Atomic vibration spectra of the metallic glass $Ni_{64}Zr_{36}$

G. F. Syrykh, M. G. Zemlyanov, and S. N. Ishmaev

''Kurchatov Institute'' Russian Science Center, 123182 Moscow, Russia

(Submitted May 8, 1997)
Fiz. Tverd. Tela (St. Petersburg) **40**, 3–6 (January 1998)

This paper describes measurements of the inelastic neutron scattering spectrum of samples of the metallic glass $Ni_{64}Zr_{36}$ grown using an isotope of Ni. These measurements were used to reconstruct the partial densities of vibrational states of the atoms Ni and Zr. A weakening of the interatomic interactions of Ni with surrounding atoms was identified, but found to be less important than numerical calculations predicted. *© 1998 American Institute of Physics.* [S1063-7834(98)00101-4]

A detailed description of the atomic structure and dynamics of disordered systems is required to understand many physical properties that characterize the amorphous state, e.g., the glass-liquid transition (which by its nature is connected with atomic vibrations),[1] the low-temperature specific heat[2] and thermal conductivity[3]; the electrical conductivity[4] and superconductivity[5] of metallic glasses, etc. In developing such a description, an important role is played by experimental verification of the available theoretical approaches.

Metallic glasses are at least two-component systems. Therefore, the most detailed information about their structure and dynamics is contained in the partial atomic radial distribution functions $\rho_{ij}(r)$ and the partial vibrational spectral functions $f_{ij}(k,\omega)$ (here i and j take on values from unity to n, where n is the number of elements in the system). When elastic and inelastic scattering of thermal neutrons are used as part of the method of isotopic contrast,[6] it becomes possible to measure the partial structure factors $S_{ij}(k)$ and partial dynamic structure factors $S_{ij}(k,\omega)$, and also to reproduce the functions $\rho_{ij}(r)$ and $f_{ij}(k,\omega)$. Although the factors $S_{ij}(k)$ have been successfully determined experimentally for

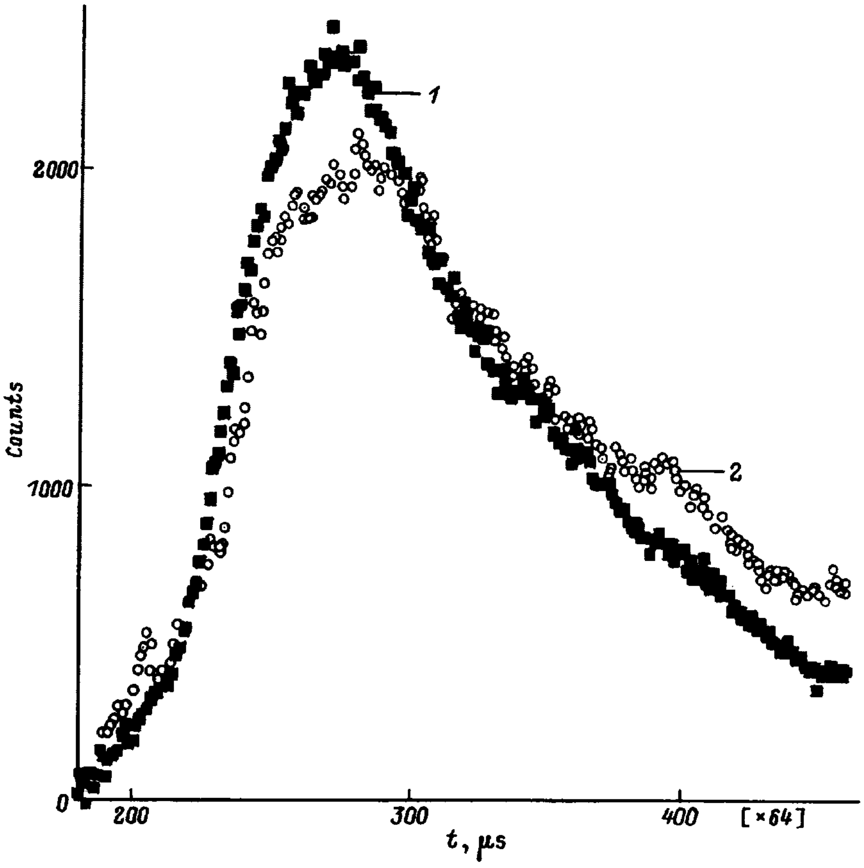

FIG. 1. Time-of-flight spectra for neutrons scattered by samples of metallic glasses. *1*—$Ni_{64}Zr_{36}$, *2*—$^{60}Ni_{64}Zr_{36}$.

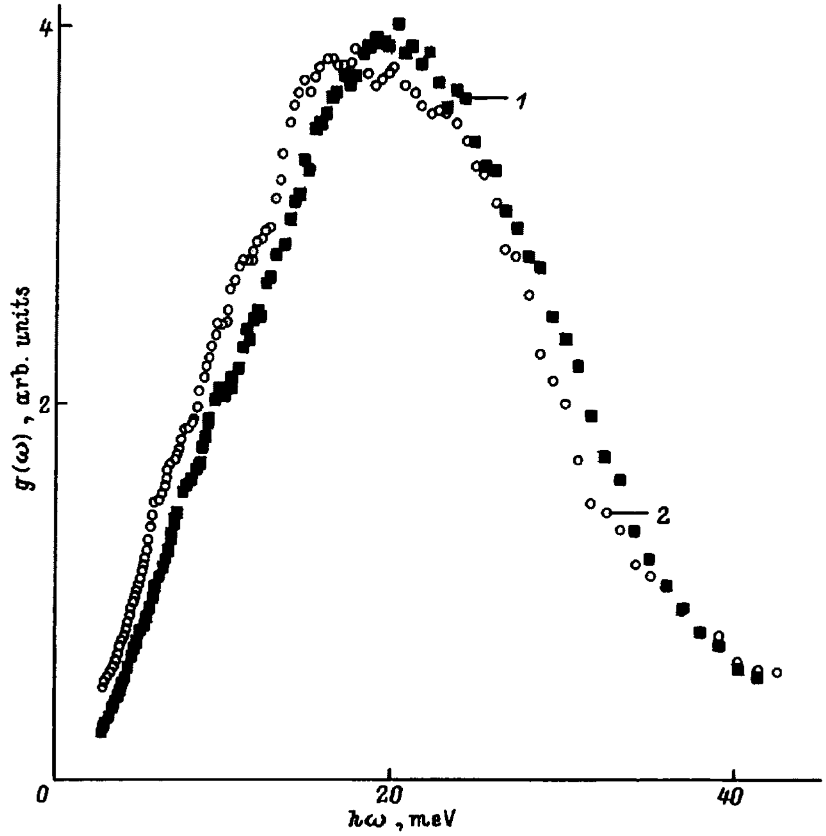

FIG. 2. Partal densities of vibrational states of Ni and Zr atoms in the metallic glass $Ni_{64}Zr_{36}$. *1*—$g_{Ni}(\omega)$, *2*—$g_{Zr}(\omega)$.

a number of metallic glasses,[7,8] the factors $S_{ij}(k,\omega)$ have yet to be determined experimentally, since these experiments require a large amount (30–40 g) of expensive isotopically enriched samples.

From a methodological point of view, it is easier to obtain information about the partial density of vibrational states $g_i(\omega)$. This information, although less detailed, is also very necessary for describing the thermodynamic properties of metallic glasses. In this paper we present the results of our experimental determination of the functions $g_{Ni}(\omega)$ and $g_{Zr}(\omega)$ for the metallic glass $Ni_{64}Zr_{36}$.

1. SAMPLE PREPARATION AND MEASUREMENTS

We prepared two chemically identical samples of $Ni_{64}Zr_{36}$ with different isotopic contents: the first sample was prepared using a natural mixture of Ni isotopes, while the second was prepared using the isotope ^{60}Ni. The metallic glasses were obtained by rapid quenching from a melt onto a rotating copper disc in an inert atmosphere (Ar). The linear velocity at the disc surface was 40 m/s. The samples were obtained in the form of ribbons of width ~ 2 mm and thickness $\sim 30\ \mu$m. The weight of the ''isotopic'' sample was 7.2 g, that of the ''natural'' sample 30 g. The amorphous state of the samples was confirmed by x-ray and neutron diffraction.

It is well known[9] that the inelastic incoherent neutron scattering spectrum $\sigma(\omega)$ from a multicomponent sample is proportional to the sum of partial densities of vibrational states of the individual elements $\sigma(\omega)$:

$$\sigma(\omega)\sim\sum_i (c\sigma/m)_i \exp(-2W_i)g_i(\omega),$$

where c, σ, and m are the concentration, total neutron scattering cross section, and atomic mass of the i-th atom respectively, and $\exp(-2W_i)$ is the Debye-Waller factor.

The dependence of the neutron scattering power of atomic nuclei on their isotopic composition ($\sigma=18.0$ and 1.08 barn for natural Ni and the isotope ^{60}Ni, respectively) allows us to recover directly the functions $g_{Ni}(\omega)$ and $g_{Zr}(\omega)$ from measurements on two samples.

The spectra $\sigma(\omega)$ were measured using a KDSOG-M spectrometer at the IBR-2 reactor[10]. The measurements were made at room temperature for scattering angles θ equal to 80,100,120, and 140°. The spectra were processed in the incoherent approximation.[11] Background measurements were made on an empty cassette. Figure 1 shows time-of-flight spectra for the scattered neutrons by the system $Ni_{64}Zr_{36}$ with different isotopic contents (the background and multiple-scattering are taken into account). For a sample prepared using natural Ni, scattering by Ni atoms dominates (the ratio of weight factors $(c\sigma/m)_{Ni}/(c\sigma/m)_{Zr}=0.89/0.11$). However, for samples with the isotope ^{60}Ni scattering primarily takes place at Zr atoms, because this same ratio equals 0.32/0.68. The qualitative difference in the spectra of neutron scattering reflects the different characters of vibrational spectra for the atoms Ni and Zr.

RESULTS AND DISCUSSION

We used the neutron scattering spectra we obtained to reconstruct the partial densities of vibrational states for Ni

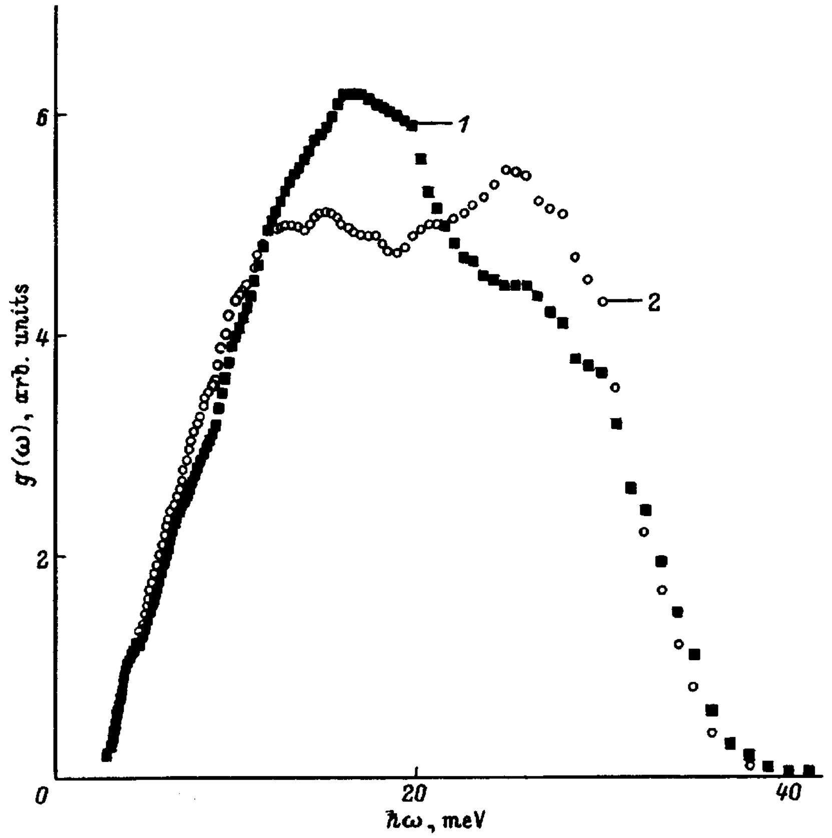

FIG. 3. Computed partial densities of vibrational states of Ni and Zr atoms in the metallic glass $Ni_{65}Zr_{35}$. *1*—$g_{Ni}(\omega)$, *2*—$g_{Zr}(\omega)$ (from Ref. 12)

and Zr atoms (Fig. 2). Debye-Waller factors and multiple scattering in the Gaussian approximation were included by iteration. Our results clearly show that the partial density of vibrational states for the heavier atom Zr (the mass ratio $m_{Zr}/m_{Ni}=1.52$) is concentrated for the most part in the range of low frequencies. However, in the vicinity of the maximum frequency of the spectrum, the contributions of Ni and Zr atoms are comparable. We calculated the second frequency moments corresponding to the partial spectra: $\langle \omega^2 \rangle_i = \int_0^\infty \omega^2 g_i(\omega) d\omega / \int_0^\infty g_i(\omega) d\omega$. Because of the finite resolution of the spectrometer, the spectra below 3 meV were approximated by a Debye function (this portion of the spectrum turns out not to have much effect on the value of $\langle \omega^2 \rangle$). The second frequency moment is related to the average force constants (B) for the interaction of a given atom with all the surrounding atoms, i.e., $\langle \omega^2 \rangle_i = B_i/m_i$. It turns out that the ratio of reciprocals of the second frequency moments taken over the spectra of Zr and Ni atoms equals 1.12, i.e., it is smaller than the mass ratio which equals 1.52. This is evidence that the interatomic interaction is weaker for the Ni atoms than for the Zr atoms.

In Ref. 12 the authors used computer simulation to calculate the partial dynamic structure factors and spectra of the partial densities of vibrational states in the metallic system $Ni_{1-x}Zr_x$. They used pairwise potentials for the interatomic interactions obtained from quantum-mechanical calculations.[13] From these it followed that the Ni-Ni interaction is considerably weaker than the Ni-Zr and Zr-Zr interactions. Figure 3 shows the computed spectra of the partial density of vibrational states for Ni and Zr atoms in the metallic glass $Ni_{65}Zr_{35}$ taken from Ref. 12. Note that the experimental and calculated energy intervals for the vibrational spectra (the difference of chemical composition can be neglected) practically coincide. However, the computed spectral distributions of vibrations of Ni and Zr atoms differ from the experimental data. The computed spectra practically coincide in the low-frequency region and near the maximum frequencies. In this case, the maximum in the vibrational density for Ni atoms occurs at lower frequencies than for Zr atoms. This causes the ratio of second frequency moments $\langle \omega^2 \rangle_{Ni}/\langle \omega^2 \rangle_{Zr}$ to equal 0.97, i.e., less than the experimental value of 1.12.

Thus, using inelastic neutron scattering and isotopic contrast, we have determined the partial densities of vibrational states in the metallic glass $Ni_{64}Zr_{36}$. The vibrational spectra of the heavy Zr atoms is shifted toward lower frequency values compared to the spectrum of Ni atoms. Nevertheless, the ratio of mean square frequencies is considerably smaller than the inverse mass ratios, which is evidence for weaker bonds between Ni atoms and their surrounding atoms. Computer simulations of the atomic dynamics in the metallic glass $Ni_{65}Zr_{35}$ predict a frequency interval that is in good agreement with the experimentally measured frequency interval, but also predict a more radical weakening of the interaction constants for the Ni atoms.

This work was carried out as part of a program of the Russian Fund for Fundamental Research (Project No. 95-02-04690).

[1] U. Bengtzelius, W. Gotze, and A. Sjolander, J. Phys. C: Sol. Stat. Phys. **17**, 5915 (1984).
[2] U. Mizutani and T. Mizoguchi, J. Phys. F: Met. Phys. **11**, 1385 (1981).
[3] I. R. Matey and A. C. Anderson, Phys. Rev. B **16**, 3406 (1978).
[4] J. Hafner, J. Non-Cryst. Solids **69**, 3253 (1985).
[5] J. Jackle and K. Frobose, J. Phys. F: Met. Phys. **10**, 1471 (1980).
[6] S. Lovesey and T. Springer, *Dynamics of Solids and Liquids by Neutron Scattering* (Springer, Berlin, 1977).
[7] S. Lefebvre, A. Quiry, J. Bigot, Y. Calvayrac, and R. Bellissent, J. Phys. F: Met. Phys. **15**, L99 (1985).
[8] E. Svab and S. N. Ishmaev, Exp. Tech. Phys. (Berlin) **36**, 89 (1988).
[9] N. A. Chernoplekov, M. G. Zemlyanov, E. G. Brovman, and A. G. Checherin, Fiz. Tverd. Tela (Leningrad) **5**, 112 (1963) [Sov. Phys. Solid State **5**, 78 (1963)].
[10] G. Baluka, A. V. Belushkin, S. I. Bragin, T. Zalecki, M. Z. Ishmukhametov, I. Natkanets, V. Oleyarchik, and Ya. Pavelchik, Preprint OIYaI No. P13-84-242, (Dubna, 1984).
[11] V. S. Oskotskiĭ, Fiz. Tverd. Tela (Leningrad) **9**, 240 (1967) [Sov. Phys. Solid State **5**, (1967)]. [*sic*]
[12] J. Hafner and M. Krajci, J. Phys.: Condens. Matter **6**, 4631 (1994).
[13] Ch. Hausleitner and J. Hafner, Phys. Rev. B **45**, 115 (1992).

Translated by Frank J. Crowne

Critical behavior of the local order parameter in $Li_2Ge_7O_{15}$:Mn^{2+}

M. P. Trubitsyn

Dnepropetrovsk State University, 320625 Dnepropetrovsk, Ukraine

(Submitted June 24, 1997)
Fiz. Tverd. Tela (St. Petersburg) **40**, 114–115 (January 1998)

[S1063-7834(98)02601-X]

Electron paramagnetic resonance (EPR) provides valuable information on local properties of crystals near structural phase transitions.[1] This work reports an EPR study of Mn^{2+} ions (0.06 and 0.2 wt %) in crystalline lithium heptagermanate $Li_2Ge_7O_{15}$ (LHG), which undergoes at $T_C = 283.5$ K a transition from the paraelectric (space group D_{2h}^{14}) to ferroelectric (space group C_{2v}^5) phase.[2,3] The spectra were measured with a Radiopan SE/X 21547 spectrometer in the X range. The samples were heated and cooled in nitrogen vapor in a standard cryostat.

An earlier calculation[4] of the spin-Hamiltonian parameters of Mn^{2+} ions in the paraphase of LHG and at the transition revealed a lowering of the local symmetry of paramagnetic centers from monoclinic (C_2) to triclinic (C_1). For magnetic fields oriented arbitrarily with respect to the crystal axes the spectral lines were found to split below T_C into two components due to the presence of ferroelectric domains in the crystal. The objective of this work was to study the temperature dependence of the split components in a temperature interval below T_C.

Figure 1 shows the temperature dependence of the position of the $m_j = -5/2$, $M_S = -3/2 \leftrightarrow -5/2$ hfs line for a magnetic field orientation $\angle \mathbf{H},\mathbf{b} = 7°$, $\mathbf{H} \perp \mathbf{c}$. The single line observed in the paraphase shifts under cooling nearly linearly toward higher fields ($\sim 7.04 \times 10^{-2}$ mT/K) because of thermal contraction of the lattice. Below T_C, the line splits into two components whose positions depend substantially on temperature. The experimental relations close to the phase transition can be described by expanding the resonance fields in powers of the local order parameter

$$H_R = H_0 + A\eta_{\text{loc}} + B\eta_{\text{loc}}^2 + \ldots, \tag{1}$$

where H_0 determines the line position in paraphase, and the expansion coefficients A and B depend on the orientation of the external magnetic field relative to the crystal axes. In a general case, $\eta_{\text{loc}}(t)$ is a function of time. The fluctuating part $\delta\eta_{\text{loc}}(t)$ contributes in first order to the width and shape of the line, and the static part $\langle \eta_{\text{loc}} \rangle$ determines the line position.

In the paraphase, $\langle \eta_{\text{loc}} \rangle = 0$, and, according to Eq. (1), the center of the line lies at $H_R = H_0$, with due account of thermal drift. The appearance of $\pm\langle \eta_{\text{loc}} \rangle \neq 0$ below T_C results in the line splitting into two components with positions

$$H_{R1,R2}(\pm\langle \eta_{\text{loc}} \rangle) = H_0 \pm A\langle \eta_{\text{loc}} \rangle + B\langle \eta_{\text{loc}} \rangle^2. \tag{2}$$

The inset to Fig. 1 shows the square of the splitting $\Delta H = H_{R1} - H_{R2} = 2A\langle \eta_{\text{loc}} \rangle$ as a function of reduced temperature $\tau = T/T_C$. We see that for $\tau \lesssim 0.96$ the experimental relation can be fitted by a straight line in accordance with the classical order-parameter exponent $\beta = 0.5$. Within $0.96 \lesssim \tau < 1$, the $\Delta H^2(\tau)$ relation deviates from the pattern predicted by the mean molecular field approximation.

The pattern of the experimental relation $H_R(T)$ (Fig. 1) indicates that the quadratic term in expansion (2) also affects noticeably the line positions. When cooled below T_C, the center of the splitting deviates from the line corresponding to thermal drift of H_0 in the paraphase (Fig. 2). As follows from Eq. (1)

$$H_C = (H_{R1} + H_{R2})/2 = H_0 + B\langle \eta_{\text{loc}} \rangle^2, \tag{3}$$

i.e. the deviation $\Delta H_C - H_0$ is proportional to $\langle \eta_{\text{loc}} \rangle^2$. Pre-

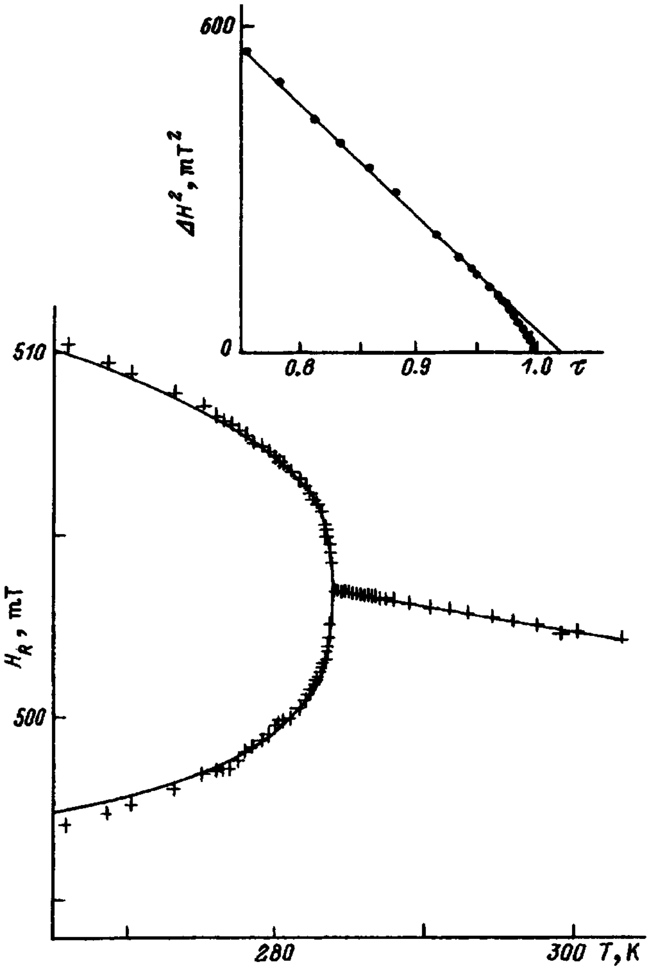

FIG. 1. Temperature dependence of the position of the $m_j = -5/2$, $M_s = -3/2 \leftrightarrow -5/2$ hfs component in the vicinity of T_C. $\angle \mathbf{H},\mathbf{b} = 7°$, $\mathbf{H} \perp \mathbf{c}$. Solid line: a plot of Eq. (4a). Inset: the square of the splitting ΔH^2 as a function of reduced temperature $\tau = T/T_C$.

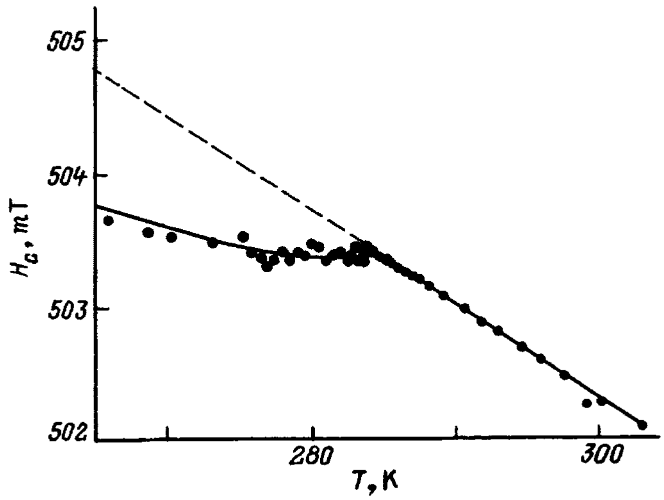

FIG. 2. Temperature dependence of the position of the H_0 line above T_C and of the splitting center H_C below the transition temperature. Dashed line depicts thermal drift of H_0 in the paraphase, solid line is a plot of Eq. (4b).

senting the local order parameter as a function of temperature, $\langle \eta_{\text{loc}} \rangle \sim (T_C - T)^{\beta}$, Eqs. (2) and (3) can be recast in the form

$$H_{R1,R2} = H_0 \pm a(T_C - T)^{\beta} + b(T_C - T)^{2\beta}, \tag{4a}$$

$$H_C = H_0 + b(T_C - T)^{2\beta}; \quad a \sim A, b \sim B. \tag{4b}$$

The values of the parameters in Eqs. (4a) and (4b) obtained by least-squares fitting for the critical interval $(\tau \sim 0.965) T_C - 10\ \text{K} \leq T < T_C (\tau = 1)$ are $T_C = 283.82$ K, $\beta = 0.32$, $a = 2.427$ mT$\cdot$K$^{-\beta}$, $b = -0.149$ mT$\cdot$K$^{-2\beta}$. A comparison of the calculated curves (solid lines in Figs. 1 and 2) with experimental data demonstrates that the temperature behavior of the quantities of interest within the critical interval is described fairly well by Eqs. (4a) and (4b) with a nonclassical value of exponent β.

The critical behavior of the local order parameter over such a broad temperature region below T_C can be attributed to specific features of the LHG, which permitted one to class it[5] among weakly polar ferroelectrics. It was pointed out[6–8] that the weakness of the long-range Coulomb forces in LHG gives rise to fluctuation effects over a considerably broader temperature interval than is the case with conventional ferroelectric materials. The value $\beta \approx 0.32$ obtained for the interval $T_C - 10\ \text{K} \leq T < T_C$ is in a good agreement with the critical exponent of the order parameter calculated within the Ising model. One may thus conclude that the properties of LHG revealed in an EPR experiment exhibit over a broad region close to T_C features characteristic of ordering transitions.

We note in conclusion that the above results are in qualitative agreement with the data of Refs. 7, 8 on the critical behavior of specific heat and elastic moduli of LHG crystals.

[1] K. A. Müller and J. C. Fayet, in *Structural Phase Transitions II*, edited by K. A. Müller and H. Thomas, Vol. **45** (1991), p. 1.

[2] H. Volenkle, F. Wittman, and H. Nowotny, Monatsch. Chem. **101**, 46 (1970).

[3] S. Haussuhl, F. Wallrafen, K. Recker, and J. Eckstein, Z. Kristallogr. **153**, 329 (1980).

[4] M. P. Trubitsyn, M. D. Volnyanskiĭ, and A. Yu. Kudzin, Kristallografiya **36**, 1472 (1991) [Sov. Phys. Crystallogr. **36**, 835 (1991)].

[5] A. K. Tagantsev, JETP Lett. **45**, 447 (1987).

[6] G. A. Smolenskiĭ, I. G. Siniĭ, A. K̂. Tagantsev, S. D. Prokhorova, V. D. Mikvabiya, and W. Windsch, Zh. Éksp. Teor. Fiz. **88**, 1020 (1985) [Sov. Phys. JETP **61**, 599 (1985)].

[7] B. A. Strukov, M. Yu. Kozhevnikov, E. L. Sorkin, and M. D. Volnyanskiĭ, Fiz. Tverd. Tela (Leningrad) **32**, 2823 (1990) [Sov. Phys. Solid State **32**, 1639 (1990)].

[8] B. A. Strukov, M. Yu. Kozhevnikov, Kh. A. Nizomov, and M. D. Volnyanskiĭ, Fiz. Tverd. Tela (Leningrad) **33**, 2962 (1991) [Sov. Phys. Solid State **33**, 1673 (1991)].

Translated by G. Skrebtsov

Relaxation of radiative defects in irradiated triglycine sulfate

O. M. Golitsyna, L. N. Kamysheva, and S. N. Drozhdin

Voronezh State University, 394693 Voronezh, Russia

(Submitted July 14, 1997)
Fiz. Tverd. Tela (St. Petersburg) **40**, 116–117 (January 1998)

Nonmonotonic temporal behavior of the temperature dependence of the conductivity of ferroelectric triglycine sulfate is observed after its irradiation by small doses of x radiation. Such behavior is associated primarily with the formation of two types of radiation defects having different lifetimes. © *1998 American Institute of Physics.* [S1063-7834(98)02701-4]

Irradiation of ferroelectric triglycine sulfate (TGS) by hard electromagnetic radiation leads to the creation of a large number of radiation defects as a result of the complex structure of this crystal.[1,2] These defects affect the properties of the crystal in a major way, primarily those properties that are determined by the behavior of its domain structure.

The system of radiation defects arising from irradiating of a TGS crystal by small doses of x radiation evolves in a complicated way with time, leading to a nonmonotonic temporal dependence of a number of measured quantities: the coefficient of static unipolarity, the pyroelectric coefficient, the internal bias field,[3] and the parameters of pulsed repolarization.[4]

It may be assumed that the formation of radiation defects also affects the conductivity of the crystal and that its temporal behavior after irradiation will also be nonmonotonic.

The aim of the present paper is to investigate the temperature dependence of the conductivity G of a crystal of TGS irradiated by small doses of x radiation.

Measurements were performed at variable current by the bridge method with the amplitude of the measuring field equal to 3V/cm at a frequency of 1,592 Hz in the quasi-static temperature regime in the temperature interval from room temperature to the Curie point T_c. The accuracy of determining G was 1%. The samples consisted of polar Y-cut wafers with dimensions $5\times5\times1$ mm, whose working surfaces were covered with electrodes of vacuum-deposited silver.

The samples were irradiated at room temperature by Ni $K\alpha$ x-radiation with photon energy 30 keV; the radiation doses did not exceed 100 kR.

It should be noted that the trends detected and adduced below are of a general nature for all the investigated samples regardless of the absolute values of their conductivity.

Figure 1 plots the temperature dependence of the conductivity of a crystal of TGS before irradiation and at various times after irradiation by a dose of 40 kR.

As can be seen from Fig. 1, immediately after irradiation the conductivity decreases by almost an order of magnitude over the entire temperature interval investigated (curve *2*). Roughly a day later the overall level of the conductivity has risen back up (curve *3*), approaching the values of G obtaining for the unirradiated crystal (curve *1*). With the further passage of time a continuous drop of the conductivity is observed (curves *4* and *5*), proceeding with a large relaxation time.

Such behavior of the conductivity was not observed in the paraelectric phase. The values of G before and after irradiation essentially coincide.

Figure 2 plots the time dependence of the conductivity $G(t)$ of an irradiated crystal, obtained at different temperatures. It can be seen that these curves have a pronounced nonmonotonic character which is apparently due to the formation in TGS of two types of defects having a decisive effect on the state of the domain structure. The defect type responsible for the appearance of the first maximum in $G(t)$, arises quickly and disappears just as quickly. The second defect type, associated with the second maximum, is characterized by significantly larger times—both of formation and of transformation into a stable configuration.

On the basis of the results of EPR studies of irradiated TGS crystals,[5] it may be conjectured that the defects of the first type are metastable $\dot{C}H_2COOH$ radicals, forming in glycine I, while the defects of type two are stable $NH_3^+\dot{C}HCO_2^-$ radicals, forming on glycines II and III. Both of the indicated

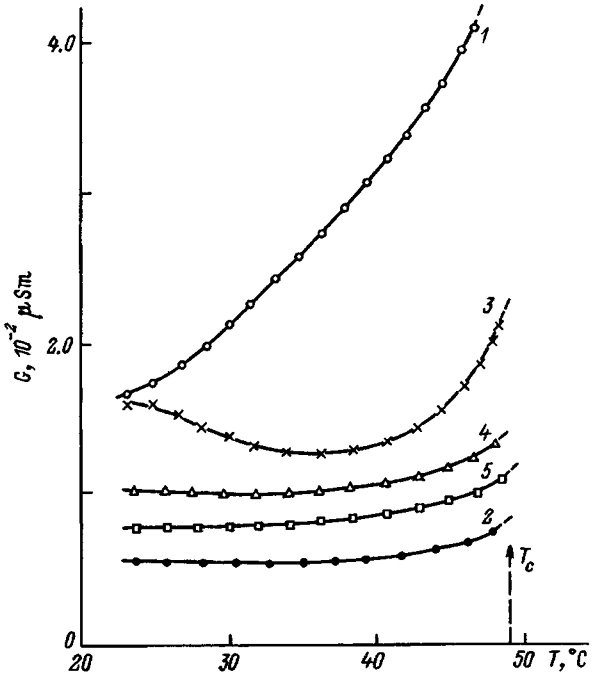

FIG. 1. Temperature dependence of the conductivity G in a TGS crystal before (*1*) and after (*2–5*) irradiation. *2*—after 20 min, *3*—24 h, *4*—46 h, *5*—102 h. Irradiation dose $D=40$ kR.

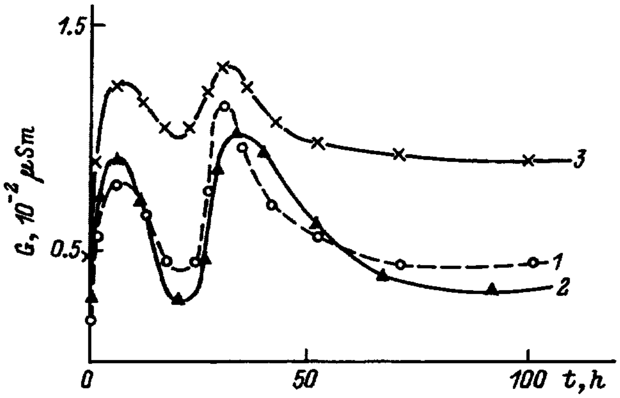

FIG. 2. Time dependences of G for an irradiated TGS crystal at different temperatures T(°C): *1*—27, *2*—36,*3*—44. $D=40$ kR.

radicals stabilize the direction of polarity in the domain.[5] What probably takes place here is an anchoring of part of the domain walls, which leads to a growth of losses in the crystal at those times when the concentration of the one or the other radical becomes the largest.

The falling segments of the time dependences shown in Fig. 2 have a relaxational character and can be approximated by functions proportional to $\exp(-t/\tau)$, where τ is the relaxation time, whose values, as calculations show, lie within the limits 5–7 h for the first maximum (τ_1) and 25–30 h for the second $(\tau/2)$, which testifies on behalf of diffusional behavior of the nascent radiation defects.[3,6]

Both relaxation times vary markedly with temperature (Fig. 3). The extrema in the dependences of $\tau_1(T)$ and $\tau_2(T)$ are found in the low-temperature region of spontaneous instability of the domain structure of the TGS crystal.[7,8] Growth of the values of τ in this temperature interval is apparently connected with an increase in the number of domain walls, where such an increase is characteristic for the given temperature region. Interaction of the domain walls with the radiation defects in this case increases the setup time of the new equilibrium state in the defect system.

The nonmonotonic temperature dependence of the conductivity relaxation times reflecting the corresponding evolution of the system of radiation defects created in TGS by small doses of x radiation has been observed here apparently for the first time.

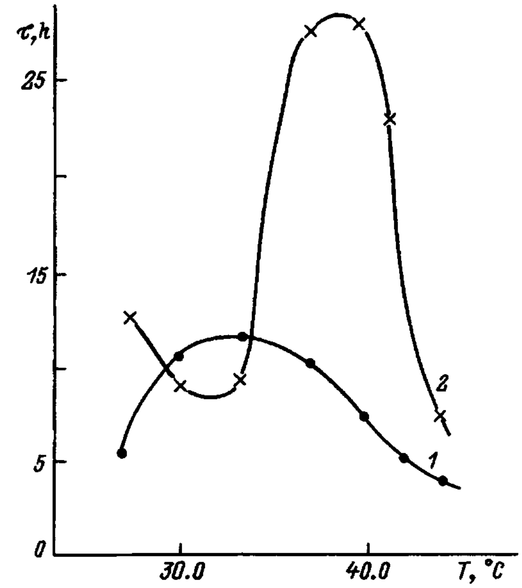

FIG. 3. Temperature dependence of the conductivity relaxation times for an irradiated crystal of TGS: *1*—τ_1, *2*—τ_2. $D=40$ kR.

Since the discussed relaxation processes in the system of defects interacting with the domain walls are thermally activated, we can estimate the activation energies (W) of these processes from the Arrhenius relation: $\tau=\tau_0 \exp(-W/kT)$. The values of W for the above-indicated first and second defect type turn out to be equal respectively to $W_1 \cong 1.0$ eV and $W_2 \cong 2.0$ eV, which correlates with the estimates of W made in Refs. 6, 9, and 10 on the basis of other experimental techniques and confirms the conjecture made in Ref. 6 of a proton conductivity mechanism in irradiated TGS crystals.

[1] E. V. Peshikov, *Action of Radiation on Ferroelectrics* [in Russian], Fan, Tashkent, 1972.

[2] M. E. Lines and A. M. Glass, *Principles and Applications of Ferroelectrics and Related Materials* (Clarendon Press, Oxford, 1977).

[3] L. N. Kamysheva, S. N. Drozhdin, and O. M. Seryuk, Zh. Tekh. Fiz. **58**, 1607 (1988) [Sov. Phys. Tech. Phys. **33**, 971 (1988)].

[4] L. N. Kamysheva, O. M. Golitsyna, S. N. Drozhdin, A. D. Maslikov, and A. B. Barbashina, Fiz. Tverd. Tela (St. Petersburg) **37**, 388 (1995) [Phys. Solid State **37**, 209 (1995)].

[5] A. P. Dem'yanchuk, *Abstract of Candidate's Dissertation*, Kiev (1976).

[6] L. I. Dontsova, N. A. Tikhomirova, and L. A. Shuvalov, Kristallografiya **39**(1), 158 (1994) [Crystallogr. Rep. **39**, 140 (1994)].

[7] O. M. Seryuk, L. N. Kamysheva, S. N. Drozhdin, and A. B. Barbashina, Fiz. Tverd. Tela (Leningrad) **30**, 540 (1988) [Sov. Phys. Solid State **30**, 308 (1988)].

[8] S. D. Milovidova, A. S. Sidorkin, A. M. Savvinov, and A. I. Maslakov, Fiz. Tverd. Tela (Leningrad) **28**, 2541 (1986) [Sov. Phys. Solid State **28**, 1423 (1986)].

[9] L. I. Dontsova, *Abstract of Doctoral Dissertation*, Voronezh (1991).

[10] B. Hilcher and M. Michalczyk, Ferroelectrics **22**, 721 (1978).

Translated by Paul F. Schippnick

Microscopic theory of the electro-acoustic echo in order–disorder antiferroelectrics

M. B. Belonenko and S. V. Nazarenko

Volgograd State University, 400062 Volgograd, Russia

(Submitted May 22, 1997; resubmitted June 16, 1997)
Fiz. Tverd. Tela (St. Petersburg) **40**, 118–121 (January 1998)

A microscopic theory of the electro-acoustic echo (EAE) is proposed for the case in which two pulses of a variable electric field act on an antiferroelectric. This theory augments the phenomenological theory proposed for the purpose of interpreting experiments on the main regularities of the electro-acoustic echo in order–disorder antiferroelectrics. The deuterization effect and ''pre-polarization'' effect are explained. The shape of the echo signal is derived analytically and it is shown that this shape depends on the time interval between pump pulses.

[S1063-7834(98)02801-9]

1. The action on matter of pulsed methods makes it possible to obtain nontrivial information about the dynamics and kinetics of excitations, which it is frequently impossible to obtain by steady-state methods. In the case of nonlinear systems, those pulsed methods stand out that allow one to obtain an echo response signal. The high efficiency and informativeness of such methods are determined by the fact that their use eliminates reversible phase scattering of the signal induced in the material.

In experiments carried out recently and of interest to us,[1,2] the main regularities of the electroacoustic echo were successfully detected and delineated in the antiferroelectric (AFE) Rs, which is a typical representative of AFE's with hydrogen bonds. It should also be noted that the theoretical explanation of the experimental regularities provided in Ref. 1, based on the phenomenological theory, does not take account of all aspects of the dynamics of AFE's characterized by the presence of an order–disorder phase transition. The most serious inadequacies that arise in a phenomenological description of AFE's are the absence of a correct dispersion law for the excitations and the frequency limits of the region of applicability.[3,4] The maximum frequency at which the phenomenological approach is applicable tends to zero as the phase transition point is approached.

2. As is well known, AFE's of order–disorder type are described most completely and consistently within the framework of the pseudospin formalism,[3–5] In this formalism the Heisenberg equations of motion for the mean values of the pseudospin operators of a two-sublattice AFE, augmented by relaxation terms in the random-phase approximation, have the form[4,6]

$$\frac{d\langle S^x_{j\alpha}\rangle}{dt}=M_{j\alpha}\langle S^y_{j\alpha}\rangle-(\langle S^x_{j\alpha}\rangle-\langle\overline{S^x_{\alpha}}\rangle)\left(\frac{\cos\phi}{T_1^*}+\frac{\sin\phi}{T_2^*}\right),$$

$$\frac{d\langle S^y_{j\alpha}\rangle}{dt}=\Omega\langle S^z_{j\alpha}\rangle-M_{j\alpha}\langle S^x_{j\alpha}\rangle-\langle S^y_{j\alpha}\rangle/T_2^*,$$

$$\frac{d\langle S^z_{j\alpha}\rangle}{dt}=-\Omega\langle S^x_{j\alpha}\rangle-(\langle S^z_{j\alpha}\rangle-\langle\overline{S^z_{\alpha}}\rangle)\left(\frac{\cos\phi}{T_2^*}+\frac{\sin\phi}{T_1^*}\right),\tag{1}$$

where $\langle\overline{S^x_\alpha}\rangle$ and $\langle\overline{S^z_\alpha}\rangle$ are the equilibrium mean values of the pseudospin operator $S^x_{j\alpha}$ and $S^z_{j\alpha}$ for the α lattice, $\langle\overline{S^x}\rangle=\langle\overline{S^x_1}\rangle=\langle\overline{S^x_2}\rangle$, $\langle\overline{S^z_1}\rangle=\overline{z}=-\langle\overline{S^z_q}\rangle$, T_1^*, T_2^* are the longitudinal and transverse relaxation times of the pseudospins.

$$\tan\phi=|\langle\overline{S^z_\alpha}\rangle|/|\langle\overline{S^x_\alpha}\rangle|,$$

$$M_{j1}=\sum_i J_{ij}\langle S^z_{i2}\rangle+2\mu E_j(t)+d\frac{\partial U(z',t)}{\partial z'}+\Delta,$$

$$M_{j2}=\sum_i J_{ij}\langle S^z_{i1}\rangle+2\mu E_j(t)+\frac{\partial U(z',t)}{\partial z'}-\Delta.$$

In Eqs. (1) $\alpha=1,2$ is an index labelling the sublattices, $S^x_{j\alpha}$ and $S^z_{j\alpha}$ have the sense of the tunneling operator and the electrical dipole moment operator of the jth unit cell of the α-labelled sublattice, Ω is the tunneling integral, $J_{ij}<0$ is the exchange integral, Δ is the asymmetry parameter of the potential for the proton on a hydrogen bond, μ is the AFE dipole moment of the cell, and $E_j(t)$ is the variable electric field applied to the sample. Here it is assumed that a transverse sound wave is excited in the sample, propagating along the polar axis (the z' axis), and also a polarized sound wave propagating along the y' axis; consequently, the displacement vector has only one nonzero component: $(U(z',t),0,0)$. Note that the case of the linear piezo effect with corresponding piezo modulus d is considered. The coordinate system x',y',z' is bound by the crystallographic axes and the coordinate system x,y,z is defined in pseudospin space.

In the case considered here, the equation for propagation of the sound wave has the form[7]

$$\ddot{U}=V_0^2\frac{d^2U}{dz'^2}-\frac{d}{\rho}\frac{d(\langle S^z_1+\langle S^z_2\rangle)}{dz'},\qquad (\dot{\ })=\frac{\partial()}{\partial t},\tag{2}$$

where ρ is the density of the crystal, V_0 is the velocity of the acoustic wave in the absence of pseudospin–phonon coupling.

Representing the index j, which describes the position of the pseudospins in the lattice, as a pair of indices (n,k), where n numbers the planes parallel to the $x'y'$ plane, and k indicates the position of the pseudospin inside such a plane, we transform to the continuum limit

$$\langle S^z_{(n\pm1)k\alpha}\rangle=\langle S^z_{nk\alpha}\rangle\pm a\frac{d\langle S^z_{nk\alpha}\rangle}{dz'}+\frac{a^2}{2}\frac{d\langle S^z_{nk\alpha}\rangle}{dz'^2}+\cdots\ .$$

Here the equations describing the dynamics of the pseudospin variables take the form

$$\langle\dot{S}^x_\alpha\rangle=M_\alpha\langle S^y_\alpha\rangle-\left(\langle S^x_\alpha-\overline{\langle S^x\rangle}\rangle\right)\left(\frac{\cos\,\phi}{T_1^*}+\frac{\sin\,\phi}{T_2^*}\right),$$

$$\langle\dot{S}^z_\alpha\rangle=-\Omega\langle S^y_\alpha\rangle-\left(\langle S^z_\alpha-\overline{\langle S^z\rangle}\rangle\right)\left(\frac{\cos\,\phi}{T_2^*}+\frac{\sin\,\phi}{T_1^*}\right),$$

$$\langle\dot{S}^y_\alpha\rangle=\Omega\langle S^z_\alpha\rangle-M_\alpha\langle S^x_\alpha\rangle-\langle S^y_\alpha\rangle/T_2^*\,,$$

$$M_1=L\langle S^z_2\rangle+K\frac{\partial\langle S^z_2\rangle}{\partial z'^2}+2\mu E(t)+d\frac{\partial U}{\partial z'}+\Delta,$$

$$M_2=L\langle S^z_1\rangle+K\frac{\partial\langle S^z_1\rangle}{\partial z'^2}+2\mu E(t)+d\frac{\partial U}{\partial z'}-\Delta,$$

$$L=\sum_k\,(J_{nk,nk'}+2J_{(n+1)k,nk'}),\quad K=a^2\sum_k\,J_{(n+1)k,nk'}\,. \tag{3}$$

3. Despite the above simplifications, system (2), (3) is still quite complicated to solve. Therefore we limit ourselves to an analysis of the effective equations describing the dynamics of the envelopes of the direct and return electroacoustic (EA) waves. Note that, since the characteristic relaxation time of the pseudospin T_1^*, T_2^* is 10^{-11}–10^{-12} s while the characteristic period of the oscillations of the electroacoustic wave is 10^{-7}–10^{-8} s, the pseudospin subsystem of the AFE can be assumed to track the variations in the external RF field and the acoustic wave field. Mathematically, such adiabatic behavior can be expressed by setting $\langle\dot{S}^\alpha_\beta\rangle=0$ in Eqs. (3). Then

$$\langle S^z_1\rangle=\overline{\langle S^z_1\rangle}+a_{11}\chi+a_{21}\chi^2-a_{31}\chi^3+b_1\frac{\partial^2\chi}{\partial z'^2}\cdots,$$

$$\chi=2\mu E(t)+d\frac{\partial U}{\partial z'},$$

$$\langle S^z_2\rangle=\overline{\langle S^z_2\rangle}+a_{12}\chi+a_{22}\chi^2-a_{32}\chi^3+b_2\frac{\partial^2\chi}{\partial z'^2}\cdots \tag{4}$$

(expressions for the coefficients a_{ij} and b_i are given in Appendix A). Differentiating the equation for the nonzero component of the displacement vector U with respect to z' and setting $\partial U/\partial z'=f$, we have

$$\ddot{f}-v_0^2\frac{\partial^2 f}{\partial z'^2}+\frac{d}{\rho}\frac{\partial}{\partial z'^2}(\langle S^z_1\rangle+\langle S^z_2\rangle)=0. \tag{5}$$

To investigate Eq. (5) further, we employ the multiscale expansion method,[8–10] according to which we seek the solution of Eq. (5) in the form

$$f=\varepsilon f^{(1)}+\varepsilon^2 f^{(2)}+\ldots,$$

$$f=f_+e^{i(\omega t-kz')}+f_-e^{i(\omega t+kz')}+\text{c.c},$$

$$f_\mp=f_\mp(\varepsilon t,\varepsilon^2 t,\varepsilon z')=f_\mp(T_1,T_2,Z_1),$$

$$T_n=\varepsilon^n t,\quad Z_n=\varepsilon^n z'. \tag{6}$$

In Eqs. (6) ω and k are the frequency and wave vector of the electroacoustic traveling waves, f_+ and f_- are the slowly varying amplitudes of the direct and return waves, T_n and Z_n are slow variables, ε is a formally small parameter that characterizes the deviation of the parameters of the system from equilibrium.

We apply the multiscale expansion method, successively eliminating the rapidly oscillating secular terms in each order of the expansion of f in the parameter ε. Thus, from the requirement of eliminating the secular terms to first order in ε we get the dispersion equation for the waves, which has the form

$$l(\omega,k)=-\omega^2+k^2\left(V_0^2+\frac{d^2}{\rho}(a_{11}+a_{12})+\frac{d^2}{\rho}k^2(b_1+b_2)\right)=0. \tag{7}$$

The corresponding equation for the secular terms, obtained in the second order in ε, leads to equations describing wave packets moving with group velocity V_{gr}

$$\frac{\partial f_\mp}{\partial T_1}\mp V_{\text{gr}}\frac{\partial f_\mp}{\partial Z_1}=0,$$

$$V_{\text{gr}}=\frac{d\omega}{dk}l_k/l_\omega,\quad l_k=\frac{dl(\omega,k)}{dk}. \tag{8}$$

Before writing down the equations that arise when we eliminate the secular terms in the third order in ε, let us specify the time dependence of the external variable field. We assume that

$$E(t)=(1/2)E_1E_1f(Z_1)\{\theta(T_2)-\theta(T_2+\tau_1)\}e^{i(\omega t-kz')}$$
$$+(1/2)E_2\{\theta(T_2+\tau_1+\tau)$$
$$-\theta(T_2+\tau_1+\tau_2+\tau)\}e^{2i\omega t}+\text{c.c.}, \tag{9}$$

in the cases of experiments for observing the $\omega-2\omega$ echo and in the case of experiments for observing the $\omega-\omega$ echo, the factor $e^{2i\omega t}$ in the second term must be replaced by $e^{i\omega t}$. In (9), E_1, E_2, τ_1, and τ_2 are the amplitudes and durations of the first and second pulses, respectively, τ is the interpulse time interval, $f(Z)$ is the shape of the envelope of the first pulse, and $Z=Z_1-V_{\text{gr}}T_1$. Thus, eliminating the secular terms, we obtain

$$\pm i\frac{\partial f_\pm}{\partial T_2}+\frac{1}{2}\frac{d^2\omega}{dk^2}\frac{\partial^2 f_\pm}{\partial Z^2}+\frac{Q}{I_\omega}|f_\pm|^2f_\pm+\widetilde{Q}|f_\mp|^2f_\mp$$
$$+\frac{(1\pm 1)}{2}\frac{Q_1}{I_\omega}E_1f(Z)=0, \tag{10}$$

at the time of action of the first pulse; in the interval between pulses and after termination of the second pulse we have Eq. (10) without the last term. At the time of action of the second pulse, we must add the term $RE_2f^*_\mp$ on the left-hand side of Eq. (10) for the $\omega-2\omega$ scheme, and the term $\widetilde{R}\widetilde{E}^2_2f^*_\pm$ for the $\omega-\omega$ scheme. The coefficients $Q,\widetilde{Q},\theta_1,R,\widetilde{R}$ in Eq. (10) are given in Appendix B.

4. Since, before the external variable field is switched on, the sample is found in a state of thermodynamic equilibrium, the initial conditions for Eq. (10) are written as $f_\mp|_{T_2=0}=0$. Further we note that system of equation (10) can be considered as a system of nonlinear Schrödinger equations (NSE) with a perturbation.[11] For their solution we employ the Karpman–Maslov method.[12] The solution of the equations for the scattering factors $c_{11}(\lambda)$ and $c_{12+}(\lambda)$, which define the dynamics of the envelope of the direct electroacoustic wave at times $0<T_2<\tau_1+\tau_0$, is

$$c_{12+}(\lambda)=1,$$

$$c_{11}(\lambda)=-i\left(\left|\frac{Q}{2l_{\omega}^{3}}\right|\right)^{1/2}\frac{Q^{*}E_1^{*}}{l_{\omega}}\,\frac{\Phi(\lambda)}{4\lambda^{2}i}$$

$$\times[e^{4i\lambda^{2}\tau_1}-1]e^{4i\lambda^{2}(\tau_1+\tau+T_2)}, \tag{11}$$

where $\Phi(\omega)$ is the Fourier transform of the first pulse,

$$\Phi(\lambda)=\beta\int_0^{\infty}dZf(Z)e^{-2i\lambda\beta Z}.$$

The interaction of the second pulse with the direct wave is parametric and generates the second wave. Note that in the $\omega-2\omega$ scheme this interaction proceeds directly whereas in the case when a second pulse is fed in with frequency ω, the parametric interaction takes place in two steps: first, as a consequence of the nonlinear properties of the crystal a harmonic with doubled frequency is generated, which then interacts parametrically with the direct wave. The return wave propagates in the $-z'$ direction with group velocity equal to the group velocity of the direct wave and is recorded as an echo-signal. As follows from the form of the terms R and $\widetilde{R}$, excitation of the return wave is possible only if the conditions $d\neq 0$ and $\langle\overline{S_1^z}\rangle=-\langle\overline{S_2^z}\rangle\neq 0$ are satisfied. These conditions are satisfied in an external zero constant field only when the crystal has been pre-polarized (i.e., kept for a sufficiently long time in an external constant field which is then switched off during the course of the experiment). Such conditions of echo detection were realized in the experiments reported in Refs. 1 and 2 for the $\omega-2\omega$ and $\omega-\omega$ schemes.

The scattering factors $c_{11}(\lambda)$ and $c_{12}(\lambda)$, defining the dynamics of the return wave, in the approximation of noninteracting waves, for $T_2>\tau+\tau_1+\tau_2$ are

$$c_{12}(\lambda)=I,$$

$$c_{11}(\lambda)=-i\left(\left|\frac{Q}{2l_{\omega}^{3}}\right|\right)^{1/2}RE_2^{*}\Phi(\lambda)\,\frac{\sin(4\lambda^{2}\tau_2)}{4\lambda^{2}}$$

$$\times e^{-4i\lambda^{2}(T_1-2\tau_1-2\tau)}(-i)$$

$$\times\left(\left|\frac{Q}{2l_{\omega}^{3}}\right|\right)^{1/2}\frac{\theta^{*}E_1^{*}}{l_{\omega}}\left[\frac{e^{4i\lambda^{2}\tau_1}-1}{4\lambda^{2}i}\right], \tag{12a}$$

for the case of an $\omega-2\omega$ echo, and

$$c_{12}(\lambda)=I,$$

$$c_{11}(\lambda)=i\left(\left|\frac{Q}{2l_{\omega}^{3}}\right|\right)^{1/2}\widetilde{R}\widetilde{E}_2^{*}\Phi(\lambda)$$

$$\times\frac{\sin(4\lambda^{2}\tau_2)}{4\lambda^{2}}e^{-4i\lambda^{2}(T_1-2\tau_1-2\tau)}(-i)$$

$$\times\left(\left|\frac{Q}{2l_{\omega}^{3}}\right|\right)^{1/2}\frac{\theta^{*}E_1^{*}}{l_{\omega}}\left[\frac{e^{4i\lambda^{2}\tau_1}-1}{4\lambda^{2}i}\right] \tag{12b}$$

for the case of detecting an $\omega-\omega$ echo.

Within the framework of the Karpman–Maslov method the amplitude of the return wave is given by[11]

$$f_{-}(Z,T_2)=\frac{1}{2\pi}\int_{-\infty}^{\infty}d\lambda e^{-2i\beta Z\lambda}\frac{Q}{2l_{\omega}^{3}}H\Phi(\lambda)\,\frac{\sin(4\lambda^{2}\tau_2)}{16\lambda^{4}}$$

$$\times(e^{-4i\lambda^{2}\tau_1}-1)\frac{\theta E_1}{l_{\omega}}e^{4i\lambda^{2}(T_2-2\tau_1-2\tau)}, \tag{13}$$

where $H=-iR^{*}E_2$ for an $\omega-2\omega$ echo and $H=-i\widetilde{R}^{*}(\widetilde{E}_2^{*})^{2}$ for an $\omega-\omega$ echo. Employing the stationary phase method, it is easy to show that the integral in Eq. (13) has a maximum at the time $T_2=2\tau+2\tau_1$. Consequently, at the time $T_2=2\tau+2\tau_1$ the amplitude of the return wave grows abruptly and is observed in the form of an echo response. For short pulse durations τ_1 and τ_2 the amplitude of the echo signal $A_e=f_{-}(T_2\approx 2\tau_1)$, is proportional to τ_1 and τ_2 according to Eq. (13). In addition, for short pulse durations it is easy to show that $A_e=f_{-}(T_2\approx 2\tau+2\tau_1)$ $\sim f(-z)$, i.e., the shape of the echo signal is the same as that of the first wave reflected about the origin. The dependence of the amplitude of the echo on the amplitudes of the variable fields is standard for echo problems: $A_e\sim E_1E_2$ ($\omega-2\omega$ echo); $A_e\sim E_1E_2^{2}$ ($\omega-\omega$ echo). Also the amplitude of the echo response $A_e\sim\Omega^{2}$. The magnitude of the tunneling integral Ω is decreased by a factor of 10–100 upon deuterization of the sample,[3,4] and, consequently, the echo signal is decreased by a factor of 10^{2}–10^{4}, which is in good agreement with experiment.

APPENDIX A:

$$\eta=\left(\frac{\cos\,\phi}{T_1^{*}}+\frac{\sin\,\phi}{T_2^{*}}\right),\qquad \varkappa=\left(\frac{\cos\,\phi}{T_2^{*}}+\frac{\sin\,\phi}{T_1^{*}}\right),$$

$$b_1=\frac{I\Psi_1b_2+k\Psi_1a_{12}}{\xi},$$

$$a_{11}=\frac{L\eta^{2}\Omega^{4}z_1z_2-(L\overline{z}_1-\Delta)\Omega^{2}\eta z_1C}{(Lz_2+\Delta)(Lz_1-\Delta)C^{2}-L^{2}\eta^{2}\Omega^{4}\overline{\overline{z}_1\overline{z}_2}},$$

$$C=(L+\Delta)^{2}\varkappa+\eta\Omega^{2}+\eta\varkappa/T_2$$

$$a_{12}=\frac{\Omega^{2}\eta\overline{z}_2(La_{11}+1)}{((L+\Delta)^{2}\varkappa+\eta\Omega^{2}+\eta\varkappa/T_2)(L\overline{z}_1-\Delta)},$$

$$\zeta=(L\overline{z}_1-\Delta)^{2}\varkappa+\eta\Omega^{2}+\eta\varkappa/T_2,$$

$$\xi=(L\overline{z}_2+\Delta)^{2}\varkappa+\eta\Omega^{2}+\eta\varkappa/T_2,$$

$$\Psi_1=\frac{\eta\Omega^{2}\overline{z}_1}{(L\overline{z}_2+\Delta)},\qquad \Psi_2=\frac{\eta\Omega^{2}\overline{z}_2}{(L\overline{z}_1-\Delta)},$$

$$a_{21}=\frac{2\varkappa a_{12}L\eta\Omega^2\overline{z}_1(La_{11}+1)(L\overline{z}_1-\Delta)-2\varkappa a_{11}(La_{12}+1)(L\overline{z}_2+\Delta)^2\zeta}{\zeta\xi(L\overline{z}_2+\Delta)-L^2\eta^2\Omega^4\overline{z}_1\overline{z}_2/(L\overline{z}_1-\Delta)},$$

$$a_{22}=(L\overline{z}_2+\Delta)\ \frac{\xi a_{21}+2\varkappa a_{11}(La_{12}+1)(Lz_2+\Delta)}{L\Omega^2\eta\overline{z}_1},$$

$$\sigma=L^2\varkappa(2a_{11}a_{22}\overline{z}_2+a_{11}a_{22}^2+2\overline{z}_2a_{12}a_{11})+2L\varkappa(a_{11}a_{12}+\overline{z}_1a_{21})+2L\varkappa(a_{11}a_{22}+a_{21}a_{12})+\varkappa a_{11}+2\varkappa\Delta a_{21},$$

$$\varphi=L^2\varkappa(2a_{12}\overline{z}_1a_{21}+a_{12}a_{11}^2+2a_{22}\overline{z}_1a_{11})-2L\varkappa\Delta(a_{11}a_{22}+a_{21}a_{11})+2L\varkappa(\overline{z}_1a_{22}+a_{11}a_{12})-2\varkappa\Delta a_{22}+\varkappa a_{12},$$

$$a_{32}=-\frac{L\psi_2\sigma-\varphi\xi}{\zeta\xi-L^2\psi_1\psi_2},\quad a_{31}=\frac{L\psi_1a_{32}+\sigma}{\zeta},$$

$$b_2=\frac{\xi k\psi_1a_{11}-kLa_{12}\psi_1\psi_2}{\zeta\xi-L^2\psi_1\psi_2}.$$

APPENDIX B:

$$\text{con }1=\frac{\tilde{d}d^2(a_{21}+a_{22})k^2}{4\tilde{d}(-a_{31}-a_{32})dk^4+\tilde{d}d(a_{11}+a_{12})k^2-\Omega^4\eta^2-k^2v_0^2},$$

$$\text{con }2=\frac{2\tilde{d}d^2(a_{21}+a_{22})}{V_0^2+\tilde{d}d^2(a_{11}+a_{12})4\tilde{d}d(a_{31}+a_{32})k^2},$$

$$R=-(a_{21}+a_{22})\tilde{d}4\mu d(ik)^2,$$

$$Q=2\tilde{d}d^2(a_{21}+a_{22})(-ik)^2\ \text{con }1+3(b_1+b_2)\tilde{d}d^3(-ik)^2,$$

$$\tilde{R}=(b_1+b_2)\tilde{d}8\mu d(ik)^2,$$

$$\tilde{Q}=2\tilde{d}d^2(a_{21}+a_{22})(-ik)^2\ \text{con }2+6(b_1+b_2)\tilde{d}d^3(-ik)^2,$$

$$\theta_1=\tilde{d}a_{12}\mu(-ik)^2+\tilde{d}(-a_{31}-a_{32})2\mu(-ik)^4.$$

[1] V. M. Berezov, V. S. Romanov, and A. B. Balakin, Ukr. Fiz. Zh. **29**, 1589 (1984).

[2] V. M. Berezov, V. S. Romanov, and A. B. Balakin, Kristallografiya **31**, 1022 (1986) [Sov. Phys. Crystallogr. **31**, 608 (1986)].

[3] V. G. Vaks, *Introduction to the Microscopic Theory of Ferroelectrics* [in Russian], Nauka, Moscow (1973), Ch. 2, 3, 5, 6.

[4] R. Blinc and B. Žekš, *Soft Modes in Ferroelectrics and Antiferroelectrics* (North-Holland, Amsterdam, 1975), Ch. 5.

[5] M. E. Lines and A. M. Glass, *Principles and Applications of Ferroelectrics and Related Materials* (Clarendon Press, Oxford, 1982), Ch. 4.

[6] M. B. Belonenko, A. R. Kessel', and M. M. Shakirzyanov, Fiz. Tverd. Tela (Leningrad) **29**, 3345 (1987) [Sov. Phys. Solid State **29**, 1919 (1987)].

[7] L. D. Landau and E. M. Lifshitz, *Theory of Elasticity*, 2nd ed. (Pergamon Press, Oxford, 1965), Ch. 1 and 3.

[8] M. J. Ablovitz and H. Segur, *Solitons and the Inverse Scattering Transform* (SIAM Press, Philadelphia, 1971), Ch. 1 and 4.

[9] R. K. Dodd, J. C. Eilbeck, J. Gibbon, and H. C. Morris, *Solitons and Nonlinear Wave Equations* (Academic Press, New York, 1988), Ch. 8.

[10] A. H. Nayfeh, *Introduction to Peturbation Techniques* (Wiley, New York, 1984), Ch. 9.

[11] G. L. Lamb, Jr., *Elements of Soliton Theory* (Wiley, New York, 1983).

[12] A. C. Newell, in *Solitons*, edited by R. K. Bullough and P. J. Caudrey (Springer-Verlag, Berlin, 1983), Vol. 6, pp. 193–267.

Translated by Paul F. Schippnick

NMR Study of ^{6}Li in LiNbO$_3$

A. V. Yatsenko

Simferopol State University, 333036 Simferopol, Russia

(Submitted August 18, 1997)
Fiz. Tverd. Tela (St. Petersburg) **40**, 122–125 (January 1998)

An experimental NMR study of the ^{6}Li isotope in single crystals of lithium niobate has been performed, along with a computer simulation of ^{6}Li NMR spectra for a crystal of congruent composition, containing defects in the cation sublattice. It is found that the mean value of the principal component of the electric field gradient tensor at the ^{6}Li nuclei is 1.48 times larger than at the ^{7}Li nuclei. It is surmised that there is a substantial difference in the character of the mobility of the ^{6}Li and ^{7}Li nuclei in the LiO$_6$ octahedra at room temperature. © *1998 American Institute of Physics.* [S1063-7834(98)02901-3]

It is well known that an NMR study of quadrupole nuclei in ferroelectrics gives very important information about the structure of the investigated objects.[1] This is most graphically clear in the case of the oxygen-octahedron ferroelectric LiNbO$_3$ in which NMR of both ^{93}Nb and ^{7}Li has been investigated. In particular, quite a few papers[2–7] have investigated the peculiarities of ^{7}Li NMR in this crystal. Nevertheless, and this pertains not only to lithium niobate but also to other lithium-containing ferroelectrics, the existence of a second stable isotope of lithium having an electric quadrupole moment, ^{6}Li with a natural abundance of 7.5%, is usually completely ignored. The main reasons why NMR of ^{6}Li has received so little attention are its small gyromagnetic ratio, low sensitivity, small nuclear quadrupole moment eQ, almost two orders of magnitude smaller than that of ^{7}Li, and, as a consequence, the low information content of the experiment. Indeed, earlier NMR experiments for ^{6}Li in LiNbO$_3$ demonstrated only the fundamental possibility of observing the corresponding signals;[8] however, no effort to compare the results of NMR of ^{6}Li and of ^{7}Li has been made.

At the present time, it is implicitly assumed that ^{6}Li and ^{7}Li in LiNbO$_3$ are structurally equivalent.[9] Therefore, it is possible to model the NMR spectrum of ^{6}Li by using the results of NMR experiments for ^{7}Li to determine the electric field gradient (EFG) at the lithium nuclei.

Indeed, the general expression for the quadrupole frequency shift of the transition $(m-1)\leftrightarrow m$ relative to the Larmor frequency in first-order perturbation theory (for axial symmetry of the EFG tensor) has the form

$$\Delta\nu=\frac{3e^2q_{zz}Q}{8I(2I-1)h}(3\cos^2\theta-1)(2m-1), \qquad (1)$$

where I is the nuclear spin, eq_{zz} is the principal component of the EFG tensor, θ is the angle between the Z axis of the EFG tensor and the external magnetic field $\mathbf{B}_0$, and m is the magnetic quantum number.[10] The ratio of frequency shifts of the NMR transition $(+3/2\leftrightarrow+1/2)$ for ^{7}Li $\Delta\nu_7$ (spin $I=3/2$) and the NMR transition $(+1\leftrightarrow 0)$ for ^{6}Li $\Delta\nu_6$ (spin $I=1$) for arbitrary orientation of the single crystal is given by

$$\Delta\nu_6=1.5\Delta\nu_7\frac{(eQ)_6}{(eQ)_7}, \qquad (2)$$

where $(eQ)_6=-0.064\times10^{-26}$ cm$^2\cdot/e/$ and $(eQ)_7=-4\times10^{-26}$ cm$^2\cdot/e/$ are the quadrupole moments of ^{6}Li and ^{7}Li (Ref. 11), and e is the charge of the electron.

Thus, for arbitrary orientation of the single crystal, the NMR spectrum of ^{6}Li consists of two lines shifted by $\mp\Delta\nu_6$ relative to the Larmor frequency. In the first approximation it can be assumed that the shape of these lines is determined only by the magnetic dipole–dipole interactions. The orientational dependence of the contribution of the dipole–dipole interactions to the second moment of the NMR line of ^{6}Li S_{2d-d} was calculated on the basis of structural data given in Ref. 12. The results of this calculation are plotted in Fig. 1. Since the quadrupole splitting of the NMR spectrum of ^{6}Li is not large, we chose as our main parameter for analysis the second moment of the entire NMR spectrum, defined relative to its center of gravity. The dependence $S_2(\theta)$ of the NMR spectrum of ^{6}Li, modeled according to relation (2) with the dependence $S_{2d-d}(\theta)$ taken into account assuming that the lines of the spectrum have Gaussian shape, is also plotted in Fig. 1. The same figure plots experimental data for the congruent single crystal LiNbO$_3$:Fe (0.07 mass%) with a correction for the influence of the amplitude of modulation of the magnetic field. The experiments were performed on a wide-line NMR spectrometer with autodyne sensor at $B_0=1.5$ T. To increase the signal-to-noise ratio (S/N) we used multiple collection of signals and Fourier filtration of the spectra, allowing an improvement of the signal-to-noise ratio by a factor of 1.5 without introducing additional error into the line shape.[13] The rms error of the experimental data indicated in Fig. 1 also allows for mutual drift of the magnetic field relative to the generation frequency of the sensor. Paramagnetic impurities in the given case do not lead to additional broadening of the spectrum—a sample check on a nominally impurity-free congruent single crystal revealed agreement within the limits of error with the experimental results presented in Figs. 1 and 2.

It is clear from Fig. 1 that there are substantial differences between the calculated and experimental dependence of $S_2(\theta)$. It is especially important to note the nonagreement of S_2 at the ''magic angle'' $\theta=55°$, which unambiguously indicates the existence of other line broadening mechanisms besides dipole–dipole interactions. Without specifying the reasons for additional broadening, it can be

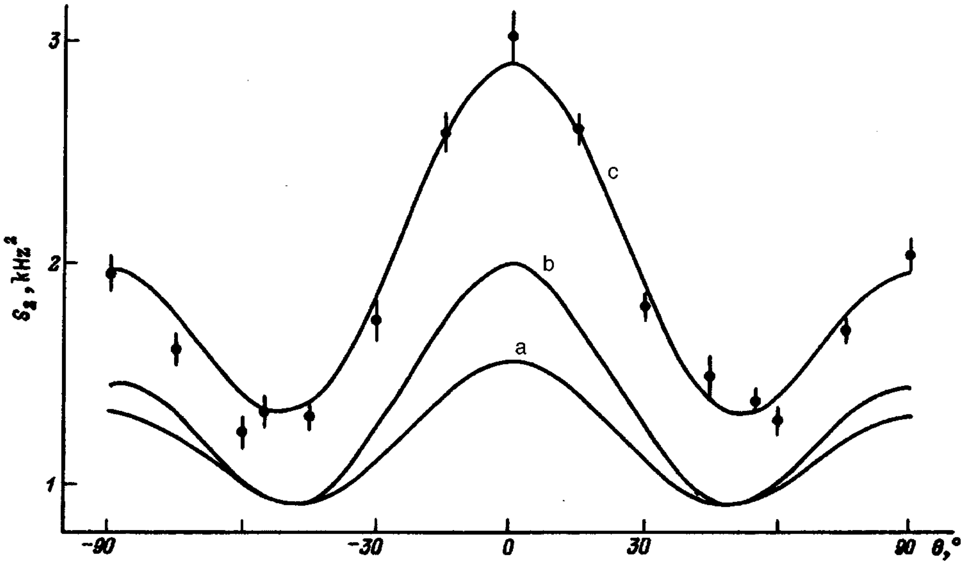

FIG. 1. Orientational dependence of the second moment of the NMR spectrum of ^{6}Li in a $LiNbO_3$ single crystal: a—due only to the magnetic dipole–dipole interactions, b—calculated according to Eq. (2) with dipole–dipole broadening taken into account, c—best fit. The points are experimental data for a single crystal of $LiNbO_3$:Fe (0.07 mass %).

assumed that the corresponding contribution to S_2 is additive with the dipole–dipole contribution and, to first order, is independent of orientation. However, even in the case in which such an additional contribution ($\simeq 0.40$ kHz^2) is taken into account, the fit aided by relation (2) is completely unsatisfactory due to significant discrepancies with the experimental data at essentially any θ, besides $\theta \simeq 55°$.

It seems improbable that the antiscreening factor of the $^6Li^+$ and $^7Li^+$ ions should differ so strongly, considering that they have the same electron shell configuration; therefore, the discrepancy between the experimental and calculated data can be eliminated only by assuming that the mean value of the electric field gradient at the ^{6}Li nuclei is larger than its mean value at the ^{7}Li nuclei. Correspondingly, the experimental data must be fitted with allowance for both additional line broadening ΔS_2 and a K-fold increase of the principal value of the EFG tensor. Comparison of different least-squares fits showed that best agreement with the experimental data obtains if we set $K = 1.48 \mp 0.02$ and $\Delta S_2 = (0.40 \mp 0.02)$ kHz^2. The best fit is shown in Fig. 1. Experimental spectra for some characteristic orientations of the crystal in the magnetic field are shown in Fig. 2.

Regarding these results, it should be noted that weak additional quadrupole satellites are present in the ^{7}Li NMR spectra of $LiNbO_3$ which could correspond to positions of the ^{7}Li nuclei with quadrupole coupling constant $C_z = 82 \mp 2$ kHz, i.e., 1.49 times larger than the generally accepted value $C_z = 55$ kHz.[2–5] To explain the complex form of the ^{7}Li NMR spectrum, it was assumed in Ref. 6 that there are several local minima of the potential of the intracrystalline electric field inside the LiO_6 octahedron which, with a certain probability, can be occupied by the ^{7}Li nuclei. Indeed, calculations of the distribution of the potential about the "classical" position of the Li^+ ions determined by x-ray and neutron scattering[12] demonstrate the presence of four minima, one of which essentially coincides with the "classical" position while the three others are arranged symmetrically about the C axis of the crystal at a distance of 0.026 nm from it.[14] Since the ^{7}Li nuclei are quite mobile, if the time it takes to switch positions τ is much less than $(C_z)^{-1}$, then the extra-axial nuclei will "feel" the average electric field gradient having axial symmetry. Such a problem of rapid reorientation was solved for the pure NMR case.[15]

Further analysis has shown[14] that the "classical" position of the ^{7}Li nuclei corresponds to the value $C_z \simeq 76$ kHz for a relative total line intensity of 0.04 (the experimental values are 82 ∓ 2 kHz and 0.06, respectively), and that the average value of C_z for the "side" positions is equal to 54 kHz.

Thus, the experimental ^{6}Li NMR results are satisfactorily explained for the case in which the ^{6}Li nuclei preferentially occupy the "classical" position on the C symmetry axis of the crystal and additional broadening of the spectral lines is associated with the effect of intrinsic defects arising as a result of nonstoichiometry in the $LiNbO_3$ crystals.

To test this assumption, we performed a computer simulation of the orientational dependence of the shape of the ^{6}Li NMR spectrum based on calculations of the electric field

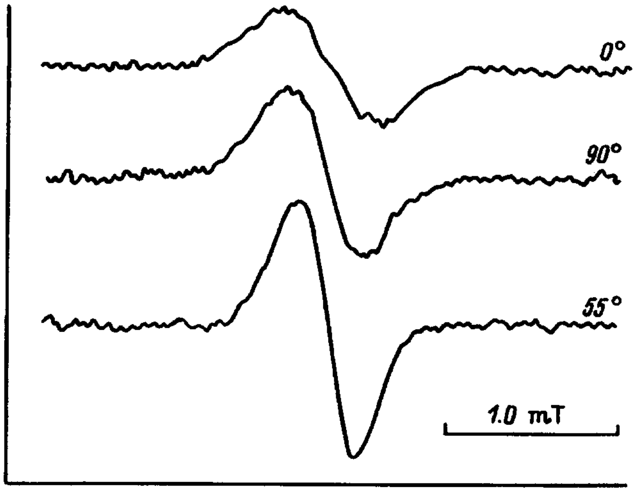

FIG. 2. Form of the NMR spectra of ^{6}Li for three orientations of the single crystal. $B_0 = 1.5$ T.

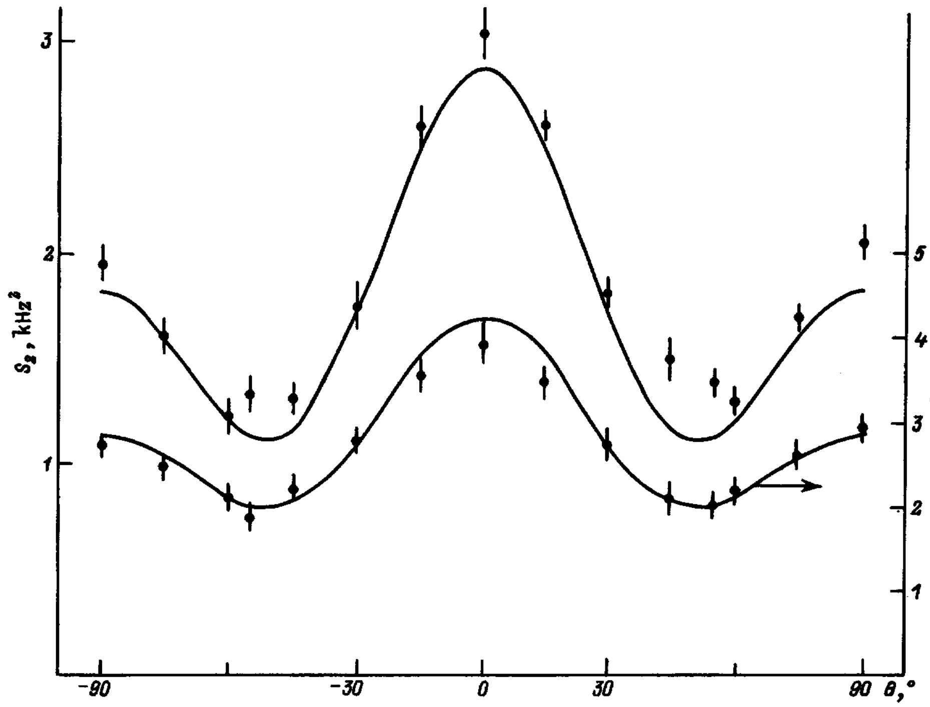

FIG. 3. Orientational dependence of S_2 and $\delta\nu$ for the NMR spectrum of ^{6}Li in a single crystal of $LiNbO_3$, calculated according to the model of randomly localized defect complexes ($Nb_{Li}+3V_{Li}$) and independent V_{Li}. The points correspond to the experimental data.

gradient in a crystal of $LiNbO_3$ with nonideal structure. The calculations were based on an ionic model assuming a random distribution of the most probable defects—complexes ($Nb_{Li}+3V_{Li}$ at the closest distances to Nb_{Li}) and spatially independent V_{Li}, where the V_{Li} are Li^+ vacancies and Nb_{Li} is the Nb^{5+} ion at the Li^+ position.[16] In the EFG calculations we used the values of the effective charges of the Li and Nb ions and of oxygen calculated in Ref. 17 by the LCAO method: $0.98/e/$, $3.67/e/$, and $-1.55/e/$, respectively. In reconstructing the shape of the spectrum we processed around 10,000 random possibilities of the EFG tensor. The orientational dependence of S_2 of the modeled ^{6}Li NMR spectrum and of the width of the resulting line $\Delta\nu$ (from the maximum of the derivative) is plotted in Fig. 3. Also shown are the corresponding experimental data. The small deviations of the orientational dependence of S_2 from the experimental values are probably explained by the absence of an account of local distortions of the structure caused by the defects.

A preliminary analysis of structural distortions caused by the defect Nb_{Li} reveals, for example, the presence of a ‘‘contraction’’ of the nearest three oxygen ions, a displacement from the *C* axis of the three nearest ^{93}Nb nuclei, etc. Calculations of the electric field gradient at the ^{93}Nb and ^{7}Li nuclei in the immediate vicinity (1.5 nm) of the defect point here to an increase in the spread both of the principal value of the EFG tensor and of the orientation of its principal axes in comparison with the results of calculations of the electric field gradient in the spatially undistorted structure.

Thus, it is very probable that at 293 K the dynamics of ^{6}Li and ^{7}Li nuclei in the $LiNbO_3$ structure differ substantially. One reason for ‘‘selective’’ population by the ^{6}Li nuclei of positions on the *C* axis may be the low concentration of this isotope and, as a consequence, the absence of collective interactions of the ^{6}Li nuclei. More definite conclusions can obviously be made only after examining the NMR spectra of ^{6}Li and ^{7}Li in $LiNbO_3$ over a sufficiently wide temperature range.

[1] V. M. Buznik, *Nuclear Magnetic Resonance in Ionic Crystals* (Nauka, Novosibirsk, 1981).

[2] G. E. Peterson, P. M. Bridenbaugh, and P. Green, J. Chem. Phys. **46**(10), 4009 (1967).

[3] V. A. Golenishchev–Kutuzov, U. Kh. Kovpillem, L. N. Rashkovich, and N. F. Evlanova, Fiz. Tverd. Tela (Leningrad) **10**, 759 (1968) [Sov. Phys. Solid State **10**, 594 (1968)].

[4] V. L. Bogdanov, V. V. Lemanov, V. P. Klyuev, and S. A. Fedulov, Fiz. Tverd. Tela (Leningrad) **10**, 1118 (1968) [Sov. Phys. Solid State **10**, 886 (1968)].

[5] T. K. Halstead, J. Chem. Phys. **53**(9), 3427 (1970).

[6] A. V. Yatsenko and N. A. Sergeev, Ukr. Fiz. Zh. **30**(1), 118 (1985).

[7] A. V. Yatsenko, Fiz. Tverd. Tela (St. Petersburg) **37**, 2203 (1995) [Phys. Solid State **37**, 1200 (1995)].

[8] A. V. Yatsenko, *Abstract of Candidate's Dissertation*, Leningrad State Univ. (1985).

[9] J. E. Riley, Jr., Ferroelectrics **75**(1–2), 59 (1987).

[10] A. G. Lundin, É. I. Fedin, *NMR Spectroscopy* [in Russian], Moscow, 1986.

[11] Bruker Almanac. Tables (1991).

[12] Yu. S. Kuz'minov, *The Electro-optical and Nonlinear-Optical Crystal Lithium Niobate* [in Russian], Moscow, 1987.

[13] A. V. Yatsenko and V. Yu. Kornienko, Ukr. Fiz. Zh. **41**(5–6), 636 (1996).

[14] A. V. Vatsenko and N. A. Sergeev, *Ext. Abstracts of the 28th AMPERE Congress*, Canterbury, England (1996), p. 279.

[15] A. Abragam, *The Principles of Nuclear Magnetism* (Clarendon Press, Oxford, 1961).

[16] E. M. Ivanova, N. A. Sergeev, and A. V. Yatsenko, Ukr. Fiz. Zh. **42**(1), 47 (1997).

[17] W. Ching, Gu Zong-Quan, and Xu Yong-Nian, Phys. Rev. B **50**(3), 1992 (1994).

Translated by Paul F. Schippnick

Heat pulses in the second-sound regime

V. D. Kagan

A. F. Ioffe Physico-technical Institute, Russian Academy of Sciences, 194021 St. Petersburg, Russia

(Submitted June 10, 1997)
Fiz. Tverd. Tela (St. Petersburg) **40**, 126–127 (January 1998)

At low temperatures, heat propagates in crystals in the form of collective excitations—second-sound waves. How the parameters of the phonon system of the crystal can be determined from the shape of the heat pulse is considered here. © *1998 American Institute of Physics.* [S1063-7834(98)03001-9]

To describe thermal phenomena we can replace the crystal lattice in the harmonic approximation by a set of independent quasiparticles—phonons. Anharmonic forces give rise to processes of interconversion of phonons of different branches, as a result of which the phonon distribution function relaxes to its equilibrium (Planck) form. This being the case, it would seem that collective excitations slowly varying in space and time are impossible in the phonon system. But phonon–phonon collisions divide into normal and resistive. Normal collisions describe conversions of phonons of different branches which conserve energy and momentum. Therefore these collisions conserve the total momentum and energy of the entire phonon system. Resistive processes, which include phonon scattering by impurities and lattice defects, scattering at the boundaries of the sample, and phonon–phonon conversions in transfer processes, conserve energy but not momentum. At low temperatures normal collisions can be significantly stronger than resistive. Thus, normal collisions unite the phonon gas into a single system possessing elasticity, and a perturbation of the phonon distribution function does not relax but propagates in the form of a wave. Such a collective excitation in the phonon gas, i.e., in the gas of acoustic quanta is called a second-sound wave.

A direct means of detecting such a wave is to examine the propagation of heat pulses. Narayanamurti[1] has experimentally isolated a slow heat pulse whose intensity maximum propagated with the speed of second sound. All subsequent experiments have applied the same means of observing second sound.[2] The speed is very characteristic, but is by no means the only characteristic of the heat pulse. Efforts have been made to extract the characteristics of the phonon system from experimental pulse data. However, the absence of a rigorous theory for the propagation of heat pulses in the second-sound regime hinders the interpretation of the experimental data. The present paper constructs such a theory.

In a harmonic second-sound wave the frequency ω and wave vector k are related by the equation[3]

$$kv-\omega=-b\omega^3\tau_n^2+i(1/\tau_R+\omega^2\tau_n). \tag{1}$$

The velocity v is smaller by a factor of $\sqrt{3}$ than the velocity of first sound averaged over all branches. The imaginary term in Eq. (1) describes attenuation: τ_R is the relaxation time of the resistive collisions, τ_n is the relaxation time of the normal collisions, and b is a number of the order of unity. The dispersion equation (1) allows one to obtain an equation for the envelope of a pulse consisting of sound waves. The variation of the temperature T in the pulse satisfies the equation

$$v\frac{\partial T}{\partial x}+\frac{\partial T}{\partial t}=-b\tau_n^2\frac{\partial^3 T}{\partial t^3}-\frac{1}{\tau_R}T+\tau_n\frac{\partial^2 T}{\partial t^2}. \tag{2}$$

All terms on the right side are correction terms, and it is possible to use in them both space and time derivatives.

It is necessary to impose a boundary condition on Eq. (2) whereas in its altered form in which spatial derivatives appear on the right side, an initial condition is required. Of more importance, however, is the left side of the equation, which defines its hyperbolic character. Depending on whether an initial or boundary condition is used, the equation has different solutions. Between these solutions there is a break which occurs along the characteristic of the equation passing through the initial space-time point $x=vt$. In the region $x<vt$, it is necessary to use a boundary condition and, in the region $x>vt$, an initial condition. The temporal maximum of the pulse falls into the first region, so that we should solve Eq. (2) with a boundary condition. The authors of Ref. 4 used an initial condition, which is, generally speaking, invalid.

We write the solution of Eq. (2) using the Fourier method,

$$T(x,t)=\int_{-\infty}^{\infty}d\omega\,\exp\left[-i\omega t+i\frac{x}{v}(\omega-b\omega^3\tau_n^2)-\frac{x}{v\tau_R}-\tau_n\omega^2\frac{x}{v}\right]\int_{-\infty}^{\infty}\frac{dt'}{2\pi}T(0,t')e^{i\omega t'}. \tag{3}$$

We will not keep the small dispersion term in the exponential, but expand with respect to it, keeping the first nonvanishing term. Assuming the initial pulse to be short, we neglect its temporal extent in comparison with the scale characterizing the received pulse

$$T(x,t)=\left(\frac{1}{2\pi}\int dt'\,T(0,t')\right)\exp\left(\frac{-x}{v\tau_R}\right),$$

$$\int_{-\infty}^{\infty} d\omega\left(1-ib\frac{x}{v}\tau_n^2\omega^3\right)\exp\left[-i\omega\left(t-\frac{x}{v}\right)-\omega^2\frac{x\tau_n}{v}\right]. \quad (4)$$

As it propagates, the pulse acquires the universal shape

$$T(x,t)=\frac{A}{\sqrt{x}}\left[1-\frac{3}{4}b\frac{v}{x}\left(t-\frac{x}{v}\right)\right]$$
$$\times\exp\left\{-\frac{x}{v\tau_R}-\left(t-\frac{x}{v}\right)^2\frac{v}{4x\tau_n}\right\}. \quad (5)$$

If we neglect the dispersion term, then the maximum of the heat pulse propagates with the velocity of second sound and its width is determined by the point in the sample at which the pulse is received and the relaxation time τ_n. Taking the dispersion term into account changes the position of the pulse intensity maximum

$$t_{\max}=\frac{x}{v}-\frac{3}{2}b\tau_n. \quad (6)$$

Thus, by calculating the speed of second sound, we can determine the relaxation time τ_n from the difference between the true position of the pulse maximum and the simple expression for it—the first term in expression (6).

The meaning of the connection between the shift in the intensity maximum and the dispersion term was stated in Ref. 1. However, the determination of this meaning in that paper was completely incorrect since the authors used only the dispersion equation (1) and did not have Eq. (6). They may have suspected it, but it is hard to say from their paper with complete certainty how they linked the shift time and the relaxation time.

Equation (5) allows us to determine the characteristics of the phonon system from experiments on the propagation of heat pulses. Taking the dispersion term into account allows us, to determine the relaxation time τ_n according to (6) by calculating the speed of second sound. In addition, it can be seen from (5) that the width of the pulse depends only on τ_n, not on τ_R. Correspondingly, it is possible to determine τ_n and their pulse widths.

We may add a few words about Ref. 4 since this paper is frequently cited.[1,2]

First, the authors of Ref. 4 did not take the dispersion term into account $(b=0)$. Second, they used a modified form of Eq. (2) whose right side contains only spatial derivatives. On this equation they imposed an initial condition, which, as noted above, does not correspond to the conditions of the experiment. However, they assumed the temperature to be concentrated at the initial instant of time near the origin. Correspondingly, they arrived at the following form of the heat pulse:

$$T(x,t)=\frac{B}{\sqrt{t}}\exp\left\{-\frac{t}{\tau_R}-\frac{\left(t-\frac{x}{v}\right)^2}{4t\tau_n}.\right\} \quad (7)$$

Near the pulse maximum $(x=vt)$ this relation differs only slightly from Eq. (5) but, at large times, pulse spreading is present in it and grows with time but is not present in (5).

[1] V. Narayanamurti and R. C. Dynes, Phys. Rev. Lett. **28**(22), 1461 (1972).
[2] V. A. Danil'chenko, V. N. Poroshin, and O. G. Sarbeĭ, JETP Lett. **30**, 196 (1979).
[3] V. L. Gurevich, *Kinetics of Phonon Systems* [in Russian], Nauka, Moscow, 1980.
[4] C. C. Ackerman and R. A. Guyer, Ann. Phys. (N.Y.) **50**(1), 128 (1968).

Translated by Paul F. Schippnick

Lattice dynamics and specific heat of the manganese antimonide Mn_2Sb

V. M. Ryzhkovskiĭ and T. D. Sokolovskiĭ

Institute of the Physics of Solid State and Semiconductors, Academy of Sciences of Belarus, 220072 Minsk, Belarus

(Submitted June 24, 1997)
Fiz. Tverd. Tela (St. Petersburg) **40**, 128–131 (January 1998)

Manganese cation binding energy, dispersion curves, total phonon spectrum, and temperature dependence of the lattice and magnetic contributions to specific heat of Mn_2Sb have been calculated. © *1998 American Institute of Physics.* [S1063-7834(98)03101-3]

Manganese antimonide Mn_2Sb crystallizes in the Cu_2Sb tetragonal structure ($C38$, space group $4/nmm$) with two structurally nonequivalent cation positions, Mn I and Mn II. The compound is a ferrimagnet $T_C = 550$ K) because of antiparallel ordering of magnetic moments on the Mn I and Mn II ferromagnetic sublattices. The manganese I and II cations have different charges and magnetic moments depending on the nearest environment. Taking the trivalent state of the antimony anions, assuming only integer values of the charge for the manganese cations as well, and taking into account the symmetry of the anion environment for the two cation species, one comes to $Mn^{+}Mn^{2+}Sb$ for the formal configuration of this compound.[1] The atomic magnetic moments of cations I and II are, respectively, 2.0 and 3.8 μ_B.[2] Manganese antimonide is a convenient subject for studying both the structural and magnetic properties of matter.

This work reports calculations of the temperature dependence of the specific heat of ferrimagnetic Mn_2Sb crystal, with inclusion not only of the lattice but of magnetic contribution as well. To determine the first, we calculated the phonon energy in the Born approximation[3] and the correction for the anharmonicity of atomic vibrations in the crystal. The magnetic contribution to specific heat was calculated in accordance with Néel theory[4] developed to explain the physical properties of ferrites.

The unit cell of the crystal contains two Mn_2Sb molecules and, therefore, according to dynamic lattice theory, for each value of the wave vector there should exist 18 normal vibrational modes found from coupled second-order differential equations of motion, provided one knows the parameters of the system, which determine the interaction between ions in the crystal. To find these parameters, we calculated the binding energies for different ion pairs taking into account the nearest five coordination spheres.

1. CALCULATION OF THE BINDING ENERGY OF THE MANGANESE CATIONS

For illustration, consider the binding energy of a pair of nearest-neighbor manganese cation species I and II. The main contribution to the binding energy comes from Coulomb interaction between the nuclei and electrons[5]

$$U_c = Z_a Z_b / R + \int\int \rho_a \rho_b dv_1 dv_2 / r_{12} - Z_b \times \int \rho_a dv_1 / r_{1b} - Z_a \int \rho_b dv_2 / r_{2a}, \tag{1}$$

where Z_a and Z_b are the nuclear charges of cations a and b, R is the distance between the cation centers, r_{12} is the distance between electrons 1 and 2, v_1 and v_2 are the volumes occupied by the cations, and ρ_a and ρ_b are the cation electronic densities calculated from the radial wave functions of the electrons in the manganese cations, using wave functions found by the self-consistent Hartree–Fock method.[6]

The exchange energy of two atoms (ions) was determined in the form

$$U_e = \int [(\rho_a + \rho_b) u_c(\rho_a + \rho_b) - \rho_a u_c(\rho_a) - \rho_b u_c(\rho_b)] dv, \tag{2}$$

where u_c is the exchange-energy density in the Bloch-Dirac electron-gas approximation. The kinetic and correlation energies were calculated using an equation similar to (2), but with the corresponding energy density.

Figure 1 shows the total binding energy U (curve *5*) and its components (curves *1–4*) as a function of separation between the manganese cation centers. Examining Fig. 1 (curve *5*), we see that the manganese cations I and II reach a stable state at a distance $R_1 \approx 3$ Å, which accords with experimental data on interatomic separations in the crystal.

Here we introduce a simplifying assumption that the interatomic interaction parameters by Born theory[3] can be expanded in longitudinal and transverse parameters of de Launay[7]

$$A_i = U''(R)_i|_{R=R_0}, \quad B_i = R_i^{-1} U'(R)_i|_{R=R_0}, \tag{3}$$

where R_i is the radius of the ith coordination sphere of a given ion, A_i and B_i are the longitudinal and transverse components of the bond parameters for ions of the ith sphere, and $U'(R)$ and $U''(R)$ are the first and second derivatives of the binding energy for the corresponding ion pair.

2. PHONON SPECTRUM CALCULATION FOR THE Mn_2Sb CRYSTAL

The conditions for stability of ion motion in manganese antimonide lead to the following dispersion relations

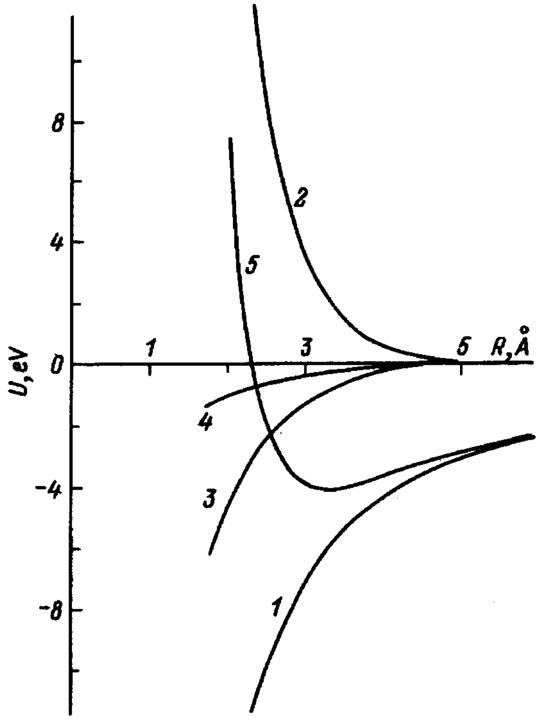

FIG. 1. Binding energy of Mn^+ and Mn^{2+} ions. *1* Coulomb energy, *2* kinetic energy, *3* correlation energy, *4* exchange energy, *5* total Mn^+Mn^{2+} binding energy.

$$|D(\mathbf{q})-\nu^2E|=0, \tag{4}$$

where $D(\mathbf{q})$ is an 18×18 dynamic matrix whose elements are trigonometric functions of the wave vector coordinates, E is an 18×18 identity matrix, and ν is the normal-mode frequency of the manganese antimonide lattice. Solving Eq. (4) for ν^2, one obtains 18 normal-mode frequencies for all wave vectors in the unit cell of reciprocal space. In particular, Fig. 2 shows dispersion curves along two high-symmetry directions of the manganese antimonide crystal, [100] and [110]. We see some of the optical vibration branches to be degenerate, while the acoustical modes do not exhibit degeneracy.

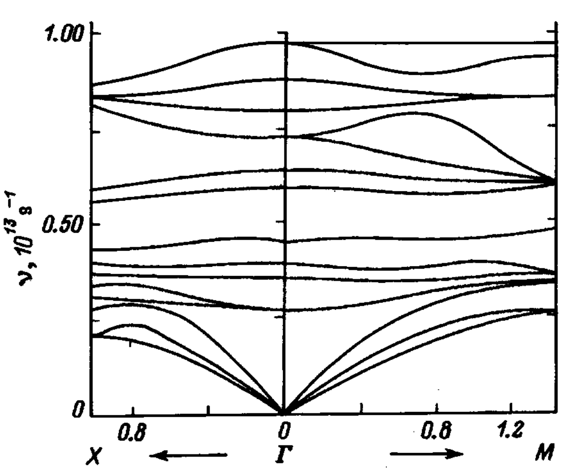

FIG. 2. Dispersion curves of normal vibrations of Mn_2Sb along the [100] and [110] directions in the first Brillouin zone.

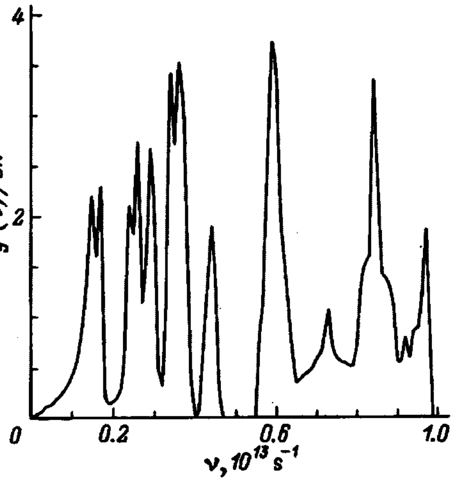

FIG. 3. Total phonon spectrum of Mn_2Sb.

Next the total phonon spectrum of manganese antimonide was calculated by the method of Blackmann.[8] To do this, secular equation (4) was solved at 64000 sites of the unit cell of reciprocal lattice under the conditions used to construct the dispersion curves. As a result, a distribution function $g(\nu)$ was found without application of any smoothing procedure (Fig. 3). The first three maxima counting from the origin correspond to the acoustic vibrations of the Mn_2Sb lattice, and the others, to optical vibrations.

3. LATTICE SPECIFIC-HEAT CALCULATIONS FOR Mn_2Sb

The temperature dependence of the specific heat of Mn_2Sb lattice at constant volume was determined from the equation

$$C_V=9R\int_0^{\nu_m}g(\nu)(h\nu/kT)^2\exp(h\nu/kT)/\times[\exp(h\nu/kT)-1]^2, \tag{5}$$

where integration was performed over the normal vibration frequency using the phonon spectrum $g(\nu)$.

Curve *1* in Fig. 4 displays the specific heat of the Mn_2Sb lattice at constant volume calculated in the harmonic approximation using Eq. (5). We also calculated the contribution of lattice anharmonicity to the specific heat of manganese antimonide. It is known that at comparatively high temperatures the first- and second-order anharmonicities give a correction to specific heat, which is directly proportional to the absolute temperature, with the coefficient of proportionality being a complex function[9,10] of the second, third, and fourth derivatives of the binding energy with respect to the distance between the crystal ion centers. The calculation yielded 0.00275 J/(mol·K^2) for the coefficient of anharmonicity for Mn_2Sb.

It is known that the electronic contribution to specific heat is, in the first approximation, also directly proportional to absolute temperature and is 0.42 J/(mol·K^2) at $T=100$ K.[11] Curve *2* in Fig. 4 includes the sum of these two corrections. The lattice specific heat of manganese anti-

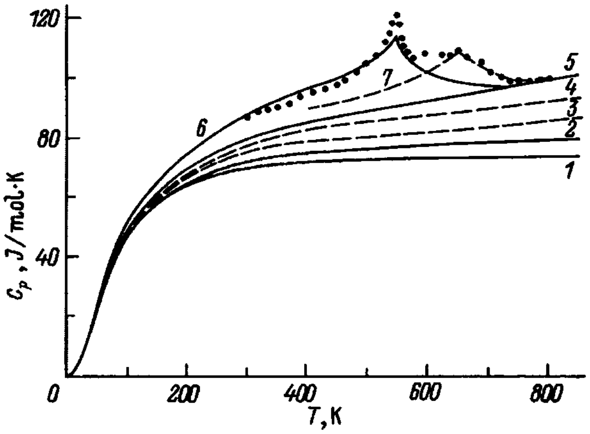

FIG. 4. Specific heat of Mn_2Sb. *1* specific heat C_v without inclusion of anharmonicity, *2* specific heat C_v including anharmonicity, *3* and *4* data on C_v from Ref. 11, *5* specific heat C_p including anharmonicity and the electronic contribution, *6* specific heat C_p with inclusion of the magnetic contribution of Mn_2Sb, *7* magnetic contribution to specific heat of MnSb.

monide at constant pressure, C_p, was calculated through C_v in accordance with the Grüneisen approximation

$$C_p=(1+GT)C_V \tag{6}$$

and is depicted in Fig. 4 by curve *5*.

4. CALCULATION OF THE MAGNETIC CONTRIBUTION TO THE SPECIFIC HEAT OF Mn_2Sb

Since Mn_2Sb is a ferrimagnet for $T<T_C=550$ K, one can apply Néel theory to its study.[4] To do this, we calculate the temperature dependence of internal magnetic energy U_M within the 0–800-K range, including the phase-transition region at 550 K, in the molecular field approximation of Weiss[12]:

$$U_M=-0{,}5(H_1M_1+H_2M_2), \tag{7}$$

where H_1 is the magnetic field acting on the Mn^+ cation from the nearest-neighbor Mn^{2+} cations, H_2 is the magnetic field of the nearest-neighbor Mn^+ cations interacting with the Mn^{2+} cation, and M_1 and M_2 are the magnetizations of the Mn^+ and Mn^{2+} sublattices, respectively.

As follows from Néel theory, in the zero external-magnetic-field approximation the quantities H and M of the two magnetic sublattices are linearly related:

$$\begin{aligned} H_1&=\Gamma_{11}M_1+\Gamma_{12}M_2, \\ H_2&=\Gamma_{12}M_1+\Gamma_{22}M_2, \end{aligned} \tag{8}$$

where Γ_{ij} are the Weiss molecular-field coefficients found from the equality

$$\Gamma_{ij}=2Z_{ij}J_{ij}/(N_jg_ig_j\mu_B), \quad (i,j=1,2), \tag{9}$$

Z_{ij} is the number of the nearest-neighbor cations on sublattice j to cation i, N_j is the number of cations j in the lattice, and J_{ij} are the exchange integrals for the interaction between cations i and j.

Since cations on the same sublattice have equal magnetic moments, one can write

$$\begin{aligned} M_1&=A_1B_S(C_1H_1/T), \\ M_2&=A_2B_S(C_2H_2/T), \end{aligned} \tag{10}$$

where $B_S(x)$ is the Brillouin function.

Solving coupled equations (8) and (10) by iterations yields self-consistent values of the spontaneous magnetization and the corresponding sublattice magnetic fields H_1 and H_2 as functions of temperature. This permits one to calculate the internal magnetic energy U_M from Eq. (7) and, subsequently, the magnetic contribution to specific heat

$$C_M=dU_M(T)/dT. \tag{11}$$

Curve 6 in Fig. 4 shows the total specific heat of Mn_2Sb as a function of temperature calculated by us. The experimental data[11] are shown by dots.

We see that the experimental curve $C_p=f(T)$ differs strongly for $T>T_C$ from our calculation for Mn_2Sb. The pattern of the curve can be readily explained if we recall the specific crystallochemical features of manganese pnictides having the Cu_2Sb structure.[13] Mn_2Sb attains stoichiometric composition (δ phase) only at high temperatures ($T\cong 1000$ K). At $T=300$ K, δ phase with excess cation component is stable. Therefore a Mn_2Sb sample (δ phase) quenched from 1100 K remains at room temperature in a thermodynamically nonequilibrium state and changes its composition under heating with precipitation of the excess nickel-arsenide–type ferromagnetic phase ε, which has a higher magnetic disordering temperature and, thus, contributes to the magnetic component of specific heat for $T>T_C=550$ K.

To gain a quantitative support for this interpretation, we carried out an additional calculation of the magnetic specific heat of MnSb (ε phase) in the molecular-field approximation. Since in a ferromagnet the magnetic sublattices are identical, one can use in the calculation Eqs. (7)–(11), provided one takes equal molecular-field coefficients ($\Gamma_{11}=\Gamma_{12}=\Gamma_{22}$), as well as the magnetizations ($M_1=M_2$) and magnetic fields ($H_1=H_2$), and assumes correct signs of the interactions. The results of the calculation are shown by dashed line 7 in Fig. 4.

We see that the experimental relation $C_p=f(T)$ can be described within the 500–750-K temperature range by a superposition of the magnetic contributions to specific heat of the δ and ε phases obtained from the calculation.

Thus straightforward calculation not only of the dynamic lattice characteristics but also of the magnetic properties of the Mn_2Sb crystal has permitted a theoretical determination of the temperature dependence of the specific heat of Mn_2Sb, which is found to agree satisfactorily with the corresponding experimental data. This provides support for the validity of the model used and for the character of the temperature-induced crystallochemical changes in Cu_2Sb-type manganese pnictides,[13] which were established by magnetometry, x-ray diffraction studies, and thermography.

---

[1] J. B. Goodenough, *Magnetism and the Chemical Bond* [Interscience, New York, 1963; Metallurgiya, Moscow, 1968].

[2] N. N. Sirota and V. M. Ryzhkovskiĭ, Fiz. Tverd. Tela (Leningrad) **16**, 2643 (1974) [Sov. Phys. Solid State **16**, 1714 (1974)].

[3] M. Born and K. Huang, *Dynamical Theory of Crystal Lattices*, (Oxford

University Press, 1954) [Russian transl., IL, Moscow, 1958].
[4] M. L. Néel, Ann. de Phys. **3**, 137 (1948).
[5] R. G. Gordon and Y. S. Kim, J. Chem. Phys. **56**, 3122 (1972).
[6] *Methods of Atomic and Molecular Electronic-Structure Calculations* [in Russian] (Ed. by Veselov, LGU, 1975).
[7] J. de Launay, Solid State Phys. **2**, 219 (1956).
[8] M. Blackmann, Proc. R. Soc. London, Ser. A **148**, 384 (1934); *Ibid.* **149**, 117 (1935).
[9] G. Leibfried and W. Ludwig, *Theory of Anharmonic Effects in Crystals*, Solid State Phys. **12**, 276 (1961) [Russ. transl., IL, Moscow, 1963].
[10] T. D. Sokolovskiĭ, Izv. Belarus Akad. Nauk., Ser. Fiz. Mat. No. 1, 97 (1988).
[11] N. E. Askheim and F. Gronvold, J. Chem. Thermodynamics **1**, 153 (1969).
[12] J. S. Smart, *Effective Field Theories of Magnetism* [W. B. Saunders, London, 1966; Mir, Moscow, 1968].
[13] V. M. Ryzhkovskiĭ, V. P. Dymont, and I. L. Pashkovskiĭ, Dokl. Belarus Akad. Nauk **40**, No. 2, 64 (1996).

Translated by G. Skrebtsov

Localization of acoustic phonons in a layered lattice

A. P. Zhernov and E. P. Chulkin

Russian Science Center ''Kurchatov Institute'', 123182 Moscow, Russia;
Institute of Superconductivity and Solid-State Physics, 101000 Moscow, Russia;
Physicotechnical Institute, 726000 Izhevsk, Russia

(Submitted July 29, 1997)
Fiz. Tverd. Tela (St. Petersburg) **40**, 132–141 (January 1998)

The possibility of weak localization of acoustic phonons in a nonideal layered-crystal lattice is studied. Analytical expressions are obtained for the thermal conductivity and diffusion coefficient tensors at low temperatures. The role of specific processes of interference scattering of phonons by phonon density fluctuations near defects under conditions of weak interaction between the layers is analyzed. It is shown that because of such processes a substantial renormalization of the diffusion coefficient in the presence of strong diagonal disorder is possible at relatively low frequencies, where the dispersion laws for the acoustic phonons display quasi-two-dimensional properties. A nonstandard low-temperature dependence of the thermal conductivity of the layered systems BSCCO and BSYCO is discussed. © *1998 American Institute of Physics.* [S1063-7834(98)03201-8]

A great deal of attention is now being devoted to the matter of weak localization of phonons as well as sound waves in disordered compounds. A number of general questions have been investigated for standard three-dimensional lattices (see, for example, Refs. 1–8).

In a previous work, we also studied phonon localization. Special attention was devoted to systems with resonantly scattering impurity centers, when cross splitting of the spectrum is possible and localization thresholds arise. Models in which systematic solutions can be obtained have been analyzed (see the cases of harmonic and anharmonic systems in Refs. 9–10 and 11–12). We employed the theoretical results obtained to explain the low-temperature behavior of the reciprocal of the decay length of ultrasound in amorphous dielectrics[13] (we have in mind the temperature interval where a plateau is observed in the thermal conductivity) and the temperature dependence of the thermal conductivity of parahydrogen quantum crystals with heavy neon and argon scatterers.[14]

In the present paper we discuss the possibility of weak localization of vibrational excitations in some nonideal, strongly anisotropic, harmonic lattices. It is assumed that the individual layers of such lattices are weakly coupled to one another and display two-dimensional properties. Two types of acoustic vibrational modes are studied. They have the following distinguishing feature. In the case of modes of the first type the corresponding displacement vectors are oriented parallel to the layers where the atoms interact strongly. For modes of the second type the displacement vector is perpendicular to the layers. As is well known, such waves are reminiscent of flexural waves in noninteracting layers and are termed ''flexural oscillations.'' They were first studied by Lifshits (see, for example, Ref. 15).

The dispersion law for flexural oscillations is quadratic in the long-wavelength part of the spectrum. Such modes have been observed in investigations of the thermal properties of graphite and boron nitride as well as layered crystals with a large number of atoms of different kinds in a unit cell, for example, in the compound $CsDy(MoO_4)_2$.[16] In a model of disorder, we confine our attention to the case of diagonal disorder. Specifically, we investigate the frequency dependence of the diffusion-coefficient tensor. The two-particle lattice Green's function averaged over the impurity configurations is determined with allowance for ''coherent backscattering'' processes. We note that the questions of weak phonon localization in strongly anisotropic layered lattices have virtually not been addressed in the literature.

In the theory developed below, we discuss the nonstandard temperature dependence of the thermal conductivity of single crystals of layered systems: the high-T_c superconductor $Bi_2Sr_2CaCu_2O_{8+y}$ (BSCCO) and its dielectric analog $Bi_2Sr_2YCu_2O_8$ (BSYCO).

1. LATTICE THERMAL CONDUCTIVITY AND DIFFUSION COEFFICIENT

Let us consider a crystal with isolated impurity atoms. We shall describe its dynamical properties by a Hamiltonian of the form

$$H=H_0+H_i,$$

$$H_0=\frac{1}{2M_0}\sum_{s,\alpha}(p_s^\alpha)^2+\frac{1}{2}\sum_{s,s'}\sum_{\alpha\alpha'}\Phi_{\alpha\alpha'}^{ss'}u_s^\alpha u_{s'}^{\alpha'},$$

$$H_i=\frac{1}{2}\left(\frac{1}{M}-\frac{1}{M_0}\right)\sum_{s,\alpha}c_s(p_s^\alpha)^2.$$

Here H_0 is the Hamiltonian of the unperturbed harmonic atomic lattice and H_i is the perturbation introduced by impurities in this system. The quantities u_s^α and p_s^α are Cartesian components of the displacement and momentum operators of the s-th atom (s is the site index), M and M_0 are, respectively, the masses of the atoms of the impurity and regular lattices, and $\Phi_{\alpha\alpha'}^{ss'}$ are the elements of the second-order force-parameter matrices. It is assumed that disorder is diagonal. In other words, we neglect the change in the force parameters near impurities, i.e. defects are assumed to be isotopic. The factor c_s equals 0 if a matrix atom is located at the s-th site and 1 if a point defect is located at this site. In what follows, the symbol $\langle \ldots \rangle_c$ denotes averaging over the impurity configurations that are realized. The configurational average $\langle c_s \rangle_c = c$, i.e. it equals the impurity concentration.

For the sake of simplicity, it is assumed that the force-parameter matrices are diagonal with respect to the Cartesian indices. To simplify the equations, we denote by s the collection of site (s) and Cartesian (α) indices.

The lattice thermal conductivity tensor $\varkappa_{\alpha\alpha'}$ is expressed in terms of the correlation function of the energy-flux operators $\mathbf{f}$. We have (see, for example, Ref. 17)

$$\varkappa_{\alpha\alpha'} = \frac{1}{2T^2 V} \int_{-\infty}^{\infty} dt \langle \langle f_\alpha(t), f_{\alpha'}(0) \rangle \rangle_c , \tag{1}$$

where T is the temperature and V is the cell volume of the lattice. The symbol $\langle ... \rangle$ denotes averaging over the equilibrium thermodynamic distribution with Hamiltonian H. The quantity f_α appearing in Eq. (1) is defined as

$$f_\alpha = \frac{1}{2} \sum_{s,s'} \Phi^{ss'}_{\alpha\alpha'} u^\alpha_s \frac{p^{\alpha'}_{s'}}{M_{s'}} R^{ss'}_\alpha , \quad R^{ss'}_\alpha = R^\alpha_s - R^\alpha_{s'} , \tag{2}$$

where R^α_s is a component of the radius vector of the s-th lattice site.

Substituting the explicit form of the Hamiltonian H of the system and the relations (2), the expression (1) can be represented in the form

$$\begin{aligned} \varkappa_{\alpha\alpha'} = {} & \frac{1}{3\pi T^2} \sum_{s,s'} \sum_{s_1,s_1'} R^{ss'}_\alpha R^{s_1 s_1'}_{\alpha'} \Phi_{s,s'} \Phi_{s_1,s_1'} \\ & \times \int_0^\infty d\omega \omega^2 n(\omega)(n(\omega)+1) \\ & \times \langle G^+_{ss_1}(\omega) G^-_{s_1' s'}(\omega) \rangle_c , \\ n(\omega) = {} & (\exp(\omega/T) - 1)^{-1}. \end{aligned} \tag{3}$$

Here $G^+_{ss'}$ denote the retarded and advanced single-particle lattice Green's functions (G functions). These G functions are "assembled" on the basis of the dynamic atomic-displacement operators u_s. We note that $G_2 = \langle G^+ G^- \rangle_c$ is a two-particle Green's function.

We are studying a layered crystal. Its lattice possesses axial symmetry. The tensor $\varkappa$ has two principal values, which we denote by $\varkappa_\parallel$ and $\varkappa_\perp$.

Let us switch in Eq. (3) from the site to the momentum representation. After a series of transformations, we obtain for the diagonal α-the component of the thermal conductivity a sum of the contributions of phonon modes of two types. They correspond to vibrational modes arising with a displacement of the atoms in the plane of the layer and along the z axis (l and b modes below). Specifically,

$$\begin{aligned} \varkappa_{\alpha\alpha} = {} & \frac{1}{NT^2} \sum_{\mathbf{k}j} \omega_j^2(\mathbf{k}) n(\omega_j(\mathbf{k}))(n(\omega_j(\mathbf{k}))+1) \\ & \times D^{(j)}_{\alpha\alpha}(\omega_j(\mathbf{k})), \quad j = l,b \end{aligned} \tag{4}$$

(N is the number of lattice atoms per unit volume). By definition

$$\begin{aligned} D^{(j)}_{\alpha\alpha'}(\omega) = {} & \frac{1}{g_j(\omega)} \sum_{\mathbf{kk}'} v^{(j)}_\alpha(\mathbf{k}) v^{(j)}_{\alpha'}(\mathbf{k}') \omega_j(\mathbf{k}) \omega_j(\mathbf{k}') \\ & \times G^{(j)}_2(\mathbf{k};\mathbf{k}';\omega). \end{aligned} \tag{5}$$

In Eqs. (4) and (5) $\omega_j(\mathbf{k})$ and $\mathbf{v}^{(j)} = \partial\omega_j(\mathbf{k})/\partial\mathbf{k}$ are, respectively, the dispersion law and group velocity of the phonon mode with quasimomentum $\mathbf{k}$ and $g_j(\omega)$ is the spectral function of the partial density of vibrational states. It is assumed that $\omega_j^2(\mathbf{k}) = \Sigma_s \Phi^{0s}_{xx} \cos(\mathbf{k}\cdot\mathbf{R}_s)$. If $j = b$, then ω_b^2 can be expressed in terms of Φ^{0s}_{zz} (see Sec. 3). Moreover, we have assumed that the spatial Fourier components of the two- and single-particle G functions are related by the equality

$$G^{(j)}_2(\mathbf{k},\mathbf{k}',\omega) = \lim_{\Omega\to 0} \langle G^{(j)+}_{\mathbf{k},\mathbf{k}'}(\omega) G^{(j)-}_{\mathbf{k},\mathbf{k}'}(\omega - \Omega) \rangle_c .$$

It is assumed that the configurationally-averaged single-particle Green's function of the j-th mode is described by a relation of the form

$$\overline{G}^{(j)+}_{(k)}(\omega) = \left(\omega^2 - \omega_j^2(\mathbf{k}) - i \frac{\omega}{\tau^{(j)}_i(\omega)} \right)^{-1} . \tag{6}$$

Here $\omega/\tau^{(j)}_i(\omega)$ is the imaginary part of the polarization operator, corresponding to an elastic interaction of phonon modes with point defects, and (see, for example, Ref. 17)

$$1/\tau^{(j)}_i(\omega) = \sigma_m \omega^3 g_j(\omega^2), \tag{7}$$

where

$$\sigma_m = \frac{\pi}{2} c \left(\frac{M - M_0}{M_0} \right)^2 = \frac{\pi}{2} c \varepsilon^2$$

is the diagonal-disorder parameter.

We shall elucidate the physical meaning of the factor D (5). Note that the probability that a localized excitation which has arisen at the sth site at time $t = 0$ reaches the site s' at the time $t \neq 0$ is proportional to the factor

$$W_{ss'}(t) = [\dot{G}_{ss'}(t)]^2.$$

The Fourier component of the factor W, averaged over the realizations of the impurity configurations, can be expressed in terms of the Fourier component of the two-particle Green's function $G_2 = \langle G^+ G^- \rangle_c$ by the relation

$$\begin{aligned} W(\mathbf{q}) & = N^{-1} \sum_{\mathbf{kk}'} \omega(\mathbf{k}) \omega(\mathbf{k}') G_2(\mathbf{k};\mathbf{k}';\omega) \\ & = N^{-1} \sum_{\mathbf{kk}'} \omega(\mathbf{k}) \omega(\mathbf{k}') \langle G^+_{\mathbf{kk}'}(\omega) G^-_{\mathbf{k}'\mathbf{k}}(\omega) \rangle_c . \end{aligned}$$

Hence it follows that $D_{\alpha\alpha'}(\omega)$ is a component of the diffusion-coefficient tensor. An expression for the coefficient D in the form (5) for phonon modes is also given in, for example, Refs. 17–19.

As is well known, in the case of dielectrics at extremely low temperatures the phonon mean-free paths l_{ph} are determined by the geometric dimensions of the sample. At comparatively high temperatures l_{ph} is dictated by anharmonic umklapp processes. At intermediate temperatures the mean-free path is sensitive to defects (see, for example, Ref. 20). The relation (4) describes, to a reasonable degree of accuracy, the behavior of $\varkappa$ at intermediate temperatures.

In Sec. 2 we present a model of a layered lattice and give the parameters $\omega_j(\mathbf{k})$, $\nu_\alpha^{(j)}(\mathbf{k})$, and $g_j(\omega)$ of the phonon spectrum that appear in the expressions for the thermal conductivity and the diffusion coefficient. In Sec. 3 the two-particle Green's function $G_2(j)(\mathbf{k};\mathbf{k}';\omega)$ is determined in the weak-localization regime and the longitudinal and transverse components $D_\parallel^{(j)}$ and $D_\perp^{(j)}$ of the partial diffusion coefficients are also determined. In Sec. 4 heat-conduction experiments are discussed.

2. MODEL OF THE CRYSTAL LATTICE

1) *Dispersion law.* We shall assume that the interaction between atoms in the crystal lattice is much stronger in the basal plane $(x0y)$ than along the z axis. In other words, the coupling between the individual layers of the lattice is weak. For the sake of simplicity, we assume that vibrations with displacement vector $\mathbf{u}$ lying in the $x0y$ plane are independent of vibrations along the z axis.

In the general case the frequencies of the acoustic vibrational modes are eigenvalues of the Fourier component of the matrix of second-order dynamic force parameters. This matrix is expressed by a relation of the form

$$\Phi_{\alpha\alpha'}(\mathbf{k})=\sum_s \Phi^{0s}_{\alpha\alpha'}(\cos(\mathbf{k}\mathbf{R}_s)-1). \tag{8}$$

We shall study vibrational modes with relatively low frequencies. The corresponding values of the quasimomenta $\mathbf{k}$ are bounded by the condition

$$ak_{x(y)}\ll 1. \tag{9}$$

The quantity bk_z need not be small. Here and below $\{a,b\}$ are components of a translational vector of the lattice (a—lattice parameter in the layer and b—a parameter characterizing the distance between the layers).

We shall give the dispersion law for longitudinal vibrations of atoms in the plane of the layer. According to the definition (8) and the condition (9), we have

$$M_0\omega_l^2(\mathbf{k})\approx-\frac{1}{2}\sum_{s_\parallel}\Phi^{0s_\parallel}_{xx}R^x_{s_\parallel}R^x_{s_\parallel}\mathbf{k}_\parallel^2 +\frac{1}{2}\sum_{s_\perp}\Phi^{0s_\perp}_{xx}(\cos(\mathbf{k}_\perp\mathbf{R}_{s_\perp})-1), \tag{10}$$

where $\mathbf{k}_\parallel^2=k_x^2+k_y^2$ and $k_\perp \parallel z$. We note that the force parameters $\Phi^{0s_\parallel}_{xx}$ and $\Phi^{0s_\perp}_{xx}$ characterize the interaction in the $x0y$ plane and along the z axis. It was assumed above that

$$|\Phi^{0s_\perp}_{xx}|\ll|\Phi^{0s_\parallel}_{xx}|. \tag{11}$$

Assuming that only nearest-neighbor atoms interact, we obtain instead of the expression (10)

$$\omega_l^2(\mathbf{k})\approx v_\parallel^{(l)2}\mathbf{k}_\parallel^2+2\omega_1^2\sin^2\frac{bk_\perp}{2},\quad v_\parallel^{(l)}=a\omega_3/2. \tag{12}$$

Here $\nu_\parallel^{(l)}$ is the longitudinal velocity of sound of the l-th mode. The frequencies ω_1 and ω_3 can be expressed in terms of the parameters $\Phi^{0x_\perp}_{xx}$ and $\Phi^{0s_\parallel}_{xx}$. On the basis of the inequality (11) $\omega_1^2\ll\omega_3^2$.

Let us now consider modes of the flexural type. Using Eqs. (8) and (9), we can write

$$M_0\omega_b^2(\mathbf{k})\approx-\frac{1}{2}\sum_{s_\parallel}\Phi^{0s_\parallel}_{zz}(R^x_{s_\parallel})^2\mathbf{k}_\parallel^2+\frac{1}{4}\sum_{s_\parallel}\Phi^{0s_\parallel}_{zz}(R^x_{s_\parallel})^4\mathbf{k}_\parallel^4 -\frac{1}{2}\sum_{s_\perp}\Phi^{0s_\perp}_{zz}\sin^2\frac{bk_\perp}{2}. \tag{13}$$

As is well known, in the general case, when there are no stresses the tensor

$$S_{\alpha\alpha',\alpha_1\alpha_1'}=\sum_s\Phi^{0s}_{\alpha\alpha'}R_s^{\alpha_1}R_s^{\alpha_1'}$$

is symmetric under an interchange of pairs of indices α,α' and α_1, α_1'. For the situation at hand this means that

$$\sum_{s_\parallel}\Phi^{0s_\parallel}_{zz}R^x_{s_\parallel}R^x_{s_\parallel}=\sum_{s_\perp}\Phi^{0s_\perp}_{xx}R^z_{s_\parallel}R^z_{s_\parallel}. \tag{14}$$

Hence it follows that the dispersion law for flexural modes (since the first term in Eq. (13) is overdefined) should contain three characteristic force parameters: Together with the parameters $\Phi^{0s_\perp}_{zz}$ and $\Phi^{0s_\parallel}_{zz}$ ($|\Phi^{0s_\parallel}_{zz}|\approx|\Phi^{0s_\parallel}_{xx}|$) there also arises the parameter $\Phi^{0s_\perp}_{xx}$. The quantity $\Phi^{0s}_{\alpha\alpha}$ is determined predominantly by the central forces. Therefore the transverse force parameters are much smaller than the longitudinal force parameters. As a result, since the interlayer interaction is weak, we have

$$|\Phi^{0s_\perp}_{xx}|\ll|\Phi^{0s_\perp}_{zz}|\ll|\Phi^{0s_\parallel}_{zz}|. \tag{15}$$

Using Eq. (14), we obtain instead of Eq. (13)

$$\omega_b^2(\mathbf{k})\approx\omega_1^2b^2\mathbf{k}_\parallel^2+\left(\frac{\tilde{\omega}_3a^2}{\pi}\right)^2\mathbf{k}_\parallel^4+2\omega_2^2\sin^2\left(\frac{bk_\perp}{2}\right). \tag{16}$$

The three force parameters (15) correspond to three characteristic frequencies. These frequencies satisfy the conditions $\omega_1^2\ll\omega_2^2\ll\tilde{\omega}_3^2$. For simplicity, we assume below that the frequencies ω_3 and $\tilde{\omega}_3$ appearing in Eqs. (12) and (16) are of the same order of magnitude and we make no distinctions between them.

We call attention to the following circumstance. We assume that the interatomic interaction force is strongly anisotropic. At the same time, it is assumed that the cell parameters can have a different order of magnitude (we consider both cases $a\approx b$ and $a\ll b$). In principle, if in describing flexural vibrations attention is confined to the interaction only between nearest neighbors in the basal plane, then the rotational invariance of the interaction potential energy between lattice atoms as a whole can be destroyed. The point is that, in reality, the atomic bonds are covalent in crystal lattices having a layered structure and the potential is a multiparticle, and not pair potential. Therefore, generally speaking, to describe flexural modes it is necessary to take account of the fact that interatomic interactions in the basal plane actually extend over several coordination spheres.

So, we have determined the anisotropic dispersion laws for the l and b modes. Let us analyze the corresponding expressions (12) and (16). It follows from these expressions that at low frequencies, right down to ω_1, the quantities ω_l and ω_b both depend on, generally speaking, both components of the quasimomenta $\mathbf{k}_\perp$ and $\mathbf{k}_\parallel$. If the frequency of the longitudinal mode lies in the interval $2\omega_1^2 \leqslant \omega_l^2 < \omega_3^2$, then the second term in Eq. (12) is comparatively small. For this reason, ω_l is virtually independent of the transverse component $\mathbf{k}_\perp$ of the quasimomentum. As a result of this, the dispersion law for the l-th mode for such frequencies approximately corresponds to the case of a two-dimensional lattice. At the same time, for a flexural mode in the interval $\omega_2^2 \leqslant \omega_b^2 \leqslant \omega_3^2$ the first and third terms in the expression for ω_b (16) can be neglected. Then, ω_b does not depend on the component $\mathbf{k}_\perp$ of the quasimomentum and is proportional to $\mathbf{k}_\parallel^2$. Thus, the dispersion law for ω_b in a narrower interval is also found to be quasi-two-dimensional.

See Ref. 21 for a detailed exposition of the model.

2) *Partial spectral densities of vibrational states.* The partial spectral function $g_{l,b}(\omega^2)$ of the squared phonon density of states is defined as

$$g_{l,b}(\omega^2) = \frac{1}{N} \sum_{\mathbf{k}} \delta(\omega^2 - \omega_{l,b}^2(\mathbf{k})). \tag{17}$$

In specific calculations, it is convenient to switch in Eq. (17) from summation over $\mathbf{k}$ to integration of $d\mathbf{k}$. In a layered lattice it is convenient to replace the sum $\Sigma_{\mathbf{k}}$ by

$$\frac{a^2 b}{(2\pi)^3} \int_{-\pi/b}^{\pi/b} dk_\perp \int_0^{2\pi} d\varphi \int dk_\parallel \ldots . \tag{17a}$$

Let us consider the spectral density of the longitudinal modes $g_l(\omega^2)$. Using the relations (12), (17), and (17a), we obtain after a series of transformations

$$g_l(\omega^2) \approx \begin{cases} \dfrac{1}{\pi^2 \omega_3} \cos^{-1}\left[\dfrac{\omega_1^2 - \omega^2}{\omega_1^2}\right], & 0 < \omega^2 \leqslant 2\omega_1^2, \\ \dfrac{1}{\pi \omega_3^2}, & 2\omega_1^2 \leqslant \omega^2 < \omega_3^2. \end{cases} \tag{18}$$

Let us comment on the equation (18). First, at low frequencies $0 < \omega^2 < 2\omega_1^2$ it is applicable when the conditions $ak_{x(y)} \leqslant 1$ and $bk_z \leqslant 1$ hold simultaneously (then $g_l(\omega^2) \sim \omega/\omega_3^2 \omega_1$). It remains valid when $k_{x(y)} a \leqslant 1$ and the condition $bk_z \leqslant 1$ breaks down. It is also interesting that in the interval $2\omega_1^2 \leqslant \omega^2 < \omega_3^2$ the function is virtually frequency-independent.

Let us now consider the case of flexural vibrations. It can be shown on the basis of the relations (16), (17), and (17a) that

$$g_b(\omega^2) \approx \begin{cases} \dfrac{\sqrt{2}}{(2\pi^2)} \dfrac{a^2}{b^2} \dfrac{\omega}{\omega_1^2 \omega_2}, & 0 < \omega^2 < \omega_1^2, \\ \dfrac{1}{4\sqrt{2}} \dfrac{1}{\omega_2 \omega_3} \cos^{-1}\left(\dfrac{\omega_*}{\omega}\right), & \omega_1^2 < \omega_*^2 < \omega^2 < \omega_2^2, \\ \dfrac{\pi}{8} \dfrac{1}{\omega_3 \omega}, & 2\omega_2^2 < \omega^2 < \omega_3^2 \end{cases} \tag{19}$$

(a derivation of Eq. (19) is given in the Appendix). We note that the quantity g_b is an increasing function of frequency for $\omega \leqslant \omega_2$. In the region $2\omega_2^2 < \omega^2 < \omega_3^2$, however, it is a decreasing function (in contrast to g_l).

We call attention to the fact that the functions g_l and g_b are defined, by means of Eqs. (18) and (19), in practically the entire low-frequency range.

3. DIFFUSION COEFFICIENT IN THE CASE OF AN ANISOTROPIC IRREGULAR HARMONIC SYSTEM

We are studying lattices for which the spectrum of acoustic modes contains no points of degeneracy. For this reason, the contributions of the l and b modes to the diffusion coefficient are independent of one another. On this basis, we proceed to determining the two-particle functions $G_2^{(l)}$ and $G_2^{(b)}$.

1) *Bethe–Salpeter equation.* The Green's function $G_2^{(j)}$, where $j = \{l, b\}$, can be represented as a series in powers of the defect concentration c. In the case of a harmonic atomic system with point-type defects, the individual terms in the series in the coordinate representation can be represented diagrammatically as follows:

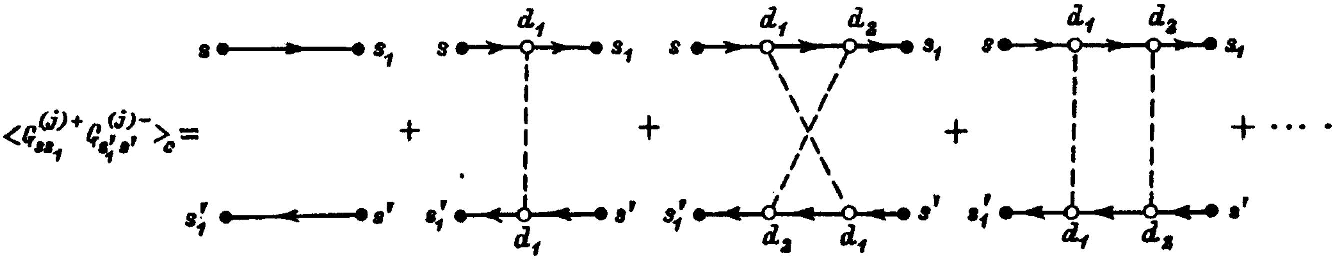

(20)

Here $s \to s' = \overline{G_{ss'}^J}$ is the configurationally averaged single-particle Green's function for a type-j mode. The indices s and d designate arbitrary and impurity sites in the lattice. The dashed line represents the "seed" vertex $\Gamma_j = c t_j^+ t_j^-$, where $t_j^\pm = \lambda(1 - \lambda \overline{G_{ss}^{(j)\pm}})^{-1}$ is the single-site scattering matrix. To simplify the notation, we have set $\lambda = (M - M_0)\omega^2$ (see the derivation of Eq. (20) in Ref. 9).

We note that the expansion (20) formally contains all diagrams that describe the renormalization of the single-particle G function of an irregular lattice and do not contain an interaction between the incoming lines. The first three diagrams containing an interaction between incoming lines are shown. They describe single and double scattering.

The equation (20) can be written in the momentum representation in the form

$$\begin{aligned} G_2^{(j)}(\mathbf{k},\mathbf{k}',\omega) &= \lim_{\Omega\to 0}\langle G^{(j)+}_{\mathbf{k},\mathbf{k}'}(\omega)G^{(j)-}_{\mathbf{kk}'}(\omega-\Omega)\rangle_c \\ &= \lim_{\Omega\to 0}\left(\overline{G^{(j)+}_{\mathbf{k}}}(\omega)\overline{G^{(j)-}_{\mathbf{k}}}(\omega-\Omega)\right. \\ &\quad\times\left(\delta_{\mathbf{kk}'}+\sum_{\mathbf{k}_1}U_j(\mathbf{k},\mathbf{k}_1;\omega,\Omega)\right. \\ &\quad\left.\left.\times G_2^{(j)}(\mathbf{k}_1,\mathbf{k}',\omega,\Omega)\right)\right). \end{aligned} \tag{21}$$

Relations of this kind are called Bethe–Salpeter equations.

The Green's function $\overline{G^{(j)+}_{\mathbf{k}}}(\omega)$ appearing here is given by Eq. (6). Next, we assume that only the ''fan'' diagrams, i.e. the second, fourth, and similar diagrams in Eq. (20), contribute to the vertex part U_j. Diagrams of this type describe inverse coherent scattering processes and determine the weak-localization regime. We have

$$\begin{aligned} &U_j(\mathbf{k},\mathbf{k}';\omega,\Omega) \\ &\quad=\frac{\Gamma_j}{N}\left(1-\frac{\Gamma_j}{N}\sum_{\mathbf{k}_1}\overline{G^{(j)+}_{\mathbf{k}_1}}(\omega)\overline{G^{(j)-}_{\mathbf{k}_1-\mathbf{q}}}(\omega-\Omega)\right)^{-1}, \\ &\mathbf{q}=\mathbf{k}+\mathbf{k}'. \end{aligned}$$

Significantly, the vertex parts Γ_j satisfy the Ward identity

$$c(t_j^+(\omega)-t_j^-(\omega))=\frac{\Gamma_j}{N}\sum_{\mathbf{k}}(\overline{G^{(j)+}_{\mathbf{k}}}(\omega)-\overline{G^{(j)-}_{\mathbf{k}}}(\omega)).$$

Hence we find, on the basis of Eqs. (6) and (7), for the frequency range $0\leqslant\omega^2\leqslant\omega_3^2$

$$\Gamma_j(\omega)\approx\frac{1}{\pi}\frac{\omega}{\tau_i^{(j)}(\omega)g_j(\omega^2)}. \tag{22}$$

2) *Diffusion vertices.* We shall determine explicitly the vertex parts $U_j(\mathbf{q};\omega;\Omega)$ in the weak-localization regime where

$$ql_{\mathrm{ph}}^{(j)}\ll 1,\quad \Omega\tau_i^{(j)}(\omega)\ll 1. \tag{23}$$

Here $l_{\mathrm{ph}}^{(j)}=\nu^{(j)}\tau_i^{(j)}(\omega)$ is the mean-free path of a type-*j* phonon.

In the low-frequency limit $0<\omega^2\leqslant 2\omega_1^2$, where the lattice can be regarded as being three-dimensional, according to Refs. 2 and 9 the vertex part U_j is described by the relations

$$\begin{aligned} U_j(\mathbf{q};\omega;\Omega) &= \frac{\omega}{(\tau_i^{(j)}(\omega))^2}\frac{1}{\pi g_j(\omega^2)}\frac{1}{(\dot{D}(\omega)q^2-i\Omega)}, \\ \dot{D} &= \frac{1}{3}v_j^2\tau_i^{(j)}(\omega). \end{aligned} \tag{24}$$

Let us proceed to intermediate frequencies, where the phonon modes behave as quasi-two-dimensional excitations. In the case of the *l*-th mode it can be shown, using Eqs. (12), (18), and (21), that in the interval $2\omega_1^2\leqslant\omega^2<\omega_3^2$

$$U_l(\mathbf{q};\omega;\Omega)\approx\frac{\omega\omega_3^2}{(\tau_i^{(l)}(\omega))^2}\frac{1}{(R_l(\mathbf{q},\omega)\tau_i^{(l)}(\omega)-i\Omega)}. \tag{25}$$

where

$$\begin{aligned} R_l(\mathbf{q},\omega) &= \frac{q_\parallel^2 v_\parallel^{(l)2}}{2}\left(1-\frac{\omega_1^2}{\omega^2}\right)+\frac{\omega_1^4}{2\omega^2}\sin\frac{q_\perp b}{2}, \\ q_\parallel^2 &= q_x^2+q_y^2,\quad q_\perp\| z. \end{aligned}$$

For the type-*b* mode, we have, using Eqs. (16), (19), and (21), in the frequency interval $2\omega_2^2<\omega^2<\omega_3^2$

$$U_b(\mathbf{q};\omega;\Omega)\approx\frac{2\omega^2\omega_3}{\pi^2(\tau_i^{(b)}(\omega))^2}\frac{1}{(R_b(\mathbf{q},\omega)\tau_i^{(b)}(\omega)-i\Omega)}, \tag{26}$$

where

$$\begin{aligned} \mathbf{R}_b(\mathbf{q},\omega) &= 2q_\parallel^2 v_\parallel^{(b)2}(\omega)\left(1-\frac{\omega_2^2}{\omega^2}\right)+\frac{\omega_2^4}{2\omega^2}\sin^2\frac{q_\perp b}{2}, \\ v_\parallel^{(b)} &= \frac{1}{\pi}\sqrt{\omega\omega_3}. \end{aligned}$$

It is assumed that $\omega\approx\omega_j(\mathbf{k})$, so that $\nu_\parallel^{(b)}(\omega)\approx\frac{a}{\pi}\sqrt{\omega_b(\mathbf{k})\omega_3}$—the group velocity of the flexural mode. We note that the expressions (24)–(26) have a similar structure.

3) *Determination of the diffusion coefficient in the weak-localization regime.* We shall find the eigenvalues of the tensor $D^{(j)}$ in the situation when the conditions (23) hold. On the basis of the relations (5) and (21) we can set

$$\{D_\parallel^{(j)},D_\perp^{(j)}\}=\{D_\parallel^{(j,1)},D_\perp^{(j,1)}\}-\{D_\parallel^{(j,2)},D_\perp^{j,2}\}, \tag{27}$$

where

$$\begin{aligned} \{D_\parallel^{(j,1)},D_\perp^{(j,1)}\} &= \frac{1}{4\pi g_j(\omega)}\lim_{\Omega\to 0}\sum_{\mathbf{k}}\left\{\frac{\partial\omega_j^2(\mathbf{k})}{\partial\mathbf{k}_\parallel},\frac{\partial\omega_j^2(\mathbf{k})}{\partial\mathbf{k}_\perp}\right\} \\ &\quad\times\overline{G^{(j)+}_{\mathbf{k}}}(\omega)\overline{G^{(j)-}_{\mathbf{k}}}(\omega+\Omega), \end{aligned} \tag{28}$$

$$\begin{aligned} \{D_\parallel^{(j,2)},D_\perp^{(j,2)}\} &= \frac{1}{4\pi g_j(\omega)}\lim_{\Omega\to 0}\sum_{\mathbf{q}\leqslant\mathbf{q}_j^{(\parallel)},\mathbf{q}_j^{(\perp)}}U_j(\mathbf{q};\omega,\Omega) \\ &\quad\times\sum_{\mathbf{k}}\left\{\frac{\partial\omega_j^2(\mathbf{k})}{\partial\mathbf{k}_\parallel},\frac{\partial\omega_j^2(\mathbf{k})}{\partial\mathbf{k}_\perp}\right\}\overline{G^{(j)+}_{\mathbf{k}}}(\omega) \\ &\quad\times\overline{G^{(j)-}_{\mathbf{k}}}(\omega+\Omega)\overline{G^{+}_{\mathbf{k}+\mathbf{q}}}(\omega)\overline{G^{(j)-}_{\mathbf{k}+\mathbf{q}}}(\omega+\Omega). \end{aligned} \tag{29}$$

The first term in Eq. (27) is the diffusion coefficient neglecting the processes described by the fan diagrams. The second term determines the change in the value of the coefficient as a result of the contribution of the fan diagrams (i.e. as a result of specific interference scattering processes occurring near defects). In lattices with a strongly anisotropic interatomic interaction force the summation over **q** is bounded by the two small quantities $q_j^{(\parallel,\perp)} \approx \pi / l_{\parallel,\perp}^{(j)}(\omega)$. If $a \approx b$, then the mean-free path length $l_{\parallel,\perp}^{(j)} = \nu_{\parallel,\perp}^{(j)} \tau_i^{(j)}(\omega)$. However, if the cell parameters a and b differ substantially, i.e. $a \ll b$, then a situation where $q_j^{(\perp)} \approx \pi / b$ can be realized.

We confine ourselves below to the static case $\Omega \rightarrow 0$. Let us first study the p mode. In the low-frequency three-dimensional region $0 < \omega^2 \leqslant 2\omega_1^2$ (indicated below by the index 1), we find instead of Eq. (28), on the basis of the explicit form of the dispersion law (12) and a series of transformations,

$$\{D_\parallel^{(l,1)}, D_\perp^{(l,1)}\}_1 \approx \left\{ \frac{\omega_1^2 \tau_i^l(\omega)}{2\pi g_l(\omega)\omega\omega_3^2} \left[4v_\parallel^{(l)2} Z_\parallel^{(l)}\left(\frac{\omega^2}{\omega_1^2}\right), v_\perp^2 Z_\perp^{(l)}\left(\frac{\omega^2}{\omega_1^2}\right) \right] \right\}_1, \tag{30}$$

where

$$Z_\parallel^{(l)}(x) = (x-1)\cos^{-1}(1-x) + \sqrt{2x - x^2},$$

$$Z_\perp^{(l)}(x) = \cos^{-1}(1-x) - (1-x)\sqrt{2x - x^2}.$$

In the limit $\omega \rightarrow 0$, we obtain from Eq. (30) the standard expression for the diffusion coefficient

$$\{D_\parallel^{(l,1)}, D_\perp^{(l,1)}\}_1 \approx \frac{1}{3}\{\tau_i^{(l)}(\omega)[4v_\parallel^{(l)2}, v_\perp^{(l)2}]\}_1. \tag{31}$$

As shown in Refs. 2 and 9, the interference term (29) as compared with the quantities which are determined by the expressions (30) and (31) is of the order of

$$-\frac{3a^2 b}{2\pi^2 g_l(\omega)\tau_i^{(l)2}(\omega) v_\parallel^{(l)3}}. \tag{32}$$

When the phonon modes relax by a Rayleigh relaxation mechanism, this correction (which is of the order of $c^2(\omega^6/\omega_D^6)$, where ω_D is the Debye frequency) is small. But, when resonantly scattering impurity centers are present in the system, cross splitting of the vibrational branches is possible. The group velocity of the phonons is found to be small near gaps. Here it is important to allow for the interference mechanism. For a layered lattice this case requires a special analysis.

Let us determine the diffusion coefficient $D^{(l)}$ in the region $2\omega_1^2 \leqslant \omega^2 < \omega_3^2$ (it is denoted by the index $2l$), where the dispersion law for the l modes is quasi-two-dimensional. To this end, we integrate Eq. (28) $dk_\parallel$, using the residue theorem, and then over $dk_\perp$ directly. We obtain

$$\{D_\parallel^{(l,1)}, D_\perp^{(l,1)}\}_{2l} \approx \left\{ \frac{1}{2\pi g_l(\omega)} \frac{\tau_i^l(\omega)}{\omega\omega_3} [4v_\parallel^{(l)2}(\omega^2 - \omega_1^2), \omega_1^4 b^2] \right\}_{2l}.$$

Next, let us examine Eq. (29). Similar calculations yield

$$\{D_\parallel^{(l,2)}, D_\perp^{(l,2)}\}_{2l} \approx \left\{ \frac{1}{2\pi g_l(\omega)\omega^2} \sum_{\mathbf{q} \leqslant \mathbf{q}_l^{(\parallel)}, q_l^\perp} \frac{1}{R_l(\mathbf{q},\omega)} \times [4v_\parallel^{(l)2}(\omega^2 - \omega_1^2), \omega_1^4 b^2] \right\}_{2l}.$$

Let us obtain an explicit expression for $\Sigma_{\mathbf{q} \leqslant \mathbf{q}_l^{(\parallel)}} R_l^{-1}$. If $b \ll l_\perp^{(l)}$, then

$$\sum_{\mathbf{q} \leqslant \mathbf{q}_l^{(\parallel)}, q_l^\perp} \frac{1}{R_i(\mathbf{q},\omega)} = \frac{a^2 b}{(2\pi)^2} \int_{-\pi/l_\perp^{(l)}}^{\pi/l_\perp^{(l)}} dq_\perp \int_0^{\pi/l_\parallel^{(l)}} \times \frac{dq_\parallel^2}{q_\parallel^2 \frac{v_\parallel^{(l)2}}{2}\left(1 - \frac{\omega_1^2}{\omega^2}\right) + \frac{\omega_1^4 \tau_i^{(l)}(\omega)}{2\omega^2} \sin^2 \frac{q_\perp b}{2}}$$

$$\approx \frac{2a^2}{\pi^2} \frac{1}{v_\parallel^{(l)2} \tau_i^{(l)}(\omega)\left(1 - \frac{\omega_1^2}{\omega^2}\right)} \times \frac{b}{l_\perp} \ln\left[2\sqrt{2} \frac{l_\perp}{b} \frac{\omega}{\tau_i^{(l)} \omega_1^2} \right]$$

(here and below $l_\parallel = l_{\mathrm{ph},\parallel}$, $l_{\mathrm{ph},\perp} = l_\perp$). Let us combine the terms of the standard and interference types. The result is

$$\{D_\parallel^{(l)}, D_\perp^{(l)}\}_{2l} \approx \left\{ \left[v_\parallel^2 \tau_i^{(l)}(\omega)\left(1 - \frac{\omega_1^2}{\omega^2}\right), \frac{b^2 \omega_1^4 \tau_i^{(l)}(\omega)}{2\omega^2} \right] \times F^{(l)}(\omega) \right\}_{2l}, \tag{33}$$

$$F^{(l)}(\omega) \approx 1 - \frac{2}{\pi} c\varepsilon^2 \frac{\omega^2}{\omega_3^2} \frac{1}{\left(1 - \frac{\omega_1^2}{\omega^2}\right)} \frac{b}{l_\perp} \ln\left[\sqrt{2}\pi \frac{l_\perp}{b} c\varepsilon^2 \frac{\omega^4}{\omega_1^2 \omega_3^2} \right] \tag{34}$$

(the relation (34) remains valid for $l_\perp \approx b$).

Let us now consider b modes of the flexural type. In the interval $0 < \omega^2 < 2\omega_2^2$ their vibrational spectrum is three-dimensional. In consequence, the effect of coherent backscattering processes on the coefficient $D^{(b)}$ can be neglected. In the region $2\omega_2^2 < \omega^2 < \omega_3^2$ the dispersion law $\omega_b(\mathbf{k})$ is approximately the same as in a two-dimensional lattice. In such a situation the renormalization of the factor $D^{(b)}$ by the interference mechanism must be finite.

Specifically, for flexural modes in the long-wavelength limit, when $0 < \omega^2 < \omega_1^2$, we have instead of Eq. (28)

$$\{D_\parallel^{(b,1)}, D_\perp^{(b,1)}\}_1 \approx \left\{ \frac{1}{3} \tau_i^{(b)}(\omega)[1v_\parallel^{(b)2}, v_\perp^{(b)2}] \right\}_1, \tag{35}$$

where $\tau_i^{(b)}$ is determined by the relation (7) and $\nu_\parallel^{(b)} = b\omega_1$ and $\nu_\perp^{(b)} = b\omega_2/\sqrt{2}$.

The situation in the frequency range $\omega_1^2 < \omega^2 < \omega_2^2$ (which we mark by the symbol $2b$) is as follows. In the expression for ω_b^2 (16) the term proportional to ω_1^2 can be neglected. The remaining two terms are of the same order of magnitude. To calculate the integrals in Eq. (28), we introduce the frequency ω_* satisfying the inequalities $\omega_1 < \omega_* < \omega < \omega_2$. We integrate once again over $dk_\parallel$ using the residue theorem and over $dk_\perp$ directly. The result is

$$\{D_\parallel^{(1,b)}, D_\perp^{(1,b)}\}_{2b} \approx \left\{ \frac{\pi}{4\sqrt{2}} \frac{\tau_i^{(b)}(\omega)\omega}{\omega_2\omega_3 g_b(\omega)} \left[\frac{8}{\pi^2}\omega_3\omega a^2 \times \left(\sin z - \frac{\sin^3 z}{3} \right), \frac{\omega^2 b^2}{2} \times \left(z - \frac{\sin 2z}{2} \right) \right] \right\}_{2b},$$

$$z = \cos^{-1}\left(\frac{\omega_*}{\omega} \right). \tag{36}$$

Finally, let us consider the region $\omega_2^2 \ll \omega^2 \ll \omega_3^2$ (which we mark by the symbol $3b$), where the frequency $\omega_b \sim k_\parallel^2$. If $b \ll l_\perp$, then it can be shown that

$$\{D_\parallel^{(b)}, D_\perp^{(b)}\}_{3b} = \left\{ \left[\frac{8}{\pi} a^2 \omega_3 \omega \tau_i^{(b)}(\omega), \frac{\pi}{4} b^2 \frac{\omega_2^4}{\omega^2} \tau^{(b)} \right] \times F^{(b)}(\omega) \right\}_{3b}, \tag{37}$$

where

$$F^{(b)}(\omega) \approx 1 - \frac{c\varepsilon^2}{4} \frac{\omega}{\omega_3} \frac{1}{1-\omega_2^2/\omega^2} \frac{b}{l_\perp} \ln\left[\frac{\pi^2}{2\sqrt{2}} \frac{l_\perp}{b} c\varepsilon^2 \frac{\omega^3}{\omega_2^2\omega_3} \right] \tag{38}$$

(the expression for the factor $F^{(b)}$ (38) holds approximately for $b \approx l_\perp$ also).

We shall now make a few comments concerning the expressions obtained for the coefficients $D^{(l,b)}$. It follows directly from the relations (33),(34) and (37),(38) that in the case of strong nondiagonal disorder, when the parameter $c\varepsilon^2$ is of the order of several tenths and larger, the interference mechanism can strongly change the values of the diffusion coefficient D. We also underscore the fact that the equations (30)–(34) and (35)–(38) together make it possible to investigate the contributions of the longitudinal and flexural modes to the low-temperature thermal conductivity under conditions when elastic scattering of these modes by defects is the dominant relaxation mechanism.

We performed numerical calculations of the factors $F^{(l)}$ (34) and $F^{(b)}$ (38). Frequency intervals where the frequencies of the longitudinal and flexural modes are virtually independent of the transverse component $k_\perp$ of the quasimomentum were studied. It was also assumed that $l_{\mathrm{ph},\perp} \approx b$. In the calculations for both the l and b modes the parameter $c\varepsilon^2$ was varied from 0.25 to 1. Moreover, the values of ω_1/ω_3 and ω_2/ω_3 were varied. The values of these ratios are determined by the ratio of the force parameters characterizing the interaction along the z axis and in the xOy plane. The computational results for the factors $F^{(l,b)}(\omega)$ are presented in Figs. 1 and 2. Hence one can see that, first, in the case of strong nondiagonal disorder the partial diffusion coefficients in the "quasi-two-dimensional" regions can change very considerably. In principle, for $c\varepsilon^2 > 1$ a gap appears in the spectrum $D(\omega)$. Second, as the interlayer interaction becomes weaker, the renormalizations of the standard diffusion coefficient increase.

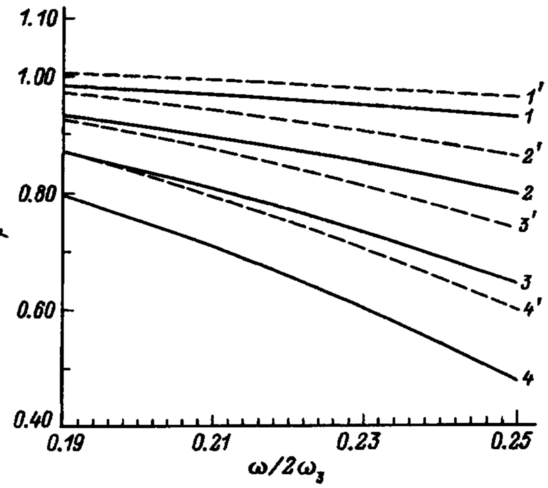

FIG. 1. $F^{(l)}$ versus $\omega/2\omega_3$. $c\varepsilon^2$: *1,1'*—0.25, *2,2'*—0.50, *3,3'*—0.75, *4,4'*—1.00. $\omega_1/\omega_3 = 0.15$ (*1–4*) and 0.1 (*1'–4'*).

4. ON THE NATURE OF THE LOW-TEMPERATURE PLATEAU IN THE THERMAL CONDUCTIVITY OF THE COMPOUNDS BSCCO AND BSYCO

The question of the unusual temperature dependence of the thermal conductivity of single crystals of the layered systems of the high-T_c superconductor BSCCO and its dielectric analog BSYCO is being discussed in the literature (see, for example, Refs. 22–24). It is customarily assumed that in these systems heat is transferred predominantly by phonons in a wide temperature range from 10 to 100 K. Here it is very interesting that there is a plateau in the thermal conductivity

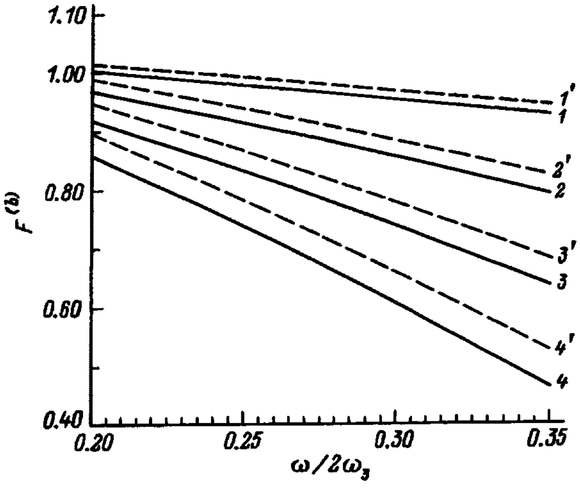

FIG. 2. $F^{(b)}$ versus $\omega/2\omega_3$. $c\varepsilon^2$: *1,1'*—0.25, *2,2'*—0.50, *3,3'*—0.75, *4,4'*—1.00. $\omega_2/\omega_3 = 0.3$ (*1–4*) and 0.25 (*1'–4'*), $\omega_1/\omega_3 = 0.15$ (*1–4*) and 0.1 (*1'–4'*).

of BSCCO and BSYCO in the temperature interval $10 \leqslant T \leqslant 30$ K (such a plateau is absent in the curve $\varkappa$ versus T for 1–2–3 superconductors, which are three-dimensional with respect to phonon properties; in addition, $\varkappa$ grows monotonically in this temperature interval (see, for example, Ref. 24). In other words, the thermal conductivity possesses features which are characteristic for heat transfer in amorphous dielectrics. The authors of the experimental works also note strong cationic disordering in real crystals as a result of cationic nonstoichiometry in bismuth and strontium-containing layers.

At the same time, it is well known that the bismuth cuprates $Bi_2Sr_2Ca_{n-1}Cu_nO_{4+2n}$, where $n = 1$, 2, and 3, possess a crystal lattice having pseudotetragonal symmetry $I4/mmm - D_{4h}^{17}$ and a block structure. They consist of alternating layers of the rock salt type –BiO–SrO– and oxygen-defect perovskite type Ca–CuO_2. The distinguishing feature of Bi-based compounds is the weak coupling of the Bi–O layers because of their relatively large spacing ≈ 3 Å. This property makes bismuth compounds similar to mica. Specifically, in Refs. 25–28 the optical spectra of these compounds were studied and it was concluded that the phonon subsystem is quasi-two-dimensional. In Ref. 28 it was concluded, on the basis of an analysis of inelastic incoherent neutron scattering spectra obtained by the isotopic contrast method, that the interaction between the structural blocks BiO-SrO and Ca-CuO_2 is weak.

In Sec. 3 it is established that at low frequencies under conditions of strong disorder a strong renormalization of the diffusion coefficient occurs as a result of specific interference processes. As a result of such a renormalization of the diffusion coefficient, a plateau can arise in an obvious way in the low-temperature dependence of the thermal conductivity (see, for example, Refs. 2 and 9).

In summary, on this basis it can be conjectured that the phonon subsystem in the compounds BSCCO and BSYCO at low temperatures exhibits two-dimensional heat-transport properties. On the basis of the results obtained in the present work, it is possible to explain qualitatively the plateau observed experimentally in the temperature dependence of the thermal conductivity of irregular BSCCO and BSYCO single crystals as being due to the action of specific impurity interference processes. Coherent backscattering processes play an important role here to the extent that the interaction between the layers is relatively weak.

So, we have discussed the question of the weak localization of acoustic vibrational modes in a nonideal, strongly anisotropic, harmonic crystal lattice. It was assumed that the layers of the lattice are weakly coupled with one another and exhibit two-dimensional properties. Two types of vibrational modes with displacement vectors oriented parallel and perpendicular, respectively, to the layers were studied. The vibrational modes of the first type are longitudinally polarized excitations and the modes of the second type are reminiscent of flexural waves in noninteracting layers.

Analytical expressions were obtained for the thermal conductivity and diffusion-coefficient tensors in the case of diagonal disorder for the temperature range where the phonon mean-free path is determined by scattering by point defects. It was shown that in definite frequency intervals, where the dispersion laws of the acoustic phonon modes exhibit two-dimensional properties, as a result of specific interference processes strong renormalization of the diffusion coefficient can occur under conditions of strong disorder. As the interaction between layers becomes weaker, the renormalization of the diffusion coefficient increases. It was noted that, in the theory developed, the plateau observed experimentally in the temperature dependence of the thermal conductivity at low temperatures ($10 \leqslant T \leqslant 30$ K) in nonideal single crystals of layered systems of the high-T_c superconductor BSCCO and its dielectric analog BSYCO can be explained qualitatively as being due to the strong renormalization of the diffusion coefficient.

We call attention to the fact that, in the above-studied case of layered lattices with heavy impurities, well-determined quasilocal modes do not arise in the quasi-two-dimensional region, i.e. so-called resonantly scattering impurity centers are not present (see Refs. 29–31). However, if the disorder is nondiagonal, then quasilocal modes can exist in the two-dimensional region. We shall investigate this case elsewhere.

We thank D. A. Zhernov for preparing the computer file for this manuscript. We are grateful to N. M. Plakid and Ah. Shober for encouragement and A. N. Taldenkov, M. G. Zemlyanov, and P. P. Parshin for valuable remarks.

This work was supported by Grant No. 96-02-16602-a from the Russian Fund for Fundamental Research.

5. APPENDIX

We shall derive the relation (19) for the spectral density of the flexural modes. First, in the frequency range $\omega_1^2 < \omega^2 < 2\omega_2^2$ the term proportional to ω_1^2 can be neglected in the expression for ω_b^2 (16). The two remaining terms, which are proportional to ω_2 and ω_3, are of the same order of magnitude. Using Eqs. (17) and (17a), it can be shown that

$$g_b(\omega^2) \approx \frac{a}{4\pi} \int dk_\parallel^2 \frac{1}{\sqrt{\omega^2 - \omega_3^2 a^2 k_\parallel^4}} \frac{1}{\sqrt{2\omega_2^2 - \omega^2 + \omega_3^2 a^4 k_\parallel^4 / \pi^4}}.$$

We introduce the frequency ω_* satisfying the relations $\omega_1 < \omega_* < \omega < \omega_2$. Then for $\omega_* < \omega$ we have the approximate equality

$$g_b(\omega^2) \approx \frac{1}{4\sqrt{2}} \frac{1}{\omega_2 \omega_3} \cos^{-1}\left(\frac{\omega_*}{\omega}\right). \tag{A1}$$

In the interval $2\omega_2^2 < \omega^2 < \omega_3^2$ the frequency $\omega_b \sim k_\parallel^2$. The term proportional to ω_2 is comparatively small. Consequently, we have

$$g_b(\omega^2) \approx \frac{1}{(2\pi)^2} \int \frac{d(k_\perp b)}{2\omega_3} \pi^2 \int \frac{d\left(k_\parallel \frac{a^2 \omega_3}{\pi^2}\right)}{\omega \sqrt{Y\left(\frac{\omega_2}{\omega}, k_\perp b\right)}}$$

$$\times\,\delta\left(\frac{k_{\parallel}a^{2}\omega_{3}}{\pi^{2}}-\omega\sqrt{Y\left(\frac{\omega_{2}}{\omega},k_{\perp}b\right)}\right),\tag{A2}$$

where

$$Y\left(\frac{\omega_{2}}{\omega},k_{\perp}b\right)=1-2\,\frac{\omega_{2}^{2}}{\omega^{2}}\sin^{2}\frac{k_{\perp}b}{2}.$$

We obtain from Eq. (A2)

$$g_{b}(\omega^{2})\approx\frac{1}{4\omega_{3}\omega}K\left(\frac{2\omega_{2}^{2}}{\omega^{2}}\right).$$

Here, to simplify the notation we denote by

$$K(m)=\int_{0}^{\pi/2}\frac{d\varphi}{\sqrt{1-m\,\sin^{2}\,\varphi}}$$

the complete elliptic integral of the first kind. Since $\omega_{2}^{2}<\omega^{2}$, $m\approx 0$, and $K(0)\approx\pi/2$. As a result, we find

$$g_{b}(\omega^{2})\approx\frac{\pi}{8}\,\frac{1}{\omega_{3}\omega}.\tag{A3}$$

The relations (A1) and (A3) determine g_{b} in the intermediate-frequency range.

[1] T. R. Kirkpatrik, Phys. Rev. B **31**, 5746 (1985).
[2] E. Akkermans and R. Maynard, Phys. Rev. B **32**, 7860 (1985).
[3] J. E. Graebner, B. Golding, and L. C. Allen, Phys. Rev. B **34**, 5696 (1986).
[4] Qian-Jin Chu, Zhao-Oing Zhang, Phys. Rev. B **38**, 4906 (1988).
[5] H. Bottger and M Theuerkauf, Phys. Status Solidi B **150**, 73 (1988).
[6] M. P. Albada, M. B. Mark, and A. Lagendijk, in *Scattering and Localization of Classical Waves in Random Media*, edited by P. Sheng, World Scientific, Singapore, 1990, p. 97.
[7] C. M. Soukoulis, S. Datta, and C. M. Economou, Phys. Rev. **49**, 3800 (1994).
[8] Ping Sheng, Minyao Zhou, Zhao-Qing Zhang, Phys. Rev. Lett. **72**, 234 (1994).
[9] A. P. Zhernov, E. I. Salamatov, and E. P. Chulkin, Phys. Status Solidi B **165**, 355 (1991).
[10] A. P. Zhernov, E. I. Salamatov, and E. P. Chulkin, Phys. Status Solidi B **168**, 81 (1991).
[11] A. P. Zhernov and E. P. Chulkin, Fiz. Tverd. Tela (St. Petersburg) **36**, 2302 (1994) [Phys. Solid State **36**, 1254 (1994)].
[12] A. P. Zhernov and E. P. Chulkin, Phys. Status Solidi B **193**, 67 (1996).
[13] A. P. Zhernov and E. P. Chulkin, Zh. Éksp. Teor. Fiz. **109**, 602 (1996) [JETP **82**, 321 (1996)].
[14] A. P. Zhernov, Phys. Status Solidi B **193**, 311 (1996).
[15] I. M. Lifshits, Zh. Éksp. Teor. Fiz. **22**, 475 (1952).
[16] É. E. Anders, I. N. Kudryavtsev, and K. É. Nemchenko, Fiz. Tverd. Tela (Leningrad) **34**, 2069 (1992) [Sov. Phys. Solid State **34**, 1106 (1992)].
[17] H. Bettger, in *Principles of the Theory of Lattice Dynamics*, Akademie-Verlag, Berlin, 1983.
[18] R. J. Elliot, J. A. Krumhansl, and P. L. Leath, Rev. Mod. Phys. **46**, 465 (1974).
[19] E. N. Economou, in *Green's Function in Quantum Physics*, 2nd edition, Springer-Verlag, New York, 1983.
[20] R. Berman, *Thermal Conduction in Solids* [Clarendon Press, Oxford, 1976; Mir, Moscow, 1979].
[21] A. M. Kosevich, *Crystal Lattice Theory* [in Russian], Vishcha Ihkola, Khar'kov, 1988.
[22] P. B. Allen, X. Du, L. Mihaly, and L. Forro, Phys. Rev. B **49**, 9073 (1994).
[23] V. B. Efimov and L. P. Mezhov-Deglin, JETP Lett. **62**, 952 (1995).
[24] A. N. Taldenkov, A. V. Inyushkin, and S. Yu. Shabanov, Sverkhprovodimost' **7**, 1502 (1994).
[25] A. A. Bush, I. N. Goncharuk, and Yu. É. Kitaev, Zh. Éksp. Teor. Fiz. **102**, 1587 (1992) [Sov. Phys. JETP **75**, 857 (1992)].
[26] Yu. Kitaev, M. F. Limonov, and A. G. Panfilov, Phys. Rev. B **49**, 9933 (1994).
[27] Yu. É. Kitaev, M. F. Limonov, A. P. Mirgorodskiĭ, A. G. Panfilov, and R. A. Évarestov, Fiz. Tverd. Tela (St. Petersburg) **36**, 865 (1994) [Phys. Solid State **36**, 475 (1994)].
[28] P. P. Parshin, M. G. Zemlyakov, A. V. Irodova, P. I. Soldatov, and S. Kh. Suleĭmanov, Fiz. Tverd. Tela (St. Petersburg) **38**, 1665 (1996) [Phys. Solid State **38**, 919 (1996)].
[29] M. A. Ivanov and Yu. V. Skripnik, Fiz. Tverd. Tela (Leningrad) **32**, 2965 (1990) [Sov. Phys. Solid State **32**, 1722 (1990)].
[30] M. A. Ivanov and Yu. V. Skripnik, Ukr. Fiz. Zh. **35**, 1856 (1990).
[31] M. A. Ivanov, A. M. Kosevich, E. S. Syrkin, Yu. V. Skripnik, I. A. Gospodarev, and S. B. Feodos'ev, Fiz. Nizk. Temp. **19**, 434 (1993) [Low Temp. Phys. **19**, 305 (1993)].

Translated by M. E. Alferieff

Neutron diffraction study of high-pressure-induced structural changes in the ammonium halogenides ND_4Br and ND_4Cl

A. M. Balagurov, D. P. Kozlenko, and B. N. Savenko

Joint Institute for Nuclear research, 141980 Dubna, Moscow District, Russia

V. P. Glazkov and V. A. Somenkov

Kurchatov Institute, 123182 Moscow, Russia

(Submitted June 4, 1997)
Fiz. Tverd. Tela (St. Petersburg) **40**, 142–146 (January 1998)

Structural changes in the deuterated ammonium halogenides ND_4Br and ND_4Cl have been studied by neutron time-of-flight diffraction up to pressures of 45 and 35 kbar, respectively. Data on the equations of state and pressure dependence of the deuterium position parameter have been obtained. A comparison with the hydrogen-containing analogs showed that isotopic substitution of deuterium for hydrogen affects only slightly the compressibility of the systems under study, although the effect is noticeable for ND_4Cl. It has been established that the order-disorder transition from the phase with random deuterium distribution (CsCl cubic structure, space group $Pm3m$) to the ordered phase (same structure, space group $P\bar{4}3m$) occurs in both compounds at the same critical value of the position parameter $u=0.153\pm 0.002$, which is apparently the same for all ammonium halogenides, and, possibly, for other systems of this structural type as well. © *1998 American Institute of Physics.* [S1063-7834(98)03301-2]

The effect of high pressure on the ammonium halogenides NH_4Br, NH_4Cl, NH_4I, and their deuterated analogs is dealt with in a large number of experimental and theoretical studies. This may be attributed to the ammonium halogenides being a comparatively simple and convenient subject for investigation, as well as to the remarkable pattern of the pressure-induced phase transitions they undergo. At room temperature the ammonium bromide and chloride have CsCl-type cubic structure, with deuterium distributed randomly over the possible sites, which corresponds to orientational disorder of ammonium ions[1] (phase II in Fig. 1a). Application of pressure orders deuterium in both systems, which is usually treated as a reorientational transition to a phase with parallel ammonium-ion ordering[2,3] (phase III for ND_4Cl and phase IV for ND_4Br in Fig. 1b; we shall subsequently call it phase IV in both cases). Raman spectra of ammonium halogenides indicate the existence of one more phase, phase V, appearing at high pressures.[3–5] While this phase also has the CsCl structure,[6] the positions of the hydrogen atoms in it are still unknown, and its existence cannot be explained in terms of the currently available theories.

The mechanisms driving the phase transitions in ammonium halogenides can be established by studying their structure and atomic dynamics at high pressures, which can be most appropriately done by neutron scattering. The IBR-2 pulsed reactor was used previously together with DN-12 diffractometer to investigate the structural changes occurring in ND_4Cl at pressures up to 25 kbar, and the dynamics of NH_4Cl up to 40 kbar.[7] The results of this investigation suggest that the transition to the new phase V is connected with the onset of a structural instability at high pressures.

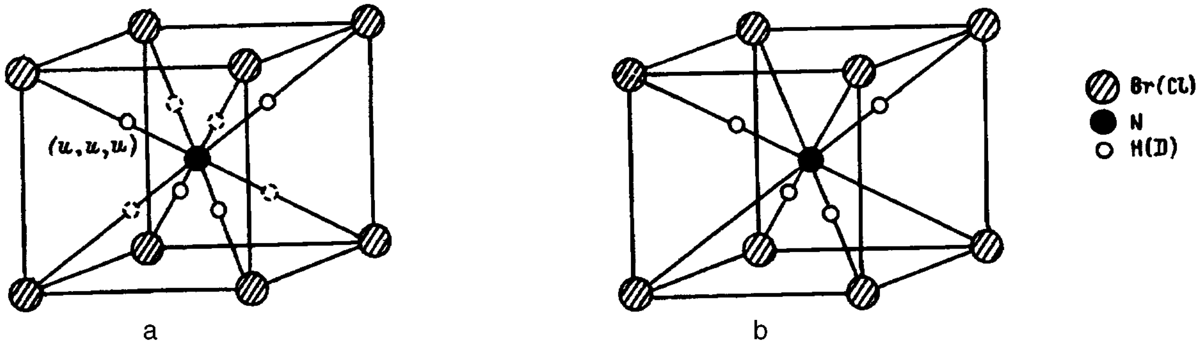

FIG. 1. Structure of ND_4Br and ND_4Cl at (a) normal (phase II) and (b) high (phase IV) pressure. Hydrogen (deuterium) atoms occupy (u,u,u)-type positions, where $u=l_{\text{N-D}}/\sqrt{3}$ is the position parameter, $l_{\text{N–D}}$ is the N–D bond length, and a is the lattice constant. At normal pressure deuterium atoms can occupy two sets of positions specified by solid and dashed symbols.

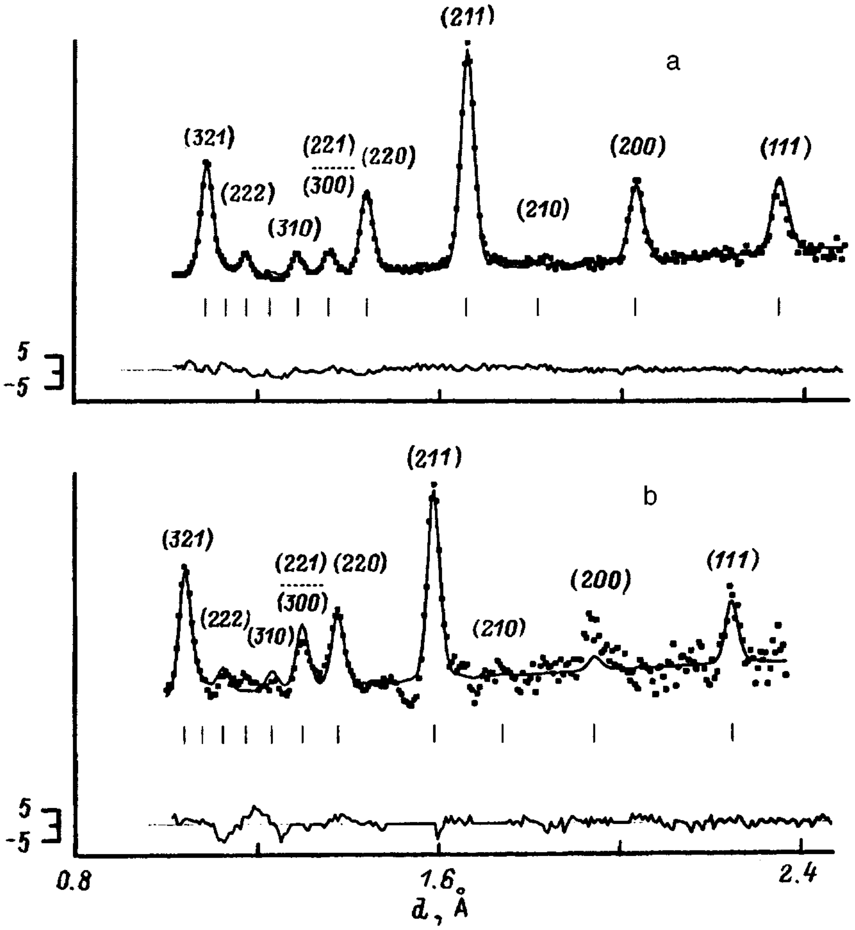

FIG. 2. Parts of ND_4Br diffraction spectra measured at (a) 0 and (b) 31 kbar, normalized against effective neutron flux and refined by the Rietveld procedure. Scattering angle $2\theta = 90°$. The experimental points are complemented by a calculated profile and a difference curve normalized to rms deviation.

The present paper reports the results of a neutron diffraction study of structural changes in the deuterated ammonium halogenides ND_4Br (at pressures of up to 45 kbar), and in ND_4Cl (up to 35 kbar). This choice of the deuterated compounds permitted us to improve the background in neutron diffraction measurements and to evaluate possible isotope effects in compressibility.

1. EXPERIMENTAL

The experiments were carried out with a DN-12 diffractometer[8] on the IBR-2 pulsed reactor in Neutron Physics Laboratory at the Joint Institute for Nuclear Research. Samples about 2.5 mm^3 in volume were compressed in a high-pressure sapphire-anvil chamber,[9] and the scattered neutrons were measured with two dia. 800-mm annular detectors, each consisting of 16 ^{3}He counters, placed at scattering angles of 45 and 90°, respectively. The diffractometer resolution at a wavelength $\lambda = 2$ Å and a scattering angle $2\theta = 90°$ is $\Delta d/d = 0.02$. ND_4Br was studied at normal pressure and 10, 26, 31, 40, and 45 kbar, and ND_4Cl, at normal pressure and 13, 25, and 35 kbar. The pressure in the chamber was determined to within 0.5 kbar from the shift of the ruby luminescence line. All experiments were performed at room temperature. Recording one diffraction spectrum took up, on the average, about 20–30 h.

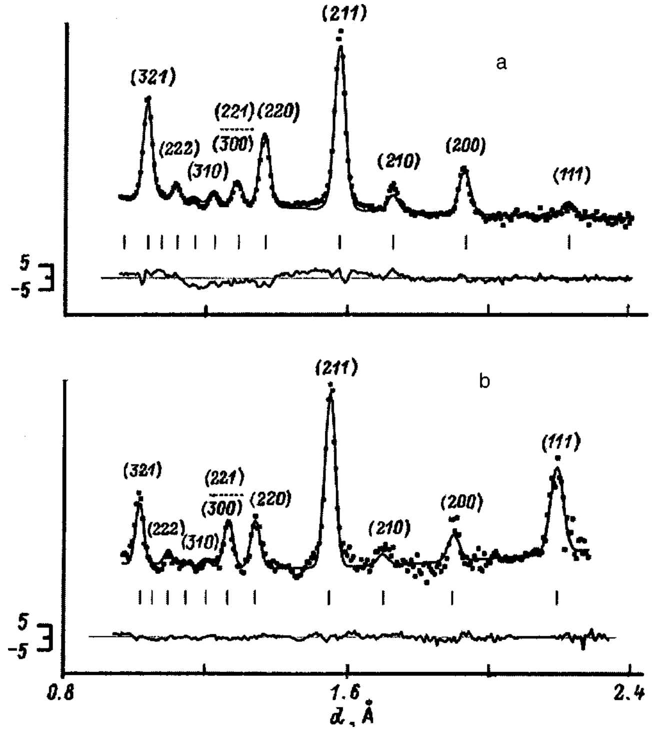

FIG. 3. Parts of ND_4Cl diffraction spectra measured at (a) 0 and (b) 13 kbar, normalized against effective neutron flux and refined by the Rietveld procedure. Scattering angle $2\theta = 90°$. The experimental points are complemented by a calculated profile and a difference curve normalized to rms deviation.

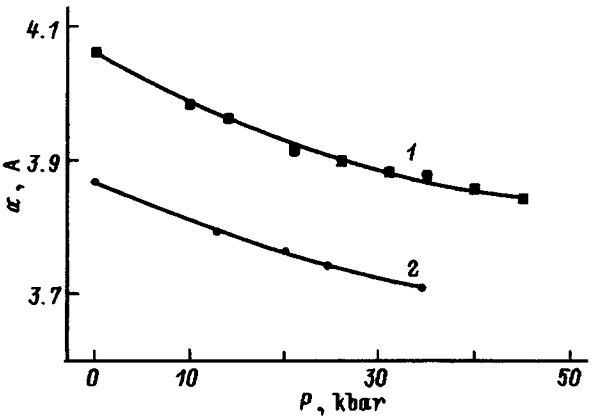

FIG. 4. Pressure dependence of the lattice constant of (*1*) ND_4Br and (*2*) ND_4Cl. The experimental errors are within the size of the symbols.

TABLE I. Compressibility of ND_4Br and ND_4Cl together with data for NH_4Br and NH_4Cl from Ref. 10.

	Ammonium bromide		Ammonium chloride	
	B_0, kbar	B_1	B_0, kbar	B_1
Our results for ND_4Br and ND_4Cl	146 ± 8	7.0 ± 0.6	202 ± 8	5.3 ± 0.6
Piston displacement technique for NH_4Br and NH_4Cl	164	4.8	167	6.7
Ultrasound measurements for NH_4Br and NH_4Cl	159	7.7	176	8.2

2. RESULTS AND DISCUSSION

Figures 2 and 3 show, respectively, parts of diffraction spectra of ND_4Br and ND_4Cl obtained at normal and high pressures and refined by the Rietveld procedure. An increase of pressure results in both systems in a reorientational II-IV phase transition accompanied by parallel ordering of ammonium ions, which is evidenced most clearly by the change in the intensities of the (111) and (221)/(300) peaks. Earlier studies established for the pressure of this transition at room temperature $P\sim25$ kbar (Ref. 3) for ND_4Br (in our experiment it was observed within $26<P<31$ kbar) and $P\sim6$ kbar (Ref. 2) for ND_4Cl, which is not in conflict with our data.

The Rietveld procedure applied to the diffraction spectra measured at normal pressure refined the cell parameter a, the position parameter of deuterium atoms u, and the thermal factor of deuterium B_D. The spectra taken at high pressures were treated with fixed values of B_D obtained at $P=0$: $B_D=3.95$ Å^2 for ND_4Br and $B_D=2.9$ Å^2 for ND_4Cl. The refinement was performed within the well-known models (space group $Pm3m$ for phase II and $P\overline{4}3m$ for phase IV).

The pressure dependences obtained for the lattice parameter a are presented in Fig. 4, and Fig. 5 shows the equations of state interpolated by Burch's equation of the type

$$P=(3/2)B_0(x^{-7/3}-x^{-5/3})[1+3/4(B_1-4)(x^{-2/3}-1)],$$

where $x=V/V_0$ is the relative volume change, B_0 and B_1 are empirical parameters having the meaning of the bulk modulus at equilibrium ($B_0=-VdP/dV|_{V=V_0}$) and of its first derivative with respect to pressure ($B_1=dB_0/dP$). The calculated values of B_0 and B_1 are presented in Table I together with data on NH_4Br and NH_4Cl taken from Ref. 10. While the isotope effect in compressibility of the compounds under study is very weak, it is more pronounced for ammonium chloride. At the same time isotopic substitution of deuterium for hydrogen leads to a noticeable increase of temperature (and a decrease of pressure) of the phase transitions in ammonium halogenides (see Table II).

The observed increase of the position parameter with pressure (Fig. 6) is primarily due to the halogen ions being forced toward the molecular ammonium ion (Fig. 7). While compression practically does not affect the N-D bond length, one can see a trend to its growth at high pressures.

An analysis of the behavior of the position parameter shows that the reorientational II-IV phase transition occurs in both compounds at the same critical value $u_{cr1}=0.153\pm0.002$ (in accordance with our data, the pressure of the II-IV transition for ND_4Br was taken $P=28$ kbar). Linear extrapolation of the u relations toward higher pressures indicates that the transition to phase V discovered recently by Raman spectroscopy takes place in both systems also at the same value of the position parameter $u_{cr2}\sim0.172$. The pressures for the IV-V transition were taken from Ref. 4. This should be regarded only as an estimate, since the $u(p)$ relation in the high-pressure region is possibly nonlinear. The critical values thus found are apparently the same for all ammonium halogenides and, possibly, for all systems of this structural type as well.

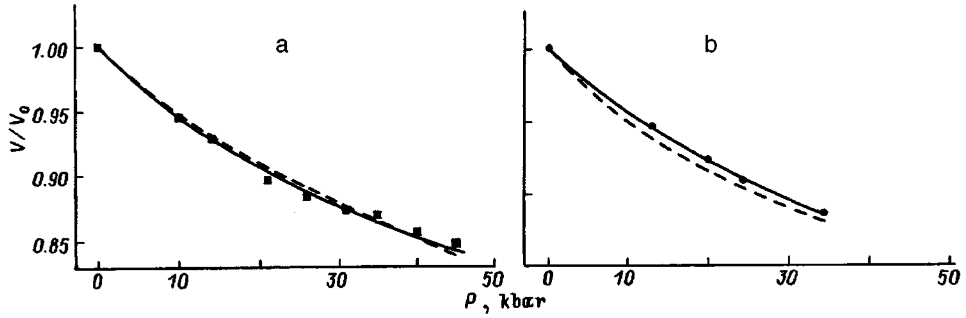

FIG. 5. Equations of state for (a) ND_4Br and (b) ND_4Cl. Dashed lines-data for NH_4Br and NH_4Cl from Ref. 10.

TABLE II. Isotope effects in the II→IV reorientational phase transition.

Parameter	NH_4Cl	ND_4Cl	NH_4Br	ND_4Br
Transition temperature, K at normal pressure (Ref. 2)	243	249	-	-
at $P=2$ kbar (Ref. 11)	-	-	204	212
Transition pressure, kbar at $T=220$ K (Ref. 11)	-	-	4	3
at room temperature (Ref. 12)	7	6	-	-

These values of u_{cr1} and u_{cr2} permit one to make certain assumptions concerning the behavior of the structure of ammonium iodide under compression using the pressures of the II-IV and IV-V transitions from Refs. 4, 5. The assumed pressure dependence of the position parameter for $ND_4I(NH_4I)$ is shown in Fig. 6 by dashed line I. The conclusion on the phase transition II-IV for NH_4I made in Ref. 5 was based, however, only on weak changes in the Raman spectrum, which are possibly not connected with structural changes in the system at all. A calculation using the compressibility data for NH_4I from Ref. 10 yields for the N-D bond length at 27 kbar (the pressure for the II-IV transition in NH_4I at room temperature) $l_{\text{N-D}}=1.1$ Å, which exceeds by almost 10% those obtained for this pressure for ND_4Br and ND_4Cl. The value $P=27$ kbar is pointed out[12] to be only a rough estimate of the pressure of the II-IV transition for NH_4I at room temperature, while in actual fact it is substantially higher. Therefore version II of the assumed behavior of ND_4I (Fig. 6) is more probable, although an increase ofthe N-D bond length under pressure may indeed take place and is determined by the anion polarizability.

Since the pressure-induced reorientational phase transitions in ND_4Br and ND_4Cl occur at close or the same critical values of the structural parameters, it would be interesting to check whether this relation holds also for other representatives of this class of compounds, in particular, for ND_4Cl, and for other phase transitions (u_{cr2}).

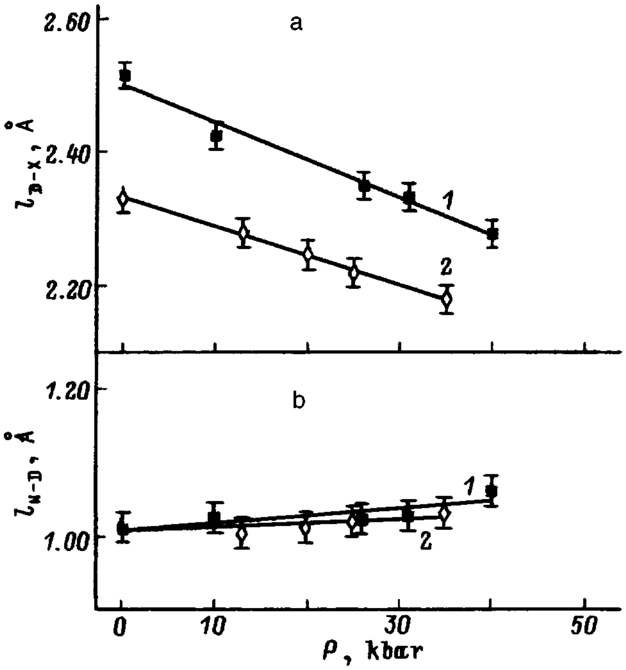

FIG. 7. Pressure dependences of (a) D-X interatomic spacing ($X=$Br, Cl) and (b) N-D bond length. *1* ND_4Br, *2* ND_4Cl.

One may conjecture that the same critical values for pressure-driven phase transitions in structures characterized by a position parameter are connected with an instability of the crystal structure which sets in at certain values of the parameter, as is the case with the critical relations of ionic radii for phase transitions involving a change in coordination number in ionic structures not having such a parameter.

The authors express their gratitude to S. L. Platonov and N. N. Parshin for assistance in preparation of the experiments.

Support of the Russian Fund for Fundamental Research (Grants 97-02-16622 and 97-02-17587) is gratefully acknowledged.

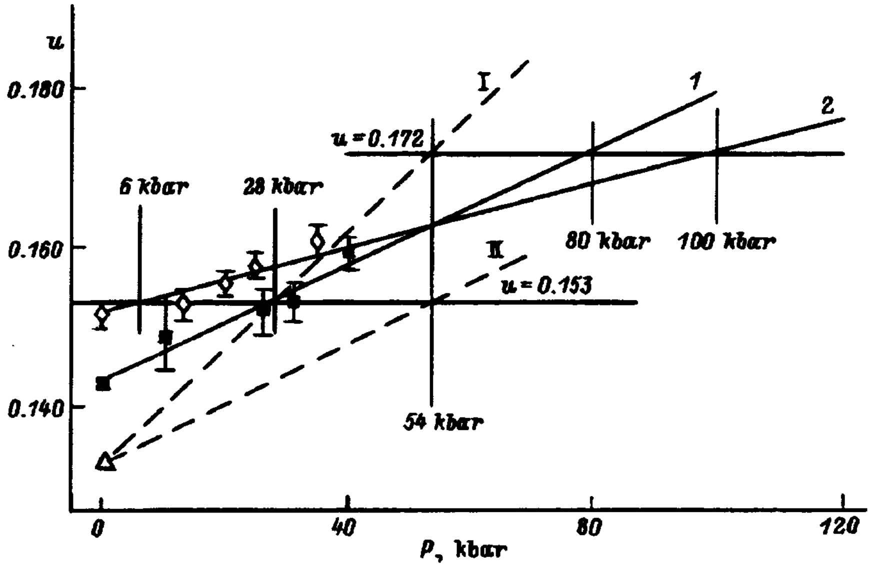

FIG. 6. Pressure dependences of the deuterium position parameter for (*1*) ND_4Br and (*2*) ND_4Cl and conjectured dependences for ND_4I (I and II). The phase transitions are shown to occur at the same values of the position parameter.

[1] M. A. Anisimov, V. M. Zaprudskiĭ, G. A. Mil'ner, and E. I. Ponomarenko, Zh. Éksp. Teor. Fiz. **80**, 787 (1981) [Sov. Phys. JETP **53**, 397 (1981)].

[2] C. W. F. T. Pistorius, Prog. Solid State Chem. **11**, 1 (1976); J. Chem. Phys. **50**, 1436 (1969).

[3] A. Schwake, K. R. Hirsch, and W. B. Holzapfel, J. Chem. Phys. **75**, 2532 (1981).

[4] A. M. Heyns, K. R. Hirsch, and W. B. Holzapfel, Solid State Commun. **29**, 351 (1979).

[5] A. M. Heyns, K. R. Hirsch, and W. B. Holzapfel, J. Chem. Phys. **73**, 105 (1980).

[6] O. Schulte and W. B. Holzapfel, High Press. Res. **4**, 321 (1990).

[7] A. M. Balagurov, B. N. Savenko, A. V. Borman, V. P. Glazkov, I. N. Goncharenko, V. A. Somenkov, and G. F. Syrykh, High Press. Res. **14**, 55 (1995).

[8] V. L. Aksenov, A. M. Balagurov, S. L. Platonov, B. N. Savenko, V. P. Glazkov, I. V. Naumov, V. A. Somenkov, and G. F. Syrykh, High Press. Res. **14**, 181 (1995).

[9] V. P. Glazkov and I. N. Goncharenko, Fiz. Tekh. Vys. Davl. **1**, 56 (1991).

[10] S. N. Vaidya and G. C. Kennedy, J. Phys. Chem. Solids **32**, 951 (1971).

[11] W. Press, J. Eckert, D. E. Cox, C. Rotter, and W. Kamitakahara, Phys. Rev. B **14**, 1983 (1976).

[12] P. Anderson and R. G. Ross, J. Phys. C **20**, 4737 (1987).

Translated by G. Skrebtsov

On electrostatic models of a metal-insulator phase transition in crystalline semiconductors with hydrogen-like impurities

N. A. Poklonskiĭ and A. I. Syaglo

Belorussian State University, 220050 Minsk, Belorus

(Submitted August 5, 1997)
Fiz. Tverd. Tela (St. Petersburg) **40**, 147–151 (January 1998)

Two well-known models for calculating the critical density N_C of a metal-insulator transition, as a function of the Bohr radius a_H of an isolated impurity as temperature $T \rightarrow 0$ K, are refined by making allowance for the screening of ions by electrons hopping along impurities. In one model, the transition at N_{C1} is explained by the appearance of delocalized electrons as the impurity band is displaced into the allowed-energy band as a result of a decrease in the electron (hole) affinity of ionized impurities. In the other model the transition is explained by an unbounded increase in the static permittivity of the crystal as the density of impurity atoms increases to N_{C2}. The obtained approximations $N_{C1}^{1/3} a_H \approx 0.24$ and $N_{C2}^{1/3} a_H \approx 0.20$ for the degree of compensation $K=0.01$ describe existing experimental data for $1 < a_H < 10$ nm. © *1998 American Institute of Physics.* [S1063-7834(98)03401-7]

1. The critical dopant density N_C at which a metal-insulator transition occurs is determined experimentally by the vanishing of the static conductivity on the metal side at $N_C = N_{C1}$ for $T \rightarrow 0$ K.[1–10] In the experiments of Refs. 10–12, the criterion for finding N_C is that the static permittivity of the crystal sample inreases without bound as the dopant density inceases to $N_C = N_{C2}$. It is thought[5,10] that $N_{C1} \approx N_{C2}$.

Models elaborating the well-known approaches (see, for example, Refs. 5 and 10) to estimating N_{C1} have been proposed recently.[13–17] In Ref. 13, the metal-insulator transition for $T \rightarrow 0$ is attributed to the "metallization" of the impurity band, which lies far from the allowed-energy band. In Ref. 14, allowance is made for screening of ions by free electrons only; the transition occurs as a result of an interaction of neutral and ionized donors, resulting in broadening and displacement of their levels into the c band. According to Ref. 15, a semiconductor passes into a metallic state when a possibility for growth of so-called "plasma metal drops"—regions of the semiconductor where donors are comlpetely ionized and the electron gas is degenerate—appears. In Refs. 16 and 17, the metal-insulator transition in strongly compensated semiconductors is explained by percolation of c-band electrons (on the metal side of the transition) and their localization in large-scale fluctuations of the random potential (on the dielectric side).

In the model of Ref. 18, adjustable parameters (in the dependence of the ionization energy of the dopants on their density) were used to find N_{C2}, and in Ref. 19 only a scheme for estimating N_{C2} in terms of the charge-carrier mobility threshold is proposed.

We note that in the models of Refs. 5 and 10–19 estimates of the values of N_{C1} and N_{C2} were considered separately. Moreover, in the interpretation of the experimental data on the dependence of N_{C1} and N_{C2} on the parameters of the semiconductor and the impurity atoms different expressions were used for the Bohr localization radius of an electron (hole)

$$a_H = \frac{e^2}{8\pi\varepsilon I_d}, \tag{1}$$

$a_H = 4\pi\varepsilon\hbar^2/me^2$, $a_i = \hbar\sqrt{2mI_d}$ (where I_d is the ionization energy of an isolated hydrogen-like impurity), $\varepsilon = \varepsilon_r\varepsilon_0$ is the static permittivity of the undoped crystal, ε_0 is the permittivity of empty space, m is the effective electron mass in one valley of the c-band (holes in one subband of the v-band), e is the electron charge, and for a free hydrogen atom $a_H = a_B = a_i$. It seems that a_H is better for describing bound states on the insulator side of the transition, since it does not include the effective electron (hole) mass, which has a straightforward meaning only for a delocalized state.

Our objective in the present paper is to refine the expressions for calculating the dependence of the critical densities N_{C1} and N_{C2} of the metal-insulator transition in weakly compensated semiconductors as a function of the Bohr radius a_H of the dopants.

2. Let us examine a n-type semiconductor in the limit $T \rightarrow 0$ with hydrogen-like donor density $N = N_0 + N_+$ and compensation K of donors by acceptors. The equation of electric neutrality is

$$N_+ = KN + n, \tag{2}$$

where n is the density of free (delocalized) electrons.

We assume that in the limit $T \rightarrow 0$ the average density of ionized donors

$$N_+ = N - N_0 = N\int_{E_F+E_d}^{\infty} = \frac{N}{2}\operatorname{erfc}\left(\frac{E_F+E_d}{\sqrt{2}W_d}\right) \tag{3}$$

is determined by the Gaussian distribution

$$P_d = (\sqrt{2\pi}E_d)^{-1}\exp(U_d^2/2W_d^2)$$

of the ionization energies of neutral donors relative to the mean value E_d; the Fermi level E_F and E_d are measured from the energy of the c-band bottom ($E_c = 0$) of the undoped crystal.

Assuming that the ionized donors and acceptors are point charges, the rms fluctuation W_d of the potential energy U_d of an ionized donor, assuming a purely Coulomb interaction of the donor only with the nearest point charge, is[20]

$$W_d\left(\sum_{j=1}^{3}\int_0^\infty P_j u_j^2 dr\right)^{1/2}\approx 1.64\frac{e^2}{4\pi\varepsilon}\left(\frac{8\pi}{3}N_+\right)^{1/3}, \tag{4}$$

where $P_j dr = 4\pi r^2 C_j \exp[-(4\pi/3)r^3\Sigma_{j=1}^3 C_j]dr$ is the Poisson probability that a point charge of the j-th kind located at a distance from r to $r+dr$ is closest to the ionized donor; $\Sigma_{j=1}^3 C_j = N_+ + KN + n = 2N_+$ is the charged-particle density in the crystal; $|u_j(r)| = e^2/4\pi\varepsilon r$ is the modulus of the Coulomb interaction energy of the two closest charges; and, $\overline{U_d} = \Sigma_{j=1}^3 \int_0^\infty P_j u_j dr = 0$.

We note that, assuming complete ionization of the impurities, W from Eq. (4) agrees with the value of the width, measured at temperature $50\ \mathrm{K} < T < 120\ \mathrm{K}$ by the method of capacitance-voltage characteristics, of the acceptor band formed in p-Si by boron atoms with density $N \approx 2\times 10^{18}\ \mathrm{cm}^{-3}$.[21]

The electron density in the c-band in the limit $T\to 0$ is, neglecting the exchange energy of the electrons,[22,23]

$$n=\int_{-\infty}^{E_F}P_n dU_n\int_0^{k_F(U_n)}\frac{\nu k^2}{\pi^2}dk=\frac{\nu(2m)^{3/2}}{3\pi^2\hbar^3}\times\int_{-\infty}^{E_F}(E_F-U_n)^{3/2}P_n dU_n, \tag{5}$$

where $P_n = (\sqrt{2\pi}W_n)^{-1}\exp(-U_n^2/2W_n^2)$ is the Gaussian distribution of the potential energy of an electron delocalized over the crystal; ν is the number of equivalent valleys (minima of the kinetic energy for different values of the quasimomentum $\hbar k$ in the Brillouin zone); and, $\overline{U_n} = 0$.

We shall now take account of the fact that on the insulator side of the transition the thermal wavelength $\pi\hbar/\sqrt{3mk_BT}$ of a free electron over which averaging of the random electric potential occurs[24] is much longer than $R = (8\pi N_+/3)^{-1/3}$—the average radius of the region containing a single charged point particle. Then $E_n \ll W_d$ and the tail of the electronic density of states of the c-band can be neglected in the limit $T\to 0$. On the metal side of the transition ($n\approx N$) in an ideal Fermi gas the wavelength of an electron with average energy $3E_F/5$ equals $\sqrt{5/3}\pi/(3\pi^2 n/\nu)^{1/3}$ and is comparable to R, so that $W_n \approx W_d$.

So, following the arguments given in Ref. 24, we employ for the rms fluctuation of the potential energy of an electron in the c-band the approximation

$$W_n = W_d\,\theta(N-N_{C1}), \tag{6}$$

where $\theta(N-N_{C1}) = 0$ for $N \leqslant N_{C1}$ and $\theta(N-N_{C1}) = 1$ for $N > N_{C1}$.

Next, we take into account the fact that the ionization energy E_d, appearing in Eq. (3), of an ''average'' donor depends on the density of dopants and compensating impurities.[25] The correlation interaction of mobile, positively charged, donor states (i.e. electronic vacancies migrating by hopping), stationary negatively charged acceptors, and free electrons decreases the donor ionization energy. According to Ref. 20, the energy difference between an ionized donor with the charge cloud screening it and a neutral donor determines the average ionization energy[1)]

$$E_d = I_d - \frac{3e^2}{16\pi\varepsilon(\lambda+d)}, \tag{7}$$

where λ is the screening length of an ionized donor, $d \approx 0.554(N(1+K))^{-1/3}\theta(N_{C1}-N)$ is the average minimum distance between charged point particles in the crystal in the case of the hopping mechanism of electron migration along donors; $d=0$ on the metal side of the transition. The quantity $I_d - E_d$ can be interpreted as the decrease in the electron affinity of a positively charged donor as a result of screening of the donor.

In the limit $T\to 0$ the screening length λ of the electrostatic field[27] is

$$\lambda^{-2} = -\frac{e^2}{\varepsilon}\left(\frac{\partial N_+}{\partial E_F}-\frac{\partial n}{\partial E_F}\right) = \frac{e^2}{\varepsilon}\left(\frac{N}{\sqrt{2\pi}W_d}\exp\left(-\frac{(E_F+E_d)^2}{2W_d^2}\right)+\frac{\partial n}{\partial E_F}\right), \tag{8}$$

where the first term reflects the contribution of electrons which hop from neutral to ionized donors to the screening and the second term reflects the contribution of free electrons.

We note that the calculation of W_d, λ, and E_d neglected the contribution of neutral donors to the permittivity ε of the crystal lattice.

Let us now examine the ''insulator'' solution ($n=0$) of the system of equations (2)–(8), where Eq. (3) gives a unique relation between the degree of compensation K of donors by acceptors and the ration $(E_F+E_d)/W_d$. As N increases, the Fermi level E_F approaches the c-band and reaches $E_C = 0$ at donor density $N = N_{C1}$. As a result, besides electrons hopping along donors, free electrons also participate in the screening. In consequence, E_d rises sharply above the c-band bottom (then, formally, $E_d < 0$ and the Bohr radius a_B must be used on the metal side of the transition). Then, λ becomes less than the critical screening length of the Coulomb potential $\lambda_c = a_B/1.16$ at which an ion has no bound electronic states.[28] In other words, as N varies continuously, the solution of the system of equations (2)–(8) jumps from an insulator state ($n=0$) to a metal state ($n=(1-K)N$). This is a metal-insulator transition. The Mott criterion[29] of the transition is

$$E_F(N_C) = 0. \tag{9}$$

In our model, the quantity N_{C1} implicitly depends on the Bohr radius a_H of a hydrogen-like impurity (compare Refs. 15 and 17). The threshold for delocalization of c-band electrons on the insulator side of the transition coincides with $E_C = 0$. Near the transition on the metal side, as a result of the appearance of the tails of the c-band density of states ($W_n \approx W_d$), the Fermi level lies below E_C but above the mobility threshold.

We note that for some values $N < N_{C1}$ the system of equations (2)–(8) has, besides an insulator solution, a metal solution also. According to Ref. 30, the solution determining the equilibrium state of the system is determined by minimizing the free energy, the minimum being equal to the energy of the system in the limit $T \rightarrow 0$. Near the metal–insulator transition on the insulator side the volume free-energy density F of electrons on donors and in the c-band is obtained from Eqs. (2) and (5) in the form

$$F = N \int_{-\infty}^{E_F + E_d} (U_d - E_d) P_d dU_d + \frac{\nu (2m)^{3/2}}{2\pi^2 \hbar^3} \int_{-\infty}^{E_F} P_n dU_n \int_{U_n}^{E_F} (E - U_n)^{1/2} E dE, \quad (10)$$

where the energy is measured from $F_C = 0$.

It follows from Eq. (10) that for all N for which there exist two solutions of the system of equations (2)–(8) F is less for the insulator solution N_{C1}.

We note that in Refs. 14 and 19 hysteresis of the solution of the electric-neutrality equation was also observed in the N-dependence of n when screening of the impurity ions only by conduction electrons is taken into account, but in Ref. 14 it was not determined which solution is stable and in Ref. 19 the stability criterion was expressed in terms of the electron mobility threshold.

In Refs. 11 and 12 the insulator-metal transition for $T \rightarrow 0$ is determined experimentally from the condition that the static permittivity $\varepsilon_\alpha = \varepsilon_{r\alpha} \varepsilon_0$ of a macroscopic crystalline sample inceases without bound as $N \rightarrow N_{C2}$; the criterion for a transition has the form

$$\varepsilon_{r\alpha}(N_C) \rightarrow \infty. \quad (11)$$

The quantity $\varepsilon_{r\alpha}$ relates the local electric field E_l acting on each polarizable particle with the average macroscopic field E_{av}.[31,32] Taking account of the superposition of the electric fields of both the atoms of the crystal matrix with density N_h and $(1-K)N$ neutral donors with polarizability α, we have (compare with Refs. 18 and 33)

$$E_l = E_{\text{av}} + \left(\frac{N_h \alpha_h}{\beta_h} + \frac{(1-K)N\alpha}{3} \right) E_l, \quad (12)$$

where α_h is the polarizability of a matrix atom and β_h takes account of the point symmetry of the undoped crystal (in the Clausius-Mossotti model $\beta_h = 3$).

The polarizability of a neutral hydrogen-like donor[34] is

$$\alpha = 18\pi [a_H(N)]^3, \quad (13)$$

where $a_H(N) = e^2/8\pi\varepsilon_r\varepsilon_0 E_d$ is the Bohr radius of a donor with average ionization energy $E_d(N)$ according to Eq. (7). According to the data in Refs. 5, 11, and 12, for $N < N_{C2}$ the average radius $0.62[(1-K)N]^{-1/3}$ of the spherical region containing one neutral donor is more than 2.5 times greater than $a_H(N)$, so that we are justified in using the lattice permittivity $\varepsilon = \varepsilon_r \varepsilon_0$ in $a_H(N)$.

The total polarizability of matrix atoms and neutral donors is[32]

$$(N_h \alpha_h + (1-K)N_\alpha)\varepsilon_0 E_l = (\varepsilon_{r\alpha} - 1)\varepsilon_0 E_{\text{av}}. \quad (14)$$

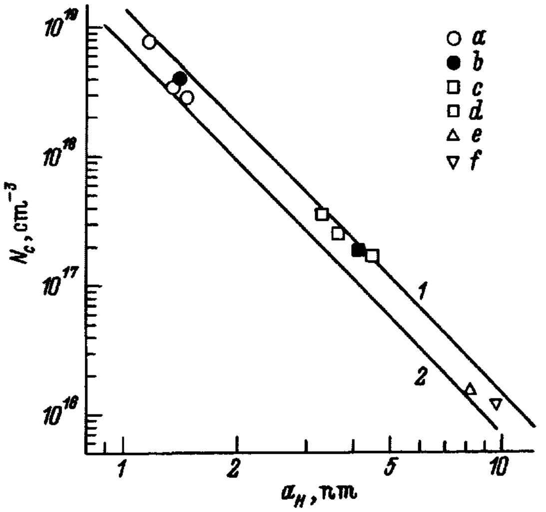

FIG. 1. Critical density N_C of metal–insulator transition versus Bohr radius a_H of an isolated impurity for Si:As,[1] Si:P,[2] Si:Sb,[3] (a); Si:B[4] (b), Ge:As,[5] Ge:P,[5] Ge:sb[6] (c), Ge:Ga[7,8] (d), n-InP[9] (e), n-GaAs[9] (f). Curves *1, 2*—calculation of N_{C1} and N_{C2} at $K = 0.01$.

Setting $\beta_h = 3$ (as if the matrix atoms formed a simple cubic lattice or were distributed randomly[32]), we have from Eqs. (12) and (14)

$$\varepsilon_{r\alpha} = \varepsilon_r + \frac{(\varepsilon_r + 2)^2 (1-K)N\alpha}{9 - (\varepsilon_r + 2)(1-K)N\alpha}. \quad (15)$$

According to Eq. (15), the condition (11) for a metal-insulator transition assumes the form

$$N_{C2} = \frac{9}{(\varepsilon_r + 2)(1-K)\alpha}. \quad (16)$$

According to the models of Refs. 33 and 18 for $\varepsilon_{r\alpha}(N)$, the critical density N_{C2} is $\varepsilon_r(\varepsilon_r + 2)/3$ and ε_r times larger than the value given by Eq. (16) for the same values of α. We note that in Ref. 18 adjustable parameters were used in the dependence of ε_d on N in order to make $\varepsilon_{r\alpha}(N)$ agree with experiment.

3. Figure 1 shows the critical densities N_{C1} for a metal-insulator transition as a functon of the Bohr radius a_H of the impurity according to Eq. (1) for Si ($\varepsilon_r = 11.47$) doped with the following atoms: As($I_d = 53.8$ meV, $N_{C1} \approx 7.8 \times 10^{18}$ cm^{-3}),[1] P($I_d = 45.6$ meV, $N_{C1} \approx 3.5 \times 10^{18}$ cm^{-3}),[2] Sb($I_d = 42.7$ meV, $N_{C1} \approx 2.9 \times 10^{18}$ cm^{-3}),[3] B($I_a = 44.4$ meV, $N_{C1} \approx 4.1 \times 10^{18}$ cm^{-3});[4] for Ge($\varepsilon_r = 15.4$) doped with the following atoms: As($I_d = 14.2$ meV, $N_{C1} \approx 3.5 \times 10^{17}$ cm^{-3}),[5] P($I_d = 12.88$ meV, $N_{C1} \approx 2.5 \times 10^{17}$ cm^{-3}),[5] Sb($I_d = 10.45$ meV, $N_{C1} \approx 1.7 \times 10^{17}$ cm^{-3}),[6] Ga($I_a = 11.32$ meV, $N_{C1} \approx 2 \times 10^{17}$ cm^{-3});[7,8] for n-InP ($\varepsilon_r = 11.8$, $I_d \approx 7$ meV, $N_{C1} \approx 1.5 \times 10^{16}$ cm^{-3})[9] and for n-GaAs ($\varepsilon_r = 12.4$, $I_d \approx 6$ meV, $N_{C1} \approx 1.2 \times 10^{16}$ cm^{-3}).[9] The values of N_{C2} for Si:As, Si:P, Si:Sb, and Ge:Sb[11,12] are actually equal to N_{C1}. The curves *1* and *2* represent the calculations of N_{C1} and N_{C2} according to Eqs. (9) and (16) with $K = 0.01$. The curve *1* for N_{C1} in the chosen coordinates does not depend on the dielectric characteristics of the material. For the curve *2* (N_{C2} versus a_H) it was assumed that $\varepsilon_r = 12$, which corresponds to the average relative permittivity of the crystal lattice of the semiconductors listed above.[35,36] The curves *1* and *2* are approximated by

$$N_{C1}^{1/3}a_H\approx 0.24,\quad N_{C2}^{1/3}a_H\approx 0.20.. \tag{17}$$

A relation similar to Eqs. (17) was obtained in Ref. 5 from an analysis of experimental data on N_C versus the Bohr radius of impurities in different semiconductors.

We note that N_{C1} and N_{C2} given by the expressions (17) agree with the value $N_{C1}\approx 10^{14}$ cm^{-3} presented in Ref. 5 for n-InSb ($\varepsilon_r\approx 17.8$, $I_d\approx 0.7$ meV, $a_H\approx 5.8$ nm).

The proposed models describe a metal–insulator transition at finite K, when there is a possibility for hopping migration of electrons (electronic vacancies) along impurity atoms even as the temperature $T\to 0$ K. In the compensation range $0.01\leqslant K\leqslant 0.2$, N_C is virtually constant and increases as K increases from 0.2 to 0.5 (N_{C1} more strongly and N_{C2} more weakly), in qualitative agreement (especially N_{C1}) with the experimental compensation dependence $N_C(K)$.[37] For $K>0.5$, the model overestimates the values of N_{C1} compared with the experimental data,[37,38] since it neglects the fluctuations of the c- and v-band edges on the insulator side of the transition.

Our models for calculating N_{C1} and N_{C2} are inapplicable for $K\to 0$ as the temperature $T\to 0$, since they neglect the contribution of the interaction of neutral donors with one another to W and E_d. In consequence, the upper Hubbard band is neglected in the calculations, i.e. the existence of donors in a negatively charged state.

4. In summary, in the present work two well-known electrostatic models of the metal-insulator transition for strongly doped crystalline semiconductors in the limit $T\to 0$ were refined. Approximate relations (17) were given for the critical dopant densities N_{C1} and N_{C2} of the transition in the electric conductivity and in permittivity with compensation $0.01\leqslant K\leqslant 0.5$ in the range of Bohr radii of isolated impurities $1<a_H<10$ nm.

We are grateful to A. G. Zabrodskiĭ for helpful remarks concerning this work.

This work was performed as part of the program ‘‘Low-dimensional systems’’ of the Ministry of Education of the Republic of Belorus. One of us (N.A.P.) thanks the INTAS program (Grant INTAS-94-4435) for support.

1) The equation (7) is supported by the experimental data on E_d for hydrogen-like impurities in lightly doped semiconductors,[25,26] specifically, when the width W_d of the impurity band is much larger than the average thermal energy $3k_BT/2$.

---

[1] P. F. Newman and D. F. Holcomb, Phys. Rev. B **28**, 638 (1983).
[2] P. Dai, Y. Zhang, and M. P. Sarachik, Phys. Rev. B **49**, 14039 (1994).
[3] A. P. Long and M. Pepper, J. Phys. C **17**, L425 (1984).
[4] P. Dai, S. Bogdanovich, Y. Zhang, and M. P. Sarachik, Phys. Rev. B **52**, 12434 (1995).
[5] P. P. Edwards and M. J. Sienko, Phys. Rev. B **17**, 2575 (1978).
[6] S. B. Field and T. F. Rosenbaum, Phys. Rev. Lett. **55**, 522 (1985).
[7] A. G. Zabrodskiĭ, A. G. Andreev, and M. V. Alekseenko, Fiz. Tekh. Poluprovodn. **26**, 431 (1992) [Sov. Phys. Semicond. **26**, 244 (1992)].
[8] K. M. Itoh, E. E. Haller, L. A. Reichertz, E. Kreysa, T. Shutt, A. Commings, W. Stockwell, B. Sadoulet, J. Muto, J. W. Farmer, and V. I. Ozhogin, in *Abstract Booklet of the International Conference on Electron Localization and Quantum Transport in Solids (August 3–6, 1996)*, Inst. Phys. Pol. Acad. Sci. Ustron., Jaszowiec, Poland, 1996, p. 15.
[9] T. I. Voronina, A. N. Dakhno, O. V. Emel’yanenko, T. S. Lagunova, and S. P. Starosel’tseva, Fiz. Tekh. Poluprovodn. **22**, 1230 (1988) [Sov. Phys. Semicond. **22**, 779 (1988)].
[10] R. N. Bhatt, Physica B **146**, 99 (1987).
[11] T. G. Castner, Philos. Mag. B **42**, 873 (1980).
[12] T. G. Castner, N. K. Lee, H. S. Tan, L. Moberly, and O. Symko, J. Low Temp. Phys. **38**, 447 (1980).
[13] A. A. Likal’ter, Zh. Éksp. Teor. Fiz. **107**, 1996 (1995) [JETP **80**, 1105 (1995)].
[14] V. M. Mikheev, Fiz. Tverd. Tela (St. Petersburg) **36**, 994 (1994) [Phys. Solid State **36**, 540 (1994)].
[15] D. N. Bychkovskiĭ, O. V. Konstantinov, and B. V. Tsarenko, Fiz. Tekh. Poluprovodn. **29**, 152 (1995) [Semiconductors **29**, 80 (1995)].
[16] A. G. Zabrodskiĭ, Fiz. Tekh. Poluprovodn. **14**, 1492 (1980) [Sov. Phys. Solid State **14**, 1245 (1980)].
[17] M. I. Daunov, I. K. Kamilov, and V. A. Elizarov, Fiz. Tverd. Tela (St. Petersburg) **37**, 2276 (1995) [Phys. Solid State **37**, 1245 (1995)].
[18] S. Dhar and A. H. Marshak, Solid-State Electron. **28**, 763 (1985).
[19] J. Jackle, Philos. Mag. B **46**, 313 (1982).
[20] N. A. Poklonskiĭ, A. I. Syaglo, and F. N. Borovik, Fiz. Tekh. Poluprovodn. **30**, 1767 (1996) [Semiconductors **30**, 924 (1996)].
[21] H. D. Barder, K. S. Lee, and J. E. Jones, Solid-State Electron. **19**, 365 (1976).
[22] E. O. Kane, Solid-State Electron. **28**, 3 (1985).
[23] N. A. Poklonskiĭ and A. I. Syaglo, Zh. Prikl. Spektrosk. **64**, 363 (1997).
[24] J. Ziman, *Models of Disorder: The Theoretical Physics of Homogeneously Disordered Systems* [Cambridge University Press, Cambridge, 1979; Mir, Moscow, 1982] p. 574.
[25] A. G. Andreev, V. V. Voronov, G. I. Voronkova, A. G. Zabrodskiĭ, and E. A. Petrova, Fiz. Tekh. Poluprovodn. **29**, 2218 (1995) [Semiconductors **29**, 1157 (1995)].
[26] L. V. Govor, V. P. Dobrego, and N. A. Poklonskiĭ, Fiz. Tekh. Poluprovodn. **18**, 2075 (1984) [Sov. Phys. Semicond. **18**, 1292 (1984)].
[27] N. A. Poklonskiĭ, Izv. Vyssh. Uchebn. Zaved. Fiz. **27**, 41 (1984).
[28] M. Dineĭkhan and G. V. Efimov, Fiz. Elem. Chastits At. Yadra **26**, 651 (1995).
[29] N. F. Mott, *Metal–Insulator Transitions* [Russian translation], Nauka, Moscow, 1979.
[30] L. D. Landau and E. M. Lifshitz, *Statistical Physics* [Pergamon Press, New York; Nauka, Moscow, 1976] p. 67.
[31] V. G. Ginzburg and E. G. Maksimov, Sverkhprovodimost’ **5**, 1543 (1992).
[32] I. E. Tamm, *The Principles of the Theory of Electricity* [in Russian], Nauka, Moscow, 1989, p. 100.
[33] G. M. Castellan and F. Seitz, in *Proceedings of Conference on Semiconducting Materials*, Butterworths, London, 1951.
[34] L. D. Landau and E. M. Lifshitz, *Quantum Mechanics* [Pergamon Press, New York; Nauka, Moscow, 1989] p. 343.
[35] O. Madelung [Ed.], *Semiconductors: Group IV Elements and III–V Compounds*, Springer-Verlag, Berlin, 1991.
[36] T. M. Lifshits, Prib. Tekh. Eksp. **1**, 10 (1993).
[37] A. G. Zabrodskiĭ, M. V. Alekseenko, and A. G. Andreev, in *25th All-Union Conference on Low-Temperature Physics* [in Russian], Physicotechnical Institute, Leningrad, 1988, Pt. 3, p. 60.
[38] H. Fritzsche, Philos. Mag. B **42**, 835 (1980).

Translated by M. E. Alferieff

Dephasing of local vibrations of a two-dimensional dipole system

V. M. Rozenbaum

Institute of Surface Chemistry, Ukrainian Academy of Sciences, 252022 Kiev, Ukraine

(Submitted March 31, 1997)
Fiz. Tverd. Tela (St. Petersburg) **40**, 152–155 (January 1998)

Anharmonically coupled, high- and low-frequency branches of vibrational excitations of a two-dimensional dipole system on a substrate are studied. It is shown that independent low-frequency resonance modes characterized by a two-dimensional wave vector belonging to the first Brillouin zone of the dipole lattice arise as a result of the harmonic interaction of phonons in the dipole system and in the substrate. The positions and widths of the spectral lines of the high-frequency local vibrations, which in the general case depend on the dispersion laws and lifetimes of the resonance modes, are calculated for low-temperature orientational states of degenerate dipoles on triangular and square lattices. © *1998 American Institute of Physics.* [S1063-7834(98)03601-6]

The anisotropy and long range of dipole-dipole interactions in two-dimensional lattice systems of different orientationally-mobile polar objects[1,2] lead to nontrivial dispersion laws for low-frequency excitations. For example, the frequency distribution function of orientational vibrations of a triangular lattice of degenerate dipoles at low temperatures T is proportional to the 3/2 power of the frequency[3] whereas for a square lattice, as a result of the ordering effect of thermodynamic fluctuations, the distribution function vanishes in a definite range of low frequencies that is proportional to $T^{1/2}$.[4–6] The most convenient method for detecting such excitations is to measure the spectroscopic characteristics of easily observable local vibrations associated with a change in the absolute values of the dipole moments.

Substantial progress in describing local vibrations of adsorbed molecules has been made on the basis of an exchange dephasing model,[7,8] in which allowance is made for the biquadratic anharmonic coupling $u_r^2 u_\varphi^2$ between the displacement u_r of a high-frequency vibration of the molecule and the displacement u_φ of a low-frequency resonance vibration.[9] This model made it possible to obtain a number of exact solutions[10–12] describing the shape of the spectral line of a local vibration and also to take into account the degeneracy of the low-frequency deformation vibrations and their intrinsic anharmonicity.[13,14] The presence of other types of anharmonic coupling, for example, of the form $u_r u_\varphi^2$, affects only the renormalization of the biquadratic anharmonicity constant.[15] This enables wide use of this model for describing experimental spectra by matching the required values of the parameters.

In the case when the density of adsorbed molecules is quite high, their vibrational modes become collectivized[3,16] and undergo additional frequency shifts as a result of the vibrational Stark effect produced by the static electric fields of neighboring polar molecules.[17] Dephasing of collectivized high-frequency modes of an adsorbate on noninteracting low-frequency resonance vibrations of molecules was studied in Ref. 18. On the other hand, it is well known that the formation of ordered structures of adsorbed molecules with orientations tilted with respect to the surface (as, for example, in the system CO and CO_2 on a NaCl (100) surface[19,20]) results in a strong interaction of the low-frequency deformation modes of the adsorbate[21] that should be especially sensitive to orientational phase transitions occurring in such systems.

In the present paper it is shown that the states of a system consisting of substrate phonons and laterally interacting low-frequency vibrations of adsorbed polar molecules that are harmonically coupled with the substrate can be divided into independent groups of states classified according to a wave vector **K** belonging to the first Brillouin zone of a two-dimensional dipole lattice. Since the phonon density of states in the substrate is many times higher than the density of the vibrational modes of the adsorbate, in the **K**-dependent group of states each adsorption mode is associated with a quasicontinuous phonon spectrum. This makes it possible to regard the low-frequency collectivized mode $\omega_\varphi(\mathbf{K})$ of the adsorbate as a resonance vibration with a renormalized frequency $\tilde{\omega}_\varphi(\mathbf{K})$ and inverse lifetime $\eta_{\mathbf{K}}(\tilde{\omega}_\varphi(\mathbf{K}))$. The parameters introduced appear in the equations of the exchange dephasing model with interacting low-frequency modes. In many cases, the width of the band $\omega_r(\mathbf{K})$ of local vibrations and the magnitude $\eta_{\mathbf{K}}(\tilde{\omega}_\varphi(\mathbf{K}))$ of the resonance are much smaller than the widths of the bands of the low-frequency vibrations of the adsorbate. Then low-temperature asymptotic expressions can be easily obtained for the shift and width of the spectral line of the local vibrations. In the present paper such expressions are presented for a system of degenerate dipoles on triangular and square lattices.

We shall represent the complete Hamiltonian of the vibrational excitations of a system consisting of high- and low-frequency modes of a dipole system and substrate phonons in the form

$$H = H_r + H_l + H_{\mathrm{anharm}}, \quad H_l = H_\varphi + H_S + H_{\mathrm{int}}. \tag{1}$$

Here H_r and H_φ are the Hamiltonians of the high- and low-frequency vibrations of the adsorbed molecules interacting via a dipole-dipole interaction:

$$\begin{aligned}H_{r,\varphi}=&\sum_{\mathbf{R}}\frac{p^2_{r,\varphi}(\mathbf{R})}{2m_{r,\varphi}}+\frac{1}{2}\sum_{\mathbf{R},\mathbf{R}'}[m_{r,\varphi}\omega^2_{r,\varphi}\delta_{\mathbf{R},\mathbf{R}'}\\&+\Phi_{r,\varphi,\mathrm{lat}}(\mathbf{R}-\mathbf{R}')]u_{r,\varphi}(\mathbf{R})u_{r,\varphi}(\mathbf{R}')\\&=\sum_{\mathbf{K}}\hbar\omega_{r,\varphi}(\mathbf{K})[b^+_{r,\varphi}(\mathbf{K})b_{r,\varphi}+1/2],\end{aligned}\qquad(2)$$

$u_{r,\varphi}(\mathbf{R})$ and $p_{r,\varphi}(\mathbf{R})$ are the displacements and generalized momenta of the molecular vibrations with a high frequency ω_r and a low frequency ω_φ at the $\mathbf{R}$-th site of the adsorption lattice, which are characterized by the reduced masses m_r and m_φ; $b^+_{r,\varphi}(\mathbf{K})$ and $b_{r,\varphi}(\mathbf{K})$ are creation and annihilation operators for the collectivized adsorbate modes with squared frequencies $\omega^2_{r,\varphi}(\mathbf{K})=\omega^2_{r,\varphi}+\tilde{\Phi}_{r,\varphi,\mathrm{lat}}(\mathbf{K})/m_{r,\varphi}$, where $\tilde{\Phi}_{r,\varphi,\mathrm{lat}}(\mathbf{K})$ are the Fourier components if the force-constant functions $\Phi_{r,\varphi,\mathrm{lat}}(\mathbf{R})$, which depend on the orientations of the corresponding vibrational displacements. The quantity H_{h-l} describes the biquadratic anharmonic interaction

$$H_{h-l}=\Phi_4\sum_{\mathbf{R}}u_f^2(\mathbf{R})u_\varphi^2(\mathbf{R})\qquad(3)$$

(Φ_4 is the corresponding anharmonicity constant), H_S describes the substrate phonons and is given by

$$H_S=\sum_{\mathbf{k}_\parallel,\sigma}\hbar\omega_S(\mathbf{k}_\parallel,\sigma)(b^+_{\mathbf{k}_\parallel,\sigma}b_{\mathbf{k}_\parallel,\sigma}+1/2),\qquad(4)$$

and H_{int} gives the harmonic coupling of the low-frequency vibrations of the adsorbate and substrate

$$H_{\mathrm{int}}=\sum_{\mathbf{R},\alpha,\beta}\Phi^{\alpha\beta}_{\mathrm{int}}e^\alpha_\varphi u_\varphi(\mathbf{R})u^\beta_S(\mathbf{R}),\qquad(5)$$

where e_φ is a unit vector of the orientation of the vibrations $u_\varphi(\mathbf{R})$, $u^\beta_S(\mathbf{R})$ is the Cartesian projection of the displacement of a substrate atom possessing mass M and located at the site $\mathbf{R}$ of the adsorption lattice onto the β axis, and Φ_{int} is the corresponding matrix of force constants.

The quantum states of the phonons in the representation (4) are characterized by a longitudinal (with respect to the plane of the surface) wave vector $\mathbf{k}_\parallel$; all other quantum numbers (which take account of the quasiparticle motion in the transverse direction, its polarization, and (implicitly) the structural arrangement of the atoms in the unit cell of the crystal) are denoted by σ. This representation is convenient because it enables immediate use of the translational symmetry of the system in the longitudinal direction and makes it possible to write the displacement $u_S(\mathbf{R})$ in the form

$$\begin{aligned}u^\alpha_S(\mathbf{R})&=(MN_0)^{-1/2}\sum_{\mathbf{k}_\parallel,\sigma}C^\alpha_{\mathbf{k}_\parallel,\sigma}e^{ik_\parallel\cdot\mathbf{R}}\tilde{u}_S(\mathbf{k}_\parallel,\sigma),\\ \tilde{u}_S(\mathbf{k}_\parallel,\sigma)&=\left(\frac{\hbar}{2\omega_S(\mathbf{k}_\parallel,\sigma)}\right)^{1/2}(b_{\mathbf{k}_\parallel,\sigma}+b^+_{-\mathbf{k}_\parallel,\sigma}),\end{aligned}\qquad(6)$$

where $C^\alpha_{\mathbf{k}_\parallel,\sigma}$ are unitary matrices that realize the transformation to normal coordinates $\tilde{u}_S(\mathbf{k}_\parallel,\sigma)$, and N_0 is the number of adsorption-lattice sites in the main region. Substituting into Eq. (5) the relations (6) and the analogous series expansion of $u_\varphi(\mathbf{R})$ in the wave vector $\mathbf{K}$ yields an expression containing the following sum:

$$\sum_{\mathbf{R}}e^{i(\mathbf{k}_\parallel+\mathbf{K})\cdot\mathbf{R}}=N_0\sum_{\mathbf{B}}\delta_{\mathbf{k}_\parallel+\mathbf{K},\mathbf{B}}.\qquad(7)$$

Here the summation over $\mathbf{B}=n_1\mathbf{B}_1+n_2\mathbf{B}_2$ extends over all nonequivalent integral linear combinations of the reciprocal adsorption-lattice vectors $\mathbf{B}_1$ and $\mathbf{B}_2$. Indeed, the first Brillouin zone for the vectors $\mathbf{k}_\parallel$ is determined by the unit cell of the crystal and, for this reason, can be larger than the first Brillouin zone for the adsorbate lattice. Thus, subgroups of vectors $\mathbf{B}-\mathbf{K}$ are formed from the entire collection of wave vectors $\mathbf{k}_\parallel$, and the expression (5) in the Heitler–London approximation, which simplifies all formulas below, assumes the form

$$H_{\mathrm{int}}=\hbar\sum_{\mathbf{K},\nu}[\chi_{\mathbf{K},\nu}b_\varphi(\mathbf{K})b^+_S(\mathbf{K},\nu)+\mathrm{h.c.}],\qquad(8)$$

where

$$\begin{aligned}\chi_{\mathbf{K},\nu}=&\frac{1}{2}[Mm_\varphi\omega_\varphi(\mathbf{K})\omega_S(\mathbf{B}-\mathbf{K},\sigma)]^{-1/2}\\&\times\sum_{\alpha,\beta}e^\alpha_\varphi\Phi^{\alpha\beta}_{\mathrm{int}}C^\beta_{\mathbf{B}-\mathbf{K},\sigma},\end{aligned}\qquad(9)$$

h.c. represents the hermitian conjugate of the first term, and the new quantum number ν corresponds to the collection of quantum number σ and $\mathbf{B}$.

The summation over $\mathbf{k}_\parallel$ and σ in Eq. (4) can also be represented as a sum over the variables $\mathbf{K}$ and ν, changing correspondingly the expressions for the variables in the summand also. Then, a fundamental result follows from Eqs. (1), (2), (4), and (8): The Hamiltonian H_l of the low-frequency adsorbate and substrate modes is a sum of the Hamiltonians $H_l(\mathbf{K})$, i.e. it is diagonal in the representation of the adsorbate wave vector $\mathbf{K}$. This makes it possible to switch independently in each diagonal block $H_l(\mathbf{K})$ to new normal coordinates, as done in, for example, Ref. 14, and to determine the spectral function of the low-frequency resonance vibrations of the system of adsorbed molecules

$$L_{\mathbf{K}}(\omega)=\frac{\tilde{\eta}_{\mathbf{K}}(\omega)}{[\omega-\omega_\varphi(\mathbf{K})-\tilde{P}_{\mathbf{K}}(\omega)]^2+\pi^2\tilde{\eta}^2_{\mathbf{K}}(\omega)},\qquad(10)$$

where

$$\begin{aligned}\tilde{\eta}_{\mathbf{K}}(\omega)&=\sum_\nu|\chi_{\mathbf{K}\boldsymbol{\nu}}|^2\delta(\omega-\omega_{\mathbf{K}\boldsymbol{\nu}}),\\ \tilde{P}_{\mathbf{K}}(\omega)&=\int_0^\infty\frac{\tilde{\eta}_{\mathbf{K}}(\tilde{\omega})d\tilde{\omega}}{\omega-\tilde{\omega}}.\end{aligned}\qquad(11)$$

The resonance frequency $\tilde{\omega}_\varphi(\mathbf{K})$ is found by setting to zero the expression in the square brackets in Eq. (10), and the resonance width equals $\eta_{\mathbf{K}}(\tilde{\omega}_\varphi(\mathbf{K}))=2\pi\tilde{\eta}_{\mathbf{K}}(\tilde{\omega}_\varphi(\mathbf{K}))$. The quantity $\tilde{P}_{\mathbf{K}}(\omega)$ describes in this case the interaction of the low-frequency molecular vibrations via the substrate.

In second-order perturbation theory with respect to the biquadratic anharmonicity constant Φ_4, the spectral function introduced above determines the position of the maximum and the width of the spectral line of the high-frequency vibrations of the adsorbate

$$\omega_0=\omega_r(0)+\frac{\gamma}{N_0}\sum_{\mathbf{K}}\int_{-\infty}^{\infty}d\omega[n(\omega)+1/2]L_{\mathbf{K}}(\omega), \quad (12)$$

$$2\Gamma_0=\frac{2\pi\gamma^2}{N_0^2}\sum_{\mathbf{K},\mathbf{K}'}\int_{-\infty}^{\infty}d\omega n(\omega)[n(\omega+\omega_r(0)-\omega_r(\mathbf{K})) +1]L_{\mathbf{K}+\mathbf{K}'}(\omega)L_{\mathbf{K}'}(\omega+\omega_r(0)-\omega_r(\mathbf{K})), \quad (13)$$

where

$$\gamma=\frac{\hbar}{m_r m_\varphi \omega_r \omega_\varphi}\Phi_4, \quad n(\omega)=\left[\exp\left(\frac{\hbar\omega}{k_{\mathrm{B}}T}\right)-1\right]^{-1}, \quad (14)$$

k_B is Boltzmann's constant, and T is the absolute temperature.

The integrals over ω in Eqs. (12) and (13) can be easily calculated for narrow resonance functions (10), where all slowly varying functions of ω are replaced by their values at the point $\omega=\tilde{\omega}_\varphi(\mathbf{K})$. In this case we obtain the following simplified expressions for the characteristics (12) and (13):

$$\omega_0=\omega_r(0)+\frac{\gamma}{N_0}\sum_{\mathbf{K}_1}[n_1+1/2] =\omega_r(0)+\gamma\int_{-\infty}^{\infty}d\omega[n(\omega)+1/2]\rho_\varphi(\omega), \quad (15)$$

$$2\Gamma_0=\frac{\gamma^2}{N_0^2} \times\sum_{\mathbf{K}_1,\mathbf{K}_2}\frac{n_1(n_2+1)(\eta_1+\eta_2)[(\Omega_1-\Omega_2)^2+(\eta_1-\eta_2)^2/4]}{(\Omega_1-\Omega_2)^4+(\eta_1^2+\eta_2^2)(\Omega_1-\Omega_2)^2/2+(\eta_1^2-\eta_2^2)^2/4}, \quad (16)$$

where

$$n_i=n(\Omega_i), \quad \eta_i=\eta_{K_i}(\Omega)_i, \quad i=1,2,$$

$$\Omega_1=\tilde{\omega}_\varphi(\mathbf{K}_1),\Omega_2=\tilde{\omega}_\varphi(\mathbf{K}_2)+\omega_r(\mathbf{K}_1-\mathbf{K}_2)-\omega_r(0); \quad (17)$$

$$\rho_\varphi(\omega)=\frac{1}{N_0}\sum_{\mathbf{K}}\delta(\omega-\tilde{\omega}_\varphi(\mathbf{K})) \quad (18)$$

is the low-frequency distribution function for the system of adsorbed molecules. In the special case of no lateral interactions of the low-frequency adsorbate modes and also no interactions of these modes via the substrate, when $\tilde{\omega}_\varphi(\mathbf{K})=\omega_\varphi$, relation (16) reduces to Eq. (48) of Ref. 18.

We call attention to the fact that, in the present approximation, the shift of the spectral line of a local vibration is determined only by the low-frequency distribution function $\rho_\varphi(\omega)$ and does not depend on the width $\eta_{\mathbf{K}}(\tilde{\omega}_\varphi(\mathbf{K}))$ of the resonances. However, the expressions (13) or (16) for the width of a spectral line of a local vibration contain resonance widths that compete with the widths of the low-frequency vibrational bands $\tilde{\omega}_\varphi(\mathbf{K})$ of the adsorbate. If these band widths are much larger than the widths of the resonances, then the latter can be neglected and Eq. (16) can be rewritten as

$$2\Gamma_0=\frac{2\pi\gamma^2}{N_0^2}\sum_{\mathbf{K}_1,\mathbf{K}_2}n_1(n_2+1)\delta(\Omega_1-\Omega_2). \quad (19)$$

If, moreover, the bands of local vibrations are much narrower than the bands of the low-frequency vibrations of the adsorbate, then the quantities $2\Gamma_0$ will also be determined only by the functions $\rho_\varphi(\omega)$

$$2\Gamma_0=2\pi\gamma^2\int_{-\infty}^{\infty}d\omega n(\omega)[n(\omega)+1]\rho_\varphi^2(\omega). \quad (20)$$

Let us calculate the temperature dependences of the frequency shift $\Delta\omega_0(T)$ and width $2\Gamma_0$ of the spectral function of local vibrations for triangular and square lattices of degenerate dipoles. In the first case, the low-temperature asymptotic expression of the function $\rho_\varphi(\omega)$ is $\rho_\varphi(\omega)=0.1062(I/V)^{5/4}\omega^{3/2}$, where I is the moment of inertia of the angular vibrations of the dipole and $V=\mu^2/a^3$ is the characteristic dipole-dipole interaction energy (μ is the dipole moment and a is the lattice constant).[13] Substituting this function into Eqs. (15) and (20), we obtain

$$\Delta\omega_0(T)/\gamma=0.1893\varkappa^{5/4}\tau^{5/2},$$

$$2\Gamma_0/(\hbar\gamma^2/V)=0.5109\varkappa^{3/2}\tau^4. \quad (21)$$

Here the two dimensionless parameters $\varkappa=\hbar^2/IV$ and $\tau=Ik_BT/\hbar^2$ describe the ratio of the rotational constant $\hbar^2/I$ to the dipole energy V and the ratio of the thermal energy k_BT to the rotational constant, respectively. For real systems, the first parameter is always small and the second can assume values which are both smaller and larger than 1. The relations (21) hold when $\varkappa\tau\ll 1$.

In the case of a square lattice, thermodynamic fluctuations order the relative orientations of the dipole moments in the sublattices (initially degenerate in the ground state) and lead to the appearance of a temperature-dependent energy gap in the spectrum of orientational vibrations[5]

$$\omega_\varphi^2(\mathbf{K})\approx C_0T+(Va^2/I)(C_xK_x^2+C_yK_y^2), \quad (22)$$

where $C_x=0.1447$, $C_y=1.7873$, and C_0 is a constant. The square-root temperature-dependence of the energy gap in the dispersion law $\omega_\varphi(\mathbf{K})$ was also noted in Ref. 4. Substituting the long-wavelength asymptotic expression (22) into Eq. (18), we obtain the low-frequency distribution function

$$\rho_\varphi(\omega)=\frac{I}{2\pi V\sqrt{C_xC_y}}\omega\Theta(\omega-\sqrt{C_0T}) \quad (23)$$

($\Theta(\omega)=1$ for $\omega>0$ and $\Theta(\omega)=0$ for $\omega<0$), which gives, using Eqs. (15) and (20),

$$\Delta\omega_0(T)/\gamma=\frac{\varkappa\tau^2}{2\pi\sqrt{C_xC_y}} \times\begin{cases}\sqrt{C_0/\tau}\exp(-\sqrt{C_0/\tau}), & \tau\ll 1,\\ \pi^2/6 & \tau\gg 1,\end{cases}$$

$$2\Gamma_0/(\hbar\gamma^2/V)=\frac{\varkappa\tau^3}{2\pi\sqrt{C_xC_y}}\times\begin{cases}(C_0/\tau)\exp(-\sqrt{C_0/\tau}, & \tau\ll 1,\\ \pi^2/3, & \tau\gg 1.\end{cases}\tag{24}$$

It is interesting that the presence of the Θ function, which is responsible for the appearance of long-range order in the system under study, in the frequency distribution function (23) leads to an explicit exponential dip in the shift of the maximum and in the width of the spectral line of a local vibration.

This work was supported by the State Fund for Fundamental Research of the Ukrainian State Committee on Science and Technology (Project 2.4/308).

[1] V. M. Rozenbaum, V. M. Ogenko, and A. A. Chuĭko, Usp. Fiz. Nauk **161**, 79 (1991) [Sov. Phys. Usp. **34**, 883 (1991)].
[2] V. M. Rozenbaum, Phys. Rev. B **53**, 6240 (1996).
[3] V. M. Rozenbaum, Zh. Éksp. Teor. Fiz. **99**, 1836 (1991) [Sov. Phys. JETP **72**, 1028 (1991)].
[4] K. M. S. Bajaj, R. Mehrotra, D. Kumar, and V. Soni, Europhys. Lett. **27**, 153 (1994).
[5] V. M. Rozenbaum, JETP Lett. **63**, 663 (1996).
[6] V. M. Rozenbaum, Zh. Éksp. Teor. Fiz. **111**, 669 (1997) [JETP **84**, 368 (1997)].
[7] C. B. Harris, R. M. Shellby, and P. A. Cornelius, Phys. Rev. Lett. **38**, 1415 (1977).
[8] R. M. Shellby, C. B. Harris, and P. A. Cornelius, J. Chem. Phys. **70**, 34 (1979).
[9] B. N. J. Persson and R. Ryberg, Phys. Rev. B **32**, 3586 (1985).
[10] A. A. Makarov and V. V. Tyakht, Poverkhnost', No. 8, 18 (1988).
[11] A. I. Volokitin, Surf. Sci. **224**, 359 (1989).
[12] D. C. Langreth and M. Persson, Phys. Rev. B **43**, 1353 (1991).
[13] V. M. Rozenbaum, Phys. Lett. A **165**, 275 (1992).
[14] V. M. Rozenbaum, Zh. Éksp. Teor. Fiz. **102**, 1381 (1992) [Sov. Phys. JETP **75**, 748 (1992)].
[15] K. Burke, D. C. Langreth, M. Persson, and Z.-Y. Zhang, Phys. Rev. B **47**, 15 869 (1993).
[16] V. M. Rozenbaum, Zh. Éksp. Teor. Fiz. **107**, 536 (1995) [JETP **80**, 289 (1995)].
[17] D. K. Lamber, G. P. M. Poppe, and C. M. J. Wijers, J. Chem. Phys. **103**, 6206 (1995).
[18] B. N. J. Persson, F. M. Hoffmann, and R. Ryberg, Phys. Rev. B **34**, 2266 (1986).
[19] J. Heidberg, E. Kampshoff, R. Kuhnemuth, M. Suhren, and H. Weiss, Surf. Sci. **269/270**, 128 (1992).
[20] J. Heidberg, E. Kampshoff, R. Kuhnemuth, and O. Schonekas, Surf. Sci. **269/270**, 120 (1992).
[21] V. M. Rozenbaum, Phys. Lett. A **176**, 249 (1993).

Translated by M. E. Alferieff

The behavior of thermopower in the $YBa_{2-x}La_xCu_3O_y$ system. Correlation between the band parameters in normal state and critical temperature

V. É. Gasumyants and E. V. Vladimirskaya

St. Petersburg State Technical University, 195251 St. Petersburg, Russia

I. B. Patrina

Institute of Silicate Chemistry, Russian Academy of Sciences, 195155 St. Petersburg, Russia

(Submitted February 21, 1997)
Fiz. Tverd. Tela (St. Petersburg) **40**, 17–22 (January 1998)

The thermopower in the $YBa_{2-x}La_xCu_3O_y$ system ($x=0-0.5$) has been studied. An analysis made in terms of the narrow-band model revealed trends in the variation of the main band parameters with increasing lanthanum concentration. The dependence of the conduction band width on lanthanum concentration was found to pass through a weak minimum at $x=0.05-0.1$, which correlates in position with the maximum in the concentration dependences of the critical temperature and degree of sample orthorhombicity. The results obtained and their comparison with Fe, Co→Cu substitution data permit a conclusion that the main factor affecting the properties of the $YBa_2Cu_3O_y$ system under nonisovalent substitution of various cations is the increasing disorder in the chain-oxygen subsystem caused by increasing impurity content. [S1063-7834(98)00401-8]

Doping is a widely recognized method of studying the properties of various materials, in particular, of high-T_c superconductors. A comparative analysis of samples of the high-T_c system $YBa_2Cu_3O_y$ (Y-123) with, differently distributed substitutions, permits one to gain information on the role and mechanism of the effect of various structural elements of the lattice on superconductivity and other properties of this compound.

Although the superconducting properties of $YBa_2Cu_3O_y$, as also of other high-T_c compounds, originate from the existence in their structure of CuO_2 layers, it is of interest to study the effect not only of oxygen deficiency and of a partial substitution of copper by other metals, but of nonisovalent substitutions of other cations as well. Indeed, doping of this kind introduces additional charge, which affects considerably the structural and superconducting properties, as well as the carrier concentration and, on the whole, the properties of the electronic system in its normal state.

The influence of impurities on the properties of solid solutions of the type $Y_{1-x}M_xBa_2Cu_3O_y$, $YBa_{2-x}M_xCu_3O_y$, and $YBa_2Cu_{3-x}M_xO_y$ depends on the valence ratio of the substituting and replaced elements. For instance, by partially replacing the Y-123 cations by ions with different valences one can vary within a broad range the oxygen content, which, depending on the actual type and degree of substitution, can both increase above the stoichiometric value $y=7$ in the case of Fe^{3+}, Co^{3+}, $Al^{3+}\rightarrow Cu^{2+}$ (Refs. 1–3), Eu^{3+}, $La^{3+}\rightarrow Ba^{2+}$ (Refs. 4–8) substitutions, and decrease for the $Ca^{2+}\rightarrow Y^{3+}$ substitution (Refs. 5, 9).

Our previous studies showed that an analysis of the behavior of transport coefficients within the narrow-band model can yield information on changes in the band parameters caused by deviations from stoichiometry.[10–12] Our investigation of the effect of oxygen deficiency[10,11] and of the nonisovalent Fe, Co→Cu substitutions[10,12] revealed that the properties of the normal phase, superconductivity, and band parameters of $YBa_2Cu_3O_y$ are dominated by the state of the oxygen subsystem, namely, by the content and distribution pattern of chain oxygen. Since $Ln^{3+}\rightarrow Ba^{2+}$ substitution, where Ln stands for a rare-earth element, also leads, similarly to the Fe, Co→Cu case, to an increase of the oxygen content y above its stoichiometric value, it appeared of interest to compare these two ways of acting on the oxygen subsystem.

Many of the authors studying the effect of nonisovalent substitution of Ba on the properties of Y-123 use lanthanum as impurity, since the ionic radii of Ba ($r_i=1.35$ Å) and La ($r_i=1.33$ Å) are very close. An increase in La content in $YBa_{2-x}La_xCu_3O_y$ results in an increase of y to ≈ 7.13 for $x=0.46$ (Ref. 6) or ≈ 7.2 for $x=0.5$ (Ref. 5). A significant feature of the influence of lanthanum is the passage of orthorhombic distortion $(b-a)$ through a maximum at La contents from $x_c=0.05$ (Refs. 7, 8) to $x_c=0.1$ (Ref. 6), which coincides in position with that in the $T_c(x)$ relation observed near $x\approx 0.05-0.06$ (Refs. 7, 13) or $x\approx 0.1$ (Refs. 6, 14). An obvious reason for the increase in $(b-a)$ with lanthanum content for $x\leqslant x_c$ is believed[6] to be additional filling by oxygen of the O(1) sites in Cu(1)O chains in this concentration region. For $x\geqslant x_c$, the additional oxygen atoms fill the O(5) vacancies, and it is this that reduces orthorhombic distortion up to a transition to tetragonal structure. Note that the formal average copper valence, whose variation was connected by many authors with the doping-induced drop of the critical temperature in Y-123, grows monotonically with increasing x throughout the lanthanum concentration range studied. Thus while for $x>x_c$ one may be justified in seeing a correlation between the formal average copper valence and T_c (Refs. 6, 7), in the initial region the increase of T_c cannot be associated with an increase of formal carrier concentration.

Studies of transport properties in the $YBa_{2-x}La_xCu_3O_y$

TABLE I. Oxygen content and unit cell parameters of $YBa_{2-x}La_xCu_3O_y$, samples.

x	y	a, Å	b, Å	$b-a$, Å	c, Å
0.0	6.95	3.822	3.885	0.063	11.670
0.05	6.98	3.820	3.894	0.074	11.655
0.1	6.99	3.823	3.895	0.072	11.650
0.2	7.03	3.819	3.890	0.071	11.650
0.3	7.10	3.828	3.879	0.051	11.640
0.4	7.14	3.857	3.857	0	11.600
0.5	7.17	3.853	3.853	0	11.580

system are extremely scarce. It is known that the variation of resistivity ρ in absolute magnitude and of the shape of the $\rho(T)$ relation with increasing La content is similar, on the whole, to that observed with increasing oxygen deficiency in Y-123. The width of the superconducting transition ΔT was found[13] to decrease with increasing La content up to $x=x_c$. There has been no systematic study of thermopower in $YBa_{2-x}La_xCu_3O_y$.

Accordingly, the objective of this work was to study the behavior of thermopower in $YBa_{2-x}La_xCu_3O_y$ samples $(x=0-0.5)$, to perform its analysis in terms of the narrow-band model, and to obtain information on transformation of the band spectrum and on the relation of its parameters with the critical temperature, as well as to compare the results obtained with data relating to nonisovalent substitution of the chain copper.

1. SAMPLE CHARACTERIZATION

Single-phase ceramic samples of composition $YBa_{2-x}La_xCu_3O_y$ $(x=0-0.5)$ were prepared by standard ceramic technology from the oxides of yttrium, lanthanum, and copper and barium carbonate. The final treatment consisted in maintaining the samples in an oxygen flow at $T=450°$ C for two hours, with subsequent slow cooling (with a rate of about 2 °C/min) to room temperature.

The single-phase state of the samples was verified by x-ray diffraction and visually with a microscope to not worse than 1%, and the oxygen content was determined by iodometric titration to within $\pm 0.01-0.02$. The data on the oxygen content and lattice parameters are presented in Table I. We see that an increase in lanthanum content results in a gradual growth of y. X-ray diffraction analysis showed that, for small x, the lattice parameter a changes little and b increases, with the magnitude of orthorhombic distortion $(b-a)$ increasing to reach a maximum at $x=0.05-0.1$. As x increases still more, parameter b begins to decrease, and a, increase, and near $x\approx 0.4$ a transition from orthorhombic to tetragonal symmetry takes place. Parameter c decreases monotonically throughout the lanthanum concentration range studied. The observed trends in the variation of the lattice parameters and oxygen content are in good agreement with other available data.[5–8]

2. RESULTS OF ELECTROPHYSICAL MEASUREMENTS

Temperature dependences of resistivity, $\rho(T)$, and thermopower, $S(T)$, were measured on all samples within the temperature range $T=T_c-300K$ by a technique described elsewhere.[12] Table II lists some results of the electrophysical measurements and the data on the critical temperature extracted from the resistive superconducting transition. For all samples, the resistivity drops linearly with decreasing temperature, with the slope of $\rho(T)$ decreasing monotonically with increasing lanthanum concentration (see $\rho_{300\,K}/\rho_{100\,K}$ ratio in Table II). Figure 1 shows the dependence of $T_c(\rho=0)$ on lanthanum content. The critical temperature is the highest in samples with $x=0.05-0.1$, and further increase of lanthanum content results in a monotonic decline of T_c. As for the width of the transition, it slightly decreases compared to undoped $YBa_2Cu_3O_y$ in the $x=0.05$ sample, to start again to rise (see Table II). The observed change in the superconducting transition parameters is in accord with literature data[6,7,13,14] and, besides, agrees qualitatively with the case of Co→Cu substitution, where an increase in impurity concentration also entails a growth of the oxygen content.[12] Note that it is at the lanthanum concentration $x=0.05-0.1$ that the samples approach maximum orthorhombicity and the stoichiometric value of oxygen content (compare data in Tables I and II).

The temperature dependence of the thermopower of the samples is shown graphically in Fig. 2. The features observed in $S(T)$ are typical of the Y-Ba-Cu-O high-T_c superconductors, namely, the constancy or weak variation of S in

TABLE II. Electrophysical data for $YBa_{2-x}La_xCu_3O_y$ samples.

x	$\rho_{300\,K}$, mΩ·cm	$\rho_{100\,K}$, mΩ·cm	$\rho_{300\,K}/\rho_{100\,K}$	T_c^m, K	ΔT, K	T_c^0, K	$S_{300\,K}$, μV/K
0.0	3.8	1.7	2.53	89.7	3.0	87.3	0.8
0.05	3.5	1.5	2.33	89.8	1.1	88.8	1.3
0.1	1.6	0.7	2.20	91.2	3.2	89.5	6.3
0.2	2.9	1.4	2.07	90.5	5.8	86.9	9.3
0.3	4.2	2.1	2.00	84.2	8.7	76.8	16.6
0.4	2.9	1.5	1.93	73.5	10.9	62.8	18.5
0.5	4.8	2.8	1.71	57.3	11.6	50.9	39.7

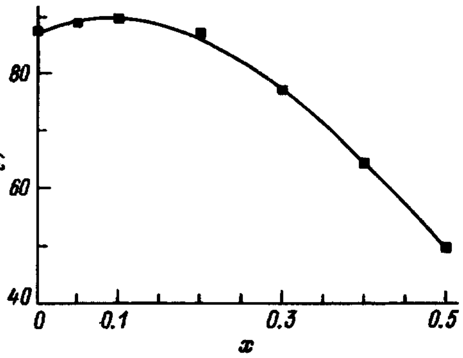

FIG. 1. Critical temperature *vs* lanthanum content in $YBa_{2-x}La_xCu_3O_y$.

the high-temperature domain for samples with slight deviations from stoichiometry (up to $x=0.2$) and the presence in the $S(T)$ curve of a maximum at $T=120-200$ K. As the lanthanum content increases, one observes a substantial increase of thermopower in absolute magnitude (see Fig. 2 and Table II) and a shift of the $S(T)$ maximum toward higher temperatures accompanied by its broadening. Thus the transformation of the $S(T)$ relations in $YBa_{2-x}La_xCu_3O_y$ samples is similar, on the whole, to the case of increasing oxygen deficiency or increasing content of a nonisovalent impurity, Fe or Co, which substitute for copper, in $YBa_2Cu_3O_y$.

A comparison of the obtained experimental results with available data[10,12] on Fe, Co→Cu substitutions shows that the absolute values of S in $YBa_{2-x}La_xCu_3O_y$ samples increase substantially less than those for samples doped by iron or cobalt with the corresponding degrees of substitution. Also, the $T_c(x)$ dependence is significantly weaker in the first case. Thus one can maintain the existence of a stable correlation between the values of S and T_c with increasing amount of doping under nonisovalent substitution in different sublattices, namely, the stronger increase of thermopower is paralleled by a sharper decrease of the critical temperature. Note also that the $\rho(T)$ relations for $YBa_{2-x}La_xCu_3O_y$ samples remain linear up to $x=0.5$, whereas in $YBa_2Cu_{3-x}M_xO_y$ (M=Fe, Co) at low temperatures they exhibit superconducting behavior at larger substitutions ($x\geqslant 0.2$ and $x\geqslant 0.3$ for M=Fe and Co, respectively[12]). This shows that localization of states with increasing impurity content is less in $YBa_{2-x}La_xCu_3O_y$ than it is in $YBa_2Cu_{3-x}M_xO_y$ (M=Fe, Co).

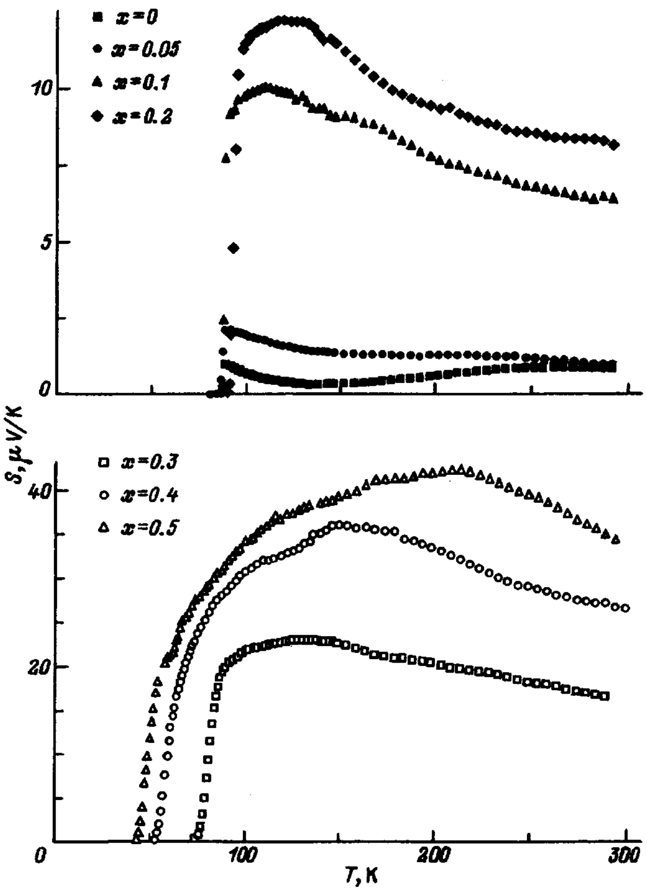

FIG. 2. Temperature behavior of the thermopower in $YBa_{2-x}La_xCu_3O_y$.

3. DISCUSSION OF EXPERIMENTAL DATA AND CONCLUSIONS

Our experimental data were examined in terms of a phenomenological model[10] of electron transport in narrow conduction-band materials. The model assumes the existence in the band spectrum of high-T_c compounds of a narrow (about 0.1 eV) density-of-states peak near the Fermi level. It was shown[10] that this assumption permits one to obtain analytical expressions for the temperature dependences of transport coefficients, which can then be used to derive the three model parameters characterizing the properties of the carrier system in normal state from the experimental data on the temperature dependence of the thermopower. These parameters are the band filling by electrons F, which is the ratio of the number of electrons to the total number of states in the band, the total effective conduction-band width W_D, and the effective width of the interval of delocalized states W_σ. This model gives the following expression for the thermopower

$$S=-\frac{k_B}{e}\left\{\frac{W_\sigma^*}{\sinh W_\sigma^*}\left[\exp(-\mu^*)+\cosh W_\sigma^*-\frac{1}{W_\sigma^*}\right.\right.$$
$$\times(\cosh\mu^*+\cosh W_\sigma^*)$$
$$\left.\left.\times\ln\frac{\exp(\mu^*)+\exp(W_\sigma^*)}{\exp(\mu^*)+\exp(-W_\sigma^*)}\right]-\mu^*\right\}, \qquad (1)$$

where

$$\mu^*\equiv\mu/k_BT=\ln\frac{\sinh(FW_D^*)}{\sinh[(1-F)W_D^*]}, \qquad (2)$$

μ is the chemical potential, k_B is the Boltzmann constant, e is the electronic charge, $W_D^*\equiv W_D/2k_BT$, and $W_\sigma^*\equiv W_\sigma/2k_BT$.

Our earlier analysis of the transport properties in the $YBa_2Cu_3O_y$ system made for different oxygen contents[10,11] and with copper replaced partially by transition metals (iron and cobalt) (Refs. 10, 12) showed that a deviation from stoichiometry leads to an increase in band filling, a widening of the conduction band, and a simultaneous change of the ratio W_σ/W_D, which signals an increase in the degree of state

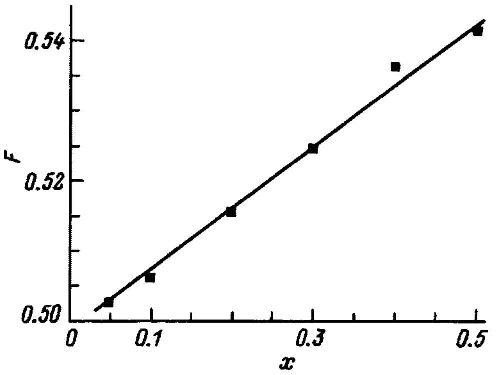

FIG. 3. Band filling by electrons *vs* lanthanum content in $YBa_{2-x}La_xCu_3O_y$.

localization. We attributed these effects to growing disorder in the chain oxygen subsystem. Note that the widening of the conduction band, which results in a drop in the density of states at the Fermi level, correlates well with the decrease in T_c. Since, as already mentioned, an increase in lanthanum content acts on the oxygen subsystem similarly to the Fe, Co→Cu substitutions, it appeared of interest to follow the transformation of the band spectrum in $YBa_{2-x}La_xCu_3O_y$ and to compare the effect of lanthanum, on the one hand, and of iron and cobalt, on the other, on the conduction band parameters and critical temperature.

We used Eqs. (1) and (2) to obtain calculated dependences $S(T)$, which were found to be in good agreement with experiment, and determined the model parameters for all the samples studied. Figures 3 and 4 present the concentration dependences of the band filling by electrons and of the energy parameters obtained for the $YBa_{2-x}La_xCu_3O_y$ system. The band filling grows weakly and practically linearly with x (Fig. 3). The observed weak increase of F can be due to a slight undercompensation of the excess charge, which is introduced into the system in the $La^{3+}\rightarrow Ba^{2+}$ substitution, by the increasing oxygen content (see Table I). As for the band width, on the whole W_D and W_σ increase. Note, however, one more essential feature. As seen from Fig. 4, the $W_D(x)$ and $W_\sigma(x)$ relations for $YBa_{2-x}La_xCu_3O_y$ exhibit a weak minimum at $x=0.1$. As already mentioned, it is at this value of lanthanum content that $T_c(x)$ passes through a maximum, and the oxygen content approaches most closely the value $y=7$. These observations can be explained in the following way. As a result of the additional filling by oxygen of the O(1) sites at a low lanthanum content, the oxygen subsystem reaches at $x\approx 0.1$ the maximum degree of order [which is evidenced by the maximum orthorhombicity and minimum width of the superconducting transition (see Tables I and II)]. It is this factor that accounts for the minimum in the concentration dependences of the band parameters, which, in its turn, leads to the maximum density of states at the Fermi level, $D(E_F)$, and, accordingly, to the highest critical temperature. Further increase of x is accompanied by filling of the oxygen vacancies O(5), thus giving rise to the onset and gradual increase of disorder in the oxygen subsystem. This causes a growth of W_D and W_σ and, in accordance with our ideas on a connection between W_D and T_c, leads to a decrease of the critical temperature.

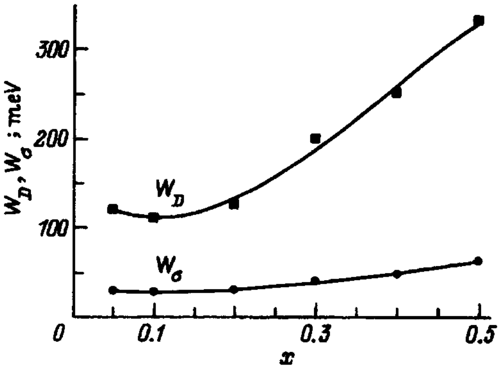

FIG. 4. Conduction-band energy characteristics *vs* lanthanum content in $YBa_{2-x}La_xCu_3O_y$.

Thus the observed variation of the critical temperature in $YBa_{2-x}La_xCu_3O_y$ is in accord with the pattern of band structure transformation throughout the lanthanum concentration range covered. In their turn, the $W_D(x)$, $W_\sigma(x)$, and $F(x)$ relations can be explained in a noncontradictory way through an analysis of structural changes in the lattice induced by lanthanum introduction. The observed correlation between the nonmonotonic variation in the degree of chain-oxygen ordering and the conduction-band width is an additional argument for the Anderson localization mechanism being operative in $YBa_2Cu_3O_y$.

The connection between the band parameter variation and critical temperature revealed here is similar to the one observed in studies of $YBa_2Cu_3O_y$ samples with different oxygen content[10,11] or different copper substitution by 3*d* metals.[10,12] The properties of the $YBa_{2-x}La_xCu_3O_y$ system, similar to the case of Fe, Co→Cu substitution, are primarily affected by an increase in oxygen content above the stoichiometric level, $y>7$, and by the associated increase of disorder in the chain-oxygen subsystem with increasing impurity concentration. All quantitative differences between the $F(x)$, $W_D(x)$, and $W_\sigma(x)$ relations obtained on samples of the above lots can be explained by analyzing the changes in the oxygen subsystem induced by various impurities, with due account of their valence and oxygen coordination. This lends support to our earlier conclusion that the factor determining the band parameters and the critical temperature of $YBa_2Cu_3O_y$ is the state of the oxygen subsystem.

Thus our study of the effect of partial substitution of lanthanum for barium on the transport and superconducting properties of the $YBa_2Cu_3O_y$ system has produced the following main results.

1) The $T_c(x)$ dependence of $YBa_{2-x}La_xCu_3O_y$ samples exhibits a maximum at $x=0.05-0.1$ corresponding to the oxygen content $y\approx 7$ and maximum orthorhombicity, which shows that for this lanthanum content the oxygen subsystem is most ordered;

2) An increase of lanthanum content in $YBa_{2-x}La_xCu_3O_y$ results in an increase of the thermopower in absolute magnitude and a shift of the maximum in the $S(T)$ relation toward higher temperatures. The behavior of the $S(T)$ dependence in $YBa_{2-x}La_xCu_3O_y$ is qualitatively

similar to that observed with increasing oxygen deficiency in $YBa_2Cu_3O_y$ or with increasing content of the nonisovalent impurities Fe and Co substituting for copper, although the growth of the absolute values of S in the case of lanthanum substitution for barium is noticeably weaker than that for samples doped by iron or cobalt at the corresponding degree of substitution;

3) An analysis of the $S(T)$ relations made in terms of the narrow-band model has revealed trends in variation of the band parameters of $YBa_{2-x}La_xCu_3O_y$ with increasing lanthanum content. The band filling by electrons grows with lanthanum content, and a weak minimum appears in the $W_D(x)$ and $W_\sigma(x)$ relations at $x=0.1$, after which W_D and W_σ start to grow. On the whole, the band spectrum transformation in $YBa_{2-x}La_xCu_3O_y$ follows the pattern observed to occur with growing oxygen deficiency or Fe, Co→Cu substitution;

4) Similar to the case of nonisovalent chain-copper substitutions, the $W_D(x)$, $W_\sigma(x)$, $F(x)$, and $T_c(x)$ relations correlate with the pattern of structural changes induced in the $YBa_2Cu_3O_y$ lattice by lanthanum incorporation, primarily with changes in the oxygen subsystem. Thus we have obtained an additional confirmation of the dominant role the disorder in chain oxygens plays in the transport properties in the normal, the superconductivity, and the band parameters in the $YBa_2Cu_3O_y$ high-T_c superconducting system;

5) Our results support the existence of a correlation between the variation of the band parameters (primarily of the conduction-band width) and the critical temperature found earlier for samples doped by various $3d$ metals, which, however, is more clearly pronounced in the present case since the changes in both these quantities are nonmonotonic. This provides an additional argument for the onset of Anderson localization in nonstoichiometric $YBa_2Cu_3O_y$.

[1] J. M. Tarascon, P. Barboux, P. F. Miceli, L. H. Greene, G. W. Hull, M. Eibschutz, and S. A. Sunshine, Phys. Rev. B **37**, 7458 (1988).

[2] Y. Xu, R. Sabatini, A. R. Moodenbaugh, Yi. Zhu, S.-G. Shyu, M. Suenaga, K. W. Dennis, and R. W. MaCallum, Physica C **169**, 205 (1990).

[3] X. Y. Zhou, H. Zhang, and Q. R. Zhang, Phys. Status Solidi A **119**, K145 (1990).

[4] V. E. Gasumyants, V. I. Kaidanov, and E. V. Vladimirskaya, Chin. J. Phys. **31**, 999 (1993).

[5] A. Tokiwa, Y. Syono, M. Kikuchi, R. Suzuki, T. Kajitani, N. Kobayashi, T. Sasaki, O. Nakatsu, and Y. Muto, Jpn. J. Appl. Phys. **27**, L1009 (1988).

[6] R. Liang, M. Itoh, T. Nakamura, and R. Aoki, Physica C **157**, 83 (1989).

[7] A. Manthiram and J. B. Goodenough, Physica C **159**, 760 (1989).

[8] V. S. Grunin, I. B. Patrina, M. M. Pivovarov, M. V. Razumeenko, N. P. Baranskaya, I. A. Drozdova, and V. L. Makarov, Sverkhprovodimost' (KIAE) **3**, 2242 (1990).

[9] B. Fisher, J. Genossar, C. G. Kuper, L. Patlagan, G. M. Reisner, and A. Knizhnik, Phys. Rev. B **47**, 6054 (1993).

[10] V. E. Gasumyants, V. I. Kaidanov, and E. V. Vladimirskaya, Physica C **248**, 255 (1995).

[11] V. É. Gasumyants, S. A. Kaz'min, V. I. Kaidanov, V. I. Smirnov, Yu. M. Baikov, and Yu. P. Stepanov, Sverkhprovodimost' (KIAE) **4**, 1280 (1991).

[12] E. V. Vladimirskaya, V. É. Gasumyants, and I. B. Patrina, Fiz. Tverd. Tela (St. Petersburg) **37**, 1990 (1995) [Phys. Solid State **37**, 1084 (1995)].

[13] J. J. Neumeier, Appl. Phys. Lett. **61**, 1852 (1992).

[14] R. G. Buckley, D. M. Pooke, J. L. Tallon, M. R. Presland, N. E. Flower, M. P. Staines, H. L. Johnson, M. Meylan, G. V. M. Williams, and M. Bowden, Physica C **174**, 383 (1991).

Translated by G. Skrebtsov

X-Ray-Diffractometry of structural changes occurring in surface layers of silicon in the process of laser diffusion of boron

A. P. Petrakov and E. A. Golubev

Syktyvkar State University, 167001 Syktyvkar, Russia

(Submitted July 8, 1997)
Fiz. Tverd. Tela (St. Petersburg) **40**, 156–160 (January 1998)

The effect of laser diffusion of boron on the structure of surface layers in silicon single crystals was investigated by diffracted-reflection curve and three-crystal x-ray diffractometry methods. Deformation and static Debye–Waller factor distribution profiles were determined numerically by varying the parameters of the problem. *© 1998 American Institute of Physics.* [S1063-7834(98)03701-0]

The electric characteristics of semiconductor materials largely depend on their impurity content.[1] Doping is usually performed by thermal diffusion[2] or ion implantation.[3] Among other methods for introducing impurities into the surface region of single crystals, laser doping, which makes it possible to obtain a sharper impurity distribution front, merits the greatest attention.[4–6] Lasers have a wide range of application in semiconductor technology. They enable not only doping but also annealing of defects that form in the process of thermal diffusion[7] and ion implantation.[8–11]

The introduction of an impurity induces structural changes in the crystal lattice. These changes can be detected with two- and three-crystal x-ray diffractometers. Analysis of the diffracted reflection of x-rays makes it possible to determine the deformation profile, thickness, and defect density of the surface layer as well as the impurity concentration profile.[12–17]

Out objective in the present work is to investigate by two- and three-crystal x-ray diffractometry the structural changes occurring in the surface layers of silicon single crystals during laser diffusion of boron.

1. EXPERIMENTAL PROCEDURE

Boron films, 400 Å thick, were sputtered on the (111) surface of single-crystal silicon plates. Sputtering was performed on 0.5 mm thick plates in vacuum using a free-running millisecond ruby laser. Film thickness was determined according to the position of the interference peaks in the x-ray total external reflection curves.[18]

All plates were divided into three groups and irradiated on the sputtered-film side with a pulsed ruby laser. The pulse duration was equal to 0.5 ms and the pulse energy density was equal to 23 J/cm^2. Two other groups were irradiated with a continuous-wave CO$_2$ laser. One group was irradiated on the silicon-substrate side and the other was irradiated on the film side. Irradiation lasted for 1 s with energy density 300 J/cm^2.

The change occurring in the structure of the surface region of the single crystals as a result of the diffusion of impurity from the sputtered films was investigated with an x-ray diffractometer in two- and three-crystal schemes with Cu $K\alpha_1$ radiation. In three-crystal diffraction, the measurements were performed in the $\theta-2\theta$ regime (the angular velocity of the analyzer is two times that of the sample) and in a regime in which the analyzer is scanned and the rotation angle of the sample is fixed. The diffractometer possessed a silicon slit monochromator with (111) double reflection. A silicon single crystal but with (111) single reflection was also used as the analyzer.

2. EXPERIMENTAL RESULTS AND DISCUSSION

Figure 1 displays experimental and theoretical curves of the diffracted reflection of x-rays measured in the $\theta-2\theta$ regime. The intensity of the incident radiation was taken to be 1, a zero angle corresponds to the exact Bragg position, and large angles have a positive sign and small angles a negative sign. It is evident from Fig. 1 that the intensity on the ‘‘tails’’ of the curves for substrate-side irradiation with ruby and CO$_2$ lasers is higher for positive angles than for negative angles. The curve for the sample irradiated with a CO$_2$ laser on the sputtered-film side is symmetric.

Figure 2 displays the reduced intensity function of the same samples $P(\alpha)=kI_m\alpha^2$, where I_m is the intensity of the main peak in the three-crystal curves, measured in the regime in which the analyzer is scanned and the rotation of the sample is fixed at angles α ranging from -120 to -15 angular seconds and from 15 to 120 angular seconds; k is a normalization constant, determined from the condition $P(\alpha)=1$ for unirradiated crystals in the experimental range of angles.[12] Maxima appeared in the functions on the positive-angle side after substrate-side irradiation with ruby and CO$_2$ lasers. Such a well-expressed maximum is not observed with film-side irradiation with a CO$_2$ laser.

Diffuse peaks due to scattering of x-rays by defects are present in the three-crystal curves of the irradiated samples. The symmetric part of the integrated intensity of the diffuse scattering (integrated over the emergence angle) as a function of the rotation angle of the sample is displayed on a double-logarithmic scale in Fig. 3. The symmetric part was determined from relation $I_s=[I(\alpha)+I(-\alpha)]/2$ and is presented in units of the intensity I_0 of the radiation incident on the sample. The experimental points for all samples fall on straight lines, the tangent of whose slope is close to 2. The intensities of the diffuse peaks in the case of film-side irradiation with ruby and CO$_2$ lasers are almost identical, while

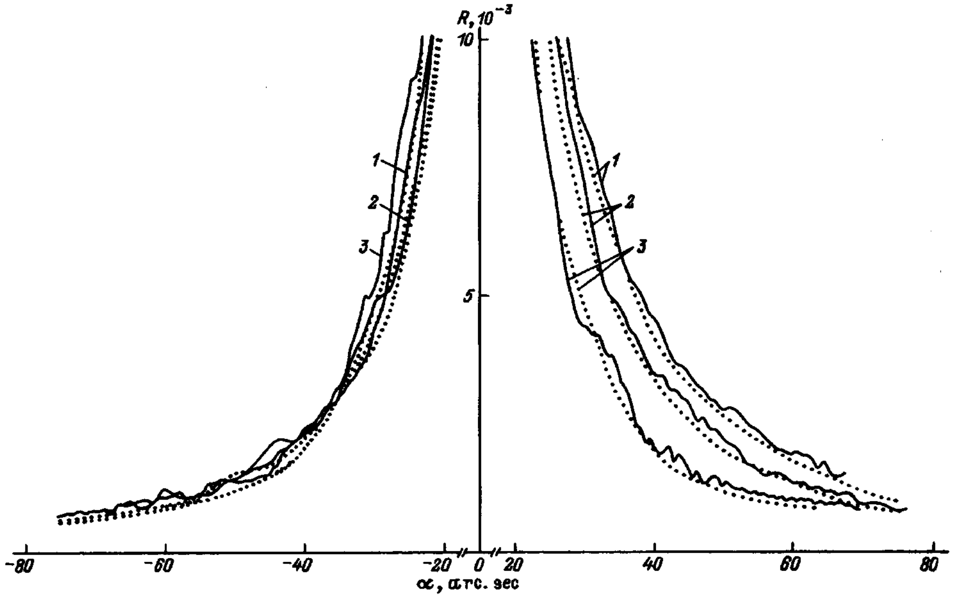

FIG. 1. Experimental (solid lines) and almost identical computed (dotted lines) $\theta-2\theta$ diffracted reflection curves for samples irradiated with a ruby laser (*1*) and a CO_2 laser (*2*, *3*). *1*, *2*—on the substrate side, *3*—on the film side.

the intensities are much higher for substrate-side irradiation with a CO_2 laser.

Figure 4 displays profiles of the deformation $\Delta d(z)/d$ and static Debye–Waller factor $f(z)$, using which makes possible an almost exact fit of the theoretical $\theta-2\theta$ curves to the experimental curves. The static Debye–Waller factor is understood to be the statistically averaged phase factor $\exp(i\mathbf{h}\cdot\mathbf{u}(z))$, where **h** is the diffraction vector and **u** is the displacement field.[19] The theoretical curves were constructed on the basis of the Topen equations of the dynamic theory of diffraction of x-rays taking account of two states of polarization and contraction.[16]

As a starting approximation for numerical modeling, the deformation profile was taken in the form of the distribution function of the impurity concentration arising in the surface layer with standard thermal diffusion.[13] Besides the deformation profile, the following were varied: the thickness of the diffusion layer, the maximum deformation, and profile of the spatial distribution $f(z)$. The following were used in the starting approximation: the thickness—calculated according to the width of the function $P(\alpha)$,[11] the maximum deformation—calculated according to the angular position of the maxima of the functions $P(\alpha)$ assuming a stepped profile, and the profile of the spatial distribution $f(z)$—calculated according to the intensity of the main peaks in the three-crystal curves.[20]

It is evident from the figure that the deformation profile of the crystal lattice of the samples irradiated with a ruby laser possesses a maximum at some distance from the surface. The deformation of samples irradiated with a CO_2 laser on the substrate side is maximum at the surface. It is impossible to construct a deformation profile for samples irradiated with CO_2 laser on the film side, since the $\theta-2\theta$ curves for such samples are virtually symmetric and are identical to the theoretical curve of the undeformed crystal (Fig. 1). The ab-

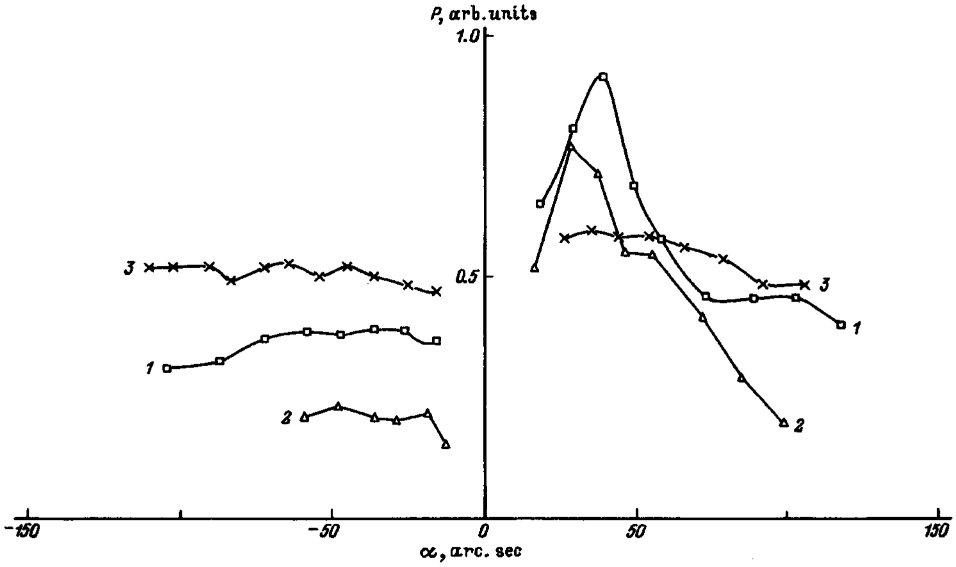

FIG. 2. Reduced intensity functions for samples after laser irradiation. The numbering of the curves (*1*, *3*) is the same as in Fig. 1.

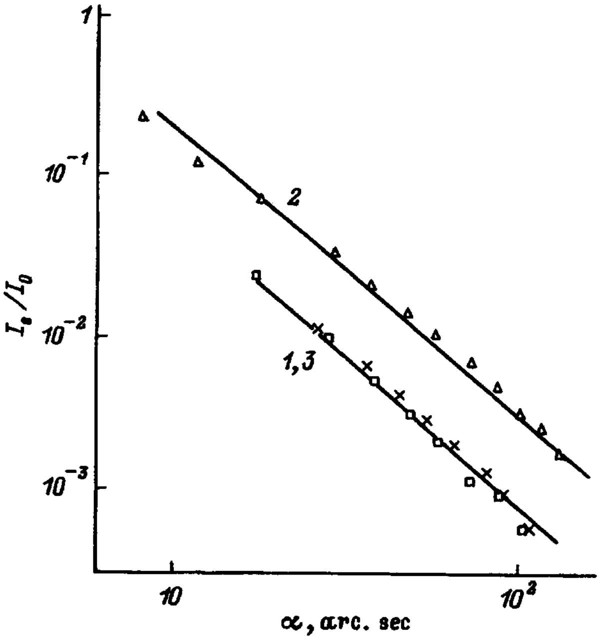

FIG. 3. Integrated intensity of the diffuse peak versus sample rotation angle. The numbering of the curves (*1, 3*) is the same as in Fig. 1.

sence of deformation is confirmed also by curve 3 in Fig. 2, which has no sharp maximum.

Both the ruby and CO$_2$ laser radiations are absorbed by the boron film, because the silicon plate is virtually transparent to CO$_2$ radiation. As a result, the film is heated and the temperature of the silicon substrate is determined by its thermal conductivity. For millisecond irradiation a temperature gradient arises as a result of heat conduction and a quasiuniform temperature distribution over the thickness of the samples is characteristic for laser irradiation for 1 s.[4] Thus, in the first case the diffusion of the impurity is due to concentration and temperature gradients while in the second case only to a concentration gradient.

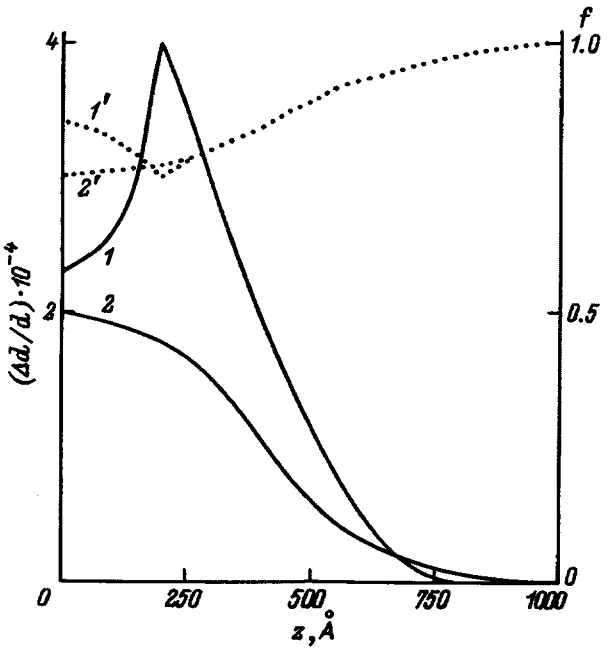

FIG. 4. Profiles of the spatial distribution of deformation $\Delta d(z)/d$ (*1, 2*) and static Debye–Waller factor $f(z)$ for samples irradiated with a ruby laser ($1',2'$) and a CO$_2$ laser on the substrate side ($2',2'$).

The intensity of the "tails" of the two-crystal curves increases after irradiation. This could be due to scattering of x-rays by the deformed lattice or by defects. Measurements in the $\theta-2\theta$ regime virtually preclude detection of radiation scattered by defects. An increase in the intensity on the positive-angle side of the $\theta-2\theta$ curves of samples irradiated with ruby and CO$_2$ lasers on the substrate side (Fig. 1) indicates the existence of negative deformation. This is also confirmed by the presence of maxima in the functions $P(\alpha)$ on the positive-angle side for the corresponding samples (Fig. 2). The sign of the deformation is explained by the fact that boron diffusing in the lattice occupies predominantly lattice sites, and since its covalent radius (0.88 Å) is smaller than that of silicon (1.17 Å), the lattice is compressed.

The absence of deformation in samples irradiated with a CO$_2$ laser on the film side does not exclude diffusion of the impurity. It is possible that diffusion occurred, but the impurity concentration that it produced was so low that the method employed did not permit detecting the lattice deformation associated with this impurity. Therefore, for such a CO$_2$ laser irradiation geometry almost the entire film is vaporized and the increase in the intensity of the "tails" of the two-crystal curves is explained by scattering by the defects that are produced. The defects are predominantly randomly distributed dislocations, as is indicated by the arrangement of the experimental points along a straight line, the tangent of whose slope equals 2, in Fig. 3.

The generation of dislocations led to the formation of slightly disoriented blocks of a mosaic structure that dynamically scatter x-rays. This is indicated by the fact that the width of the main peaks in the three-crystal curves increase after irradiation to a constant value that is independent of the rotation angle of the sample.[21] Similar defects were detected in samples irradiated on the substrate side as well as in samples irradiated with a ruby laser. The difference is only in the dislocation density, which was determined according to the width of the main peaks in the three-crystal curves.[21] The peaks have a width of 11 angular seconds in the case of film-side irradiation with a CO$_2$ laser and 15 angular seconds in the case of substrate-side irradiation, corresponding to dislocation densities 8.8×10^4 and 5.0×10^5 cm^{-2}, respectively. The dislocation density in samples irradiated with a ruby laser is the same as in samples irradiated on the film side with a CO$_2$ laser.

The generation of dislocations could be due to lattice deformation caused by the presence of an impurity or thermal action. However, dislocation generation is due to thermal action, since the stresses due to deformation as estimated from $\sigma=\varepsilon E/2\nu$, where ε is the lattice deformation, $E=1.66\times10^{11}$ N/m^2 is Young's modulus, and $\nu=0.28$ is the Poisson ratio, equals 1.2×10^8 Pa even with maximum deformation $\varepsilon=4\times10^{-4}$ (Fig. 4); this is less than the tensile strength of silicon $\sigma_0=2\times10^8$ Pa.[23]

Deformation is directly proportional to the density of boron in lattice sites. For the (111) reflection this relation is given by $\varepsilon = 1.44\beta C$, where $\beta = -4.97\times 10^{-24}$ is the deformation coefficient, determined by the difference of the covalent radii of the boron and silicon atoms.[23] Therefore the depth distribution of the boron concentration has the same form as the deformation profiles presented in Fig. 4 for the corresponding samples.

The arrangement of the deformation maxima at some distance from the surface in samples irradiated with a ruby laser can be explained by the partial evaporation of the diffused boron from the surface region during cooling. In the case of substrate-side irradiation with a CO_2 laser, the boundary of the film with the surface is heated, as a result of which the film prevents evaporation. Film-side irradiation with the same radiation results mainly in the evaporation of the film.

The maximum boron density reaches $C = 5.6\times 10^{19}$ cm^{-3} in the case of irradiation with a ruby laser and $C = 2.8\times 10^{19}$ cm^{-3} in the case of film-side irradiation with a CO_2 laser. Such a high density is explained by the nonequilibrium nature of the processes and is observed in the case of laser diffusion of other impurities.[6]

The following conclusions can be drawn on the basis of our x-ray diffraction investigations. Laser diffusion of boron from a surface film into silicon can be conducted with both 1-ms ruby radiation and 1-s CO_2 radiation. In the latter case substrate-side irradiation is best. The maximum boron density in CO_2-laser-irradiated samples is observed near the surface. The density profile of boron diffused under the action of ruby radiation has a sharp maximum which is shifted into the bulk of the crystal. Laser diffusion is accompanied by the generation of dislocations.

We thank V. A. Bushuev for helpful discussions and valuable remarks.

[1] V. S. Vavilov, V. F. Kiselev, and B. N. Mukashev, *Defects in the Volume and on the Surface of Silicon* [in Russian], Nauka, Moscow, 1990.

[2] D. Shaw [Ed.], *Atomic Diffusion in Silicon in Semiconductors* [Plenum Press, New York, 1973; Mir, Moscow, 1975].

[3] F. F. Komarov, A. P. Novikov, V. S. Solov'ev, and S. Yu. Shiryaev, *Structural Defects in Ion-Implanted Silicon* [in Russian], 1990.

[4] V. E. Borisenko, *Solid-Phase Processes in Semiconductors During Pulsed Heating* [in Russian], Nauka Tekhnika, 1991.

[5] S. G. Kiyak, Izv. Akad. Nauk SSSR **53**, 417 (1989).

[6] V. I. Fistul' and A. M. Pavlov, Fiz. Tekh. Poluprovodn. **17**, 854 (1983) [Sov. Phys. Semicond. **17**, 535 (1983)].

[7] R. T. Young and J. Narayan, Appl. Phys. Lett. **33**, 14 (1978).

[8] A. V. Dvurechenskiĭ, G. A. Kachurin, E. V. Nidaev, and L. S. Smirnov, *Pulsed Annealing of Semiconductor Materials* [in Russian], Nauka, 1982.

[9] A. A. Zav'yalova, R. M. Imamov, M. V. Koval'chuk, Yu. V. Koval'chuk, and A. A. Lomov, Pis'ma Zn. Tekh. Fiz. **8**, 653 (1982) [Sov. Tech. Phys. Lett. **8**, 284 (1982)].

[10] V. A. Bushuev and A. P. Petrakov, Pis'ma Zh. Tekh. Fiz. **18**, 77 (1992) [Sov. Tech. Phys. Lett. **18**, 271 (1992)].

[11] V. A. Bushuev and A. P. Petrakov, Fiz. Tverd. Tela (St. Petersburg) **35**, 355 (1993) [Phys. Solid State **35**, 181 (1993)].

[12] A. M. Afanas'ev, P. A. Aleksandrov, and R. M. Imamov, *X-Ray-Diffraction Diagnostics of Submicron Layers* [in Russian], Nauka, Moscow, 1989.

[13] V. Holy and J. Kubena, Czech. J. Phys. B **32**, 750 (1982).

[14] R. N. Kyutt, P. V. Petrashen, and L. M. Sorokin, Phys. Status Solidi A **60**, 381 (1980).

[15] V. G. Kohn, M. V. Kovalchuk, R. M. Imamov, and E. E. Lobanovich, Phys. Status Solidi A **64**, 435 (1981).

[16] V. A. Bushuev and A. P. Petrakov, Kristallografiya **40**, 1043 (1995) [Crystallogr. Rep. **40**, 968 (1995)].

[17] V. A. Bushuev and A. P. Petrakov, Kirstallografiya **40**, 1050 (1995) [Crystallogr. Rep. **40**, 974 (1995)].

[18] M. A. Andreeva, S. F. Borisova, and S. A. Stepanov, Poverkhnost', No. 4, 5 (1985).

[19] V. A. Bushuev, Fiz. Tverd. Tela (Leningrad) **31**, 70 (1989) [Sov. Phys. Solid State **31**, 1877 (1989)].

[20] A. P. Petrakov and V. A. Bushuev, Pis'ma Zh. Tekh. Fiz. **19**, 92 (1993) [Tech. Phys. Lett. **19**, 637 (1993)].

[21] V. A. Bushuev and A. P. Petrakov, Poverkhnost', No. 9, 64 (1992).

[22] W. R. Runyan, *Silicon Semiconductor Technology*, McGraw-Hill, New York, 1965.

[23] M. Servidori, A. Zani, and G. Garulli, Phys. Status Solidi A **70**, 691 (1982).

Translated by M. E. Alferieff

Wide-band approximation in the problem of charge transfer of a desorbed particle at a metal surface

S. Yu. Davydov

A. F. Ioffe Physicotechnical Institute, Russian Academy of Sciences, 194021 St. Petersburg, Russia

(Submitted June 10, 1997; resubmitted August 8, 1997)
Fiz. Tverd. Tela (St. Petersburg) **40**, 161–163 (January 1998)

Electron transfer processes between a desorbed particle and a metal surface (charge transfer) are studied in the approximation of a wide but finite band. The effect of a change in the width of the surface band produced by adsorbed atoms on the emission probability of neutrals and ions is investigated. © *1998 American Institute of Physics.* [S1063-7834(98)03801-5]

1. Substrates coated with a layer of alkali metal are ordinarily used in the experimental study of charge transfer of scattered or sputtered atoms (ions).[1,2] When the density of atoms in such a layer changes, only the change in the work function of the system is taken into account in the theory (see, for example, Ref. 3); the change in the band structure of the system is neglected. This is because, as a rule, the infinitely wide band approximation is used in the theory of charge transfer. This approximation is not applicable *a priori* for the problem of a varying adatom density, since the surface band produced by overlapping quasilevels shifts, broadens, and changes shape as the adatom density increases.[4–8] The present paper examines the role of broadening of the surface band in the formation of the charge composition of the scattered (sputtered) flux.

2. The Anderson Hamiltonian

$$H(t)=\sum_k \varepsilon_k c_k^+ c_k+\varepsilon_a(t)a^+a+\sum_k V_k(t)(c_k^+a+\text{h.c.}) \tag{1}$$

with a time-dependent position $\varepsilon_a(t)$ of the quasilevel of an adatom and the interaction energy $V_k(t)$ of an adatom with a metal substrate is widely used to describe the charge transfer of atoms (ions) in the process of scattering by the surface of a solid (or sputtering or desorption).[1,2] Here ε_k is the dispersion law of the metal electrons in the substrate, $c_k^+(c)$ is the creation (annihilation) operator of an electron in the state $\mathbf{k}$, and $a^+(a)$ is the creation (annihilation) operator of an electron in the level ε_a. For simplicity, the spin index is dropped.

From the Heisenberg equations of motion, setting $V_k(t)=u(t)V_k$, we obtain the equation

$$i\frac{\partial \widetilde{C}_a(t)}{\partial t}=-\frac{i}{\pi}u^*(t)\int_{t_0}^{t}dt'u(t')\widetilde{c}_a(t')\times\exp[i\varepsilon_a(t-t')]K(t-t')+\Phi(t), \tag{2}$$

where

$$K(t-t')=\int_{-\infty}^{+\infty}d\omega\Delta(\omega)\exp[-i\omega(t-t')],$$

$$\Delta(\omega)=\pi\sum_k |V_k|^2\delta(\omega-\varepsilon_k),$$

$$\widetilde{c}_a(t)=\exp(i\varepsilon_a t)c_a(t), \tag{3}$$

$\Phi(t)$ is an inhomogeneous term (see Ref. 1). Here and below the system of units in which $\hbar=1$ is used.

Ordinarily, the following procedure is used to convert the integrodifferential equation (2) into a differential equation. First, it is assumed that the factor $|V_k|^2$ in the expression for $\Delta(\omega)$ can be taken outside the summation, averaging the term over $\mathbf{k}$ in a corresponding manner, $|V_k|^2\rightarrow V^2$. Then

$$\Delta(\omega)=\pi V^2\rho(\omega), \tag{4}$$

where

$$\rho(\omega)=\sum_k \delta(\omega-\varepsilon_k) \tag{5}$$

is the density of states of the substrate. In the infinitely wide-band approximation it is assumed that $\rho(\omega)=\text{const}$. Then it follows from Eqs. (3) that $K(t-t')\propto\delta(t-t')$, which transforms Eq. (2) into a differential equation.

3. An attempt to go beyond the infinitely wide-band approximation, using a time-dependent Anderson Hamiltonian, was undertaken in Refs. 9 and 10, where a model of two finite-width bands separated by a gap was studied. I also call attention to Ref. 11, where the special case of a time-independent position ε_a of an adatom level and interaction matrix element $V(t)$ differing from zero only in a definite time interval is studied.

In the present work I employ the approximation of a wide but finite conduction band in the substrate, whose density of states $\rho(\omega)$ is given by the expression

$$\rho(\omega)=\begin{cases}\dfrac{1}{D}, & |\omega|<D,\\ 0, & |\omega|>D.\end{cases} \tag{6}$$

Here the center of the s band, having a width $2D$ and containing two electrons, is taken as the point of zero energy. Substituting expressions (6) and (4) into Eq. (3), we obtain

$$K(t-t')=\pi V^2\frac{\sin[D(t-t')]}{D(t-t')}. \tag{7}$$

For sufficiently large D the function K has, at $t=t'$, a sharp maximum with a width of the order of $1/D$. If it is permissable to regard the functions $u(t)$ and $\widetilde{c}_a(t)$ in Eq. (2) as constants in this time interval, then removing them from the integrand substantially simplifies the calculations. For example, for $D=1$ eV the characteristic time interval $\tau_1=1/D=3.3\times10^{-16}$ s. If the desorbed ion moves with velocity $v=10^6$ cm/s and the interaction potential V changes over a characteristic distance of the order of 3 Å, then the desorbed atom interacts with the surface during a characteristic time interval $\tau_2\approx3\times10^{-14}$ s. Therefore Eq. (2) admits the simplification described above. Then, repeating all calculations of Ref. 1 we obtain the following expressions for the occupation probability $\langle n_a(\infty)\rangle$ of the level of a particle flying off (moving to infinity) with velocity $\nu=\text{const}$:

1) $\varepsilon_a>0$

$$a)\ \ \varepsilon_a>\varepsilon_f,\quad n_a=\frac{\Delta}{(\Delta^2+\Lambda^2)^{1/2}}[\pi-\arctan(\Delta/\Lambda)]^{-1}\times\exp\left\{\frac{(\varepsilon_f-\varepsilon_a)}{\gamma v}[\pi-\arctan(\Delta/\Lambda)]\right\},\tag{8}$$

$$b)\ \ \varepsilon_a<\varepsilon_f,\quad n_a=1-\frac{\Delta}{(\Delta^2+\Lambda^2)^{1/2}}[\arctan(\Delta/\Lambda)]^{-1}\times\exp\left[-\frac{(\varepsilon_f-\varepsilon_a)}{\gamma v}\arctan(\Delta/\Lambda)\right],\tag{9}$$

2) $\varepsilon_a<0$

$$a)\ \ \varepsilon_a>\varepsilon_f,\quad n_a=-\frac{\Delta}{(\Delta^2+\Lambda^2)^{1/2}}[\arctan(\Delta/\Lambda)]^{-1}\times\exp\left[-\frac{(\varepsilon_f-\varepsilon_a)}{\gamma v}\arctan(\Delta/\Lambda)\right],\tag{10}$$

$$b)\ \ \varepsilon_a<\varepsilon_f,\quad n_a=1-\frac{\Delta}{(\Delta^2+\Lambda^2)^{1/2}}[\pi+\arctan(\Delta/\Lambda)]^{-1}\times\exp\left\{-\frac{(\varepsilon_f-\varepsilon_a)}{\gamma v}\times[\pi+\arctan(\Delta/\Lambda)]\right\}.\tag{11}$$

Here

$$\Delta=\begin{cases}\dfrac{\pi V^2}{D}, & |\varepsilon_a|<D,\\ 0, & |\varepsilon_a|>D,\end{cases}\tag{12}$$

$$\Lambda=\frac{V^2}{D}\ln\left|\frac{D+\varepsilon_a}{D-\varepsilon_a}\right|\tag{13}$$

and γ is the characteristic reciprocal of the decay length of the hybridization potential: $V\propto\exp(-\gamma z)$, where z is the distance from the surface of the substrate to the desorbed particle. In Eqs. (8)–(13) the notation $n_a\equiv\langle n_a(\infty)\rangle$ and $\varepsilon_a\equiv\varepsilon_a(\infty)$ was introduced.

I underscore once again that in deriving the expressions (8)–(13) we studied a finite but wide band. For this reason we could neglect all oscillation effects occurring in two-level systems[1–3] provided that the quasilevel of the adatom lies inside the band and sufficiently far from the band edges (i.e. the quasilevel is displaced from the edges by an amount greater than the band half-width).

4. As an illustration, let us examine the simple particular case $|\varepsilon_a|\ll D$. For $\varepsilon_a>0$ and $\varepsilon_a>\varepsilon_f$ we obtain

$$n_a=\frac{2}{\pi}\exp\left[-\frac{\pi(\varepsilon_a-\varepsilon_f)}{2\gamma v}\right]Q_1,$$

$$Q_1=\left(1-\frac{4\varepsilon_a}{\pi^2D}\right)\exp\left[-\frac{2\varepsilon_a(\varepsilon_a-\varepsilon_f)}{D\gamma v}\right].\tag{14}$$

As D increases, Q_1 and n_a increase and the particle charge $Z_a\equiv(1-n_a)$ decreases. For $\varepsilon_a>0$ and $\varepsilon_a<\varepsilon_f$ we have

$$n_a=1-\frac{2}{\pi}\exp\left[-\frac{\pi(\varepsilon_f-\varepsilon_a)}{2\gamma v}\right]Q_2,$$

$$Q_2=\left(1+\frac{4\varepsilon_a}{\pi^2D}\right)\exp\left[\frac{2\varepsilon_a(\varepsilon_f-\varepsilon_a)}{D\gamma v}\right].\tag{15}$$

If D increases, then Q_2 decreases, n_a increases, and Z_a decreases. Therefore, for a level ε_a lying above band center the probability $P^+\propto Z_a$ of ions escaping decreases with increasing band width.

For $\varepsilon_a<0$ and $\varepsilon_a>\varepsilon_f$ n_a is given by Eqs. (14) and for $\varepsilon_a<0$ and $\varepsilon_a<\varepsilon_f$ is given by Eqs. (15), i.e., in the present case the ion yield increases with D. The reason for this effect is that the shift of the quasilevel of an adatom $\Lambda\propto\varepsilon_a/D$. As band width increases, the shift decreases, the adatom quasilevel shifts to band center, and the filling of the adatom increases for a level lying above band center and decreases otherwise. This result also holds for an arbitrary ratio of ε_a and D. The effect of a change in band width on the probability of ions escaping is proportional to the quantity $|\varepsilon_a(\varepsilon_a-\varepsilon_f)|$.

We note that both in the tight-binding model[12,13] and in the free-electron approximation,[14] the width of the surface band is proportional to a^{-2}, where $a=a(\theta)$ is the distance between nearest neighbors, which depends on the relative adatom density $\theta=N_m/N_m(\text{ML})$. Since $N_m=a^{-2}$ and $N_m(\text{ML})=d^{-2}$, where d is the distance between the nearest neighbors in a monolayer (ML), we have

$$D(\theta)\propto D(\text{ML})\cdot\theta.$$

In the case when the adatoms interact via a dipole-dipole interaction the concentration shift $\delta\varepsilon_f$ of the Fermi level of the adsorption system equals

$$\Delta\varphi=\Phi\theta(1-n_m),\quad \Phi=4\pi e^2\lambda N_{\text{ML}},\tag{16}$$

where λ is half the length of the dipole formed by the adsorbed ion and its image in the metal substrate and n_m is the number of electrons on the adatom.[14,15] For alkali-metal atoms, if λ is set equal to the half-sum of their ionic and atomic radii and d is taken as the distance between the nearest neighbors in the alkali-metal crystal, then $\Phi\cong15-20$ eV. Therefore $\Phi(1-n_m)$ and $D(\text{ML})$ are of the same order of magnitude and both effects must be taken into account on the same grounds.

We also note that in describing the concentration dependences of the yield of atoms (ions) in electron-stimulated desorption allowance must be made for the change in the width of the surface band (see, for example, Ref. 16).

This work was performed as part of the program ''Surface atomic structures.''

[1] R. Brako and D. M. Newns, Rep. Prog. Phys. **52**, 655 (1989).

[2] J. Los and J. J. C. Geerlings, Phys. Rep. **190**, 133 (1990).

[3] H. Nakanshi, H. Kasai, and A. Okiji, Surf. Sci. **197**, 515 (1988).

[4] S. Yu. Davydov, Fiz. Tverd. Tela (Leningrad) **19**, 3376 (1977) [Sov. Phys. Solid State **19**, 1971 (1977)].

[5] S. Yu. Davydov, Fiz. Tverd. Tela (Leningrad) **20**, 1752 (1978) [Sov. Phys. Solid State **20**, 1013 (1978)].

[6] S. Yu. Davydov, Fiz. Tverd. Tela (Leningrad) **20**, 1998 (1978) [Sov. Phys. Solid State **20**, 1153 (1978)].

[7] S. Yu. Davydov, Fiz. Met. Metalloved. **47**, 481 (1979).

[8] S. Yu. Davydov, Poverkhnost', No. 8, 17 (1991).

[9] S. Yu. Davydov, A. V. Radyushchin, and A. A. Shaporenko, in *Abstracts of Reports at the 10th All-Union Conference on the Surface–Ion Interaction* [in Russian], Moscow, 1991, Vol. 2, p. 53.

[10] D. Yu. Davydov, A. V. Radyushin, and A. A. Shaporenko, Vacuum **44**, 923 (1993).

[11] M. Yu. Gusev, D. V. Klushin, I. F. Urazgil'din, and S. V. Sharov, Zh. Éksp. Teor. Fiz. **103**, 2102 (1993) [JETP **76**, 1047 (1993)].

[12] W. Harrison, *Electronic Structure and the Properties of Solids* [Freeman, San Francisco, CA, 1980; Mir, Moscow, 1983, Vol. 1].

[13] W. A. Harrison, Phys. Rev. B **27**, 3592 (1983).

[14] C. Kittel, *Introduction to Solid State Physics*, Wiley, New York, 1976, 5th edition [Russian translation, Nauka, Moscow, 1978].

[15] J. P. Muscat and D. M. Newns, J. Phys. C **7**, 2630 (1983).

[16] V. N. Ageev, O. P. Burmistrova, and B. V. Yakshinskii, Surf. Sci. **194**, 101 (1988).

Translated by M. E. Alferieff

Positron investigations of free-volume elements in polymer gas-separation membranes

V. P. Shantarovich and Z. K. Azamatova

Institute of Chemical Physics, Russian Academy of Sciences, 117334 Moscow, Russia

Yu. A. Novikov

Institute of General Physics, Russian Academy of Sciences, 117942 Moscow, Russia

(Submitted June 30, 1997)
Fiz. Tverd. Tela (St. Petersburg) **40**, 164–167 (January 1998)

This work is a part of an investigation aimed at converting the positron method into a tool for quantitative investigations of microdefects in polymers. The number (10^{19} cm^{-3}) and effective radii (0.2–2.8 nm) of elementary free volumes in polymer gas-separation membranes polytrimethyl silylpropine (PTMSP) and porous polyphenylene oxide (PPO 200 and 70 m^2/g) are estimated on the basis of positron data. The calculations are facilitated by using the mutually complementary programs PATFIT and CONTIN as well as by the possibility of estimating the diffusion coefficients of positronium in PPO samples having different specific surface areas. [S1063-7834(98)03901-X]

Investigations of free-volume elements (FVEs) in polymer systems is of great interest, since many mechanical and physicochemical properties of polymers depend on the size and number of such elements. At the same time, until very recently, no direct methods for investigating the number and sizes of FVEs were available. Under these conditions the possibilities of the positron-annihilation (PA) method appear to be very attractive. They were noted from the moment the ''free-volume'' model first appeared.[1] According to this model, positronium—a bound system consisting of a positron and an electron (symbol P_s)—strives to occupy an FVE before annihilating, and the annihilation characteristics (lifetimes and intensities of long-lived components in the temporal distribution of the annihilation radiation) yield information about the number and size of the defects (free volumes).[2–4] Until recently, the PATFIT program was used to calculate the annihilation characteristics. This program analyzes the temporal distribution of the annihilation radiation in terms of several exponentials which are characterized by decay rates $\lambda_i/1/\tau_i$ and intensities I_i. Gregory and Jean[5,6] were the first to use the inverse Laplace transform for this distribution in order to obtain a continuous distribution of the positron lifetimes in the annihilation spectrum (CONTIN program). This makes it possible, in principle, to obtain the size distribution of elementary free volumes (FVEs).

In the present work, we employed both programs (PATFIT and CONTIN) to study the unusually long (for polymers) lifetimes of positronium (elements of free volume) in polymethyl silylpropine (PTMSP), used as a nonporous gas-separation membrane, as well as in porous polyphenylene oxide (PPO 200 and 70 m^2/g), which is a porous gas-separation membrane.[7] The high concentration of these volumes gives rise to anomalously high permeability of the membranes and the appearance of a second component (with respect to the standard positronium component τ_3, I_3 near 6 ns for PTMSP and approximately up to 30 ns in porous PPO) in the temporal distribution of the annihilation radiation. Evidently, the two components correspond to the presence of two groups of pores of different sizes. Our preliminary PTMSP data were recently confirmed by Consolati *et al.*[8] and Ito *et al.*[9] In Ref. 8, PATFIT analysis of the temporal distributions of positron annihilation in PTMSP showed a superlong-lived component τ_4 whose lifetime for an evacuated sample reached 13 ns with the same intensities I_4 as in our measurements. This attests to permeability of the pores and the presence of, together with collisional annihilation, a chemical reaction between positronium and atmospheric oxygen in pores.[10] The CONTIN program was used in Ref. 9 to obtain a continuous pore-size distribution in evacuated PTMSP as well as in a sample filled with a plasticizer agent. In contrast to atmospheric oxygen, the plasticizer was chemically inert with respect to positronium and introducing the plasticizer into pores did not produce quenching (shortening of the lifetime) but rather it inhibited the formation of positronium (suppression of the intensity I_4 component). The component I_3 increased at the same time. This can be explained both by the partial filling of large pores with the plasticizer (increase in the number of smaller defects) and by an increase in the probability for capture of positronium at previously existing small defects with complete closing of large defects (vanishing of an alternative channel).

Continuing our investigations in this direction, we report our first results on simultaneous application of the PATFIT and CONTIN programs for the above-mentioned PTMSP and PPO samples under atmospheric conditions (see Table I and Figs. 1 and 2). The error introduced in the estimates of the pore radius by neglecting the chemical reaction of positronium with atmospheric oxygen can be estimated by comparing with the lifetime data for PTMSP.[8] This error is found to be very appreciable and can reach 50–80% for pore radii in PTMSP. We proceeded from the well-known and widely used Tao-Eldrup equation.[2,3] Having PPO samples with a

TABLE I. Comparison of the results of PATFIT and CONTIN analysis of the temporal distributions of the annihilation radiation in a nonporous PTMSP gas-separation membrane and homogeneous PPO.

	PTMSP		Homogeneous PPO	
Distribution parameter	PATFIT	CONTIN	PATFIT	CONTIN
τ_1,ns	0.136±0.006	0.13	0.141±0.008	0.15
τ_2,ns	0.360±0.010	0.40	0.370±0.008	0.35
τ_3,ns	1.520±0.012	1.75	1.780±0.140	2.30
τ_4,ns	5.580±0.020	5.63	3.060±0.130	
I_1,%	23.90 ±1.40	24.5±0.4	18.35 ±1.50	14.6±1.2
I_2,%	29.40 ±1.30	26.7±0.7	50.46 ±1.21	54.0±2.0
I_3,%	5.58 ±0.02	5.4±0.8	15.38 ±2.65	31.0±0.6
I_4,%	40.50 ±0.30	42.9±3.0	15.80 ±2.97	

characterized specific surface area and estimating the pore radii, at least with the above-indicated error, it was tempting to estimate the order of magnitude of the diffusion coefficient D of positronium before it is captured in a pore since, if this coefficient is known, it is possible not only to determine the relative pore-size distribution according to R but also the absolute density N (from the capture rates calculated from the annihilation characteristics $\nu = 4\pi DRN$ (Ref. 11)).

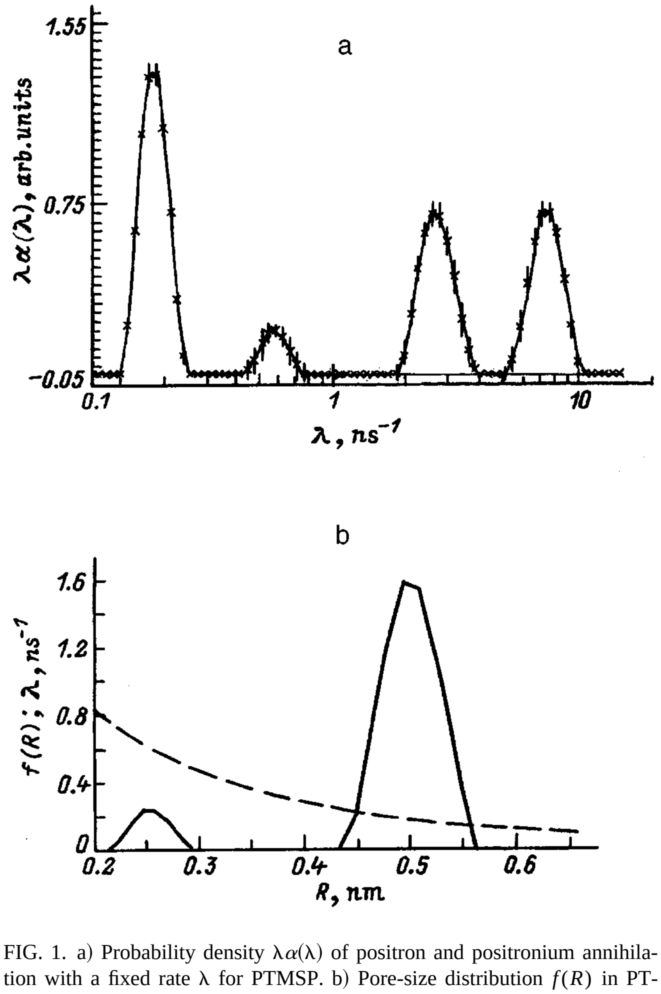

FIG. 1. a) Probability density $\lambda\alpha(\lambda)$ of positron and positronium annihilation with a fixed rate λ for PTMSP. b) Pore-size distribution $f(R)$ in PTMSP (solid line) according to data on the positronium components $I_3\tau_3$ and $I_4\tau_4$ (two left-hand peaks on the annihilation-rate scale). The dashed line represents the computed dependence,[3] used for obtaining the pore sizes, of the annihilation rate λ on the pore radius R.

The measurements were performed with an ORTEC spectrometer, assembled in the ''fast-fast'' arrangement having a resolution of 230 ps (the full width at half-height of the peak of instantaneous coincidences). The total statistical sample for each curve consisted of at least 10^7 counts.

The results obtained with the PATFIT and CONTIN analysis of the positron lifetime spectra of PTMSP and nonporous (homogeneous) PPO are presented in Table I. Single-crystal silicon, whose lifetime spectrum contains the single component 220 ps, was used as the standard sample. One can see that homogeneous PPO possesses a spectrum that is characteristic for ordinary polymer materials. Although PATFIT distinguishes two components τ_3 and τ_4 here, these components are quite close (their intensities are within 15% of each other). Just as in the case of PTMSP, the CONTIN program, which was employed in the annihilation rate interval 0.1–15 ns^{-1} with 75 points in the solution, describes them by a single wide peak near 2.3 ns with an intensity of 31%. At the same time, PTMSP, which is distinguished by an

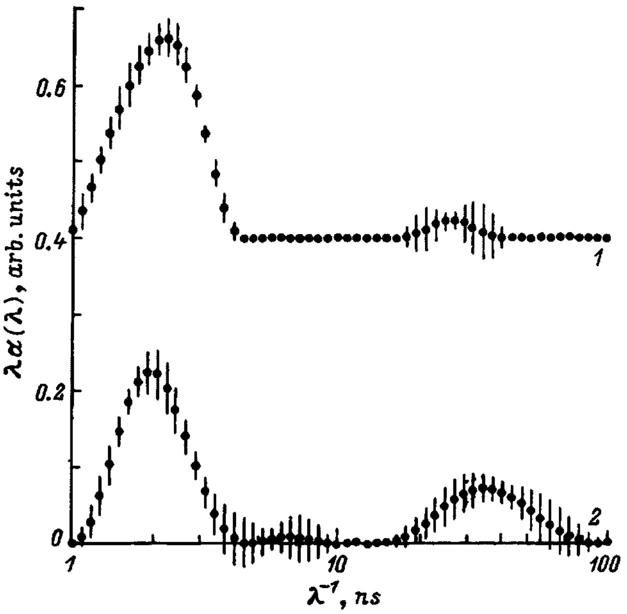

FIG. 2. CONTIN data on the probability density of positronium annihilation with a fixed lifetime ($\tau = \lambda^{-1}$) in PPO: 70 (*1*) and 200 m^2/g (*2*). In the PATFIT program these components correspond to intensities I_3 and I_4 with average times τ_3 and τ_4, respectively.

unusually high permeability, has a lifetime of 5.58 ns with a very high intensity of 40.5%. The PATFIT and CONTIN data for PTMSP agree very well with one another. This is explained by the fact that the correct choice of the resolution function was made in the PATFIT analysis. Figure 1a demonstrates the annihilation probability distribution $\lambda\alpha(\lambda)$ with a fixed rate λ (Ref. 5) for positrons and positronium in PTMSP and Fig. 1b shows the pore-size distribution obtained for PTMSP with the CONTIN data and the well-known equations (from Refs. 2 and 3) relating the positronium lifetime with the pore size. We also note that, according to existing ideas,[11,12] the $I_1\tau_1$ component corresponds to a combination of processes leading to the annihilation of singlet positronium and delocalized positrons and in many cases the $I_2\tau_2$ component is due, at least partially, to the annihilation of positrons localized at small defects in microregions of high density (ordering) in the experimental material. However, this process is not discussed here in more detail.

Let us now consider the data for porous PPO. Figure 2 (curves 1, 2) shows the CONTIN results for the positronium part of the positron lifetime spectra in PPO membranes with specific surface areas of 70 and 200 m^2/g. Ninety points were used for the solution in the wider interval $0.01-15$ ns^{-1}. As one can see, for the 200 m^2/g sample, even under atmospheric conditions, the longest-lived positronium component (right-hand peak), whose intensity equals 6.5% according to the PATFIT data, is characterized by an average lifetime of 35 ns. This is somewhat longer than the value τ_4 which we presented earlier for this material.[4] As noted in Ref. 4, for such long positronium lifetimes it is no longer entirely correct to use the equations of Refs. 2 and 3, which neglect the characteristic annihilation rate of triplet positronium (0.007 ns^{-1}) compared with the annihilation rate of positronium in a pore. The correction[4] gives somewhat larger (by approximately 30%) pore radii than the values calculated according to Refs. 2 and 3. Ultimately, it can be concluded that according to the positron data pores with a radius of approximately 1.4 nm are present in PPO 200 m^2/g even under atmospheric conditions. Now, using this specific surface area as the upper limit of this quantity for the sample in the atmosphere, it can be stated that the pore density $N<3.3\times10^{19}$ g^{-1} or, assuming the density of the polymer material to be approximately 1 g/cm^3, $N<3.3\times10^{19}$ cm^{-3} and the average distance between defects (pores) $\lambda>0.3\times10^{-6}$ cm. Further, according to the calculations in Ref. 4, even if degassing PPO 200 m^2/g triples the lifetime, which ordinarily is not achieved, this will correspond to doubling of the defect radius. For a fixed surface area, this means that the pore density decreases and, correspondingly, the distance between the pores increases. Thus, it is found that $0.3\times10^{-6}<\lambda<0.5\times10^{-6}$ cm. Judging from the large change occurring in the intensity of the longest-lived peak when the specific surface changes from 200 to 70 m^2/g (Fig. 2), the positronium diffusion length $\lambda_D^{Ps}=(6D\tau)^{1/2}$ before localization at a defect is close to λ and it can be assumed that it falls within the same limits. Taking the lifetime τ of nonlocalized positronium to be approximately equal to the lifetime of free positrons (0.3 ns), we find that $5\times10^{-4}<D_{Ps}<1.5\times10^{-4}$ cm^2/s. We note that in a previous work[11] we used the value 10^{-4} cm^2/s as an estimate of the defect density in PTMSP. It turns out that the number of defects united by the right-hand peak in Fig. 1b and calculated from the capture rate ν according to the ratio $\nu/4\pi DR$ is several units times 10^{19} cm^{-3}.

In conclusion, we note that attempts to estimate the diffusion coefficient of nonlocalized positronium have been made previously,[13,14] with the estimate in Ref. 14 applied to resins. The equation (2) from Ref. 4, relating the ratio $I_3/(I_2+I_3)$ to the positronium diffusion coefficient, was used. In a three-component description, this ratio approximately equals the probability of positronium escaping into a pore. However, even this approach is not perfect because it is difficult to distinguish the exact amount of delocalized positronium against the background formed by free-positron annihilation. At the same time, it is interesting that the value $D_{Ps}=0.2\times10^{-4}$ cm^2/s, which is close to the lower limit of our estimate, was obtained in Ref. 14.

The smallness of the value obtained for the diffusion coefficient as compared with the value $D_+=10^{-1}$ cm^2/s[15] characteristic for free positrons in polymers shows that the diffusate is positronium and not a positron, whose localization in a pore could be accompanied by the formation of positronium.

Evidently, the accuracy of our estimates can be increased by working with degassed samples.

We are grateful to Professor R. B. Gregory (Kent State University, USA) for kindly providing the CONTIN code.

This work was supported by (Grant No. 95-03-08325) from the Russian Fund for Fundamental Research.

[1] W. Brandt and J. Spirn, Phys. Rev. **142**, 231 (1966).
[2] S. J. Tao and J. Chem. Phys. **56**, 5499 (1972).
[3] M. Eldrup, D. Lightbody, and J. N. Sherwood, Chem. Phys. **63**, 51 (1981).
[4] V. P. Shantarovich, O. P. Yampol'skiĭ, and I. B. Kevdina, Khim. vys. énerg. **28**, 53 (1994).
[5] R. B. Gregory and Zhu Yongkang in *Positron and Positronium Chemistry*, edited by Y. C. Jean, World Scientific, Singapore, 1991, p. 136; R. B. Gregory, J. Appl. Phys. **70**, 4665 (1991).
[6] Q. Deng and Y. C. Jean, Macromolecules **26**, 30 (1993).
[7] Yu. P. Yampolskii, V. P. Shantarovich, and F. P. Chernyakovskii *et al.* J. Appl. Polym. Sci. **47**, 85 (1993).
[8] G. Consolati, J. Genco, M. Pegoraro, and L. Zanderighi, J. Polym. Sci. Pt B: Polym. Phys. B **34**, 357 (1996).
[9] K. Okamoto, K. Tanaka, M. Ito, H. Kita, and Y. Ito, in *Proceedings of the tenth International Conference on Positron Annihilation*, edited by Yuan-Jin He and Y. C. Jean, Mat. Sci. Forum. Trans Tech. Publ., Switzerland, 1995, Vol. **175–178**, p. 743.
[10] A. D. Mokrushina, A. O. Tatur, and V. P. Shantarovich, Izv. Vyssh. Uchebn. Zaved., Ser. khim. **6**, 1216 (1973).
[11] V. P. Shantarovich, Yu. P. Yampol'skiĭ, I. B. Kevdina, Z. K. Azamatova, and V. S. Khotimski, Vysokomolekulyar. soedineniya A **39**, 445 (1997).
[12] V. P. Shantarovich, J. Rad. Nucl. Chem. Articles **210**, 357 (1996).
[13] K. Venkatesvaran, K. J. Cheng, and Y. C. Jean, J. Chem. Phys. **88**, 2465 (1984).
[14] B. Brandt and R. Paulin, Phys. Rev. Lett. **21**, 193 (1968).
[15] M. Maurino and W. Brandt, Bull. Am. Phys. Soc. **24**, 72 (1979).

Translated by M. E. Alferieff

Electron spectroscopy of fluoridated fullerene films

A. L. Shakhmin, N. V. Baranov, and M. A. Khodorkovskiĭ

Russian Science Center ''Applied Chemistry,'' St. Petersburg, Russia

S. V. Murashov

All-Russia Science Center ''S. I. Vavilov State Optical Institute,'' St. Petersburg, Russia

(Submitted June 8, 1997)
Fiz. Tverd. Tela (St. Petersburg) **40**, 168–172 (January 1998)

The chemical and energy structures of highly fluoridated fullerene films have been investigated. Analysis of the complex structure of carbon 1*s* spectra showed the presence of C–F and C–F2 fragments as well as nonfluoridated carbon atoms with an overwhelming quantity of C–F bonds. The band gap in fluoridated-fullerene and its films was estimated to be 8.0 eV and energy loss on an interband transition at 11 eV was also observed. Comparison of the valence-band spectra of the experimental samples showed that the valence band of fluoridated fullerenes is divided into anionic and cationic parts (similarly to alkali-halide crystals) and suggests that fluoridated fullerenes possess the corresponding properties, making it possible to find new materials with wide practical applications. © *1998 American Institute of Physics.* [S1063-7834(98)04001-5]

Interest and the number of publications concerning fullerene are shifting in a direction away from the investigation of its properties to the investigation of the properties of its derivatives and compounds. This shift is connected with the search for possible applications of new materials. In the present work we investigated by electron spectroscopy powders of fullerene and fluoridated fullerene as well as films obtained from these materials.

The experimental samples were prepared from fullerene soot (the mixture C_{60}(86%)+C_{70}(14%)). Fluoridated films were prepared from fluoridated fullerene powder, obtained from fullerene soot produced at the Russian Science Center ''Applied Chemistry'' by gas-phase fluoridation with molecular fluorine (90%F_2+10%N_2) in a flow-through–diffusion system. A batch of fullerene soot powder was fluoridated in a reactor in a period of four days with temperature varying from 19 to 170 °C until the powder acquired a light-yellow color. According to the empirical formula, the nominal composition of the fluoridated fullerene so obtained (calculated for C_{60}) was $C_{60}F_{46}$.

Fullerene-soot and fluoridated-fullerene films were obtained in situ by thermal sputtering of the corresponding powder on aluminum foil, precleaned by ionic etching. During sputtering the vacuum in the chamber was not worse than 5×10^{-8} torr. The sputtering process was monitored with a quadrupole mass spectrometer with a mass range of up to 2000. Sputtering was performed with controllable heating up to 350 °C. In the course of sputtering of the fluoridated-fullerene film, the mass spectra showed the appearance and appreciable growth of a peak due to atomic fluorine (19 amu) and molecular fluorine (38 amu) after 250 °C and, starting at 290 °C, the appearance of intense signals with masses 720 amu (C_{60}) and 840 amu (C_{70}), their double ions, and a large quantity of masses ranging from 300 to 400 amu. At the same time, clear signals in the mass range 720–1800 amu (except for 840 amu) that could be attributed to fullerene with different degrees of fluoridation were not observed.

Thus, according to the mass spectra, fluoridated-fullerene powder predominantly decomposes into fluorine (including atomic fluorine) and fullerene on heating. The presence of a large number of peaks in the range 400–600 amu attests to decomposition of some fluoridated fullerenes into large fragments, which is characteristic for highly fluoridated fullerenes.[1] The evaporated components were deposited on room-temperature aluminum foil. In the process, first, the formation of a fullerene film and fluoridation of the film could occur simultaneously and, second, fullerene could be fluoridated in the gas cloud between the sputtering cell and the surface of the sample, which were separated by a distance not greater than 1 cm. The film obtained under ultrahigh-vacuum conditions was moved into an x-ray photoelectron spectrometer, where its energy structure was investigated.

The x-ray photoelectron spectra (XPS) of all samples were obtained with a Perkin Elmer ESCA-5400 spectrometer using Mg $K\alpha$ radiation. The energy of the spectrometer was calibrated with respect to the $4f_{7/2}$ level of gold; the binding energy of this level was taken to be 84.00 eV.

In the course of the investigations of all samples, survey spectra, 1*s* spectra of O, C, and F, and valence-band spectra were recorded and the curve of the difference current through the sample was also recorded. The charging effect for fluoridated-fullerene samples was taken into account according to the 1*s* fluorine peak, whose energy was taken to be the binding energy of the F_{1s} line for teflon (688.75 eV).[2]

The atomic composition calculated for the experimental samples from the XPS spectra is presented in Table I. According to this table, the degree of fluoridation of $C_{60}F_x$ pow-

TABLE I. Atomic composition of fluoridated-fullerene powder and film (in atomic percent) with different photoelectron collection angles.

	Powder	Film		
Element	45°	30°	45°	80°
F	46	34.7	34.7	36.5
O	7	2.1	3.3	2.2
C	47	63.2	62.0	61.3

der is somewhat higher than that obtained by weighing. The C_{1s} spectra obtained for both the fluoridated-fullerene film and the powder is characterized by a complex shape, implying the presence of a large number of components corresponding to different chemical states of the carbon atoms (Fig. 1). It should be noted that irradiation of the sample with low-energy (10 eV) electrons in order to compensate the charging does not change the shape and the relative positions of the features in the C_{1s} spectrum. The spectrum shifts along the energy scale as a whole. This attests to the fact that the surface of the sample is uniformly charged and makes it possible to interpret the characteristic features of the spectrum taking their relative position into consideration. The F_{1s} spectrum, in contrast to that of carbon, has no distinct features for both fluoridated samples. This is characteristic for fluorine, which has approximately the same binding energy in different compounds with carbon.[2] The survey spectrum obtained for the fluoridated-fullerene film shows that the thickness of the obtained film is, at least, much larger than the emergence depth of electrons with energies of about 1100 eV (>25 Å), since the aluminum peaks corresponding to the $2s$ and $2p$ levels are not present in the spectrum and the binding energy (535.5 eV) of the small oxygen peak is substantially different from that obtained for the initial aluminum surface (533.0 eV). As one can see from Table I, oxygen is also present in the fluoridated-fullerene powder in an amount equal to 7% with O_{1s} binding energy 535.3 eV at the maximum (with allowance for charging according to F_{1s}); in addition, the O_{1s} spectrum has two features with energies ~ 532.7 and ~ 530.7 eV. The binding energy at the maximum is close to the binding energy of oxygen in water,[2] and this component can be regarded as being adsorbed from

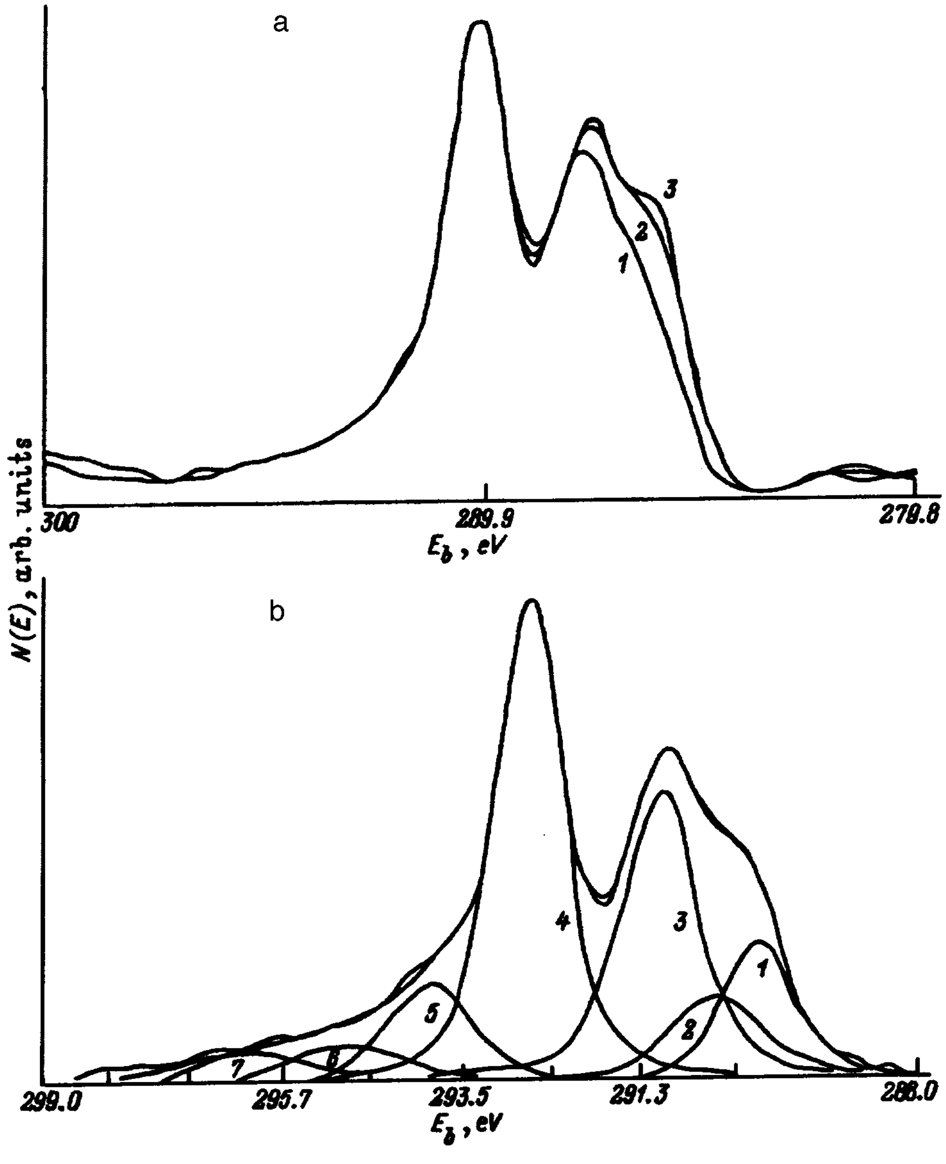

FIG. 1. a) $1s$ spectra of carbon for different photoelectron collection angles. *1*—80°, *2*—45°, *3*—30°. b) Decomposition of the $1s$ spectrum of carbon with a collection angle of 45°.

TABLE II. Decomposition of the C_{1s} spectrum of a fluoridated-fullerene film into individual components.

Peak No. (Fig. 1b)	E_b, eV	Relative peak intensity, %
1	285.83	10.69
1	286.59	7.17
3	287.61	28.07
4	290.05	42.29
5	291.93	8.11
6	293.6	2.32
7	295.1	1.36

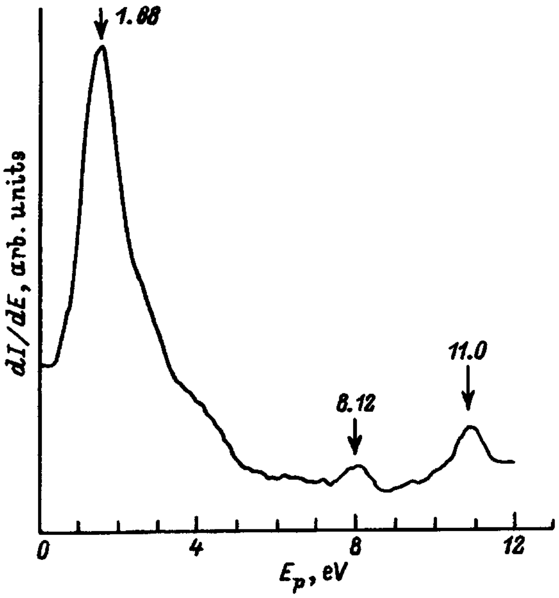

FIG. 2. First derivative of the difference current flowing through a fluoridated-fullerene film versus incident-electron energy.

atmospheric water. The remaining two components can be attributed to oxygen bound with fullerene, similarly to Ref. 3. The O_{1s} peak obtained on a fluoridated-fullerene film has a maximum at 535.5 eV and a small shoulder at 533.5 eV; it can be interpreted similarly to the oxygen in powder. No oxygen peak is observed in the fullerene films obtained in the same manner.

The atomic composition of the powder and film of fluoridated fullerene in Table I is given for different photoelectron collection angles. This corresponds to the depth of the analysis in the range 10–30 Å.

It is evident from Table I that the film is quite homogeneous within the thickness analyzed. The small increase in the amount of carbon near the surface can be attributed to underfluoridation at the end of the sputtering process, but the difference in the values is less than the error in the experimental determination of the atomic concentration. At the same time, these changes can be indirectly supported by Fig. 1a, which displays the C_{1s} spectra obtained from a fluoridated-fullerene film at different electron collection angles. It is evident from this figure that the low-energy characteristics of the spectrum are more intense at the surface of the film than in the volume; it is logical to attribute this increase, with allowance for the binding energy, to carbon atoms that do not bind with fluorene.

The results of the decomposition of the C_{1s} spectrum into individual components are presented in Fig. 1b. The fact that, as noted above, the shape of the spectrum is virtually the same for different conditions of charging of the surface of the sample suggests the following picture of chemical bonds in the fluoridated-fullerene film.

1) Judging from the binding energy of the components, it is logical to attribute the three low-energy peaks to carbon atoms which do not form any bonds with fluorine but which do possess a different number of nearest-neighbor carbon atoms which do have bonds with fluorine. As a result of the presence of such neighbors, the binding energy of the atom changes by about 0.3 eV (according to the estimate in Ref. 4) on account of each bond of a neighboring atom with fluorine.

2) The largest peak, at 290.05 eV, corresponds to carbon atoms which have one bond with fluorine. Judging from the atomic density and the numerical decomposition given for the C_{1s} spectrum in Table II, we conclude that these atoms comprise 26% of the total number of carbon atoms and therefore the same number of fluorine atoms are bound with them. There remains another 9% of fluorine atoms that can form CF_2 fragments with carbon. Correspondingly, these carbon atoms will comprise approximately 7.3% of the total number of carbon atoms; this is quite close to the intensity of the peak at 291.93 eV. Thus, this peak is due to CF_2 fragments. The peaks with energies 295.1 and 293.6 eV are too weak for serious analysis; they could be due to both carbon atoms possessing more than two bonds with fluorine and, what is more likely, carbon atoms possessing, besides bonds with two fluorine atoms, an adequate number of fluoridated carbon atoms as nearest neighbors.

To estimate the band gap in the film obtained, the valence-band spectra and the spectrum of the difference current, flowing through the sample in the case when a fluoridated-fullerene film is irradiated with electrons with energies from 0 to 12 eV, and the XPS of electron energy losses after the F_{1s} peak were measured.

Peaks in the curve of the first derivative of the difference current through the sample are observed at 1.68, 8.12, and 11 eV (Fig. 2). The peak at 1.68 eV corresponds to the band gap in C_{60} and could be due to nonfluoridated fragments of C_{60} at the surface. Since the low-energy primary electrons are scattered primarily in the surface layer (where the fluorine concentration is lower), the peak at 1.68 eV has the highest intensity. On this basis, it can be concluded that quite substantial structural formations of nonfluoridated fullerene exist in the surface layer of the experimental film. The feature at 8.12 eV apparently characterizes the band gap in the fluoridated-fullerene film. This value of the band gap agrees with the fact that the highly fluoridated fullerene film obtained on aluminum foil was visually transparent, which attests to a much larger band gap than in fullerene (according to different authors the band gap in fullerene ranges from 1.2 to 1.95 eV[5,6]), and it agrees with the loss spectrum after the F_{1s} peak in the XPS (Fig. 3), where the band gap is estimated to be of the order of 8.0 eV. The large shoulder in the fluorine peak is apparently due to surface scattering in the C_{60}

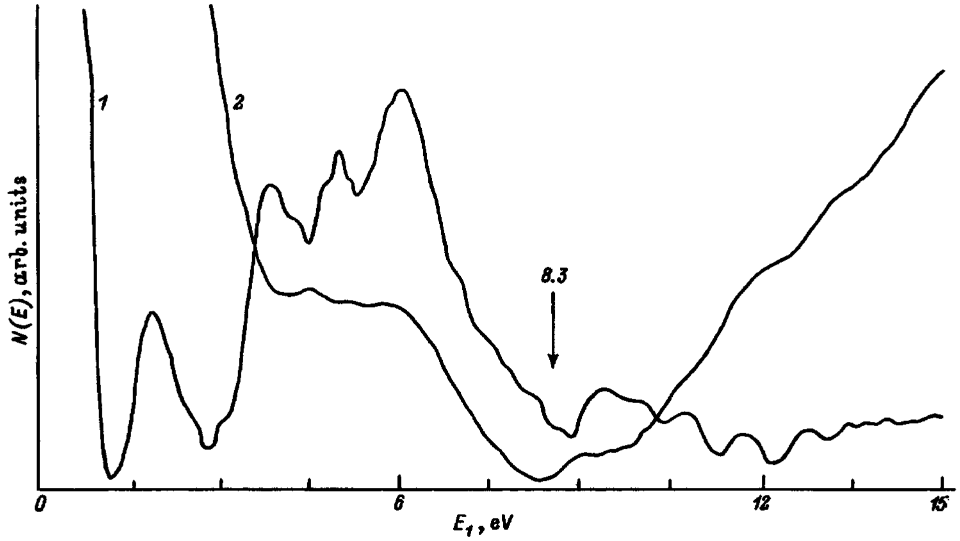

FIG. 3. Photoelectron energy-loss spectra. *1*—After the 1*s* peak of carbon for a fullerene film, *2*—after the 1*s* peak of fluorine for a fluoridated-fullerene film.

film. The feature at 11 eV in the curve of the difference current (Fig. 2) could be due to transitions from the maximum of the density of states of the valence band (feature *A* in Fig. 4) into the conduction-band bottom.

Figure 4 displays the valence-band spectrum of a fluoridated-fullerene film. The shape of this spectrum is substantially different from that of the spectrum of the starting fullerene. Comparing the spectra shows that while a number of features at the valence-band top have the same energy, the fluoridated-fullerene film has a much higher density of states at the valence-band top (similarly to the valence-band spectrum of teflon). The maximum density (feature *A*) lies approximately 3–4 eV below the valence-band top, in good agreement with the position of the feature at 11 eV in Fig. 2. Comparing the valence bands shows that, as a result of charge transfer to fluorine, the region of the σ orbitals of the valence band of the fluoridated-fullerene film is shifted to higher energies than in the case of the corresponding region of the valence band in fullerene and the valence-band top in the fluoridated-fullerene film is formed mainly by the $2p$ states of fluorine. Thus, the valence band of the fluoridated-fullerene film consists of a low-energy subband (anionic) formed by the states of fluorine atoms and a high-energy (cationic) subband formed by the states of carbon, i.e. it is similar to the bands in alkali-halide crystals (AHCs).[7] On the basis of the similarity of the valence bands and band gaps,[7] it can be expected that highly fluoridated fluorine and its films will possess a number of properties which are characteristic for AHCs. For example, it could be possible to produce simple and practicable, highly efficient, secondary-electron emitters, including emitters based on fluoridation of oriented structures of tubular fluorines.

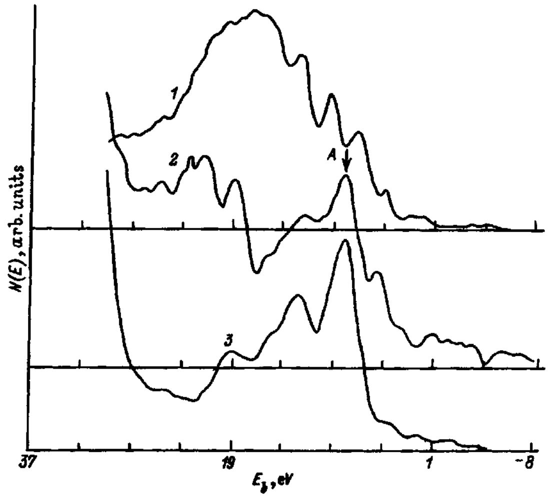

FIG. 4. Valence-band spectra of the starting fullerene (*1*), fluoridated-fullerene (*2*), and teflon (*3*).

This work was performed as part of the State Scientific and Technical Program ''Urgent directions in condensed-media physics'' (direction ''Fullerenes and atomic clusters'') and was financed by the Fund of the Public Union of Scientists for Intellectual Collaboration ''Intellekt.''

[1] H. Selig, C. Lifshiz, T. Peres, J. E. Fischer, A. R. McGhile, W. J. Romanow, J. P. McCauley, and A. B. Smith, J. Am. Chem. Soc. **113**, 5475 (1991).
[2] V. I. Nefedov, *Reference Data for X-Ray Spectroscopy of Chemical Compounds* [in Russian], Moscow, 1984.
[3] V. Vijayakrishnan, A. K. Santra, T. Pradeep, R. Sesshadri, R. Nagarajan, and C. N. Ramachandra Rao, J. Chem. Soc. Chem. Commun. , 198 (1992).
[4] D. M. Cox, S. D. Cameron, A. Tuinman, A. Gakh, J. L. Adcock, R. N. Compton, E. W. Hagaman, K. Kniaz, J. E. Fischer, R. M. Strongin, M. A. Cichy, and A. B. Smith, J. Am. Chem. Soc. **116**, 1115 (1994).
[5] R. Kuzuo, M. Terauchi, M. Tanaka, Y. Saito, and H. Shimonara, Jpn. J. Appl. Phys. **30** (10 B), 4817 (1991).
[6] S. Saito and A. Oshiyama, Phys. Rev. Lett. **66**, 2637 (1991).
[7] Ch. Yu. Lushchik and A. Ch. Lushchik, *Decay of Electronic Excitations with Formation of Defects in Solids* [in Russian], Moscow, 1989.

Translated by M. E. Alferieff

Elastic moduli of single-crystal C_{60}

N. P. Kobelev, R. K. Nikolaev, Ya. M. Soĭfer, and S. S. Khasanov

Institute of Solid-State Physics, Russian Academy of Sciences, 142432 Chernogolovka, Moscow District, Russia

(Submitted June 4, 1997)
Fiz. Tverd. Tela (St. Petersburg) **40**, 173–175 (January 1998)

The matrix of elastic constants of the fcc phase of solid C_{60} has been determined experimentally from measurements of the the velocity of 5 MHz ultrasound in single-crystal samples with different crystallographic orientations. The following values were obtained for the elastic moduli: $C_{11}=14.9\pm0.9$ GPa, $C_{12}=8.8\pm1.0$ GPa, and $C_{44}=6.6\pm0.18$ GPa. The results are compared with theoretical estimates of the elastic moduli and data obtained in previous measurements of the elastic characteristics of solid C_{60}. © *1998 American Institute of Physics.* [S1063-7834(98)04101-X]

In recent years the study of the physical properties of a new class of molecular crystals—fullerites, which consist of giant, highly symmetric, carbon clusters, has attracted increasing attention from investigators. Solid C_{60} is one of the most striking representatives of this class of materials.

The present study is devoted to an experimental determination of the elastic moduli of single-crystal C_{60}. It is necessary to know the elastic constants, which reflect the parameters of the intermolecular interaction in the crystal, in order to analyze the thermal and mechanical properties, to calculate an entire series of fundamental characteristics, and so on. Moreover, they can serve as a criterion for assessing the correctness of theoretical models describing the intermolecular interaction in fullerite. However, the matrix of the elastic moduli of solid C_{60} has still not been determined experimentally. Only measurements of the elastic properties of polycrystalline, more precisely, compacted, samples of fullerite,[1] measurements of Young's modulus of small single-crystal samples,[2,3] and measurements on polycrystalline films[4,5] have been available. This was clearly insufficient. Full-scale measurement of the matrix of elastic moduli became possible only in the present work, for which C_{60} single crystals with adequate dimensions and a high degree of perfection were obtained.

Such single crystals were produced by a modified method of growth from the gas phase. At present, mainly two methods are used to obtain C_{60} crystals: crystallization from solution[6] and growth from the gas (vapor) phase.[7] The main drawbacks of the first method are that the growing crystal traps the solvent and the samples obtained have a block structure. The more promising method is growth from the gas phase by sublimation and desublimation of the starting powder. However, the C_{60} single crystals so obtained are small and they contain many defects. While growing C_{60} single crystals from the gas phase, we observed that the perfection and geometric dimensions of the signal crystals produced can be increased substantially by using as the starting material very small C_{60} crystals which are precleaned by repeated vacuum sublimation. In this connection, the initial single crystals were prepared as follows: 100–150 mg of chromatographically purified, 99.95% pure, C_{60} fullerene powder was placed in an 8–10 mm diameter and 250 mm-long quartz ampule, which was evacuated to 10^{-6} Torr and heated to 300 °C. Organic solvents and volatile impurities were removed in a dynamic vacuum within 8–10 h. Next, the samples were subjected to triple vacuum sublimation. The yield of purified crystals was equal to $\approx70\%$ of the initial charge by weight. These crystals were placed back into the 8–10 mm in diameter and 150 mm long quartz ampul, which was evacuated to 10^{-6} torr and sealed. The ampul was placed into a horizontal two-zone furnace. The growth process occurred under the following conditions: sublimation temperature of 600 °C, crystallization temperature of 540 °C, and crystal growth time of 8–12 h. Next, the crystals were slowly cooled together with the furnace. As a result, we obtained quite large (up to 30 mg), well-faceted C_{60} crystals.

The structural state, degree of perfection, and orientation of the single crystals obtained were checked by x-ray structural analysis. The crystals were fcc at room temperature with lattice parameter $a=14.17$ Å. The external faceting of the crystals consisted mainly of {111} planes. Samples with the ''correct'' faceting consisted of octahedra sectioned along the {100} and {110} planes. The overwhelming majority of the crystals consisted of growth twins, whose distinguishing morphological feature was the presence of concave, dihedral angles of the external shape. As a rule, the growth twins were constructed as follows: A sample possessed a central part with developed {111} octahedral faces, on one or several of which grew a twin ''cap.'' For this reason, for purposes of the present work, crystals with a large nontwin central part were selected from the relatively large number of single crystals and the twin ''caps'' were mechanically detached. The samples prepared from these crystals for measurements of the elastic properties consisted of plane-parallel plates, one plane of which was the growth surface with the corresponding crystallographic orientation; the other plane was either mechanically ground parallel to the first plane or it was a cleavage plane (for some samples with {111} orientation).

Since solid C_{60} room temperature is cubic at the matrix of the elastic constants has three independent components: C_{11} C_{12}, and C_{44}. These elastic constants were determined by an acoustic method. The velocities of longitudinal and

TABLE I. Measurements of the sound velocities and geometric parameters of single-crystalline solid C_{60} samples.

Sample No.	Orientation	Characteristic cross section, mm×mm	Thickness, mm	ν_l, 10^5 cm/s	ν_t, 10^5 cm/s
1	⟨111⟩	4×3	1.36	3.38±0.12	1.575±0.035
2	⟨111⟩	4×3	1.14	3.35±0.15	1.61 ±0.045
3	⟨111⟩	1.5×1.2	1.20	3.36±0.15	1.58 ±0.045
4	⟨111⟩	2.2×1.5	2.10	3.39±0.075	
5	⟨100⟩	4×4	1.39	3.00±0.1	1.97 ±0.045
6	⟨100⟩	3×1.5	1.80	2.96±0.075	1.98 ±0.03
7	⟨110⟩	4×1.5	2.67	3.27±0.07	

transverse sound waves at 5 MHz in samples of different orientations were measured by the echo-pulse method in a transmission scheme. The echo-pulse method that we employed was specially modified for measurements of thin samples. The basic instrumental arrangement was as follows. A signal from a built-in high-frequency quartz oscillator was fed into a circuit forming a timing sync pulse, a circuit forming the delay of the oscillograph trigger, and a circuit forming a probe pulse, which consisted of a short ($\approx 1\ \mu$s) radio pulse with a 5 MHz carrier frequency and a nearly Gaussian, shape phase-synchronized with the radio pulse. This radio pulse was fed into a wide-band low-Q piezoelectric transducer, which provided excitation of ultrasonic vibrations and was glued to one of the faces of the sample. The undetected signal received from a similar piezoelectric trasnducer glued to the opposite face of the sample was fed into the oscillograph input. The propagation time of the received echo pulses in the sample was determined, using the delay circuit, according to the position of the top of the central half-period of these pulses on the oscillograph screen. In the case of short samples or strong damping in the material, the passage time of ultrasound through the sample was estimated as the difference of the delay times (relative to the sync pulse) of the signal received by the piezoelectric transducer with (piezoelectric transducer–sample–piezoelectric transducer) and without (direct acoustic contact between the piezoelectric transducers) the sample present. This scheme made it possible to determine the passage time of ultrasound through the sample to within $\approx 0.01\ \mu$s.

Table I lists the geometric characteristics of the experimental samples and the results of measurements of the sound velocities. The values of the elastic moduli of solid C_{60} calculated on the basis of these measurements are given in Table II. The experimental values of the velocities, measured with a high degree of accuracy, of transverse ultrasonic waves in the directions [100] ($\rho\nu_t^2 = C_{44}$) and [111] ($\rho\nu_t^2 = (C_{11} - C_{12} + C_{44})/3$) directions and longitudinal waves in the direction [100] ($\rho\nu_l^2 = C_{11}$) were used in the calculation. The remaining data served for additional checking. For comparison, Table II also gives the elastic constants for the fcc phase of solid C_{60}, which were obtained theoretically in Ref. 8, where the interatomic Buckingham potential was used for calculating the intermolecular interaction and the electrostatic interaction was taken into account. As one can see, the experimental and theoretical values are in satisfactory agreement with one another.

TABLE II. Experimental and theoretical values of the elastic moduli C_{ij} (GPa) of the fcc phase of solid C_{60} (300 K).

C_{11}	C_{12}	C_{44}	$C_{11} - C_{12}$	
14.9±0.9	8.8±1.0	6.6±0.18	6.1±0.45	Experiment
13.8	6.6	7.0	7.2	Theory of Ref. 8

The Debye temperature θ for the fcc phase of solid C_{60} can be determined, using the well-known relation

$$\theta = \frac{h}{k} \cdot \left(\frac{9N}{4\pi V} \right)^{1/3} \cdot \left(-\frac{1}{v_l^3} + \frac{2}{v_t^3} \right)^{-1/3}, \tag{1}$$

from the values obtained for the elastic moduli. Here N is the number of molecules in a unit cell, V is the cell volume, v_l and v_t are the average values of the longitudinal and transverse sound velocities, and h and k are the Planck and Boltzmann constants, respectively. The average values of the elastic moduli must be calculated in order to obtain the average values of the sound velocities. Such average values characterize polycrystalline materials in which the anisotropy is averaged as a result of the disordered orientation of individual single-crystal grains. In performing the averaging, we determined the bulk modulus K from the equation $K = (C_{11} + 2C_{12})/3$ and the shear modulus G from the relation[9] $G = ((C_{11} - C_{12})/2C_{44})^{2/5}$. All other elastic constants of the polycrystal material (Young's modulus E, the longitudinal modulus C_l, and the Poisson ratio ν) were estimated from G and K using the well-known relations between the elastic moduli of an isotropic medium. The computational results are presented in Table III. The average sound velocities are 3.3×10^5 cm/s for longitudinal sound and 1.7×10^5 cm/s for transverse sound. This gives a Debye temperature ~ 66 K.

The averaging performed here, of the elastic moduli, also makes it possible to compare the results obtained in the present experiment with the measurements of the elastic properties performed on compacted samples[1] and polycrystalline films[4] of C_{60} (Table III). As one can see, the values of the elastic moduli of compacted C_{60} are approximately 30% lower than those obtained for the single-crystal material. This is apparently due to the structural imperfection of the compacted samples. The elastic moduli for the polycrystalline film are also lower than for the single-crystal C_{60}. In this case, the discrepancy between the results could also be due

TABLE III. Isotropic moduli of polycrystalline C_{60}, calculated from the values of the moduli C_{ij} of a single crystal, and data from previous works.

K, GPa	G, GPa	C_l, GPa	E, GPa	ν	References
10.8±0.75	4.85±0.18	17.2±0.45	12.6±0.45	0.306±0.012	This work
8.4±0.5	3.75±0.1	13.4±0.4	9.8±0.4	0.305±0.02	Ref. 1
6.4±0.5	4.1±0.2	13.3±0.8	12±1	0.18±0.04	Ref. 4.

to the exsitence of crystallographic texture in the film samples.

To compare the results obtained in the present work with the measurements of the elastic properties of single-crystal C_{60} performed by other authors,[2,3] who estimated only Young's modulus, the crystal orientation being essentially unknown, we estimated on the basis of the elastic constants determined in the present work Young's modulus for the most characteristic orientations: $E_{[100]}=8.3\pm 0.6$ GPa, $E_{[110]}=13.2\pm 1$ GPa, and $E_{[111]}=16.3\pm 1.2$ GPa. The value 19 ± 5 GPa was obtained in Ref. 2 and 15.9 GPa was obtained in Ref. 3. It can be assumed that in both cases the orientation of the crystals was close to [111], and in this case the agreement between the values obtained is acceptable.

In summary, the results of most previous estimates of the elastic properties of solid C_{60} agree with our measurements. The exception is Ref. 5, where measurements of oscillations of thin fullerite films gave values for the elastic moduli that were 3 to 5 times higher than our estimates. In our opinion, this could be due to photopolymerization of the very thin fullerite films used in Ref. 5. The appearance of covalent bonds between C_{60} molecules results in strong stiffening of the elastic characteristics of fullerite.[10]

We thank B. Sh. Bagautdinov and R. A. Dilanyan for assisting in the x-ray-structural investigations.

This work was performed as part of the State Scientific and Technological Program ''Urgent problems in condensed-state physics: fullerenes and atomic clusters.''

[1] N. P. Kobelev, A. P. Moravskiĭ, Ya. M. Soĭfer, I. O. Bashkin, and O. G. Rybchenko, Fiz. Tverd. Tela (St. Petersburg) **36**, 2732 (1994) [Phys. Solid State **36**, 1491 (1994)].

[2] S. Hoen, N. G. Chopra, and X.-D. Xiang *et al.*, Phys. Rev. B **46**, 12737 (1992).

[3] X. D. Shi, A. R. Kortan, and J. M. Williams *et al.*, Phys. Rev. Lett. **68**, 827 (1992).

[4] H. Coufal, K. Meyer, and R. K. Grygier *et al.*, Appl. Phys. A **59**, 83 (1994).

[5] C. B. Eom, A. F. Hebard, and L. E. Tremble *et al.*, Science **259**, 1887 (1993).

[6] V. V. Ratnik, A. V. Talyzin, P. P. Syrnikov, and L. M. Sorokin, Fiz. Tverd. Tela (St. Petersburg) **37**, 565 (1995) [Phys. Solid State **37**, 308 (1995)].

[7] M. Tachibana, M. Michiyama, and H. Sakuma *et al.*, J. Cryst. Growth **166**, 883 (1996).

[8] E. Burgos, E. Halas, and H. G. Bonadeo, Phys. Rev. B **49**, 15 544 (1994).

[9] K. S. Aleksandrov, Dokl. Akad. Nauk SSSR **164**, 800 (1965) [Sov. Phys. Dokl. **10**, 893 (1966)].

[10] N. P. Kobelev, Ya. M. Soifer, and I. O. Bashkin *et al.*, Mol. Mater. **7**, 261 (1996).

Translated by M. E. Alferieff

Spin correlations in $YBa_2(Cu_{1-x}F_x)_3O_{7+y}$ ceramic

G. P. Kopitsa, V. V. Runov, and A. I. Okorokov

B. P. Konstantinov St. Petersburg Institute of Nuclear Physics, Russian Academy of Sciences,
188350 Gatchina, Leningrad Province, Russia

(Submitted April 10, 1997)
Fiz. Tverd. Tela (St. Petersburg) **40**, 23–26 (January 1998)

To detect scattering by magnetic correlations and to estimate their characteristic space scale, $YBa_2(Cu_{1-x}Fe_x)_3O_{7+y}$ ceramic with $x=0.13$ and $y=0.4$ is investigated by the small-angle scattering of polarized neutrons. The measurements are carried out in the range of temperatures $15\ K \leqslant T \leqslant 315\ K$ and magnetic fields $0 < H \leqslant 4500$ Oe. Anomalies in the temperature curves of the intensity $I(T,q)$ (where q is the momentum transfer) and the polarization $P(T,q)$ are observed in the temperature range $T < 40$ K. Interference between nuclear and magnetic scattering is also observed in this temperature range. The observed phenomena are interpreted as scattering by magnetic correlations having a scale $70\ Å < R < 370\ Å$. Irreversible effects and the type of magnetic ordering are discussed. © *1998 American Institute of Physics.* [S1063-7834(98)00501-2]

Despite the abundance of papers published in the last few years, the system of high-temperature (high-T_c) superconductors $YBa_2(Cu_{1-x}Fe_x)_3O_{7+y}$ continues to hold the attention of researchers for its bearing on the question of coexistence of magnetism and superconductivity.

According to Mössbauer spectroscopy,[1–3] in the low-temperature range the Fe atoms in this system exhibit magnetic ordering, predominantly of the spin-glass type, and at the same time the superconducting state is preserved for $x \leqslant 0.15$ with sufficient oxygen enrichment. This hypothesis has been corroborated in several studies employing diverse experimental techniques.[4,5] However, the type of magnetic ordering and its characteristic scale within which neutron-scattering experiments might be feasible, remain an open question, even though such experiments have actually been performed. Specifically, in the only small-angle neutron-scattering experiment known to us, Katano *et al.*[5] have observed an extremely weak temperature dependence of neutron scattering at $T \leqslant 20$ K, which the authors, drawing on data from magnetic measurements, have interpreted as scattering by magnetic fluctuations without any further analysis of the hypothesized magnetic scattering, because of its smallness above the background of nuclear scattering. In the ceramic, as we know from Ref. 6 and as remarked in Ref. 5, very strong small-angle nuclear scattering is observed as a result of nuclear density fluctuations, highly recommending the use of polarized neutrons for the *a priori* observation of weak magnetic scattering above the nuclear background. Garcia-Muñoz *et al.*[7] have performed diffraction measurements on $YBa_2(Cu_{0.9}Fe_{0.1})_3O_{7+y}$ ceramic using polarized neutrons. However, they observed only paramagnetic scattering in the temperature range 1.5–300 K without any signs of long-range or short-range magnetic ordering, contradicting the premises from Mössbauer spectroscopy.

In the present study we have detected scattering by spin correlations in the investigated ceramic at $T \leqslant 40$ K. The form of the momentum dependence of small-angle magnetic scattering and the irreversibility of the temperature dependence of the polarization during cooling and heating of the sample are indicative of possible magnetic ordering of the spin-glass type in the given system in the low-temperature range.

1. DESCRIPTION OF THE EXPERIMENT

According to Ref. 8, the investigated system is single-phase with a superconducting transition temperature $T_c \cong 9$ K. The measurements were performed on two samples of the same composition and different thicknesses. One of them was in the shape of a cylinder of length 25 mm and diameter 9 mm, and the other comprised a plate of dimensions $25 \times 8\ mm^2$ of thickness 3 mm. Polarization effects and scattering are proportionately weaker for a thin sample, and their observation is naturally more difficult. In measurements on the thin sample, however, we were able to disregard multiple nuclear scattering in analyzing the dependence of the scattering on the momentum transfer.

The temperature measurements were carried out in an RNK 10-300 cryorefrigerator in the range $15\ K \leqslant T \leqslant 315\ K$ within error limits $\Delta T/T \leqslant 10^{-2}$. The sample was placed between the poles of an electromagnet, which permitted measurements to be performed in the magnetic field range $0 < H \leqslant 4500$ Oe. The electromagnet had a large angular aperture and could be rotated in the horizontal plane through angles $0 \leqslant \varphi \leqslant 30°$ (φ is the angle between the field vector $\mathbf{H}$ and the momentum vector $\mathbf{q}$), thereby affording the possibility of changing the direction of the applied magnetic field relative to $\mathbf{q}$.

The experiment was carried out in the VVR-M reactor at the Institute of Nuclear Physics in St. Petersburg in conjunction with the Vektor multidetector apparatus for the small-angle scattering of polarized neutrons.[9] A multichannel analyzer enabled measuring the polarization of the scattered neutrons

$$P(T,q)=\frac{I(\uparrow)-I(\downarrow)}{I(\uparrow)+I(\downarrow)},$$

where $I(\uparrow)$ and $I(\downarrow)$ are the intensities of neutrons parallel and antiparallel to the field vector **H**, respectively, simultaneously for 20 scattering angles. For the measurement of magnetic-nuclear interference the analyzer was removed, and the difference in the scattered-neutron intensities $\Delta(T,q)=I(\uparrow)-I(\downarrow)$ was measured. The main parameters were established in this experiment: the average neutron wavelength $\lambda=9$ Å, $\Delta\lambda/\lambda\cong 0.22$, the range of momentum transfers 2.7×10^{-3}Å$\leqslant q\leqslant 3\times10^{-2}$ Å^{-1}, and the polarization of the incident beam $P_0\cong 0.94$.

2. RESULTS AND DISCUSSION

Several measurement cycles have been carried out under various temperature measurement conditions and in various magnetic fields, in which reproducibility of the results was observed. The most detailed investigation was conducted in the low-temperature range 15 K$\leqslant$T$\leqslant$55 K, where a slight anomaly, no more than 2%, was observed in the scattering intensity near 20 K. In the range $T>55$ K, on the other hand, no variations were observed in $P(T,q)$ outside the statistical error limits. It should be noted at once that neither temperature variations of $P(T,q)$ in the scattered beam (i.e., for $q>2.7\times10^{-3}$Å^{-1}) nor variations of $I(T,q)$ and $P(T,q)$ with the magnitude and direction of the field **H** in the investigated range were detected beyond the statistical error limits. Variations of $I(T,q)$ and $P(T,q)$ with the cooling rate and temperature cyclings were also not found. On the other hand, the conditions for variations existed. It is likely that the statistical measurement accuracy and possibly the magnetic field range were too small to observe such effects.

Typical temperature curves $P(T,0)$ for neutrons scattered within the limits of the central counter ($q\leqslant 2.7\times10^{-3}$ Å^{-1}) under various measurement conditions are shown in Fig. 1. The temperature dependence of the scattering $\Delta(T)$ is shown in Fig. 2. It is evident from Figs. 1 and 2 that the observed temperature dependences in $P(T)$ and $\Delta(T)$ are extremely small, not exceeding 1%, but are statistically resolvable in the experiment and have a pronounced double-trough profile with two minima and a maximum at $T\approx 26$ K. The observable difference of $\Delta(T)$ from zero is attributable to interference between nuclear and magnetic scattering and, as will be shown below, characterizes the upper bound of the visible scale of magnetic correlations in the given measurements. It has been shown[10] that the difference $\Delta(q)=I(\uparrow)-I(\downarrow)$ is proportional to two terms:

$$\Delta(q)\sim 2\,\mathrm{Re}[\langle\psi_0\psi_m^*\rangle+\langle\psi_n\psi_m\rangle]. \tag{1}$$

It follows from the law of conservation of the number of particles that

$$\int \Delta(q)dq=0. \tag{2}$$

The first term in Eq. (1) corresponds to interference of the direct beam and magnetic scattering, and the second is associated with interference between nuclear and magnetic scattering (ψ_0, ψ_n, and ψ_m are the wave functions of unscattered neutrons and neutrons scattered by the nuclear and magnetic potentials, respectively). We recall that the sign of the magnetic interaction potential depends on the direction of polarization of the neutrons relative to the field and, accordingly, this fact can be utilized to separate the nuclear-magnetic interaction term. In the Born approximation the amplitudes of nuclear and magnetic scattering are expressed in terms of the Fourier transforms of (respectively) the nuclear and magnetic densities of scattering lengths (contrast): $\delta b^{n,m}=b^{n,m}(\mathbf{r})-\overline{b^{n,m}}$, where $b^{n,m}(\mathbf{r})$ and $\overline{b^{n,m}}$ are the local and average scattering lengths in the sample, respectively. The interference term is therefore proportional to the cross-correlation function of magnetic and nuclear fluctuations of the density of neutron scattering lengths. It follows from condition (2) that the terms in expression (1) must have opposite signs. This means that $\Delta(q)$ must have opposite signs in the ranges $q<q_{\min}$ (i.e., in the region of the direct beam, where $q_{\min}$ is the minimum resolvable momentum of the instrument) and $q>q_{\min}$ (i.e., in the scattering-dominated region). The change of sign of $\Delta(q)$ in the regions of the direct beam and scattered neutrons has been demonstrated[10] in measurements of the interference effect in superconducting YBCO ceramic. Owing to the difference in the signs of

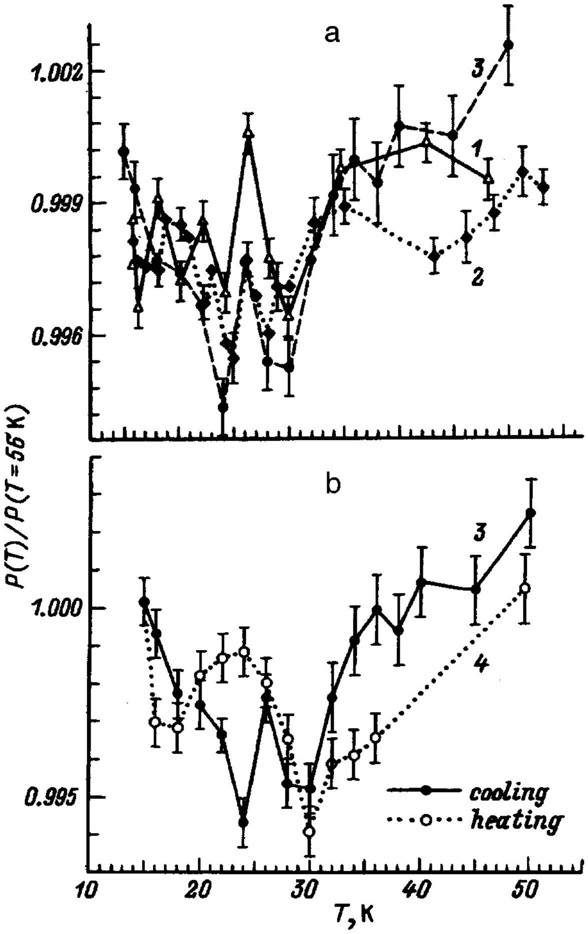

FIG. 1. Temperature dependence of the polarization of neutrons scattered within the limits of the direct beam ($q\leqslant 2.7\times10^{-3}$Å^{-1}), measured for a sample of thickness 9 mm in various T-measurement regimes and in various magnetic fields H. a: *1*) "Zero-field" ($H\approx 2$ Oe) cooling at the rate ≈ 2 K/h; *2*) repeated cooling at the same rate in a field $H=4500$ Oe parallel to **q** ($\varphi=0$); *3*) cooling in a field $H=4500$ Oe, $\varphi=30°$, at the rate ≈ 1.4 K/h. b: *3, 4*) cooling-heating cycle in a field $H=4500$ Oe, $\varphi=30°$.

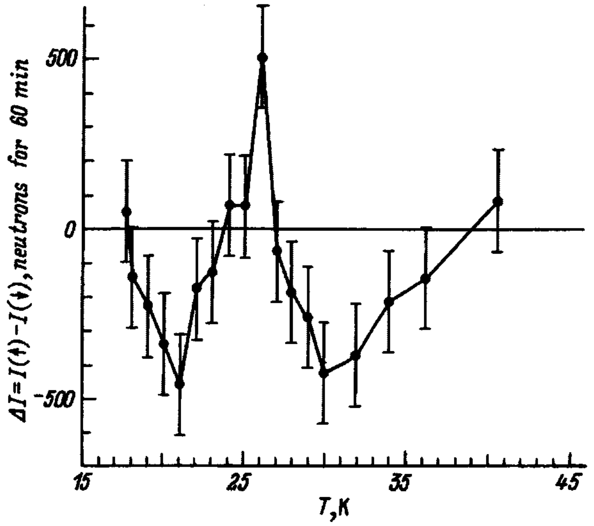

FIG. 2. Temperature dependence of the difference in the intensities of neutrons $\Delta(T)=I(\uparrow)-I(\downarrow)$ scattered within the limits $q\leq 2.7\times 10^{-3}\,\text{Å}^{-1}$ with polarizations in the same direction (↑) and in the opposite direction (↓) to the magnetic field, from measurements on a sample of thickness 9 mm with cooling in a field $H=4500$ Oe, $\varphi=30°$.

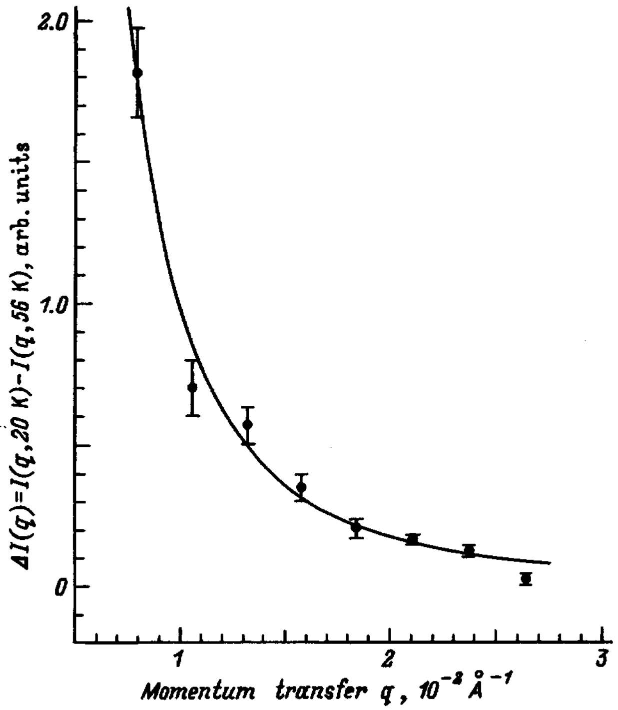

FIG. 3. Momentum dependence of the intensity of magnetic scattering of neutrons [difference $\Delta I(q)=I(q,20\,\text{K})-I(q,56\,\text{K})$], from measurements on a sample of thickness 3 mm with cooling in a field $H=50$ Oe. The points represent the experimental results, and the curve represents numerical calculation by a modified Gaussian technique using the equation $\Delta I(q)=A(q^2+\kappa^2)^2$.

the terms in (1), interference is observed as an effect having a certain sign [i.e., $\Delta(q)\neq 0$, including $q=0$] when scattering takes place and the instrumental resolution is sufficient to distinguish between scattering and the direct beam. In other words, the characteristic space scale of the visible scattering system obeys $R\leq R_{\max}$, where $R_{\max}\approx 1/q_{\min}$ is the limiting resolution of the instrument. In the given experiment $R_{\max}\approx 370$ Å. This estimate of the scale of magnetic correlations is further confirmed by the results of an analysis of the low-temperature momentum dependence of the excess scattering intensity: $\Delta I(q)=I(q,20\,\text{K})-I(q,56\,\text{K})$, shown in Fig. 3. Scattering is satisfactorily described by the functional relation $\Delta I(q)\approx 1/(q^2+\kappa^2)^2$ with the characteristic radius $R=\kappa^{-1}$ equal to 100 ± 30 Å. However, the statistical error is too large to decide the form of the dependence of the scattering intensity on the momentum transfer for a specific form of the correlation function. The data are described with essentially the same reliability by the relation $\Delta I(q)\approx q^{-n}$, where $n=2.5\pm 0.1$, so that now the characteristic radius must be interpreted as a consistent estimate obtained from an analysis of interference and as a lower bound of the scale. Summarizing, we conclude that the experimentally observed scale of magnetic correlations lies in the interval $70\,\text{Å}<R<370\,\text{Å}$.

A definite model capable of describing magnetic-nuclear interference in the sample is nonexistent at the present time. However, $\Delta(q)$ is observed to have the opposite sign from that obtained in the observation[10] of interference in YBCO ceramic at $T<T_c$ and $H<1000$ Oe with the magnetic field applied after cooling in zero field. In Ref. 10 it is shown that interference occurs in scattering at voids penetrated by the magnetic field. The opposite sign of the interference effect in the investigated samples indicates that the interference-producing variations of the nuclear and magnetic scattering densities occur in phase in the sample, i.e., their maxima (minima) coincide. The average induction $\langle B\rangle$ in the sample can be estimated from depolarization data with allowance for the estimated characteristic scale of magnetic correlations on the basis of, for example, the Halpern-Holstein equation.[11] Within the framework of this model (i.e., based on the assumption that for each ith inhomogeneity of diameter $d_i\approx\langle d\rangle\approx R$ the induction $\delta B_i\approx\langle B\rangle$, and the number of inhomogeneities $N=L/\langle d\rangle$, where L is the thickness of the sample) the average induction can be estimated to lie between the bounds $200\,\text{G}<\langle B\rangle<400$ G at the 0.5% depolarization level.

The statistical accuracy achieved in the experiment is insufficient to determine the type of magnetic correlations with the necessary reliability, but the experimentally observed graphical form of the function $P(T)$ is to some extent similar to the $P(T)$ obtained in a study[12] of the paramagnet-spin glass transition in a disordered magnetic material with competing exchange interaction. An analogy is observed in the noncoincidence of the maxima of $I(T,q)$ and $P(T)$ and in the stretching of the transition temperature, but mainly it is evident from Fig. 1b that the same kind of irreversibility as in Ref. 12 is observed in our system cooling and heating and is a definite property of spin-glass systems. It is possible that the double-trough profile of the observed anomalies in the polarization $P(T)$ and in the magnetic-nuclear interference $\Delta(T)$ is associated with the existence of the previously postulated[13] two types of ordering in the given system, which depend on the spin state of the Fe atoms, as determined by their oxygen environment. Further investigations will be needed to answer these questions.

The authors are grateful to S. V. Maleev for valuable discussions, to M. K. Runova for data-processing assistance, and to S. V. Grigor'ev, S. Klimko, and O. V. Radionov for assistance with the measurements. One of us (GPK) thanks the St. Petersburg government for individual financial support (young investigator award for ''Candidate Projects.'')

This work has been carried out in the VVR-M reactor with financial support from the Ministry of Science of Russia (Reg. No. 01-48), also under the auspices of the Russian Program ''Neutron Studies of Matter,'' and with partial support from the Russian Fund for Fundamental Research (Project L-EN 96-1596755).

[1] Z. Q. Qiu, Y. W. Du, H. Tang, J. C. Walker, W. A. Bryden, and K. Moorjani, J. Magn. Magn. Mater. **69**, L221 (1987).

[2] T. Tamaki, T. Komai, A. Ito, Y. Maeno, and T. Fujita, Solid State Commun. **65**, 43 (1988).

[3] I. S. Lyubutin, V. G. Terziev, and A. Ya. Shapiro, Hyperfine Interact. **61**, 1105 (1990); I. S. Lyubutin, T. V. Dmitrieva, and V. G. Terziev, Zh. Éksp. Teor. Fiz. **102**, 1615 (1992) [Sov. Phys. JETP **75**, 873 (1992)].

[4] I. Mirebeau, M. Hennion, G. Coddens, T. E. Phillips, and K. Moorjani, Europhys. Lett. **9**, 181 (1989); I. Mirebeau, M. Hennion, J. Dianoux, V. Caignaert, and K. Moorjani, J. Appl. Phys. **67**, 4521 (1990).

[5] S. Katano, T. Matsumoto, A. Matsushita, T. Hatano, and S. Funahashi, Phys. Rev. B **41**, 2009 (1990).

[6] A. I. Okorokov, V. V. Runov, A. D. Tret'yakov, S. V. Maleev, and B. V. Toperverg, Zh. Éksp. Teor. Fiz. **100**, 257 (1991) [Sov. Phys. JETP **73**, 143 (1991)].

[7] J. L. Garcia-Muñoz, J. Rodriguez-Carvajal, O. Schaerpf, X. Obradors, S. H. Kilcoyne, and R. Cywinski, Physica C **185–189**, 1173 (1991).

[8] A. M. Balagurov, G. M. Mironova, I. S. Lyubutin, V. G. Terziev, and A. Ya. Shapiro, Sverkhprovodimost' (KIAE) **3**, 615 (1990).

[9] S. V. Grigor'ev, O. A. Gubin, G. P. Kopitsa, A. I. Okorokov, V. V. Runov, and A. D. Tret'yakov, PIYaF Preprint No. 2028 [in Russian], B. P. Konstantinov Institute of Nuclear Physics, Russian Academy of Sciences, Gatchina, 1995.

[10] B. Toperverg, G. Gordeyev, A. Okorokov, V. Runov, M. Runova, L. Axelrod, S. Grigoriev, I. Lazebnik, G. Kopitsa, A. Brulet, R. Kahn, R. Papoular, J. Rossat-Mignod, H. Eckerlebe, R. Kampmann, and R. Wagner, PIYaF Preprint No. 2071 [in Russian], B. P. Konstantinov Institute of Nuclear Physics, Russian Academy of Sciences, Gatchina, 1997.

[11] O. Halpern and T. Holstein, Phys. Rev. **59**, 960 (1941).

[12] V. V. Runov, S. L. Ginzburg, B. P. Toperverg, A. D. Tret'yakov, A. I. Okorokov, and E. I. Mal'tsev, Zh. Éksp. Teor. Fiz. **94**(1) 325 (1988) [JETP **67**, 181 (1988)].

[13] I. S. Lyubutin and T. V. Dmitrieva, Zh. Éksp. Teor. Fiz. **105**, 954 (1994) [JETP **78**, 511 (1994)].

Translated by James S. Wood

Van Hove singularity in Raman scattering spectra of high-T_c superconductors

O. V. Misochko

Institute of Solid State Physics, Russian Academy of Sciences, 142432 Chernogolovka, Moscow District, Russia

E. Ya. Sherman

Moscow Institute of Physics and Technology, 141700 Dolgoprudnyĭ, Moscow District, Russia

(Submitted May 22, 1997)
Fiz. Tverd. Tela (St. Petersburg) **40**, 27–31 (January 1998)

Experimental data are presented which supporting observation of an extended van Hove singularity in Raman spectra of high-T_c superconductors. Excitation of large-momentum electron-hole pairs is proposed as a possible mechanism of the scattering. © *1998 American Institute of Physics.* [S1063-7834(98)00601-7]

The singularity in the density of electron states $\nu(\varepsilon)$ (ε is the electron energy) lying close to the Fermi level is attracting considerable interest as a possible cause of the high transition temperature T_c and of the unusual properties of superconducting cuprates in normal state.[1,2] A variety of experimental data relating, in particular, to thermopower, anomalous isotope effect, and specific heat, provide an indirect support for the assumption of a high density of states in the vicinity of the Fermi level. Various band-structure models, in particular, those based on the magnetic polaron concept,[3] also indicate the existence of such a singularity. At the same time only data obtained from angle-resolved photoemission spectra[4] offered a direct proof for the existence of an extended van Hove singularity at some points of the Brillouin zone denoted subsequently $\mathbf{k}_{\upsilon H}$. In the vicinity of such points the carrier dispersion law is strongly anisotropic and can be written in the form describing a saddle-point extended along the y axis:

$$\varepsilon(\mathbf{k})=\frac{1}{2}\left(\frac{K_x^2}{m}-\frac{K_y^2}{M}\right)-E_0,\quad \mathbf{K}=\mathbf{k}-\mathbf{k}_{\upsilon H} \tag{1}$$

where $M \gg m$, m is of the order of the free-electron mass m_0, E_0 is the distance to the Fermi level ($E_F=0$), and $\mathbf{k}$ is the electron momentum. (For the sake of simplicity, we assume $\hbar=1$.) The value of E_0 derived from photoemission measurements for hole (p-type) superconductors is typically 25 meV (200 cm^{-1}), i.e., it lies in the IR region. Hence this singularity may be seen in IR absorption and/or Raman scattering of light, the methods usually employed for studies of excitation in this energy range. The photoemission method has a good angular but comparatively poor (about 10 meV) spectral resolution, which in order of magnitude coincides with E_0. The Raman method possesses two essential advantages over photoemission spectra. First, its spectral resolution is more than twenty times that of the latter, and second, optical techniques are capable of probing surface layers of a crystal with thickness of the order of light penetration depth $\delta \sim 1000$ Å, whereas photoemission measurements reach only to depths up to 50 Å.

This work reports the temperature and polarization dependences of the Raman scattering intensity in various high-T_c superconductors with different amounts of doping (i.e. oxygen concentrations). Experimental data (Sec. 2) indicate the presence, in the A_{1g} scattering spectra of superconducting crystals, of a broad low-intensity line in the frequency-transfer region Ω of about 200 cm^{-1}. At the same time this line is not seen in B_{1g} and B_{2g} spectra of superconducting crystals nor in all studied scattering symmetries for nonsuperconducting crystals. (Since orthorhombic distortions affect only weakly the tetragonal symmetry of CuO_2 layers, we describe the light scattering in terms of this symmetry.) We believe that this peak (line) should be identified with an extended van Hove singularity in the electronic spectrum. A quantitative analysis of the mechanism of electronic light scattering in the vicinity of the singularity described by Eq. (1) is given in Sec. 2.

1. EXPERIMENTAL RESULTS

The experiments were performed in backscattering geometry $\overline{z}(\mathbf{e}_S,\mathbf{e}_I)z$, where $\mathbf{e}_I, z$ and $\mathbf{e}_S, \overline{z}$ are the polarizations and directions of incident and scattered light, respectively, on standard equipment including a liquid-nitrogen–cooled multichannel detector. The electronic subsystem was excited by the various spectral lines emitted by Ar$^+$, He-Ne, and He-Cd lasers. The pump laser power was maintained below 10 W/cm^2 in order to avoid overheating of the crystals under study. The spectral resolution in each experiment was better than 3 cm^{-1}. The laser spot position was monitored with a microscope to within about 10 μm. All spectra were deconvoluted properly using the spectral function of the system and normalized to the incident intensity. The experiments were carried out on the following high-quality crystals:

a) $YBa_2Cu_3O_{7-x}$ (Y-123) with transition temperatures $T_c=92$ and 57 K, and a nonsuperconducting crystal;
b) $YBa_2Cu_4O_8$ (Y-124) with $T_c=79$ K;
c) $Bi_2Sr_2CaCu_2O_{8+x}$ (Bi-2212) with $T_c=90$ K;
d) $Tl_2Ba_2CuO_{6+x}$ (Tl-2201) with $T_c=90$ K.

The oxygen concentration in the samples was preset by annealing in an oxygen atmosphere. The transition temperature of each crystal was determined from magnetic measurements, and the crystallographic orientation, by x-ray diffraction. As follows from the T_c data, the Y-124 and Tl-2201 were overdoped, and the Bi-2212 samples were close to op-

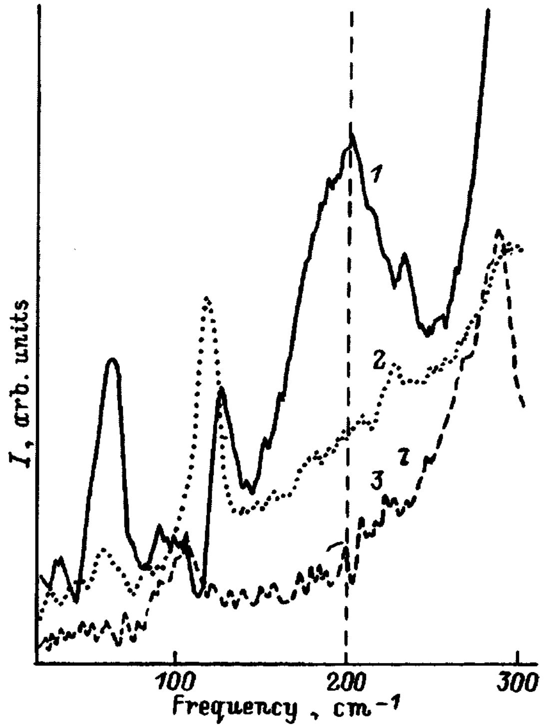

FIG. 1. Polarization dependences of Raman scattering intensity in Bi-2212 ($T_c = 90$ K) at $T = 5$ K. *1*/A_{1g}, *2*/B_{2g}, *3*/B_{1g}.

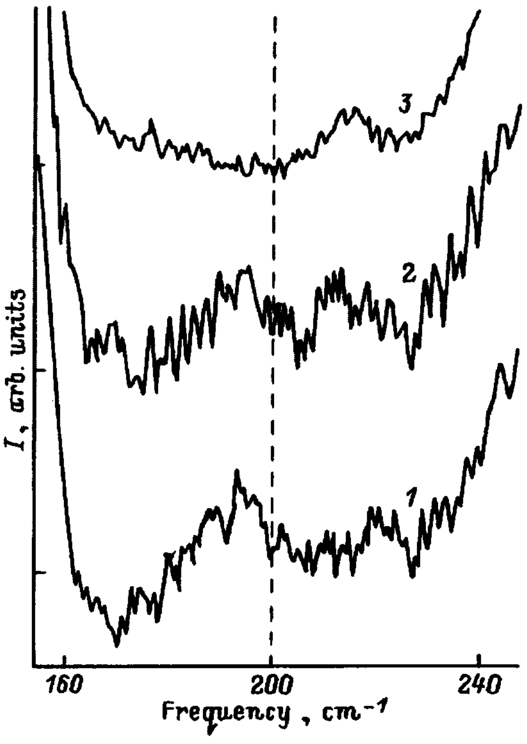

FIG. 2. Raman scattering spectra of Y-124 ($T_c = 79$ K) obtained in A_{1g} polarization at different temperatures. T(K): *1*/10, *2*/190, *3*/295.

timal. Before measurements, the samples were cleaned in methanol to remove surface impurities. Measurements on bismuth-based crystals were made on as-cleaved surfaces.

Raman scattering spectra of high-T_c superconductors contain a large number of comparatively narrow phonon lines against an intense continuum originating from scattering by excitations of the electronic subsystem. Below T_c the continuum deforms to produce a broad peak, whose intensity and position depend on the incident and scattered polarizations. In our experiments redistribution of the continuum was also observed, but since the ‘‘superconducting’’ peak (seen above 500 cm^{-1} in the A_{1g} scattering geometry) lies far from the assumed position of the van Hove singularity, we shall not discuss the effects associated with the superconducting transition. For all cuprate superconductors the complete structure of the phonon spectrum is well known. The spectrum is usually dominated by diagonal phonons exhibiting interesting properties, such as a decrease of the B_{1g} phonon frequency (340 cm^{-1}) in the superconducting state of the yttrium-barium cuprate. Nondiagonal phonons were observed to exist only in Y-123 crystals.

At the same time the electronic continuum demonstrates in all the superconducting crystals studied thus far one common feature, namely, a weak broad peak around 200 cm^{-1}. The fact that this peak is a common characteristic, and that it lies close to the energy of the van Hove singularity derived from photoemission spectra, provided a motivation for its comprehensive investigation.

We start with the polarization dependences of the peak intensities. Figure 1 presents the data obtained for Bi-2212 crystals in different polarizations. We see that the peak is the strongest in the A_{1g} geometry ($\mathbf{e}_I \| \mathbf{e}_S$) and is not seen in crossed polarizations corresponding to the B_{1g} ($\mathbf{e}_I \| x', \mathbf{e}_S \| y'$) and B_{2g} ($\mathbf{e}_I \| x, \mathbf{e}_S \| y$) scattering geometries.

Let us turn now to the temperature dependence of scattering. In yttrium- and thallium-based crystals the peak was not seen at room temperature, became increasingly more pronounced as the temperature was lowered, and was retained in the superconducting state. For the Y-124 crystal this effect is shown in Fig. 2. By contrast, in Bi-2212 crystals this peak is present already at room temperature.

To analyze the influence of doping on the position of this peak, we compared Y-123 samples with the oxygen concentrations providing different critical temperatures. In crystals with $T_c = 92$ and 57 K, the peaks were in approximately the same positions. The peak vanished if the crystal became nonsuperconducting because of the oxygen concentration being too low (Fig. 3). Sm→Y and Nd→Y substitutions did not reveal any noticeable dependence of the observed effects on the rare-earth species.

Summing up the experimental data, we can say that we have observed a broad maximum which, while being weak, was nevertheless essentially above the background noise, and peaks around 200 cm^{-1} in the fully symmetric A_{1g} scattered component of superconducting crystals. The peak position does not change within the pump-light wavelength region of 633 to 442 nm, and the peak itself exhibits a resonant behavior. Since the peak is observed in Y-124 crystals, it is certainly not of defect origin, because Y-124 is a stable stoichiometric compound. The observation of this peak in bismuth- and thallium-based crystals argues in support of its being due to the CuO_2 layers, which are common building blocks in all the crystals studied here. A comparison of the

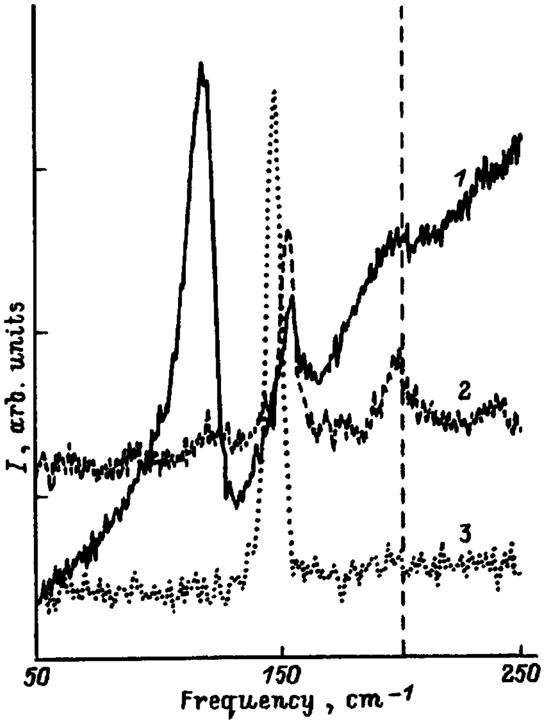

FIG. 3. Comparison of A_{1g} spectra obtained on Y-123 crystals of three types at $T=10$ K. T_c(K): *1*/92, *2*/57, *3*/nonsuperconducting crystal.

peak position with the photoemission data[5] for Y-123 and Y-124 shows that it is close to the position of the van Hove singularity, whereas the polarization and temperature dependences of the peak intensities are due to the extended pattern of the spectrum. Note that the temperature dependence of the peak supports its electronic rather than phonon nature, because the phonon-mode intensity in Raman scattering should decrease with temperature and follow the Bose distribution for the phonon occupation numbers. At the same time the van Hove singularity should become more pronounced for $T \leqslant E_0$, since it is not smoothed by temperature effects in this region. Photoemission measurements made on Bi-2212 crystals[6] likewise yield a close position of the Raman peak to E_0. We are not aware of the corresponding data for Tl-2201. We believe, however, that the peak observed there is of the same nature as that in yttrium- and bismuth-based crystals, since it exhibits a similar pattern. We believe therefore that the peaks observed in all the crystals are due to an extended van Hove singularity.

Since light scattering is determined by the electronic properties of a crystal, a singularity in the density of states should obviously manifest itself in light scattering. The mechanism of this manifestation is discussed qualitatively in the following Section.

2. DISCUSSION OF RESULTS

Consider possible mechanisms of Raman scattering of light by electronic states in the vicinity of the van Hove singularity.

The vertex (matrix element) describing electron interaction with photons for given polarizations of the incident (frequency ω_I) and scattered (frequency ω_S) light can be written[7]

$$\gamma(\mathbf{k},\omega)=\mathbf{e}_I\mathbf{e}_S+\frac{1}{m_0}\sum_{j,f}\left[\frac{\langle j|\hat{\mathbf{p}}\mathbf{e}_S|f\rangle\langle j|\hat{\mathbf{p}}\mathbf{e}_I|f\rangle}{\varepsilon_f(\mathbf{k}-\varepsilon_j(\mathbf{k})+\omega_I}\right) + \frac{\langle j|\hat{\mathbf{p}}\mathbf{e}_I|f\rangle\langle f|\hat{\mathbf{p}}\mathbf{e}_S|j\rangle}{\varepsilon_j(\mathbf{k})-\varepsilon_f(\mathbf{k})-\omega_S}. \qquad (2)$$

In Eq. (2), $\hat{\mathbf{p}}$ is the momentum operator, and summation is performed over all allowed transitions connecting the band electronic states $|j\rangle$ and $|f\rangle$ with energies $\varepsilon_j(\mathbf{k})$ and $\varepsilon_f(\mathbf{k})$, respectively. The interband momentum-matrix elements depend substantially on $\mathbf{k}$ and possibly vanish at high-symmetry points and/or lines in the Brillouin zone.[8] Carrier motion results in fluctuations in $\gamma(\mathbf{k},\omega)$, thus giving rise to elastic and inelastic light scattering. In other words, scattering transfers energy from light to excitations of the electronic subsystem associated with various types of carrier motion.

It is usually assumed that only extremely long-wavelength excitations with momenta $q_\delta \sim 1/\delta$ can be seen in light scattering spectra. In the vicinity of the van Hove singularity, however, the Fermi velocity $v_F \sim \sqrt{E_0/m_0} \sim 5\times 10^6$ cm/s is so small that the transferred frequency, estimated for a pure metal as $\Omega \sim v_F q_\delta$, does not exceed $10\ \mathrm{cm}^{-1}$. For an isotropic three-dimensional metal with impurities, a finite q_δ can explain the scattering pattern only for energies up to 10 meV.[9] To consider scattering within a broader frequency region, one will have to invoke various momentum relaxation mechanisms, which can become manifest in two mutually dependent ways.[10–12] First, momentum relaxation results in finite damping of excitations with extremely small $q \sim 1/\delta$,[10,11] i.e. in their finite spectral density within a frequency interval of width of order $1/\tau_r$, where τ_r is the characteristic relaxation time. This damping produces a maximum in intensity at $\Omega \sim \tau_r^{-1}$. Second, the finite damping τ_r allows contribution to Raman scattering of elementary excitations with a large ($q \gg q_\delta$) momentum.

It is reasonable to assume that the time τ_r satisfies the inequality $\tau_r \leqslant E_0^{-1}$, i.e., $\tau_r \leqslant 3\times 10^{-14}$ s. The corresponding mean free path $l = v_F \tau_r \sim 15$ Å, and, by virtue of the uncertainty in $\mathbf{k}$, the possible momentum transfer to the electronic subsystem is evaluated as $q_l \sim 1/l \gg q_\delta$ and determined by the mean free path rather than by the light penetration depth. This mechanism allows scattering within a frequency interval of order $v_F q_l$, which can be larger than E_0. Consider this mechanism, which corresponds to finite-momentum excitations and is similar in many ways to light scattering near the van Hove singularity in the phonon spectrum,[13] in more detail. The Feynman diagram describing Raman scattering is presented in Fig. 4a, and the corresponding excitation, in Fig. 4b. The electron excited by light (photoelectron) interacts with all other carriers to create an electron-hole pair with momentum $\mathbf{q}$. Since the momentum of the incident and scattered photon is extremely small because of the large light wavelength $\lambda \sim \delta \sim 1000$ Å, in order for it to be conserved a momentum $-\mathbf{q}$ should be transferred to the crystal in the course of phonon excitation and/or scattering from impurities (Fig. 4a depicts the ‘‘phonon’’ process). Hence this mecha-

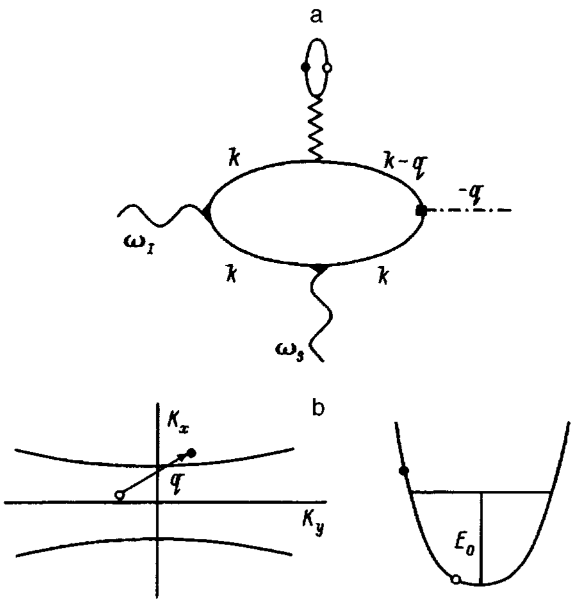

FIG. 4. (a) ''Phonon'' process describing Raman scattering with finite momentum transfer. Solid line relates to electron, wavy line–to photon, and dot-and-dash line–to phonon. Broken line corresponds to interaction between electrons, **k** is the photoelectron momentum. (b) Excitation produced in scattering.

nism is determined both by interaction between electrons, which plays an important part in all high-T_c superconductors, and by the momentum relaxation rate. The corresponding intensity $I(\Omega)$ is proportional to $V^2\tau_r^{-1}$, where V is the matrix element of carrier interaction, and $\tau_r=\min(\tau_{\text{imp}},\tau_{e-p})$, where τ_{e-p} and τ_{imp} are, respectively, the relaxation times associated with electron-phonon interaction and impurity scattering. Neglecting temperature-induced effects, the scattering intensity at frequency Ω in this process can be evaluated as

$$I(\Omega)\sim|R|^2\int_{-E_0}^{0}\nu(\varepsilon)\nu(\varepsilon+\Omega)d\varepsilon, \tag{3}$$

where R is the matrix element of the process, such that $|R|^2\sim V^2\tau_r^{-1}$, $\varepsilon<0$ for occupied states, and $\varepsilon+\Omega>0$ for empty states. For $\Omega\ll E_0$, the small phase volume of possible excitations results in low scattering intensity. For $\Omega\gg E_0$, the density of states decreases, which results in a decrease of scattering intensity. As follows from this simple consideration, the intensity should pass through a maximum at a transferred frequency Ω determined by E_0. The fact that $\varepsilon(\mathbf{k})$ in Eq. (1) depends only on K_x and is nearly independent of K_y due to the extended nature of the van Hove singularity increases the scattering probability, since the contribution to the scattering intensity at a given frequency Ω comes from excitations occupying a comparatively large volume in momentum space in the vicinity of the Fermi surface.

Note that excitation of finite-momentum pairs implies that Raman scattering redistributes carriers in **k** space of the electronic subsystem (Fig. 4b). The dependence of the matrix element of electron interaction with photons, $\gamma(\mathbf{k},\omega)$, in Eq. (2) on electron momentum results in a change of crystal polarizability as a result of particle redistribution and, hence, in light scattering.

A quantitative investigation of the position of the peak and of its shape involving a detailed structure of the electronic spectrum will be done in a separate publication and will be based on the concept of magnetic polaron formation in CuO_2 sheets.

The authors are grateful to A. Abrosimov, G. Emel'chenko, and M. Kulakov for the crystals used in this study.

[1] R. S. Markiewicz, Int. J. Mod. Phys. B **5**, 2037 (1991).
[2] C. C. Tsuei, C. C. Chi, D. M. Newns, P. C. Pattnaik, and M. Däumling, Phys. Rev. Lett. **69**, 2134 (1992); D. M. Newns, C. C. Tsuei, R. P. Hübener, P. J. M. van Bentum, P. C. Pattnaik, and C. C. Chi, Phys. Rev. Lett. **73**, 1695 (1994).
[3] A. F. Barabanov, V. M. Berezovskiĭ, É. Zhasinas, and L. A. Maksimov, Zh. Éksp. Teor. Fiz. **110**, 1480 (1996) [JETP **83**, 819 (1996)].
[4] Z.-X. Shen, Science **267**, 343 (1995).
[5] A. A. Abrikosov, J. C. Campuzano, and K. Gofron, Physica C **214**, 73 (1993); K. Gofron, J. C. Campuzano, A. A. Abrikosov, M. Lindroos, A. Bansil, H. Ding, D. Kölling, and B. Dabrawski, Phys. Rev. Lett. **73**, 3302 (1994).
[6] D. S. Dessau, Z.-X. Shen, D. M. King, D. S. Marshall, L. W. Lombardo, P. H. Dickinson, A. G. Loeser, J. DiCarlo, C.-H. Park, A. Kapitulnik, and W. E. Spicer, Phys. Rev. Lett. **71**, 2781 (1993).
[7] A. A. Abrikosov and V. M. Genkin, Zh. Éksp. Teor. Fiz. **65**, 842 (1973) [Sov. Phys. JETP **38**, 417 (1973)].
[8] G. L. Bir and G. E. Pikus, *Symmetry and Strain-Induced Effects in Semiconductors* [Wiley, New York, 1975; Nauka, Moscow, 1972].
[9] L. A. Fal'kovskiĭ, Zh. Éksp. Teor. Fiz. **95**, 1146 (1989) [Sov. Phys. JETP **68**, 661 (1989)].
[10] A. Zawadowski and M. Cardona, Phys. Rev. B **42**, 10732 (1990).
[11] B. Kh. Baĭramov, V. A. Voĭtenko, and I. P. Ipatova, Usp. Fiz. Nauk **163**, No. 5, 67 (1993).
[12] O. Misochko and E. Ya. Sherman, Physica C **222**, 219 (1994).
[13] E. N. Dolgov and E. Ya. Sherman, Fiz. Tverd. Tela (St. Petersburg) **35**, 1218 (1993) [Phys. Solid State **35**, 620 (1993)].

Translated by G. Skrebtsov

Influence of the pinning of Abrikosov vortices on the propagation of surface magnetostatic waves in a ferromagnet-superconductor structure

Yu. I. Bespyatykh and V. D. Kharitonov

Branch of the Institute of Radio Engineering and Electronics, Russian Academy of Sciences,
141120 Fryazino, Moscow Province, Russia

V. Vasilevskiĭ

Polytechnic Institute, 26-600 Radom, Poland

(Submitted June 25, 1997)
Fiz. Tverd. Tela (St. Petersburg) **40**, 32–35 (January 1998)

The influence of surface-layer vortex pinning in a type-II superconductor on the propagation of surface magnetostatic waves in a ferromagnet-superconductor structure is analyzed. The pinning is assumed to be strong enough to prevent vortex displacement under the influence of the Lorentz force generated by the surface magnetostatic waves, so that the ground state of the superconductor is determined by the elastic properties of the vortex lattice and by pinning. In the given model the problem reduces to the analysis of the wave spectrum in the scattered field created by the disordered vortex surface layer. A calculation shows that the influence of this field on the surface magnetostatic-wave spectrum is slight and, hence, degradation of the shielding properties of the superconductor does not take place in the presence of strong vortex pinning (as opposed to the ferromagnet-ideal superconductor structure). © *1998 American Institute of Physics.* [S1063-7834(98)00701-1]

1. The interaction of Abrikosov vortices with magnetostatic waves in a ferromagnet-superconductor structure has been investigated in a number of papers. The entrainment of a vortex structure by a magnetostatic wave has been discussed theoretically[1] and observed experimentally.[2] Popkov[3] has investigated the possibility of the amplification of a magnetostatic wave by a magnetic stream of vortices. A detailed study of the influence of the coupling of a superconductor vortex lattice with the magnetization of a ferromagnet on the spectrum of surface magnetostatic waves (SMSWs) in hybrid structures is reported in Refs. 4–9. In particular, a nonmonotonic dependence of the SMSW on the angle φ between the direction of wave propagation and the direction of the magnetizing field $\mathbf{H}_0$ (or on the frequency ω at a fixed angle φ) has been predicted theoretically[4] and observed experimentally.[5] An analysis of a structure containing an ideal superconductor without pinning has shown[7–9] that the displacement of the vortices under the influence of the Lorentz force exerted by SMSWs from the plane parallel to the ferromagnet-superconductor interface for small angles φ and sufficiently large wave numbers can be substantial, and this fact, in turn, causes the SMSW penetration depth to increase. In other words, the shielding properties of the superconductor deteriorate, and the wave spectrum more closely resembles the SMSW spectrum in a ferromagnet-vacuum structure. It has also been shown[7–9] that SMSW attenuation due to the loss of part of its energy in viscous motion of the vortices can significantly exceed the intrinsic magnetic attenuation and attenuation due to two-magnon scattering processes.

2. The major influence of defects on the physical properties of superconductors, the high-T_c variety in particular, is well known.[10] Of top priority, therefore, is the investigation of SMSW propagation in a hybrid structure with a nonideal superconductor. We assume that the pinning of vortices in the surface layer is strong enough to counteract their displacement under the influence of SMSWs. This means that the critical pinning current density j_c must be much higher than the SMSW-induced surface current density j_m. According to estimates,[1] $j_m \sim 3.5\times 10,^6$ A/cm^2. The condition $j_c \gg j_m$ is met, for example, by defects of the void or macroinclusion type, because[11] they can raise the critical current to within the vicinity of the vaporization current ($j_c \sim 2\times 10^7$ A/cm^2). In the adopted model the equilibrium position of the surface vortices is determined entirely by the elastic properties of the vortex lattice and the surface pinning forces, whereas the influence of vortex coupling with the magnetization in the ground state of the superconductor can be disregarded. We also ignore thermal fluctuations.

3. We consider a structure consisting of a ferromagnetic layer ($-L \leqslant y \leqslant 0$) and, contiguous with it, a superconducting half-space ($y > 0$) in a tangential magnetizing field $\mathbf{H}_0 \parallel \mathbf{n}_z$, which is higher than the saturation field of the ferromagnet. We describe the superconductor in the London approximation and assume, in addition, that $k\lambda_L \ll 1$, where $\mathbf{k} = (k_x, k_z)$ is the SMSW wave vector, and λ_L is the London penetration depth. We write the Gibbs potential of the system in the form

$$G = G_m + G_u + G_{\text{stray}} + G_{\text{int}} + G_{\text{pin}}, \tag{1}$$

where G_m is the magnetization excitation energy, G_u is the vortex interaction energy, and G_{stray} is the vortex scattering field (expressions for G_m, G_u, and G_{stray} are given in Ref. 9).

We write the interaction energy G_{int} of the magnetization with vortices in the form (in the integrand we retain the term $\sim M_{\mathbf{k}}^z$, which is omitted in Refs. 6 and 9 but will be needed below)

$$G_{\mathrm{int}}=B\int\frac{d\mathbf{k}}{4\pi^2}k_z\int_{-L}^{0}dy\,e^{ky}\left[\frac{\mathbf{k}\cdot\mathbf{M}_{\mathbf{k}}(y)}{k}+iM^{y}_{\mathbf{k}}(y)\right]u^{y}_{-\mathbf{k}}(0), \tag{2}$$

where B is the magnetic induction in the superconductor, $\mathbf{M}_{\mathbf{k}}$ and $\mathbf{u}_{\mathbf{k}}(y)$ are the Fourier components of the magnetization and the vortex displacements, respectively. Equation (2) is identified with the jump of the normal component of the magnetic induction at the surface of the superconductor; this component is proportional to the y component of the vortex displacement.[12]

Finally, we write the surface pinning energy G_{pin} in the form

$$G_{\mathrm{pin}}=-\int\frac{d\mathbf{k}}{4\pi^2}F_{\mathbf{k}}u^{y}_{-\mathbf{k}}(0), \tag{3}$$

where $F_{\mathbf{k}}$ is a random pinning force density with zero mean. From the condition of the minimum of the Gibbs potential in the given approximation we obtain

$$u^{y}_{\mathbf{k}}(0)=\zeta_{\mathbf{k}}F_{\mathbf{k}}/c_{11}k_z\,, \tag{4}$$

where c_{11} is the compression modulus of the vortex lattice, and $\zeta_{\mathbf{k}}$ is a dimensionless parameter of the order of unity, which is given in Ref. 13 We note, in contrast with the bulk random pinning model,[14] that the rms displacement of a surface-layer vortex as determined from Eq. (4) is finite and preserves long-range positional order.

4. In light of the foregoing discussion, the effective magnetic field of the ferromagnet (ignoring exchange and anisotropy) has the form

$$\mathbf{H}_{\mathrm{eff}}=\mathbf{H}_0+\mathbf{H}+\mathbf{H}_{\mathrm{stray}}\,, \tag{5}$$

where $\mathbf{H}$ is the dipole field, and $\mathbf{H}_{\mathrm{stray}}$ is the scattering field (magnetic stray field), which depends on the pining-induced displacement of the vortices from their ideal positions; its Fourier component is determined from Eq. (2):

$$\mathbf{H}_{\mathrm{stray}}(\mathbf{k},y)=-\frac{\partial G_{\mathrm{int}}}{\partial\mathbf{M}_{-\mathbf{k}}(y)}=\frac{1}{4\pi^2}H_0u^{y}_{\mathbf{k}}(0)k_ze^{ky}\times\left(\frac{k_x}{k}\mathbf{n}_x+i\mathbf{n}_y+\frac{k_z}{k}\mathbf{n}_z\right) \tag{6}$$

(this equation is written with allowance for the fact that $B\approx H_0$ in the given range of fields). The problem therefore reduces to the investigation of SMSW propagation in the random field $\mathbf{H}_{\mathrm{stray}}$ generated by the ‘‘frozen’’ displacements of surface-layer vortices.

Above all we note that the presence of the field $\mathbf{H}_{\mathrm{stray}}$ in the structure renders the ground state of the ferromagnet inhomogeneous:

$$\mathbf{M}(\mathbf{r},t)=\mathbf{M}_0+\mathbf{M}(\mathbf{r})+\mathbf{m}(\mathbf{r},t). \tag{7}$$

Linearizing the static form of the Landau-Lifshitz equation ($M_z\approx M_0$, $M^{x,y}\ll M_0$), we obtain the system of equations for $M^{x,y}$

$$\Omega_HM^{x}_{\mathbf{k}}(y)+\frac{k_x}{2}\int_{-L}^{0}dy'\times\left\{\left[\frac{k_x}{k}M^{x}_{\mathbf{k}}(y')+i\,\mathrm{sgn}(y-y')M^{y}_{\mathbf{k}}(y')\right]e^{-k|y-y'|}+\left[\frac{k_x}{k}M^{x}_{\mathbf{k}}(y')+iM^{y}_{\mathbf{k}}(y')\right]e^{k(y+y')}\right\}+\frac{1}{4\pi^2}\Omega_H\frac{k_zk_x}{k}e^{ky}u^{y}_{\mathbf{k}}(0)=0,$$

$$(\Omega_H+1)M^{y}_{\mathbf{k}}(y)+\frac{k}{2}\int_{-L}^{0}dy'\left\{\left[-M^{y}_{\mathbf{k}}(y')+i\frac{k_x}{k}\times\mathrm{sgn}(y-y')M^{x}_{\mathbf{k}}(y')\right]e^{-k|y-y'|}+\left[M^{y}_{\mathbf{k}}(y')-i\frac{k_x}{k}M^{x}_{\mathbf{k}}(y')\right]e^{k(y+y')}\right\}-\frac{i}{4\pi^2}\Omega_Hk_ze^{ky}u^{y}_{\mathbf{k}}(0)=0, \tag{8}$$

where $\Omega_H=H_0/4\pi M_0$. The solution of the system (8) has the form

$$M^{x}_{\mathbf{k}}(y)=\frac{ik\sin\varphi\cos\varphi H_0u^{y}_{\mathbf{k}}(0)}{8\pi^3D_0(\Omega_H+1)}[(1+\eta^0_{\mathbf{k}})\times(\eta^0_{\mathbf{k}}-\sin^2\varphi)e^{q^0_{\mathbf{k}}(y+L)}+(1-\eta^0_{\mathbf{k}})\times(\eta^0_{\mathbf{k}}+\sin^2\varphi)e^{-q^0_{\mathbf{k}}(y+L)}],$$

$$M^{y}_{\mathbf{k}}(y)=\frac{q^0_{\mathbf{k}}\cos\varphi H_0u^{y}_{\mathbf{k}}(0)}{8\pi^3D_0(\Omega_H+1)}[(1+\eta^0_{\mathbf{k}})\times(\eta^0_{\mathbf{k}}-\sin^2\varphi)e^{q^0_{\mathbf{k}}(y+L)}-(1-\eta^0_{\mathbf{k}})\times(\eta^0_{\mathbf{k}}+\sin^2\varphi)e^{-q^0_{\mathbf{k}}(y+L)}], \tag{9}$$

where

$$q^0_{\mathbf{k}}=\eta^0_{\mathbf{k}}k,\quad \eta^0_{\mathbf{k}}=\sqrt{(\Omega_H+\sin^2\varphi)/(\Omega_H+1)},$$

$$D_0=e^{q^0_{\mathbf{k}}L}(1+\eta^0_{\mathbf{k}})(\eta^0_{\mathbf{k}}-\sin^2\varphi)-e^{-q^0_{\mathbf{k}}L}(1-\eta^0_{\mathbf{k}})(\eta^0_{\mathbf{k}}+\sin^2\varphi).$$

5. We now consider elementary excitations $\mathbf{m}(\mathbf{r},t)$ propagating against the background of the inhomogeneous ground state (9). The effective field in the dynamic Landau-Lifshitz equation has the same form (5), but now contains a high-frequency part, which is easily determined from the solution of the magnetostatic boundary-value problem. Transforming to Fourier components and linearizing, we obtain the system of equations (omitting the factor $e^{-i\omega t}$)

$$-i\Omega m^{y}_{\mathbf{k}}(y)+\Omega_Hm^{x}_{\mathbf{k}}(y)+\frac{k_x}{2}\int_{-L}^{0}dy'\times\left\{\left[\frac{k_x}{k}m^{x}_{\mathbf{k}}(y')+i\,\mathrm{sgn}(y-y')m^{y}_{\mathbf{k}}(y')\right]e^{-k|y-y'|}+\left[\frac{k_x}{k}m^{x}_{\mathbf{k}}(y')+im^{y}_{\mathbf{k}}(y')\right]e^{k(y+y')}\right\}$$

$$\begin{aligned}
&+\frac{1}{4\pi M_0}\int\frac{d\mathbf{k}}{(2\pi)^2}H^z_{\text{stray}}\\
&\times(\mathbf{k}-\mathbf{k}',y)m^x_{\mathbf{k}'}(y)+\frac{i}{2M_0}\int\frac{dk'}{(2\pi)^2}k'_zM^x_{\mathbf{k}-\mathbf{k}'}(y)\\
&\times\int_{-L}^{0}dy'\Bigg\{\Bigg[\frac{i\mathbf{k}\cdot\mathbf{m}_{\mathbf{k}'}(y')}{k'}\\
&-\operatorname{sgn}(y-y')m^y_{\mathbf{k}}(y')\Bigg]e^{-k'|y-y'|}\\
&+\Bigg[\frac{i\mathbf{k}\cdot\mathbf{m}_{\mathbf{k}'}(y')}{k'}-m^y_{\mathbf{k}'}(y')\Bigg]e^{k'(y+y')}\Bigg\}=0,
\end{aligned}$$

$$\begin{aligned}
&i\Omega m^x_{\mathbf{k}}(y)+(\Omega_H+1)m^y_{\mathbf{k}}(y)+\frac{k}{2}\\
&\times\int_{-L}^{0}dy'\Bigg\{\Bigg[-m^y_{\mathbf{k}}(y')+\frac{ik_x}{k}\\
&\times\operatorname{sgn}(y-y')m^x_{\mathbf{k}'}(y')\Bigg]e^{-k|y-y'|}\\
&+\Bigg[m^y_{\mathbf{k}}(y')-\frac{ik_x}{k}m^x_{\mathbf{k}}(y')\Bigg]e^{k(y+y')}\Bigg\}+\frac{1}{4\pi M_0}\\
&\times\int\frac{d\mathbf{k}}{(2\pi)^2}H^z_{\text{stray}}(\mathbf{k}-\mathbf{k}',y)m^y_{\mathbf{k}'}(y)+\frac{i}{2M_0}\\
&\times\int\frac{d\mathbf{k}}{(2\pi)^2}k'_zM^y_{\mathbf{k}-\mathbf{k}'}(y)\int_{-L}^{0}dy'\Bigg\{\Bigg[\frac{i\mathbf{k}'\cdot\mathbf{m}_{\mathbf{k}'}(y')}{k'}\\
&-\operatorname{sgn}(y-y')m^y_{\mathbf{k}'}(y')\Bigg]e^{-k'|y-y'|}\\
&+\Bigg[\frac{i\mathbf{k}'\cdot\mathbf{m}_{\mathbf{k}'}(y')}{k'}-m^y_{\mathbf{k}'}(y')\Bigg]e^{k(y+y')}\Bigg\}=0,
\end{aligned}$$

$$\Omega=\omega/\omega_m,\qquad \omega_m=4\pi\gamma M_0. \tag{10}$$

We seek a solution of the system (10) in the form

$$\begin{aligned}
m^x_{\mathbf{k}}(y)&=A_{\mathbf{k}}e^{q_{\mathbf{k}}y}+B_{\mathbf{k}}e^{-q_{\mathbf{k}}y}+\int d\mathbf{k}'[A^{(1)}_{\mathbf{k}'}e^{(q_{\mathbf{k}'}+\overset{0}{q}_{\mathbf{k}-\mathbf{k}'})y}\\
&\quad+A^{(2)}_{\mathbf{k}'}e^{(q^{\mathbf{k}'}-\overset{0}{q}_{\mathbf{k}-\mathbf{k}'})y}+B^{(1)}_{\mathbf{k}'}e^{-(q_{\mathbf{k}'}+\overset{0}{q}_{\mathbf{k}-\mathbf{k}'})y}\\
&\quad+B^{(2)}_{\mathbf{k}'}e^{(-q_{\mathbf{k}'}+\overset{0}{q}_{\mathbf{k}-\mathbf{k}'})y}],\\
m^y_{\mathbf{k}}(y)&=C_{\mathbf{k}}e^{q_{\mathbf{k}}y}+D_{\mathbf{k}}e^{-q_{\mathbf{k}}y}+\dots,
\end{aligned}$$

which takes into account the renormalization of the ground state of the ferromagnet due to inhomogeneities. As a result of expressing all the coefficients in terms of $C_{\mathbf{k}}$ and $D_{\mathbf{k}}$, we obtain a system of integral equations for these two quantities, which is conveniently written in the matrix form

$$\hat{\Pi}^{(0)}(\mathbf{k})\mathbf{C}_{\mathbf{k}}+\int\frac{d\mathbf{k}'}{(2\pi)^2}\hat{\Pi}^{(1)}(\mathbf{k},\mathbf{k}')C_{\mathbf{k}'}=0, \tag{11}$$

where the column vector $\mathbf{C}_{\mathbf{k}}=\binom{C_{\mathbf{k}}}{D_{\mathbf{k}}}$, the second-rank square matrix $\hat{\Pi}^{(0)}$ corresponds to the system of perturbations, and the matrix $\hat{\Pi}^{(1)}$ corresponds to the perturbation introduced by the displacements of surface-layer vortices. The matrix $\hat{\Pi}^{(0)}(\mathbf{k})$ has the form

$$\hat{\Pi}^{(0)}(\mathbf{k})=\begin{pmatrix} k-q_{\mathbf{k}}\alpha^{(-)}_{\mathbf{k}}\sin\varphi & k+q_{\mathbf{k}}\alpha^{(+)}_{\mathbf{k}}\sin\varphi\\ \dfrac{e^{-q_{\mathbf{k}}L}(1+\alpha^{(-)}_{\mathbf{k}}\sin\varphi,}{q_{\mathbf{k}}+k} & \dfrac{-e^{-q_{\mathbf{k}}L}(1+\alpha^{(+)}_{\mathbf{k}}\sin\varphi)}{q_{\mathbf{k}}-k}\end{pmatrix}. \tag{12}$$

Here we have introduced the notation

$$q^2_{\mathbf{k}}=\eta^2_{\mathbf{k}}k^2=1-\Omega_H\cos^2\varphi/[\Omega_H(\Omega_H+1)-\Omega^2],$$

$$\alpha^{(\pm)}_{\mathbf{k}}=\frac{\Omega^2(\eta^2_{\mathbf{k}}-1)\pm\eta_{\mathbf{k}}\sin\varphi}{\Omega_H(\eta^2_{\mathbf{k}}-1)-\sin^2\varphi}.$$

The condition $\det\hat{\Pi}^{(0)}(\mathbf{k})=0$ gives the well-known[15] SMSW spectrum in the perturbation-free system (i.e., in the ferromagnet-ideal metal system),

$$\tanh q_{\mathbf{k}}L=\frac{q_{\mathbf{k}}\mathbf{k}\omega_H\cos^2\varphi}{(q^2_{\mathbf{k}}\sin^2\varphi-k^2)\omega_H+(q^2_{\mathbf{k}}-k^2)(\omega\sin\varphi+\omega_m\sin^2\varphi)},$$

$$\omega_H=\gamma H_0.$$

The explicit expression for the matrix $\hat{\Pi}^{(1)}(\mathbf{k},\mathbf{k}')$ is too cumbersome to write out here.

We solve the system (11) by iterations, using a procedure similar to that in Refs. 16 and 17 with averaging over the random vortex displacements in each step; by virtue of relation (4) this operation is equivalent to averaging over a random pinning force. Since we are not discussing a microscopic pinning model here, it is more practical to work with the spectral density $W(\mathbf{k})$ of the binary correlation function of the vortex displacements, which is given by the relation

$$\langle u^y_{\mathbf{k}}(0)u^y_{\mathbf{k}'}(0)\rangle=(2\pi)^2\sigma^2W(\mathbf{k})\delta(\mathbf{k}+\mathbf{k}'), \tag{13}$$

where σ denotes the standard deviation. For estimates we adopt the simplest form of the spectral density $W(\mathbf{k})\sim k_0/(k_0^2+k^2)^{3/2})$, where k_0 is the correlation length.

Omitting the intermediate calculations, we give the final results for SMSWs propagating in the direction perpendicular to the field $\mathbf{H}_0$.

For thick ferromagnetic plates ($kL\gg 1$) the relative attenuation is

$$\frac{\operatorname{Im}k}{k}\approx\frac{1}{\pi^3\sqrt{2}}\left(\frac{\sigma}{L}\right)^2\sqrt{\frac{\omega_H}{\omega_m+2\omega_H}}\,e^{kL}\times\begin{cases}8k_0L/\ln\delta, & \ln\delta\gg k_0L,\\ (\ln\delta/k_0L)^2, & \ln\delta\ll k_0L,\end{cases} \tag{14}$$

where $\delta=\Gamma/\omega_m$, and Γ is the natural attenuation of SMSWs (for yttrium iron garnet films $\delta\sim 10^{-3}-10^{-4}$).

Calculations for thin plates ($kL\ll 1$) give

$$\frac{\mathrm{Im}\,k}{k}\approx\frac{1}{\pi^3}\left(\frac{\sigma}{L}\right)^2\frac{\omega_H}{\sqrt{\omega_m(\omega_m+\omega_H)}}\times\begin{cases}\sqrt{2}k_0L/\sqrt{kL}\ \ln\,\delta, \\ \sqrt{kL}\ \ln\,\delta\gg k_0L, \\ 16^{-1}[(\omega_H+\omega_m)/\omega_m]^{3/2}kL(\ln\,\delta/k_0L)^2, \\ \sqrt{kL}\ \ln\,\delta\ll k_0L.\end{cases}$$

Assuming for estimates that $k=10^2\ \mathrm{cm}^{-1}$, $L=10\ \mu\mathrm{m}$, $H_0=500$ Oe, and $\sigma\sim k_0^{-1}\sim d$, where $d=(2^{1/2}/3^{1/4})\times(\Phi_0/H_0)^{1/2}$ is the period of the vortex lattice (Φ_0 is the quantum of magnetic flux), we find that the relative SMSW attenuation due to the investigated scattering mechanism is at least one or two orders of magnitude smaller than the natural attenuation. The corresponding frequency shift is equally small, so that the wave spectrum essentially coincides with the SMSW spectrum in the ferromagnet-ideal metal structure.

Consequently, strong vortex pinning completely ''restores'' the shielding properties of the superconductor from the case of unpinnned vortices.

This work has received support from the Russian Fund for Fundamental Research (Grant 96-02-17283a).

[1] A. F. Popkov, Zh. Tekh. Fiz. **59**(9), 112 (1989) [Sov. Phys. Tech. Phys. **34**, 1023 (1989)].

[2] V. S. Babushkin and N. A. Morozova, Pis'ma Zh. Tekh. Fiz. **17**(19), 1 (1991) [Sov. Tech. Phys. Lett. **17**, 681 (1991)].

[3] A. F. Popkov, Pis'ma Zh. Tekh. Fiz. **15**(15), 9 (1989) [Sov. Tech. Phys. Lett. **15**, 332 (1989)].

[4] Yu. I. Bespyatykh, A. D. Simonov, and V. D. Kharitonov, Pis'ma Zh. Tekh. Fiz. **16**(23), 27 (1990) [Sov. Tech. Phys. Lett. **16**, 896 (1990)].

[5] V. I. Zubkov, B. M. Lebed', É. G. Lokk, V. D. Kharitonov, V. I. Shcheglov, and S. V. Yakovlev, Pis'ma Zh. Tekh. Fiz. **18**(15), 5 (1992) [Sov. Tech. Phys. Lett. **18**, 476 (1992)].

[6] Yu. I. Bespyatykh, V. Vasilevskiĭ, M. Gaĭdek, A. D. Simonov, and V. D. Kharitonov, Fiz. Tverd. Tela (St. Petersburg) **35**, 2983 (1993) [Phys. Solid State **35**, 1466 (1993)].

[7] Yu. I. Bespyatykh, V. Vasilevskiĭ, V. D. Kharitonov, and V. I. Shcheglov, Pis'ma Zh. Tekh. Fiz. **21**(18), 27 (1995) [Tech. Phys. Lett. **21**, 736 (1995)].

[8] Yu. I. Bespyatykh, V. Vasilevskiĭ, V. D. Kharitonov, and V. I. Shcheglov, Pis'ma Zh. Tekh. Fiz. **22**(11), 7 (1996) [Tech. Phys. Lett. **22**, 433 (1996)].

[9] Yu. I. Bespyatykh, V. Vasilevskiĭ, M. Gaĭdek, and V. D. Kharitonov, Fiz. Tverd. Tela (St. Petersburg) **37**, 3049 (1995) [Phys. Solid State **37**, 1680 (1995)].

[10] L. N. Bulaevskiĭ, V. L. Ginzburg, A. A. Sobyanin, and A. A. Stratonnikov, Usp. Fiz. Nauk **157**, 539 (1989) [Sov. Phys. Usp. **32**, 277 (1989)].

[11] G. S. Mkrtchyan and V. V. Shmidt, Zh. Éksp. Teor. Fiz. **61**, 367 (1971) [Sov. Phys. JETP **34**, 195 (1972)].

[12] E. H. Brandt, J. Low Temp. Phys. **42**, 557 (1981).

[13] Yu. I. Bespyatykh, V. Vasilevskiĭ, M. Gaĭdek, and V. D. Kharitonov, Fiz. Tverd. Tela (St. Petersburg) **37**, 2611 (1995) [Phys. Solid State **37**, 1434 (1995)]; erratum: Fiz. Tverd. Tela (St. Petersburg) **38**, 3200 (1996) [Phys. Solid State **38**, 1747 (1996)].

[14] A. I. Larkin, Zh. Éksp. Teor. Fiz. **58**, 1466 (1970) [Sov. Phys. JETP **31**, 784 (1970)].

[15] G. A. Bugal'ter and I. A. Gilinskiĭ, Izv. Vyssh. Uchebn. Zaved. Radiofiz. **32**, 1187 (1989).

[16] A. I. Urazakov and L. A. Fal'kovskiĭ, Zh. Éksp. Teor. Fiz. **63**, 2297 (1972) [Sov. Phys. JETP **36**, 1214 (1973)].

[17] Yu. I. Bespyatykh, V. Vasilevskiĭ, M. Gaĭdek, and V. D. Kharitonov, Fiz. Met. Metalloved. **80**(5), 5 (1995).

Translated by James S. Wood

Electron paramagnetic resonance of deep boron acceptors in 4*H*-SiC and 3*C*-SiC crystals

P. G. Baranov, I. V. Il'in, and E. N. Mokhov

A. F. Ioffe Physicotechnical Institute, Russian Academy of Sciences, 194021 St. Petersburg, Russia

(Submitted May 30, 1997)
Fiz. Tverd. Tela (St. Petersburg) **40**, 36–40 (January 1998)

EPR spectra of deep boron in 4*H*-SiC and 3*C*-SiC crystals have been observed and studied. Two sites in 4*H*-SiC produced deep-boron EPR signals, quasi-cubic *k* and hexagonal *h*. In both cases the deep-boron center symmetry is close to axial along the *c* crystal axis, and the *g* factor anisotropy is about an order of magnitude larger than that for shallow boron centers. In the 3*C*-SiC crystal, the deep-boron symmetry is also close to axial along one of the four ⟨111⟩ directions. The model proposed for the deep boron center with acceptor properties is B_{Si}-v_C, where B_{Si} is the boron substituting for silicon, and v_C is the carbon vacancy, with the B_{Si}-v_C direction coinciding in 4*H*SiC with the hexagonal axis of the crystal for both *k* and *h* positions. In the cubic 3*C*-SiC crystal, there are four equivalent deep boron centers, which represent B_{Si}-v_C pairs with the bond directed along one of the four ⟨111⟩ crystal directions.
[S1063-7834(98)00801-6]

Silicon carbide finds an ever increasing application as a promising material for microelectronics devices designed for operation in extreme environmental conditions.

Boron, representing a major acceptor impurity in silicon carbide, creates two levels in the gap corresponding to two types of defects (see Ref. 1 and references therein). 6*H*-SiC contains a shallow and a deep boron center with activation energies of 0.35–0.39 and 0.55–0.75 eV, respectively. Both centers were detected by deep-level transient spectroscopy.[2–4]

The main and most informative method for investigating defect structure at atomic level is electron paramagnetic resonance (EPR). Recent publications[5–7] report detection and study of EPR spectra of deep-level boron in 6*H*SiC. A number of anisotropic signals assigned to deep boron were earlier observed by optically detected magnetic resonance (ODMR).[8–10] ODMR spectra were derived from intensity changes in the luminescence band associated with deep boron in 6*H*-SiC and 4*H*-SiC crystals.

The hexagonal polytype 4*H*SiC and cubic polytype 3*C*SiC are modifications of silicon carbide having the largest application potential. Besides, these polytypes have a comparatively simple crystal lattice, which appears important for better understanding of the microscopic structure of deep boron centers. This work reports detection and investigation of deep boron by EPR in 4*H*-SiC and 3*C*-SiC crystals.

1. EXPERIMENTAL

We studied the 4*H* and 3*C* polytypes of SiC grown by the Lely and sandwich sublimation methods.[11] In the latter case growth was in vacuum at 1850–2000 °C. The growth rate was 0.8–1 mm/h. The desired polytype was prepared by properly choosing the off-stoichiometric vapor-phase composition. When the vapor was enriched with silicon, 3*C*-SiC crystals were obtained. By contrast, enrichment of the vapor phase with carbon, which was achieved by adding tin vapor, resulted in the growth of the 4*H* polytype. The crystals were *n* type, with an uncompensated donor-impurity concentration of $5\times10^{16}-3\times10^{18}$ cm^{-3}.

Boron exhibits fast diffusion in silicon carbide.[12] Therefore we studied, as a rule, samples doped with boron by diffusion. The diffusion was carried out in vacuum-tight graphite containers at 1900–2300 °C. The diffusion time was varied from 0.5 to five hours. The source used in diffusion was natural-abundance boron or the ^{10}B or ^{11}B isotopes. After diffusion, the near-surface, heavily-boron-doped layer about 0.010 mm thick and with concentration $>5\times10^{18}$ cm^{-3} was removed from the sample. Note that high-quality 3*C*-SiC crystals did not convert to hexagonal polytypes during the high-temperature annealing.

2. RESULTS OF THE EXPERIMENT

A. 4*H*-SiC hexagonal crystal

Figure 1 shows EPR spectra of a 4*H*-SiC crystal doped by diffusion with ^{11}B. The spectra were taken at 4 K for different magnetic-field orientations relative to the hexagonal (*c*) axis of the crystal. The rotation was performed in the $\{11\overline{2}0\}$ plane. As shown earlier for 6*H*SiC,[5–7] the low-field part of the spectrum is due to the deep-boron centers. This part of the spectrum is marked in Fig. 1 with a horizontal section indicating roughly the magnetic-field region containing deep-boron signals at different orientations. The signals belonging to deep-boron centers are denoted by dB. In contrast to the 6*H*-SiC polytype, 4*H*SiC has, besides a hexagonal site (*h*), only one quasi-cubic site (*k*), and this manifests itself in the EPR spectrum presented in Fig. 1. The signals due to the deep-boron centers in the *h* and *k* positions have practically the same intensity, whereas in the 6*H*-SiC crystal the signal with the lower *g* factor, which belongs to two

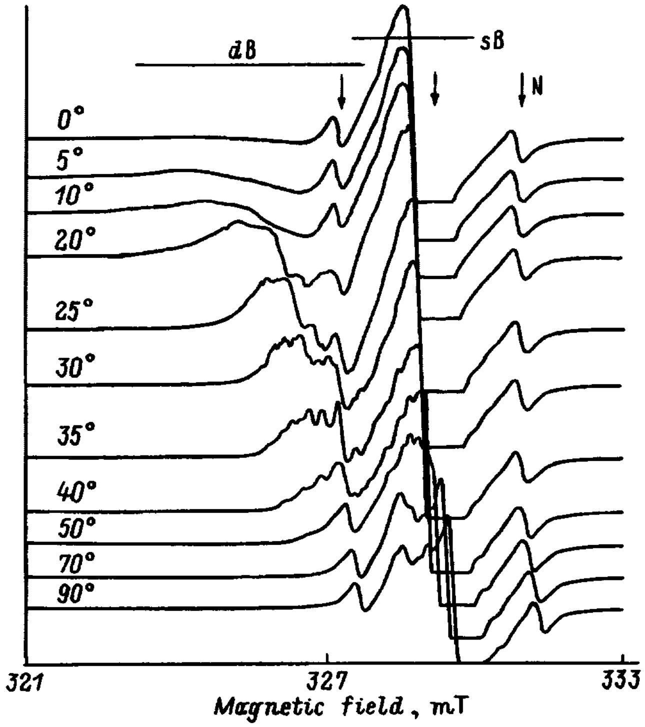

FIG. 1. Orientational dependence of deep-boron EPR spectra in $4H$-SiC:^{11}B measured in X range at 4.2 K. The rotation was made in the $\{11\overline{2}0\}$ plane. Vertical arrows identify the extreme nitrogen hfs components.

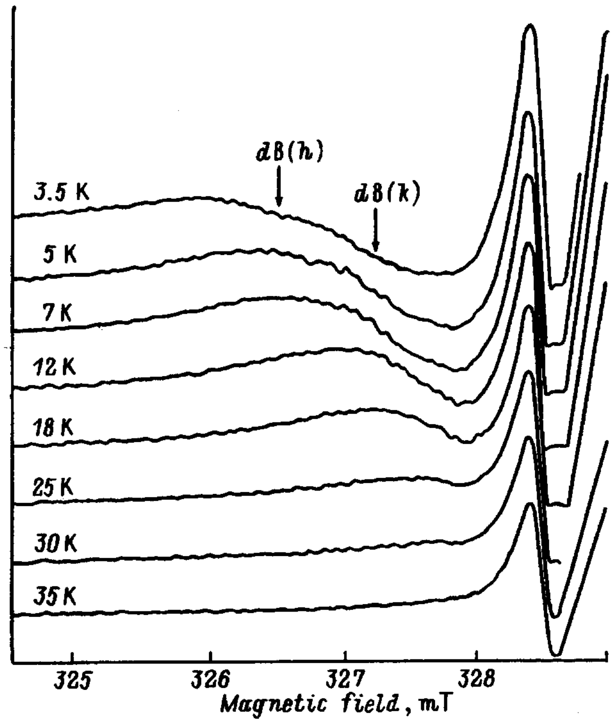

FIG. 2. Temperature dependence of deep-boron EPR spectra in $4H$-SiC:^{11}B measured in X range in $\mathbf{B}\| c$ orientation.

quasi-cubic positions with practically equal g factors, is about two times stronger.[5–7] Thus the present study permits an unambiguous assignment of the signal with the maximum g factor to the hexagonal position, and the second, to the quasi-cubic one.

The high-field part of the EPR spectrum denoted by sB in Fig. 1 corresponds to shallow boron, and the two nearly isotropic lines with a ~3.6-mT splitting, to the extreme hfs nitrogen-donor components (from the inner part of the crystal, which was not fully compensated during the boron diffusion).

The EPR spectra in Fig. 1 confined within the 20–40° interval between the magnetic-field direction and the c axis of the crystal contain a resolved structure caused by hyperfine interaction of the unpaired electron with the ^{11}B nucleus. Native boron consists of two stable isotopes, ^{10}B (19.8% abundance) and ^{11}B (80.2%), with spins $I=3$ and 3/2, respectively. Figure 1 shows an EPR spectrum obtained on a $6H$-SiC crystal doped with ^{11}B. The spectrum should contain in this case one or several groups of lines, with four equidistant hfs lines in each group. It is this situation that is seen qualitatively in Fig. 1 in the 20–50° interval. The resolution vanishes for angles close to 0°, leaving only two broad overlapping lines. Measurements carried out at higher frequencies on $6H$-SiC crystals revealed a scatter in the g factors which, for orientations close to $\mathbf{B}\| c$, destroys spectral resolution. The hfs splittings at $\theta=35°$ are ~2 mT and ~3 mT for dB (h) and dB (k), respectively.

Deep-boron EPR spectra shown in Fig. 1 can be analyzed using the following spin Hamiltonian

$$H=\mu_B \mathbf{B} g \mathbf{S}+\mathbf{S} A \mathbf{I}-g_I \mu_N \mathbf{B}\mathbf{I}, \tag{1}$$

where the electronic and nuclear (^{11}B) spins are $S=1/2$ and $I=3/2$, respectively, g and A are tensor quantities characterizing the electronic g factor and hyperfine interaction with the boron nucleus, μ_B is the Bohr magneton, and g_I is the nuclear g factor of ^{11}B. The spectra can be approximately characterized by axial symmetry along the c axis of the crystal. At 4 K, $g_{\|}=2.029$ and 2.024 for the h and k deep-boron positions, respectively, and $g_{\perp}\cong 2.0$. Figure 2 displays the temperature behavior of the deep-boron EPR spectrum in $4H$SiC:^{11}B obtained in the X range in $\mathbf{B}\| c$ orientation. We readily see that the deep-boron EPR lines shift with increasing temperature toward higher magnetic fields, which implies that $g_{\|}$ decreases with increasing temperature and approaches 2.0. This effect was earlier observed for deep-boron, deep-aluminum, and deep-gallium centers.[6,7] Apparently, as the temperature increases, the first to disappear are deep-boron spectra associated with the h position, dB (h), followed above 30 K by EPR signals of the deep boron occupying the k sites, dB (k), leaving only the EPR spectrum of the shallow boron.

B. 3*C*-SiC hexagonal crystal

Figure 3 illustrates the orientational dependence of EPR spectra observed in $3C$SiC:^{11}B. The spectra were measured in the X range at 4 K. The crystal was rotated around the $\langle 110\rangle$ direction. The spectra are seen to be essentially anisotropic. The simplest spectrum is observed in the $\mathbf{B}\|\langle 100\rangle$ orientation, which implies for a cubic crystal that the principal symmetry axis of the defect is along $\langle 111\rangle$. The low-field spectrum consisting of one group of four lines, marked appropriately in Fig. 3 for the $\mathbf{B}\|\langle 100\rangle$ orientation, belongs to the deep boron, whereas the stronger high-field signal origi-

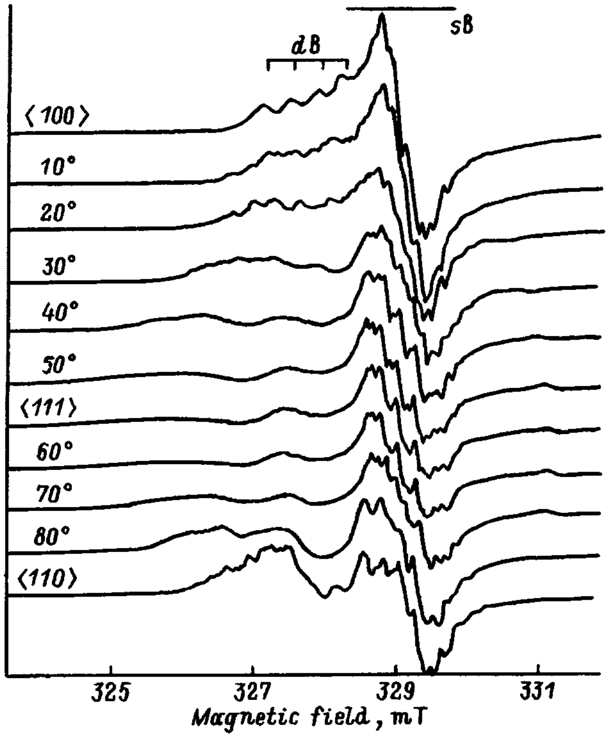

FIG. 3. Orientational dependence of deep-boron EPR spectra in $3C$-SiC:^{11}B measured in X range at 4.2 K. The rotation was made about the ⟨110⟩ direction.

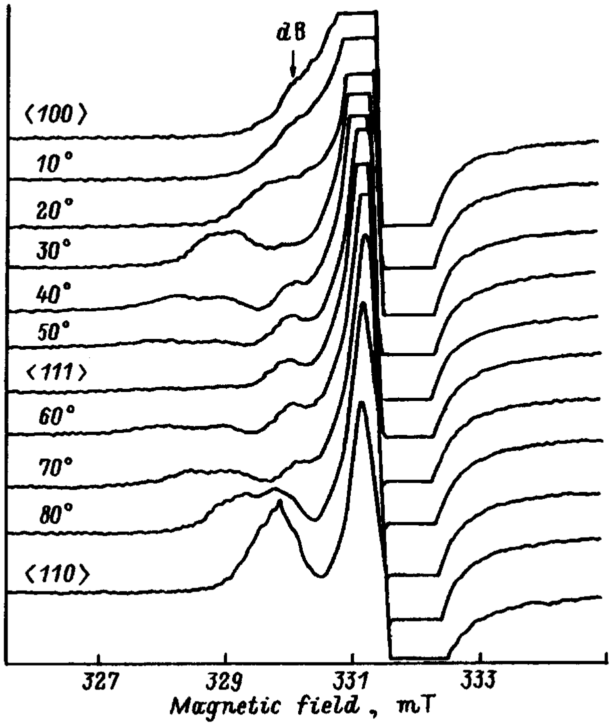

FIG. 4. Orientational dependence of deep-boron EPR spectra in $3C$-SiC:^{10}B measured in X range at 4.2 K. The rotation was made about the ⟨110⟩ direction.

nates from the shallow boron. The splitting into four lines spaced by about 0.3 mT is caused by hyperfine interaction, which follows unambiguously from the experiments with $3C$SiC:^{10}B discussed below. Substitution of ^{10}B for ^{11}B should affect substantially the spectrum, because the hyperfine structure for the former isotope should consist of seven unresolved components with a separation three times smaller than that in the case of ^{11}B, in other words, one should observe now one unresolved broad line, whose total width should be, however, slightly less than the envelope for ^{11}B with unresolved hyperfine structure. Figure 4 presents EPR spectra observed in the ^{10}B-doped $3C$-SiC crystal. As expected, the EPR spectra that we assign to deep boron no longer contain the resolved structure observed in Fig. 3 at some angles, for instance, the center of the unresolved line for the $\mathbf{B}\|\langle 100\rangle$ orientation is shown by an arrow, and for orientations close to $\mathbf{B}\|\langle 111\rangle$ the overlapping unresolved lines have become slightly narrower. Thus the spectrum we are discussing is indeed due to boron. A comparative analysis of the spectra in Figs. 3 and 4 permits one to separate the line splittings due to hyperfine interaction from those originating from the anisotropy of the g factors because of the existence of magnetically nonequivalent deep-boron positions. Unfortunately, the X range does not allow one to find all spin-Hamiltonian parameters for deep boron. Estimates show the symmetry of the centers to be close to axial along ⟨111⟩, and the g factor in this direction to be $g_{\|}\cong 2.025$. Similarly to the hexagonal SiC polytypes, $g_{\perp}\cong 2.0$. Interpretation of EPR spectra of $3C$SiC in the X range presents certain difficulties, since the widths of the deep-boron lines are comparable to the line shifts in different orientations. We have at present no possibility for concluding unambiguously whether the double lines observed for close to $\mathbf{B}\|\langle 111\rangle$ orientations in Figs. 3 and 4 are due to the centers having lower than axial symmetry (such a lowering of symmetry for deep boron was observed by us[5–7] in the case of $6H$SiC) or to the presence in the crystal of an $6H$-SiC impurity, which could partially form in the course of high-temperature boron diffusion. One clearly sees in Fig. 3 an additional satellite on the high magnetic-field side, whose position is orientation dependent, with the maximum field for its position observed for $\mathbf{B}\|\langle 111\rangle$. In this case, the line is separated from the $g=2.0$ position by about 1.5 mT. Figure 5a presents temperature behavior of the EPR spectrum of deep boron in $3C$SiC:^{11}B measured in X range in the $\mathbf{B}\|\langle 111\rangle$ orientation. We readily see that the temperature at which deep-boron EPR signals are no longer seen (about 20 K) correlates fully with that of the satellite line disappearance, which indicates that the latter belongs to deep boron. Such a satellite line was observed also in $6H$-SiC crystals in orientations close to $\mathbf{B}\perp c$, and, in addition, experiments[5–7] with $6H$-SiC crystals enriched in the ^{13}C isotope showed unambiguously that this line is not caused by hyperfine interaction with ^{13}C. Shown for comparison in Fig. 5b is the temperature dependence of the deep-boron EPR spectrum in $6H$SiC:^{11}B obtained in X range in the $\mathbf{B}\perp c$ orientation. One could apparently isolate here also the second low-field component with a splitting of about 3 mT.

3. DISCUSSION

An analysis of deep-boron EPR spectra based on the assumption that the deep-boron symmetry is close to axial,

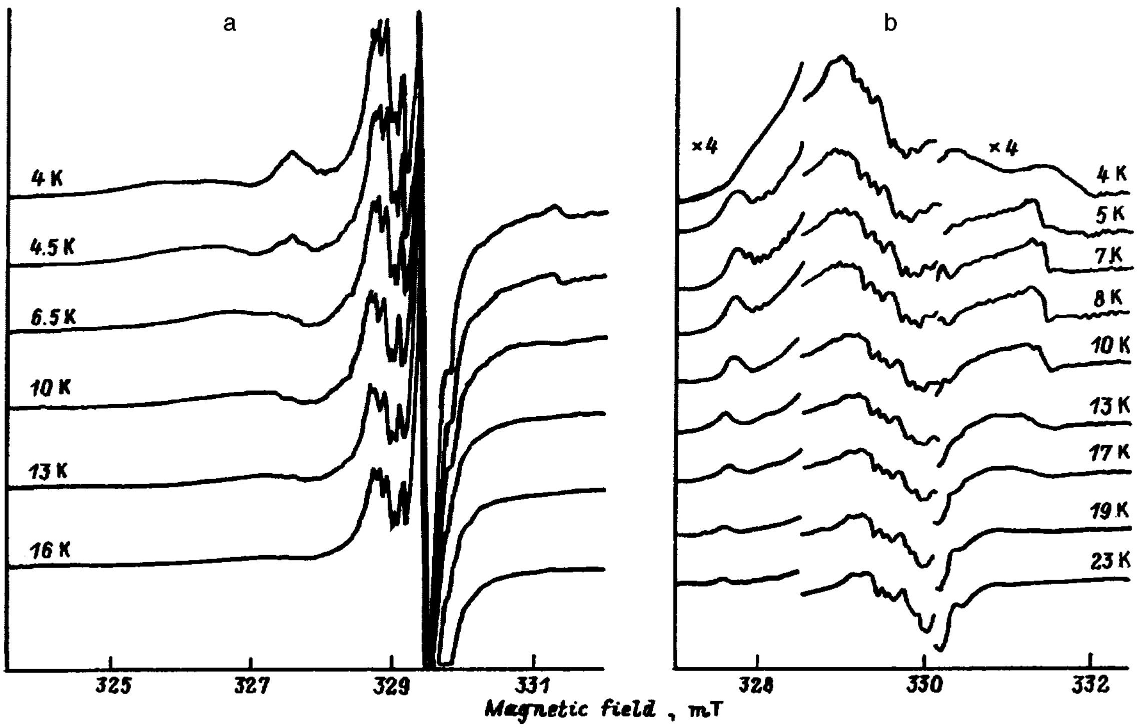

FIG. 5. Temperature behavior of deep-boron EPR spectra in X range obtained (a) in $3C$-SiC:^{11}B crystal with $\mathbf{B}\|\langle 111\rangle$ and (b) in $6H$-SiC:^{11}B crystal with $\mathbf{B}\perp c$.

and on the strong anisotropy of deep-boron compared to shallow-boron spectra in ^{13}C-enriched crystals, led to a conclusion that deep boron in the acceptor state in $6H$-SiC crystals represents a B_{Si}-v_C pair, with the bond directed along the c axis for both the hexagonal and the two quasi-cubic positions.[5–7] Our present investigation suggests that the deep-boron acceptor center in $4H$SiC is also a B_{Si}-v_C pair, with the bond aligned with the c axis in both hexagonal and quasi-cubic position. While this model can be used for cubic $3C$SiC as well, this crystal has four nonequivalent deep-boron centers representing B_{Si}-v_C pairs with the bond aligned with one of the four $\langle 111\rangle$ axes.

Note one more essential point. An earlier analysis of the mechanism of boron diffusion in SiC led to a conclusion that the boron states taking part in diffusion are the B_C-v_C associates. It would be difficult, however, to assign the EPR spectra of deep boron to this configuration. It may be argued that mobile associates created in the near-surface layer of a sample dissociate to a considerable extent during the diffusion anneal with a release of v_C, which is subsequently captured by B_{Si} to form the stronger associate B_{Si}-v_C.

The line broadening observed to occur in the $\mathbf{B}\|c$ orientation ($\mathbf{B}\|\langle 111\rangle$ in $3C$SiC) and, as a consequence, the strong decrease in EPR signal intensity in this orientation, may be caused by a stress-induced scatter in the $g_{\|}$ factors. The satellite lines observed by us are possibly due to hyperfine interaction with ^{29}Si. In order to reliably establish the electronic structure of deep-boron centers, one has to make an ENDOR study at high EPR frequencies, as well as carry out experiments on SiC crystals enriched with the ^{29}Si isotope.

Partial support of the Volkswagen Stiftung (Grant I/70958) and of the Russian Fund for Fundamental Research (Grant 96-02-16927) is gratefully acknowledged.

[1] G. Pensl and R. Helbig, in *Advances in Solid State Physics*, Vol. 30, edited by U. Rössler (Vieweg, Braunschweig, 1990), p. 133.
[2] M. M. Anikin, A. A. Lebedev, A. L. Syrkin, and A. V. Suvorov, Fiz. Tekh. Poluprovodn. **19**, 114 (1985) [Sov. Phys. Semicond. **19**, 69 (1985)].
[3] W. Suttrop, G. Pensl, and P. Laning, Appl. Phys. A **51**, 231 (1990).
[4] V. S. Ballandovich and E. N. Mokhov, Fiz. Tekh. Poluprovodn. **29**, 370 (1995) [Semiconductors **29**, 187 (1995)].
[5] P. G. Baranov and E. N. Mokhov, Semicond. Sci. Technol. **11**, 489 (1996); Fiz. Tverd. Tela (St. Petersburg) **38**, (1996) [Phys. Solid State **38**, (1996)].
[6] P. G. Baranov, I. V. Ilyin, and E. N. Mokhov, Solid State Commun. **100**, 371 (1996).
[7] P. G. Baranov, Defect Diffus. Forum **148–149**, 129 (1997).
[8] N. G. Romanov, V. A. Vetrov, P. G. Baranov, E. N. Mokhov, and V. G. Oding, Pisma Zh. Tekh. Fiz. **11**, 1168 (1985) [Sov. Tech. Phys. Lett. **11**, 483 (1985)].
[9] P. G. Baranov, N. G. Romanov, V. A. Vetrov, and V. G. Oding, in *Proceedings of the 20th International Conference in Physics of Semiconductors*, edited by E. M. Anastassakis and J. D. Joannopoulos (World Scientific, Singapore, 1990), Vol. 3, p. 1855.
[10] P. G. Baranov and N. G. Romanov, Appl. Magn. Reson. **2**, 361 (1991); Mater. Sci. Forum **83–87**, 1207 (1992).
[11] Yu. A. Vodakov, E. N. Mokhov, M. G. Ramm, and A. D. Roenkov, Krist. Tech. **14**, 729 (1979).
[12] Yu. A. Vodakov and E. N. Mokhov, in *Silicon Carbide-1973* (South Carolina Univ. Press, 1974), p. 508.

Translated by G. Skrebtsov

Classical analogs to the Chalker–Coddington model

S. N. Dorogovtsev

A. F. Ioffe Physicotechnical Institute, Russian Academy of Sciences, 194021 St. Petersburg, Russia

(Submitted May 30, 1997)
Fiz. Tverd. Tela (St. Petersburg) **40**, 41–47 (1998)

A description is given of a classical analogs to the Chalker–Coddington model, i.e. of a lattice model of the integer quantum Hall effect, which has recently been used to investigate intensively mesoscopic conductance fluctuations at the plateau transition. It is shown that the corresponding classical problem is current percolation through bonds forming a two-dimensional percolation-cluster hull. It is also shown that, in contrast to standard percolative problems, the scaling relations for conductance, as also the conductance distribution function for finite samples, contains only the critical correlation-length exponent in the problem under study. It is known that such relations developed for the integer quantum-Hall effect likewise contain only the critical correlation-length exponent. It is finally concluded that this essential feature of the quantum Hall effect is determined not so much by its quantum nature as by the geometry of the problem.
[S1063-7834(98)00901-0]

The Chalker-Coddington model[1,2] is presently the most popular lattice model for the integer quantum Hall effect. It permits one to describe in a sufficiently simple and revealing way the so-called plateau transition in the quantum Hall effect at zero temperature.[3] Recent studies reported strong fluctuations of conductance in mesoscopic samples directly at this transition.[4] The conductance distribution functions in this regime and the behavior of the conductance of small samples in the vicinity of the plateau transition were successfully investigated within the Chalker-Coddington model both numerically[5,6] and by the renormalization-group (RG) method in real space.[7]

It turned out that the average conductance of a small sample is connected with its linear dimensions L and the deviation from the transition point Δ through the following scaling relation which includes only the critical exponent ν of the localization length:

$$\langle G\rangle = g(L^{1/\nu}\Delta), \tag{1}$$

where $g(x)$ is a scaling function (we shall explain the meaning of Δ in the Chalker–Coddington model later). The conductance distribution function $P(G)$ at the plateau transition does not depend on dimension L at all.

It would seem that the conductance of classical percolative systems should behave in a radically different way at criticality. Consider, for instance, the bond percolation problem, where the scaling relation connecting averaged conductance of a sample of dimension L with the deviation of the conducting-bond concentration p from the percolation threshold p_c

$$\langle\sigma\rangle(p,L) = L^{-t/\nu} s[L^{1/\nu}(p-p_c)] \tag{2}$$

contains both the ‘‘static’’ correlation-length exponent ν and the ‘‘dynamical’’ critical-conductance exponent t [$s(x)$ is the scaling function].[8–11] The general expression for the conductance distribution function at the threshold also contains the dynamical critical exponent:

$$P(\sigma,L) = f(L^{t/\nu}\sigma). \tag{3}$$

At first sight, this significant difference between the quantum and classical problems should not appear strange. Indeed, in the quantum problem the conductance is expressed through the transmission matrix,[12] and the critical localization-length exponent cannot be called ‘‘static,’’ whereas in classical percolation problems separation of the critical exponents into static and dynamic is a radical issue (see, e.g., a comprehensive discussion in a review[13]). Now does this imply that there is nothing in common between the quantum and classical problem? We are going to prove here that this is not so. We shall show that the classical analog of the Chalker–Coddington model is the percolation problem where, in contrast to the standard formulation, the scaling relations for the conductance and resistance distribution function at the percolation threshold contain only the static critical exponents, which are determined, as usually, by the form of the percolating cluster, namely,

$$\langle\sigma\rangle = L^{-d_h} s[L^{1/\nu}(p-p_c)] \tag{4}$$

and

$$P(\sigma,L) = f(L^{d_h}\sigma). \tag{5}$$

Here d_h, as we shall see, is the fractal dimension of the percolating cluster hull, i.e. the static critical exponent. It is known that in a two-dimensional problem this quantity is directly expressed through the critical correlation-length exponent: $d_h = 1 - 1/\nu$.[14]

We shall thus verify that the conductance of the classical analog of the Chalker–Coddington model exhibits common features with that in the quantum problem, in that the corresponding scaling relations contain only exponent ν. Rather than presenting a rigorous proof, however, we shall restrict ourselves to a very instructive and straightforward calculation of critical exponents of the classical problem.

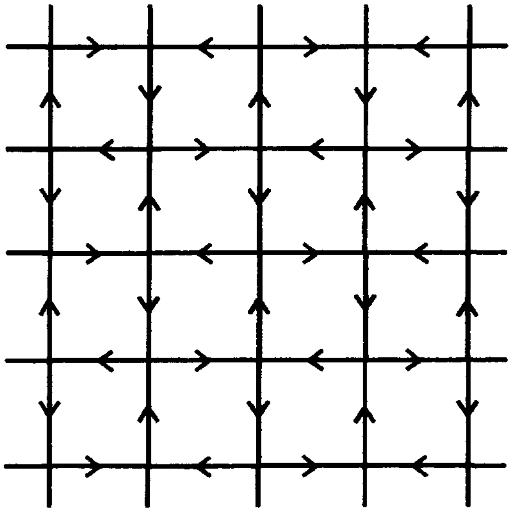

FIG. 1. Directed-bond lattice used in the Chalker–Coddington model and in the model under study. The bond arrows specify the directions in which a particle may walk.

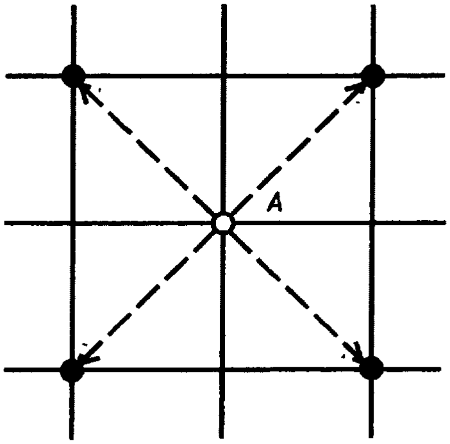

FIG. 2. Lattice sites which can be reached by a particle from site A in two steps.

1. CHALKER–CODDINGTON MODEL AND SPIRAL RANDOM WALK

We shall first recall the Chalker–Coddington model.[1] A quantum particle (an electron) can propagate through bonds on a square lattice in the directions shown in Fig. 1. On scattering from a lattice site, the particle can turn either to the left with a probability amplitude r, or to the right, with a probability amplitude t, with the scattering, r, and transmission, t, probability amplitudes related in the standard way: $|r|^2+|t|^2=1$. (To avoid ''right turns'' and ''left turns,'' one can introduce two appropriately chosen matrices for different lattice sites, namely, one scattering matrix for the sites sum of coordinates whose, $i+j$, is an even number, and another one, which is related to the first through the transformation of rotation by an angle $\pi/2$, for the sites whose coordinate sum is odd.[1,5,15]) Walk over the bonds results in accumulation of random phases, over which one shall have to perform averaging when the calculation of concrete quantities is reached. The constraint on possible directions of motion models the magnetic field and simplifies considerably the quantum localization problem. Delocalization in the square lattice under study occurs at $|t|^2=1/2$, which is the plateau transition point in the integer quantum-Hall effect. The parameter of deviation from this critical point, Δ, which enters Eq. (1), can be expressed through $|t|$ as $\Delta\equiv\|t|-1/\sqrt{2}|$.

Obviously enough, to the Chalker–Coddington quantum problem corresponds directly the following simple classical problem of random walk on a square lattice. We assume that after a step from one lattice site to its nearest neighbor a classical particle can walk to the left (to the nearest site) with a probability p, and to the right, with a probability $1-p$. No second steps in the same direction are allowed. Such random walk belongs to the spiral class.[16]

If we prescribe the direction of the first step of the particle, all its subsequent possible walks on the lattice will form the same pattern that is used in the Chalker–Coddington model (Fig. 1). (Strictly speaking, depending on whether the first step was made in the horizontal or vertical direction we shall obtain two patterns with opposite directions of the corresponding bonds.)

It is clear that such random walk represents, generally speaking, a non-Markovian process, since the direction of a step depends on that of the preceding one. In two cases, however, this process reduces to the Markovian pattern. If $p\ll 1$, the particle will walk most of the time around plaquettes, with only infrequently hopping from one plaquette to its neighbor. Actually, we have here usual random walk between plaquettes with a probability $p/4$ to move to one of the four sides after each step. Let the linear dimension of the lattice cell be a, and the time between steps, τ. The neighboring plaquettes involved in such walk lie diagonally (Fig. 1), so that their separation is $\sqrt{2}a$. Using the standard relations,[17] we come to the following expression for the diffusion coefficient in this regime:

$$D=\frac{(\sqrt{2}a)^2}{4\tau}4p=\frac{2a^2p}{\tau}. \tag{6}$$

In the second case, the probabilities of left and right steps are equal, $p=1/2$. Note that, irrespective of the direction of the preceding step, the particle will enter after two steps with equal probability one of the four sites marked in Fig. 2. Thus in two steps the particle moves along the diagonal of the square-lattice cell again by $\sqrt{2}a$ with a probability of 1/4 for each of the four possible directions. Thus

$$D=\frac{(\sqrt{2}a)^2}{4\tau/2}4\cdot\frac{1}{4}=\frac{a^2}{4\tau}. \tag{7}$$

So, as could have been expected, the classical problem which directly corresponds to the Chalker–Coddington model contains no hint whatsoever of the criticalities occurring in plateau transitions in the quantum Hall effect. To find something similar to this in the classical domain, we shall have to invoke percolation problems.[18]

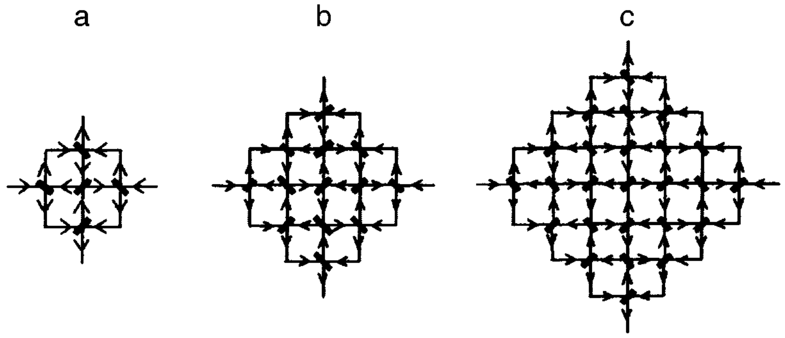

FIG. 3. Clusters used to construct renormalization-group transformations. The scaling factor is 2, 3, and 4 for clusters a, b, and c, respectively. The mirrors at the sites are arranged arbitrarily.

2. CHALKER-CODDINGTON MODEL AND THE PERCOLATION PROBLEM

Consider the following percolating problem. Double-sided mirrors are placed at the sites of a square network with a unit lattice constant. The mirrors are tilted at an angle of $+\pi/4$ or $-\pi/4$ to the horizontal, so that the trajectory of particle motion over the bonds is given uniquely by the mirror arrangement. Denote the lattice site coordinates by (i,j). Let the probability that the mirror tilt angle at a given site is $(-1)^{i+j}\pi/4$ be p, while that for the mirror tilt angle to be $(-1)^{i+j}\pi/4$ is $(1-p)$ (see Fig. 3).

We note immediately that particle trajectories in such a problem do not branch, do not meet, and do not intersect one another. Therefore they can be either closed, or begin and end at the sample boundary.

For $p=0$ and $p=1$, the mirrors are arranged in a checkerboard pattern, and the lattice is actually divided into plaquettes not connected with one another, and it is only around them that the particle can move. One can also readily see (we shall verify this directly later) that only for $p=1/2$ can a particle move to infinity. (Light can pass through such a mirror system only for $p=1/2$!) Thus percolation can exist in this problem at the only point $p=1/2$. In the quantum problem, this corresponds to delocalization at $|t|^2=1/2$.

We should like to stress that we can arrange our mirrors also on a lattice with bonds oriented as they are in the Chalker–Coddington model (Figs. 1 and 3). As a result, the direction of particle motion becomes fixed, so that, for instance, for $p=0$ the particle will move around a plaquette counterclockwise, and for $p=1$, clockwise. As for the trajectory pattern itself and the behavior at criticality, they certainly do not change.

We have thus formulated a model in which quantum interference between different particle trajectories is excluded in principle because the direction of scattering at each site is rigidly fixed. In place of the quantum scattering matrix we have classical mirrors at lattice sites, which determine uniquely (for the given mirror configuration) where the particle should be scattered, to the right or left. The averaging over the phase advance of a quantum particle in the Chalker–Coddington model is replaced in our case by that over different mirror configurations. Despite the fundamental differences between the quantum and classical problems, we shall find that they have common features as well.

We should mention an earlier treatment of a considerably more complex percolative problem, with gyrotropy incorporated to describe the effect of a strong magnetic field, the so-called gyrotropic percolation.[19]

How could this problem be related to the conventional percolation approach? Let us first forward some general considerations, after which we shall verify them by direct calculation of the critical exponents. If the probability p is neither zero nor one, the system is divided into a multiplicity of clusters of two types. In the first of them, the mirrors at the (i,j) sites are tilted at an angle $(-1)^{i+j}\pi/4$ to the horizontal, while in clusters of the second type the mirror tilt angle is $(-1)^{i+j}\pi/4$. For $p\geqslant 1/2$, conventional percolation can take place over regions of the first type, and for $p\leqslant 1/2$, over regions of the second. One can readily check that particle trajectories pass in our problem along the boundaries separating clusters of different types. (An exception to this are the trajectories circling around unit plaquettes inside such clusters.) Thus our problem actually reduces to description of particle motion through bonds along the percolating cluster hull in the conventional percolation model.[14,20–22] In continuum percolation problems this corresponds to motion along equipotentials near the percolation threshold.[23,24]

The above considerations can in no case be considered rigorous. They need serious substantiation. Here we shall simply use the position-space RG method to find the critical exponents for the problem under study with an accuracy high enough to check what are actually mere assumptions. If they are correct, the critical correlation-length exponent of our problem will coincide with that in the conventional two-dimensional percolation. As for the fractal dimension of an infinite trajectory for $p=1/2$ obtained in our case, it should coincide with that of the percolating cluster hull in the conventional percolation model [see Eqs. (4) and (5)].

The method of position-space renormalization, also called renormalization group in real space (see, e.g., Refs. 25–27), turns out to be particularly simple in our case. It is found that the clusters most suitable for constructing RG transformations of probability p are those shown in Fig. 3a,b,c for the scaling factor b of 2, 3, and 4, respectively. One can readily verify that the number of sites in each such cluster is $n=b^2+(b-1)^2$.

Let the bonds in the clusters be oriented as shown in Fig. 3. It is easy to see that if for a given mirror configuration the trajectory starting on the left reaches, say, the upper bond, then the trajectory starting on the right will without fail go down. Therefore there is only one way to perform an RG transformation, namely, one has to determine the probability

p' with which the trajectory starting on the right will eventually come up if the corresponding probability for a site is p or $1-p$, depending on the actual site number (see formulation of the model in the beginning of the Section). Note that in order to find p' one will have to make a brute-force search through 2^n possible mirror configurations.

For a cluster with $b=2$ (Fig. 3a), brute-force search through configurations with due account of their weights yields the following transformation for probability p:

$$p'(p)=2p^2(1-p)^3+8p^3(1-p)^2+5p^4(1-p)+p^5. \tag{8}$$

By the way, transformation (8) has the same form as that of the renormalization group for the simplest self-dual cluster in the conventional bond percolation problem.[25–27] It turns out that this coincidence occurs only in the $b=2$ case.

Because the clusters considered here are symmetrical, RG transformations yield the precise value of the percolation threshold. Indeed, the fixed transformation point $p'(p_c)=p_c$ is precisely one half, $p_c=1/2$.

In order to find the critical exponent ν of the correlation length ξ, we shall use the standard procedure.[25–27] If before the RG transformation the correlation length in the critical region was $\xi=c_0|p-1/2|^{-\nu}$, where c_0 is a constant, then after the transformation it will be expressed through the renormalized probability p' in the following way: $\xi=bc_0|p'-1/2|^{-\nu}$, since the linear dimension of the cell increased b times. As a result

$$\nu=\frac{\ln b}{\ln|dp'(p=1/2)/dp|}. \tag{9}$$

Inserting Eq. (8) in this expression for $b=2$ yields $\nu=1.4277$.

The RG transformation for a cluster with $b=3$ (here the number of sites $n=13$, see Fig. 3b) is found as simply but looks more cumbersome

$$\begin{aligned}p'(p)=\,&3p^3(1-p)^{10}+38p^4(1-p)^9+209p^5(1-p)^8\\&+627p^6(1-p)^7+1089p^7(1-p)^6+1078p^8\\&\times(1-p)^5+677p^9(1-p)^4+283p^{10}(1-p)^3\\&+78p^{11}(1-p)^2+13p^{12}(1-p)+p^{13}.\end{aligned} \tag{10}$$

Using now relations (9) with $b=3$ and (10), one can readily find a more accurate value for the critical correlation-length exponent: $\nu=1.3797$.

The number of configurations to be searched for clusters with $b=3$ and 4 is already quite large, and therefore it is reasonable to use for this purpose a computer, especially because the algorithm for selecting the configurations contributing to p' is extremely simple.

Let the coordinates of the center of the cluster be (0,0). One selects such mirror configurations for which the particle trajectory starting on the left, at point $(-b,0)$, ends at $(0,b)$ on top. Denote the coordinates of the site visited by the particle at kth step by $(i(k),j(k))$. Introduce for each cluster site a quantity $d(i,j)=\pm1$, which is $+1$ if the site mirror is tilted at $+\pi/4$ to the horizontal, and -1, if the mirror tilt angle is $-\pi/4$. At sites external to the cluster (with coordinates of the type of $(-b+1,\pm1),(b-1,\pm1)$ and so on, see Fig. 3) we shall also place mirrors and tilt them so as to force the particle to remain inside the cluster.

It is easy to check that the coordinates of the particle after each step are related to its position at the preceding steps through the following relations

$$\begin{cases}i(k+1)=i(k)+d[i(k),j(k)][j(k)-j(k-1)]\\ j(k+1)=j(k)+d[i(k),j(k)][i(k)-i(k-1)]\end{cases}. \tag{11}$$

Therefore it is not difficult to calculate the complete trajectory of the particle for each mirror arrangement and select the desirable configurations.

Such a simple brute-force search through 2^{35} configurations for the $b=4$ cluster shown in Fig. 3c yields immediately the relation

$$\begin{aligned}p'(p)=\,&4p^4(1-p)^{21}+102p^5(1-p)^{20}+1230p^6\\&\times(1-p)^{19}+9272p^7(1-p)^{18}+48718p^8\\&\times(1-p)^{17}+188512p^9(1-p)^{16}+553496p^{10}\\&\times(1-p)^{15}+1252416p^{11}(1-p)^{14}+2198498p^{12}\\&\times(1-p)^{13}+3001802p^{13}(1-p)^{12}+3204984p^{14}\\&\times(1-p)^{11}+2715264p^{15}(1-p)^{10}+1854463p^{16}\\&\times(1-p)^9+1032857p^{17}(1-p)^8+471428p^{18}\\&\times(1-p)^7+175870p^{19}(1-p)^6+53028p^{20}(1-p)^5\\&+12646p^{21}(1-p)^4+2300p^{22}(1-p)^3\\&+300p^{23}(1-p)^2+25p^{24}(1-p)+p^{25},\end{aligned} \tag{12}$$

which can be used by means of Eq. (9) to find the critical correlation-length exponent $\nu=1.3627$.

We see that the values of exponent ν obtained by the renormalization group procedure with b set successively to 2, 3, and 4 approach 4/3, which is the exponent for conventional percolation in two dimensions. Since this convergence is monotonic, it appears reasonable to extrapolate this series to $b\to\infty$.[25–27] As usual, the extrapolation is not a rigorous and unique procedure and can be performed, for instance, in the following way. Let us plot the values of ν obtained in this way as a function of reciprocal powers $b^{-\alpha}$, where index $\alpha>0$ is, in principle, arbitrary. We construct a curve described by a quadratic polynomial through these points. The intercept of this curve on the vertical axis yields the desired extrapolated value of $\nu(b\to\infty)$.

Clearly, the result of the extrapolation depends essentially on the index α we choose. For example, for $\alpha=1$ we obtain $\nu(b\to\infty)=1.340$. It turns out that the value $\nu(b\to\infty)=1.335$ closest to 4/3 is obtained if we take $\alpha=1.335$. This is certainly nothing but an amusing coincidence. At least we could not find an explanation for it. In any case, extrapolation results in values of ν very close to the correlation-length exponent for conventional percolation, which supports our conjectures. Note that earlier estimates of exponent ν in such a problem used the procedure based on the transfer matrix method and yielded $\nu=1.29\pm0.04$.[3]

In conclusion to this Section, we touch briefly on another problem with site mirrors, which would appear to be close to ours. In this model, the probability for a mirror to be tilted at an angle of $+\pi/4$ is p, and that of a tilt angle of $-\pi/4$, is $1-p$ for *each* site. In this case for $p=0$ particles or light can propagate along one diagonal of the lattice, and for $p=1$, along the other diagonal. One can easily check, however, that for arbitrarily small p or $1-p$ light will already propagate along both lattice diagonals. Indeed, in this case light can penetrate into an $N\times N$ lattice along one diagonal to a distance of order N, and along the other, to a distance of order pN. Thus in this model, in contrast to the one discussed here, there are no exponential correlations and no traditional percolation threshold.

3. RESISTANCE AND CONDUCTANCE DISTRIBUTION FUNCTIONS

Consider now the behavior of the resistance and conductance at criticality in our model. What distribution functions will be obtained for them at $p=1/2$ in the case of a finite sample? What is the fractal dimension of an infinite trajectory for $p=1/2$?

In principle, finding these distribution functions is a very complex problem. One should construct an RG transform for the corresponding distribution functions and find their stationary point, which is the universal distribution function being sought. Actually, one has to solve a complex nonlinear integral equation. This can be done only approximately, and the procedure involved is usually extremely time consuming (see, e.g., Ref. 7). One succeeds in solving analytically such problems only in one dimension, or by means of the fairly forced method of Migdal-Kadanov.[11]

Rather than invoking sophisticated procedures, we shall make use of the extremely simple approach, first proposed for such problems by Kirkpatrick,[8] which nevertheless gives quite satisfactory results. (It should be stressed, however, that this approach is certainly not capable of yielding accurate results.) In our case it looks as follows. Before the RG transformation, we shall replace the distribution function in the length of trajectories passing, for instance, from the left upward (see Fig. 3) with a delta function, in other words, we shall assume that for $b=1$ the distribution function has the form $Q_0(l)=\delta(l-2)$ (the bond length on a square lattice or, which in our case is the same, the bond resistance are assumed to be unity).

Let us find the form the distribution function in bond length assumes after the RG transformation at the percolation threshold, i.e. where it has a universal form. (Obviously, the exact distribution function can be found in this way only for $b\to\infty$.) To determine the scaling exponents [see Eqs. (4) and (5)], the distribution function obtained is again replaced by a delta function. The question of where this delta function should best be placed is postponed until later. This function is usually constructed at the point of mean resistance or mean conductance. (Since the trajectories neither branch nor intersect one another, the length of such a trajectory $l\equiv R$ plays the part of resistance, and its inverse, $l^{-1}\equiv\sigma$, of conductance.) In order to find the critical exponent we are looking for, it remains to compare these values with the corresponding value before the RG transformation, i.e., 2 or 1/2, respectively, in the first and second case.

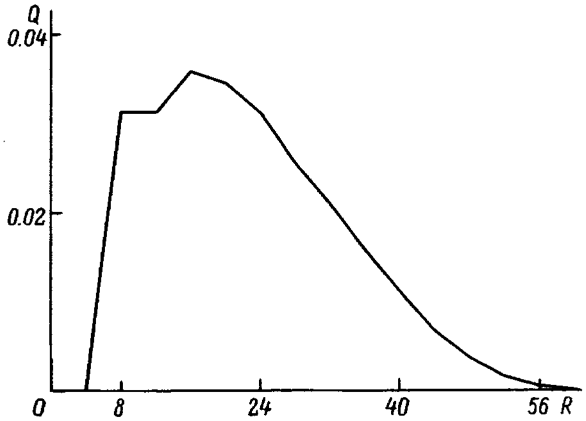

FIG. 4. Resistance distribution function $Q(R)$ obtained after renormalization-group transformation with $b=4$ (See Fig. 3c). The discrete values at points $R=2b+4k$, $k=0,1,2,\ldots,b^2-b$ are connected by a line.

Let us perform this procedure successively for the RG transformations with the scaling factors 2, 3, and 4 (see clusters in Fig. 3). In the search through configurations described in the preceding Section (we set now $p=1/2$ from the very beginning), we calculate for each configuration the length of the trajectory which leads, for instance, from the left upwards. The distribution functions thus obtained for the lengths of such trajectories (i.e. cluster resistances) and conductances have the forms shown in Figs. 4 and 5, which are the distributions obtained after the action on the delta function of the RG transformation with the scaling factor $b=4$.

Actually, the conductance distribution $Q(R)$ is obtained in the form of a set b^2-b+1 of discrete values $Q(R)\delta_{R,(2b+4k)}$, $k=0,1,2,\ldots,b^2-b$, placed with an equal step of four from $R=2b$ to $R=2b(2b-1)$, which are the minimum and maximum possible trajectory lengths in the cluster, respectively. After smoothing, this distribution can be readily used to construct the conductance distribution $P(\sigma)=Q(\sigma^{-1})/\sigma^2$.

Already after applying transformations with small $b=3$ and $b=4$, the distributions thus found turn out to be close to one another. Therefore, for example, from the shape of the

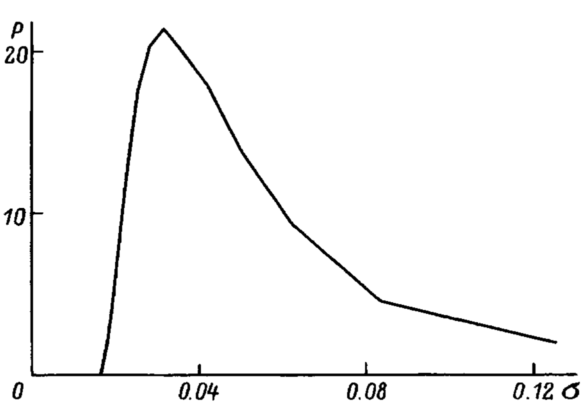

FIG. 5. Conductance distribution function $P(\sigma)$ obtained after renormalization-group transformation with $b=4$ (See Fig. 3). The vanishing of the distribution function at the conductance $\sigma=[2b(2b-1)]^{-1}=1/56$ is a consequence of the cluster used being finite.

conductance distribution $P(\sigma,b=4)$ derived for a cluster with scaling factor $b=4$ (see Fig. 5) one can form an idea of the universal distribution introduced by Eq. (5). As follows from this relation, the universal distribution function $f(x)=P(4^{-d_h}x,b=4)$. The above procedure does not naturally permit us to establish the shape of the distribution function for small and large conductances.

In order to find the critical exponent d_h introduced in Eq. (5), one will have to replace, in the way described above, the calculated distributions by delta functions constructed, for instance, around the mean resistance or mean conductance. Obviously enough, since the conductance distribution (Fig. 5) is more asymmetric than the resistance distribution (Fig. 4), the solution obtained for the critical exponent by the first approach should be substantially more accurate than that derived by the second. In the first case we can use Eq. (5) and the requirement of universality of the distribution function at criticality to obtain the following general relation for exponent d_h:

$$d_h^r=\ln\left(\frac{\langle R\rangle}{2}\right)/\ln b. \tag{13}$$

The relation to be used to calculate the exponent from mean conductance is somewhat different:

$$d_h^\sigma=\ln\left(\frac{\langle \sigma\rangle}{1/2}\right)/\ln b. \tag{14}$$

The upper indices r and σ on d_h indicate the way by which the calculation is performed. It should be stressed that we actually calculate the fractal dimension of our trajectory at percolation threshold.

The calculation of the critical exponent using Eqs. (13) and (14) yields convergent series $d_h^r=1.7549$, 1.7485, 1.7454 and $d_h^\sigma=1.4764$, 1.5289, 1.5623 for clusters with $b=2$, 3, and 4, respectively.

Extrapolations constructed by means of the same extrapolating functions as the ones used in the preceding Section yield the following values: $d_h^r(b\to\infty)=1.738$ and $d_h^\sigma(b\to\infty)=1.655$. As already mentioned, the first value should be substantially closer to the truth than the second. This gives us an idea of the error with which the answer has been found. Thus the approximate value of the exponent (1.738) is very close to the fractal dimension of the hull of the conventional percolating cluster, $d_h=1+1/\nu=7/4$. This result supports our assumptions.

Thus, despite its seeming simplicity, the Chalker–Coddington model is fairly complex because of the complexity in the interference accompanying propagation of a quantum particle through a system posessing a large number of scattering centers. The nature of quantum localization in it still remains not fully clear. For instance, one does not know accurately enough the critical localization-length exponent (see, e.g., a comprehensive discussion in Ref. 7). As for the classical percolation analog of this model considered here, it allows a very simple description of the critical behavior and reveals some common features with its prototype, namely, the critical relationships for resistance and conductance and their distribution functions at percolation threshold contain only exponent ν. One may thus conclude that this property is a consequence not of the quantum nature of the plateau transition in the integer quantum-Hall effect but rather of the common geometry of the two problems.

We note in conclusion that we have used here extremely simple and straightforward methods of critical-exponent calculation, and have not employed any sophisticated calculational procedures like the Monte Carlo approach, which, generally speaking, is applicable to such problems. Nevertheless, the critical exponents were obtained with a remarkably high accuracy which is difficult to reach in studies of the conventional percolation problem.

There are two reasons responsible for such a high accuracy. First, the trajectories along which a particle can move are in this situation very simple, namely, they cannot meet, branch, or intersect one another. This simplifies considerably the RG calculational procedure. Second, the clusters for the RG transformations were chosen very conveniently. Note that the cluster shown in Fig. 3a was used[7] in a study of the Chalker-Coddington model.

The author is grateful to A. V. Gol'tsev, S. A. Ktitorov, E. K. Kudinov, A. M. Monakhov, A. N. Samukhin, B. N. Shalaev, and Yu. A. Firsov for the numerous fruitful discussions.

Partial support of the Russian Fund for Fundamental Research (Grant 97-02-18283-a) is gratefully acknowledged.

[1] J. T. Chalker and P. D. Coddington, J. Phys. C **21**, 2665 (1988).
[2] G. V. Mil'nikov and I. M. Sokolov, JETP Lett. **48**, 536 (1988).
[3] D.-H. Lee, Z. Wang, and S. Kivelson, Phys. Rev. Lett. **70**, 4130 (1993).
[4] D. H. Cobden and E. Kogan, Phys. Rev. B **54**, R17316 (1996).
[5] S. Cho and M. P. A. Fisher, Phys. Rev. B **55**, 1637 (1997).
[6] Z. Wang, B. Jovanović, and D.-H. Lee, Phys. Rev. Lett. **77**, 4426 (1996).
[7] A. G. Galstyan and M. E. Raikh, Phys. Rev. B (in press).
[8] S. Kirkpatrick, Rev. Mod. Phys. **45**, 574 (1973).
[9] T. Nakayama, K. Yakubo, and R. L. Orbach, Rev. Mod. Phys. **66**, 381 (1994).
[10] C. Tsallis and A. C. N. de Magalhães, Phys. Rep. **268**, 305 (1996).
[11] A. N. Samukhin, V. N. Prigodin, and L. Jastrabik, Phys. Rev. Lett. **78**, 5276 (1997).
[12] D. S. Fisher and P. A. Lee, Phys. Rev. B **23**, 6851 (1981).
[13] M. B. Isichenko, Rev. Mod. Phys. **64**, 961 (1992).
[14] H. Saleur and B. Duplantier, Phys. Rev. Lett. **58**, 2325 (1987).
[15] S. Cho and M. P. A. Fisher, Phys. Rev. B **55**, 1025 (1997).
[16] D. S. McKenzie, Phys. Rep. **27C**, 35 (1976).
[17] A. Isihara, *Statistical Physics* [Academic Press, New York, 1971; Mir, Moscow, 1973].
[18] S. A. Trugman, Phys. Rev. B **27**, 7539 (1983).
[19] S. N. Dorogovtsev, Fiz. Tverd. Tela (Leningrad) **28**, 3020 (1986) [Sov. Phys. Solid State **28**, 1699 (1986)].
[20] R. F. Voss, J. Phys. A **17**, L373 (1984).
[21] R. M. Ziff, Phys. Rev. Lett. **56**, 545 (1986).
[22] P. Grassberger, J. Phys. A **19**, 2675 (1986).
[23] R. Zallen and H. Scher, Phys. Rev. B **4**, 4471 (1971).
[24] A. V. Gruzinov, M. B. Isichenko, and Ya. L. Kalda, Zh. Éksp. Teor. Fiz. **97**, 476 (1990) [Sov. Phys. JETP **70**, 263 (1990)].
[25] J. L. Cardy and S. Ostlund, Phys. Rev. B **25**, 6899 (1982).
[26] J. P. Straley, J. Phys. C **10**, 1903 (1977).
[27] P. J. Reynolds, W. Klein, and H. E. Stanley, J. Phys. C **10**, L167 (1977).

Translated by G. Skrebtsov

Anisotropy of the hopping conductivity in $TlGaSe_2$ single crystals

S. N. Mustafaeva, V. A. Aliev, and M. M. Asadov

Institute of Physics, Academy of Sciences of Azerbaidzhan, 370065 Baku, Azerbaidzhan

(Submitted June 10, 1997)
Fiz. Tverd. Tela (St. Petersburg) **40**, 48–51 (January 1998)

The temperature dependences of the conductivities parallel and perpendicular to the layers in layered $TlGaSe_2$ single crystals are investigated in the temperature range from 10 K to 293 K. It is shown that hopping conduction with a variable hopping length among localized states near the Fermi level takes place in $TlGaSe_2$ single crystals in the low-temperature range, both along and across the layers. Hopping conduction along the layers begins to prevail over conduction in an allowed band only at very low temperatures (10–30 K), whereas hopping conduction across the layers is observed at fairly high temperatures ($T \leqslant 210$ K) and spans a broader temperature range. The density of states near the Fermi level is determined, $N_F = 1.3 \times 10^{19} \text{eV} \cdot \text{cm}^3)^{-1}$, along with the energy scatter of these states $J = 0.011$ eV and the hopping lengths at various temperatures. The hopping length R along the layers of $TlGaSe_2$ single crystals increases from 130 Å to 170 Å as the temperature is lowered from 30 K to 10 K. The temperature dependence of the degree of anisotropy of the conductivity of $TlGaSe_2$ single crystals is investigated. © *1998 American Institute of Physics.* [S1063-7834(98)01001-6]

Single crystals of $TlGaSe_2$ are typical representatives of layered semiconductors and are of considerable interest to scientists for their intriguing physical properties. Among the latter are strong anisotropy of the electronic characteristics due to the uniqueness of their crystal structure. According to crystallographic data, the structure of $TlGaSe_2$ is described by the space group $C2/c(C_{2h}^6)$. The primitive cell contains eight formal units of $TlGaSe_2$. This compound has a monoclinic, pseudotetragonal structure with parameters $a = b = 10.75$, $c = 15.56$ Å, and $\beta = 100°$. The interatomic distances are equal to 3.45 Å (Tl–Se), 3.92 Å (Se–Se), and 3.42 Å (Tl–Tl).[1,2]

So far many physical properties of these single crystals and the charge transfer processes in them have been investigated in detail. However, our analysis of the published papers shows that the authors have been preoccupied with charge transfer processes in the allowed bands of these crystals, assuming that the main conductivity contribution is from carriers moving from one allowed band to another or from impurity states into one of the allowed bands.

It is important to note that the $TlGaSe_2$ single crystals studied so far have p-type conductivity, a high electrical resistivity, and a low density of free carriers. These crystals are characterized by an abundance of localized states in the band gap;[3,4] for example, Karpovich *et al.*[3] have established that the conductivity activation energy in the temperature range 290–400 K is equal to 0.8–1.1 eV for various $TlGaSe_2$ samples. The localized levels are attributable the presence in these crystals of structural defects such as vacancies, inclusion impurities, and dislocations. In locations where the ideal periodicity of the crystal structure breaks down, states occur with energies lying in an interval forbidden in the ideal crystal. In other words, in contrast with bands associated with the crystal as a whole, the additional levels correspond to states localized at crystal defects. The high density of localized states in the band gap [of the order of $10^{19} (\text{eV} \cdot \text{cm}^3)^{-1}$; Refs. 4 and 5] endow these crystals with an energy structure resembling that of amorphous semiconductors. The amorphous state is characterized by the presence of highly deformed and even broken chemical bonds, which tend to acquire acceptor properties. The role of these defects is especially pronounced for crystals having a layered structure. The existence of such defects is explained, in particular, by a high density of states near the Fermi level.

One possible charge transfer mechanism in amorphous and compensated semiconductors is thermally activated hopping. Charge carriers hop from one center localized in the band gap to another center, with the emission or absorption of a phonon. Hopping conduction is usually observed at low temperatures, where it prevails over the conduction of thermally excited carriers in an allowed band.

Here we present the results of a study of charge transfer processes in a layered $TlGaSe_2$ single crystal in a static electric field. The crystals were grown by Bridgman directional crystallization from a melt $TlGaSe_2$ at a rate of 5–10 K/min. The conductivity of the prepared samples was determined both along and across the layers in the single crystals. Indium was melted into the single crystals to form an ohmic contact with $TlGaSe_2$. Samples had thicknesses of the order of $100-130\ \mu$m. The contacts were applied to them on the side faces in such a way as to direct the electric current along the natural strata of the single crystal, i.e., perpendicular to the C axis. The distance between the contacts was $l = 0.10-0.15$ cm. We denote the conductivity of the samples along the layers by $\sigma_{\perp c}$. Other $TlGaSe_2$ samples were prepared in a sandwich configuration designed to direct the electric current across the natural layers of the single crystals, i.e., along the C axis of the single crystal. We denote the conductivity of the $TlGaSe_2$ samples in this configuration by $\sigma_{\parallel c}$.

The amplitude of the static electric field applied to the samples ($F = 10^2 - 10^3$ V/cm) corresponded to the ohmic region of the $I-V$ curve.

The conductivities of the samples were measured in the

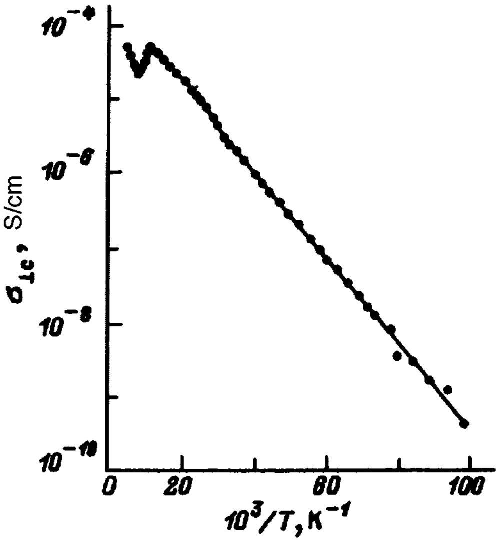

FIG. 1. Temperature dependence of the conductivity along the layers of $TlGaSe_2$ single crystals in the ohmic regime.

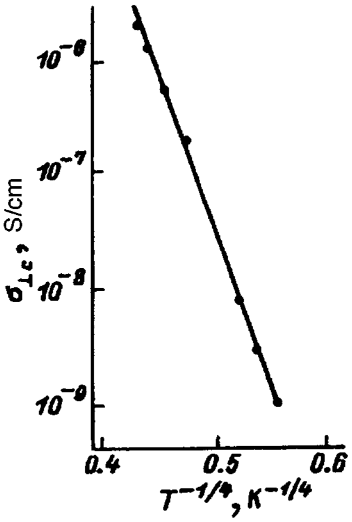

FIG. 2. Low-temperature conductivity of $TlGaSe_2$ single crystals along their layers in Mott coordinates.

temperature range from 10 K to 293 K. During the measurements the sampleswere in a Utreks helium cryostat with a temperature stabilization system (stabilization error 0.02 K).

Figure 1 shows the temperature dependence of the electrical conductivity $\sigma_{\perp c}$ in the temperature range 10–232 K. The conductivity $\sigma_{\perp c}$ decreases exponentially as the temperature is lowered from 232 K to 150 K. In this temperature range the main contribution to the conductivity is from carriers activated from a shallow impurity level $E_t = 0.04$ eV. With a further reduction in temperature the conductivity increases, attaining a maximum at $T = 104$ K. The anomalous behavior of $\sigma_{\perp c}$ in this temperature interval is probably attributable to phase transitions, whose presence is further confirmed by measurements of the heat capacity and the optical properties of the $TlGaSe_2$ single crystals in the temperature interval 100–120 K (Ref. 6). At $T < 104$ K the conductivity $\sigma_{\perp c}$ again decreases as the temperature is lowered, with a variable activation energy. In the low-temperature range (10–30 K) the experimental points provide a poor fit to a straight line in coordinates ($\log \sigma_{\perp c}, 10^3/T$) (Fig. 1). The approximate activation energy of the conductivity in this temperature range is ~ 0.01 eV. However, these points straighten out fairly well in coordinates ($\log \sigma_{\perp c}, T^{-1/4}$) (Fig. 2). This experimental result indicates that hopping conductivity with a variable hopping length among localized states in the vicinity of the Fermi level is observed in the $TlGaSe_2$ single crystals in the indicated temperature range. In this type of conductivity the plot of $\log \sigma = f(T^{-1/4})$ should be a straight line with slope T_0 (Ref. 7):

$$\sigma \sim \exp[-(T_0/T)^{1/4}], \tag{1}$$

$$T_0 = \frac{16}{N_F k a^3}, \tag{2}$$

where N_F is the density of states near the Fermi level, k is the Boltzmann constant, $a = 1/\alpha$ is the localization radius, and α is the decay constant of the localized-carrier wave function $\psi \sim e^{-\alpha r}$.

From Fig. 2 we find the value $T_0 = 5.4 \times 10^5$ K. Knowing T_0, we determine the density of localized states near the Fermi level from Eq., (2). We obtain $N_F = 1.3 \times 10^{19} (\mathrm{eV \cdot cm^3})^{-1}$. In calculating N_F, we assume that the localization radius $a \approx 30$ Å (Ref. 7) by analogy with a GaSe single crystal, which is the binary analog of the $TlGaSe_2$ single crystal.

The value of N_F agrees in order of magnitude with our results obtained earlier in a study of the hopping conductivity of $TlGaSe_2$ single crystals in alternating electric fields, $N_F = 5.4 \times 10^{19} (\mathrm{eV \cdot cm^3})^{-1}$ (Ref. 5), and also with the results of Darvish *et al.*,[4] who obtained $N_F = 1.3 \times 10^{19} (\mathrm{eV \cdot cm^3})^{-1}$. For their calculations, however, they set $a = 8$ Å. Localization radii of this order are usually assumed for amorphous materials;[8] for $TlGaSe_2$ (a ternary analog of GaSe), however, it is recommended to use $a \approx 30$ Å, which has been obtained experimentally for GaSe single crystals.[7]

We use the equation

$$R(T) = \frac{3}{8} a T_0^{1/4} T^{-1/4} \tag{3}$$

to determine the carrier hopping length R at various temperatures. The value of R increases from 130 Å to 170 Å as the temperature is lowered from 30 K to 10 K. It is evident that the average hopping length is five times the average distance between carrier localization centers. From the condition[8]

$$\frac{4}{3} \pi R^3 N_F \frac{J}{2} = 1 \tag{4}$$

we find the scatter of trapping states near the Fermi level: $J = 0.011$ eV. The true density of deep-level traps, determined from the equation $N_t = N_F J$, is equal to $1.4 \times 10^{17} \mathrm{cm}^{-3}$.

The foregoing discussion applies to the case of the in-layer conductivity $\sigma_{\perp c}$ of the single crystals. The temperature dependence of the conductivity $\sigma_{\parallel c}$ along the C axis of the single crystal exhibits a somewhat different behavior. The conductivity of samples prepared in the sandwich con-

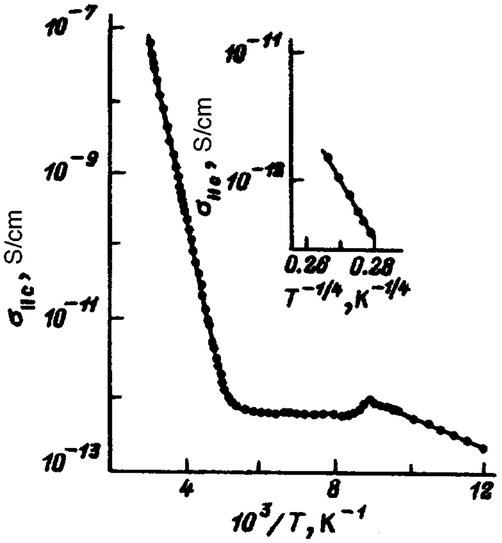

FIG. 3. Temperature dependence of the conductivity $\sigma_{\parallel c}$ in $TlGaSe_2$ single crystals in coordinates $\log\sigma_\parallel$ versus $10^3/T$. Inset: the same in coordinates $\log\sigma_\parallel$ versus $T^{-1/4}$.

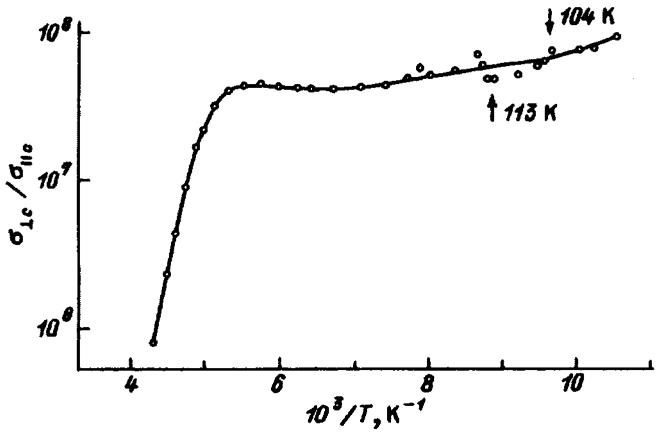

FIG. 4. Temperature dependence of the conductivity anisotropy of $TlGaSe_2$ single crystals.

figuration was measured in the temperature interval 96–293 K (Fig. 3). Unfortunately, $\sigma_{|c}$ could not be measured at lower temperatures, because the currents in the samples were too low. The high-temperature branch of the $\sigma_{\parallel c}(T)$ curve has an exponential character. In the temperature interval 210–293 K this curve has a slope of 0.54 eV. Below 210 K the conductivity activation energy decreases continuously, and at $T \leqslant 165$ K the conductivity $\sigma_{\parallel c}$ becomes almost independent of the temperature. At $T = 113$ K, however, the $\sigma_{\parallel c}(T)$ curve is observed to have a small conductivity ''peak.'' As mentioned above, a phase transition takes place in $TlGaSe_2$ single crystals in the temperature interval 100–120 K. A continuous decrease of the conductivity activation energy to zero in $TlGaSe_2$ singles crystals at low temperatures has been reported previously,[3] but the cause of this behavior of σ has not been established in Ref. 3.

We attribute the monotonic decay of the conductivity $\sigma_{\parallel c}$ with decreasing temperature to the hopping of carriers among localized states near the Fermi level. The same dependence, replotted in coordinates $(\log\sigma_{\parallel c}, T^{-1/4})$, is shown in the inset to Fig. 3. The slope of this graph is $T_0 = 3.4 \times 10^6$ K. For the density of localized states near the Fermi level we obtain $N_F = 2 \times 10^{18} (\mathrm{eV \cdot cm^3})^{-1}$. As mentioned above, from the results of conductivity measurements along the $TlGaSe_2$ layers we obtain $N_F = 1.3 \times 10^{19} (\mathrm{eV \cdot cm^3})^{-1}$, almost an order of magnitude higher than the value of N_F obtained from the $\sigma_{\parallel c}$ measurements. The disparity is most likely attributable to the anisotropic spatial distribution of defects in the investigated crystals. The carrier hopping lengths across the layers of the single crystals, determined from Eq. (3), are equal to 129 Å at 200 K and to 136 Å at 165 K. In the temperature interval discussed above a phonon is absorbed in the hopping of a carrier from one localized center to another. The existence of an activation energy is associated with the scatter of the localized levels. As the temperature is lowered, the probability of carrier hops to spatially more distant but energetically closer centers increases, and this is the reason for the decay of the hopping activation energy and the increase in the hopping length as the temperature decreases. Finally, there comes a time at which the conductivity ceases to depend on the temperature, in which case carrier hops take place with the emission of phonons. We assume that the temperature-dependent conductivity observed in $TlGaSe_2$ is nothing other than zero-activation hopping conductivity.

Our experimental results have shown that a hopping mechanism of charge transfer among states localized near the Fermi level is operative at low temperatures, both along and across the layers of $TlGaSe_2$ single crystals. It must be noted, however, that hopping conduction along the layers of the single crystals begins to prevail over conduction in an allowed band only at very low temperatures (10–30 K), whereas hopping conduction across the layers is observed at fairly high temperatures ($T \leqslant 210$ K) and spans a broader temperature range.

Figure 4 shows the temperature dependence of the degree of anisotropy of the conductivity $\sigma_{\perp c}/\sigma_{\parallel c}$ of $TlGaSe_2$ single crystals in the range 96–232 K. It is evident from Fig. 4 that as the temperature is lowered from 232 K to 180 K, $\sigma_{\perp c}/\sigma_{\parallel c}$ rises abruptly at first (more than 50-fold) and then forms a plateau in the interval 180–135 K, after which $\sigma_{\perp c}/\sigma_{\parallel c}$ slowly continues to increase until at 96 K it attains the value 9×10^7, which is two orders of magnitude greater than the value of $\sigma_{\perp c}/\sigma_{\parallel c}$ at $T = 232$ K. It is important to note the moderate scatter of the experimental points as phase-transition temperatures (104 K and 113 K) are approached. These segments are indicated by arrows in Fig. 4

[1] T. J. Isaaks and J. D. Feichther, J. Solid State Chem. **14**, 260 (1975).
[2] D. Müller and H. Hahn, Z. Anorg. Allg. Chem. **438**, 258 (1978).
[3] I. A. Karpovich, A. A. Chervova, and L. I. Demidova, Izv. Akad. Nauk SSSR, Neorg. Mater. **8**, 70 (1972).
[4] A. M. Darvish, A. É. Bakhyshov, and V. I. Tagirov, Fiz. Tekh. Poluprovodn. **11**, 780 (1977) [Sov. Phys. Semicond. **11**, 458 (1977)].
[5] S. N. Mustafaeva, S. D. Mamedbeĭli, and I. A. Mamedbeĭli, Neorg. Mater. **30**, 626 (1994).

[6] S. G. Abdullaev, A. M. Abdullaev, K. K. Mamedov, and N. T. Mamedov, Fiz. Tverd. Tela (Leningrad) **26**, 618 (1984) [Sov. Phys. Solid State **26**, 375 (1984)].

[7] S. N. Mustafaeva, Neorg. Mater. **30**, 619 (1994).

[8] N. F. Mott and E. A. Davis, *Electronic Processes in Non-Crystalline Materials* [Clarendon Press, Oxford, 1971; Mir, Moscow, 1974].

Translated by James S. Wood

Physical characteristics of electron-induced dichroism in vitreous arsenic trisulfide

O. I. Shpotyuk

Lvov Scientific-Research Institute of Materials, 290031 Lvov, Ukraine;
Institute of Physics at the Pedagogical University, 42200 Czestochowa, Poland

V. O. Balitskaya

Lvov Scientific-Research Institute of Materials, 290031 Lvov, Ukraine

(Submitted February 5, 1997; resubmitted June 11, 1997)
Fiz. Tverd. Tela (St. Petersburg) **40**, 52–56 (January 1998)

The dependence of the electron-induced dichroism effect in vitreous As_2S_3 on the photon energy of the probe radiation and on the temperature of subsequent thermal anneals is investigated. The effect is observed to be completely suppressed after prolonged storage of the samples (10–15 days) following electron irradiation. It is shown by induced-reflection Fourier-transform IR spectroscopy that the observed effect is associated with processes involving the formation of oriented defects in the form of undercoordinated atomic pairs in the glass structural matrix. © *1998 American Institute of Physics.* [S1063-7834(98)01101-0]

Recent detailed studies of the influence of absorbed light (photoinduced phenomena) (Ref. 1) and high-energy penetrating radiation (radiation-induced phenomena) (Refs. 2 and 3) on amorphous chalcogenide semiconductors have led to the disclosure of a profound similarity between these phenomena. It has been established that the mechanism of photostructural and radiation-structural transformations is governed by processes involving the formation of coordination defects, i.e., defects induced by switchings of chemical bonds; the accompanying relaxation processes are capable of spanning structural zones on an average scale of the order of several interatomic distances.[1–4] Subsequent investigations have shown that this conclusion applies not only to scalar phenomena (isotropic changes in the physical properties of the amorphous chalcogenide semiconductor), but also to vector phenomena, in particular, to photoinduced and radiation-induced dichroism, which appears under the influence of linearly polarized light[5,6] and a directed stream of accelerated electrons,[7] respectively.

At first glance, the radiation analog of vector photoinduced phenomena in amorphous chalcogenide semiconductors (linear or circular dichroism, birefringence[5,6]) should be rendered impossible by the nonpolarization of high-energy radiation, specifically γ rays, which produce the most significant changes in the physical properties.[2] Nonetheless, it has been shown earlier[7] that the difference between the absorption coefficients of probe light having its polarization plane oriented parallel and perpendicular to the stream of accelerated electrons can be determined for cubic samples of vitreous $v-As_2S_3$ previously irradiated by accelerated electrons ($E=2.8$ MeV).

Continuing the work begun in Ref. 7, we have investigated the spectral profiles of electron-induced dichroism in vitreous $v-As_2S_3$, the temperature dependence of this effect, its time variations, and the microstructural mechanism.

1. EXPERIMENTAL PROCEDURE

The investigated $v-As_2S_3$ samples were prepared from components of extreme purity (at least 99.999%) in quartz ampoules previously cleaned and dehydrated and then evacuated.[7] The samples were prepared at a maximum temperature of 1050 K, and the ampoules were furnace-cooled. The samples were shaped into cubes 6–8 mm on a side, whose faces were polished to a high degree of cleanliness.

The samples were irradiated by a collimated beam of accelerated electrons having an energy of 2.8 MeV at fluences ranging from $\Phi=10^{15}$ cm^{-2} in the direction perpendicular to the BB_1C_1C plane (Fig. 1). We arbitrarily designate this plane of the cube by the symbol $\parallel$ in accordance with the parallelism of its normal vector to the direction of the electron beam. The probe light beam had a diameter of 2–3 mm and passed through the sample at a distance of 1.5–2 mm from the BB_1C_1C plane. Analogously, we identify the $ABCD$ plane of the cube by the symbol $\perp$. The accelerated electrons essentially achieved total penetration of the light-probed zone (penetration depth $\sim 5-6$ mm; Ref. 8) under the stated conditions.

We thus determined two orthogonal directions for probe light with polarization planes parallel $(a-a)$ and perpendicular $(b-b)$ to the direction of the accelerated electron beam (Fig. 1).

The electron-induced dichroism was measured the day after electron irradiation on a Specord 40 spectrophotometer in the range 200–900 mm. Effects associated with inhomogeneity of the scalar electron-induced darkening[9] were excluded by balancing the 100% level of the instrument with the probe beam directed alternately onto opposite sides of the sample.

The degree of electron-induced dichroism was estimated by the parameter $\varkappa$ in accordance with the well-known expression[5,6]

$$\varkappa=\Delta d=(\alpha_{\parallel}-\alpha_{\perp})d=\frac{2(\tau_{\perp}-\tau_{\parallel})}{(\tau_{\perp}+\tau_{\parallel})},$$

where $\alpha(\tau_{\parallel})$ and $\alpha(\tau_{\perp})$ are the absorption (transmission) coefficients of the probe light with parallel $(a-a)$ and perpendicular $(b-b)$ orientations of the polarization plane, and d is the thickness of the sample.

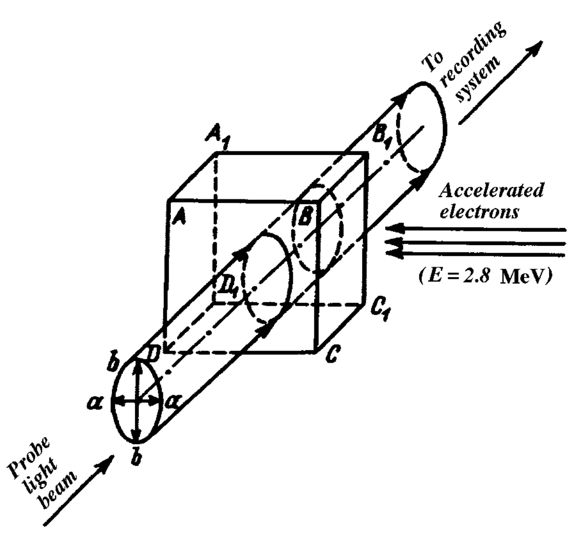

FIG. 1. Diagram illustrating the conditions for the experimental observation of electron-induced dichroism in vitreous $\upsilon-\mathrm{As_2S_3}$.

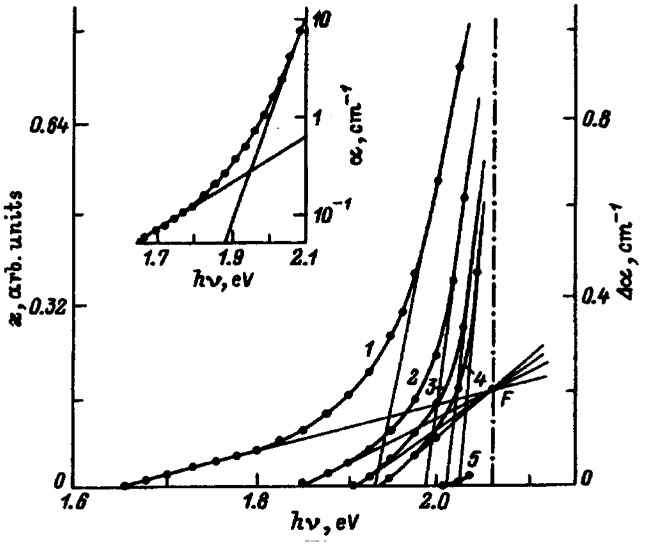

FIG. 2. Spectral curves of electron-induced dichroism in $\upsilon-\mathrm{As_2S_3}$. *1*) After irradiation by accelerated electrons at $\Phi=5\times10^{16}\mathrm{cm}^{-2}$; 2–5) after subsequent thermal anneals at various temperatures: *2*) 343 K; *3*) 373 K; *4*) 398 K; *5*) 423 K. Inset: spectral curve of the optical absorption coefficient of $\upsilon-\mathrm{As_2S_3}$.

Anisotropy of the reflection coefficient was disregarded, because it is at least an order of magnitude lower than the anisotropy of the absorption coefficient (a similar assumption is made in Ref. 6).

The microstructural mechanism of the electron-induced dichroism was investigated by induced-reflection Fourier-transform infrared spectroscopy (using a Bruker IFS 113V spectrophotometer) in the range of the vibrational bands of the main structural complexes of $\upsilon-\mathrm{As_2S_3}$ $(400-100\,\mathrm{cm}^{-1})$.[3,4] Multiple reflection spectra of $\upsilon-\mathrm{As_2S_3}$ were stored up (at least 256 in number) and were subtracted on a computer before and after electron irradiation, i.e., the investigated useful signal represented the spectrum of electron-induced reflection ΔR. Positive values obtained for this quantity, $\Delta R>0$ (additional reflection), corresponded to structural complexes formed as a result of irradiation, and negative values, $\Delta R<0$, conversely, corresponded to vanishing complexes. All the measurements were performed from planes of the cube with their normals oriented perpendicular ($ABCD$) and parallel (BB_1C_1C) to the direction of the accelerated electron beam (Fig. 1).

This technique is well suited for investigating structural changes in amorphous chalcogenide semiconductors at the level of 1% of the total concentration of transformed chemical bonds. It was first used in 1988 to identify structural transformations induced by absorbed light in thin arsenic trisulfide films.[10]

We know[11–13] that $\upsilon-\mathrm{As_2S_3}$ is characterized by distinct separation of the vibrational bands of the main structural fragments. Pyramidal $\mathrm{AsS_3}$ units and bridged As–S–As units formed by heteropolar As–S chemical bonds are characterized by a group of bands in the interval $335-285\,\mathrm{cm}^{-1}$ (Ref. 12). Molecular products with ''irregular'' homopolar As–As and S–S chemical bonds correspond to the bands 379, 340, 231, 210, 168, $140\,\mathrm{cm}^{-1}$ (Refs. 11 and 12). We have also heeded the fact that, according to factorial group analysis,[13] crystalline $\mathrm{As_2S_3}$ is characterized by four IR vibrational modes observed in the interval $335-285\,\mathrm{cm}^{-1}$ (323.1, 307.3, 301.3, and $288.9\,\mathrm{cm}^{-1}$).

To study the electron-induced dichroism mechanism, we investigated the IR Fourier spectra of the additional reflection of $\upsilon-\mathrm{As_2S_3}$ irradiated by accelerated electrons after a 2-h anneal at temperatures of 300–423 K, i.e., below and above the threshold of scalar radiation-induced darkening (390–400 K).[14]

2. EXPERIMENTAL RESULTS AND DISCUSSION

Figure 2 shows spectral curves of the parameter $\varkappa$ for $\upsilon-\mathrm{As_2S_3}$ after electron irradiation at a fluence $\Phi=5\times10^{16}\,\mathrm{cm}^{-2}$ (curve *1*) and subsequent thermal anneals at various temperatures T (curves *2–5*). It should be noted that the electron-induced dichroism effect is observed in the spectral region of the fundamental optical absorption edge of the investigated samples (see the inset to Fig. 2).

In studying the dose dependence of the electron-induced dichroism, we have found that dichroism appears after electron irradiation at fluences of at least $\Phi=5\times10^{15}\,\mathrm{cm}^{-2}$, attains a relative maximum in the interval $\Phi=5\times10^{16}-10^{17}\,\mathrm{cm}^{-2}$, and then increases slightly (by 10–15%) up to $\Phi=5\times10^{17}\mathrm{cm}^{-2}$ without appreciable saturation.

We now consider the characteristics of the electron-induced dichroism of $\upsilon-\mathrm{As_2S_3}$ after electron irradiation at a fluence $\Phi=5\times10^{16}\mathrm{cm}^{-2}$. The electron-induced dichroism is observed to have a fairly sharp edge with a slope of $6-7\,\mathrm{eV}^{-1}$ in the energy range $h\nu>1.9$ eV (curve *1* in Fig. 2). In this range the parameter $\varkappa$ attains values of 0.7–0.9, which are much higher than in the case of photoinduced dichroism.[6] Subsequent thermal annealing causes this curve to shift toward shorter wavelengths, as in the thermally induced recovery of the scalar optical properties of γ-irradiated amorphous chalcogenide semiconductors.[14] Unlike this pro-

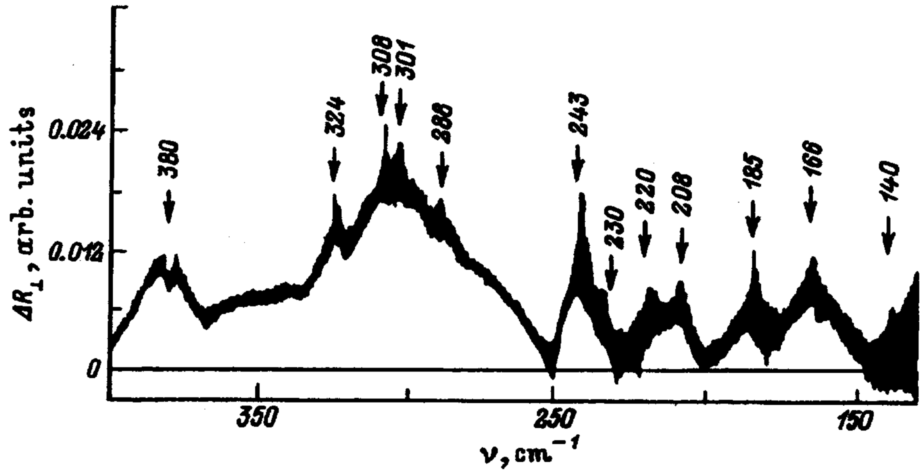

FIG. 3. Spectrum of additional reflection $\Delta R_{\perp}$ induced by thermal annealing at a temperature of 333 K for electron-irradiated $v-\mathrm{As}_2\mathrm{S}_3$.

cess, however, the thermal annihilation of electron-induced dichroism has a nonthreshold character and commences already at temperatures of 300–330 K (curves *2–4* in Fig. 2). This effect essentially vanishes altogether after thermal annealing at 420–430 K (curve 5 in Fig. 2).

At longer wavelengths ($\varkappa<0.10-0.15$) we observe a fairly elongated electron-induced dichroism ''tail,'' which becomes shorter after annealing, and now the linear continuations of the $\varkappa(h\nu)$ curve intersect at a single point F (Fig. 2). This feature distinguishes electron-induced dichroism from the analogous scalar phenomenon of radiation-induced darkening,[2,14] which produces parallel shifts of the lower part of the absorption spectrum.

We have established that electron-induced dichroism in $v-\mathrm{As}_2\mathrm{S}_3$ vanishes completely at room temperature over a period of 10–15 days, whereas the familiar photoinduced analog dies out only partially at this temperature.[6] Consequently, Lyubin and Tikhomirov's[6] scenario of the influence of external perturbing factors on native defect centers existing in amorphous chalcogenide semiconductors before irradiation, proposed to explain the mechanism of photoinduced dichroism, is scarcely applicable to our case. Moreover, we assume that the model of photoinduced topological reorientation of dipoles existing before irradiation (in the form of so-called defect pairs of alternating valence),[15] including the switching of three ''rigid'' covalent bonds,[5] is not very probable for amorphous chalcogenide semiconductors.

Taking into account the negligible concentration of native defects in thermally annealed glass in comparison with their concentration in thin films prepared under the more nonequilibrium conditions of deposition by thermal evacuation,[15] we can assume that the mechanism of electron-induced dichroism in $v-\mathrm{As}_2\mathrm{S}_3$ is not associated with reorientation, but with the electron-induced formation of new (oriented relative to the electron stream) defects.

Comparing the total spectra of $\mathbf{R}_{\perp}$ and $\mathbf{R}_{\parallel}$ of $v-\mathrm{As}_2\mathrm{S}_3$ (i.e., the spectra of reflection from the faces $ABCD$ and BB_1C_1C, respectively) immediately after electron irradiation ($\Phi=5\times10^{16}\mathrm{cm}^{-2}$), we note that the background value of $\mathbf{R}_{\perp}$ is higher than $\mathbf{R}_{\parallel}$. In addition, the vibrational band at $420\,\mathrm{cm}^{-1}$, which corresponds to As–O complexes,[16] is stronger in the $\mathbf{R}_{\perp}$ spectrum.

This condition indicates the presence of two types of electron-stimulated transformations on the surface of the investigated samples: first of all, surface damage, i.e., rheological changes (Tanaka[17] has recently investigated a similar process); second, surface oxidation due to the chemical interaction of destroyed complexes in the glass matrix with absorbed oxygen atoms, as in the case of γ-ray-induced oxidation of the surface of amorphous chalcogenide semiconductors in long-term exposure to radiation.[18] The first process is observed to take place on the ''parallel'' BB_1C_1C plane of the $v-\mathrm{As}_2\mathrm{S}_3$ cube, and the second process on the ''perpendicular'' $ABCD$ plane.

Rheological changes reduce the background radiation level $\mathbf{R}_{\parallel}$, significantly impeding the correct identification of intrinsic electron-induced structural transformations on this plane (at any rate up to temperatures of 390–400 K, at which processes of recovery of the reflectivity of the damaged surface begin to set in as a result of thermal healing of the previously formed macrodefects). The onset of vacancion clusters, cracks, microscopic voids, crystalline inclusions, and other macrodefects in the amorphous chalcogenide semiconductor after exposure to high-energy radiations has also been observed by a number of other authors.[19–21]

The second process (electron-induced oxidation) does not exert any appreciable influence on the vibrational spectrum of $v-\mathrm{As}_2\mathrm{S}_3$ in the range of the bands of the principal structural units of the matrix ($400-100\,\mathrm{cm}^{-1}$), because the stretched and bent modes of As–O complexes are situated in a shorter-wavelength region ($\nu>400\,\mathrm{cm}^{-1}$).[16]

Figure 3 shows the spectrum of additional reflection $\Delta R_{\perp}$, induced by thermal annealing at $T=333\,\mathrm{K}$, for electron-irradiated ($\Phi=5\times10^{16}\mathrm{cm}^{-2}$) $v-\mathrm{As}_2\mathrm{S}_3$.

More than ten additional-reflection ($\Delta R_{\perp}$) bands can be discerned, corresponding to various structural complexes of $v-\mathrm{As}_2\mathrm{S}_3$ based on heteropolar (As–S) and homopolar (As–As and S–S) covalent chemical bonds. The results indicate a significant rise in their concentration in the investigated samples after thermal annealing. The most pronounced increase is characteristic of complexes with heteropolar As–S chemical bonds, which in Fig. 3 correspond to bands of the $\Delta\mathbf{R}_{\perp}$ spectrum in the range $335-285\,\mathrm{cm}^{-1}$ (Refs. 12 and 13). This effect is not observed in nonirradiated samples annealed at temperatures below $T=440-450$ K (Ref. 22).

When the annealing temperature is raised from 390 K to 400 K, the intensity of the $v-\mathrm{As}_2\mathrm{S}_3$ vibrational modes shown in Fig. 3 is further amplified. This is particularly true of the modes of structural complexes having homopolar chemical bonds (379, 340, 243, 231, 188, 168, and 140 cm^{-1}). In other words, electron-induced defects created by the destruction of heteropolar As–S bonds are more unstable and sensitive to the thermal annealing conditions (being restored at relatively low temperatures).

At temperatures above 390–400 K the received additional-reflection signal is more complex. Two components are discernible in the $\mathbf{\Delta R}_{\perp}$ spectrum: 1) a component similar to the one shown in Fig. 3 but with stronger bands in the region of vibrational modes corresponding to homopolar chemical bonds; 2) a component representing the switching of chemical bonds due to the thermal annihilation of defects responsible for scalar radiation-structural transformations.[3] The second component appears only after annealing at temperatures above the threshold of thermal recovery of the irradiated $v-\mathrm{As}_2\mathrm{S}_3$ (390–400 K).[14] Also under these conditions the rheological electron-induced flaws (macrodefects) on the BB_1C_1C plane partially vanish, the background reflection $R_{\parallel}$ from this plane increases significantly, and restoration of the characteristic brightness of the investigated samples in reflected light is visually observable after thermal annealing. All the same, a precise numerical evaluation of the two additional-reflection components in the $\mathbf{\Delta R}_{\parallel}$ spectrum is rendered difficult by their overlap.

Consequently, the structural framework of electron-irradiated $v-\mathrm{As}_2\mathrm{S}_3$ samples contains a definite concentration of defects in the form of broken chemical bonds (which are restored during thermal annealing),[15,23] and they are responsible for the vector electron-induced dichroism effect. Such defects comprise atoms having an incompletely saturated valence (undercoordinated atoms).[22,23] The dissociation of chemical bonds in amorphous chalcogenide semiconductors is essentially homolytic, i.e., the electrons initially forming a covalent bond become delocalized at a single atom after destruction of the bond;[15] consequently, unpaired spins do not appear during the formation of such defects, and the resulting defects are essentially pairs of oppositely charged, undercoordinated atoms. The total electroneutrality of the samples is therefore unchanged by irradiation, and a stable electron-induced EPR signal is not received (at room temperature); this result is consistent with well-established experimental data.[2]

Using the model of a random structural framework of $v-\mathrm{As}_2\mathrm{S}_3$ (Ref. 15) and taking the experimental results into account (Fig. 3), we can conclude that the defects in question are heteroatomic pairs $(\mathrm{As}_2^+,\mathrm{S}_1^-)$ as well as homoatomic pairs $(\mathrm{As}_2^-,\mathrm{As}_2^+)$ and $(\mathrm{S}_1^-,\mathrm{S}_1^+)$. The superscripts indicate the charge state of the atom, and the subscripts give the number of covalent-bound nearest neighbors. The difference between the electronegativities of the arsenic and sulfur atoms[24] is taken into account in forming the heteropolar pair $(\mathrm{As}_2^+,\mathrm{S}_1^-)$. Such defects are metastable, existing in the investigated samples immediately after irradiation at room temperature and vanishing at higher temperatures, in perfect agreement with the plotted temperature curves of electron-induced dichroism. An investigation of the temporal stability of the electron-induced dichroism shows that the annihilation process also takes place at room temperatures with a characteristic longevity of 10–15 days.

The initiating factor of defect formation is the elastic scattering of electrons by sulfur nuclei, which displaces atoms from their equilibrium positions and subsequently results in the destruction of covalent chemical bonds.[8,23,25] The effective formation of displacive radiation defects in amorphous chalcogenide semiconductors is attributable to the low threshold energies associated with the large contributions of van der Waals and other intermolecular interactions.[1,15] This explanation is supported by the agreement of the calculated concentrations of defects formed in $v-\mathrm{As}_2\mathrm{S}_3$ by the displacement of atoms by a subthreshold mechanism[23] and of undercoordinated atomic pairs responsible for the induced IR reflection signal in Fig. 3.

The undercoordinated defect pairs are oriented predominantly along the propagation direction of the electron beam (owing to the orientation of the atomic displacements) and, in the final analysis, can be regarded as oriented electric dipoles generating the observed electron-induced dichroism effect.

The broken heteropolar As–S (1) and the homopolar As–As and S–S (3) chemical bonds are restored after the annihilation of $(\mathrm{As}_2^+,\mathrm{S}_1^-)$, $(\mathrm{As}_2^-,\mathrm{As}_2^+)$, and $(\mathrm{S}_1^-,\mathrm{S}_1^+)$ defects, respectively. It follows from the inclusion of the dissociation energy of various chemical bonds in $v-\mathrm{As}_2\mathrm{S}_3$ (Ref. 15) that the first annihilation process is dominant over the other two, in good agreement with the experimental results of induced-reflection Fourier-transform IR spectroscopy.

The electron-induced dichroism effect vanishes in $v-\mathrm{As}_2\mathrm{S}_3$ at annealing temperatures around $T=420-430$ K. According to our estimates (based on a comparison of the intensities of the vibrational bands of stretched modes of complexes with heteropolar As–S bonds before and after electron irradiation), the concentration of completely annihilated undercoordinated atoms is $\sim 9-12\%$.

It has been shown earlier that similar broken-coordination defects formed at high γ-irradiation doses (in which case they lack a predominant orientation) are a source of additional photodarkening of these samples, thereby forming a structural channel of radiation sensitization.[23]

This work has been carried out as part of Project No. 2.4/13 of the National Fund for Fundamental Research of Ukraine.

[1] S. R. Elliott, J. Non-Cryst. Solids **81**, 71 (1986).
[2] O. I. Shpotyuk and A. O. Matkovskii, J. Non-Cryst. Solids **176**, 45 (1994).
[3] O. I. Shpotyuk, Phys. Status Solidi A **145**, 69 (1994).
[4] O. I. Shpotyuk, Phys. Status Solidi B **183**, 365 (1994).
[5] S. R. Elliott and V. K. Tikhomirov, J. Non-Cryst. Solids **198–200**, 669 (1995).
[6] V. M. Lyubin and V. K. Tikhomirov, Fiz. Tverd. Tela (Leningrad) **33**, 2063 (1991) [Sov. Phys. Solid State **33**, 1161 (1991)].
[7] O. I. Shpotyuk and V. A. Balitskaya, Zh. Prikl. Spektrosk. **63**, 566 (1994).
[8] A. K. Pikaev, *Modern Radiochemistry: Fundamental Principles, Experimental Technique and Methods* [in Russian], Nauka, Moscow, 1985.
[9] R. M. Gural'nik, S. S. Lantratova, V. M. Lyubin, and S. S. Sarsembinov,

Fiz. Tverd. Tela (Leningrad) **24**, 1334 (1982) [Sov. Phys. Solid State **24**, 757 (1982)].

[10] V. N. Kornelyuk, I. V. Savitskiĭ, L. I. Khirunenko, O. I. Shpotyuk, and I. I. Yaskovets, Zh. Prikl. Spektrosk. **50**, 444 (1989).

[11] D. W. Scott, J. P. McCullough, and F. H. Kruse, J. Mol. Spectrosc. **13**, 313 (1964).

[12] U. Strom and T. P. Martin, Solid State Commun. **29**, 527 (1979).

[13] T. Mori, K. Matsuishi, and T. Arai, J. Non-Cryst. Solids **65**, 269 (1984).

[14] O. I. Shpotyuk, Zh. Prikl. Spektrosk. **46**, 122 (1987).

[15] A. Feltz, *Amorphous Inorganic Materials and Glasses* [Weinheim, New York, 1993; Mir, Moscow, 1986].

[16] I. I. Rosola, P. P. Puga, V. V. Khiminets, and D. V. Chepur, Ukr. Fiz. Zh. **26**, 1875 (1981).

[17] K. Tanaka, in *Abstracts of NATO Advanced Research Workshop on ''Physics and Applications of Non-Crystalline Semiconductors in Optoelectronics''* (Chisinau, Moldova, 1996), p. 29.

[18] O. I. Shpotyuk, Ukr. Fiz. Zh. **23**, 509 (1987).

[19] Sh. Sh. Sarsembinov, R. M. Gural'nik, B. S. Zhakupbekov, Yu. I. Krotov, and S. Ya. Maksimova, Fiz. Khim. Stekla **13**, 143 (1987).

[20] A. M. Andriesh, E. V. Kulakov, and I. P. Kulyak, Kvantovaya Élektron. **12**, 1981 (1985) [Sov. J. Quantum Electron. **15**, 1310 (1985)].

[21] A. Ya. Vinokurov, A. N. Garkavenko, and L. I. Litinskaya, Avtometriya **5**, 28 (1988).

[22] V. N. Kornelyuk, Visnik Lvov. Univ. Ser. Fiz. B **22**, 92 (1989).

[23] A. O. Matkovskiĭ, S. B. Ubizskiĭ, and O. I. Shpotyuk, Fiz. Tverd. Tela (Leningrad) **32**, 1790 (1990) [Sov. Phys. Solid State **32**, 1042 (1990)].

[24] S. S. Batsanov, *Electronegativity and Effective Charges of Atoms* [in Russian], Znanie, Moscow, 1971.

[25] M. I. Klinger, Izv. Akad. Nauk Latv. SSR Ser. Fiz. Tekh. Nauk **4**, 58 (1987).

Translated by James S. Wood

Electrical and magnetic properties of $CeNi_4In$ with Ce in saturated valence state

M. D. Koterlin, B. S. Morokhivskiĭ, R. R. Kutyanskiĭ, I. D. Shcherba, and Ya. M. Kalychak

L'vov State University, 290005 L'vov, Ukraine

(Submitted May 22, 1997)
Fiz. Tverd. Tela (St. Petersburg) **40**, 7–9 (January 1998)

Measurements of the electrical resistance, thermopower, and magnetic susceptibility of $CeNi_4In$ have been carried out within the 4.2–400 K range, with Ce in saturated valence state. It is shown that this state of Ce in metallic compounds is characterized by formation of a fine structure in the density of states near the Fermi level, which is qualitatively different from the case of usual intermediate-valence state. © *1998 American Institute of Physics.* [S1063-7834(98)00201-9]

The nature of the saturated valence state of cerium in metallic compounds plays a major role in the valence instability of rare-earth elements.[1] In contrast to usual intermediate-valence states, cerium in saturated-valence state exhibits comparatively weak correlation effects and a high stability of the f-shell occupation n_f ($n_f \simeq 0.65-0.70$) in relation to a number of external factors (temperature, pressure, substitution-induced changes in lattice parameters).[1–4]

Starting with the approximation of extreme localization of Ce f states in metallic systems, saturated valence may be considered as a nonmagnetic Kondo state with a high characteristic temperature $T_{sf} \sim 10^3$ K.[5] At the same time there are experimental and theoretical data[6,7] indicating an essentially band character of f states in saturated-valence conditions. The available information is still insufficient even for a qualitative description of the Ce saturated-valence state at the microscopic level. This stresses the need of further investigation of this phenomenon in various crystal matrices.

This communication reports a study of the electrical and magnetic properties of a new compound, $CeNi_4In$ [$MgSnCu_4$ cubic structure, space group $F\overline{4}3m$ (Ref. 8)], with cerium in saturated-valence state. To separate quantitatively the contribution of this Ce state to the electrical properties of $CeNi_4In$ at high temperatures, we used the isostructural compound with Nd.

The compounds were prepared by direct arc melting in purified argon of nickel (99.91% pure), indium (99.99%), and the rare earth metal (pure to not worse than 99.85%). Homogenization anneal was performed at 900 K for 150 h. The alloy lattice constants determined with a DRON-2.0 diffractometer (Fe $K\alpha$ radiation) were in good agreement with published data.[8]

The sample preparation and measurement techniques were described elsewhere.[9] The valence state of Ce was determined from x-ray L_{III} absorption spectra 300 K (see Ref. 10). The thermopower was measured with respect to Cu.

Figure 1 displays an experimental Ce L_{III} absorption spectrum and its deconvolution into the components (a Gaussian describing the $2p$-$5d$ transition and an arctan-like line approximating the band absorption edge) corresponding to the conventional ionic configurations $Ce^{3+}(4f^1)$ and $Ce^{4+}(4f^0)$. The occupation number of the f shell derived from the intensity ratio of the principal lines was found to be $n_f \sim 0.70 \pm 0.03$, which corresponds to the state of saturated valence in metallic compounds.

Figures 2 and 3 present the temperature dependences of electrical resistivity ρ and thermopower S for RNi_4In (R=Ce, Nd). The $\rho(T)$ relation for $CeNi_4In$ is similar to that observed for intermediate-valence Ce compounds[11] (Fermi-liquid behavior $\rho \sim AT^2$ with $A = 2.4 \times 10^{-3}$ $\mu\Omega\text{cm}\cdot\text{K}^{-2}$ for $T < 60$K, negative curvature of $\rho(T)$ where one expects $\rho \sim T$ for $T > 100$ K). In the case of $NdNi_4In$, the $\rho(T)$ behavior follows qualitatively the Bloch-Grüneisen law. The absence of a clearly pronounced $\rho = \text{const}$ section for $T \to 0$ is apparently due to carrier scattering by Nd^{3+} magnetic ions. This additional scattering does not present with qualitative evaluation of the contribution of the valence-unstable Ce states ($\Delta\rho$) to the total ρ. We see that within the temperature range covered $\Delta\rho$ does not saturate (see inset in Fig. 2), which is in qualitative accord with the expected large value of T_{sf}($>$400 K) characterizing the valence-saturated Ce. In contrast to systems where Ce has an intermediate valence state,[11] the $S(T)$ relation for $CeNi_4In$ does not exhibit the characteristic positive contribution with a maximum. A com-

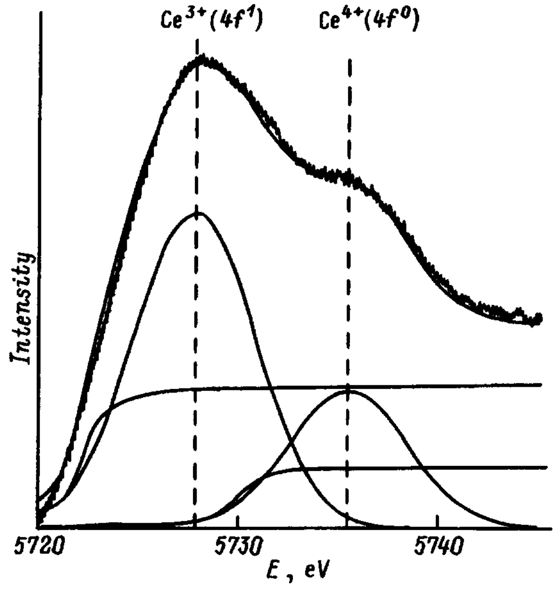

FIG. 1. Experimental x-ray L_{III} absorption spectrum of Ce in $CeNi_4In$ and its deconvolution.

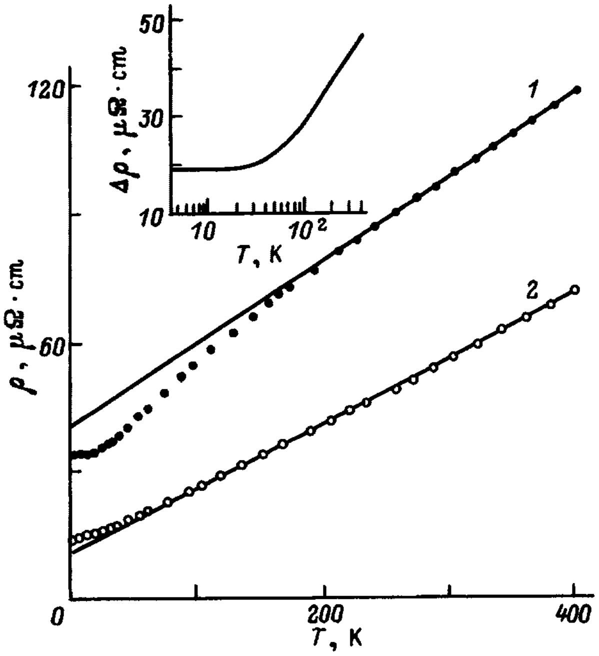

FIG. 2. Temperature dependences of the electrical resistance of RNi_4In [R=Ce (*1*) and Nd (*2*)]. The inset shows the contribution of the valence-unstable state of Ce to total electrical resistance against log temperature.

parison of the high-temperature portions in $S(T)$ for $CeNi_4In$ and $NdNi_4In$ suggests a negative contribution of the Ce saturated-valence state to thermopower. This behavior of the $S(T)$ relations was earlier observed by us in the case of $CeNi_5$ with valence-saturated Ce, when Ni was replaced successively by p elements (Al, Ga, Si, Ge).[3,4] Remarkably, in the case of p elements of the In group, $S(T)$ relations similar in behavior to that presented in Fig. 3 for $CeNi_4In$ are observed for $CeNi_4Al$ and $CeNi_4Ga$. The additional negative contribution to $S(T)$ for $T<100$ K can be attributed to electron-phonon interactions.[12]

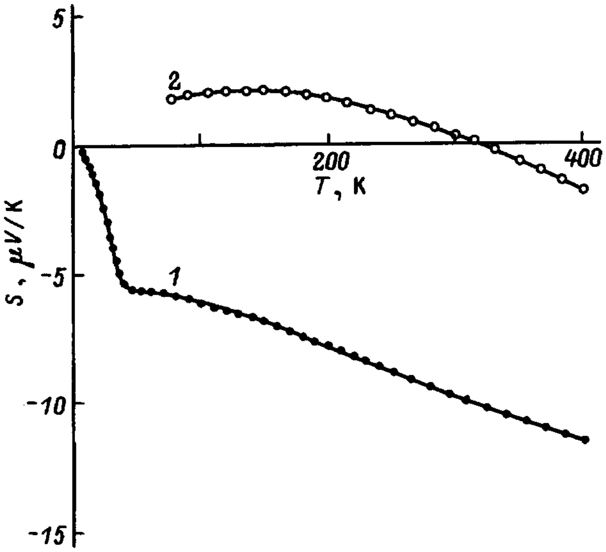

FIG. 3. Temperature dependences of the thermopower of RNi_4In [R=Ce (*1*) and Nd (*2*)].

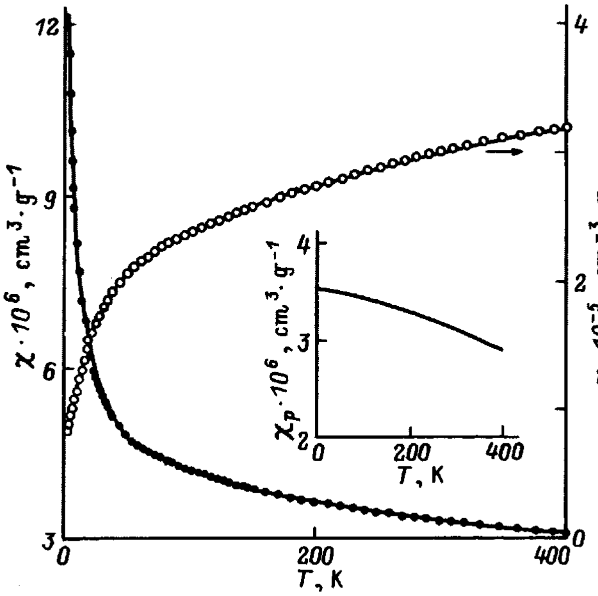

FIG. 4. Temperature dependences of the magnetic susceptibility of $CeNi_4In$. The inset shows the susceptibility component due to the valence-unstable state of Ce.

Magnetic susceptibility χ of $CeNi_4In$ exhibits a complex temperature behavior and follows qualitatively the Curie-Weiss law only for $T<20$ K (Fig. 4). Taking into account possible magnetic activity of the Ni sublattice, the $\chi(T)$ relation was approximated by

$$\chi(T)=C/(T+\theta)+\chi_P(T),$$

$$\chi_P(T)=\chi_P(0)[1-bT^2\ \ln(T/T_{sf})]. \quad (1)$$

Here the first term is the Curie–Weiss component of χ, and the second, taken from Ref. 13, describes the Fermi-liquid behavior of the χ component due to the valence-unstable Ce. The smallest fitting error ($<1\%$) is obtained for $C=7.4\times10^{-5}$ $cm^3g^{-1}K^{-1}$, $\theta=4.4$ K, $\chi_P(0)=3.5\times10^{-6}$ cm^3g^{-1}, $b=-9.5\times10^{-12}$ K^{-2}, and $T_{sf}=1213$ K. This corresponds to an effective magnetic moment $\mu_{\mathrm{eff}}=0.5\,\mu_B$ on Ni ions and a Pauli component χ_P falling off with increasing T (see inset in Fig. 4). Taking for the separation of $\chi_P(T)$ the paramagnon model[14] used frequently in describing the magnetic susceptibility of metallic systems with valence-unstable Ce

$$\chi_P(T)=\chi_P(0)[1+\alpha(T/T_{sf})^2], \quad (2)$$

we obtain, with a slightly larger fitting error ($\sim1.2\%$), approximately the same values of parameters for the Ni sublattice ($C=7.9\times10^{-5}$ $cm^3g^{-1}K^{-1}$, $\theta=4.9$ K) and for the $\chi_P(T)$ component [$\chi_P(0)=3.4\times10^{-6}$ cm^3g^{-1}, $\alpha=-1.0$, and $T_{sf}=1091$ K]. In both cases, the $\chi_P(T)$ relation remarkably lacks a noticeable plateau, $\chi_P\simeq$const, for $T\ll T_{sf}$ and a maximum characteristic of Fermi-liquid systems of such type. This behavior implies[13,14] the absence of appreciable positive curvature of the density-of-states function near the Fermi level E_F, which is typically observed in systems with intermediate-valence Ce.

It is known that intermetallic compounds with Ce in intermediate-valence state exhibit near the Fermi level a narrow peak in the density of states $g_f(E)$ of width $\Gamma_f \sim T_{sf}$, which is pinned above E_F so that $S(T) \sim dg_f(E)/dE|_{E=E_F} > 0$,[15] and that their $\chi(T)$ relation is well described for $T < T_{sf}$ by Eqs. (1) and (2) and passes through a maximum at $T \sim T_{sf}$ (Refs. 11, 14). The totality of our data permits a conclusion that a density-of-states peak forms in the Fermi region below E_F. The formation possibility of such a structure is in qualitative agreement with band-structure calculations[16] made in the Anderson impurity model with strong degeneracy and with additional inclusion of spin-orbit splitting. The involvement of the $\mathrm{Ce}^{3+} J = 7/2$ multiplet in formation of an additional fine structure in the density of states near E_F appears quite possible if one takes into account that the spin-orbit splitting energy $\Delta_{so} \simeq 0.2$ eV in valence-saturated Ce (Ref. 1) is comparable to T_{sf}. Additional support for the possibility of the Ce saturated-valence state in metallic systems forming a fine structure in the density of states below the Fermi level is provided by the appearance of an additional negative contribution to the total thermopower in the $\mathrm{CeNi}_{5-x}\mathrm{M}_x$ solid solutions (M=Al, Ga, Si, Ge) and in the induced phase transition in $\mathrm{CeNi}_{5-x}\mathrm{Cu}_x$ involving a change in the valence state.[17]

We note in conclusion that the nature of forming such a structure could be clarified by numerical calculations using the model of Ref. 16, which would include real microscopic parameters of f-state coupling with band states of the crystal matrix.

[1] J. Rohler, in *Handbook on the Physics and Chemistry of Rare Earths*, edited by K. A. Gschneidner, Jr., L. Eyring, and S. Kufner (North-Holland, Amsterdam, 1989), Vol. 10, p. 453.

[2] V. A. Shaburov, Yu. P. Smirnov, A. E. Sovestnov, and A. V. Tyunis, JETP Lett. **41**, 259 (1981).

[3] M. D. Koterlin, O. I. Babich, B. S. Morokhivskiĭ, G. Ya. Len', R. V. Lutsiv, and Yu. N. Grin', Fiz. Tverd. Tela (Leningrad) **29**, 943 (1987) [Sov. Phys. Solid State **29**, 542 (1987)].

[4] M. D. Koterlin, O. I. Babich, B. S. Morokhivskiĭ, M. B. Konyk, and R. V. Lutsiv, Fiz. Tverd. Tela (Leningrad) **30**, 1612 (1988) [Sov. Phys. Solid State **30**, 873 (1988)].

[5] J. W. Allen and R. M. Martin, Phys. Rev. Lett. **49**, 1106 (1982).

[6] L. Severin and B. Johansson, Phys. Rev. B **50**, 17886 (1994).

[7] S.-H. Yang, H. Kumigashira, T. Yokoga, A. Chainani, T. Takahashi, H. Takeya, and K. Kadowaki, Phys. Rev. B **53**, R11946 (1996).

[8] V. I. Zaremba, V. M. Baranyak, and Ya. M. Kalychak, Vestn. L'vov University, Ser. Khim. **25**, 18 (1984).

[9] M. D. Koterlin, O. I. Babich, B. S. Morokhivskiĭ, L. I. Nikolaev, and A. V. Yushchenko, IMF Preprint No. 15, Kiev (1987).

[10] M. D. Koterlin, B. S. Morokhivskiĭ, I. D. Shcherba, and N. V. German, Ukr. Fiz. Zh. **38**, 262 (1993).

[11] N. B. Brandt and V. V. Moshchalkov, Adv. Phys. **33**, 373 (1984).

[12] S. Cabus, K. Gloos, U. Gottwick, S. Horn, M. Klemen, J. Kübler, and F. Steglich, Solid State Commun. **51**, 909 (1984).

[13] S. Misawa, Physica B **149**, 162 (1988).

[14] M. T. Béal-Monod and J. M. Lawrence, Phys. Rev. B **21**, 5400 (1980).

[15] M. D. Koterlin and R. V. Lutsiv, in *Physics and Chemistry of Rare-Earth Semiconductors* [In Russian], edited by K. E. Mironov (Nauka, Novosibirsk, 1990).

[16] N. E. Bickers, D. L. Cox, and J. W. Wilkins, Phys. Rev. B **36**, 2036 (1987).

[17] R. V. Lutsiv, M. D. Koterlin, O. I. Babich, and O. I. Bodak, Fiz. Tverd. Tela (Leningrad) **26**, 1182 (1984) [Sov. Phys. Solid State **26**, 716 (1984)].

Translated by G. Skrebtsov

Temperature dependence of the magnetic susceptibility in IV-VI semiconductors

B. A. Volkov and O. M. Ruchaĭskiĭ

P. N. Lebedev Physics Institute, Russian Academy of Sciences, 117924 Moscow, Russia

(Submitted April 2, 1997; resubmitted July 7, 1997)
Fiz. Tverd. Tela (St. Petersburg) **40**, 57–62 (January 1998)

The magnetic susceptibility of IV-VI semiconductors with a quasirelativistic electron spectrum is investigated. [S1063-7834(98)01201-5]

The specific attributes of the band structure of IV-VI compounds are such that their investigation can often be confined to the contribution of certain characteristics of electrons exclusively within a small neighborhood of the band gap (which are described by a Dirac-type equation[2]) on the assumption that the contribution of all other band electrons is constant. The investigation of the magnetic properties of such compounds,[3] PbTe(Ga) in particular, leads to the problem of the magnetic susceptibility of a Dirac gas of free electrons. From another angle, this problem is equally interesting as a means of tracing, for example, the influence of interband transitions and the finiteness and anisotropy of the spectrum on the magnetic response, and also for assessing the contribution of impurities to the susceptibility.

1. GENERAL STATEMENT OF THE PROBLEM

The unperturbed Hamiltonian has the form

$$\hat{\mathcal{H}}_0=\hat{\alpha}_i v_{ij}\hat{p}_j+\hat{\beta}\Delta,$$

or it can be written in the expanded matrix form

$$\hat{\mathcal{H}}_0=\begin{pmatrix}\Delta & \hat{\sigma}_i v_{ij}\hat{p}_j\\ \hat{\sigma}_i v_{ij}\hat{p}_j & -\Delta\end{pmatrix}. \tag{1}$$

Here $\hat{\sigma}=(\sigma_x,\sigma_y,\sigma_z)$ denotes the Pauli spin matrices, $\hat{\mathbf{p}}=-i\nabla$ (in all intermediate equations we have set $\hbar=1$), $\Delta=(1/2)\varepsilon_g$ is the half-width of the band gap, and v_{ij} is a tensor representing the interband transition matrix element. To simplify matters for the time being, we consider the isotropic case, when the tensor can be written in the form $v_{ij}=v\,\delta_{ij}$. The magnetic field is included in the Hamiltonian by the customary gauge-invariant operation

$$\hat{\mathcal{H}}_0=\begin{pmatrix}\Delta & v\sigma\left(\hat{\mathbf{p}}-\dfrac{e}{c}\mathbf{A}\right)\\ v\hat{\sigma}\left(\hat{\mathbf{p}}-\dfrac{e}{c}\mathbf{A}\right) & -\Delta\end{pmatrix}. \tag{2}$$

Adopting the usual definition of the current density operator

$$\hat{\mathbf{j}}=\frac{\delta\hat{\mathcal{H}}}{\delta\mathbf{A}}=ev\begin{pmatrix}0 & \hat{\sigma}\\ \hat{\sigma} & 0\end{pmatrix}, \tag{3}$$

we can rewrite Eq. (2) in the form

$$\hat{\mathcal{H}}=\hat{\mathcal{H}}_0+\hat{V}=\hat{\mathcal{H}}_0-\frac{1}{c}\,\hat{\mathbf{J}}\cdot\mathbf{A}. \tag{4}$$

The average value of the operator (3) is determined by means of the density matrix

$$\langle\hat{\mathbf{J}}(x)\rangle=\mathrm{tr}(\hat{\mathbf{J}}\hat{\rho}), \tag{5}$$

and the density matrix is obtained from the Green's function of the Schrödinger equation in an external field:

$$\hat{\rho}(x,x')=\oint_C\frac{d\omega}{2\pi i}\,\hat{G}_\omega(x,x'). \tag{6}$$

Here the integration is carried out along the real ω axis, and the contour C encloses only occupied states. The average value of the current density operator is related to the field through the response function Q_{ij}:

$$\langle\hat{\mathbf{J}}(x)\rangle_i=\int d^3x'\,Q_{ij}(x-x')A_j(x'), \tag{7}$$

where $\langle\hat{\mathbf{J}}_i$ is the ith component of the vector $\langle\hat{\mathbf{J}}$. From now on, since the velocity tensor v_{ij} is isotropic, we shall assume everywhere that $Q_{ij}=\delta_{ij}Q$. The transformation to Fourier components in Eq. (7) yields

$$\mathbf{j}_\mathbf{q}=\int d\mathbf{x}e^{-i\mathbf{q}\cdot\mathbf{x}}\langle\hat{\mathbf{J}}(\mathbf{x})\rangle=Q(\mathbf{q})\mathbf{A}_\mathbf{q}. \tag{8}$$

Here $\boldsymbol{A}_\boldsymbol{q}$ denotes the Fourier components of the field $\mathbf{A}$. In the investigated system the free Green's function is given by the equation

$$\hat{G}^{(0)}_\omega(\mathbf{p})=\frac{1}{\omega^2-\varepsilon^2(\mathbf{p})}\begin{pmatrix}\omega+\Delta & v(\hat{\sigma}\mathbf{p})\\ v(\hat{\sigma}\mathbf{p}) & \omega-\Delta\end{pmatrix}, \tag{9}$$

where $\varepsilon(\mathbf{p})=\sqrt{\Delta^2+v^2\mathbf{p}^2}$ is the dispersion law. The following expression for the Green's function in the external field $\mathbf{A}$ can be written on the basis of Eq. (4);

$$\hat{G}_\omega(\mathbf{p})\simeq\hat{G}^{(0)}_\omega(\mathbf{p})+\hat{G}^{(0)}_\omega(\mathbf{p})\hat{V}\hat{G}^{(0)}_\omega(\mathbf{p}) \tag{10}$$

(to determine the response to a weak field, it is sufficient to know the Green's function in the first order with respect to $\mathbf{A}$). The density matrix described by the first term of Eq. (10) is the zero-field density matrix of the system and does not contribute to the average current density operator. Consequently, with allowance for (7) Eq. (10) assumes the form

$$\langle\hat{\mathbf{J}}\rangle=\oint_C\frac{d\omega}{2\pi i}\,\mathrm{Tr}(\hat{\mathbf{J}}\hat{G}^{(0)}_\omega\hat{V}\hat{G}^{(0)}_\omega). \tag{11}$$

Transforming to Fourier components in Eq. (11) and taking Eqs. (4) and (8) into account, we obtain the following equation for Q ($\mathbf{n}$ is the unit vector in the direction of the field $\mathbf{A}$):

$$Q(\mathbf{q})=-\frac{1}{c}\oint_C\frac{d\omega}{2\pi i}\int\frac{d\mathbf{p}}{(2\pi)^3}\,\mathrm{Tr}[(\hat{\mathbf{J}},\mathbf{n})\hat{G}^{(0)}_{\omega}\times(\mathbf{p})\mathrm{Tr}(\hat{\mathbf{J}},\mathbf{n})\hat{G}^{(0)}_{\omega}(\mathbf{p}+\mathbf{q})]. \quad (12)$$

In Eq. (12) the trace operator applies only to ''spinor'' indices, i.e., the indices of four-row matrices [see Eq. (1)]. It is convenient to go over to the representation of the Green's function (9). Then, taking Eq. (3) into account, we have

$$Q_1(\mathbf{q})=-\frac{e^2v^2}{c}\oint_C\frac{d\omega}{2\pi i}\int\frac{d\mathbf{p}}{(2\pi)^3}\,\mathrm{Tr}[(\hat{\sigma},\mathbf{n})\hat{G}_{11}(\mathbf{p})\times(\hat{\sigma},\mathbf{n})\hat{G}_{22}(\mathbf{p}+\mathbf{q})],$$

$$Q_2(\mathbf{q})=-\frac{e^2v^2}{c}\oint_C\frac{d\omega}{2\pi i}\int\frac{d\mathbf{p}}{(2\pi)^3}\,\mathrm{Tr}[(\hat{\sigma},\mathbf{n})\hat{G}_{12}(\mathbf{p})\times(\hat{\sigma},\mathbf{n})\hat{G}_{21}(\mathbf{p}+\mathbf{q})], \quad (13)$$

In Eqs. (13) G_{AB} denotes the elements of the matrix (9) $(A,B=1,2)$, every such element, in turn, is a 2×2 matrix, the trace operator applies only to indices of these matrices, i.e., to ''spin'' indices, and the total response function is

$$Q(\mathbf{q})=2[(Q_1(\mathbf{q})+Q_2(\mathbf{q})]. \quad (14)$$

The following remark is essential before we proceed with specific calculations. To determine the static magnetic susceptibility χ_0, it is sufficient to know $Q(\mathbf{q})$ to within quantities of the order of q^2. In fact, if we invoke the relation between the current **j** and the sample magnetization **M**: $\mathbf{j}=c\,\mathrm{curl}\mathbf{M}$, along with the relation $\mathbf{H}=\mathrm{curl}\mathbf{A}$ and Eq. (8), we readily obtain

$$\chi_0=\lim_{\mathbf{k}\to0}\left(\frac{Q_{\mathbf{k}}}{ck^2}\right). \quad (15)$$

2. CALCULATION OF THE SUSCEPTIBILITY FOR $\mu=0$.

It is useful to begin by determining the susceptibility at zero temperature and for ''half-filling'' (the chemical potential lies in the band gap). In this case the contour of integration C in (6) encloses only states of the lower band, i.e., $-\infty<\omega<-\Delta$. The quantity $Q(\mathbf{q})$ is calculated in two stages in accordance with Eq. (14):

$$Q_1(\mathbf{q})=-\frac{e^2v^2}{c}\int\frac{d\mathbf{p}}{(2\pi)^3}\oint_C\frac{d\omega}{2\pi i}\times\frac{2(\omega^2-\Delta^2)}{[\omega^2-\varepsilon^2(\mathbf{p})][\omega^2-\varepsilon^2(\mathbf{p}+\mathbf{q})]}$$

$$=\frac{e^2v^2}{4\pi^2cq}\int dp\left[\frac{p(\varepsilon_+-\varepsilon_-)}{v^2}-\frac{p^3}{\varepsilon_p}\ln\left|\frac{\varepsilon_p+\varepsilon_+}{\varepsilon_p+\varepsilon_-}\right|\right]. \quad (16)$$

Here $p=|\mathbf{p}|$, $q=|\mathbf{q}|$ (the integration in the last equation in (16) is carried out with respect to the absolute value of the momentum **p**), $\varepsilon_\pm=\sqrt{\Delta^2+v^2(p\pm q)^2}$, and $\varepsilon_p=\sqrt{\Delta^2+v^2p^2}$. The two factors in the denominator of the integrand in the first equation derives from the trace of the two-row unit matrix. The calculation of $Q_2(\mathbf{q})$ is more complicated, because this term depends on the relative orientation of the vectors **q** and **n**. Expanding the trace of the four σ-matrices, we obtain

$$Q_2(\mathbf{q})=-\frac{e^2v^4}{c}\int\frac{d\mathbf{p}}{(2\pi)^3}\frac{\Omega(\mathbf{p},\mathbf{q},\mathbf{n})}{[\varepsilon(\mathbf{p})+\varepsilon(\mathbf{p}+\mathbf{q})]\varepsilon(\mathbf{p})\varepsilon(\mathbf{p}+\mathbf{q})}. \quad (17)$$

The function $\Omega(\mathbf{p},\mathbf{q},\mathbf{n})$ is defined as follows:

$$\Omega(\mathbf{p},\mathbf{q},\mathbf{n})=\begin{cases}2p_x^2-p^2-p_zq, & \mathbf{n}\perp\mathbf{q},\\ 2p_z^2-p^2+p_zq, & \mathbf{n}\parallel\mathbf{q}.\end{cases}$$

Here the vector **q** is directed along the z axis, and the direction of **n** in the first row is chosen along the x axis. Only the transverse part of the vector potential has physical significance; hence, $Q_2^{\parallel}\equiv0$. The following renormalization of the response $Q(\mathbf{q})$ will be useful in our subsequent calculations:

$$Q(\mathbf{q})\to\widetilde{Q}(\mathbf{q})=Q_\perp+\frac{1}{2}Q_\parallel. \quad (18)$$

Making the change of notation $\Delta\to v\Delta$, from Eq. (17) we obtain

$$Q_2(q)=\frac{e^2v}{8\pi^2c}\int dp\left[\frac{p^2}{\varepsilon_p}-\frac{p(\varepsilon_+-\varepsilon_-)}{q}+\frac{p}{q\varepsilon_p}\times\left(p^2-\frac{q^2}{2}\right)\ln\left|\frac{\varepsilon_p+\varepsilon_+}{\varepsilon_p+\varepsilon_-}\right|\right]. \quad (19)$$

Under the renormalization (18) we have $Q_1(\mathbf{q})\to\widetilde{Q}_1(\mathbf{q})=(3/2)Q_1(\mathbf{q})$, because $Q_1(\mathbf{q})$ does not depend on the relative orientation of **q** and **n**. In addition it is important to note that the vector potential $\mathbf{A}=\mathrm{const}$ also does not generate current, i.e., $\widetilde{Q}(0)\equiv0$, so that from now on we drop all terms that do not contain q. For $\widetilde{Q}(q)$ we finally obtain

$$\widetilde{Q}(q)=2\left(\frac{e^2v}{8\pi^2c}\right)\int_0^\infty dp\left[\frac{5p(\varepsilon_+-\varepsilon_-)}{2q}-\frac{2p^3}{q\varepsilon_p}\times\ln\left|\frac{\varepsilon_p+\varepsilon_+}{\varepsilon_p+\varepsilon_-}\right|-\frac{pq}{2\varepsilon_p}\ln\left|\frac{\varepsilon_p+\varepsilon_+}{\varepsilon_p+\varepsilon_-}\right|\right]. \quad (20)$$

As mentioned, it is sufficient to know the response function in the second order with respect to q [see Eq. (15)]. The expansion of the logarithms in the integrand out to $O(q^5)$ yields the following result for (20):

$$\widetilde{Q}(q)=-2\frac{e^2vq^2}{8\pi^2c}\int_0^\infty dp\left[\frac{p^2}{2\varepsilon_p^3}+\frac{p^3}{3\varepsilon_p}\left(\frac{3p^3}{2\varepsilon_p^6}-\frac{p}{\varepsilon_p^4}\right)\right]$$

$$\simeq-\frac{e^2vq^2}{6\pi^2c}\ln\frac{\Delta v}{\Delta} \quad (21)$$

[all the terms in this equation diverge as $\ln p$ in the limit $p\to\infty$, the term containing $p(\varepsilon_+-\varepsilon_-)$ in the integrand of (20) yields terms that converge in the limit $p\to\infty$ and is therefore omitted in (21), and the divergence is eliminated by cutting off the integral over p in (21) at a large value Λ]. The susceptibility is deduced from this result on the basis of Eq. (15) ($\hbar$ is restored in the final equation):

$$\chi = -\frac{e^2 v}{6\pi^2 c^2 \hbar} \ln\frac{\Lambda v}{\Delta} = -\frac{\alpha}{6\pi^2}\frac{v}{c}\ln\frac{\Lambda v}{\Delta}, \qquad (22)$$

where $\alpha = e^2/\hbar c$ is the fine-structure constant. To within the logarithm, this equation is similar to the well-known Landau susceptibility equation

$$\chi_L = -\frac{e^2 v_F}{12\pi^2 c^2 \hbar} = -\frac{e^2 p_F}{12\pi^2 c^2 \hbar m}.$$

The result (22) agrees with the analogous expression obtained in Ref. 4. Assuming that Λv is of the order of the atomic energy scale and that the ratio v/c is of the order of 10^{-2}, we estimate χ to be of the order of 10^{-5}, which is much larger than the susceptibility of ordinary materials, $\sim 10^{-6}$.

3. CALCULATION OF THE RESPONSE FOR ARBITRARY FILLING

The filling is described by the chemical potential μ or by the corresponding momentum p_0 ($|\mu| = \sqrt{\Delta^2 + v^2 p_0^2}$). It is convenient to separate the response into two components: $\chi = \chi^{(0)} + \delta\chi$. Here $\chi^{(0)}$ is the susceptibility (22) corresponding to $\mu = 0$, and $\delta\chi$ is the contribution associated with nonzero μ. The definition of $\delta\chi$ is the same as in the preceding section [see (12)] except that the integration is now carried out with respect to occupied states as described by the equation $\Delta < |\omega| < |\mu|$. It is obvious at the outset that the result is not going to depend on the sign of μ; we therefore assume everywhere below that μ is positive. For the contribution to the response function from $\delta\chi$ we obtain

$$\delta Q(\mathbf{q}) = 2(\delta Q_1(\mathbf{q}) + \delta Q_2(\mathbf{q})).$$

The definitions of $\delta Q_1(\mathbf{q})$ and $\delta Q_2(\mathbf{q})$ are analogous to (13) except that now the integration over the frequency is confined to the limits $\Delta < \omega < \mu$.

From $\delta\widetilde{Q}(q)$ we obtain

$$\delta\widetilde{Q}(q) = \frac{e^2 v}{4\pi^2 c}\int_0^{p_0} dp\left(\frac{2p^3}{\varepsilon_p q} + \frac{pq}{2\varepsilon_p}\right)\ln\left|\frac{2p+q}{2p-q}\right|. \qquad (23)$$

To determine the susceptibility, we can expand the integrals in Eq. (23) as functions of the parameter q. After subtraction of the response function for $q = 0$, this operation gives

$$\delta\widetilde{Q}(q) = \frac{e^2 v q^2}{4\pi^2 c}\left(\frac{1}{6}\int_0^{p_0}\frac{dp}{\varepsilon_p} + \frac{1}{2}\int^{p_0}\frac{dp}{\varepsilon_p}\right)$$
$$= \frac{e^2 v q^2}{6\pi^2 c}\operatorname{arcsinh}\frac{p_0 v}{\Delta}.$$

The contribution to the susceptibility is finally described by the equation

$$\delta\chi = \frac{e^2 v}{6\pi^2 c^2 \hbar}\operatorname{arcsinh}\frac{p_0 v}{\Delta} = \frac{\alpha}{6\pi^2}\frac{v}{c}\operatorname{arcsinh}\frac{p_0 v}{\Delta}. \qquad (24)$$

In the limit $p_0 \to \infty$ (or, more precisely, $p_0 \to \Lambda$) we have $\operatorname{arcsinh}(p_0 v/\Delta) \to \ln(p_0 v/\Delta)$, and Eq. (24) goes over to (22) with the opposite sign, as it should in the absence of carriers. In the opposite limit ($p_0 \to 0$) the susceptibility goes over to

$$\delta\chi \to \frac{e^2 p_0 v^2}{6\pi^2 c^2 \hbar\Delta} = \frac{e^2 p_0}{6\pi^2 c^2 \hbar m^*} = 2|\chi_L|, \qquad (25)$$

where $m^* = \Delta/v^2$ is the effective mass, which can be obtained by expanding the dispersion law $\varepsilon_p = \sqrt{\Delta^2 + v^2 p^2}$ for small momentum. The susceptibility (25) coincides with the total susceptibility of a noninteracting electron gas, which is the sum of the Pauli susceptibility and the Landau susceptibility and is equal in absolute value to $2|\chi_L|$. We obtain the final equation for the magnetic susceptibility in the form

$$\chi = \frac{e^2 v}{6\pi^2 c^2 \hbar}\left[\ln\frac{\Lambda v}{\Delta} - \operatorname{arcsinh}\frac{p_0 v}{\Delta}\right]$$
$$= -\frac{e^2 v}{6\pi^2 c^2 \hbar}\ln\frac{\Lambda v}{p_0 v + |\mu|} \qquad (26)$$

[the sign of the modulus of μ in the last equation again underscores the fact that Eq. (26) is identical for positive and negative values of the chemical potential].

For $\Delta \ll \mu < \Lambda v$ Eq. (26) goes over to an expression consistent with (22) but with Δ replaced by μ:

$$\chi \simeq -\frac{e^2 v}{6\pi^2 c^2 \hbar}\left[\ln\frac{\Lambda v}{\Delta} - \ln\frac{p_0 v}{\Delta}\right] = -\frac{e^2 v}{6\pi^2 c^2 \hbar}\ln\frac{\Lambda}{p_0}$$
$$\simeq -\frac{e^2 v}{6\pi^2 c^2 \hbar}\ln\frac{\Lambda v}{\mu}. \qquad (27)$$

4. ANISOTROPY OF THE SUSCEPTIBILITY FOR $\mu = 0$

The susceptibility of the gas in the anisotropic case can be calculated by analogy with the preceding case. For simplicity we consider an axisymmetric system, in which the tensor velocity matrix element v_{ij}, resolved along the principal axes, is described by two constants and has the from $(v_\perp, v_\perp, v_\parallel)$.

In this case the magnetic susceptibility again has two components in the principal axes ($\chi_\parallel$ and $\chi_\perp$), corresponding to orientation of the magnetic field **H** parallel and perpendicular to the anisotropy axis (z axis). The calculation of the susceptibility in this case is analogous to the calculation in Sec. II, but with corrections for the anisotropic dispersion law and the orientation of the vectors **A** and **q** relative to the anisotropy axis. Nonetheless, a change of integration variables reduces the calculation to the isotropic case. The corresponding velocity matrix element is then determined from the condition of invariance of the total number of states with energies lower than the cutoff energy (which for IV-VI semiconductors is of the order of the average ionicity gap Δ_{ion}; Ref. 1). Consequently, for the case $\mathbf{H}\| z$ we obtain

$$\chi_\parallel = -\frac{e^2 v_\perp^2}{6\pi^2 c^2 v_\parallel \hbar}\ln\frac{\Delta_{\text{ion}}}{\Delta}, \qquad (28)$$

and for $\mathbf{H}\perp z$

$$\chi_\perp = -\frac{e^2 v_\parallel}{6\pi^2 c^2 \hbar}\ln\frac{\Delta_{\text{ion}}}{\Delta}. \qquad (29)$$

For $v_\parallel = v_\perp = v$, Eqs. (28) and (29) go over to (22) ($\Lambda v = \Delta_{\text{ion}}$). It should be noted that the domain of validity of

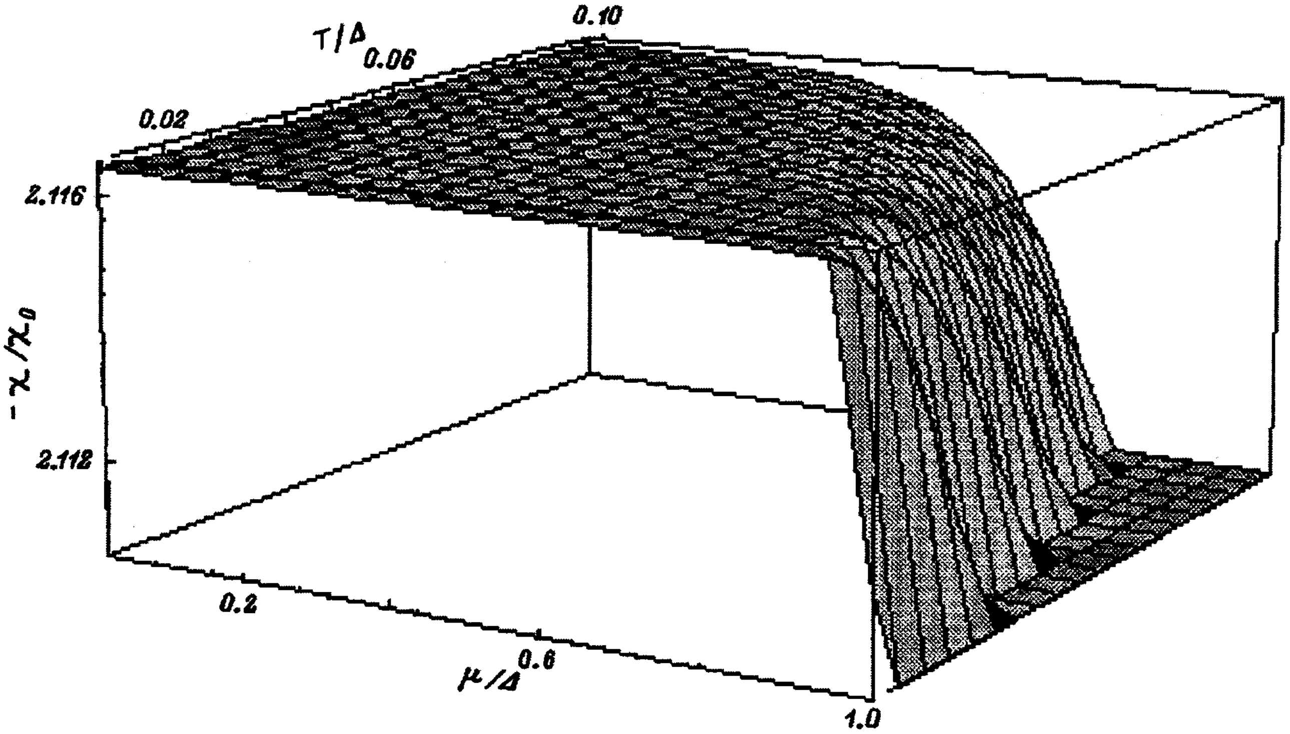

FIG. 1. Magnetic susceptibility versus chemical potential μ and temperature T.

Eqs. (28) and (29) is bounded by the condition whereby $\Delta_{\text{ion}}/v_{\perp}$ and $\Delta_{\text{ion}}/v_{\parallel}$ (corresponding to the cutoff momenta) must not exceed the Brillouin momentum.

5. SUSCEPTIBILITY AT FINITE TEMPERATURE

The susceptibility is also easily determined for a free gas at finite temperature. The procedure for determining it is exactly analogous to the one described above except for a modification of the method of determining the density matrix from the Green's function: The relation between these quantities is now given by the following equation instead of Eq. (6):

$$\hat{\rho}(x,x')=\oint_C \frac{d\omega}{2\pi i}\,\hat{G}_{\omega}(x,x')n_F(\omega). \tag{30}$$

The function $n_F(\omega)$ is the ordinary Fermi distribution function. In Eq. (30) the integration is carried out along a contour enclosing all frequencies. Equations (13) now go over to

$$Q_1(\mathbf{q})=-\frac{e^2v^2}{c}\int\frac{d\mathbf{p}}{(2\pi)^3}\oint_{-\infty}^{\infty}\frac{d\omega}{2\pi i}\times\frac{1}{\exp((\omega-\mu)/T)+1}\,\frac{2(\omega^2-\Delta^2)}{(\omega^2-\varepsilon^2(\mathbf{p}))(\omega^2-\varepsilon^2(\mathbf{p}+\mathbf{q}))}$$

and similarly for $Q_2(\mathbf{q})$. A repetition of the previous calculations yields an expression for $\widetilde{Q}(q)$ similar to (23):

$$\widetilde{Q}(q)=-\frac{e^2v}{4\pi^2c}\int_0^{\infty}dp\left(\frac{2p^3}{\varepsilon_p q}+\frac{pq}{2\varepsilon_p}\right)\times f(\varepsilon_p,\mu,T)\ln\left|\frac{2p+q}{2p-q}\right|. \tag{31}$$

In Eq. (31) we have introduced the function $f(\varepsilon_p,\mu,T)=n_F(-\varepsilon_p)-n_F(\varepsilon_p)$. From this equation we obtain the following result for the magnetic susceptibility:

$$\chi(\mu,T)=-\frac{e^2v}{6\pi^2c^2}\int_0^{\infty}\frac{dp}{\varepsilon_p}f(\varepsilon_p,\mu,T)=-\frac{e^2v}{6\pi^2c^2}\int_0^{\infty}\frac{dp}{\varepsilon_p}\,\frac{\sinh(\varepsilon_p/T)}{\cosh(\varepsilon_p/T)+\cosh(\mu/T)}. \tag{32}$$

The behavior of χ as a function of T and μ is shown in Fig. 1. The chemical potential and the temperature (referred to the half-width of the band gap) are plotted along the horizontal axis, and the ratio of the susceptibility (with the opposite sign) to the quantity $\chi_0=(e^2v/6\pi^2c^2)\approx1.2\times10^{-6}$ is plotted along the vertical. The temperature is varied from zero to 0.1Δ, which roughly corresponds to 100 K, and the position of the chemical position is varied from the middle of the band gap to the bottom of the conduction band ($0\leqslant\mu\leqslant\Delta$). It is important to note that the susceptibility remains diamagnetic for all possible values of T and μ. [Diamagnetism is attributable to the fact that the function $f(\varepsilon_p,\mu,T)$ is positive. The response becomes paramagnetic when the function f changes sign, but this is possible only at negative temperature T, i.e., in the presence of population inversion.]

It is readily verified that Eq. (32) goes over to (22) in the limit $T\to0$ for $\mu=0$, and for nonzero μ it goes over to an expression identical to (26). From Eq. (32) we can deduce the asymptotic behavior for

$$\mu,\Delta\gg T\quad\text{and}\quad|\mu-\Delta|\sim T. \tag{33}$$

Under these conditions the function $f(\varepsilon_p,\mu,T)$ can be written in the form $1-n_F(\varepsilon_p)$. In this case the term with $f=1$ in

(32) corresponds to the susceptibility contribution from the completely filled lower band and, by the first condition in (33), coincides with (22). By the second condition in(33) we can assume that the carriers in the upper band are nondegenerate and that $n_F(\varepsilon_p)$ is a Boltzmann distribution. In this case the susceptibility has the form,

$$\delta\chi(\mu,T)=\frac{e^2v}{6\pi^2c^2}\int_0^\infty\frac{dp}{\varepsilon_p}\exp\left(\frac{\mu-\varepsilon_p}{T}\right). \tag{34}$$

The main contribution to (34) is from states near the bottom of the band, where $\varepsilon_p\approx\Delta+(p^2/2\Delta)$; it suffices to retain the momentum dependence only in the exponential function. We then obtain

$$\delta\chi(\mu,T)\simeq\frac{e^2v}{6\pi^2c^2}\exp\left(\frac{\mu-\Delta}{T}\right)\int_0^\infty\frac{dp}{\Delta}\exp\left(-\frac{p^2}{2\Delta T}\right)$$
$$=\frac{e^2v}{6\pi^2c^2}\exp\left(\frac{\mu-\Delta}{T}\right)\frac{\sqrt{2\pi\Delta T}}{2\Delta}. \tag{35}$$

To clarify this expression, it must be noted that the carrier density in the upper band under the same assumptions is given by the equation

$$\delta n=\mathrm{tr}(\hat{\rho}(x,x'))=2\int_0^\infty\frac{d\mathbf{p}}{(2\pi)^3}\exp\left(\frac{\mu-\varepsilon(\mathbf{p})}{T}\right)$$
$$\approx\exp\left(\frac{\mu-\Delta}{T}\right)\frac{\sqrt{2\pi(T\Delta)^3}}{2\pi^2}.$$

In this light Eq. (35) now assumes the form [see also the comments to Eq. (25)]

$$\delta\chi(\mu,T)\simeq\frac{e^2v^4\hbar^2\delta n}{6c^2T\Delta^2}=\frac{2}{3}\frac{\delta n}{T}\left(\frac{e\hbar}{2m^*c}\right)^2 \tag{36}$$

(the correct power of v is automatically restored here). This equation coincides with the well-known equation for the total susceptibility of a Boltzmann electron gas [see also Eq. (25)]:

$$\chi=\frac{2}{3}\frac{n}{T}\left(\frac{e\hbar}{2mc}\right)^2.$$

Finally, we can determine the asymptotic behavior of (32) for $\mu,\Delta\ll T<\Lambda v$. To make such an estimate, we separate the integral in Eq. (32) into two temperature intervals. The contribution of the high-energy term is dominant at high T, so that the following expression is obtained for the susceptibility in the limit $T\rightarrow\infty$:

$$\chi(\mu,T)=-\frac{e^2v}{6\pi^2c^2\hbar}\ln\frac{\Lambda v}{T}. \tag{37}$$

This expression is again similar to Eqs. (22) and (27) with the appropriate substitutions.

In closing, it is important to note that the computational method graphically demonstrates the origin of the diamagnetic response in such systems. Indeed, as is readily perceived, it follows from Eq. (13) that the contribution of $Q_1(\mathbf{q})$ is identical for the cases $\mathbf{A}\perp\mathbf{q}$ and $\mathbf{A}\|\mathbf{q}$. Consequently, the susceptibility is attributable to the term $Q_2(\mathbf{q})$ originating from off-diagonal elements of the Hamiltonian (1), i.e., elements describing interband transitions. Moreover, the given diagramming technique can be used to choose the gauge best suited to the subsequent calculations, rather than to fix it *a priori*. The method should prove far more convenient and straightforward in calculating, for example, susceptibility corrections due to impurities and weak localization associated with the latter.

This work has received partial financial support from the Russian Fund for Fundamental Research (Projects 96-02-16701a and 96-02-19022a).

[1] B. A. Volkov and O. A. Pankratov, Zh. Éksp. Teor. Fiz. **75**, 1362 (1978) [Sov. Phys. JETP **48**, 687 (1978)].

[2] G. L. Bir and G. E. Pikus, *Symmetry and Strain-Induced Effects in Semiconductors* (Israel Program for Scientific Translations, Jerusalem; Wiley, New York, 1972).

[3] A. M. Vasil'eva, B. A. Volkov, T. M. Voloshok, and S. V. Kuvshinnikov, JETP Lett. **61**, 786 (1995).

[4] L. A. Fal'kovskiĭ, A. V. Brodovoĭ, and G. V. Loshkarev, Zh. Éksp. Teor. Fiz. **80**, 334 (1981) [Sov. Phys. JETP **53**, 170 (1981)].

Translated by James S. Wood

Characteristics of the temperature dependence of the EPR spectrum of a layered GaSe:Gd crystal

S. S. Ishchenko and A. A. Klimov

Institute of Semiconductor Physics, National Academy of Sciences of Ukraine, 252028 Kiev, Ukraine

(Submitted June 2, 1997)
Fiz. Tverd. Tela (St. Petersburg) **40**, 63–65 (January 1998)

The temperature dependence of the axial constants b_2^0 characterizing the fine structure of the EPR spectra of Gd^{3+} in a layered GaSe crystal is investigated. The compound GaSe:Gd contains three types of centers, in which Gd^{3+} is associated with Li^+ or Na^+ ions situated in the interlayer space. The influence of these ions on the phonon spectrum of the crystal is studied. It is shown that the lithium atoms are too small to have any appreciable influence on low-frequency optical vibrations (the E'' mode), which govern the behavior of the temperature curve. Here $b_2^0(T)$ remains linear in the temperature range well below the Debye temperature Θ_D; this is a characteristic feature of layered structures. Sodium, on the other hand, completely suppresses the E'' mode, so that, for centers associated with it, the temperature dependence of $b_2^0(T)$ exhibits the same behavior as for ordinary (nonlayered) crystals, where linearity is observed only for $T>\Theta_D$. *© 1998 American Institute of Physics.* [S1063-7834(98)01301-X]

Within layer atoms in layered crystals are connected by strong ionic-covalent bonds, whereas weak bonds of the van der Waals type are active between the layers. The presence of the weak bonds creates low-frequency ($\omega=10-100\ \mathrm{cm}^{-1}$), low-dispersion optical branches in the phonon spectrum of the layered crystal,[1–3] which are responsible for anomalies in various kinds of temperature dependences.[4–6]

In an electron paramagnetic resonance (EPR) study of layered GaSe:Mn^{2+} (Ref. 6) the unusual behavior of the temperature dependence of the constant b_2^0 characterizing the interaction of the electron spin of a paramagnetic center with the axial crystal field has in fact been successfully explained by low-frequency optical modes. An anomaly has been reported in Ref. 6 in that the linear part of the $b_2^0(T)$ curve extends into the temperature range well below the Debye temperature Θ_D ($\Theta_D\simeq 300$ K for GaSe).

The EPR spectrum of GaSe:Gd^{3+} has been investigated.[7] It has been established that Gd^{3+} replaces a covalent-bound pair of gallium Ga_2^{4+} atoms and is situated in the center of the layer. Electron-nuclear double resonance measurements have disclosed that alkali-metal ions (Li^+ or Na^+) exist between the layers in the vicinity of paramagnetic centers, where they act as charge compensators. These ions were present in the crystal as uncontrolled impurities.

Since Li^+ and Na^+ shunt interaction between the layers in this configuration and, hence, exert a significant influence on the generation of low-frequency optical modes, it is instructive to investigate the variations induced in the temperature dependences of the EPR spectra by the presence of an impurity in the gap between layers. The results of such an investigation are given below.

The measurements were carried out on a Varian E-12 EPR spectrometer. The sample was placed in a double quartz tube with helium gas blown through it. The sample temperature was varied by regulating the temperature of the gas flow and was measured by a special sensor placed in direct contact with the sample. The errors of the measurement quantities did not exceed the following upper limits: $\Delta T\leqslant 2$ K; $\Delta b_2^0\leqslant 2\times10^{-4}\ \mathrm{cm}^{-1}$.

Two types of interlayer gaps v and w exist in the polytype-ε GaSe lattice, where the volume of w is much larger than the volume of v (Refs. 7 and 8). The dimensions of the Na^+ ion significantly exceed v and are commensurate with w. For this reason sodium is found only in the w gap (we label it Na_w^+. The dimensions of Li^+ are such that it can exist in both gaps, forming both L_v^+ and L_w^+. Consequently, the ε-GaSe:Gd crystal is characterized by three types of paramagnetic centers: $\mathrm{Li}_w^+\mathrm{Gd}^{3+}w$, $\mathrm{Li}_v^+\mathrm{Gd}^{3+}v$, and $\mathrm{Na}_w^+\mathrm{Gd}^{3+}w$ (the closest interlayer gaps or ions contained in them are indicated to the left and to the right of Gd^{3+}). The complete set of parameters of these centers and a detailed description of their EPR spectra are given in Ref. 7. We have investigated the temperature dependence $b_2^0(T)$ for these centers. The corresponding curves are shown in Fig. 1. Also shown for comparison in the same figure is the temperature dependence for Mn^{2+} centers, taken from Ref. 6.

It is evident from Fig. 1 that curves *2* and *3* associated with lithium centers are similar to curve *1* (Ref. 6) and can therefore be described by the expression[5,6]

$$b_2^0(T)=b_{2(0)}^0+b_{2(1)}^0\cdot\coth(\omega/2kT), \tag{1}$$

where ω is the frequency of the low-frequency optical mode having the strongest influence on the constant b_2^0 and extending the linear part of the temperature curve into the low-temperature region, and $b_{2(0)}^0$ and $b_{2(1)}^0$ are parameters that depend on the nature of the center and its interaction with the crystal field and with phonons. Equation (1) is obtained by expanding b_2^0 with respect to the relative displacements of the atoms, averaging, and retaining only low-frequency optical phonons in the second-order terms of the expansion. Acoustic modes—flexural modes in particular[9]—and the dilatation or compression of the crystal are ignored here. It has

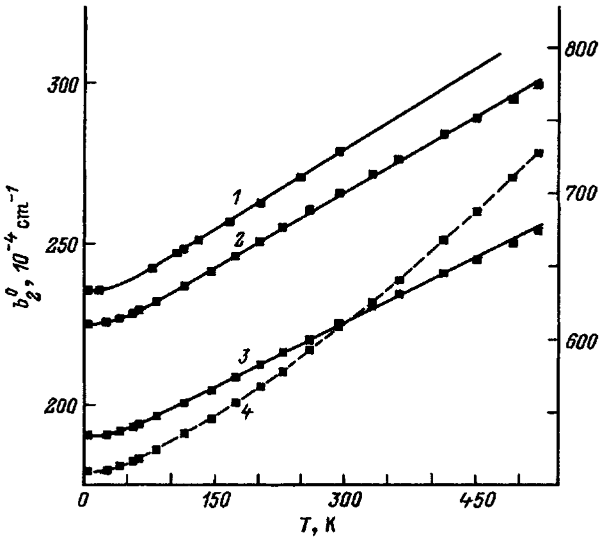

FIG. 1. Temperature dependence of the constant b_2^0 characterizing the EPR spectra of paramagnetic centers in a layered GaSe crystal. *1)* Mn^{2+}; *2)* $Li_w^+Gd^{3+}w$; *3)* $Li_v^+Gd^{3+}v$; *4)* $Na_w^+Gd^{3+}w$. The solid curves for centers *1–3* represent the theoretical curves obtained from Eq. (1), and the points represent the experimental data. The dashed curve for center 4 represents an approximation of the experimental data. The absolute values of b_2^0 are plotted along the vertical axis. The right vertical scale corresponds to center 1, and the left scale to centers *2–4*.

been shown[6,10] that this approximation yields fairly good agreement between theory and experiment for layered crystals of the GaSe type.

Curves *2* and *3* in Fig. 1 are satisfactorily described by Eq. (1) for the following values of the parameters. For a $Li_w^+Gd^{3+}w$ center: $b_{2(0)}^0 = 218\times10^{-4}$ cm^{-1}, $b_{2(1)}^0 = 406\times10^{-4}$ cm^{-2}, $\omega = 58$ cm^{-1}; for a $Li_v^+Gd^{3+}v$ center: $b_{2(0)}^0 = 184\times10^{-4}$ cm^{-1}, $b_{2(1)}^0 = 349\times10^{-4}$ cm^{-2}, $\omega = 60$ cm^{-1}.

In contrast, curve *4* in Fig. 1, which is associated with a $Na_w^+Gd^{3+}w$ center, differs significantly from curves *1–3*. It cannot be described by Eq. (1) and is more similar to the temperature curves $b_2^0(T)$ for ordinary (nonlayered) crystals. The nonlinearity of the dependence in the range $T < \Theta_D$ indicates the suppression of low-frequency optical modes in this case.

These results can be interpreted as follows. According to Polian *et al.*,[1] low-frequency optical vibrations with $\omega \simeq 56$ cm^{-1} (E'' mode) are generated in layered GaSe, where the atoms execute motion perpendicular to the normal to the layer. The strong bonds turn easily in this case, and the atoms in adjacent layers slide relative to each other. In such deformations the role of the elastic force is taken mainly by weak interlayer bonds, so that the vibration frequency is lower than the usual. The E'' mode significantly deforms the nearest-neighbor environment of the paramagnetic center and, hence, strongly modulates b_2^0. As a result, the mode completely determines the temperature behavior of b_2^0, as has indeed been observed[6] for Mn^{2+} and for the $Li_v^+Gd^{3+}v$ and $Li_w^+Gd^{3+}w$ centers in our experiments.

The influence of ions situated in the interlayer space on the E'' mode depends on the position and size of the ion (Fig. 2). The structure of the v gap is such that an ion situated in it, even with dense packing (such that the ionic radius R_u is commensurate with the effective gap radius R_v), does not really inhibit the E''-mode vibrations. In the case of the w gap, on the other hand, the E'' mode can exist only if $R_u \ll R_w$. For $R_u \simeq R_w$ vibrations are no longer possible, because the atoms in the adjacent layers lose their ability to slide relative to each other (Fig. 2). Owing to the small size of the lithium ions, the E'' mode is preserved both for Li_v^+ and for Li_w^+. For the Na_w^+ ion, on the other hand, this mode is completely suppressed.

The physical properties of the layered GaSe crystal classify it has a quasi-two-dimensional structure. The presence of a sodium ion in the interlayer space renders the crystal locally three-dimensional. This effect is responsible for the similarity of the $b_2^0(T)$ curve for the $Na_w^+Gd^{3+}w$ center to the temperature curves of nonlayered structures, which usually exhibit nonlinear behavior only in the temperature range $T < \Theta_D$.

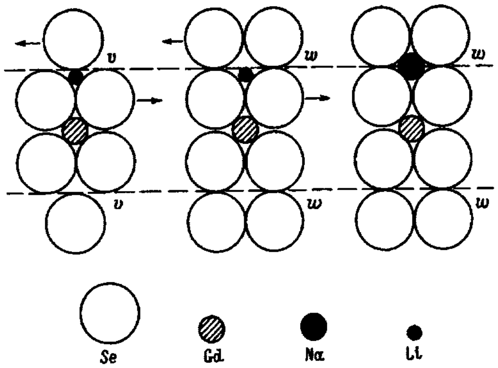

FIG. 2. Models of Gd^{3+} centers in GaSe. The horizontal dashed lines represent the boundaries of the layer. The arrows indicate the direction of motion of selenium atoms in adjacent layers in the E'' mode.

---

[1] A. Polian, K. Kune, and A. Kuhn, Solid State Commun. **19**, 1079 (1976).

[2] G. L. Belen'kiĭ and V. B. Stopachinskiĭ, Usp. Fiz. Nauk **140**, 233 (1982) [*sic*].

[3] V. V. Artamonov, L. I. Berezhinskiĭ, M. P. Lisitsa *et al.*, Fiz. Tverd. Tela (Leningrad) **17**, 3621 (1975) [Sov. Phys. Solid State **17**, 2355 (1975)].

[4] E. S. Syrkin and S. B. Feodos'ev, Fiz. Nizk. Temp. **8**, 760 (1982) [Sov. J. Low Temp. Phys. **8**, 493 (1982)].

[5] M. F. Deĭgen, S. S. Ishchenko, V. I. Konovalov, and S. M. Okulov, Fiz. Tverd. Tela (Leningrad) **20**, 476 (1978) [Sov. Phys. Solid State **20**, 276 (1978)].

[6] S. S. Ishchenko, V. I. Konovalov, and S. M. Okulov, Fiz. Tverd. Tela (Leningrad) **21**, 287 (1979) [Sov. Phys. Solid State **21**, 174 (1979)].

[7] A. A. Klimov, V. G. Grachev, S. S. Ishchenko *et al.*, Fiz. Tverd. Tela (Leningrad) **29**, 28 (1987) [Sov. Phys. Solid State **29**, 16 (1987)].

[8] A. Kuhn, A. Chevy, and R. Chevalier, Phys. Status Solidi **31**, 469 (1975).

[9] M. D. Glinchuk, V. E. Goncharuk, D. L. Lyfar' *et al.*, Fiz. Tverd. Tela (Leningrad) **18**, 15 (1976) [Sov. Phys. Solid State **18**, 7 (1976)].

[10] S. S. Ishchenko, *Radiospectroscopy* [in Russian], Perm. Univ., Perm (1985), p. 209.

Translated by James S. Wood

Relaxation of the conductivity of CsI-Tl after excitation by subnanosecond electron pulses

B. P. Aduev and V. N. Shvaĭko

Kemerovo State University, 650043 Kemerovo, Russia

(Submitted June 9, 1997)
Fiz. Tverd. Tela (St. Petersburg) **40**, 66–67 (January 1998)

The pulsed conductivity is investigated for a CsI-Tl crystal having a Tl^+ concentration $\mathrm{N}=8\times10^{17}\mathrm{cm}^{-3}$ and excited by an electron beam (0.2 MeV, 50 ps, $10^2-10^4 A/cm^2$). It is shown that the amplitude of the conduction current pulse is almost an order of magnitude lower than for ''pure'' CsI crystals irradiated under like conditions. The conduction current relaxation time is preserved up to $\tau=100$ ps in this case. Under the experimental conditions, therefore, the lifetime of electrons in the conduction band is controlled by trapping at Tl^+ centers. The electron capture cross section at a Tl^+ center is determined: $\sigma=7\times10^{-16}$ cm^2, which agrees in order of magnitude with estimates of the capture cross section for a neutral trapping center. © *1998 American Institute of Physics.* [S1063-7834(98)01401-4]

Investigations of the transient conductivity of CsI crystals excited by subnanosecond electron beams have been reported in recent papers.[1,2] It has been shown that the conduction current pulse in CsI relaxes at room temperature in a time ~1 ns, obeying second-order kinetics. A linear dependence of the amplitude of the conduction current pulse on the excitation density is observed here. This behavior and a comparison with optical experiments[3,4] have led to the conclusion that the observed relaxation time is associated with the coherent transfer of conduction-band electrons, limited by recombination with V_k centers. Processing of the experimental curves within the framework of the model provides an estimate of the electron mobility: $\mu=(8\pm2)$ cm^2/V·s, which agrees in order of magnitude with the mobility of band electrons and corroborates the preceding conclusion.

These considerations have stimulated interest in setting up a detailed experiment on CsI crystals doped with a controlled impurity. If the impurity concentration is sufficiently high and if the lifetime of conduction-band electrons is determined primarily by the impurity, the capture cross section of an electron by an impurity center can be determined from the measured relaxation time of the conduction current:

$$\sigma=(v\tau N)^{-1}, \tag{1}$$

where v is the thermal electron velocity ($v=1.75\times1.75$ cm^3/s at $T=300$ K), and N is the impurity concentration.

The CsI crystals used in the study were doped with Tl^+ ions to a concentration $\mathrm{N}=8\times10^{17}\mathrm{cm}^{-3}$. The excitation source was an electron accelerator (0.2 MeV, 50 ps, 10^2-10^4 A/cm^2). The temporal resolution of the experimental procedure was 150 ps. The relaxation time, which can be estimated from convolution-integral processing of the experimental results, has a value $\gtrsim20$ ps. Measurements performed on samples of identical dimensions and at identical excitation density have shown that the amplitude of the conduction current pulse in CsI-Tl is approximately an order of magnitude lower than in pure CsI, and the relaxation time is abruptly curtailed. Consequently, the electron lifetime is limited by the dominant reaction $\mathrm{Tl}^+ + e^- \rightarrow \mathrm{Tl}^0$ under our experimental conditions. Oscillograms of the time-shifted excitation and conduction current pulses are shown in Fig. 1 (the center of the excitation pulse is taken as the origin). The oscillograms are processed by means of the convolution integral

$$R(t)=\int_0^t W(t')F(t-t')dt', \tag{2}$$

where $R(t)$ is the observed experimental dependence, $W(t')$ is the profile of the excitation pulse, and $F(t-t')$ is the impulse response function. In our situation the excitation pulse is found to be well described by a normal distribution $W(t)=\exp(-2t^2/w^2)$, where $w=180$ ps is the Gaussian parameter characterizing the pulse duration. The function $F(t)$ is assumed to have the form $F(t-t')=\exp[(t'-t)/\tau]$. The dashed curve is calculated from Eq. (2) with the parameter $\tau=100$ ps. Using Eq. (1) and the values of the quantities in it, we calculate the cross section $\sigma=7\times10^{-16}$ cm^2, which agrees in order of magnitude with estimates for the capture cross section at a neutral center.

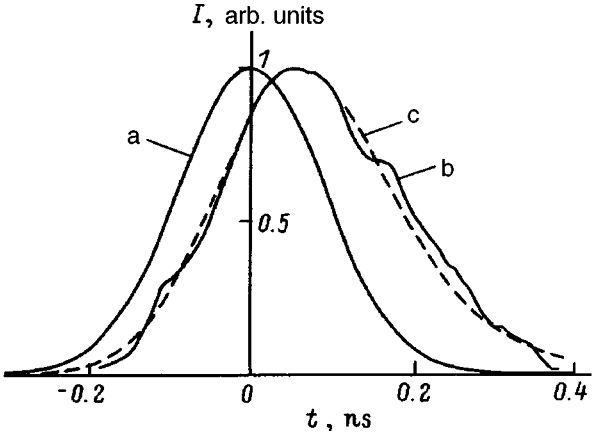

FIG. 1. Oscillograms of the excitation pulse (a) and the conduction current pulse (b), together with the calculated oscillogram (c).

[1] B. P. Aduev, G. M. Belokurov, and V. N. Shvaĭko, Fiz. Tverd. Tela (St. Petersburg) **37**, 2537 (1995) [Phys. Solid State **37**, 1392 (1995)].
[2] B. P. Aduev, A. V. Igolinskiĭ, and V. N. Shvaĭko, Fiz. Tverd. Tela (St. Petersburg) **38**, 948 (1996) [Phys. Solid State **38**, 525 (1996)].
[3] É. D. Aluker, R. G. Deĭch, and G. S. Dumbadze, Pis'ma Zh. Tekh. Fiz. **14**, 2132 (1988) [Sov. Tech. Phys. Lett. **14**, 925 (1988)].
[4] É. D. Aluker, R. G. Deĭch, and G. S. Dumbadze, Izv. Akad. Nauk Latv. SSR Ser. Fiz. Tekh. Nauk **17**(4) (1987).

Translated by James S. Wood

Influence of pulsed laser radiation on the real structure of CdTe single crystals

I. L Shul'pina, N. K. Zelenina, and O. A. Matveev

A. F. Ioffe Physicotechnical Institute, Russian Academy of Sciences, 194021 St. Petersburg, Russia

(Submitted June 19, 1997)
Fiz. Tverd. Tela (St. Petersburg) **40**, 68–72 (January 1998)

Back-reflection x-ray diffraction topography is used the measure the real structure of the surface layer of CdTe single crystals. It is found that the structural changes depend mainly on the laser power, on the presence of a doping impurity, and on the orientation and profile of the sample surface. Three distinct and conspicuous phenomena are discussed: overall improvement of the real structure of the surface layer, the periodic relief of the crystal surface, and twin mosaic structure. © *1998 American Institute of Physics.* [S1063-7834(98)01501-9]

Various types of laser processing of materials, including laser impurity injection, are among the latest technologies used in the design of modern devices. In application to Si, GaAs, and CdTe crystals, laser impurity injection is used to form ohmic and rectifying contacts, and this doping technique is enjoying increasingly widespread acceptance.[1,2] However, irradiation-induced structural defects can have a strong influence on the electrical characteristics of devices. A great deal has yet to be investigated in this area; information on the structural changes in CdTe crystals, which are highly sensitive to heat,[5] is particularly scarce. The main advantage of laser injection over other doping techniques in regard to semiinsulating CdTe crystals is the confinement of heating to a thin surface layer. The main structural transformations in CdTe are also expected to take place in a thin layer and should be significant. There is hope for the possibility of detecting the changes by back-reflection x-ray topography.[6,7]

Cadmium telluride is a highly absorbing material, and the x-ray diffraction examination of it has unique characteristics. The latter have been thoroughly studied[7–9] and are such that Cu $K\alpha$ radiation can be used to analyze the structure of a surface layer a few micrometers thick, essentially without any concern for the contribution of its normally mosaic dislocation bulk structure, which can be observed by Mo $K\alpha$ radiation. For this reason we have adopted reflection x-ray topography as the principal method for investigating structural changes taking place in CdTe in exposure to high-intensity pulsed radiation under conditions close to those encountered in the injection of doping impurities.

1. EXPERIMENTAL CONDITIONS AND DESCRIPTION OF THE SAMPLES

For the investigation we used an OGM-40 pulsed laser with two heads: ruby (wavelength $\lambda = 0.694$ μm) and neodymium ($\lambda = 1.06$ μm); the pulse duration was 20 ns in both cases. The radiation beam from the ruby laser is absorbed in a surface zone of the investigated CdTe crystal (absorption coefficient $K = 6\times10^4$ cm^{-1}; Ref. 10), causing it to heat up. The absorption of radiation from the neodymium laser by the crystal is weak ($K = 1-3$ cm^{-1}; Ref. 10); we therefore used CdTe samples coated with a vacuum-evaporated film of a doping impurity (e.g., Al), which was removed chemically after irradiation. The sample was irradiated on the side opposite the deposited film. Upon begin absorbed in the film, the laser radiation heated the contact zone of the crystal.

A photoconductive cell with an output diameter of 0.7 cm was used to focus the radiation and to equalize its intensity over the beam cross section. The sample was mounted tightly against the output end of the photoconductive cell. It was irradiated over a wide range of energies: $(0.2-1.8)$ J/cm^2.

The investigated CdTe crystals were grown from the melt in the zero-gradient heat field of the furnace.[11] Samples having dimensions $8\times8\times1.5$ mm were cut from single-crystal wafers oriented primarily along the (111) plane. The surfaces of the samples were prepared by abrasive polishing and subsequent chemical polishing.

The real structure of the crystals was investigated by reflection x-ray diffraction topography. Primary Cu $K\alpha$ radiation and a series of reflections were used. The extraction of the crystals in reflection and the estimation of their degree of structural imperfection (e.g., blocks, the presence of macrostresses, large inclusions, etc.) were performed in a URT or KRS chamber using a Start television system, and detailed examinations were made on photographic plates for nuclear photographs of the MK type with emulsion thicknesses of 15 μm and 50 μm.

The crystals selected for the investigations were free of blocks and had a most homogeneous real structure. However, subgrains, small-angle boundaries, and macrostresses were present in the samples. The dislocation densities, estimated from auxiliary photographs of the 444 reflection by Mo $K\alpha$ radiation, had values in the interval $10^{-4}-10^5$ cm^{-2}. The dislocation structure had a typical mosaic character. A distinctive attribute of the real structure of the samples was the presence of shallow, sparse, circular inclusions, presumably Te (Ref. 12). The largest solitary inclusions of this type generated dislocations along the $\langle110\rangle$ directions. They show up as stars on the topograms.

2. PROCEDURE OF THE INVESTIGATIONS

The real structure of the as-prepared samples could be characterized on the basis of topograms obtained in Cu $K\alpha$ radiation and the 444 reflection in a single-crystal photographic arrangement, because essentially all important structural defects are displayed under these conditions, with the

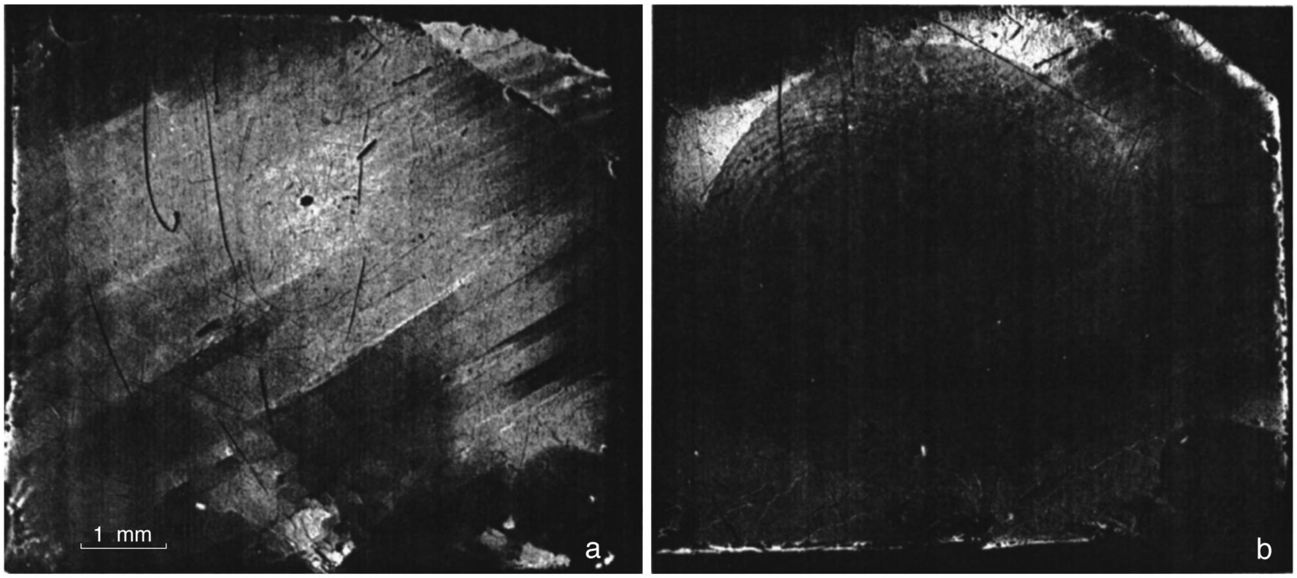

FIG. 1. Structural transformation of the surface layer of a CdTe sample as a result of irradiation by a neodymium laser at energy ~0.3 J/cm^2. a) Before irradiation; b) after irradiation, Cu $K\alpha$ radiation, 620 reflection; the object in the lower right corner is a circular marker.

exception of dislocations (which are poorly or not at all visible). After laser irradiation, on the other hand, particularly at low energies ~0.3−0.5 J/cm^2, this technique was found to be inadequate, and an attempt was made to find more sensitive crystal photography conditions.

The asymmetric 422, 531, 331, 440, 620, and 711 reflections were tested for (111)-oriented crystals. The beam penetration depth t was calculated for them according to the equation

$$t=\frac{2.3}{\mu[\csc(\theta+\alpha)+\csc(\theta-\alpha)]},$$

where μ is the linear x-ray absorption coefficient, θ is the Bragg angle, and α is the tilt angle of the reflecting plane relative to the surface of the sample. The penetration depth decreased from 4 μm to 0.7 μm for this set of reflections, and for the 444 reflection it was equal $t=6.7$ μm. This is the thickness of the crystal surface layer capable of contributing, in principle, to the formation of diffraction images of defects.

The last reflections in the above-stated series were found to be the most sensitive to weak surface flaws induced by laser irradiation under our conditions. The 620 reflection was chosen as the working line on the basis of practical photographic considerations. For this reflection the angle of incidence of rays on the crystal is 5.6° (2.6° for the 711 reflection) with the crystal surface precisely oriented along the (111) plane. Recording of the topograms in these reflections did not require scanning of the crystal and the photographic plate (scanning is mandatory for other reflections). A two-crystal arrangement was used to determine the physical nature of the patterns observed in the topograms (see below). The monochromator in this case was a Ge crystal.

3. RESULTS

Laser irradiation in the energy interval (0.2–0.3) J/cm^2 is followed by overall improvement in the structure of the surface layer, as the topograms reveal in three distinct effects (Figs. 1a and 1b): First, the total reflection intensity diminishes in the irradiated zone relative to the nonirradiated sample surface, corresponding to enhancement of the structural perfection of the crystals. Second, tiny scratches introduced in the technological irradiation process heal over. Third, we see enhancement of the contrast of individual defects, including inclusions, which increase in number, while those existing prior to irradiation increase in size. The latter effect is attributable to stress relaxation around the inclusions, which renders them more detectable through their generation of dislocations. Accordingly, dislocations around large inclusions are dispersed farther away. This behavior is unquestionably promoted by heating of the surface layer of the crystal.

A periodic pattern similar to an interference pattern is observed in the topograms at energies above 0.3 J/cm^2, appearing as rings or loops with a period that diminishes toward the periphery (Figs. 2a and 2b). The visibility of this pattern clearly depends on the irradiation energy. At near-threshold energies ≈0.3 J/cm^2 it is only visible in the 620 and 711 reflections, whereas at higher energies it is visible in 440, 531, and even 422.

The configuration of the patterns differs for different samples, strongly implying a dependence of the type of pattern on the profile of the sample surface, which is not perfectly flat, but acquires a certain convexity as a result of prolonged chemical polishing.

From the standpoint of the formation of an x-ray diffraction image, the pattern can be attributed either to a periodic deformation of the crystal (in the form of elastic waves generated, for example, by the high-intensity pulsed irradiation) or to its periodic surface relief.

We have taken the following approach to the explanation of the observed pattern. We first attempted to determine whether a given pattern is associated with modification of the

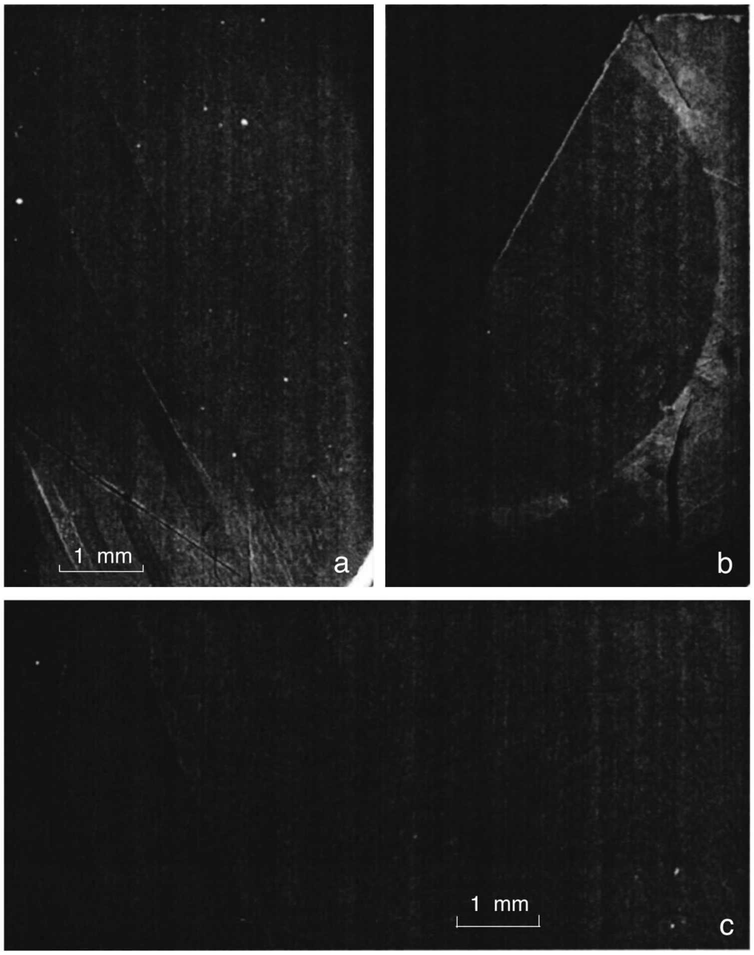

FIG. 2. Structural transformation of the zone irradiated by a ruby laser, Cu $K\alpha$ radiation. Onset of recrystallization structure: a) local at $E=0.8$ J/cm^2 (440 reflection); b) over the entire area at $E=1.37$ J/cm^2 (620 reflection); c) magnified fragment of topogram *a* (440 reflection).

as-prepared dislocation structure of the crystals. Unfortunately, the resolution of the topograms recorded with Mo $K\alpha$ radiation was not sufficient to arrive at a conclusive decision; in our opinion, the as-prepared dislocation structure of the crystal does not undergo any appreciable transformation.

Second, we used a two-crystal topographic recording scheme with reduced x-ray dispersion, which had no real influence on the visibility of the loops, and the results biased us in favor of periodic surface relief of the crystals as the physical cause of the observed pattern.

We should interject at this point that the pattern of periodic loops is visually observable on the crystals themselves. Moreover, a periodic structure is visible on the glass separating the crystal from the photoconductive cell, most likely originating from CdTe evaporation products formed in heating.

Inasmuch as this pattern, according to our observations, depends on the gap between the glass and the sample, which is determined by, among other conditions, the profile of the sample surface, it can be identified with the behavior of the volotile products occupying the small gap. Considerable effort continues to be devoted to the investigation of this matter, and the results of its analysis will be published later.

In this study we have investigated the structural changes of CdTe using successively incremented laser energies. A third interesting effect of irradiation is observed in this case: the formation of a mosaic twin structure.

This effect was first discerned locally in irradiation by a ruby laser at an energy of 0.8 J/cm^2. It shows up in the topograms in the form of a triangular grid with boundaries along the $\langle 211\rangle$ direction (Figs. 2a and 2c). The length of the boundaries varies from 250 μm to 50 μm.

The center of the zone with this structure does not coincide with the center of the periodic loops, but with the center of the irradiated zone. The ratio of the dimensions of the zone in two mutually perpendicular directions is 1:2.

In irradiation at an energy of 1.37 J/cm^2 this type of structure is observed over the entire area of the irradiated zone with a diameter of 7 mm except for a thin peripheral ring of width ~ 300 μm, but the actual structure is much shallower, particularly in the center of the zone (Fig. 2b). The length of the mosaic cell boundaries here is ~ 30 μm and increases to ~ 50 μm toward the periphery. At high energies (1.81 J/cm^2) this type of structure is distinctly observed only in the peripheral part of the irradiated zone; in the center it becomes disordered.

The above-described type of structure is observed against the background pattern of periodic loops and does not appear to be related to this pattern.

We have attempted to elucidate the structure of the mosaic cell boundaries. In particular, we ascertained their crystallographic orientation to be along ⟨211⟩, supporting the notion of twins rather than dislocations, which are characterized by the ⟨110⟩ direction. We then determined the detectability of the three systems of directions of the ⟨211⟩ boundaries in different reflections. Only in one reflection (444) is a mosaic structure visible without any background of images of periodic loops (which are not visible in this reflection). Two rather than three systems of cell boundaries are visible in different 422 reflections, corroborating the twin character of the boundaries.

Unfortunately, our resolution was too low to enable us to observe interactions of the laser-induced twin mosaic structure with the as-prepared dislocation mosaic structure of the crystals. It seems to us, on the whole, that the observed structure can be regarded as a recrystallization structure in the somewhat liberal interpretation of this concept[13] when extended to twins of the special type encountered in semiconductor materials. It is a well-known fact that recrystallization in metals results in the formation of high-angle boundaries. During recrystallization in semiconductors the dislocation mosaic structure is probably capable of changing into a twin mosaic structure. It is possible that this structural transformation must also be accompanied by a changes in the properties of the surface layer of CdTe, as is typical of recrystallization in general.[12,13]

For irradiation by a neodymium laser in the present study the CdTe surface was coated with an Al layer by vacuum evaporation. In the structural examinations it was noted that the presence of Al in the surface layer of CdTe has a definite influence on the recrystallization and formation of the twin mosaic structure. When Al is dissolved in CdTe in large concentration, it can promote the formation of a fine-scale twin mosaic structure. Investigations are continuing in this area.

4. DISCUSSION OF THE RESULTS

We have described preliminary results of a study of laser-induced structural changes in CdTe surface layers under conditions of impurity doping. We have observed explicit evidence of structural transformation, which is not unexpected in light of the fact that laser irradiation is accompanied by heating of the surface layer of CdTe. The heating can be so intense as to cause melting of the surface layer. It is interesting to note that at an irradiation energy ~ 0.3 J/cm^2, for which the pattern of periodic loops observed by us becomes appreciable, earlier calculations[10] give the thickness of the melted layer $\sim 250-300$ Å. The real structure of the crystal surface exhibits overall improvement in this case. At the same time, however, we do not observe any significant change in the structure of the surface layer. In our opinion, a distinctly observable recrystallization and pronounced structural transformation of the surface take place at higher energies $\geqslant 0.8$ J/cm^2, which, according to the same calculations,[10] correspond to a molten thickness ~ 1400 Å. It is conceivable that this process could be controlled not only by varying the irradiation energy, but also by means of suitable coatings to inhibit evaporation of the semiconductor. We believe that an irradiation regime with distinct recrystallization promises to be the most practical for laser impurity injection.

It should be noted that the scale of the structural changes in CdTe under the influence of laser irradiation could be smaller than that observed by x-ray topography. Laser processing is known to have many ramifications,[14] but the investigation of CdTe in this setting has only just begun.

This work is partly supported by the Russian Fund for Fundamental Research, Grant No. 97-02-18331.

[1] T. Tokuyama, in *Laser and Electron Beam Processing of Materials*, edited by C. W. White and P. S. Peercy (Academic Press, New York, 1980), p. 608.

[2] C. An, H. Tews, and G. Cohen-Solad, J. Cryst. Growth **59**, 289 (1982).

[3] J. Narayan, in *Laser and Electron Beam Processing of Materials*, edited by C. W. White and P. S. Peercy (Academic Press, New York, 1980), p. 397.

[4] M. von Allmen and S. S. Lau, in *Laser and Electron Beam Processing of Materials*, edited by C. W. White and P. S. Peercy (Academic Press, New York, 1980), p. 524.

[5] A. T. Akobirova, O. A. Matveev, S. M. Ryvkin, and A. Kh. Khusainov, Fiz. Tekh. Poluprovodn. **10**, 2127 (1976) [Sov. Phys. Semicond. **10**, 1265 (1976)].

[6] A. R. Lang, in *Diffraction and Microscopic Methods in Material Science* [in Russian], Metallurgiya, Moscow (1984), p. 364.

[7] I. L. Shul'pina, Kristallografiya **39**, 270 (1994) [Crystallogr. Rep. **39**, 227 (1994)].

[8] I. L. Shul'pina, T. S. Argunova, and V. V. Ratnikov, Zh. Tekh. Fiz. **65**(4), 180 (1995) [Tech. Phys. **40**, 388 (1995)].

[9] I. L. Shulpina and T. S. Argunova, J. Phys. D **28**, A47 (1995).

[10] R. O. Bell, M. Toulermonde, and P. Siffert, J. Appl. Phys. **19**, 313 (1979).

[11] O. A. Matveev and D. V. Nakhabtsev, Inventor's Certificate No. 1431391 (June 15, 1988).

[12] J. Shen, D. K. Aidun, L. L. Regel, and W. R. Wilcox, J. Cryst. Growth **132**, 250 (1993).

[13] S. S. Gorelik and M. Ya. Dashevskiĭ, *Materials Science in Application to Semiconductors and Dielectrics* [in Russian], Metallurgiya, Moscow (1988), p. 574.

[14] F. Kh. Mirzoev, V. Ya. Panchenko, and L. A. Shelepin, Usp. Fiz. Nauk **166**, 3 (1996).

Translated by James S. Wood

Influence of uniaxial compression at 80 K on the formation of radiation defects in KCl, KBr, and KI crystals

A. Z. Bekeshev, E. T. Sarmukhanov, Sh. Zh. Sagimbaeva, S. K. Tulepbergenov, and K. Sh. Shunkeev

Aktyubinsk State University, 463000 Aktyubinsk, Kazakhstan

E. A. Vasil'chenko and A. A. Élango

Institute of Physics of Estonia, EE2400 Tartu, Estonia

(Submitted June 27, 1997)
Fiz. Tverd. Tela (St. Petersburg) **40**, 73–78 (January 1998)

The influence of uniaxial compression at 80 K on the efficiency of formation of stable radiation defects in KCl, KBr and KI crystals is investigated by absorption spectroscopy. It is found that compression along the ⟨100⟩ directions does not alter the efficiency of radiation defect formation in KCl and KBr crystals, but in KI the efficiency drops by more than an order of magnitude. It is concluded from a semiquantitative analysis that the observed difference is attributable to the impossibility of H centers fitting into the compression-reduced interstitial voids in KI, whereas several multiples of ten-percent compression is required to produce the analogous effect in KCl and KBr. [S1063-7834(98)01601-3]

It has been shown previously[1–3] that initial plastic deformation produces a large number of vacancy defects in a crystal, which take on the role of stabilizing traps for mobile electron excitations and radiation defects. The trapping of electron excitations (which is crucial at low, helium temperatures) tends to lower the efficiency of radiation defect formation, whereas the trapping of mobile radiation defects (which is important at temperatures above the temperature of delocalization of H centers) tends to raise the efficiency.

Fundamentally new and interesting possibilities for investigating the decay of electron excitations are found when a crystal is subjected directly to mechanical stress, which produces elastic deformation.[4,5] Phenomena can occur in the stressed crystal from a change in the symmetry of the lattice and can alter certain critical distances in it; the latter effect, in turn, can influence the primary act of decay of electron excitations, both radiative and nonradiative, with the formation of radiation defects (F and H pairs).

We have previously[4,5] reported preliminary studies of the influence of uniaxial compression at 80 K on the x-ray luminescence spectra of KCl, KBr, and KI crystals. We have observed a significant increase in the efficiency of intrinsic (not impurity-related) luminescence in stressed crystals. These investigations have since been extended to a CsI crystal.[6] It has been hypothesized that the cause of the enhancement of intrinsic luminescence is a decrease in the mean free path of free electron excitations (excitons and holes) when the translational symmetry of the crystal is disrupted by uniaxial compression. This process will necessarily reduce the transfer of excitation to defects and raise the efficiency of self-localization of electron excitations. A special study has been mounted to confirm and develop this hypothesis, and in the present article we focus on the specific characteristics of the nonradiative channel of decay of electron excitations.

Adsorption spectroscopy has been used to investigate the structure and formation efficiency of radiation defects in the x irradiation (at 80 K) of KCl, KBr, and KI crystals stressed in uniaxial compression at 80 K.

We also carry out a semiquantitative analysis of the possibilities of the stable formation of halogen defects at the instant of decay of electron excitations in a field of elastic displacements in stressed crystals.

The KCl and KBr crystals were grown by the Stockbarger method from raw material purified by a combination method of treatment developed at the Institute of Physics of Estonia in Tartu.[7] The final stage of purification entailed 60-fold zone melting, which had the effect of reducing the majority of impurities in the crystals to the level of $10^{-6}-10^{-8}$ mole fractions. Some of the KI crystals were grown by the Kyropoulos procedure in an inert-gas atmosphere, and others were supplied by Harshaw/Bicron, having a concentration of sodium ions at the level of $10^{-4}-10^{-5}$ mole fractions.

The crystals were stressed in vacuum along the crystallographic ⟨100⟩ direction from the end section of the crystal at 80 K directly in a nitrogen cryostat. At low temperatures, according to Refs. 8 and 9, the slip process is frozen in (the fraction of plastic deformation decreases), and the elastic limit of the crystals is raised. At 80 K, however, none of these effects radically alters the plastic properties of alkali-halide crystals. The strain of the crystal was set by means of a compressing screw (with a pitch of 1 mm per full revolution of the crystal holder), which imparted translational motion to the pressed rod. The structure of the cryostat was such that the lower limit of strain of the crystal could be set experimentally in vacuum at 80 K; the stress could be removed

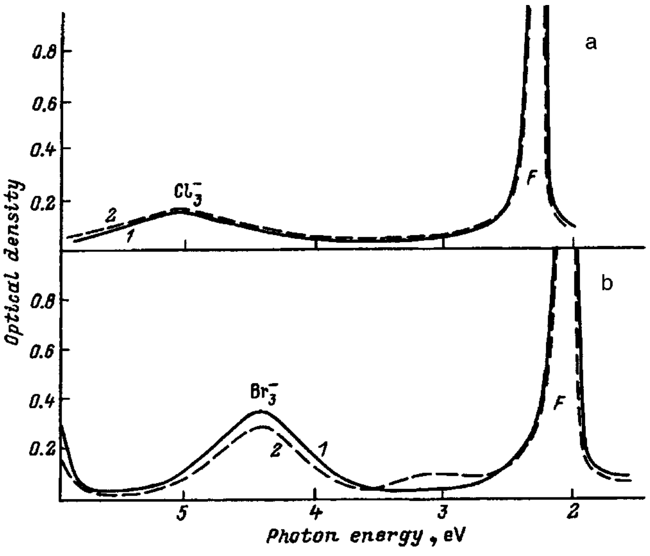

FIG. 1. Absorption spectra measured at 80 K for KCl (a) and KBr (b) crystals after 3-h x irradiation at 80 K. 1) Without deformation ($\varepsilon = 0\%$); 2) with compression ($\varepsilon = 2\%$) along ⟨100⟩ at 80 K.

at any time and restored during the experiment.

The crystals were exposed to W x rays from a URS-55 machine operating at 45 kV, 18 mA. The absorption spectra of the stressed and x-irradiated crystals were measured at 80 K by means of a Specord M40 spectrophotometer in the spectral range 1.7–6.2 eV.

The basic methodological approach was to compare the nature of the radiation defects and the efficiency of their formation during x irradiation in two samples: one unstrained and one uniaxially compressed at 80 K. To eliminate the risk imposed by inhomogeneities in the objects, the samples used for the comparative experiments were two precisely cleaved, mirror-image halves.

Figures 1 and 2 shows the excited absorption spectra of x-irradiated KCl, KBr, and KI crystals. It is evident from a comparison of the spectra of the unstrained crystals (curves *1*) and the stressed crystals (curves *2*) that the nature of the radiation defects formed in both cases does not change under load application. The principal radiation defects in all the crystals are F and X_3^- centers (X for halogen): The F and Cl_3^- centers in KCl crystals have absorption bands with maxima at 2.3 eV and 5.2 eV, respectively; the F and Br_3^- centers in KBr crystals have absorption maxima at 2.06 eV and 4.6 eV; the F and I_3^- centers in KI crystals have absorption maxima at 1.87 eV and 3.6 eV, respectively. The formation of α centers (excitation of a halogen in the field of an anion vacancy) has also been observed.

Significant changes in the formation efficiency formation of F centers under the application of stress could not be detected in the KCl and KBr crystals. Only a certain redistribution of halogen radiation defects was observed (Fig. 1b), but they did not alter the total number of generated F-center radiations.

The application of uniaxial compression has an altogether different influence on the efficiency of radiation defect formation in a KI crystal. It is evident from Fig. 2a that the number of radiation defects in a stressed crystal is more than an order of magnitude lower than those formed by isodose x irradiation of an unstressed crystal. The number of complementary F and I_3^- centers and the number of α centers both

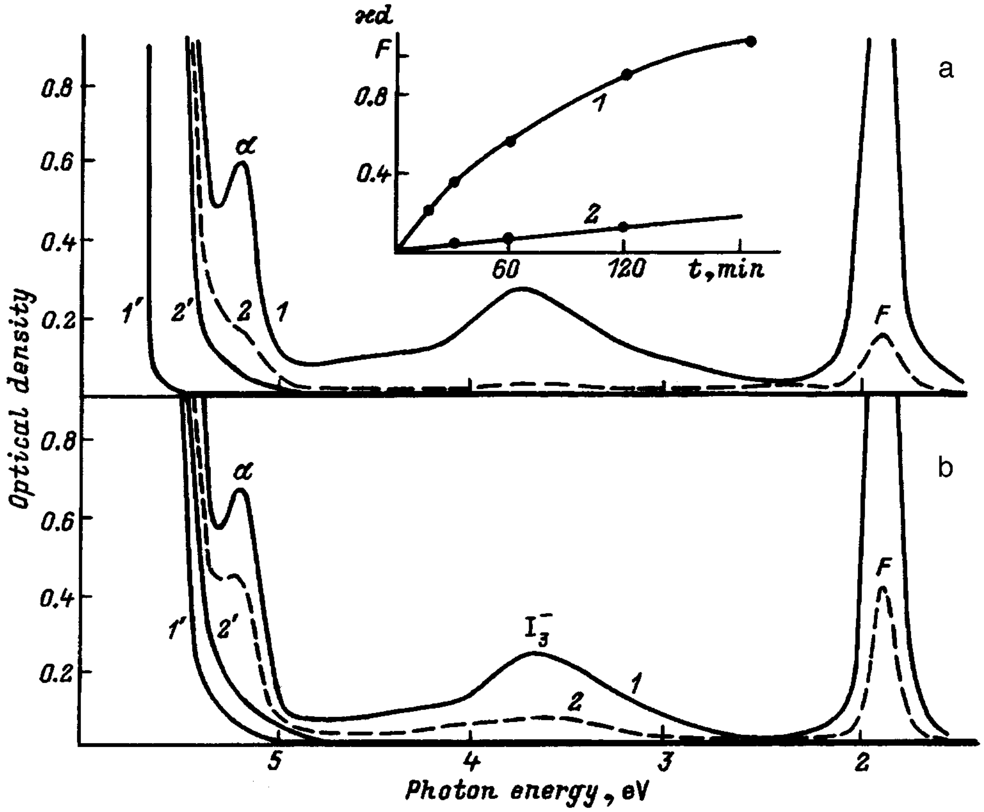

FIG. 2. Absorption spectra of KI crystals. a) As-cleaved crystal, 3-h x irradiation; b) ''defective'' crystal, 1-h x irradiation; *1′,2′*) before irradiation; *1,2*) after irradiation; *1′,1*) spectra measured without compression; *2′,2*) with compression along ⟨100⟩ to 2%. Inset: curves representing the buildup of F centers in an as-cleaved KI crystal: *1*) without deformation; *2*) with compression ($\varepsilon = 2\%$) along ⟨100⟩ at 80 K.

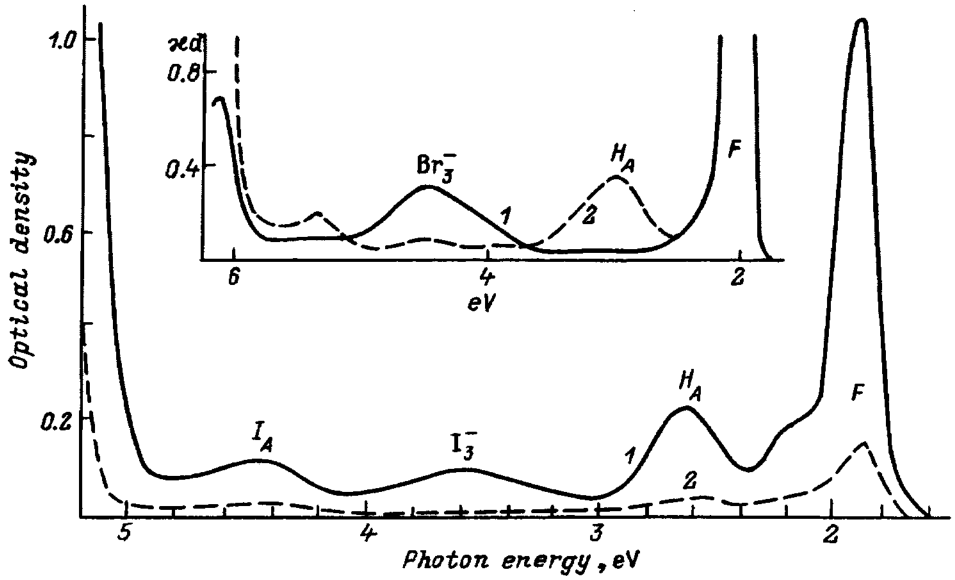

FIG. 3. Absorption spectra of KI-Na (1×10^{-3} mol. %) and KBr-Na (5×10^{-4} mol. %) (inset) at 80 K after 1-h x irradiation. *1)* Without compression; *2)* with compression at 80 K ($\varepsilon=2-3\%$) along ⟨100⟩.

decrease in this case (i.e., the efficiency of formation of α centers mimics the efficiency of formation of F and I_3^- centers). The inset to Fig. 2a shows the kinetics of defect growth as the x-irradiation dose is increased. A drop in the rate of radiation defect formation under compressive stress and the absence of the initial stage of the growth curve are clearly visible.

In view of our capability of recording the decay of fundamental absorption in a KI crystal, we also investigated the changes taking place in this spectral region. The fundamental absorption edge of the as-prepared, unstrained crystal (curve *1′* in Fig. 2a) shifts toward the low-energy end of the spectrum under the application of stress (curve *2′* in Fig. 2a). After x irradiation of the stressed crystal and annealing of the resulting radiation defects at temperatures up to 490 K the fundamental absorption edge (curve *1′* in Fig. 2b) does not fully return to the initial state, and a second compression of the crystal (curve *2′* in Fig. 2b) shifts it still farther toward the low-energy end of the spectrum. These shifts reflect the formation of predominantly vacancy defects in the course of plastic deformation of the crystal.[1] The observed shifts indicate that, under 2–3% uniaxial compression at 80 K, the crystal is not only elastically deformed,[4] but also undergoes plastic deformation, which persists after the removal of stress. We have performed control measurements to discern how plastic deformation can influence the resulting drop in efficiency of radiation defect formation in a KI crystal. Now the initial object of investigation was, in our terminology, a ''defective'' KI crystal, which had already been subjected to compression at 80 K, x irradiation of the compressed crystal at 80 K, and heating to 490 K (curve *1′* in Fig. 2b). The formation of radiation defects in this crystal is illustrated by curve *1* in Fig. 2b. When this x-irradiated crystal is again heated to 490 K to eliminate (anneal out) radiation defects (curve *2′* in Fig. 2b) and is then once again x-irradiated at 80 K, but now in the uniaxially compressively stressed state, the formation of radiation defects is again observed to diminish (curve *2* in Fig. 2b). The reduction in this case is somewhat less than for the as-prepared, unstrained crystal (Fig. 2a), but is still very pronounced. In our opinion, one of the possible causes of the slightly weaker influence of uniaxial compression in the defective crystal (Fig. 2b) is a decrease in the homogeneity of the crystal due to the formation of various vacancies. This process diminishes the uniformity and magnitude of the applied uniaxial compression throughout the total volume of the crystal.

We can assume therefore that the observed reduction in the radiative formation of stable defects under uniaxial compression in a KI crystal is attributable to elastic deformation, which lowers the point symmetry of the crystal from O_h to D_{4h} (Ref. 10).

The reduction of radiation defect formation in conjunction with lowering of the crystal symmetry can be attributed to various causes: The channel of exciton decay into F-H pairs becomes unfavorable, reverse recombinations increase as a result of the difficulties of separating primary F-H defects, or the efficiency of association of interstitial H centers decreases. The possibility of the latter phenomenon is indicated by an effect that we have observed previously[11] in KBr crystals containing a sodium impurity: a redistribution of the efficiency of association of H centers among different channels under uniaxial compression.

It has been shown that the formation efficiency of Br_3^- centers in the interaction of two H centers decreases, while the efficiency of localizing of H centers about the sodium impurity increases in a KBr-Na crystal subjected to compression. The reason for this effect is abatement of the long-range, inherently elastic, mutual interaction of two H centers.

To verify whether or not a similar effect is responsible for the reduction of radiation defect formation in a stressed KI crystal (Fig. 2), we have investigated the influence of uniaxial compression on radiation defect formation in a KI crystal containing a sodium impurity. The measurement results are shown in Fig. 3. It is evident from a comparison of curves *1* and *2* that the formation efficiency of radiation defects in a KI-Na crystal subjected to uniaxial compression, as in the pure KI crystal, decreases substantially. This fact is a significant departure from the result obtained for a KBr-Na

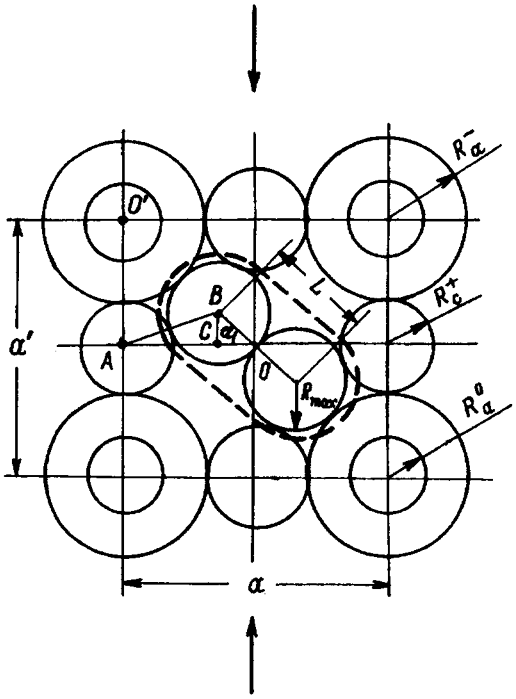

FIG. 4. Structure of the H center for the calculation of $R_{\max}$ in an fcc alkali-halide crystal in compression along the ⟨100⟩ direction.

crystal (see the inset to Fig. 3), where all that is observed is a redistribution of halogen defects (Br_3^--H_A) with conservation of the total number of resulting radiation vacancy defects (F-α centers).

We can therefore conclude on the basis of these results that the application of uniaxial compression and x irradiation at 80 K induces a substantial (by more than an order of magnitude) reduction of the formation efficiency of stable radiation defects in a KI crystal, whereas similar treatment does not alter the efficiency of radiation defect formation in pure KCl and KBr crystals. We have also established experimentally that the reduction of defect formation in a KI crystal is attributable to uniaxial elastic deformation of the crystal and that it is not related to a change in the association of primary interstitial defects in the stressed sample.

In seeking to explain the causes of the difference between the influence of uniaxial compression in KI, on the one hand, and in KCl and KBr, on the other, we make use of a recently[12] modified geometrical model of an alkali-halide crystal. According to this model, anions (X^-) are assumed to be ''elastic,'' and cations (M*) and halogen atoms (X^0) are assumed to be perfectly rigid (nondeformable). We assume that the diameter of a newly formed H center is dictated by the radius of the halogen atom ($R_a^0 0$), and the maximum possible void radius ($R_{\max}$) for occupation by the H center is determined by the elasticity of the anions. If $R_{\max} > R_a^0$, favorable conditions are established for the formation of an H center, but if $R_{\max} < R_a^0$, then the halogen atom (and, hence, the H center) does not fit in the designated void.

The maximum possible void radius for the postulated H center, according to the geometrical model[12] in Fig. 4, is

$$R_{\max} = \frac{1}{2}\sqrt{a^2 + L^2 - 2aL\cos\alpha - R_c^+}, \tag{1}$$

where R_c^+ is the cation radius, a is the lattice constant, and L is the bond length in the H center; it is defined in the interval $(R_a^+ + R_a^0) \geqslant L \geqslant 2R_a^0$.

If we assume that uniaxial compression (or tension) along the crystallographic ⟨100⟩ direction is achieved by virtue of anion elasticity, the angle α, which is an indicator of how the crystal is affected by deformation, varies as a function of the degree of elastic stress. It follows from Fig. 4 that

$$\cos\alpha = AO/OO' = 1/\sqrt{1+Q^2}, \tag{2}$$

so that $Q = a'/a = 1 \pm \varepsilon$ [Q is the relative variation of the lattice constant due to external compression or tension, a' is the lattice constant in compression (tension), and ε is the elastic strain (in %)]. The lattice dilates for $Q > 1$ and compresses for $Q < 1$. We have investigated the latter case.

Assuming that $L = 2R_a^0$ and taking Eqs. (1) and (2) into account, we find

$$R_{\max} = \frac{(a^2 - 4(R_c^+)^2)}{(8R_c^+ + 4a/\sqrt{1+(1-\varepsilon)^2})}. \tag{3}$$

The maximum elastic strain $\varepsilon_{\max}$ at which the H-center occupation condition is satisfied ($R_{\max} = R_a^0$) can be estimated from Eq. (3):

$$\varepsilon_{\max} = 1 - \sqrt{[4aR_a^0/(a^2 - 4(R_c^+)^2 - 8R_a^0 R_c^+)]^2 - 1}. \tag{4}$$

The results of calculations of $R_{\max}$ and $\varepsilon_{\max}(\%)$ for $R_{\max} = R_a^0$ are summarized in Table I.

We see that the ratio of the void radius to the radius of the halogen atom ($R_{\max}/R_a^0$) increases in the order KI→KBr→KCl, exemplifying the increasingly favorable imbedding of H centers in the corresponding crystals. We recall the well-known fact that the efficiency of radiation defect formation increases in the same order. According to our data, occupation by the H center is the fullest possible ($R_{\max}/R_a^0 = 0.999$) in the unstrained KI lattice. At the lowest

TABLE I. Parameters of the KCl, KBr, and KI lattices.

Crystal	a, Å (Ref. 12)	R_a^0, Å (Ref. 13)	$R_{\max}$, Å	$R_{\max}/R_a^0$	$\varepsilon_{\max}$, % (for $R_{\max} = R_a^0$)
KI	7.066	1.4	1.399	0.999	−0.16
KBr	6.597	1.15	1.243	1.081	24.41
KCl	6.293	1.0	1.143	1.143	43.18

Note: Here a is the lattice constant,[12] R_a^0 is the atomic radius,[13] $R_{\max}$ is the maximum possible void radius for occupation by an H center, $R_{\max}/R_a^0$ is the ratio of the void radius to the radius of the H center, and $\varepsilon_{\max}$ is the maximum strain at which an H center fits into the lattice.

compression of the KI lattice a situation arises where $R_a^0 > R_{\max}$, and it is no longer possible for the H center to fit the void. In KBr and KCl crystals the analogous changes must take place at very high compression ratios: 24.4 and 43.2, respectively. These figures indicate the presence of a large reserve of empty space for occupation by H centers.

Consequently, the phenomenon observed in this study, i.e., the marked reduction of radiation defect formation in the KI crystal under uniaxial compression at 80 K, is most likely attributable to attenuation of the nonradiative channel for the formation of F-H pairs, owing to the impossibility of H centers fitting the compression-reduced interstitial voids of the KI lattice. Not to be overlooked is the well-known (see, e.g., Refs. 14 and 15) reduction of radiation defect formation in a KI crystal by a similar mechanism when the x-irradiation temperature is lowered to 4.2 K.

In KCl and KBr crystals the formation efficiency of short-lived F, H centers scarcely changes at all in the temperature range from 80 K down to 4.2 K.[16] This behavior is also fully consistent with our present results, which show that uniaxial mechanical compression (much greater than the compression encountered in cooling) does not alter the efficiency of radiation defect formation in KCl and KBr crystals.

When the process of decay into F-H pairs weakens, the energy of the decaying electron excitation must transfer either into the radiative process or into another nonradiative process associated with the generation of a large number of lattice modes.[17] We have previously[4,5] remarked that the amplification of the intensity of intrinsic luminescence in a KI crystal uniaxially stressed at 80 K is much larger than in an analogously stressed KBr crystal. On this basis we can assume that, whereas the amplification of the luminescence intensity in KBr is mainly attributable to a reduction of losses associated with the transfer of excitation to defects in the stressed crystals, the amplification of the luminescence intensity in KI can be attributed to the same factor plus attenuation of the decay process into F-H pairs. A powerful consideration in regard to this explanation is the absence of a strict quantitative dependence in the degrees of amplification of intrinsic luminescence and reduction of impurity luminescence in KI.

The lack of any influence of uniaxial compression at 80 K on the efficiency of radiation defect formation in KCl and KBr indicates that the process of decay into F-H pairs in these crystals is highly stable against the geometrical factor. This consideration is possibly one reason why the efficiency of radiation defect formation in KCl and KBr does not diminish when the temperature is lowered to 4.2 K (Refs. 14 and 15). Thermal compressions, which drastically reduce the efficiency of defect formation in KI, are incapable of affecting the formation of F-H pairs in KCl and KBr.

In closing, we are grateful to S. M. Ryabykh for a discussion of the problem.

[1] A. T. Akilbekov, E. A. Vasil'chenko, E. T. Sarmukhanov, K. Sh. Shunkeev, and A. A. Élango, Fiz. Tverd. Tela (Leningrad) **33**, 868 (1991) [Sov. Phys. Solid State **33**, 492 (1991)].

[2] A. Lushchik, Ch. Lushchik, N. Lushchik, A. Frorip, and O. Nikiforova, Phys. Status Solidi B **168**, 413 (1991).

[3] E. Vasilchenko, E. Sarmukhanov, K. Shunkeev, and A. Elango, Phys. Status Solidi B **174**, 155 (1992).

[4] A. Z. Bekeshev, E. A. Vasil'chenko, E. T. Sarmukhanov, K. Sh. Shunkeev, and A. A. Élango, Fiz. Tverd. Tela (St. Petersburg) **36**, 330 (1994) [Phys. Solid State **36**, 180 (1994)].

[5] K. Sh. Shunkeev, E. A. Vasil'chenko, and A. A. Élango, Zh. Prikl. Spektrosk. **62**, 156 (1995).

[6] A. Z. Bekeshev, E. A. Vasil'chenko, K. Sh. Shunkeev, and A. A. Élango, Fiz. Tverd. Tela (St. Petersburg) **39**, 87 (1997) [Phys. Solid State **39**, 75 (1997)].

[7] R. I. Gindina, A. A. Maaroos, L. A. Ploom, and N. A. Yaanson, Tr. Inst. Fiz. Akad. Nauk Est. SSR **49**, 45 (1979).

[8] O. V. Klyavin, S. G. Simashko, and V. D. Yaroshevich, Fiz. Tverd. Tela (Leningrad) **13**, 3508 (1971) [Sov. Phys. Solid State **13**, 2965 (1972)].

[9] T. Suzuki and H. Koizumi, in *Physics and Chemistry of Solids, International Symposium on Lattice Defect Related Properties of Dielectric Materials* (1985), p. 117.

[10] A. A. Kaplyanskiĭ, Opt. Spektrosk. **16**, 602 (1964) [Opt. Spectrosc. **16**, 329 (1964)].

[11] A. Bekeshev, E. Vasil'chenko, K. Shunkeev, and A. Élango, Fiz. Tverd. Tela (St. Petersburg) **38**, 2394 (1996) [Phys. Solid State **38**, 1316 (1996)].

[12] S. M. Ryabykh and L. T. Bugaenko, Izv. Akad. Nauk Latv. SSR Ser. Fiz. Tekh. Nauk **2**, 77 (1990).

[13] B. K. Vaĭnshteĭn, V. M. Fridkin, and V. L. Indenbom, *Modern Crystallography*, Vol. 2 (Nauka, Moscow, 1979).

[14] J. D. Konitzer and H. N. Hersh, J. Phys. Chem. Solids **27**, 771 (1966).

[15] M. Ikezawa, K. Shirahata, and T. Kojima, Sci. Rep. Tohoku Univ. **1**, 45 (1969).

[16] R. T. Williams, Semicond. Insul. **3**, 251 (1978).

[17] Ch. B. Lushchik and A. Ch. Lushchik, *Decay of Electronic Excitations with the Formation of Defects in Solids* [in Russian], Nauka, Moscow, 1989.

Translated by James S. Wood

Activation energy of spatial separation of the components of interacting pairs

V. M. Lisitsyn, V. I. Korepanov, and A. N. Yakovlev

Tomsk Polytechnical University, 634004 Tomsk, Russia

(Submitted July 16, 1997)
Fiz. Tverd. Tela (St. Petersburg) **40**, 79–80 (January 1998)

[S1063-7834(98)01701-8]

Frenkel defect pairs in ionic crystals, created during the decay of electronic excitations, annihilate for the most part; the remainder are transformed into stable color centers and accumulate in the crystal. The temperature dependence of the efficiency of color center accumulation is complex. Of especial interest in this dependence is a segment of the temperature range in which substantial growth of the color center accumulation efficiency is observed. As we have shown, the reason for the growth in the accumulation efficiency in this range is an increase, with rising temperature, of the probability of spatial separation of the components of the radiation-generated interacting pairs via thermally activated motion of the mobile component.[1,2]

In the present paper, we use computer modeling to analyze the process of spatial separation of F–H pairs with prescribed initial distribution of the components, with the aim of determining the dependence of the activation energy of the accumulation process on the parameters governing the thermally activated motion of the mobile component of the pair in the field of the immobile component.

We adopted the following model to calculate the separation of correlated F–H pairs created during the decay of electronic excitations, where this separation takes place via thermally activated motion of the mobile component of the pair (the H center). At temperatures above that necessary for delocalization (20–60 K in alkali-halide crystals) the H center can undergo thermally activated motion via successive hops to neighboring lattice sites. Since the activation energy to reorient the H center is lower than that necessary for a hop (see, e.g., Ref. 3), the model assumes that transitions of an H center are possible in any direction regardless of its initial orientation. The H center is found in the attractive field of the F center. This is taken into account in the model by a distortion of the potential relief for motion of the H center in the immediate vicinity of the F center. The potential relief for motion of the H center in the field of the F center is depicted schematically in Fig. 1. The interaction potential of the F center with the H center is unknown. We prescribe it in the form $E(r)=-a\ \exp(-br)$ allowing us to vary both the magnitude of this interaction through the parameter a and its stength (long-range action) through the parameter b.

In the calculations we assigned the initial position of the H center to coincide with one of the lattice sites in the immediate vicinity of the F center. Then, using the Monte Carlo method we calculated the probabilities of transition of the H center from its assigned state to any possible new state via a series of successive jumps. The transition of the H center to the zero state in the model means its annihilation with the F center and disappearance. In the case when the H center winds up beyond 12 spheres of its possible positions around the F center, it is taken to have transformed into a stable center under the conditions of the experiment and to be no longer able to annihilate. The probability that an H center survives up to the prescribed time of its migration was calculated as a function of the temperature of the crystal. A given H center was assumed to have survived regardless of its coordinates (inside or outside 12 spheres around the F center). The effective activation energy of spatial separation of the interacting components of the F–H pairs (or the effective activation energy of defect accumulation) was calculated from the temperature dependence of the probability of survival of an H center.

The effective activation energy of spatial separation of the interacting F–H pairs was calculated as a function of the activation energy of migration of an H center E_{H} and the parameters of the interaction potential of an F and an H center, a and b.

Results of calculating the activation energy E_p of spatial separation of the components of F–H pairs in a crystal having the structure when the H center is initially located at a lattice site nearest the F center (the state [110] for the F center located at the origin) are presented in Table I. The calculations were performed for 10^{-8} s separation of the F–H pair following start of the experiment with the potential parameters indicated in the table. As the calculations show, the effective activation energy of spatial separation of the components of the F–H pairs E_p is independent of the acti-

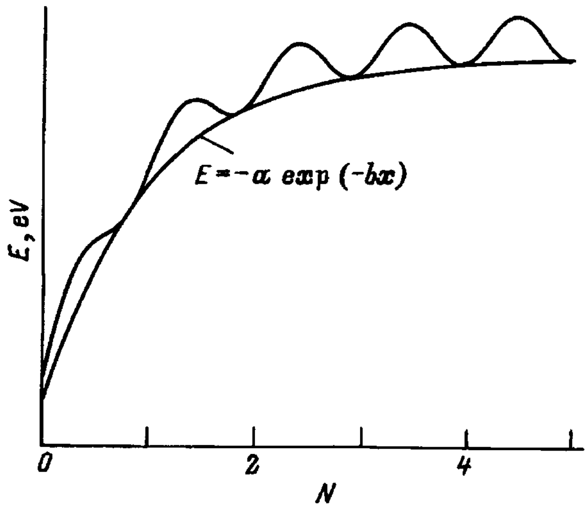

FIG. 1. Schematic form of the potential relief for motion of an H center in the field of an F center. The number of the state N denotes the order of the sphere of equivalent mutual displacements of the centers.

TABLE I. Effective activation energy E_p of spatial separation of F and H centers located on neighboring lattice sites tabulated as a function of the parameters of their interaction potential $E(r)=-a\ \exp(-br)$ and the activation energy of migration of the H center E_H in a crystal with NaCl structure.

E_H, eV	a	E_p, eV		
		$b=7$	$b=8$	$b=9$
height 0.02	6	0.0311	0.0105	0.0034
	9	0.0536	0.0199	0.0064
	12	0.0833	0.0305	0.0102
	15	0.104	0.0414	0.0149
0.04	6	0.0311	0.0105	0.0034
	9	0.0536	0.0199	0.0064
	12	0.0833	0.0305	0.0102
	15	0.104	0.0414	0.0149
0.06	6	0.0311	0.0105	0.0034
	9	0.0536	0.0199	0.0064
	12	0.0833	0.0305	0.0102
	15	0.104	0.0414	0.0149
0.08	6	0.0311	0.0105	0.0034
	9	0.0536	0.0199	0.0064
	12	0.0833	0.0305	0.0102
	15	0.104	0.0414	0.0149

vation energy of migration of an H center E_H, varies weakly with time, and tends toward a limiting value. It is found that E_p depends on the a and b parameters of the interaction potential of an F and an H center.

The activation energy of spatial separation depends on the initial distribution of the components of the separating pair. Table II, for example, presents results of a calculation of E_p for the case in which the starting states for initiation of motion of the H centers are states 1 and 2 corresponding in a crystal with NaCl structure to sites [110] and [200] relative to the F center, which are equiprobable in these two states. Table II also presents results of calculations for $E_H=0.06$ eV, $a=15$ eV, and $b=8$. The above conclusion also applies to any other values of the interaction potential parameters and E_H.

TABLE II. Dependence of the activation energy of spatial separation of F and H centers on their initial mutual displacement in a crystal with NaCl structure.

Initial distribution over states			
0	1	2	E_p, eV
0	1	0	0.0414
0	0	1	0.0076
0	0.5	0.5	0.0142

We also calculated the dependence of the activation energy of spatial separation on the interaction potential parameters and activation energy of migration of the H center in a crystal having the fluorite structure. Qualitatively, the dependence is quite similar to that described above. But for all the input parameters the same, in a crystal with fluorite structure E_p turns out to be 2–3 times lower than in a crystal with NaCl structure.

The calculations provide a qualitative picture of the separation process of correlated, close-lying, interacting Frenkel pairs formed during the decay of electronic excitations. The trajectory of the mobile component of the pair in the field of the immobile component bound with it, for example an H center in the field of an F center, has a complicated character. The trajectory depends on the ratio of the magnitudes of the barriers to jumps of the mobile component for all possible directions and also on the temperature of the crystal. At low temperatures, but still sufficient for an H center to overcome the lowest barrier to a jump, motion of an H center is terminated by annihilation with an F center as a result of one or more jumps in the direction of the F center. As the temperature is increased, the probability of jumps of an H center in a state having the same or greater distance from the F center increases, i.e., as the temperature is raised, the H center traverses a longer path before annihilation or passes beyond the limits of the interaction region. The most probable separation trajectory of an H center is a spherical spiral. This means that the speed of displacement of a mobile defect from an immobile one in whose interaction field it is found is much less than its linear velocity of motion. This is true for the motion of any defect in a crystal containing other defects. The speed of displacement of a defect should decrease sharply as it passes by another defect with which there is a mutual attraction or repulsion. This effect, obviously, can show up in tunneling processes. Retardation of the migration of a defect near another defect should lead to a growth of the efficiency of the possible tunneling processes between them.

[1] V. M. Lisitsyn, Izv. Vuzov, Fizika *2*, 86 (1979).

[2] V. M. Lisitsyn, V. I. Korepanov, and A. N. Yakovlev, Izv. Vuzov, Fizika *11*, 5 (1996).

[3] Ch. B. Lushchik and A. Ch. Lushchik, *Decay of Electronic Excitations with Defect Formation in Solids* [in Russian], Nauka, Moscow, 1989.

Translated by Paul F. Schippnick

Influence of the concentration of Ca impurity on the magnetic threshold of the magnetoplastic effect in NaCl crystals

V. I. Al'shits, E. V. Darinskaya, and O. L. Kazakova

Institute of Crystallography, Russian Academy of Sciences, 117333 Moscow, Russia

(Submitted June 5, 1997)
Fiz. Tverd. Tela (St. Petersburg) **40**, 81–84 (January 1998)

It is found experimentally that the threshold magnetic field B_c for the magnetoplastic effect, i.e., the field at which the depinning of dislocations from paramagnetic impurities in an external magnetic field begins to be observed, increases with increasing concentration C of Ca impurity in NaCl crystals in the range $C=(0.5-100)$ ppm. It is shown that the dependence $B_c(C)$ exhibits a distinct tendency toward saturation. The physical interpretation of the observed dependence rests on the notion that as the impurity concentration C increases, the average size of the impurity complexes increases and, accordingly, the local atomic configuration around the impurity atoms changes according to a definite pattern. In particular, the average number $\overline{n_v}$ of cation vacancies among the nearest neighbors increases from 1 to 6 as the number N of Ca atoms in the complex increases, and this trend, in turn, should cause the thermal vibration amplitude of the Ca atoms to increase. In other words, the phenomenon in question appears to be physically analogous in its microscopic mechanisms to the previously observed increase of B_c with increasing temperature. The proposed interpretation is further supported by good correlation of the experimental dependence $B_c(C)$ with the calculated function $\overline{n_c}(N)$. [S1063-7834(98)01801-2]

This paper is a continuation of an investigation of the magnetoplastic effect,[1–9] which entails the depinning of dislocations from paramagnetic centers in nonmagnetic crystals under the influence of a magnetic field. We assume that the depinning time τ_{dp} is determined by the evolution in the magnetic field of a spin radical pair in the system {paramagnetic pin-dislocation} to a new state, in which the spin deterrent is lifted from a particular process (e.g., electron transition) that radically alters the configuration of the system and, in particular, the energy of interaction in it, thereby releasing the dislocation from its pinning site. A physical scheme of this kind has proven itself to be highly beneficial in the interpretation of the observed influence of magnetic fields on the rates of chemical reactions,[10] photocurrents in semiconductors,[11] and a great many other processes.[12] In every case the occurrence of the corresponding phenomena has required that the spin evolution in the system under the influence of a magnetic field proceed more rapidly than the thermal randomization of spins. From this standpoint the magnetoplastic effect can only be observed as long as the depinning time τ_{dp} does not exceed the spin-lattice relaxation time τ_{sl} in the given dislocation-impurity system. According to our experimental data,[2] the time τ_{dp} is almost totally independent of the temperature and increases rapidly as the magnetic field is reduced, $\tau_{dp} \propto B^{-2}$. On the other hand, the converse property of the time τ_{sl} is well known, as it is only slightly sensitive to the magnetic field, but depends on the temperature T, decreasing as T increases. We infer, therefore, that there must be a threshold magnetic field B_c, governed by the relation

$$\tau_{dp}(B_c)=\tau_{sl}, \tag{1}$$

below which the magnetoplastic effect cannot be observed. This prediction has been fully confirmed in a recent study of ours,[5] in which we have measured the magnetic threshold B_c for NaCl, LiF, and Al crystals. The physical model described below is supported not only by the actual existence of the threshold B_c, but also by its shift in the proper direction after an independent controlled variation of the right or left side of Eq. (1). In particular, raising the temperature from 77 K to 300 K and thereby shortening the time τ_{sl} had the effect of raising the threshold B_c, and weak x irradiation, which, according to our own independent data,[6] shortens the time τ_{dp} in a fixed field B, lowered the level B_c. The existence of the magnetic threshold B_c of the magnetoplastic effect has also been confirmed in a recent study[9] of the influence of a magnetic field on the macroplasticity kinetics of LiF crystals subjected to active deformation at a constant strain rate $\dot{\varepsilon}=\text{const}$.

The objective of the present undertaking is to investigate experimentally the dependence of the threshold field B_c on the concentration of Ca impurity in NaCl crystals and to give a physical interpretation of the measured dependence.

The experimental procedure, based on observation of the mobilities of individual dislocations in crystals in an external static magnetic field without mechanical loading, is described in detail in Refs. 1–4. In particular, the mean-free-path l of the dislocations as a function of the magnetic field B, the duration t of magnetic processing of the samples, and the Ca impurity concentration C in them is determined from histograms of the dislocation paths measured by repeated chemical etching. We investigated NaCl crystals with four different Ca impurity concentrations: $C_1=0.5$ ppm, $C_2=1$ ppm, $C_3=10$ ppm, and $C_4=100$ ppm.

We have previously investigated the dependence $l(B,C,t)$ for these crystals.[1–5] Our intention here is merely

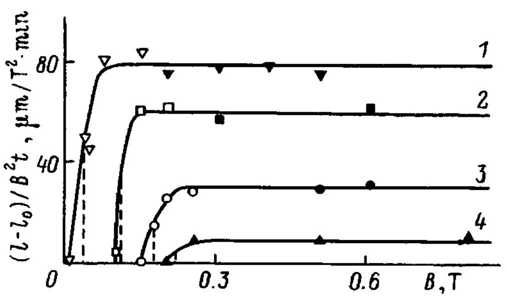

FIG. 1. Normalized mean free path of dislocations versus magnetic induction B for four Ca impurity concentrations. *1)* $C=0.5$ ppm; *2)* 1 ppm; *3)* 10 ppm; *4)* 100 ppm. The dark points of curves *1–3* are taken from Ref. 4, and those of curve *4* are taken from Ref. 5.

to augment the existing database with measurements of the dislocation mean free paths in low fields B at subthreshold levels $B<B_c$. The required functional dependence has the form

$$l=l_0+kB^2t, \qquad (2)$$

where l_0 is the background mean free path, which does not depend on the magnetic field and is governed by stray effects (e.g., the etching-out of subsurface pinning sites). As the magnetic field B is decreased, the coefficient k, which is a function of the Ca impurity concentration C but does not depend on B above the threshold, suddenly drops to zero upon passing through the threshold value $B=B_c$.

Figure 1 shows corresponding experimental plots of $k(B)=(l-l_0)/B^2t$ for four concentrations C. The most significant inference drawn from the curves is the dependence of the threshold field B_c on the Ca impurity concentration C (Fig. 2). The steep variation of $B_c(C)$ in the pure crystals with low concentrations in the vicinity of $C\sim1$ ppm gives way to a smoother behavior at concentrations $C\sim10$ ppm, distinctly tending to saturation at $C\gtrsim100$ ppm.

The observed dependence $B_c(C)$ leads to the following fairly obvious interpretation. It is a well-known fact[13–16] that the average size of impurity complexes in annealed crystals grows larger as the impurity concentration is increased. However, it has been shown[2] that this fact does not have any appreciable influence on the dependence $\tau_{dp}(B)$. More precisely, the critical frequency of rotation $\nu_c\propto B^2$ of the samples in a magnetic field, i.e., the frequency above which dislocation depinning is not observed, is identical for NaCl crystals having very different Ca concentrations. According to the model used to describe the effect,[5] this characteristic uniquely determines the time τ_{dp}:

$$\tau_{dp}=(10^{-2}-10^{-3})\nu_c^{-1}, \qquad (3)$$

implying that an elementary depinning event associated with

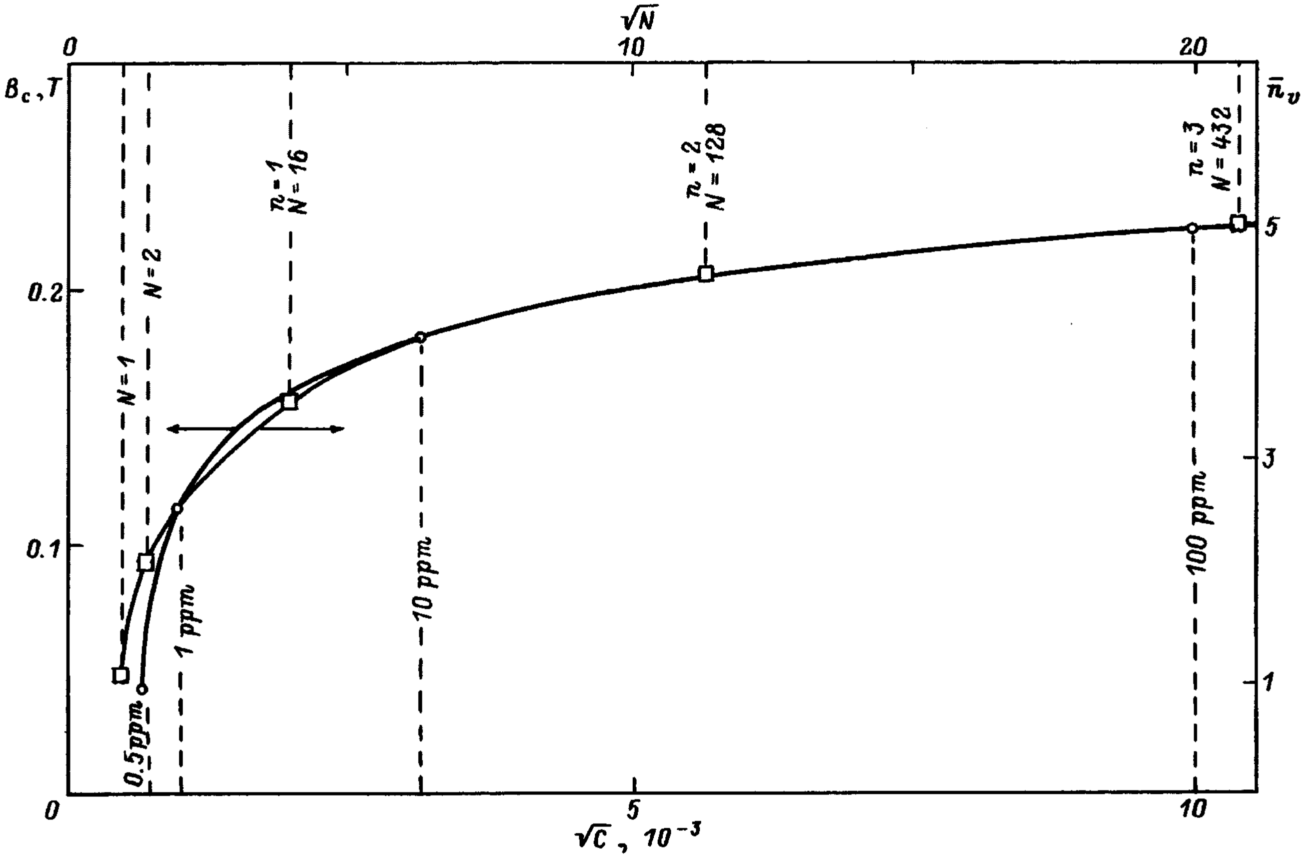

FIG. 2. Threshold magnetic field B_c versus Ca impurity concentration C, in coordinates $(B_c,\sqrt{C})$, and average number $\overline{n_v}$ of vacancies in the nearest neighborhood of a Ca impurity versus number N of Ca atoms in the complex, in coordinates $(\overline{n_v},\sqrt{N})$.

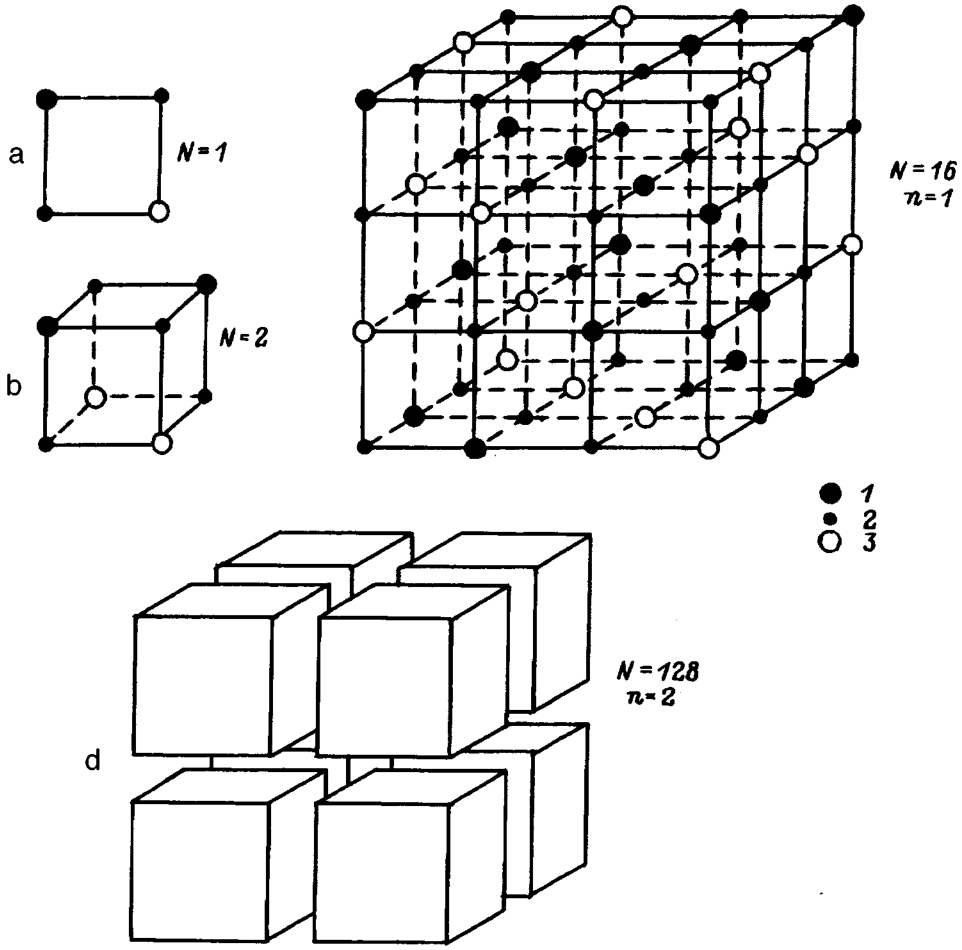

FIG. 3. Model structures of Ca complexes in NaCl crystals. *1*) Ca^{2+}; *2*) Cl^{-}; *3*) cation vacancy.

spin evolution is actually the breakoff of dislocations from individual Ca atoms rather than correlated depinning from the complex as a whole.

Consequently, according to the reported data, the proportionality factor in the relation $\tau_{dp} \propto B^{-2}$ does not depend on C. It therefore follows from Eq. (1) that the concentration dependence of the magnetic threshold B_c must be determined entirely by the function

$$B_c = \frac{\text{const}}{\sqrt{\tau_{sl}(C)}}. \tag{4}$$

The dependence $\tau_{sl}(C)$, in turn, characterizes the response of spin-lattice relaxation in the dislocation-impurity atom system to variation of the size of the impurity complexes. The physical cause of such a response can be linked to the following consideration. The response of the spin system to thermal lattice vibrations must obviously increase as the vibration amplitude increases. In particular, this is why the time τ_{sl} decreases as the temperature is raised. Clearly, the same thing happens at a fixed temperature when the number of vacancies among the nearest neighbors of each impurity atom increases. The complexes formed by the divalent Ca impurity in the ionic NaCl crystal have the distinctive feature that one cation vacancy and two Cl^{-} ions must be associated with each Ca^{2+} ion substituted for a monovalent Na^{+} ion in the complexes. It is evident from Fig. 3 that the number of vacancies n_v among the nearest neighbors of each Ca atom increases as the number N of Ca atoms in the complex increases: $n_v = 1$ for $N = 1$ (Fig. 3a), $n_v = 2$ for $N = 2$ (Fig. 3b), and for $N = 16$ in the cube-shaped complex (Fig. 3c) we have $n_v = 6$, 4, 3 or 2, depending on whether the Ca atom is situated in the interior volume $(n_v = 6)$, on the surface $(n_v = 4)$, or on an edge $(n_v = 3$ or $2)$. As N increases, the number of Ca atoms in the interior of the complex obviously increases, and the average number $\overline{n_v}$ must increase as well, tending asymptotically to 6.

Let us consider, for example, a model family of cubic complexes consisting of ‘‘unit cubes’’ having the structure shown in Fig. 3c. An n-fold increase in the edge of the cube causes the number of Ca atoms in the complex to increase to $N = 16n^3$. Figure 3d illustrates such a complex for $n = 2$ and $N = 128$. It is readily perceived that in each complex of this family the total of $N = 16n^3$ impurity atoms includes

$$N_6 = 16n^3 - 24n^2 + 10n \tag{5}$$

bulk atoms, each containing $n_v = 6$ nearest-neighbor cation vacancies,

$$N_4 = 24n^2 - 22n + 4 \tag{6}$$

surface atoms surrounding $n_v = 4$ vacancies, and

$$N_3 = 8n - 4 \tag{7}$$

and

$$N_2 = 4n \tag{8}$$

edge atoms characterized by the parameters $n_v = 3$ and $n_v = 2$, respectively. As a result, the average number $\overline{n}_v$ of vacancies surrounding impurity atoms in the given complex is equal to

$$\overline{n}_v = \frac{6N_6 + 4N_4 + 3N_3 + 2N_2}{16n^3} = 6 - \frac{12n^2 - n - 1}{4n^3}. \tag{9}$$

Figure 2 shows the function $\overline{n}_v(N)$ plotted in coordinates $\overline{n}_v, \sqrt{N})$ through the points $(N=1,\ \overline{n}_v=1)$, $(N=2,\ \overline{n}_v=2)$, and $[N=16n^3(n=1,\ 2,\ldots),\ \overline{n}_v=1]$ according to Eq. (9). The striking and surprising similarity between the $B_c(C)$ and $\overline{n}_v(N)$ curves, of course, cannot be treated as quantitative agreement between theory and experiment. Nonetheless, it most certainly lends support to the proposed physical scheme. The next step must be to establish specific relations between C and N and between B_c and $\overline{n}_v$.

So far we can only assume on the basis of Fig. 2 that the complexes in the purest NaCl crystals with Ca impurity concentrations $C_1 = 0.5$ ppm and $C_2 = 1$ ppm are composed of several impurity atoms, those in crystals with $C_3 = 10$ ppm consist of several tens of impurity atoms, and finally the complexes in crystals with a concentration $C_4 = 100$ ppm can contain hundreds of impurity atoms. And while it may be premature to discuss a new technique for the experimental determination of the average size of paramagnetic complexes, the observed sensitivity of the threshold B_c of the magnetoplastic effect to the impurity concentration C encourages the likelihood that such a technique will be found.

In closing, the authors are indebted to A. A. Urusovskaya for valuable discussions and to V. P. Kiselo and V. M. Chernov for methodological assistance.

This work has received support from the Russian Fund for Fundamental Research (Grant No. 97-02-16327).

[1] V. I. Al'shits, E. V. Darinskaya, T. M. Perekalina, and A. A. Urusovskaya, Fiz. Tverd. Tela (Leningrad) **29**, 467 (1987) [Sov. Phys. Solid State **29**, 265 (1987)].

[2] V. I. Al'shits, R. Voska, E. V. Darinskaya, and E. A. Petrzhik, Fiz. Tverd. Tela (St. Petersburg) **35**, 70 (1993) [Phys. Solid State **35**, 37 (1993)].

[3] V. I. Alshits, E. V. Darinskaya, and E. A. Petrzhik, Mater. Sci. Eng. A **164**, 322 (1993).

[4] V. I. Al'shits, E. V. Darinskaya, O. L. Kazakova, E. Yu. Mikhina, and E. A. Petrzhik, J. Alloys Compd. **211/212**, 548 (1994).

[5] V. I. Al'shits, E. V. Darinskaya, O. L. Kazakova, E. Yu. Mikhina, and E. A. Petrzhik, JETP Lett. **63**, 668 (1996).

[6] V. I. Al'shits, E. V. Darinskaya, and O. L. Kazakova, Zh. Éksp. Teor. Fiz. **111**, 615 (1997) [JETP **84**, 338 (1997)].

[7] Yu. I. Golovin and R. B. Morgunov, Fiz. Tverd. Tela (St. Petersburg) **35**, 1384 (1993) [Phys. Solid State **35**, 700 (1993)].

[8] Yu. I. Golovin and R. B. Morgunov, JETP Lett. **61**, 596 (1995).

[9] A. A. Urusovskaya, V. I. Al'shits, A. E. Smirnov, and N. N. Bekkauer, JETP Lett. **65**, 497 (1997).

[10] K. M. Salikhov, Yu. N. Molin, R. Z. Sagdeev, and A. L. Buchachenko, *Spin Polarization and Magnetic Effects in Radical Reactions* [Elsevier, Amsterdam, 1984; Nauka, Novosibirsk, 1978].

[11] V. V. Kveder, Yu. A. Osip'yan, and A. I. Shalynin, Zh. Éksp. Teor. Fiz. **83**, 699 (1982) [Sov. Phys. JETP **56**, 389 (1982)].

[12] Ya. B. Zel'dovich, A. L. Buchachenko, and E. L. Frankevich, Usp. Fiz. Nauk **155**, 3 (1988) [Sov. Phys. Usp. **31**, 385 (1988)].

[13] W. Frank, Phys. Status Solidi **29**, 797 (1968).

[14] P. Graw and F. Frohlich, Phys. Status Solidi A **55**, 479 (1979).

[15] I. Sarkozi and A. A. Predvoditelev, Kristallografiya **24**, 622 (1979) [Sov. Phys. Crystallogr. **24**, 358 (1979)].

[16] A. A. Urusovskaya, E. V. Darinskaya, R. Voszka, and J. Jansky, Cryst. Res. Technol. **16**, 597 (1981).

Translated by James S. Wood

Excess free volume and mechanical properties of amorphous alloys

V. I. Betekhtin, A. G. Kadomtsev, and A. Yu. Kipyatkova

A. F. Ioffe Physico-technical Institute, Russian Academy of Sciences, 194021 St. Petersburg, Russia

A. M. Glezer

I. P. Bardin Institute of Metallurgy and Metal Physics, 107005 Moscow, Russia

(Submitted July 2, 1997)
Fiz. Tverd. Tela (St. Petersburg) **40**, 85–89 (January 1998)

Characteristics of the excess free volume in amorphous alloys quenched from a melt are investigated and analyzed. It is established by small-angle x-ray scattering that the application of intense hydrostatic pressure causes this volume to decrease. This decrease leads to an enhancement of a number of characteristics of the mechanical properties of amorphous alloys. © *1998 American Institute of Physics.* [S1063-7834(98)01901-7]

Key problems concerning the mechanical behavior of amorphous alloys include the challenge to elucidate the atomic mechanism of heterogeneous plastic flow and the condition for generating quasibrittle cracks as an alternative mechanism to relaxing external stresses. In light of the basic similarity of the process of heterogeneous plastic flow in amorphous alloys and the process of plastic flow in crystalline materials, we are right to assume that, as in crystals, plastic deformation of amorphous alloys is determined by a combination of processes of generation, interaction, and annihilation of defects that are the basic carriers of plastic deformation.

A sufficiently detailed picture of all stages of structural relaxation and the mechanism of plastic deformation of amorphous alloys can be had from the free-volume model.[1] In our understanding of the term, the free volume consists of regions of depressed density, characterized by a definite size distribution (from fractions of an atomic diameter to hundreds of nanometers) which depends on the conditions of preparation, composition, heat-treatment regime, and a number of other factors. Within this model, we have the possibility of tracing, both theoretically and experimentally, the evolution of regions of free volume from their generation in regions of rarefaction in the melt through transformation of their shapes and redistribution over the cross section of the amorphous matrix upon quenching the melt, to modification of their morphology and size distribution parameters of these defects under various external influences. Note that in the presence of a continuous size distribution of free-volume regions, different fractions of these defects should possess substantially different activation energies and migration mechanisms.

Let us dwell briefly on experimental demonstrations of the existence of free volume in amorphous alloys quenched from melt.

1) It is well known[2] that the density of amorphous alloys is several percent lower than the density of crystalline materials of the same chemical composition. As dilatometric experiments have shown, at the structural relaxation stage, a compaction of the amorphous matrix takes place associated with partial annihilation and removal of excess free volume.

2) Small-angle x-ray scattering experiments have revealed the existence in amorphous alloys of regions with electron-density fluctuations which are several nanometers to several hundreds of nanometers in extent.[3] Changes in the characteristics of these regions in the presence and absence of surfactants, and also with progress of structural relaxation processes, give reason to suppose that the main scattering centers are the free-volume regions. It was also established in Ref. 3 that these regions play an important role in formation processes of microfissures during mechanical treatments.

3) Scanning electron microscopy and auto-ion microscopy studies have provided direct evidence of pores and submicropores which can be assigned to a certain fraction of the regions of free volume.[1] The volume density of the submicropores undergoes marked growth at the stage of dilatometrically recorded compaction when the free volume goes out of the amorphous matrix most vigorously, not only onto outer surfaces but also onto inner free surfaces.

4) In electron-microscopy studies of submicrocrystalline iron-based alloys obtained by quenching from melt, i.e., obtained using the same preparation method used to prepare the amorphous alloys, a very high volume density of prismatic dislocation loops and submicropores ($10^{10}-10^{11}$ mm^{-3}) was observed.[1] In essence, these defects, arising as a consequence of agglomeration of nonequilibrium high-temperature vacancies, make up the excess free volume of the crystal.[4] The difference from the amorphous state consists only in the fact that, as a consequence of Wolf–Bragg scattering effects, we have the possibility of easily visualizing these defects in a crystal, and also in the fact that the free-volume density in the amorphous state is two orders of magnitude larger than that which we see with an electron microscope in rapidly quenched crystals.

In general, the free volume can be divided into excess free volume and structurally induced free volume. The category of excess free volume does not impose significant restrictions on the structural model of the truly amorphous state since it can be considered as a defect of that state, and not a structural element. Removal of the excess free volume does not lead to any changes in the nature of the symmetry or the topological characteristics of the amorphous state. It is precisely this most mobile component of the free volume that is responsible for changes in the structure and physical–

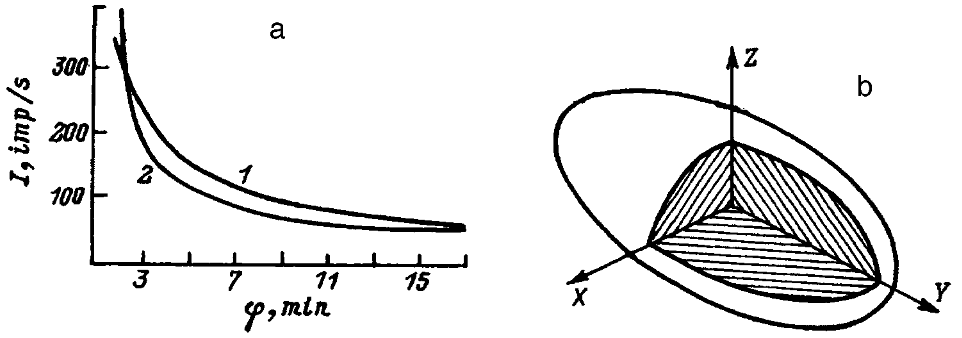

FIG. 1. Anisotropy of small-angle x-ray scattering as a function of the image direction (*1*—image in the YZ plane, *2*—image in the XZ plane) (a) and calculated shape of the scattering inhomogeneities (free volume) (b) for the investigated amorphous samples.

mechanical properties of amorphous alloys in structural relaxation stage. The structurally induced free volume is a structural element entering into the make-up of the atomic complexes determining the topological and compositional characteristics of the amorphous state. Thus, for example, in the case of the polycluster model of the amorphous state,[5] the structurally induced free volume is a necessary element at the intercluster boundaries.

All the above underscores the need for a detailed study of those characteristics of the free volume that can noticeably influence the mechanical behavior of amorphous alloys. In the present study we have undertaken an effort, using small-angle x-ray scattering, to analyze the shape of the regions of free volume and the nature of their distribution over the total volume of samples quenched from melt. The interpretation of the small-angle scattering data has so far not been unique since, in principle, several scattering sources are possible: micro-patches, particles of a second phase, and regions enriched by a dopant element or possessing an increased level of internal strains. In this light, it would be useful to introduce a physical parameter of internal action that would allow us to uniquely link the small-angle scattering characteristics with the parameters of homogeneities of a given type. Such a parameter, in our opinion, is the external hydrostatic pressure since it is well known that it is capable of effectively decreasing the porosity of a wide range of materials.[6–10] In this context, one usually observes a decrease in the average dimensions of the pores while their overall concentration remains unchanged. Motivated by this fact, we also set ourselves the goal of determining the effect of the hydrostatic pressure on the volume fraction and nature of the size distribution of the free-volume regions.

1. MATERIAL AND EXPERIMENTAL TECHNIQUE

The amorphous alloys investigated in this study, $Co_{60}Fe_{10}Si_{15}B_{10}$ (alloy 1), $Fe_{56}Co_{24}Si_{15}B_{15}$ (alloy 2), and $Fe_{78}Ni_2Si_8B_{12}$ (alloy 3), were prepared by quenching from melt in the form of strips or ribbons 30 μm thick and 5 to 10 mm wide. Structural studies confirmed the amorphous state of the alloys and the absence of any particles of a second phase.

In this study we used a small-angle x-ray chamber with Kratki collimation Mo ($K\alpha$ or Co $K\alpha$ radiation). This setup made it possible to determine the inhomogeneity parameters in the range 3–300 nm. To increase the reliability of the results, we also processed the samples independently by other methods. Hydrostatic pressures of up to 1.5 GPa were created in a high-pressure bomb in an oil medium.[8] The microhardness was measured by a specially developed technique[11] on the end-face of the strip. We also determined the tensile strength of samples cut from the strip of the amorphous alloys by stretching them with constant rate of loading to the point of tensile rupture. The temper brittleness temperature of the amorphous alloys was determined by means of a series of isochronous anneals at different temperatures with subsequent mechanical deflection testing at room temperature.

2. EXPERIMENTAL RESULTS

The small-angle x-ray scattering studies showed that the nature of the scattering for the three investigated compositions are qualitatively similar. The scattering inhomogeneities have a slightly prolate shape, and their size distribution is clearly non-uniform. The small-angle scattering indicatrices measured along the longitudinal axis of the strip (the X axis) possess greater steepness and smaller total width than those measured in the direction perpendicular to the axis of the strip (along the Y axis) (Fig. 1a).

Analysis shows that the inhomogeneities have a nearly spherical, slightly ellipsoidal shape since they are oblate relative to the normal to the surface of the strip and prolate in the plane of the strip in the Y direction. Thus, the ellipsoidal defects are oriented with their major axes perpendicular to the direction of the strip in the plane of the strip (Fig. 1b). The ratio of the major axis to the minor axis of the ellipse is 1.13–1.15. With this in mind, in what follows we will use the term ‘‘pore size,’’ similar in concept to the reduced diameter.

Processing of the indicatrix by the Guinier method together with calculation and processing of the invariant for the same alloy makes it possible to reliably distinguish at least two fractions of inhomogeneities with mean sizes around 100 and 20 nm (curve *1* in Fig. 2). In addition to this, weak scattering from inhomogeneities with sizes in the range 4–5 nm is observed, along with scattering (in the supersmall-angle range) by inhomogeneities with sizes around 250 nm. (An analysis of the nature of scattering by these inhomogeneities will be given separately.)

On the whole, the small-angle scattering pattern and its interpretation are qualitatively similar to the results obtained for Fe–B based amorphous alloys.[3]

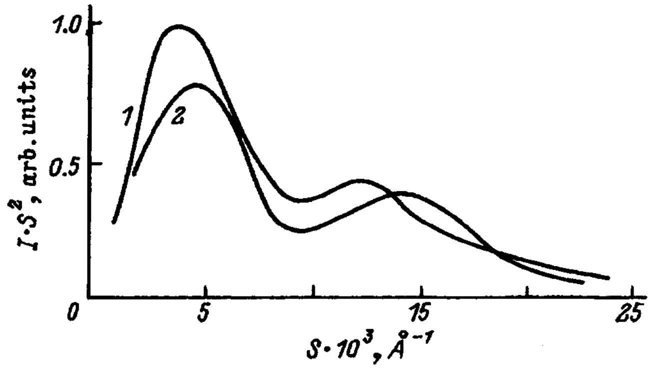

FIG. 2. Invariants of the scattering indicatrices of alloy 1 before (1) and after (2) application of hydrostatic pressure.

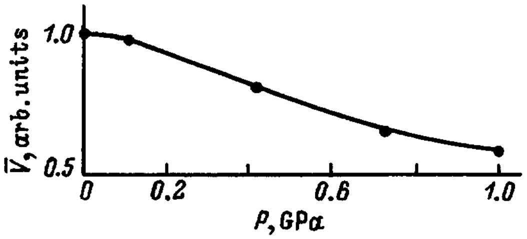

FIG. 3. Dependence of the mean pore volume on hydrostatic pressure.

The results of the application of hydrostatic pressure reduce to the following. Figure 2 displays the results of a study of inhomogeneities of scattering of amorphous alloy 1 after the application of a hydrostatic pressure of 1 GPa. It can be seen that an overall decrease of the intensity of small-angle scattering and of the mean dimensions of the readily distinguished scattering inhomogeneities is observed. Calculations show that the total volume of the scattering inhomogeneities decreased twofold on average. A detailed analysis of the trend of the curves in different coordinates, the magnitudes of the absolute scattering intensities, the outer form of the curve of the invariant and its magnitude showed that the observed scattering can be interpreted uniquely only as scattering by micro-patches (micropores). The decrease of the small-angle scattering intensity after application of hydrostatic pressure clearly proved to be associated only with a decrease in the volume of the scattering particles. Here no change is observed in the concentration or the electron densities of the scattering inhomogeneities. According to Ref. 12, if only the size of the inhomogeneities is changed, a definite relation between the change in their size (D) and the change in the scattering intensity (I) should hold. In our case (slit collimation, almost round pores) this relation has the form $D^5 \sim I_{\varphi=0}$ (Ref. 13). Indeed, for alloy 1 after application of a pressure of 1 GPa (time of action 10 s) the quantity D^5 decreased by a factor of 1.73 while the scattering intensity decreased by a factor of 1.8. The estimates confirm the cavity-like nature of the scattering inhomogeneities.

Assuming that the observed inhomogeneities are micropores, we can estimate their volume fraction. For all the alloys examined, it amounts to a few percent. It is significant that the volume-fraction estimate of scattering inhomogeneities, assumed to differ in nature, gives unreal values—more than a hundred percent.

Figure 3 plots the average pore volume of one of the fractions for alloy 1 as a function of the applied pressure (P). It can be seen that the pores begin to close up already at very small pressures $P \leqslant 0.1$ GPa. At large pressures, this process is observed to extinguish. A similar trend was obtained for other alloys and the other pore fraction.

Figure 4 plots the scattering invariant obtained for alloy 2 in its original state after quenching from melt (curve *1*) and after removing from each surface by electrolytic etching a surface layer about 3 μm thick (curve *2*). It can be seen that removal of the surface layer is followed by a substantial decrease in the size of the scattering centers, which indicates a clearly non-uniform size distribution of the inhomogeneities: the larger scattering regions become concentrated in surface regions of the ribbon-like samples while the smaller regions become concentrated in interior regions.

As is well known,[6–10] closing of the micropores almost always leads to an improvement in the physical-mechanical properties of the materials. Regarding the amorphous alloys examined in this study, we were able to establish experimentally that the application of external hydrostatic pressure increases the microhardness of the alloys on average by 7–9%. Closing the micropores has a similar effect on the tensile strength of amorphous alloys as shown by deflection testing. Thus, the tensile strength of samples of alloy 1 at 18 °C and 100 °C was 1,500 and 1,400 MPa, respectively, and, for the same samples after the application of a pressure of 1 GPa, the tensile strength at the above-indicated temperatures increased to 1,610 and 1,520 MPa, i.e., by 7–8%.

Still more interesting is the fact that, after high-pressure treatment, the temper brittleness temperature, i.e., the viscous-brittle transition temperature observed in almost all metal-metalloid amorphous alloys following annealing above a critical temperature, was observed to increase in all three amorphous alloys. Thus, for alloy 3, the transition to the brittle state after preliminary high-pressure treatment at 1 GPa takes place after annealing at a temperature 50 °C higher than in the same alloy not having undergone such treatment. Similar results were obtained for the other investigated amorphous alloys.

3. DISCUSSION

In the present study, the application of intense hydrostatic pressure to amorphous alloys lowered the volume fraction of scattering inhomogeneities and their mean size without changing the magnitude of electron-density fluctuations or the volume density of the scattering centers. Complete analogy with ordinary porous materials leaves no doubt that, in amorphous alloys quenched from melt, small-angle scattering reveals in a fundamental way the characteristics of the excess and structurally-induced free volume. The results obtained using this technique indicate unambiguously that, in addition to free volume on the atomic scale, amorphous alloys contain noticeably larger micro-patches tens and hundreds of nanometers in size.

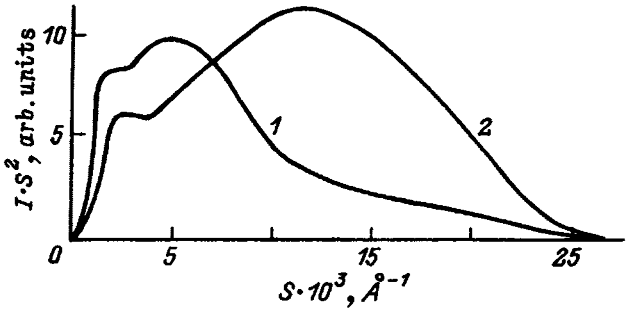

FIG. 4. Invariants of the indicatrices of amorphous alloy 2 before (1) and after (2) electrolytic etching of the surface of the ribbon-like samples.

Let us consider the possible mechanism by which the quenching parameters influence the size and shape distribution of the free-volume regions and their distribution over the cross section of the ribbon-like samples produced by rapid quenching on a rapidly rotating disk-chiller. It is first necessary that in the melt contain, before its sudden cooling on the disk, regions of rarefaction whose size and number increase with the temperature of the melt.[14] At the moment the drops of melt fall upon the cooled surface of the rapidly rotating disk, forces act on the rarefaction regions (future regions of excess free volume), whose magnitude and duration of action determine the characteristics of the free volume after the melt solidifies. An analysis of the combined action of these forces shows that the regions of free volume forming during rapid solidification of the melt should generally be ellipsoids, oblate to different degree along the axis perpendicular to the surface of the ribbon-like samples, with a different ratio of the other axes depending on the specific quenching parameters and the properties of the material. This corresponds to the experimental data shown in Fig. 1. The influence of the centrifugal forces depends on the quenching rate and is expressed in the nonequilibrium of the defect distribution over the cross section of the strip; this is also confirmed experimentally (Fig. 4). In the surface regions the mean size of the free volume is much higher than in the interior regions.

Within the framework of the above ‘‘force’’ model, the melt temperature and the effective quenching rate influence the size distribution of the free volume in two ways: The melt temperature is mainly responsible for the total number of regions having reduced density, where this number can be ‘‘frozen’’ upon quenching, and for the shift in the size distribution toward larger values when the melt temperature is raised. The effective quenching rate is responsible for the total number actually ‘‘frozen’’ defects and for the shift in the size distribution toward smaller values with growth of the effective cooling rate of the melt.

The structural model of the temper brittleness of amorphous alloys according to which annealing above some critical temperature is followed by a change in the failure was first formulated in Ref. 15. Such a change is associated with a facilitation of generation of large cracks in the micropores of relaxational origin, arising as a result of coalescence of the regions of excess free volume. Each amorphous alloy with a given size distribution of the free-volume regions has a definite critical temperature of the elastic-brittle transition, leading to the appearance of a number of pores of supercritical size sufficient for macrodestruction. The applied hydrostatic pressures, by shifting this distribution toward smaller values, obviously increase the critical temperature necessary for the formation of supercritical micropores. Thus, the experiments on the effect of hydrostatic pressure on the temper brittleness temperature described in this study, on the one hand, confirm the validity of the relaxation model of temper brittleness proposed in Ref. 15 and, on the other, reveal one more way of affecting on the critical temperature of the elastic-brittle transition in amorphous alloys.

It is significant that experiments on hydrostatic pore closing, in principle, give new information about plasticity mechanisms in amorphous alloys. It is clear that the decrease in the size of pores under pressure is possible only as a result of the occurrence of microplastic flow processes (the temperature is too low for diffusion processes to occur). Analysis of the curve in Fig. 3 reveals that the threshold pressure for onset of the closing-up process is either too low ($\lesssim .1$ GPa) or is even simply absent. Preliminary data also indicate that the degree of closing up depends on the time of action and depends weakly on the size of the pores. All of these results taken together give us reason to suppose that in the present the mechanism of viscous flow characteristic of amorphous materials is realized. In this regard, note that the closing up of pores in crystalline materials occurs by a dislocation mechanism which is characterized by the presence of a threshold pressure, the absence of a dependence of closing up on the time of action of this mechanism (in the range $10^{-3}-10^{4}$ s), and an enhancement of the degree of closing up accompanying an increase in the size of the micro-patches.[6–10]

In conclusion, let us dwell briefly on the nature of the smallest-size and largest-size fractions of the scattering inhomogeneities, of sizes 4 and 250 nm. The small-angle scattering behavior subsequent to application of pressure does not permit a unique interpretation of these fractions as submicron patches since their volume fraction hardly changes at all after the application of intense hydrostatic pressure. It seems that we are dealing here with scattering inhomogeneities of a nature requiring additional study.

Thus, on the basis of the above study we may conclude that amorphous alloys quenched from the melt contain slightly ellipsoidal submicron patches 20–100 nm in size, nonuniformly distributed over the cross section of the ribbon-like samples. The decrease in the volume fraction of these defects of the amorphous state caused by the application of intense hydrostatic pressures leads to changes in many of the mechanical properties of the investigated materials.

The authors thank the Russian Fund for Fundamental Research for financial support (Grant No. 97-02-17412) and V. I. Matveev for determining the hardness of the amorphous alloys.

[1] A. M. Glezer, B. V. Molotilov, *Structure and Mechanical Properties of Amorphous Alloys* [in Russian], Moscow, 1992.
[2] K. Suzuki, H. Fujimori, K. Hasimoto, *Amorphous Metals* [in Russian], Moscow, 1987.

[3] A. M. Glezer and V. I. Betekhtin, Fiz. Tverd. Tela (St. Petersburg) **38**, 1784 (1996) [Phys. Solid State **38**, 983 (1996)].
[4] A. M. Glezer, B. V. Molotilov, and V. V. Sosnin, Fiz. Met. Metalloved. **58**(2), 370 (1984).
[5] A. S. Bakaĭ, *Polycluster Amorphous Structures and Their Properties* [in Russian], Moscow, 1984.
[6] P. G. Cheremskoĭ, V. V. Slezov, and V. I. Betekhtin, *Pores in Solids* [in Russian], Moscow, 1990.
[7] V. I. Betekhtin, A. I. Petrov, and A. G. Kadomtsev, Fiz. Met. Metalloved. **67**(3), 5644 (1989).
[8] V. Sklenicka, V. I. Betekhtin, K. Kucharova, A. G. Kadomtsev, and A. I. Petrov, Scr. Metall. **25**, 2559 (1991).
[9] A. I. Petrov, M. V. Razuvaeva, and V. I. Betekhtin, Mekhanika Kompozit. Mater. **6**, 1112 (1989).
[10] V. I. Betekhtin and A. G. Kadomtsev, Tzement **5–6**, 16 (1991).
[11] A. M. Glezer and O. L. Utevskaya, in *Composite Precision Alloys* [in Russian], Moscow (1983), p. 78.
[12] A. Guinier and G. Fournet, *Small-Angle Sattering of X-Rays* (London, 1995).
[13] V. I. Betekhtin, A. G. Kadomtsev, V. A. Kon'kova, and A. I. Petrov, Preprint FTI No. 1076 (1986).
[14] Ya. I. Frenkel', *Introduction to the Theory of Metals* [in Russian], Leningrad, 1972.
[15] A. M. Glezer, B. V. Molotilov, and O. L. Utevskaya, Fiz. Met. Metalloved. **58**(5), 991 (1984).

Translated by Paul F. Schippnick

Dynamical theory of thermal spin fluctuations in metallic ferromagnets

V. I. Grebennikov

Institute of Metal Physics, Ural Branch of the Russian Academy of Sciences, 620219 Ekaterinburg, Russia

(Submitted April 7, 1997)
Fiz. Tverd. Tela (St. Petersburg) **40**, 90–98 (January 1998)

A self-consistent dynamical theory of thermal spin fluctuations is developed which describes their spatial correlation. It is based on the functional integral method and utilizes the quadratic representation for the electron free energy in a fluctuating exchange field with renormalized susceptibilities allowing for the interaction of various spin fluctuation modes. Interpolation between the single-site and homogeneous susceptibilities is used, where these susceptibilities are found self-consistently. The average over fluctuations takes account of both long-wavelength and local excitations. A closed system of equations is formed for both unknown quantities: the magnetization and the mean-square exchange field at a site. The basic characteristics of a specific magnet are the density of electron states and the atomic magnetic moment at $T=0$. A method is proposed for separating the relatively slow thermal-spin fluctuations from the rapid zero-spin fluctuations forming the ground state of the magnets. At $T=0$ we have a system of equations of mean field theory. The temperature excites thermal spin fluctuations, which are described by taking account of correlation in time and space. The magnetization, susceptibility, magnitude of the spin fluctuations and their distribution over momenta, and the degree of magnetic short-range order in iron are calculated as functions of the temperature in the ferromagnetic and paramagnetic phases, and also at the transition between them, the Curie temperature. © *1998 American Institute of Physics.* [S1063-7834(98)02001-2]

The effect of electron-spin-density fluctuations on the magnetic properties of metallic magnets at finite temperatures has been studied intensely for several decades.[1–4] Recent successes in the description of spin fluctuations have been linked to the use of the functional integral method based on the Stratonovich–Hubbard transformation,[5,6] which allows one to reduce the density-of-states calculations of the interacting electrons to a problem of motion of independent electrons in an external field, varying arbitrarily both in space and in time.

However, the overwhelming majority of studies have been based on the static single-site approximation,[7–12] in which the field fluctuations are determined by time-independent potentials randomly distributed over the sites of the crystal lattice. Electron scattering by them is treated within the framework of the coherent potential approximation (CPA).

This theory has explained the Curie–Weiss law for paramagnetic susceptibility. Estimates were made of the Curie temperature and showed, in general, that it is less than the value predicted by the Stoner–Wohlfahrt mean-field theory. Note that quantitative results in the study of band structures calculated from first principles[13–16] have turned out to be less successful than calculations based on model densities of states.[11,17] In most of the cited references, with the exception of Refs. 8, 9, and 12, only one-dimensional spin fluctuations along the magnetization were taken into account although it is completely obvious from general considerations that transverse fluctuations in the ferromagnetic region predominate. But such was done and is still done.[17–19]

Efforts to go beyond the single-site approximation in the CPA scheme have been limited to a consideration of the pairwise distribution function of the fluctuating static potentials at neighboring sites.[20,21]

An alternative approach was proposed by Hertz and Klenin.[22] They considered dynamical fluctuations in the so-called long-wavelength limit and obtained a generalization of the well-known random-phase approximation (RPA)[23] for the susceptibility where the latter depends on the wave vector and the frequency. Unfortunately, this theory was developed only for the paramagnetic region; therefore, the mechanism of a feedback effect of the spin fluctuations on the magnetization is completely absent from it. The authors of this theory have used it to explain the possibility of the existence of spin waves above the Curie temperature also in concrete estimates, again, based on the static approximation. Due to its great mathematical difficulties, this approach has not received further development.

Spatial correlation of spin fluctuations was examined on the basis of the Murata–Doniach model functional[24–27] and its generalizations giving the described spin fluctuations within the framework of classical statistics. In particular, recently,[27] the parameters of the effective functional were determined with the aid of first-principle calculations of the energy of spiral spin configurations, followed by a standard thermodynamic calculation. The results obtained in Ref. 27 demonstrate all of the essential features of the static approximation. These include the abrupt fall $\sim T$ of the magnetization at low temperatures, the approach of the low-temperature specific heat not to zero, but to a constant value, the need to introduce a cutoff in the wave vector, the small value of the effective magnetic moment in the Curie–Weiss law, etc. Along with this, reasonable estimates of the Curie temperature in iron, cobalt, and nickel were obtained.

A large number of studies have examined the effects of interelectron correlations in the ground state of the Hubbard model. Their influence on the temperature dependence of the properties of the transition metals has received significantly less study. In Refs. 28 and 29 the functional integral method was united with the Gutzwiller method to calculate the electron wave functions with correlation taken into account. However, here also the fluctuating field was described in the single-site static approximation. It turns out that the main effect of the electron correlations reduces to a renormalization of the coupling constant. But since its magnitude in any case is effective (it is determined from the observed magnetization at $T=0$, whether by the mean-field theory or by the variational approach), in reality the effect of the electron correlations in iron is roughly 10%, and in nickel still smaller. Note that Ref. 28 again only considered longitudinal fluctuations. Although in some sense taking electron–electron correlations into account is equivalent to taking dynamic field fluctuations into account, in the given case in essence only ''zero'' fluctuations (fluctuations in the ground state) were taken into account, and this proved to be entirely insufficient for obtaining the true temperature behavior of the main characteristics of ferromagnetic metals.

Thus, although it has been possible within the framework of the static approach to explain, either qualitatively or semiquantitatively, a number of physical properties previously amenable to description, for a quantitative description it is necessary to extend the theory by allowing fuzzy for dynamic spin fluctuations. In Ref. 3, based on the Gaussian approach, Grebennikov and Turov formulated a dynamical theory of local spin fluctuations (in the single-site scattering approximation) and found general relations between the results of the dynamic and static descriptions. Grebennikov[31] then generalized the dynamical theory to spatially correlated spin fluctuations, granted, only in the paramagnetic region. This problem was considered in connection with the problem of magnetic short-range order and the interpretation of the observed paramagnetic scattering of neutrons. An analogous problem was investigated within the framework of the static approximation by Hasegawa.[14] The development of the dynamical theory became possible after it became clear[32] that, in describing the scattering of electrons by spin fluctuations, there is no need to use the coherent potential scheme—second-order perturbation theory is quite adequate.

In the present paper, I develop a self-consistent dynamical theory of thermal fluctuations of the electron spin density in metallic ferromagnets that takes their spatial correlation into account. The input data for this theory are the density of electron states of the considered magnet and the magnetization at $T=0$. The self-consistent system of equations obtained allows one to calculate the magnetization at any temperature, the local and homogeneous susceptibilities, the mean-square fluctuating field at a site, and the associated magnetic, thermodynamic, spectroscopic, and other properties of the electron subsystem in the ferro- and paramagnetic phases, and also over the transition between them.

1. MATHEMATICAL DESCRIPTION AND MAIN APPROXIMATIONS

We will use the above-mentioned functional integral scheme. The Stratonovich–Hubbard transformation[5,6,22] allows one to reduce the problem of calculating the density of states of interacting electrons to finding the density of states of the electrons in the spatiotemporally fluctuating exchange field with subsequent integration over all possible configurations

$$Q=e^{\mathcal{F}/T}=\frac{\int DV\,\exp(-F_1(V)/T-F_0(V)/T)}{\int DV\,\exp(-F_0(V)/T)}, \tag{1}$$

where T is the temperature in energy units. The problem of the motion of the electrons in an external field formally has an exact solution. Their free energy

$$F_1(V)=T\ \mathrm{Tr}\ \ln G(V)+\mu N_e \tag{2}$$

is written in terms of the single-particle Green's function of the electrons in the external field V

$$G(V)=(z+\mu-H^0-V)^{-1}. \tag{3}$$

Here z is an energy variable that can take generally complex values, μ is the chemical potential, H^0 is the matrix of the single-particle Hamiltonian of the system (without creation and annihilation operators). Equation (1) also contains the eigenenergy of the exchange field

$$F_0=\frac{1}{2}\ \mathrm{Tr}\ \frac{V^2}{u}. \tag{4}$$

The system is described by one effective coupling constant u, which is determined below by solving the appropriate equations provided the magnetization at $T=0$ is known.

Here we use matrix notation. The trace Tr is the sum of the diagonal elements and is independent of the specific representation of the matrices. The matrix elements of the exchange field in the site representation and the temporal representation have the form

$$V_{ii'ss'}(\tau,\tau')=\boldsymbol{\sigma}\mathbf{V}_i(\tau)\,\delta_{ii'}\,\delta(\tau-\tau), \tag{5}$$

where the index i labels the lattice sites (atoms), s is the spin number, $\mathbf{V}_i(\tau)$ is the real vector exchange field at site i, $\tau\in(0;1/T)$ is ''imaginary'' time, which appears in the transformation to the interaction representation, and σ^α are the Pauli spin matrices. The Fourier transformation with respect to the spatial coordinates and time allows one to write this matrix in the momentum and frequency (energy) representation. It depends on the difference of the wave vectors and frequencies,

$$V_{qq'nn'ss'}=V_{q-q',n-n',ss'}\,. \tag{6}$$

Due to boundedness of the time interval, we use a Fourier series in the frequencies $\omega_n=2\pi nT$, which are multiples of the temperature T.

The zeroth-order Green's function G^0 is defined by Eq. (3) for $V=0$. By virtue of the time-independence and translational invariance of the one-electron Hamiltonian H it is diagonal in the $q\omega_n$ representation

$$G^0_{qq'nn'ss'}=G^0_{qns}\delta_{qq'}\delta_{nn'}\delta_{ss'}\,. \tag{7}$$

The Green's function averaged over the fluctuating field, $\langle C(V)\rangle$, which will be made use of in what follows, possesses analogous properties.

Since the matrices V and G^0, as can be seen, do not diagonalize simultaneously in real space or momentum space, Eq. (2) is purely formal, and must be simplified for practical use. Incidentally, we may note that, in the static single-site approximation, only the site-diagonal components of the Green's function and the field at $\omega=0$ remain.

We will make use of the expansion of the free energy

$$F(V)=F_1(V)=F_0(V) \tag{8}$$

over fluctuations of the field $\Delta V=V-\langle V\rangle$ about its mean value $\langle V\rangle$, which we determine from the condition that the first variation of the total free energy $\mathcal{F}$ vanish,

$$T\ \mathrm{Tr}\left(\langle G(V)\rangle+\frac{\langle V\rangle}{uT}\right)\sigma^{\alpha}=0. \tag{9}$$

The Green's function averaged over the field fluctuations enters here by virtue of Eq. (1). The average $\langle ...\rangle$ is understood to mean the integral with the distribution function

$$c(V)=\exp(-F(V)/T)\bigg/\int DV\ \exp(-F(V)/T), \tag{10}$$

in which $F(V)$ is initially assigned by Eq. (8), but in what follows we will use the quadratic approximation. Equation (9) together with the condition $(\partial\mathcal{F}/\partial\mu=0)$ of conservation of the total number of electrons

$$T\ \mathrm{Tr}\langle G(V)\rangle=N_e \tag{11}$$

are the equations of Stoner's theory for the static homogeneous exchange field $\langle V\rangle$ and the chemical potential μ. The only difference consists in the fact that the Green's function is calculated not in the mean field itself $\langle V\rangle$, as in the Stoner theory, but with the fluctuations taken into account. If we replace $\langle G(V)\rangle$ by $G(\langle V\rangle)$, then we arrive at the equations of the Stoner–Wohlfahrt mean-field theory.

In order to find the distribution function (10), we expand $F(V)$ out to terms of second order in ΔV (with Eqs. (9) and (11) taken into account)

$$\begin{aligned}F(V)&\simeq F^{(2)}(V)\\&=\frac{1}{2}T\ \mathrm{Tr}\left[\left(\frac{\delta_{\alpha\beta}}{uT}+\langle G(V)\sigma^{\alpha}G(V)\sigma^{\beta}\rangle\right)\Delta V^{\alpha}\Delta V^{\beta}\right]\\&=N\sum_{qn\alpha}\left(\frac{1}{u}-\chi^{\alpha}_{qn}\right)\Delta V^{\alpha}_{qn}\Delta V^{\alpha}_{q-n}.\end{aligned} \tag{12}$$

Equation (12) contains the definition of the bare susceptibility χ^{α}_{qn} of the electrons in the presence of the fluctuating exchange field; N is the number of atoms. Again, if we replace $G(V)$ by $G(\langle V\rangle)$, we arrive at the known formulas for the zeroth (loop) susceptibility in the RPA.

Calculation of the inhomogeneous dynamic susceptibility $\chi_{qn}=\chi_q(i\omega_n)$, a function of four variables, with subsequent summation over wave vectors q and frequencies $\omega_n=2\pi nT$ for real metals is a pointlessly complicated procedure. As the fruit of such efforts we will get only numbers: the magnetization, the homogeneous static susceptibility, and so on. On top of that, representation (12) has a fundamental inadequacy: each harmonic q gives its own contribution to the energy (12) and, consequently, to the distribution function (10), which is independent of the other harmonics, i.e., a system of non-interacting fluctuations (spin waves) obtains, which does not correspond to the physics of the phenomenon for a large number of excitations. Interaction of the modes can be taken into account very simply by introducing a local (single-site) bare susceptibility

$$\chi_l(z)=\frac{1}{N}\sum_q \chi_q(z)=\{\chi_q(z)\}, \tag{13}$$

which is the susceptibility averaged over the momenta in the Brillouin zone. We denote the operation of momentum-averaging by the symbol {...}. The local susceptibility is no longer determined by the total Green's function, but only by the single-site Green's function, which is expressed in terms of the density of electron states (DES). The corresponding formulas are given below.

The idea is to obtain the renormalized susceptibilities χ_q by interpolating between two points: χ_0 and χ_l. This allows us, on the one hand, to take account of interaction of modes and, on the other, the determine the q dependence of the susceptibility or the associated spatial correlation of the spin fluctuations. This principle of taking simultaneous account of local and spatial fluctuations is employed to calculate the average Green's function and the corresponding eigenenergy $\Delta\Sigma$. Second-order perturbation theory gives (summation is assumed over repeated indices)

$$\begin{aligned}\Delta\Sigma_{pm}&=\langle\Delta V_{qn}\langle G(V)\rangle_{p-q,m-n}\Delta V_{-q,-n}\rangle\\&\simeq\langle\Delta V_{qn}\langle G(V)\rangle_{p-q,m}\Delta V_{-q,-n}\rangle.\end{aligned} \tag{14}$$

The latter equation holds only for thermal fluctuations possessing low energy in comparison with the characteristic energies of the electron subsystem.

We introduce the principle of separating the zero fluctuations (vacuum fluctuations, in the ground state) and thermal fluctuations. The interaction of the electrons with each other generates fluctuations of the charge density and spin density both at $T=0$ and at any finite temperature. We will assume that correlation effects caused by fluctuations are already taken into account in some way in the calculation of the density of electron states at $T=0$ (by the density functional method or variational approach, etc.). It remains for us to consider only their T-dependent part, in other words the thermal fluctuations. The zero vibrations have a wide energy spectrum ΔE (of the order of the intra-atomic electron repulsion u) and short period $\Delta t=h/\Delta E$. The thermal fluctuations possess low energies $\Delta E=k_BT$ and are therefore relatively slow excitations. This latter peculiarity allows us to distinguish them from fluctuations in the ground state, that is, to detect thermal spin fluctuations in ''fast'' experiments (fast in terms of their time scale). Equilibrium thermal spin fluctuations may be considered[33] as almost static scatterers for the conduction electrons in the calculation of the kinetic properties of magnets. For this reason, from the set of all fluctuations we will consider only thermal, or temperature, spin fluctuations.

Two extreme estimates are usually used to calculate the sum over the Brillouin zone in Eq. (14): 1) $\langle G(V)\rangle_{p-q}\simeq\langle G(V)\rangle_p$; this estimate assumes that the main contribution comes from quasihomogeneous fluctuations with $q\simeq 0$. This is the so-called long-wavelength limit.[1,22] 2) In the second estimate the Green's function is replaced by the local (single-site) Green's function $g=\{\langle G(V)\rangle_{p-q}\}$. This approximation assumes that excitations with any q are roughly the same and is called the local (random) fluctuation approximation.[1,8] Our approach takes both these aspects into account—the long-wavelength and the random, see Eq. (22). Let us now turn to the characteristics of the spin fluctuations. Using the quadratic expansion for the free energies (12), we obtain the Gaussian distribution function (10), which allows us to calculate the mean value

$$\langle \Delta V^{\alpha}_{qn}\Delta V^{\alpha}_{-q,-n}\rangle=\langle|\Delta V^{\alpha}_{qn}|^2\rangle=\frac{uT}{2N}\,\frac{1}{1-u\chi^{\alpha}_{qn}}. \tag{15}$$

Summing over the odd frequencies, we obtain after analytic extension of the function to the real axis

$$\sum_n \langle|\Delta V^{\alpha}_{qn}|^2\rangle=\sum_n \frac{uT}{2N}\,\frac{1}{1-u\chi^{\alpha}_{qn}}$$
$$=\frac{u}{2N}\,\frac{2}{\pi}\int_0^{\infty}d\varepsilon\left(B(\varepsilon)+\frac{1}{2}\right)$$
$$\times\mathrm{Im}\,\frac{1}{1-u\chi^{\alpha}_{q}(\varepsilon+i0)}. \tag{16}$$

Here $B(\varepsilon)=(\exp(\varepsilon/T)-1)^{-1}$ is the Bose–Einstein function. The term proportional to 1/2 describes the contribution of the temperature-independent zero fluctuations which, as was discussed above, should be discarded (effects of zero fluctuations in the ground state were examined in Refs. 34 and 35). Because of strong localization of the Bose function at zero energy of excitation, it suffices to know the behavior of the susceptibility only in the limit $\varepsilon\rightarrow 0$.

We employ the well-known expansion[30]

$$\chi_q(\varepsilon)=\chi_q(0)_i\varphi_q\varepsilon. \tag{17}$$

Approximating the Bose function by

$$B(\varepsilon)=\begin{cases} T/\varepsilon, & \varepsilon<\pi^2T/6,\\ 0, & \end{cases} \tag{18}$$

we obtain an analytical relation for the integral in Eq. (16)

$$\sum_n \langle|\Delta V^{\alpha}_{qn}|^2\rangle=\frac{uT}{2N\lambda_q}\,\frac{2}{\pi}\,\arctan\,\frac{\pi^2uT\varphi_q}{6\lambda_q}, \tag{19}$$

where

$$\lambda_q=1-u\chi_q(0)$$

is the inverse gain factor of the susceptibility.

The first factor in (18) defines the fluctuations in the static approximation (formally in the limit $T\rightarrow\infty$). The second takes account of their dynamics and plays the role of a cutoff factor.

As was already noted, we require only the local susceptibility (13). To calculate it we used equations (12) in which we replace the average of the product by the product of the average Green's functions. As a result, we arrive at a closed system of equations.

2. CALCULATIONAL FORMULAS

The electron system in the absence of an external field is described by the density of states $\nu(\varepsilon)$ and the corresponding single-site Green's function

$$G^0(\varepsilon)=\int d\varepsilon'\,\frac{\nu(\varepsilon')}{\varepsilon-\varepsilon'}. \tag{20}$$

Here $\nu(\varepsilon)$ is the nonmagnetic density of states in the calculation per atom, per d band, per spin, which is assumed to be known. In the field V^{α}_{qn}, characterized by its mean value $\overline{V}=\langle V\rangle$ and mean-square fluctuation at a site

$$\zeta^{\alpha}=\sum_{qn}\langle|\Delta V^{\alpha}_{qn}|^2\rangle, \tag{21}$$

the diagonal spin components of the single-site Green's function $g=N^{-1}\Sigma_k\langle G(V)\rangle_k$ are given by

$$g_s(\varepsilon)=\sum_{s'=\pm}P_{ss'}G^0(\varepsilon-\Delta\Sigma_s(\varepsilon)-s'v), \tag{22}$$

where

$$v=(\overline{V}+\zeta^x+\zeta^y+\zeta^z)^{1/2},\quad P_{ss'}=\frac{1}{2}\left(1+ss'\,\frac{\overline{V}}{v}\right) \tag{23}$$

is the root-mean-square value of the exchange field and the weight of its quasihomogeneous configurations $\pm v$. The eigenenergy due to the random part of the fluctuations is equal to

$$\Delta\Sigma_s(\varepsilon)=\zeta^z g_s(\varepsilon)+(\zeta^x+\zeta^y)g_s(\varepsilon). \tag{24}$$

Due to axial symmetry here $\zeta^x=\zeta^y$. In the paramagnetic phase $\zeta^x=\zeta^y=\zeta^z$. For any fixed value of the fluctuations the values ζ^{α} solve equations for the mean field $\overline{V}$ and the chemical potential μ of standard type

$$\overline{V}=-us^z(\overline{V}),\quad n_e=n_++n_-,\quad s^z=(n_+-n_-)/2, \tag{25}$$

where

$$n_s=D\int\frac{d\varepsilon}{\pi}f\,\mathrm{Im}\,g_s(\varepsilon) \tag{26}$$

is the number of electrons with spin projection s at a site in all $D(=5)$ bands, $f(\varepsilon,T)=(\exp(\varepsilon-\mu)/T+1)^{-1}$ is the Fermi function, n_e is the total number of electrons per atom (a known quantity), and s^z is the average spin of the atom.

For $\zeta^{\alpha}=0$ the equations transform into the equations of mean-field theory. This is always true for $T=0$, and this fact makes it possible to find the effective coupling constant u provided the saturation magnetization $m_0=2\mu_Bs_0$ is known.

The magnitude of the local thermal field fluctuations is calculated from the relations

$$\zeta^{\alpha}=\left\{\frac{uT}{2\lambda^{\alpha}_q}\,\frac{2}{\pi}\,\arctan\,\frac{\pi^2\varphi^{\alpha}_l uT}{6\lambda^{\alpha}_q}\right\},\alpha=x,y,z, \tag{27}$$

where {...} denotes averaging over all momenta in the Brillouin zone, which we replace approximately by a sphere of equal volume.

The inverse gain factor

$$\lambda_q^\alpha = \lambda_0^\alpha + (\lambda_l^\alpha - \lambda_0^\alpha) q^2 / \{q^2\} \tag{28}$$

is found by interpolation over two of its values for $q=0$ and we average over q,

$$\lambda_0^\alpha = 1 - u\chi_0(0), \quad \lambda_l^\alpha = 1 - u\{\chi_q^\alpha(0)\} = 1 - u\chi_l^\alpha(0), \tag{29}$$

These values are found self-consistently in the course of the solution. In Eq. (27) φ_q has been replaced by its mean value $\varphi_l = \{\varphi_q\}$.

The local susceptibility χ_l and its derivative with respect to the energy φ_l are expressed[30] in terms of the average single-site Green's function (22)

$$\chi_l^x = -D \int \frac{d\varepsilon}{\pi} f \, \mathrm{Im}(g_+ g_-),$$

$$\varphi_l^x = d \int \frac{d\varepsilon}{\pi} \left(-\frac{df}{d\varepsilon} \right) \mathrm{Im}\, g_+ \mathrm{Im}\, g_-,$$

$$\chi_{ls} = -D \int \frac{d\varepsilon}{\pi} f \, \mathrm{Im}(d_s)^2,$$

$$\varphi_{ls} = D \int \frac{d\varepsilon}{\pi} \left(-\frac{df}{d\varepsilon} \right) (\mathrm{Im}\, g_s)^2,$$

$$\chi_l^z = (\chi_{l+} + \chi_{l-})/2, \quad \varphi_l^z = (\varphi_{l+} + \varphi_{l-})/2. \tag{30}$$

The unamplified static homogeneous spin susceptibility is obtained by numerical differentiation of the spin density (25) with respect to the magnetic field h

$$\chi_0^z = \frac{\Delta s^z}{\Delta h} = (s^z(\overline{V + h/2}) - s^z(\overline{V - h/2}))/h, \quad h \to 0. \tag{31}$$

Note that the mean exchange field $\overline{V}$ is completely analogous to the external magnetic field h (in energy units). For this reason[32] the total susceptibility $\tilde{\chi}_0^\alpha$ is related to the zero (bare, loop) susceptibility χ_0^α via the familiar gain factor

$$\tilde{\chi}_0^\alpha = \frac{\chi_0^\alpha}{\lambda_0^\alpha} = \frac{\chi_0^\alpha}{1 - u\chi_0^\alpha}. \tag{32}$$

In the absence of magnetic anisotropy any small external magnetic field induces a rotation of the large spontaneous magnetization of a ferromagnet, which entails a divergence of the susceptibility. This means we can set $\lambda_0^\alpha = 0$ for $T < T_c$. In the paramagnetic region this is no longer the case and we must use relation (31) to calculate the bare susceptibility $\chi_0^z = \chi_0^x = \chi_0^y$ and (32) to calculate the total susceptibility $\tilde{\chi}_0$ determined experimentally.

Equations (20)–(32) constitute a closed system of equations which yield the solution of the magnetic problem. Let us comment separately on its parts.

The average Green's function (22) is obtained from the following considerations. If we use the above-mentioned approximation of quasihomogeneous fluctuations[22] in its original form, then

$$\tilde{G}_k = \left\langle \frac{1}{\varepsilon - \varepsilon_k - \mathbf{V}\boldsymbol{\sigma}} \right\rangle \simeq \frac{(\varepsilon - \varepsilon_k + \overline{V\sigma^z})}{(\varepsilon - \varepsilon_k)^2 - \langle V^2 \rangle}$$

$$= \sum_{s=\pm} \frac{1}{2} \left(1 + \frac{s\overline{V\sigma^z}}{v} \right) \frac{1}{\varepsilon - \varepsilon_k - sv}. \tag{33}$$

Summing in Eq. (33) over all quasimomenta k, we obtain the single-site Green's function in the form (22), but only for $\Delta\Sigma = 0$. Here in the average over the fluctuations, to simplify the calculations we used a splitting[11] of the form $\langle V^{2n} \rangle \to \langle V^2 \rangle^n$ and $\langle V^{2n+1} \rangle \to \langle V^2 \rangle^n \langle V \rangle$. Function (33) describes only the quasihomogeneous part of the fluctuations. In order to take account of their random part, we introduce the eigenenergy $\Delta\Sigma(\varepsilon)$. Its value may be determined by minimizing the total free energy $\mathscr{F}$ in Eq. (1) with respect to $\Delta\Sigma$ in the single-site scattering approximation. This procedure leads to the equation of coherent potential theory. However, in the case of thermal fluctuations the perturbation is not large and the CPA equation takes the form (24), where the functions g_s on the right-hand side can be calculated by setting $\Delta\Sigma_s = 0$. Expression (24) can also be treated simply as a correction to the energy level in second-order perturbation theory.

Local electrical neutrality. So far in our approach we have completely neglected the interaction of the fluctuations of the charge density. Fluctuations of the exchange field generate not only changes in the spin density but also in the number of electrons at the lattice sites. Usually the contribution of the charge fluctuations in the functional integral theory is taken into account by introducing a variable charge field whose magnitude is estimated by the method of steepest descent.[8,12] We reject this procedure for two reasons. First, it complicates the calculational scheme by introducing an additional arbitrary constant, the charge coupling constant, and, second, it nevertheless completely ignores the interaction of electrons at different sites since this interaction is absent in the initial Hubbard model although it is important.

We propose a second path. It is not hard to find the local spin susceptibility, defined by the second variation of the free energy (12), given the additional condition of total electrical neutrality of the atoms. This leads to a change only in the longitudinal local susceptibility in the ferromagnetic region. The last two equations in (30) are replaced by the following new ones:

$$\frac{1}{\chi_l^z} = \frac{1}{2} \left(\frac{1}{\chi_{l+}} + \frac{1}{\chi_{l-}} \right), \quad \text{and} \quad \frac{1}{\varphi_l^z} = \frac{1}{2} \left(\frac{1}{\varphi_{l+}} + \frac{1}{\varphi_{l-}} \right). \tag{34}$$

Mixing the susceptibilities calculated according to formulas (34) and (30) with some weighing factor, it is possible to allow for partial conservation of local electric neutrality in the presence of spin fluctuations.

Averaging over directions. The proposed model in effect allows for interaction with different wave vectors q by introducing the bare susceptibility averaged over q. Of course, they interact with each other and with spin fluctuations of different polarizations. In order to somehow take this interaction into account and also simplify the theory (which is extremely necessary for its further practical use), we replace the longitudinal and transverse susceptibilities by their mean value

$$\chi^{\alpha} \to \chi = (\chi^{z} + \chi^{x} + \chi^{y})/3, \tag{35}$$

and we make an analogous substitution for φ^{α}. Here the root-mean-square spin fluctuation ζ loses its dependence on the polarization, and for each fixed temperature the main system of equations now contains only two unknown numbers ζ and $\overline{V}$ (of course, there is always one more trivial variable, the chemical potential μ). In the paramagnetic phase $\overline{V}=0$, and there only remains the root-mean-square field fluctuation at a site.

Thus, our approach may be considered as a generalization of the Stoner–Wohlfahrt mean-field theory resulting from the introduction of the additional variable ζ, the root-mean-square fluctuation of the exchange field at a site. This quantity depends explicitly on the temperature, see Eq. (22), and serves as the main source of temperature dependence of the properties of metallic magnets associated with their electron subsystem. The old source, thermal smearing of the Fermi distribution, is ineffective for integral characteristics although it can be important for describing single-particle excitations at the Fermi surface.

3. MAGNETIC SHORT-RANGE ORDER

In the functional integral theory the calculation of the spin correlation functions is equivalent to a calculation of the pairwise correlators of the field V (Ref. 1). Recall that the original problem reduces to the interaction Tr sV of the electron spin density s with the field V. Hence it follows that

$$\begin{aligned}\langle s^{\alpha}_{qn} s^{\beta}_{-q-n}\rangle &= \frac{T^2}{4}\int DV \exp\left(-\frac{F_0}{T}\right)\frac{\partial}{\partial V^{\alpha}_{qn}}\frac{\partial}{\partial V^{\beta}_{-q-n}} \\ &\quad\times \exp\left(-\frac{F_1}{T}\right)\Bigg/\int DV \exp\left(-\frac{F_0+F_1}{T}\right) \\ &= \frac{\langle V^{\alpha}_{qn} V^{\beta}_{-q-n}\rangle}{u^2} - \frac{T}{2uN}\delta^{\alpha\beta}.\end{aligned} \tag{36}$$

The last equality was obtained by integrating by parts using the explicit form of F_0 [Eq. (4)].

Invoking Eq. (15), we find the correlators for the fluctuations $\Delta s = s - \langle s\rangle$

$$\langle \Delta s^{\alpha}_{qn}\Delta s^{\alpha}_{q-n}\rangle = \frac{T}{2N}\frac{\chi^{\alpha}_{qn}}{1-u\chi^{\alpha}_{qn}}. \tag{37}$$

The correlator (37) is defined by the total susceptibility $\tilde{\chi}$ of the type (32) in complete agreement with the fluctuation–dissipation theorem. For Gaussian fluctuations, this susceptibility has the RPA form; however, the zero susceptibility χ (30) is changed due to the fluctuations.

Summing in Eq. (37) over frequencies ω_n, we obtain the correlator for coincident times

$$\langle \Delta s^{\alpha}_{q}(t)\Delta s^{\alpha}_{-q}(t)\rangle = \frac{1}{N\pi}\int_0^{\infty} d\varepsilon \left(B(\varepsilon)+\frac{1}{2}\right)\mathrm{Im}\,\frac{\chi^{\alpha}_{q}(\varepsilon)}{1-u\chi^{\alpha}_{q}(\varepsilon)}. \tag{38}$$

Function (38) determines, for example, paramagnetic scattering of neutrons with momentum transfer q. However, experimentally, the neutron energy losses ε are bounded by their small initial energy and the instrument transmission function. For this reason, in practice the integration interval on the right-hand side of Eq. (38) is $100-200$ meV. Thus, the zero (from 1/2) spin fluctuations make a small contribution, and for this reason the thermal spin fluctuations $(B(\varepsilon)\sim T/\varepsilon)$ fit into this energy window completely. By observing paramagnetic scattering of neutrons it is possible to estimate the degree of magnetic short-range order above T_c (Ref. 31). A calculation of the spin correlators in the static approximation was carried out in Refs. 14.

We obtain an explicit expression for the spatial correlator of the thermal spin fluctuations for coincident times by invoking Eqs. (38), (17)–(19), and interpolation (28),

$$\begin{aligned}\langle \Delta s^{\alpha}(r)\Delta s^{\alpha}(0)\rangle &= N\{\exp(iqr)\langle \Delta s^{\alpha}_{q}\Delta s^{\alpha}_{-q}\rangle\} \\ &= \int_0^1 dk 3k\frac{\sin(krq_D)}{rq_D}\frac{T}{u\lambda^{\alpha}_{l} b(k)\pi} \\ &\quad\times \arctan\frac{\pi^2 u T_{\varphi}}{6\lambda^{\alpha}_{l} b(k)},\end{aligned}$$

where

$$b(k) = d + k^2(1-d)/0.6, \quad d = \lambda^{\alpha}_{0}/\lambda^{\alpha}_{l}. \tag{39}$$

Here q_D is the radius of the Debye sphere in wave-vector space. The number of states contained within the Debye sphere is equal to the number of atoms per unit volume, $(4/3)\pi q_D^3 = (2\pi)^3 N/\Omega$, $\{q^2\} = 0.6q_D^2$.

At distances r satisfying the inequality $rq_D > \pi$, the Fourier transform is determined by small k, i.e., by the function $k/b(k)$, and we arrive at the well-known result

$$\begin{aligned}&\langle \Delta s^{\alpha}(r)\Delta s^{\alpha}(0)\rangle \sim \frac{1}{q_D r}\exp(-q_D r/a), \\ &a = \left(\frac{d-1}{0.6}\right)^{1/2},\end{aligned} \tag{40}$$

Thus, the ratio of gain factors for the homogeneous and local susceptibilities $d = (1-u\chi_l)/(1-u\chi_0)$ determines the spin correlation radius $r_0 = a/q_D$. For a *bcc* lattice with lattice constant a_0 it is equal to $r_0 \simeq 0.2a_0 a$. At the Curie point r_0 diverges, and the spin fluctuations (40) fall off in inverse proportion to the distance.

4. CALCULATED RESULTS FOR IRON

In what follows we assume that detailed comparative studies of various factors have already been carried out, such as the dynamics of the spin fluctuations, their spatial correlation, contributions of the transverse and longitudinal modes, and local electrical neutrality in transition metals and their alloys using densities of states calculated from first principles. Here we limit ourselves simply to an illustration of the possibilities of the proposed method in the case of iron.

As the initial density of states (DES) we take the nonmagnetic density of states[36] calculated by the density func-

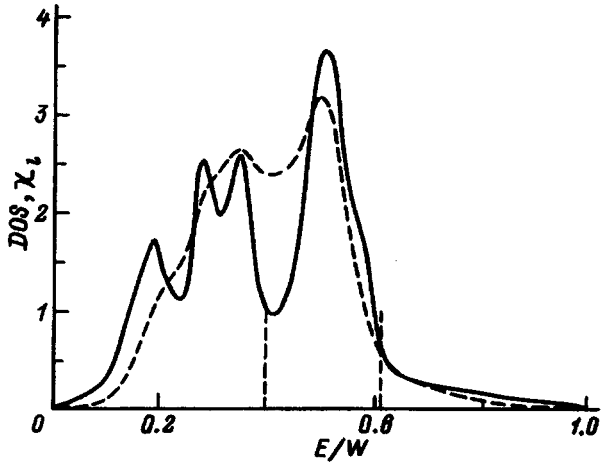

FIG. 1. Nonmagnetic density of electron states at $T=0$ (solid curve) and local susceptibility χ_l (dashed line) as functions of the position of the Fermi level ($\mu=E$). The vertical lines are the Fermi levels for electrons with different spins, energy E is in units of $W=13.4$ eV.

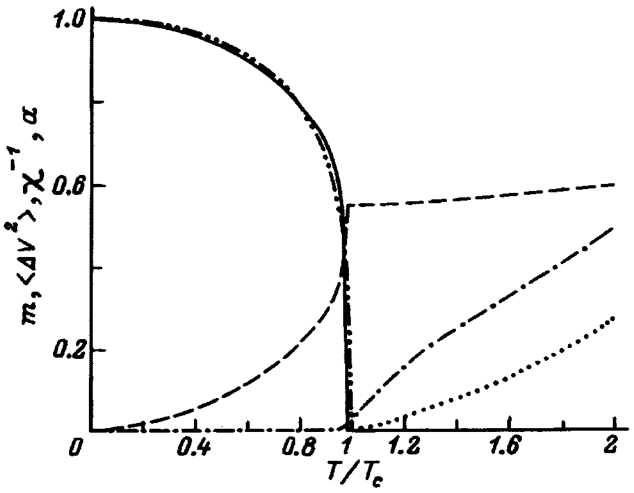

FIG. 2. The magnetization $m(T)/m(0)$ (solid line—calculation, dash–dot–dot—experiment), mean-square fluctuation of the exchange field at the site $\langle\Delta V^2\rangle/V^2(0)$ (for the exchange field in units of the exchange splitting $V(0)$ at $T=0$) (dashed curve). Above T_c: inverse susceptibility $1/\chi$ (per atom, in units of $k_B T_c^{\rm exp}/\mu_B^2$) (dotted curve), dimensionless inverse correlation radius $1/a$ (40) (dash–dot curve). All quantities plotted as functions of temperature $T/T_c^{\rm exp}$.

tional method. From it we exclude the constant $s-p$ background so that the area under the DES curve becomes equal to 10 electrons per atom. As a result, we obtain a band with total width $W=13.4$ eV and number of d electrons per atom $n_e=7.05$. Next the DES is smeared by convolving it with a Lorentzian with half-width $\Gamma=0.01W$ in order to eliminate the unphysical sharp peaks that always arise in band calculations that completely ignore the decay of one-electron states. The DES obtained by this procedure and normalized to one state, $\nu(E)$, is plotted in Fig. 1. The dashed curve in the same figure depicts the zero static local susceptibility χ_l as a function of the position of the Fermi level ($\mu=E$). Solution of the equations at $T=0$ gives the observed value of the atomic magnetic moment $m_0=2.2\mu_B$ for the exchange-coupling constant u equal to 1.29 eV.

Solutions of the system of equations (20)–(32), as functions of the temperature T normalized to the experimentally observed Curie temperature $T_c^{\rm exp}=1044$ K, are shown in Fig. 2. The calculated magnetization m essentially coincides with the experimental result depicted by the dotted line, $T_c=0.98T_c^{\rm exp}$. The paramagnetic susceptibility obeys the Curie–Weiss law with effective magnetic moment $m_{\rm eff}=3.27\mu_B$ (experimental value $3.12\mu_B$) and the paramagnetic Curie point $\theta_c=1.08T_c^{\rm exp}$. Figure 2 also shows the mean-square thermal fluctuation of the exchange field $\langle\Delta V^2\rangle=\zeta^z+\zeta^x+\zeta^y$ in units of the exchange splitting $V(0)=us_0=1.42$ eV at $T=0$, $\langle\Delta V^2\rangle/V^2(0)$, and the dimensionless reciprocal correlation radius a^{-1} (40).

The density of states at the three temperatures $T/T_c=0$, 0.89, and 2.17 are plotted in Fig. 3. These results can be compared with the photoemission spectra. The exchange splitting of the spectra is preserved at temperatures significantly exceeding T_c. Thermal spin fluctuations only smear out the corresponding structure in contrast to the results of mean-field theory, according to which splitting completely disappears in the paramagnetic state, and the spectra should reproduce the nonmagnetic density of states shown in Fig. 1.

Figure 4 plots the thermal spin fluctuations with different wave vectors in the Brillouin zone at $T=1.28T_c^{\rm exp}$, normalized to unit splitting. This quantity describes the paramagnetic scattering of neutrons.[31] The solid curve was calculated in the dynamical theory according to (38) without the zero fluctuations. The static approximation result, calculated according to (37) for $n=0$, is shown for comparison.

The corresponding dynamic correlation function, characterizing the degree of magnetic short-range order, is depicted in Fig. 5. Note that the function $\langle m^2(q)\rangle$ (Fig. 4) is the same at all sites of the reciprocal lattice, and its Fourier transform $\langle m(r)m(0)\rangle$ is defined at the sites of the direct lattice, i.e., the coordinate r takes the discrete values r_i while $m(r_i)$ is understood as the integrated moment of the electrons in the MT sphere (momentum-transfer sphere) centered at the ith atom. As can be seen, the correlation of the spin fluctuations

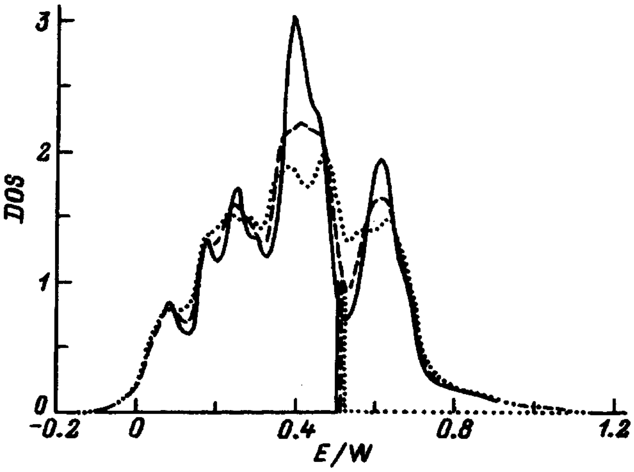

FIG. 3. Spin-integrated density of electron states at $T=0$ (solid curve), $T=0.89T_c$ (dashed curve) and $T=2.17T_c$ (dotted curve). The vertical lines correspond to the chemical potential μ.

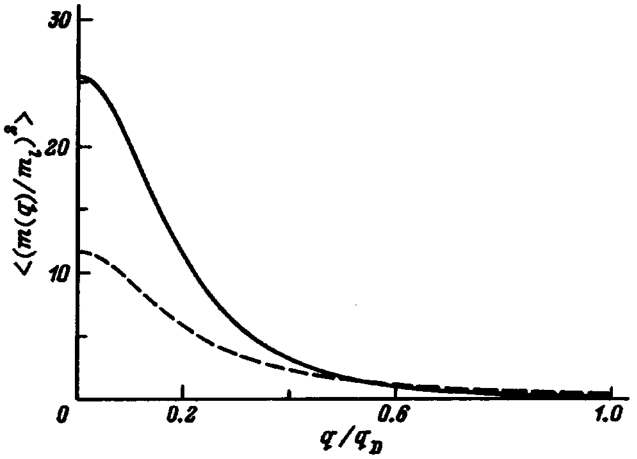

FIG. 4. Distribution of spin fluctuations over wave number q (in units of the limiting vector q_D of the Brillouin zone) in the dynamical theory (solid curve) and in the static approximation (dashed curve).

in real space is not large, but it is completely sufficient for paramagnetic scattering of neutrons to be distinctly observable.

In conclusion, we note that our theory is based on the well-known Gaussian approximation for describing the fluctuating field and at the same time differs fundamentally from previous approaches. The key point consists in separating the temperature fluctuations from the zero fluctuations (the fluctuations in the ground state at $T=0$). As a result, the dynamical problem reduces to a calculation of quasi-elastic scattering of electrons by a fluctuating exchange potential which is characterized by the mean-square thermal fluctuation at a site $\langle \Delta V^2 \rangle$. It is just this value that is calculated by the dynamical formulas and it contains an explicit temperature dependence which differs qualitatively from that obtained in the static approach. Our relations, especially in the form (16), are very similar to the well-known RPA equations, however, with a very important difference, namely, that the zero susceptibility is renormalized due to the spin fluctuations and is calculated self-consistently.

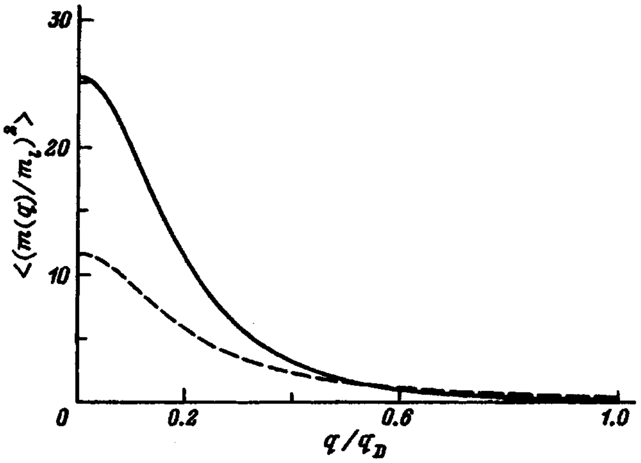

FIG. 5. Spin correlation function plotted against distance r (in units of the bcc lattice constant of iron a_0). The dashed curve is its asymptotic limit (40).

To sum up, I have proposed a simple (in terms of its final relations) theory of thermal spin fluctuations which takes account of 1) the dynamics and spatial correlation of the spin fluctuations, 2) the interaction of different spatial modes, and 3) contributions from both the long-wavelength and random spin fluctuations to the average single-site Green's function, which in fact is the sole characteristic of the electron subsystem. As input data, the mathematical scheme uses the density of electron states (e.g., based on first-principle calculations) and the atomic magnetic moment at $T=0$.

[1] T. Moriya, *Spin Fluctuations in Itinerant Electron Magnetism*, Springer-Verlag Series in Solid State Sciences, Vol. 56 (Springer-Verlag, New York, 1985).
[2] H. Capellmann (editor), *Metallic Magnetism* (Springer, Berlin, 1987).
[3] V. I. Grebennikov and E. A. Turov, *Dynamic and Kinetic Properties of Magnets* [in Russian], Nauka, Moscow (1986), pp. 9–36.
[4] V. I. Grebennikov and E. A. Turov, *Magnetic Properties of Crystalline and Amorphous Media* [in Russian], Nauka, Novosibirsk (1989), pp. 72–87.
[5] R. L. Stratonovich, Dokl. Akad. Nauk SSSR **157**, 1097 (1957).
[6] J. Hubbard, Phys. Rev. Lett. **3**(2), 77 (1959).
[7] M. Cyrot, Phys. Rev. Lett. **25**(13), 871 (1970); J. Phys. (Paris) **33**, 125 (1972).
[8] J. Hubbard, Phys. Rev. Lett. **19**(5), 2626 (1979); Phys. Rev. B **20**(11), 4584 (1979).
[9] J. Hubbard, Solid State Sci. **29**, 29 (1981).
[10] H. Hasegawa, J. Phys. Soc. Jpn. **46**(5), 1504 (1979); Solid State Commun. **31**(8), 597 (1979).
[11] H. Hasegawa, J. Phys. Soc. Jpn. **49**(1), 178; (3), 963 (1980).
[12] V. I. Grebennikov, Yu. I. Prokop'ev, O. B. Sokolov, and E. A. Turov, Fiz. Met. Metalloved. **52**(4), 679 (1981).
[13] H. Hasegawa, J. Phys. F **13**(9), 1915 (1983).
[14] H. Hasegawa, J. Phys. F **13**(12), 2655 (1983); **14**(5), 1235 (1984).
[15] B. L. Gyorffy, A. J. Pindor, J. Staunton, G. M. Stocks, and H. Winter, J. Phys. F **15**(6), 1337 (1985).
[16] J. Staunton, B. L. Gyorffy, G. M. Stocks, and J. Wadsworth, J. Phys. F **16**(11), 1761 (1986).
[17] Y. Kakehashi, J. Phys. Soc. Jpn. **50**(5), 1505; (7), 2251; (11), 3620 (1981).
[18] Y. Kakehashi, Phys. Rev. B **41**, 9207 (1990).
[19] F.-J. Shi and T.-H. Lin, Phys. Rev. B **49**(23), 16 269 (1994).
[20] T. Moriya and H. Hasegawa, J. Phys. Soc. Jpn. **48**(5), 1490 (1980).
[21] Y. Kakehashi and M. Yu, Phys. Rev. B **50**(9), 6189 (1994).
[22] J. A. Hertz and M. A. Klenin, Phys. Rev. B **10**(3), 1084 (1974); Physica B **91**, 49 (1977).
[23] T. Izuyama, D.-J. Kim, and R. Kubo, J. Phys. Soc. Jpn. **18**(7), 1025 (1963).
[24] K. K. Murata and S. Doniach, Phys. Rev. Lett. **29**(5), 285 (1972).
[25] M. Shimizu, Pers Progr. Phys. **44**(4), 329 (1981).
[26] W. Weber, B. Kirchner, and J. Voitlander, Phys. Rev. B **50**(2), 1090 (1994).
[27] M. Uhl and J. Kubler, Phys. Rev. Lett. **77**(2), 334 (1996).
[28] Y. Kakehashi and P. Fulde, Phys. Rev. B **32**(3), 1595 (1985).
[29] Y. Kakehashi, Phys. Rev. B **34**(4), 3243 (1985).
[30] V. I. Grebennikov, Fiz. Met. Metalloved. **66**(2), 227 (1988).
[31] V. I. Grebennikov, J. Magn. Magn. Mater. **84**, 59 (1990).
[32] V. I. Grebennikov, Fiz. Met. Metalloved. **64**(2), 276 (1987).
[33] E. A. Turov and V. I. Grebennikov, Physica B **159**, 56 (1989).
[34] V. I. Grebennikov and O. B. Sokolov, Fiz. Met. Metalloved. **76**(11), 5 (1993).
[35] V. I. Grebennikov and O. B. Sokolov, J. Phys.: Condens. Matter **4**(12), 3283 (1992); Phys. Status Solidi B **151**(2), 623 (1989).
[36] B. I. Rezer and V. I. Grebennikov, Fiz. Met. Metalloved. **83**(2), (1997).

Translated by Paul F. Schippnick

Production, structure, and microhardness of nanocrystalline Ni-Mo-B alloys

G. E. Abrosimova, A. S. Aronin, I. I. Zver'kova, A. F. Gurov, and Yu. V. Kir'yanov

Institute of Solid-State Physics, Russian Academy of Sciences, 142432 Chernogolovka, Moscow Region, Russia

(Submitted March 11, 1997; resubmitted June 17, 1997)
Fiz. Tverd. Tela (St. Petersburg) **40**, 10–16 (January 1998)

Radiography, differential scanning calorimetry, luminescence and high-resolution electron microscopy are used to study the production, nanocrystalline structure, stability, and microhardness of alloys from the Ni-Mo-B system containing from 27 at. % to 31.5 at. % Mo and 10 at. % B. All studies of these alloys indicated that annealing at 600 °C leads to the creation of a granular phase consisting of FCC nanocrystallites with average grain sizes of 15–25 nm, depending on the chemical composition of the alloy. Annealing these nanocrystalline samples isothermally at a temperature of 600 °C has no appreciable effect on the grain size. Structurally, the nanocrystalline phase consists of grains of an FCC solid solution of Mo and B in Ni, dispersed in an amorphous matrix that isolates them from one another. The lattice parameters of the FCC nanocrystallites depend on the alloy composition and the duration of their isothermal anneal. Within this latter time, molybdenum and boron atoms diffuse from the FCC solid-solution lattice into the surrounding amorphous matrix. The stability of the nanocrystalline structure is determined by the thermal stability of the amorphous matrix, whose crystallization temperature increases with the isothermal annealing time due to enrichment by boron and molybdenum. As the structure forms, the alloy becomes harder as the nanocrystalline grains grow in size. This relation between hardness and grain size, which is opposite to the Hall—Petch law, is explained by hardening of the amorphous matrix due to changes in its chemical composition. © *1998 American Institute of Physics.* [S1063-7834(98)00301-3]

The creation of new materials is usually driven by a need to improve the properties of known materials or to produce new combinations of these properties. The recent discovery of a new class of materials—nanocrystalline alloys—is no exception to this principle. In addition, nanocrystalline materials (in which the grain size does not exceed 50 nm) are extremely interesting subjects for research, since an appreciable fraction of their atoms are located at surfaces or in the immediate vicinity of surfaces. The unique properties of these materials stem from their ultrafinely dispersed granular structure and the large fraction of surface atoms. Nanocrystalline materials can be obtained by various methods: sputtering, electrolytic deposition, laser ablation, mechanical alloying, and crystallization of metallic glasses[1,2] (for example, a nanocrystalline structure is observed when amorphous Fe-B alloys are crystallized at high temperatures, see Ref. 3). A major impetus for the development of this last method was provided by the discoveries that nanocrystalline alloys based on Fe exhibit good magnetic softness[4] and nanocrystalline light alloys based on Al and Mg are high-strength materials.[5]

It is widely known that many mechanical properties of polycrystalline alloys depend on the grain size d. In particular, the plasticity limit of these materials, like their microhardness, obeys the Hall-Petch law

$$\sigma_\tau=\sigma_0+K_y/\sqrt{d},$$

where σ_τ is the plasticity limit, σ_0 is the frictional stress, which is independent of grain size, and K_y is a constant. Therefore, nanocrystalline materials with extremely small grain sizes are of great interest from the point of view of creating high-strength properties. However, nanocrystalline materials obtained by controlled crystallization of amorphous alloys exhibit deviations from the Hall—Petch law,[5,6] which probably indicates that the deformation mechanism is different (i.e., unlike that of ordinary polycrystalline alloys). The nanocrystalline alloys discussed in this paper, which consist of Ni with a large amount of Mo, are promising materials from the point of view of achieving good corrosion resistance and electrocatalytic properties.[7] An important property of these materials is the high thermal stability of the nanocrystalline structure. Previously, we showed[8] that the thermal stability of the nanocrystalline alloy $(Ni_{65}Mo_{35})_{90}B_{10}$, obtained by controlled crystallization of a metallic glass, is determined by the stability of the amorphous matrix that exists between the grains. The goal of this paper is to investigate the creation, structure, thermal stability, and microhardness of pre-eutectic alloys with nanocrystalline structure from the system Ni-Mo-B as well as their dependence on the concentrations of the metalloid (B) and the refractory components (Mo), and to establish a correlation between the structural and mechanical properties. We investigated these samples by electron microscopy, radiography, differential scanning calorimetry, and microhardness measurements using the Vickers method.

1. METHOD OF INVESTIGATION

In this paper, we will discuss the alloys $(Ni_{65}Mo_{35})_{90}B_{10}$, $(Ni_{70}Mo_{30})_{90}B_{10}$, and $(Ni_{70}Mo_{30})_{95}B_5$ (by batch). We used high-purity metals ($>99\%$) to prepare the alloys. Initially amorphous samples were obtained by rapid quenching from a melt on a copper disk rotating at a speed of ≈ 20 m/s (melt spinning). The thickness of the amorphous alloy ribbons was about 30 μm.

The amorphous alloys were held under isothermal conditions in a resistive oven, and then placed in ampoules that were pumped down to a vacuum of 1×10^{-5} Pa and hermetically sealed. These ampoules were placed in the oven and kept there for periods of time that varied from 1 to 600 hours.

The crystallization of the amorphous alloys was studied by differential scanning calorimetry using a DSC-7 Perkin-Elmer thermal analysis setup. The ampoules were heated in an argon atmosphere at a rate of 20 K/min.

The microhardness was measured on a PMT-3 microhardness meter at a load of 0.5 N for 20 s. Each experimental value was determined from 40 measurements with an error of about 3%. The sample structure was investigated by radiography, luminescence, and high-resolution electron microscopy. The diffraction patterns were obtained with a Siemens D-500 diffractometer, using Cu $K\alpha$ radiation. The electron microscopy studies were made using a JEM-100CX electron microscope with an accelerating voltage of 100 kV, and a high-resolution JEOL-400EX microscope (spherical aberration constant $C_s = 1.0$ mm, $U = 400$ kV). Samples for the electron microscopy were prepared by ion polishing on a GATAN600 setup.

The average grain size was determined from the broadening of peaks in the x-ray scans, using the Selyakov-Sherrer formula[9] and from dark-field electron-microscopy images. In order to determine the grain size from the broadening of the peaks, we used a special set of computer programs. When the diffraction lines under study partially overlapped, we resolved them using a set of diffraction line-resolving programs. In order to determine the lattice parameters we added a standard (Al powder). The sample was not removed from the diffractometer while the standard was deposited.

2. EXPERIMENTAL RESULTS

We investigated three alloys with the following compositions: $(Ni_{70}Mo_{30})_{90}B_{10}$ (1), $(Ni_{70}Mo_{30})_{95}B_5$ (2), $(Ni_{65}Mo_{35})_{90}B_{10}$ (3). As obtained, the alloys were amorphous: diffraction studies revealed no sign of a crystalline phase, only diffuse maxima that are typical of amorphous structures. Upon heating, these amorphous alloys proceeded to crystallize. Crystallization proceeded by a primary crystallization mechanism in which the crystals that emerge from an amorphous host (in our case, a solid solution based on Ni; see Fig. 1) have a composition different from that of the original alloy. The composition of the matrix changes as these primary crystals are liberated.

For these alloys, the lattice parameter of the nanosized grains of FCC solid solution was a function of how long they were isothermally held at 600 °C. In the alloy $(Ni_{70}Mo_{30})_{90}B_{10}$, the lattice parameter of the FCC solid solution increased from 0.3592 nm when the alloy was isothermally held in the oven for 1 hour to 0.3602 nm when held there for 360 hours; in $(Ni_{70}Mo_{30})_{95}B_5$ this treatment produced practically no change (from 0.3600 nm after 5 hours to 0.3602 nm after 360 hours); and in $(Ni_{65}Mo_{35})_{90}B_{10}$ there was a negligible decrease (from 0.3600 nm after 5 hours to 0.3597 nm after 144 hours).

The process of crystallization of these alloys is illustrated in Figs. 2a, 2b. The crystallization temperatures (T_x) determined from the differential scanning calorimetry data at a heating rate of 20 K/min were 829, 802, and 847 K for the alloys $(Ni_{70}Mo_{30})_{90}B_{10}$, $(Ni_{70}Mo_{30})_{95}B_5$, $(Ni_{65}Mo_{35})_{90}B_{10}$ respectively. Thus, the crystallization temperature of these alloys increases with increasing concentration of the metalloid (B) and the refractory component (Mo). During the period of primary crystallization, grains of a solid solution of boron and molybdenum in nickel were formed.

We studied crystallization processes in these alloys while they were annealed isothermally at a temperature of 600 °C. Figure 1 illustrates the evolution of the structure, and the way it changes with increasing oven time, which gradually increases the fraction of crystalline phase. The maxima in the diffraction patterns of the annealed alloys (Fig. 1) are caused by the presence of nanocrystallites with an FCC lattice and the residual amorphous phase, except perhaps for the pattern corresponding to a duration of 600 hours.

As we have already mentioned, crystallization of these amorphous alloys begins with the liberation of crystals of a solid solution of boron and molybdenum in Ni from the amorphous matrix. The grain size is several nanometers. Increasing the time the samples were kept in the oven at 600 °C caused these grains to increase slightly in size, but after 144 hours there was practically no change in grain size at all. Figure 3 shows the dependence of the average grain size on the oven time for all the samples we studied. The mean size was determined from electron microscopy data. In all the alloys we investigated, a nanocrystalline structure forms with an average grain size that does not exceed 28 nm. Signs of this structure are visible in Fig. 4, which shows light-field (a) and dark-field (b) images of the structure of samples of the alloy $(Ni_{70}Mo_{30})_{90}B_{10}$ after being kept isothermally for 144 hours at 600 °C.

The finest-grained nanocrystalline structures form in the alloy $(Ni_{70}Mo_{30})_{90}B_{10}$, the coarsest-grained in the alloy $(Ni_{65}Mo_{35})_{90}B_{10}$. The nanocrystalline structure is two-phase, consisting of an amorphous matrix in which grains of a solid solution with an FCC lattice are uniformly distributed. The grains have no direct contact with one another. The high-resolution image of this structure shown in Fig. 5 reveals grains separated by regions of the amorphous phase. The magnitude of defocusing was -49 nm, corresponding to Schertzer defocusing.

Plots of the changes in microhardness for the alloys versus oven time are shown in Fig. 6 (curves *1–3*). In the original state, the alloy $(Ni_{65}Mo_{35})_{90}B_{10}$ exhibits the largest microhardness, while $(Ni_{70}Mo_{30})_{95}B_5$ exhibits the smallest. The microhardness of the alloy $(Ni_{70}Mo_{30})_{90}B_{10}$ in the amorphous state essentially corresponds to that of the alloy $(Ni_{65}Mo_{35})_{90}B_{10}$, i.e., with increasing concentration of the metalloid the microhardness increases. It is also clear from Fig. 6 that the microhardnesses of all the alloys increase with the anneal duration. At the stage where the nanocrystalline

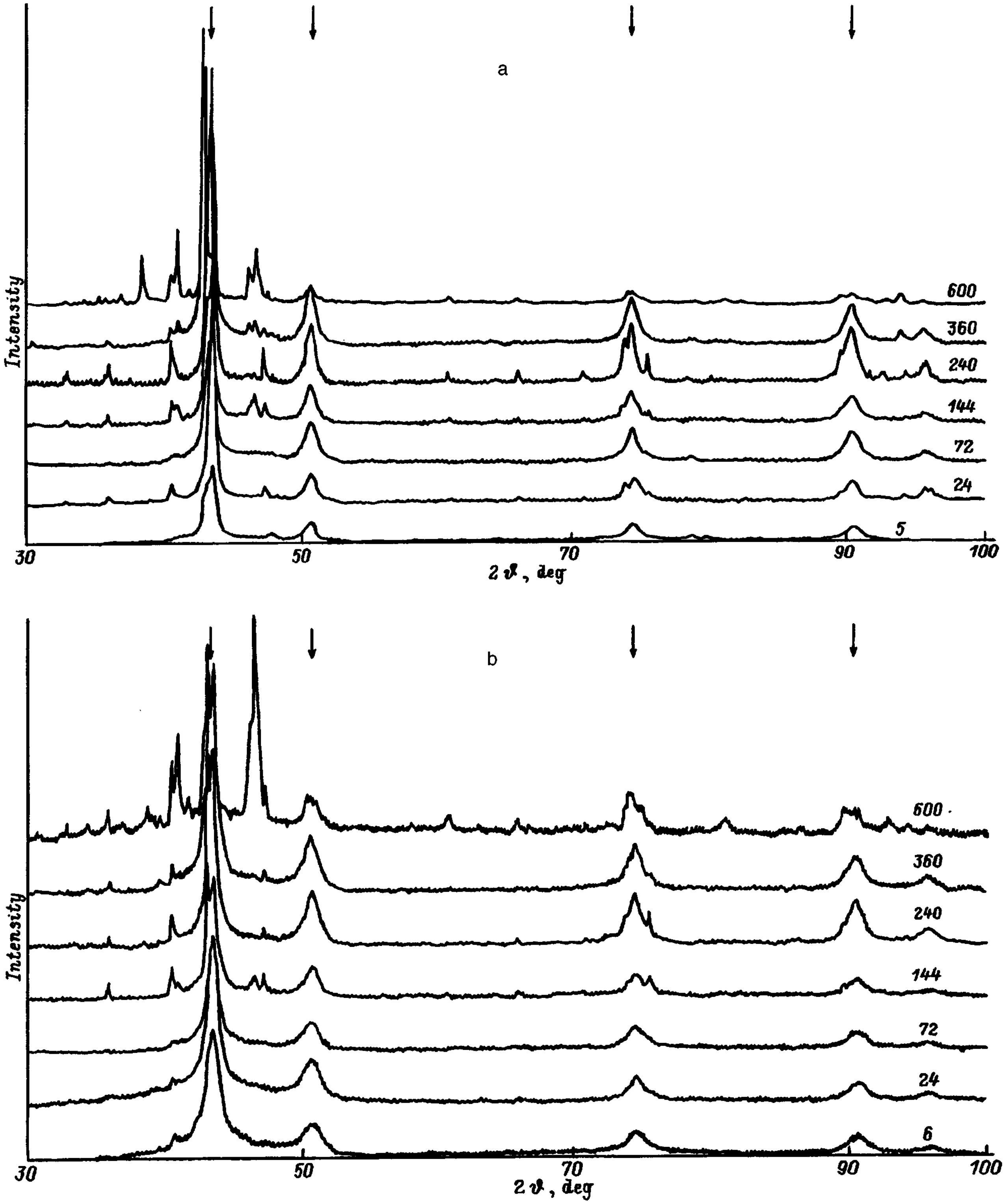

FIG. 1. Diffraction pattern of alloys annealed at 600 °C for 1-600 hours. a—$(Ni_{70}Mo_{30})_{95}B_5$, b—$(Ni_{70}Mo_{30})_{90}B_{10}$. The arrows indicate the position of lines of the FCC phase. The numbers on the curves indicate oven time (in hours).

microstructure is stable (i.e., after being kept isothermally at 600 °C for 72 to 240 hours) the microhardnesses of all the alloys practically coincide. The observed dependence (Fig. 6) correlates with the dependence of the grain size on oven time (Fig. 3). It is noteworthy that the microhardness of all the alloys drops rapidly as the nanocrystalline structure decays.

3. DISCUSSION OF RESULTS

As we have already noted, the starting alloys were amorphous. On heating they crystallize by primary crystallization due to the composition of the alloys. In primary crystallization from the amorphous matrix, crystallites of the FCC solid solution based on Ni are liberated. Since during primary

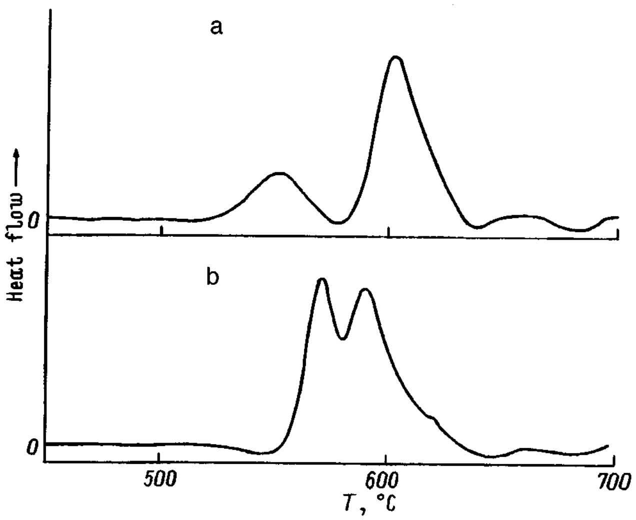

FIG. 2. Differential scanning calorimetry curves for amorphous Ni-Mo-B alloys heated at a rate of 20 K/min. a—$(Ni_{70}Mo_{30})_{95}B_5$, b—$(Ni_{70}Mo_{30})_{90}B_{10}$.

crystallization the composition of the crystals that form differs from that of the matrix, the composition of the remaining amorphous phase changes as the crystallization proceeds. For these alloys, the amorphous phase is enriched by boron and molybdenum as the fraction of crystalline phase increases. On the other hand, the composition of the liberated crystals also undergoes a change that depends on the time spent in the oven. This change in composition of the nanocrystallites causes a change in the lattice parameter. As we noted earlier, increasing the time the alloys are kept at 600 °C increases the lattice parameter of the alloy $(Ni_{70}Mo_{30})_{90}B_{10}$, leaves it unchanged in the alloy $(Ni_{70}Mo_{30})_{95}B_5$, and decreases it slightly in the alloy $(Ni_{65}Mo_{35})_{90}B_{10}$. The observed changes in lattice parameter confirm the composition of the nanocrystallites changes during their stay in the oven. Since dissolving Mo in Ni leads to an increase in the lattice parameter of the resulting Ni-based solid solution, while dissolving B in Ni leads to a decrease, these changes in lattice constant can be explained in the following way. It is well known[10] that the equilibrium concentration of Mo in Ni at 600 °C is 13.6 at. %, while for B it is less than 1 at. %. At the time of formation, the nanocrystallites consist of a supersaturated solid solution of Mo and B in Ni. While the samples are in the oven, a combined diffusion of Mo and B from the nanocrystallites occurs. It is quite likely that due to the different chemical composition of the original alloys, the initial compositions of the nanocrystallites in the alloys will also be different. Different supersaturations of the nanocrystallite solid solutions of molybdenum and boron lead to different values of the lattice parameters. The maximum lattice parameter is observed for the largest molybdenum content (the alloy $Ni_{65}Mo_{35})_{90}B_{10}$ and the minimum boron content (the alloy $(Ni_{70}Mo_{30})_{95}B_5$). As the boron concentration increases (from the alloy $Ni_{70}Mo_{30})_{90}B_{10}$ to the alloy $Ni_{70}Mo_{30})_{95}B_5$) or the Mo concentration decreases (from the alloy $Ni_{70}Mo_{30})_{90}B_{10}$ to the alloy $(Ni_{65}Mo_{35})_{90}B_{10}$, nanocrystallites with decreased values of lattice parameter form. While the samples are held isothermally in the oven, combined diffusion of molybdenum and boron into the surrounding amorphous matrix occurs. A slight decrease in the lattice parameter is observed when molybdenum leaves the nanocrystallites for the case where the amount of lost molybdenum (combined with boron) is largest, i.e., for the alloy $(Ni_{65}Mo_{35})_{90}B_{10}$ (compared to the other alloys). Since nanocrystallites of the alloy $(Ni_{70}Mo_{30})_{90}B_{10}$ lose less molybdenum, simultaneous boron diffusion into the amorphous matrix leads us to expect an increase in the lattice parameter, which is also observed. Nanocrystallites of the alloy $(Ni_{70}Mo_{30})_{95}B_5$ initially contained less boron than in the other alloys, and a larger amount of molybdenum than in the alloy $(Ni_{70}Mo_{30})_{90}B_{10}$. Therefore, the combined diffusion of molybdenum and boron from the nanocrystallites in this alloy does not lead to an appreciable change in the lattice parameter. It is noteworthy that all the experimental lattice parameters we have obtained for the FCC solid solution based on nickel are larger than the lattice parameter of pure nickel (0.353 nm). It is therefore clear that the nanocrystallites contain a large amount of molybdenum at all stages of existence of the nanocrystallite structure. Estimates of the molybdenum concentration in the nanocrystallites based on lattice parameter in accordance with Vegard's law give a value of about 20 at. %. These estimates do not take into account the presence of boron atoms in the nanocrystallite lattice.

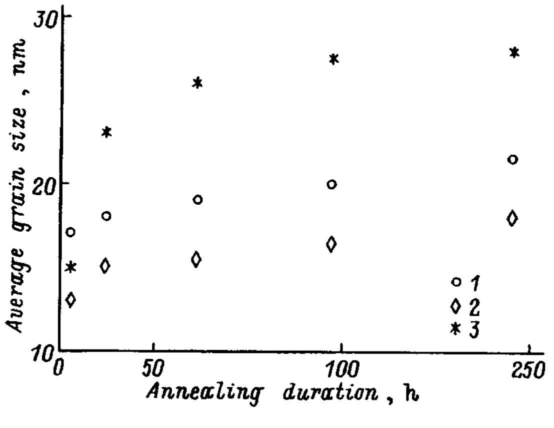

FIG. 3. Dependence of the average grain size on oven time at 600 °C. *1*—$(Ni_{70}Mo_{30})_{95}B_5$, *2*—$(Ni_{70}Mo_{30})_{90}B_{10}$, *3*—$(Ni_{65}Mo_{35})_{90}B_{10}$.

The nanocrystalline structure of the alloys investigated here has high thermal stability. The average grain size is in the range 15–20 nm, depending on processing. The oven temperature, which is roughly 0.6 of the melting temperature, is entirely adequate for recrystallization to take place in ordinary fine-crystalline alloys.[11] However, in these alloys the increase in the grain size does not remain significant for very long. Let us consider how this can be explained.

While they are in the oven, these alloys all exhibit an increase in the average size of the nanocrystallites (Fig. 3). The change is significant in the initial stage of their stay in the oven, but then the grain size almost ceases to change. During this time the amorphous matrix is enriched by molybdenum and boron. Because the amorphous matrix is situated so as to isolate the nanocrystallites from one another, it prevents their growth at one another's expense. In this way it

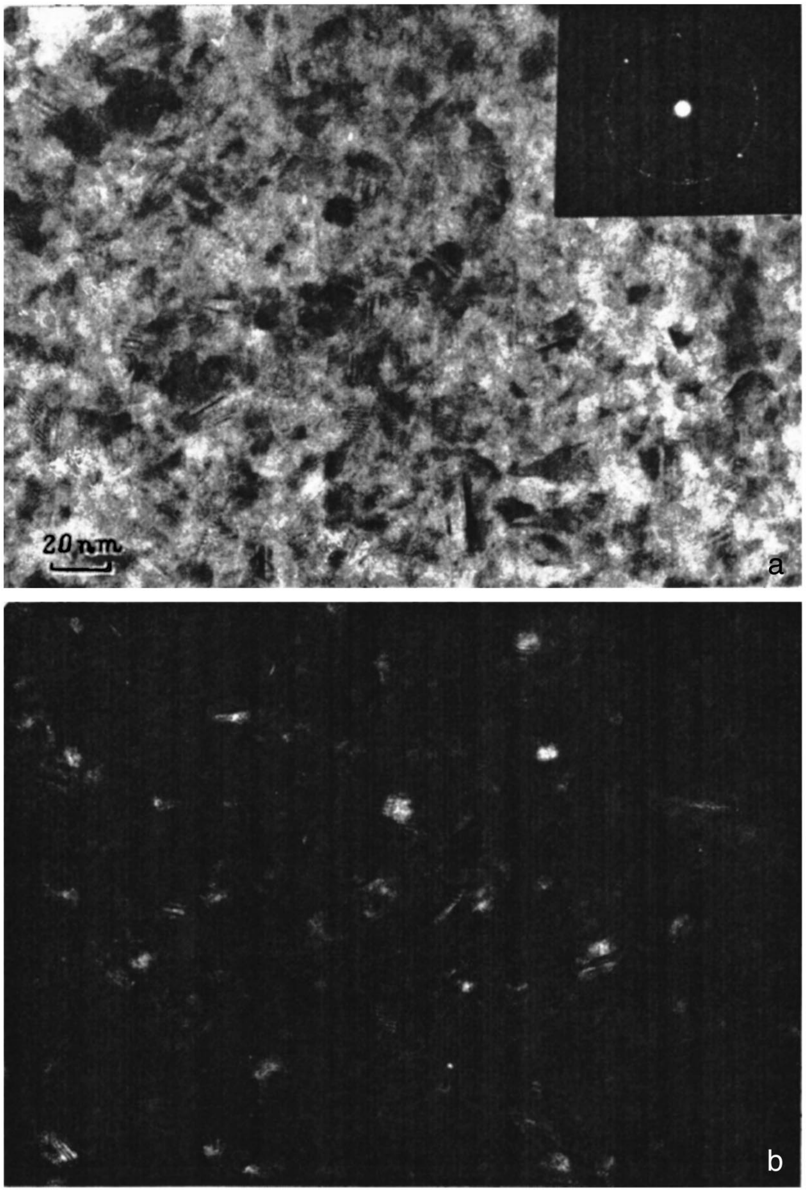

FIG. 4. Microstructure of $(Ni_{70}Mo_{30})_{90}B_{10}$ alloy after 144 hours in the oven at 600 °C. a—bright-field image, b—dark-field image.

determines the thermal stability of the nanocrystalline structure. The differential scanning calorimetry results (Fig. 2) imply that increasing the concentrations of boron and the refractory component (i.e., Mo) in the amorphous matrix leads to an increase in the crystallization temperature of the amorphous alloys. Thus, while the alloys are in the oven the chemical composition of the amorphous matrix changes, leading to an increase in its crystallization temperature and hence thermal stability.

Figure 6 shows the change in microhardness of the alloys H_V as a function of oven time. For all three alloys, as the isothermal oven time increases the microhardness increases (along with a simultaneous increase in grain size). This implies (since σ_τ is roughly equal to $H_V/3$) that the experimental dependence of the plasticity limit on grain size is opposite the Hall-Petch law (i.e., $\sigma_\tau = \sigma_0 + K_y/\sqrt{d}$, where σ_τ is the plasticity limit; the frictional stress σ_0, whose value does not depend on grain size, is the stress required to translate unpinned dislocations in the unpinned glide planes of a single crystal; and K_y is a (positive) constant connected with the propagation of strain through a grain boundary).[12] The experimental dependences shown in Fig. 6 cannot be explained in terms of dislocation interactions (the Hall-Petch law). A similar dependence of the plasticity limit on the size of the nanocrystallites was also noted in Ref. 6 in nanocrystalline alloys obtained by crystallization of metallic glasses based on Zr.

It is likely that the microhardness of these alloys is determined in large part by the amorphous matrix, and that its increase as the nanocrystallites form and grow is due to hardening of the amorphous matrix. This hardening of the amorphous matrix is a result of the redistribution of chemical components during the formation and growth of the crystallites. The largest change in microhardness occurs simultaneously with the largest change in average grain size. However, the change in composition of the grains and diffusion of molybdenum and boron from them occurs over the entire time the samples are kept in the isothermal oven. Conse-

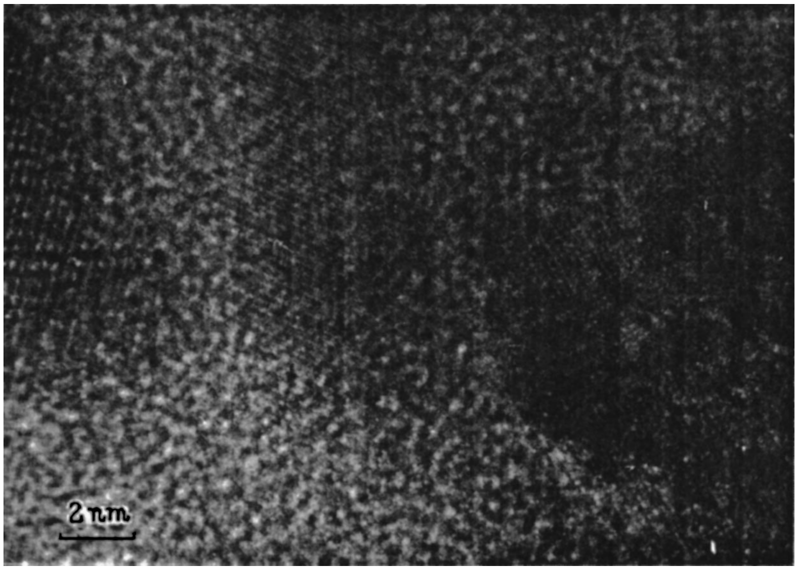

FIG. 5. High-resolution image of the structure of nanocrystalline alloys $(Ni_{65}Mo_{35})_{90}B_{10}$ after 72 (isothermal) hours in the oven at 600 °C.

quently, the change in composition of the amorphous matrix, which determines the microhardness, is largest while the grains are forming and growing, i.e., during primary crystallization, and is not a consequence of diffusion of components from the nanocrystallites while they are in the oven. During this time, the amorphous matrix is enriched by boron and molybdenum, causing its hardness to increase (H_V is larger for an amorphous alloy with increased concentrations of boron and molybdenum than H_V for an alloy with decreased concentrations; see the initial points of the curves shown in Fig. 6). It is obvious that the bulk fraction of remaining amorphous matrix depends on the concentration of Mo and B in the original alloy, and increases with its growth. Therefore alloys with larger Mo and B content should be harder. On the other hand, these alloys contain more coarse grains of the crystalline phase; therefore, we should expect them to exhibit the lowest hardness. However, at the stage of stable existence of the nanocrystalline structure the values of microhardness, taking into account measurement errors, are practically the same for all the alloys we studied, and do not depend on the grain size. Therefore the observed identical values of microhardness are most likely due to the influence of both the effects discussed above.

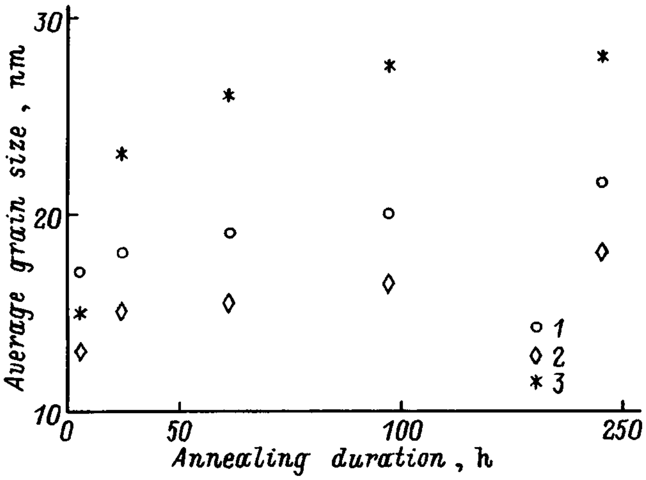

FIG. 6. Plots of microhardness (load 0.5 N) of the alloy system Ni–Mo–B versus isothermal time in the oven at 600 °C. *1*—$(Ni_{70}Mo_{30})_{95}B_5$, *2*—$(Ni_{70}Mo_{30})_{90}B_{10}$, *3*—$(Ni_{65}Mo_{35})_{90}B_{10}$.

The authors are grateful to the Russian Fund for Fundamental Research (Projects Nos. 96-02-19582 and 95-02-03759a) for financial support of this work, and also to H. Alves (Dortmund University, Federal Republic of Germany) and V. V. Molokanov (IMET, Russian Academy of Sciences, Moscow, Russia) for providing the amorphous alloy samples.

[1] G. Herzer, IEEE Trans. Magn. **25**, 3327 (1989).
[2] U. Köster, U. Schuheman, M. Blank-Bewerdorf, S. Brauer, M. Sutton, and G. P. Stephenson, Mater. Sci. Eng. A **133**, 611 (1991).
[3] G. E. Abrosimova, A. S. Aronin, and V. A. Stel'mukh, Fiz. Tverd. Tela (Leningrad) **33**, 3570 (1991) [Sov. Phys. Solid State **33**, 2006 (1991)].
[4] P. Allia, F. Vinai, M. Knobel, and T. R. Sato, Appl. Phys. Lett. **59**, 2454 (1991).
[5] Z. C. Zhong, X. Y. Jiang, and A. L. Greer, Rapidly Quenched and Metastable Materials (RG9): Book of Abstracts (Bratislava, August 25, 1996), P. 244.
[6] H. Alves, M. Ferreira, U. Köster, and B. Müller, Mater. Sci. Forum **225–227**, 769 (1996).
[7] H. Alves, M. Ferreira, U. Köster, and B. Müller, Mater. Sci. Forum **179–181**, 449 (1995).
[8] A. S. Aronin, G. E. Abrosimova, I. I. Zver'kova, Yu. V. Kir'janov, V. V. Molokanov, and M. I. Petrzhik, Rapidly Quenched and Metastable Materials: Book of Abstracts (Bratislava, August 25, 1996), P. 247.
[9] Ya. S. Umanskiĭ, Yu. A. Skakov, A. N. Ivanov, and L. N. Rastorguev, *Crystallography, Radiography, and Electron Microscopy* [in Russian], Metallurgiya, Moscow, 1982.
[10] M. Hansen and K. Anderko, *Constitution of Binary Alloys*, 2nd ed. [McGraw-Hill, New York, 1958; Metallurgizdat, Moscow, 1962].
[11] S. S. Gorelik, *Recrystallization of Metals and Alloys*, Metallurgiya, Moscow, 1978.
[12] J. P. Hirth and J. Lothe, *Theory of Dislocations* [McGraw-Hill, New York, 1967; Atomizdat, Moscow, 1972].

Translated by Frank J. Crowne

Effect of Cr^{3+} ions on the magnetic moment of ferrites of the system $CuFe_{2-x}Cr_xO_4$

L. G. Antoshina, A. N. Goryaga, and E. N. Kukudzhanova

Moscow State University (M. V. Lomonosov), 119899 Moscow, Russia

(Submitted April 23, 1997)
Fiz. Tverd. Tela (St. Petersburg) **40**, 99–100 (January 1998)

The dependence of the magnetic moment $n_{0\exp}$ of samples of the system $CuFe_{2-x}Cr_xO_4$ ($x=0.0$, 0.2, 0.3, 1.0, 1.4, 1.6, and 2.0) on their Cr^{3+} content is examined here for the first time. It is found that the experimental values of the magnetic moment $n_{0\exp}$ are much smaller than the values calculated from the cation distribution obtained previously ($n_{0\,\text{theor}}$). It is suggested that this relationship ($n_{0\,\text{theor}}>n_{0\exp}$) is due to a decrease in the magnetic moments of the Cr^{3+} ions resulting both from pairing of the t_{2g} orbitals of these cations in the octahedral sublattice and from a transfer of spin density from the ligands to the e_g orbitals of these ions. For compositions with $x>1.0$, the noncollinear magnetic structure also leads to an increase in the difference between $n_{0\,\text{theor}}$ and $n_{0\exp}$. *© 1998 American Institute of Physics.* [S1063-7834(98)02101-7]

The present paper is dedicated to a study of the dependence of the magnetic moments of ferrites of the system $CuFe_{2-x}Cr_xO_4$ on their Cr^{3+} content. There is no such information available in the literature. As a rule, a depressed value of the experimental magnetic moments $n_{0\exp}$ is observed in ferrite-chromites relative to the theoretical values $n_{0\,\text{theor}}$. This is usually linked to the presence of a noncollinear magnetic structure in the B sublattice which is responsible for the magnetic moment of ferrite-chromites. However, it is not ruled out that this situation $n_{0\exp}<n_{0\,\text{theor}}$ may also be due to other factors.

For our study we chose samples of the system $CuFe_{2-x}Cr_xO_4$ with substitution levels $x=0.0$, 0.2, 0.3, 1.0, 1.4, 1.6 and 2.0. The samples were prepared using ceramic technology. We found at $T=293$ K that the samples with chromium content $x=0.0$, 0.2, and 0.3 have tetragonally-distorted spinel structure with $c/a>1$; for $x=1.6$ and 2.0, $c/a<1$; while the samples with $x=1.0$ and 1.4 occur in the cubic phase, in agreement with the results of Ref. 1. A study of the magnetization at 4.2 K in fields up to 12 kOe is carried out here for the first time using the ballistic method. The relative error of measurement of the magnetization was 3%.

By extrapolating the linear part of the 4.2 K isotherms of $\sigma(H)$ to $H=0$ we found the value of the spontaneous magnetization σ_s, from which we calculated $n_{0\,\exp}$. The theoretical value $n_{0\,\text{theor}}$ was calculated using the cation distribution in ferrite–chromites of copper suggested in Ref. 1. Here we assumed that the magnetic moments of the ions entering the composition of these ferrites have only a spin origin and that there is collinear ordering in the A and B sublattices.

Figure 1 plots the magnetic moments $n_{0\,\exp}$ and $n_{0\,\text{theor}}$ as functions of the Cr^{3+} content in the system $CuFe_{2-x}Cr_xO_4$. The error bars shown on the $n_{0\,\text{theor}}(x)$ curve correspond to errors in the cation distribution.[1] It can be seen that the dependence $n_{0\,\exp}(x)$ differs markedly from the dependence $n_{0\,\text{theor}}(x)$: whereas $n_{0\,\exp}$ only decreases with increase of x, the theoretical value $n_{0\,\text{theor}}$, on the other hand, grows vigorously. Here it turned out that the experimental values $n_{0\,\exp}$ are significantly lower than the theoretical ones $n_{0\,\text{theor}}$. For example, in $CuFeCrO_4$ $n_{0\,\text{theor}}$ is 2.5 times larger than $n_{0\,\exp}$ whereas in copper chromite it is larger by an order of magnitude.

Earlier we found[2] that the magnetic structure of the $CuFeCrO_4$ sample, which has cubic structure, is collinear, i.e., the large difference observed in the experimental and theoretical values $n_{0\,\exp}$ and $n_{0\,\text{theor}}$ for the given sample cannot be associated with a decrease in the magnetic moment of the B sublattice as a consequence of noncollinear ordering. At the same time, in the $CuFe_{2-x}Cr_xO_4$ sample, according to neutron diffraction data, to the contray, a noncollinear magnetic structure is present in the B sublattice.

According to Goodenough,[3] in ferrite–chromites in addition to indirect exchange interactions, direct exchange interactions can take place between the magnetic cations in the B sublattice since the distances between the B cations are comparable to R_{Cr}, for which immediate overlap of the t_{2g}

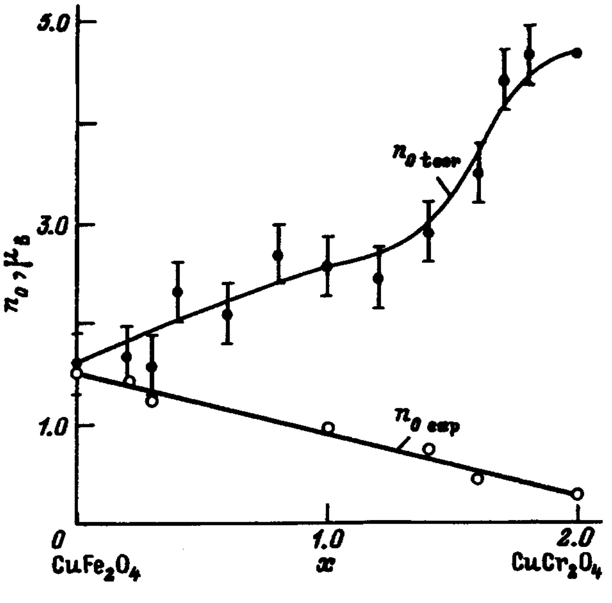

FIG. 1. Experimental, $n_{0\exp}$, and theoretical, $n_{0\,\text{theor}}$ magnetic moment plotted as functions of the Cr^{3+} content in samples of the system $CuFe_{2-x}Cr_xO_4$.

orbitals of the 3d cations is possible. Since one electron is found on each of the t_{2g} orbitals in $\mathrm{Cr}^{3+}(t_{2g}^3, e_g^0)$, pairing of their spins and, consequently, a decrease of the magnetic moment can take place as a result of such overlap.

It is well known that ferrite–chromites having the spinel structure belong to the class of compounds with a quite large covalent impurity bonding. Therefore transfer of spin density is possible in them, according to the results of Ref. 4, from the ligands to the vacant e_g orbitals of the neighboring Cr^{3+} ions. The authors of Ref. 4 assume that such a transition is energetically identical for a spin aligned with the magnetic moment of the Cr^{3+} ion and an anti-parallel spin.

Since the values of $n_{0\,\mathrm{exp}}$ are much smaller than those of $n_{0\,\mathrm{theor}}$, we believe that transfer of spin density to the Cr^{3+} ions in the system $\mathrm{CuFe}_{2-x}\mathrm{Cr}_x\mathrm{O}_4$ will take place for anti-parallel spin. Since the orbital moment of the octahedral Cr^{3+} ions is completely frozen by the crystal field, this transition will lead only to a decrease of their spin magnetic moment. In this case, the theoretical value of the Curie–Weiss constant $C_{s\,\mathrm{theor}}$ for ferrite–chromites should be larger than the experimental value in the paramagnetic region. We established this fact for the $\mathrm{CuFe}_{0.4}\mathrm{Cr}_{1.6}\mathrm{O}_4$ and $\mathrm{CuCr}_2\mathrm{O}_4$ samples. It turns out that, for a sample with $x=1.6$, the experimental value $C_{s\,\mathrm{exp}}=3.4\pm0.2$ whereas the theoretical value $C_{s\,\mathrm{theor}}=5.11$; for a sample with $x=2.0$, $C_{s\,\mathrm{exp}}=1.2\pm0.2$ while $C_{s\,\mathrm{theor}}=4.11$.

We believe that the large difference between the $n_{0\,\mathrm{theor}}$ and $n_{0\,\mathrm{exp}}$ values for samples of the system $\mathrm{CuFe}_{2-x}\mathrm{Cr}_x\mathrm{O}_4$ is associated in first order with a decrease in the magnetic moments of the Cr^{3+} ions both as a result of pairing of the t_{2g} orbitals of the cations in the octahedral lattice and as a result of transfer of spin density from the ligands to the e_g orbitals of these ions. However, it should be noted that, for copper ferrite–chromite samples with $x>1.0$ their noncollinear magnetic structure will also lead to a still larger difference between their theoretical and experimental magnetic moments.

[1] H. Ohnishi and T. Teranishi, J. Chem. Phys. **16**(1), 35 (1961).

[2] L. G. Antoshina and A. N. Goryaga, Fiz. Tverd. Tela (Leningrad) **34**, 3373 (1992) [Sov. Phys. Solid State **34**, 1805 (1992)].

[3] J. B. Goodenough, Phys. Rev. **117**, 1442 (1960).

[4] P. Freund, J. Owen, and B. F. Hann, J. Phys. C **6**, L139 (1973).

Translated by Paul F. Schippnick

Transport properties of antiferromagnetic fcc-iron alloys

G. A. Takzeĭ, I. I. Sych, and S. V. Cherepov

Institute of Magnetism, National Academy of Sciences of Ukraine, 252680 Kiev, Ukraine

(Submitted June 19, 1997)
Fiz. Tverd. Tela (St. Petersburg) **40**, 101–105 (January 1998)

A study is reported of the electrical resistance and thermopower of $Fe_xNi_{80-x}Cr_{20}$ fcc alloys within the $44 \leqslant x \leqslant 70$ at. % range. It is shown that, at low temperatures, they typically exhibit minima in the temperature dependences of electrical resistance. The appearance of these anomalies is attributed to the formation of a gap in the conduction electron spectrum due to the onset of long- or short-range antiferromagnetic order in the alloys. The effect of magnetic field on the magnetic states appearing in frustrated antiferromagnetic alloys has been studied, and an H-T magnetic phase diagram constructed.
[S1063-7834(98)02201-1]

Variation in the concentration of alloying components in the fcc alloys FeNiMn and FeNiCr along different quasibinary cuts was shown[1,2] to drive a phase transition from a long-range ferromagnetic (FM) to long-range antiferromagnetic (AFM) order. It is essential that, close to the critical concentrations where magnetic order changes type in these alloys, a spin glass (SG) state sets in.

It is of interest to establish how the onset of the above magnetic phases and states in these alloys can affect their transport properties. Of particular interest are the fcc alloys $Fe_xNi_{80-x}Cr_{20}$, which have a rich magnetic phase diagram[3] (Fig. 1). It is in these alloys that one first observed in the high iron-concentration region a reentrant temperature-driven AFM-SG transition for a frustrated Heisenberg magnet.[3,4]

The present study deals with the electrical resistance and thermopower of $Fe_xNi_{80-x}Cr_{20}$ alloys within a broad composition range and shows, by invoking data obtained in magnetic measurements, that the anomalous behavior of their transport properties is due to the formation of an energy gap in the electronic spectrum of the alloys induced by their AFM ordering. Besides, the investigation of the transport properties has permitted us to refine the magnetic structure of the alloys in the SG state, which in some cases is impossible to do by other means.

1. EXPERIMENTAL TECHNIQUES

The $Fe_xNi_{80-x}Cr_{20}$ samples were 40 mm-long wires 0.2–0.3 mm in diameter. Prior to measurements, the samples were quenched from 1400 K in water. X-ray diffraction and dilatometric analysis showed that when cooled to 4.2 K all alloys retained their original fcc state.

The electrical resistance was measured by the conventional four-probe dc technique in two current directions to exclude the effect of parasitic emf.

The temperature dependences of the alloy thermopower were studied in the 9–200-K range with respect to 99.999%-pure lead.

2. EXPERIMENTAL RESULTS AND DISCUSSION

A. Electrical resistance

Figure 2 presents typical temperature dependences of reduced electrical resistance $\Delta R(T)/R(5\,\mathrm{K}) = [R(T)-R(5\,\mathrm{K})]/R(5\,\mathrm{K})$ of $Fe_xNi_{80-x}Cr_{20}$ alloys, which, in accordance with the phase diagram in Fig. 1, undergo paramagnet-ferromagnet (PM-FM), PM-FM-SG, PM-SG, PM-AFM-SG, and PM-AFM magnetic transformations at $x=44$; 54; 60; 64 and 66; and 70 at. %, respectively. We readily see that the alloys in the AFM composition region ($x \geqslant 62$) are characterized by minima in electrical resistance, whose temperature T_m and relative depth $\Delta R(T_m)/R(5\,\mathrm{K})$ are the larger, the larger is x. Figures 1 and 2 show also that for AFM alloys $T_m < T_N$, where T_N is the Néel temperature.

For alloys with $54 \leqslant x \leqslant 60$, i.e., in the spin-glass region, minima in electrical resistance are also typical. In contrast to the AFM alloys, however, in SG state this anomaly is much weaker. It should also be pointed out that, contrary to Ref. 5, we did not observe any anomalies in electrical resistance either close to the SG freezing temperature T_G or in the vicinity of T_N. The latter observation is in accord with the results of many studies of the electrical resistance of the SG state, as well as of the frustrated FM and AFM.[6]

Consider now the effect of magnetic field on this anomaly in the electrical resistance. As seen from Figs. 3 and 4 illustrating the corresponding dependences for the AFM alloy and the spin glass, a sufficiently strong magnetic field shifts the $\Delta R(T)/R(4.2\,\mathrm{K})$ anomaly toward lower temperatures without suppressing it completely. This argues unambiguously for the observed anomalies being of magnetic nature.

Let us turn now to interpretation of the above results, which should answer at least three questions. First, why the minima in resistance are most clearly seen in AFM alloys? Second: what causes the minima in resistance in the $Fe_xNi_{80-x}Cr_{20}$ spin glass? And, finally, what is the mechanism of depression of the resistance minimum by magnetic field?

We note first that the above anomalies in the form of minima in the temperature dependences of resistance were observed also in other fcc-iron alloys [FeNiCr (Refs. 5, 7–9),

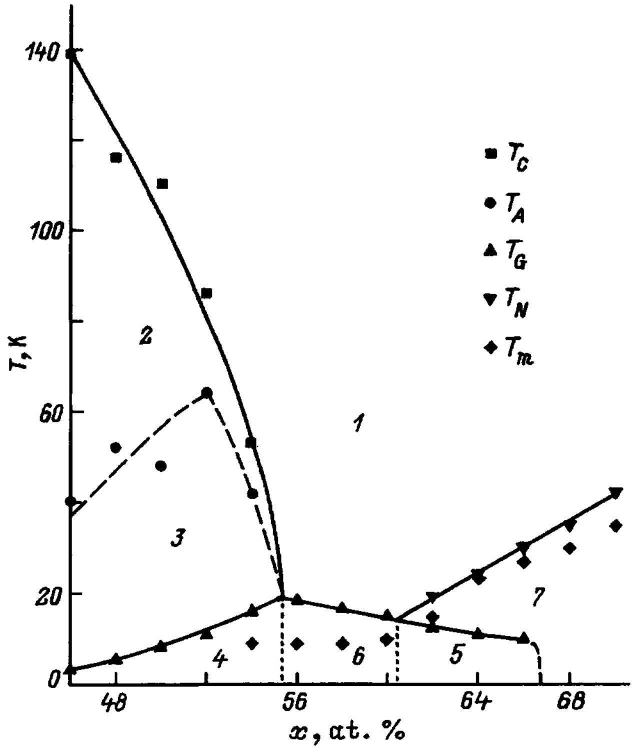

FIG. 1. Magnetic phase diagram of Fe$_x$Ni$_{80-x}$Cr$_{20}$ alloys. *1*—paramagnetic region, *2*—ferromagnetic region, *3*—coexistence of long-range FM order with local distortions of the collinear spin structure, *4* and *5*—reentrant spin glass, *6*—spin glass, *7*—antiferromagnetic region. T_C, T_N, T_G, T_m are the Curie, Néel, spin-glass freezing, and electrical-resistance-minimum temperatures, respectively, T_A is the temperature of the onset of noncollinear ferromagnetic state.

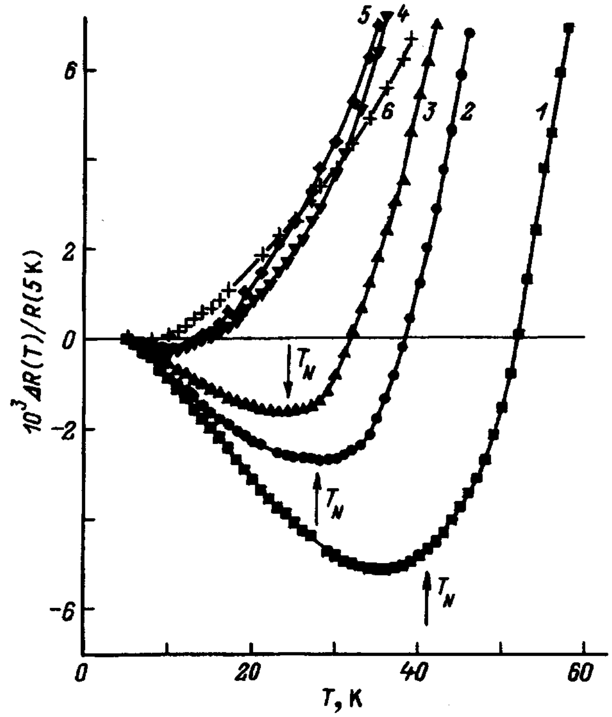

FIG. 2. Temperature dependence of the relative electrical resistance of Fe$_x$Ni$_{80-x}$Cr$_{20}$ alloys. *x*: *1*—70, *2*—66, *3*—64, *4*—60, *5*—54, and *6*—44.

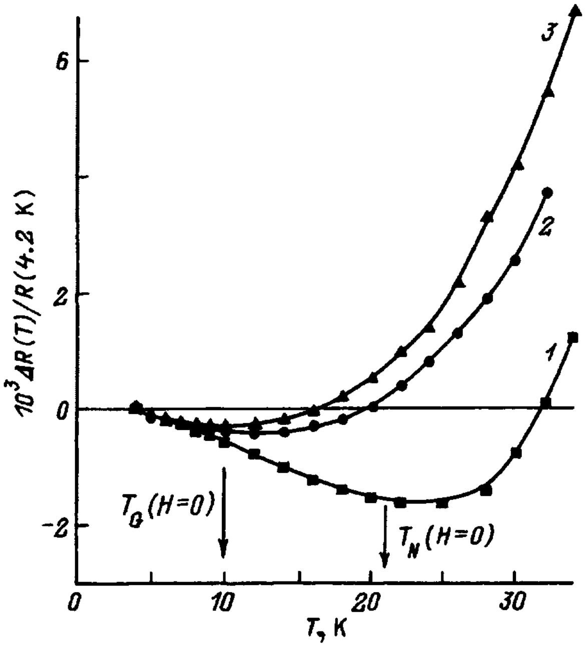

FIG. 3. Temperature dependence of the relative electrical resistance of the antiferromagnetic alloy Fe$_{64}$Ni$_{16}$Cr$_{20}$ in a magnetic field. H(kOe): *1*—0, *2*—30, *3*—50.

Fe$_{65}$(Ni$_{1-x}$Mn$_x$)$_{35}$ (Ref. 10), (Fe$_{0.65}$Ni$_{0.35}$)$_{1-x}$Mn$_x$ (Refs. 11, 12) close to the critical concentration of the onset of long-range AFM order, and were attributed to various mechanisms of conduction electron scattering, which, unfortunately, cannot describe the totality of the available

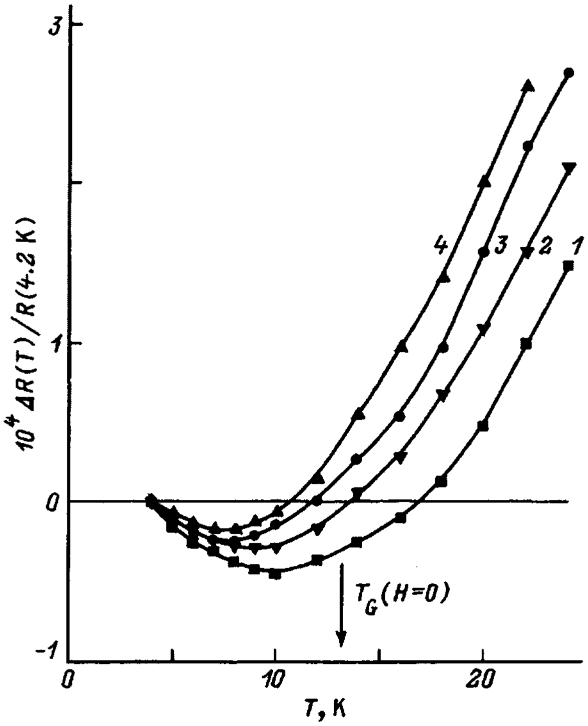

FIG. 4. Temperature dependence of the relative electrical resistance of the spin-glass alloy Fe$_{60}$Ni$_{20}$Cr$_{20}$ in a magnetic field. H(kOe): *1*—0, *2*—5, *3*—17, *4*—40.

experimental data. It should be stressed that all the above alloys are magnetically of the same nature. Therefore the reasons for the anomalous behavior of their electrical resistance should also be the same.

The resistivity ρ of the alloys of interest to us here can be presented for temperatures below T_N and T_G in the form

$$\rho(T)=\rho_0+\rho_{PH}+\rho_{EE}+\rho_{SW}+\rho_{SD}+\rho_{EG}, \tag{1}$$

where ρ_0 is the residual, temperature-independent resistivity, ρ_{PH}, ρ_{EE}, and ρ_{SW} are the contributions due to electron-phonon, electron-electron, and electron–spin-wave scattering, respectively, ρ_{SD} is the term accounting for electron scattering from randomly frozen spins in SG state, and ρ_{EG} is the contribution arising from the formation of a gap in the carrier energy spectrum.

Because of the large residual resistivity ($\rho_0 \approx 65-70\,\mu\Omega\cdot\mathrm{cm}$) of $\mathrm{Fe}_x\mathrm{Ni}_{80-x}\mathrm{Cr}_{20}$ alloys, the total contribution of the ρ_{PH}, ρ_{EE}, and ρ_{SW} terms to the resistivity is apparently fairly small. Besides, since they do not increase with decreasing temperature,[13] they cannot produce minima in the temperature dependences of the electrical resistivity of the alloys under consideration (Figs. 2–4). The ρ_{SD} term likewise cannot be responsible for the anomalies in electrical resistivity of these alloys. Indeed, below the SG freezing temperature T_G, the magnetic contribution to resistivity in classical spin-glass systems decreases with decreasing temperature.[6] At the same time in the $\mathrm{Fe}_x\mathrm{Ni}_{80-x}\mathrm{Cr}_{20}$ spin glass with $x=20$ (Fig. 4) we observe an opposite pattern. Besides, as seen from Fig. 1, the concentration dependence $T_m(x)$ of the temperature at which the resistivity is minimum correlates very well with $T_N(x)$, which is not observed for the T_G temperature. All this gives us grounds to suggest that the anomalous behavior of the electrical resistivity of the alloys is connected with the onset of AFM ordering. Or, to be more precise, one can expect that for this type of ordering an energy gap appears in the conduction electron spectrum below the Néel temperature T_N, and it is this gap that accounts for the semiconducting character of the alloy conductivity at low temperatures.

This conclusion is borne out by band parameter calculations for atomically ordering[14] and AFM[15–17] metal alloys. The net result of these calculations is that under both atomic and AFM ordering a gap at the conduction band center may appear below the ordering temperature. In the case of AFM ordering, the gap width is proportional to the relative magnetization of the AFM sublattices.[15] If the Fermi level in paramagnetic state is at the center of the conduction band, then the metal can become semiconducting for $T<T_N$. The complex shape of the Fermi surface of fcc-iron alloys allows formation of a gap, however, only in certain directions of the reciprocal lattice.[16] It thus follows that not all carriers take part in the gap conduction, since otherwise one would observe a metal-insulator transition for $T<T_N$. This conclusion is supported by the data in Fig. 2, which show that the largest increase in electrical resistance for $T<T_m$ does not exceed $\sim 0.5\%$. In other words, the comparatively weak increase in electrical resistivity below T_m can be connected with temperature-induced variations in the concentration of electrons involved in the gap conduction, which make up an insignificant part of all electrons in the system.

Thus turning back to Eq. (1), we can maintain that the main contribution to the temperature dependence of electrical resistivity of the alloys under study comes from the ρ_{PH} and ρ_{EG} terms, with the first of them decreasing, and the second, increasing with decreasing temperature.

Despite the absence of long-range AFM order in the $\mathrm{Fe}_x\mathrm{Ni}_{80-x}\mathrm{Cr}_{20}$ spin glasses ($54<x\leqslant 60$), the minimum in the temperature dependence of their electrical resistivity (Figs. 2 and 4) can be attributed to the presence in the corresponding alloys of finite-length correlations (short-range AFM order). These correlations are due to local composition fluctuations, within which each iron atom is surrounded only by iron atoms.[18] Calculations show[14,17] that local AFM ordering can also give rise to formation of an energy gap, which is the smaller, the smaller is the average length of the AFM correlations. In $\mathrm{Fe}_x\mathrm{Ni}_{80-x}\mathrm{Cr}_{20}$ alloys with $x\leqslant 55$, i.e. in the FM composition region (Fig. 1), AFM correlations of considerable length are unlikely to set in. Therefore in such alloys, for example, in the $x=44$ alloy, one should observe gap conduction, and this is supported by the experimental data of Fig. 2.

Putting off the discussion of the effect of external magnetic field on the anomalies in electrical resistivity until the third Subsection of this work, we shall consider the temperature dependence of the thermopower of $\mathrm{Fe}_x\mathrm{Ni}_{80-x}\mathrm{Cr}_{20}$ AFM alloys.

B. Thermopower

Thermopower is an electronic property which is known to be most sensitive to the band structure of metals. One may thus expect that the rearrangement of the electronic structure of $\mathrm{Fe}_x\mathrm{Ni}_{80-x}\mathrm{Cr}_{20}$ alloys resulting from their AFM ordering should affect their thermopower. Figure 5 shows the temperature dependence of thermopower S of the $\mathrm{Fe}_x\mathrm{Ni}_{80-x}\mathrm{Cr}_{20}$ alloy with $x=64$. We readily see that the thermopower undergoes a strong anomaly near the Néel temperature T_N and even reverses its sign. Interpretation of such experiments meets with serious difficulties, since it requires a detailed knowledge of the electronic structure of alloys. Nevertheless, we shall attempt to analyze the above result drawing from fairly simple considerations. We can write[13]

$$\begin{aligned} S&=\frac{\pi^2}{3}\frac{k^2T}{e}\left[\frac{\partial \ln \sigma(E)}{\partial E}\right]_{E=E_F} \\ &=\frac{\pi^2}{3}\frac{k^2T}{e}\left[\frac{\partial \ln \Lambda}{\partial E}+\frac{\partial \ln \Sigma}{\partial E}\right]_{E=E_F}, \end{aligned} \tag{2}$$

where e is the electronic charge, E_F is the Fermi energy, σ is the conductivity, Λ is the electron mean free path, and Σ is the Fermi surface area. Using the above relation and neglecting the temperature dependence of Λ, we can give a qualitative description of the temperature dependence of thermopower. Indeed, when AFM order sets in in fcc-iron alloys, part of the Fermi surface contracts because of the formation of the gap.[16] As a result, the second term in Eq. (2) becomes

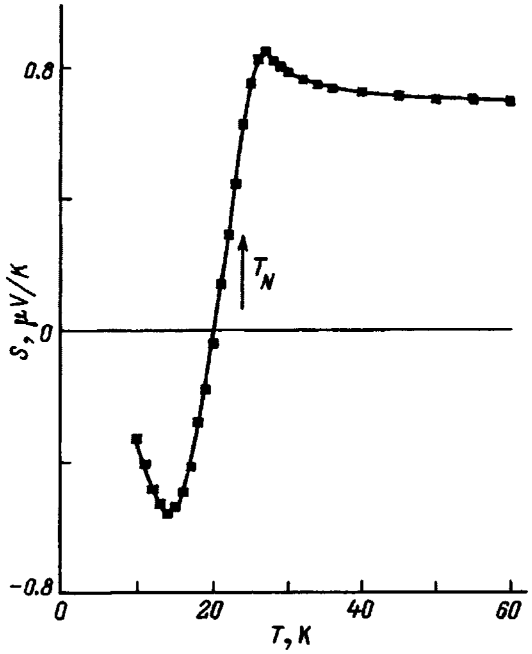

FIG. 5. Temperature dependence of the thermopower of the $Fe_{64}Ni_{16}Cr_{20}$ alloy.

negative, and thermopower can reverse its sign at temperatures below T_N, where the gap appears. It is this that occurs in reality (Fig. 5).

C. *H-T* phase diagram

Let us consider now how one could explain the effect of magnetic field on the observed electrical resistance anomalies in AFM alloys within the above model (Fig. 3). Obviously enough, total suppression of these anomalies would require magnetic fields capable of destroying AFM order in the alloys. Figure 6 presenting a magnetic phase diagram *H-T* for the $Fe_xNi_{80-x}Cr_{20}$ alloy with $x=64$ (Refs. 3, 4) shows that application to the sample of a comparatively low magnetic field $H\approx 17$ kOe suppresses long-range AFM order. In other words, regions 1 and 4 in the magnetic phase diagram (Fig. 6) correspond to the alloy in paramagnetic state. At the same time states 1 and 4 differ considerably. As seen from Fig. 3, a magnetic field $H=50$ kOe does not suppress completely the minimum in electrical resistance in this alloy, and in the $Fe_{60}Ni_{40}Cr_{20}$ spin glass too (Fig. 4). Recalling our previous discussion, this implies that, in contrast to the purely paramagnetic region 1, where no noticeable spin correlations are present, and region 2, where long-range AFM order exists, in region 4 short-range AFM order persists. In this sense, between the state of the $Fe_{64}Ni_{16}Cr_{20}$ alloy in regions 3 and 4 and that of the $Fe_{60}Ni_{20}Cr_{20}$ alloy in region 6 in Fig. 1 there is a formal similarity, namely, in all the above cases there is no long-range AFM order while there are finite-length AFM correlations. At the same time there is also a radical difference in that such correlations in region 4 in Fig. 6 exist in the presence of a sufficiently strong magnetic field in the PM matrix of the alloy, while in the SG state (region 6 in Fig. 1) or in the reentrant SG state (region 3 in Fig. 6) they coexist with the frozen-spin system.

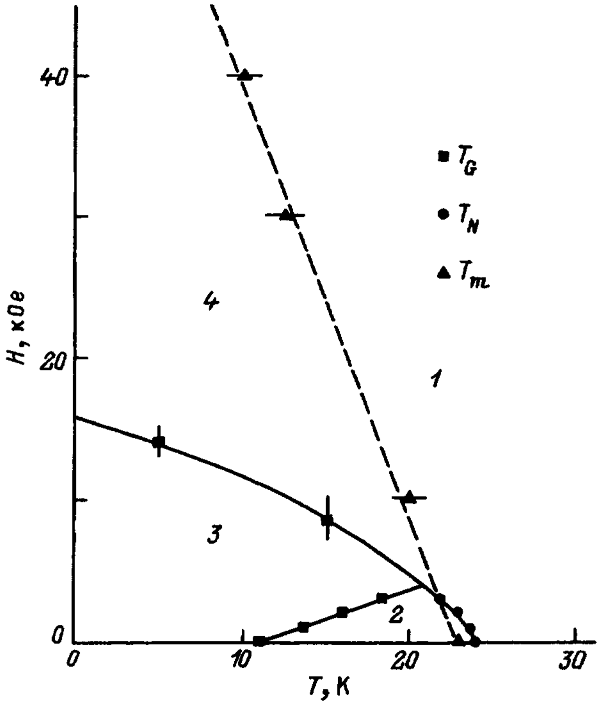

FIG. 6. *H-T* magnetic phase diagram of the $Fe_{64}Ni_{16}Cr_{20}$ alloy. *1*—paramagnetic region, *2*—antiferromagnetic region, *3*—spin-glass, *4*—coexistence of paramagnetism and short-range antiferromagnetic order. T_N—Néel temperature, T_G—spin-glass freezing temperature,[3,4] T_m—temperature of the minimum of electrical resistance (this work).

Thus the experimental data presented here and their analysis permit a conclusion that the anomalies in the electrical resistance of $Fe_xNi_{80-x}Cr_{20}$ fcc alloys in the form of minima in its temperature dependence originate from the formation of a gap in the electron conduction-band spectrum when both long- and short-range AFM order sets in in the alloys. This approach offered an explanation for the anomalous behavior of the thermopower of alloys near the Néel temperature and for the partial depression of the resistance anomalies by magnetic field in both AFM alloys and the spin glass, and made possible establishment of AFM correlations in paramagnetic state in AFM alloys placed in a sufficiently strong magnetic field.

The above concepts can be used apparently in explaining the reasons for the anomalous electrical resistance of the wide variety of antiferromagnets and spin glasses in 3*d* transition-metal alloys. Besides the compounds studied in this work, one could refer in this connection to the alloys FeNiMn,[10–12] CoMn and FeCoMn,[19] FeMnAl,[20] and some others.

We are grateful to V. F. Los' and S. P. Repetskiĭ for fruitful discussions.

[1] A. Z. Men'shikov, G. A. Takzeĭ, and A. E. Teplykh, Fiz. Met. Metalloved. **54**, 465 (1982); A. K. Majumdar and P. von Blanckenhagen, Phys. Rev. B **29**, 4079 (1984).

[2] A. Z. Men'shikov, P. Burlet, A. Chamberod, and J. L. Tholence, Solid State Commun. **39**, 1093 (1981); M. Shiga, T. Satake, Y. Wada, and Y. Nakamura, J. Magn. Magn. Mater. **51**, 123 (1985); A. Wulfes, Ch. Böttger, J. Hesse, J. Sievert, and H. Ahlers, J. Magn. Magn. Mater. **104–107**, 2069 (1992).

[3] G. A. Takzeĭ, A. M. Kostyshin, and I. I. Sych, JETP Lett. **43**, 547 (1986); Fiz. Tverd. Tela (Leningrad) **29**, 2434 (1987) [Sov. Phys. Solid State **29**, 1407 (1987)].
[4] G. A. Takzei, A. B. Surzhenko, I. I. Sych, M. V. Gavrilenko, Yu. P. Gavrilyuk, S. G. Barsov, A. L. Getalov, I. V. Golosovsky, V. P. Koptev, L. A. Kuzmin, S. M. Mikirtychyants, V. P. Plakhty, V. P. Harchenkov, and G. V. Shcherbakov, J. Magn. Magn. Mater. **118**, 77 (1993).
[5] V. I. Pecherskaya, D. N. Bol'shutkin, and I. Ya. Il'ichev, Fiz. Met. Metalloved. **50**, 300 (1980).
[6] C. Y. Hyang, J. Magn. Magn. Mater. **51**, 1 (1985).
[7] L. N. Larikov, G. A. Takzeĭ, V. S. Flis, and O. A. Shmatko, Dokl. AN USSR, Ser. A, No. 11, 1031 (1976); L. N. Larikov, G. A. Takzeĭ, and I. I. Sych, Metallofizika **2**, 30 (1980).
[8] A. V. Deryabin and V. E. Rode, Fiz. Nizk. Temp. **2**, 1450 (1976) [Sov. J. Low Temp. Phys. **2**, 710 (1976)].
[9] G. A. Takzeĭ, I. I. Sych, and A. Z. Men'shikov, Fiz. Met. Metalloved. **52**, 1157 (1981).
[10] M. Shiga and Y. Nakamura, J. Phys. Soc. Jpn. **26**, 24 (1969).
[11] Ch. Böttger and J. Hesse, Z. Phys. B **75**, 485 (1989).
[12] A. Höfer, M. Fricke, Ch. Böttger, and J. Hesse, Phys. Status Solidi A **148**, 551 (1995).
[13] J. M. Ziman, *Electrons and Phonons* [Clarendon Press, Oxford, 1960; IL, Moscow, 1962].
[14] V. F. Los and S. P. Repetsky, J. Phys.: Condens. Matter **6**, 1707 (1994); V. F. Los', S. P. Repetskiĭ, and K. P. Godlevskiĭ, Fiz. Tverd. Tela (St. Petersburg) **36**, 194 (1994) [Phys. Solid State **36**, 106 (1994)].
[15] Yu. P. Irkhin, Fiz. Met. Metalloved. **6**, 214 (1958).
[16] Y. Ishikawa, *Physics and Applications of Invar Alloys* (Maruzen Co, Tokyo, 1978).
[17] A. N. Andriotis, E. N. Economou, Qiming Li, and C. M. Soukoulis, Phys. Rev. B **47**, 9208 (1993).
[18] A. Z. Men'shikov and A. E. Teplykh, Fiz. Met. Metalloved. **44**, 1215 (1977).
[19] M. Matsui, K. Sato, and K. Adachi, J. Phys. Soc. Jpn. **35**, 419 (1973).
[20] S. S. Yan, L. Lui, F. R. Wang, Y. Xiao, S. S. Chai, and Y. Y. Li, Solid State Commun. **54**, 831 (1985).

Translated by G. Skrebtsov

Logarithmic singularity in the specific heat in the vicinity of phase transitions in uniaxial ferroelectrics

B. A. Strukov, E. P. Ragula, S. V. Arkhangel'skaya, and I. V. Shnaĭdshteĭn

Moscow State University (M. V. Lomonosov), 119899 Moscow, Russia

(Submitted May 12, 1997)
Fiz. Tverd. Tela (St. Petersburg) **40**, 106–108 (January 1998)

Using precise vacuum adiabatic calorimetry it is shown that the specific heat of the model ferroelectric crystal TGS does not exhibit the logarithmic singularity predicted by theory above the transition temperature. This discrepancy with the available specific heat data in the literature, obtained by dynamical measurements, is discussed with allowance for the maximum attainable measurement accuracy (0.3%) in the static adiabatic experiment. © *1998 American Institute of Physics.* [S1063-7834(98)02301-6]

It is well known that anomalies associated with phase transitions in intrinsic uniaxial ferroelectrics, are well described by the Landau theory of second-order phase transitions. In particular, we observed the specific-heat discontinuity predicted by the Landau theory in crystals of triglycine sulfate (TGS), a model uniaxial ferroelectric with Curie temperature $T_c = 48.2$ °C.[1–4] The magnitude of the jump agrees with the expected value to within 10–15%. At the same time, a number of papers have discussed the logarithmic contribution to the specific heat from the paraelectric phase ($T > T_c$), which reflects in the static thermodynamic functions fluctuations of the order parameter—the electrical polarization along the polar b axis. It is remarkable that the logarithmic contribution to the specific heat was noted in measurements employing the dynamical method[5–7] whereas the jumplike discontinuity was observed in measurements employing the static adiabatic method.[3] It is well known that the dynamical method possesses greater sensitivity in relative units whereas the vacuum adiabatic method possesses greater absolute accuracy, which can reach 0.1–0.3%. It is significant that, to reveal the logarithmic singularity in the temperature dependence of the specific heat, it is necessary to correctly separate out the lattice contribution, which is not associated with the phase transition and is determined by the noncritical degrees of freedom of the crystal.

The aim of the present work is a detailed comparison of accurate data on the temperature dependence of the specific heat of a crystal of TGS, obtained by vacuum adiabatic calorimetry, with the data available in the literature on the existence of the logarithmic singularity in the specific heat at $T = T_c$. Specific heat measurements were performed in the temperature interval 80–350 K on a computerized standard calorimeter capable of nearly limiting measurement accuracy (0.3%). The heating intervals were $\Delta T \sim 0.3$ K, and the mass of the sample was 1.102 g.

Figure 1 plots the temperature dependence of the specific heat of a crystal of TGS over a wide temperature range. The solid curve shows the lattice specific heat, obtained by interpolation of experimental data by the Debye and Einstein

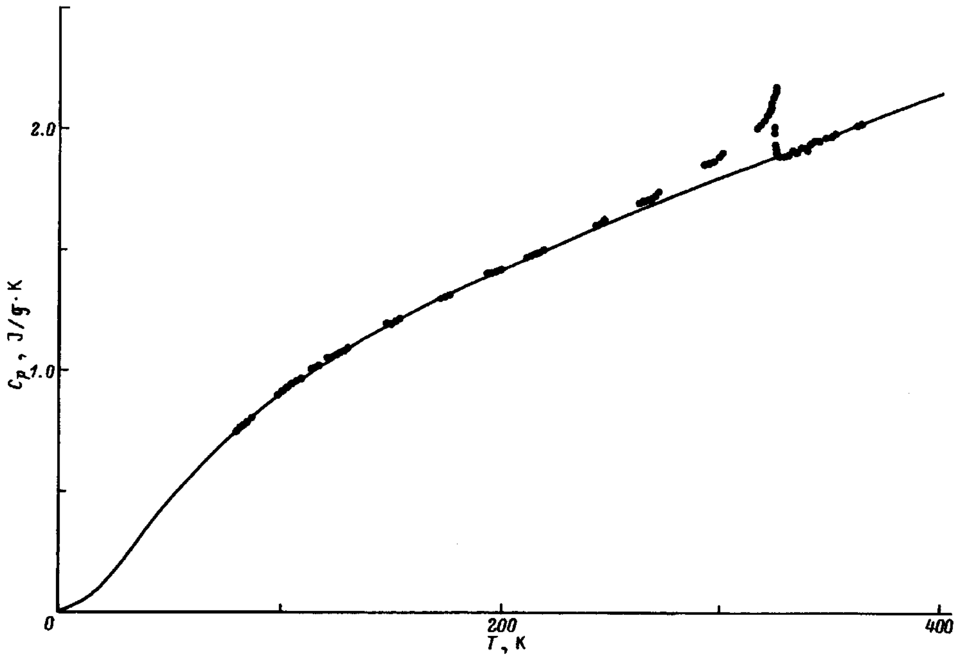

FIG. 1. Temperature dependence of the specific heat of a TGS crystal over a wide temperature interval. The solid curve is the calculated lattice specific heat.

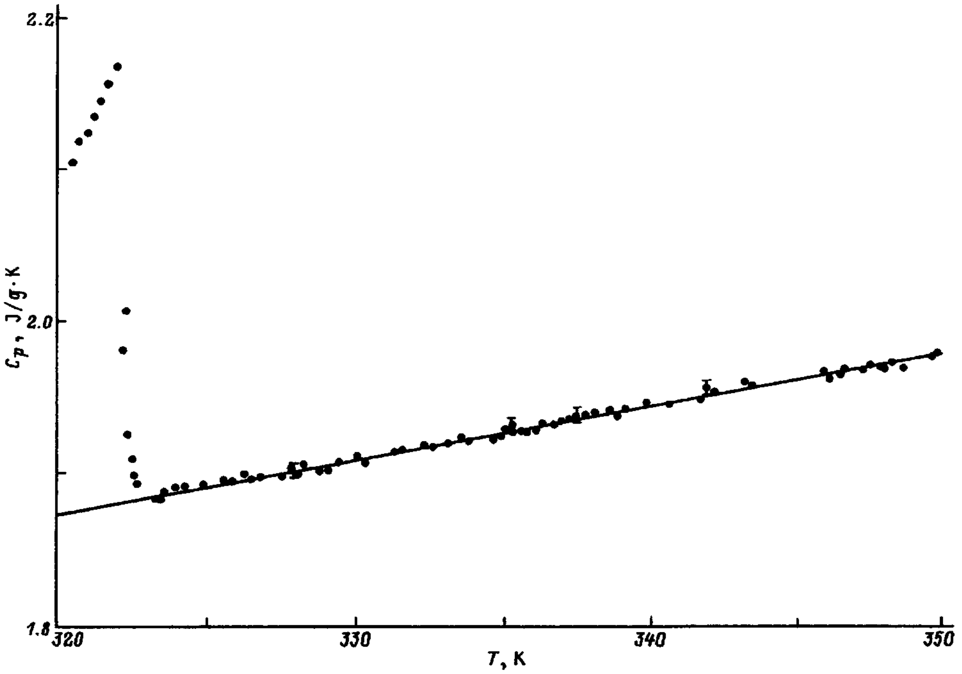

FIG. 2. Temperature dependence of the specific heat of a TGS crystal above the Curie temperature. The solid curve is the lattice specific heat. The measurement error is indicated for a few representative points (0.3%).

functions ($C_p^{\mathrm{lat}}=C_0D(\Theta_D T)+C_1E(\Theta_E/T)+C_2T$, $C_0=6.5$ J/g·K, $C_1=2.7$ J/g·K, $C_2=0.346$ J/g·K^2, $\Theta_D=215$ K, $\Theta_E=380$ K). The curve of the lattice specific heat coincides with the experimental points in the temperature interval from 80 to 250 K ($T<T_c$) and from 324 to 350 K ($T>T_c$). The excess entropy is $\Delta S=6.78$ J/mol·K, and the energy associated with the phase transition is $\Delta Q=1.998\times 10^3$ J/mol. The temperature region in the vicinity of the phase transition together with the experimental points and the lattice specific heat curve (line) is shown in Fig. 2. It can be seen that the spread of the experimental points relative to the latter curve does not exceed 0.3% and within the limits of this accuracy the measured values for $T>T_c$ do not reveal any ''excess'' specific heat (above the ''normal,'' i.e., the lattice specific heat) down to $(T-T_c)<1$ K, where ''smearing'' of the phase transition by defects shows up in the usual way. This result confirmed the above-noted ''insensitivity'' of the static method to logarithmic corrections.

As can be seen from Fig. 1, the method we used to separate out the lattice specific heat in the region of the anomaly shows that linear approximation (used in Refs. 5–7) is not satisfactory. Here taking account of the nonlinearity of the dependence $C_p^{\mathrm{lat}}(T)$ by means of the interpolation equation used leads to a decrease in the very small excess specific heat for $T>T_c$, making it experimentally undetectable.

On the other hand, it may also be supposed that a possible temperature dependence of the fluctuational contribution to the specific heat of the type $C_p-C_p^{\mathrm{lat}}=A\ \ln(T-T_c)/T_c$, observed in Refs. 5–7, lies within the limits of the spread of experimental points observed in our experiment. In this case, the coefficient A should be not larger than 7.0×10^{-3} J/g·K for the temperature interval $T_c=1-350$ K. It is well known that for the fluctuational contribution to the specific heat of uniaxial ferroelectrics the relation

$$C_p-C_p^{\mathrm{lat}}=k_{\mathrm{B}}T^2\alpha^2/(8\pi^2\delta^{3/2})\ln(T-T_c)/T_c\,,$$

is valid, where $\alpha=2\pi/C_{C-W}$ is proportional to the reciprocal of the Curie–Weiss constant and δ is the correlation parameter.[8] Using our estimate for the coefficient A, we obtain $\delta\leqslant 1.0\times 10^{-15}$ cm^{-2}. This value leads to a reasonable estimate for the correlation radius far from the phase transition: $\xi_0\sim(\delta/\alpha T_c)^{1/2}<3\times 10^{-8}$ cm.

We thus arrive at the conclusion that observation of the logarithmic correction to the specific heat in intrinsic uniaxial ferroelectrics, is only possible, if at all, for a relative measurement accuracy significantly better than 0.1%, which is unattainable under the conditions of the static adiabatic experiment, where the latter does demonstrate the agreement of the temperature dependence of the anomalous part of the specific heat with the conclusions of the Landau theory without taking the fluctuational contribution into account.

This work was carried out with the support of the Russian Fund for Fundamental Research (Grant No. (96-02-17723a).

[1] S. Hoshino, T. Mitsui, F. Jona, and R. Pepinsky, Phys. Rev. **107**, 1255 (1957).

[2] B. A. Strukov, Fiz. Tverd. Tela (Leningrad) **6**, 2862 (1964) [Sov. Phys. Solid State **6**, 2278 (1964)].

[3] A. J. Camnasio and J. A. Gonsalo, J. Phys. Soc. Jpn. **39**(2), 451 (1975).

[4] J. Del Cerro and S. Ramos, Ferroelectrics **39**(1/4), 1229 (1981).

[5] K. Ema, K. Hamano, K. Kurihara, and I. Hatta, J. Phys. Soc. Jpn. **43**, 1954 (1977).

[6] K. Ema, M. Karayama, Y. Ikeda, and K. Hamano, J. Phys. Soc. Jpn. **46**(**1**), 347 (1979).

[7] K. Ema, K. Hamano, and Y. Ikeda, J. Phys. Soc. Jpn. **46**(1), 345 (1979).

[8] A. P. Levanyuk, Izv. Akad. Nauk SSSR, Ser. Fiz. **29**(6), 879 (1965).

Translated by Paul F. Schippnick

Dielectric and photoelectric properties of $Pb(Mg_{1/3}Ta_{2/3})O_3$ crystals

A. A. Bokov, I. P. Raevskiĭ, M. A. Malitskaya, and S. M. Emel'yanov

Scientific-Research Institute of Physics, Rostov-on-the-Don University, 344104 Rostov-on-the-Don, Russia

(Submitted May 22, 1997)
Fiz. Tverd. Tela (St. Petersburg) **40**, 109–110 (January 1998)

The temperature dependence of the dielectric constant ε and the spectral dependence of the photoconductivity of $Pb(Mg_{1/3}Ta_{2/3})O_3$ crystals are investigated. The width of the band gap (3.4 eV) is determined. It is found that above the temperature of the maximum of the dielectric constant, its reciprocal $1/\varepsilon$ varies with temperature first quadratically and then according to a linear law, as is characteristic of ferroelectrics with a smeared phase transition. The smearing parameter of the transition estimated from the experimental data is close to the value calculated assuming the absence of long-range order in the arrangement of the Mg and Ta ions.

[S1063-7834(98)02401-0]

Ferroelectric phase transitions in complex disordered perovskites are accompanied, as a rule, by smeared anomalies in the temperature dependence of their physical properties. The reasons for smearing of the transitions cannot be taken as finally elucidated despite the fact that there exist several models explaining it (reviews of these models can be found in Refs. 1 and 2). In this light, experiments allowing one to assess the validity of the theoretical conclusions of the various models are essential. A large part of the experimental studies of the properties of ferroelectrics in the vicinity of the smeared phase transition were performed for $Pb(Mg_{1/3}Nb_{2/3})O_3$ (PMN) crystals. Therefore the question arises, which of the results are characteristic specifically of this compound and which are due to general regularities.

We have carried out studies of the $Pb(Mg_{1/3}Ta_{2/3})O_3$ (PMT) crystal, which is similar to PMN in composition. Data on its properties are very few in number. It is known that at -98 °C a smeared phase transition is observed in it, which is interpreted as a ferroelectric phase transition related to the existence of dielectric hysteresis loops.[3] PMT crystals are also interesting from a practical point of view. Because the linearization of the electro-optical effect characteristic of other ferroelectrics with smeared phase transition is absent in PMT crystals in electric fields whose field strength is not less than 50 kV/cm, and their dielectric constant and dielectric losses are small, they are very promising for use as light modulators.[4]

PMT crystals, light yellow in color and having the shape of parallelepipeds with sides up to 4 mm, were prepared by mass crystallization. The solvent was a lead oxide and boron oxide melt. Crystallization occured in the temperature interval 1250–1030 °C with a cooling rate of 5 °C/h. To facilitate the measurements, aquadag electrodes were deposited on the crystals.

The temperature dependence of the dielectric constant ε of the PMT crystal, measured at a frequency of 1.59 kHz, is plotted in Fig. 1. Apart from the maximum at -85 °C, corresponding to the smeared phase transition, no anomalies in the temperature interval from -190 to $+300$ °C are seen. The maximum value ε_m, around 10,000, exceeds somewhat the literature value (the crystals used in Ref. 3 had ε_m around 7,000).

In many crystals with a smeared ferroelectric phase transition, the temperature dependence of ε in the vicinity of the maximum is described by the relation

$$\frac{1}{\varepsilon}=\frac{1}{\varepsilon_m}+\frac{(T-T_m)^2}{2\varepsilon_m\sigma^2},$$

where T_m is the temperature at which ε reaches its maximum value ε_m, σ is the smearing parameter of the transition. As can be seen from Fig. 2, this relation holds in PMT with $\sigma=30$ K. The Curie-Weiss law, $1/\varepsilon=(T-T_0)/C$, is fulfilled at temperatures exceeding T_m by more than 150 K (curve *2*, Fig. 1). The Curie constant is equal to $C=1.7\times10^5$ K, and the Curie-Weiss temperature is equal to $T_0=-18$ °C, which significantly greater than T_m. Such a relationship between T_m and T_0, and also the observed tran-

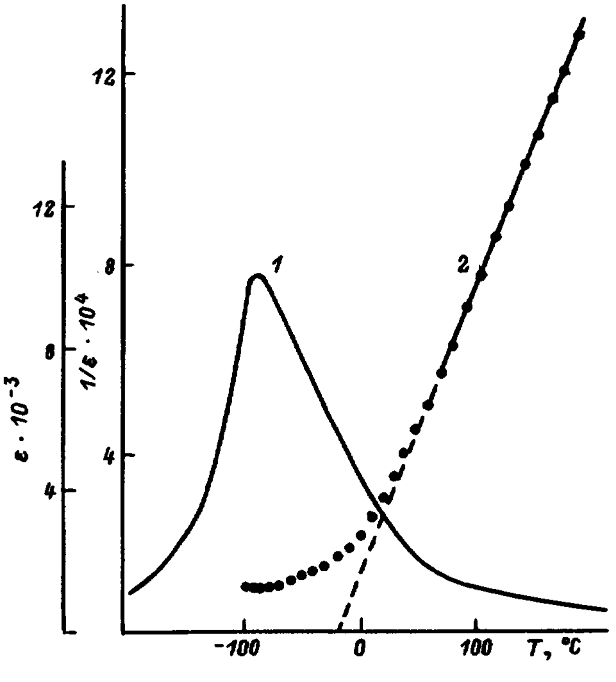

FIG. 1. Temperature dependence of the dielectric constant ε (*1*) and its reciprocal $1/\varepsilon$ (*2*) for a crystal of $Pb(Mg_{1/3}Ta_{2/3})O_3$, measured at 1.59 kHz.

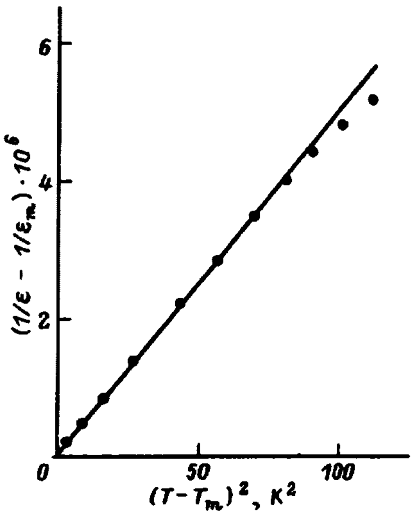

FIG. 2. Dependence of $1/\varepsilon$ on $(T-T_m)^2$ for a crystal of $Pb(Mg_{1/3}Ta_{2/3})O_3$.

sition from the quadratic dependence of $1/\varepsilon(T)$ to a linear dependence are characteristic of ferroelectrics with a smeared phase transition.[5,6]

Recently, a new model of ferroelectric phase transitions in disordered crystals was developed,[7] according to which smearing of the transition is caused by random static distortions of the ionic configuration in the unit cells, associated with a difference in the sizes of the disordered ions. Using the equations derived in Ref. 7, we can calculate the smearing parameter σ in a disordered compound or solid solution. Our calculations for PMT, which assume that the absence of long-range order in the arrangement of the Mg and Ta ions, give $\sigma = 22$ K. This is much smaller than the value obtained experimentally. Such a discrepancy may be connected with the fact that besides disorder in the arrangement of the Mg and Ta ions, other crystal defects also make a definite contribution to the smearing of the transition in these crystals.[7]

In connection with the promising characteristics of PMT for electro-optical applications, it is of interest to study those characteristics defining the optical properties of these crystals, in particular, the width of the band gap E_g. Since there is no information in the literature about E_g for PMT, we studied the photoconductivity of these crystals by the technique described in Ref. 8. In the spectral dependence of the transverse photoconductivity of PMT we detected maxima at 3.4 and 2.9 eV. These results are similar to those obtained in a study of the photoconductivity of PMN crystals, where maxima were observed at 3.4, 2.8, and 2.0 eV (Ref. 9). The maximum at 3.4 eV in PMN corresponds to the band gap, as was confirmed by the results of a study of optical absorption and electrical absorption.[9] Apparently, the photoconductivity maximum in PMT at 3.4 eV also corresponds to E_g. Note that the values of E_g in PMT and PMN are much smaller less than in triple perovskites of the type $A^{2+}B^{2+}_{1/3}B^{5+}_{2/3}O_3$, in which A can be Ba, Sr, or Ca.[10,11] This difference is due to the contribution of the *s* orbitals of lead to the formation of the band gap.[8,11]

[1] A. A. Bokov, Ferroelectrics **131**, 49 (1992).
[2] Z.-G. Ye, Ferroelectrics **184**, 193 (1996).
[3] V. A. Bokov and I. E. Melnikova, Fiz. Tverd. Tela (Leningrad) **2**, 2728 (1960) [Sov. Phys. Solid State **2**, 2428 (1960)].
[4] A. A. Berezhnoĭ, V. M. Fedulov, and K. P. Skornyakova, Fiz. Tverd. Tela (Leningrad) **17**, 2785 (1975) [Sov. Phys. Solid State **17**, 1855 (1975)].
[5] V. A. Isupov, Fiz. Tverd. Tela (Leningrad) **28**, 2235 (1986) [Sov. Phys. Solid State **28**, 1253 (1986)].
[6] A. A. Bokov, I. P. Raevskiĭ, V. G. Smotrakov, and I. M. Talysheva, Fiz. Tverd. Tela (Leningrad) **26**, 608 (1984) [Sov. Phys. Solid State **26**, 369 (1984)].
[7] A. A. Bokov, Zh. Éksp. Teor. Fiz. **111**(5), 1817 (1997) [JETP **84**, 994 (1997)].
[8] O. I. Prokopalo and I. P. Raevskiĭ, *Electrophysical Properties of Oxides of the Perovskite Family* [in Russian], Rostov-on-the-Don Univ. Press, Rostov-on-the-Don, 1985.
[9] V. A. Trepakov, N. N. Kraĭnik, and A. V. Olifir, Fiz. Tverd. Tela (Leningrad) **18**, 1751 (1976) [Sov. Phys. Solid State **18**, 1019 (1976)].
[10] J. Lecomte, J. P. Loup, G. Bosser, M. Hervieu, and B. Raveau, Solid State Ionics **12**, 113 (1984).
[11] I. P. Raevskii, S. A. Prosandeev, and I. A. Osipenko, Phys. Status Solidi B **198**, 695 (1996).

Translated by Paul F. Schippnick

An EPR study of local fluctuations in the vicinity of the ferroelectric phase transition in $Li_2Ge_7O_{15}$

M. P. Trubitsyn, M. D. Volnyanskiĭ, A. Yu. Kudzin, and T. L. Kuz'menko

Dnepropetrovsk State University, 320625 Dnepropetrovsk, Ukraine

(Submitted June 6, 1997)
Fiz. Tverd. Tela (St. Petersburg) **40**, 111–113 (January 1998)

EPR spectra of Mn^{2+} ions have been studied in the temperature interval containing the ferroelectric transition in crystalline lithium heptagermanate $Li_2Ge_7O_{15}$. The EPR linewidth and shape were measured as functions of temperature and orientation. It is shown that the critical resonance-line broadening observed to occur in the vicinity of the phase transition is due to fluctuations in the local order parameter with frequencies below 10^7 Hz. © *1998 American Institute of Physics.* [S1063-7834(98)02501-5]

$Li_2Ge_7O_{15}$ (LHG) crystals undergo a ferroelectric transition at $T_C=283.5$ K from the high-temperature paraelectric (space group D_{2h}^{14}) to ferroelectric (space group C_{2v}^5) phase accompanied by the onset of spontaneous polarization along the c axis.[1–3]

This work is a continuation of an EPR study of Mn^{2+} centers (0.06 and 0.2 wt %) in LHG crystals, whose preliminary results were published earlier.[4,5] The resonance lines were found[5] to undergo a considerable broadening and a crossover from a near-Lorentzian to a pure Gaussian profile. It was proposed that the observed effects are actually a consequence of slowed-down dynamics of the local order parameter. Concurrently, the inhomogeneous broadening of the magnetic resonance lines in the vicinity of the phase transition could be due to other reasons, for instance, to interaction of impurities with the local order parameter.[6] Therefore the character of the fluctuation contribution to the width and shape of the EPR lines requires further study.

The transformation of Mn^{2+} EPR spectra accompanying the paraelectric-ferroelectric transition can be described by the spin Hamiltonian[7]

$$\mathcal{H}_{FP}=\mathcal{H}_{PP}+\tilde{\mathcal{H}}=\left\{g\beta H+\sum b_n^m O_n^m\right\}+\sum \tilde{b}_n^m O_n^m .$$

A calculation[4] of parameters b_n^m of the spin Hamiltonian $\mathcal{H}_{PP}$ in paraphase showed the local symmetry of Mn^{2+} at T_C to lower from monoclinic C_2 to triclinic C_1. The parameters of the spin Hamiltonian $\tilde{\mathcal{H}}$ lowering the symmetry at the transition are functions of the local order parameter $\tilde{b}_n^m(\eta)$, and, thus, can be expanded in the vicinity of T_C in powers of η. Note that the expansions of the monoclinic parameters $\tilde{b}_n^m$ will contain only even, and those of the triclinic parameters, any powers of η.

It thus follows that for an arbitrary orientation of the external magnetic field **H** relative to the crystallographic axes, the resonance fields, in which microwave power is absorbed, can be expanded in powers of the local order parameter

$$H_R=H_0+A\eta+B\eta^2+\ldots, \tag{1}$$

where H_0 corresponds to the line position in the paraphase, and $\eta(t)=\langle\eta\rangle+\delta\eta(t)$ can be presented as a sum of a static, $\langle\eta\rangle$, and time-dependent, $\delta\eta(t)$, part. The expansion coefficients $A(\theta,\varphi)$ and $B(\theta,\varphi)$ depend on external-field orientation with respect to the crystal axes, with A being determined by the triclinic, and B, by the monoclinic parameters b_n^m. It was shown[6,8] that, if the resonance fields are linearly related to the order parameter $(B\sim 0)$, the fluctuation contribution $\delta\eta$ to EPR linewidth can be obtained in an analytical form for two limiting cases. If the fluctuations are fast compared to the characteristic EPR frequencies in an experiment, the regime is dynamic, and the critical contribution in the vicinity of T_C^+ can be written

$$\delta H_{CR}\sim A^2(\theta,\varphi)k_BT|T-T_C/T_C|^{-\nu}, \tag{2}$$

where k_B is the Boltzmann constant, and ν is the critical correlation-length exponent. If the fluctuations may be considered static on the EPR time scale, we have for the critical contribution to the linewidth

$$(\delta H_{CR})^2\sim A^2(\theta,\varphi)k_BT\{1-\mathrm{const}|T-T_C/T_C|^{\nu}\}. \tag{3}$$

According to Eqs. (2) and (3), at the transition δH_{CR} behaves differently with temperature in the two limiting cases, namely, in the dynamic mode (2) δH_{CR} diverges, and in the static regime (3) it takes on a finite value. The lack of precise data on the critical exponents quite frequently does not permit one to separate unambiguously the intervals where the above approximations are applicable by analyzing the temperature-dependent parts of Eqs. (2) and (3). It was shown[6] that the actual mode realized in an experiment can be identified by studying the orientation dependences of the critical linewidth, namely, in the dynamic limit $\delta H_{CR}\sim A^2(\theta,\varphi)$, while in the static case $\delta H_{CR}\sim A(\theta,\varphi)$.

We have performed therefore a study of the orientation and temperature dependences of the linewidth and shape of the $m_j=-5/2$ hfs component of the $M_S=-3/2\leftrightarrow-5/2$ high-field electronic transition for temperatures above T_C. The EPR spectra were obtained on a Radiopan SE/X 2547 radiospectrometer in the X range. The samples were heated and cooled in nitrogen vapor in a standard cryostat capable of holding the sample temperature stable to within ± 0.02 K around T_C.

Figure 1 shows angular dependences of the linewidth defined as the distance between the extrema of the derivative of the absorption line with the field **H** deviating from the **b**

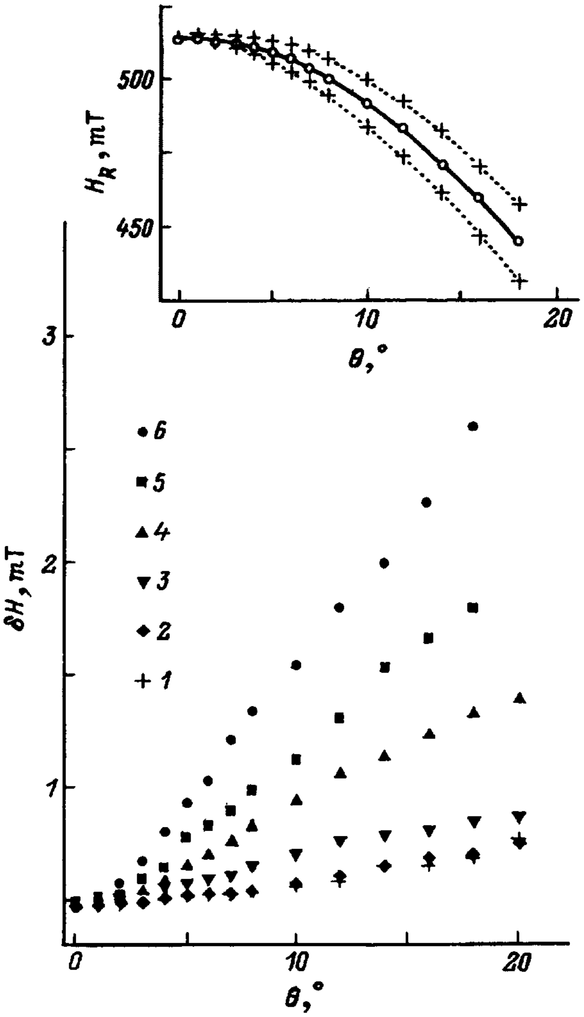

FIG. 1. Angular dependences of the width of the $m_j = -5/2$ hfs component of the $M_S = -3/2 \leftrightarrow -5/2$ transition for different temperatures (K). *1*—$T_C + 39.9$, *2*—$T_C + 14.2$, *3*—$T_C + 3.7$, *4*—$T_C + 1.2$, *5*—$T_C + 0.4$, *6*—$T_C + 0.1$. $T_C = 283.7$ K. $\theta = \angle \mathbf{H}, \mathbf{b}$, $\mathbf{H} \perp c$. Inset: angular dependences of the line position in the paraphase at $T = 284.1$ K (solid line) and of the split components in the ferroelectric phase at $T = 273.2$ K (dashed line).

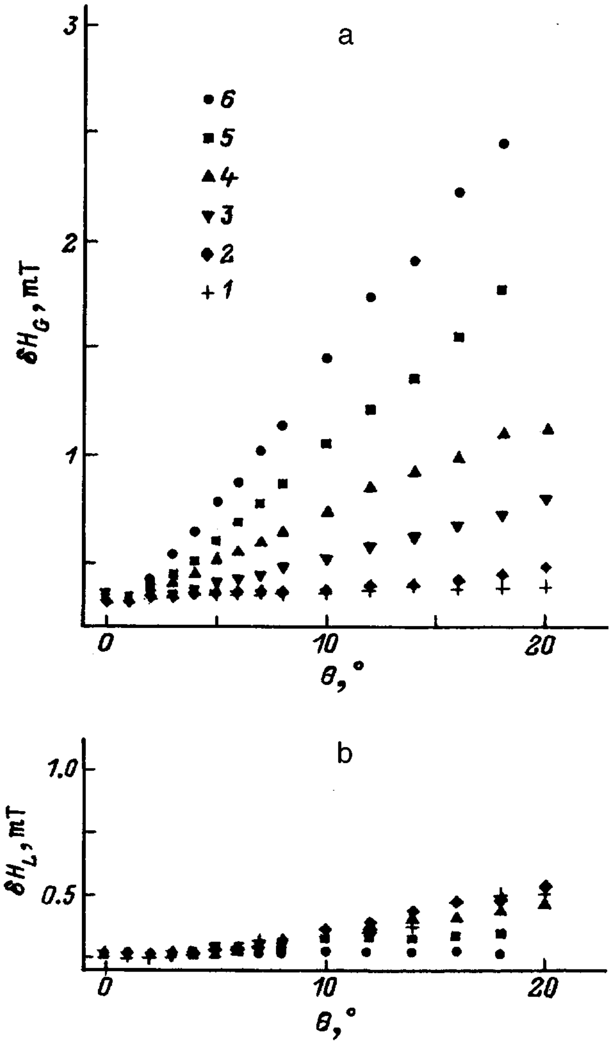

FIG. 2. Angular dependences of (a) Gaussian and (b) Lorentzian linewidth components for different temperatures, *1–6*, specified in the caption to Fig. 1. Notation of curves *1–6* is the same as in Fig. 1.

axis in the (**a**,**b**) plane. The measurements could be performed only within the θ interval 0–20°, since for larger angles the analysis of spectra was made difficult by superposition of the hfs sextets corresponding to the $M_S = -3/2 \leftrightarrow -5/2$ and $M_S = -1/2 \leftrightarrow -3/2$ electronic transitions. As seen from Fig. 1, the resonance line broadens as one approaches the transition, with the magnitude of broadening depending substantially on angle θ. The inset to Fig. 1 shows also the angular dependences of the position of the line under study above T_C and of the two split components, which are observed below the transition point and are due to the local order parameter $\pm\langle\eta\rangle$ becoming nonzero. Correlation of the linewidth anisotropy at T_C^+ with the angular dependence of the line splitting below T_C ($\Delta H \sim \langle\eta\rangle$) provides a direct indication that the EPR line broadening in the vicinity of the phase transition is governed by fluctuations in the local order parameter. As seen from Fig. 1, the anisotropy in the critical contribution to linewidth reflects the symmetry of the polar phase even before the transition, for $T > T_C$.

A comparison of the data presented in Fig. 1 shows clearly that for $\mathbf{H} \| \mathbf{b}$ no noticeable broadening is observed near T_C^+, and there is no splitting below T_C. Deviation from this orientation results in a progressive increase of critical broadening for T_C^+ and of the domain splitting for $T < T_C$. The reason for this behavior is clear; indeed, the absence of splitting in the ferroelectric phase for $\mathbf{H} \| \mathbf{b}$ implies that coefficient $A(\theta = 0) = 0$, and, thus, the relation of resonance fields to the local order parameter (1) should be determined by the term $B\eta^2$. The small broadening for T_C^+ in the principal orientation shows that the fluctuation contribution given by the quadratic term in Eq. (1) may be neglected, thus making it possible to use Eqs. (2) and (3) in an analysis of experimental data.

It should be pointed out that the shape of the resonance line also depends on temperature and angle θ. Therefore in order to separate the critical contribution to linewidth δH_{CR}, we performed computer modeling of the experimental line profile in the form of a convolution of a Lorentzian with a Gaussian

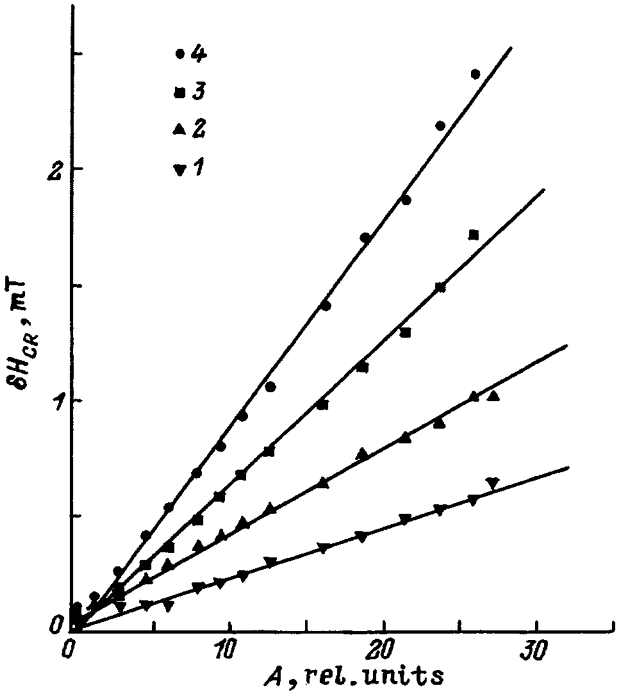

FIG. 3. Critical contribution to EPR linewidth as a function of parameter A for different temperatures (K). *1*—$T_C+3.7$, *2*—$T_C+1.2$, *3*—$T_C+0.4$, *4*—$T_C+0.1$.

$$F(H)=\int L(H-H_C/\delta H_L)G(H_C-H_0/\delta H_G)dH_C,$$

where H_0 determines the line center, and the fitting parameters δH_L and δH_G relate to the homogeneous and inhomogeneous contributions to linewidth, respectively. The results of the least-squares fitting are shown in Fig. 2. We readily see that the Lorentzian width δH_L practically does not depend on temperature, and that the critical line broadening near T_C is determined by the considerable increase of the inhomogeneous Gaussian component δH_0. Thus the contribution to critical linewidth can be derived from the relation

$$\delta H_{CR}^2(\theta,T)=\delta H_C^2(\theta,T)-\delta H_G^2(\theta,T^*=323.6\ \mathrm{K}).$$

Here the Gaussian width $\delta H_G(\theta,T^*)$ is assumed as a baseline, so that no noticeable broadening effects are observed for $T^*=T_C+39.8$ K within the whole θ interval studied.

$A(\theta)$ can be determined by direct measurement of the domain splitting (see inset to Fig. 1). As seen from expansion (1), the appearance of $\langle\eta\rangle\neq 0$ below T_C results in a line splitting, whose magnitude $\Delta H(\theta)=H_{R1}(\theta,+\langle\eta\rangle)-H_{R2}(\theta,-\langle\eta\rangle)=2A(\theta)\langle\eta\rangle$ reflects directly the angular dependence of parameter $A(\theta)$.

Figure 3 displays the dependences of the critical linewidth δH_{CR} on A. Although the error of δH_{CR} determination increases as one moves away from T_C, a linear dependence $\delta H_{CR}\sim A$ appears preferable over a quadratic one for all the above relations. Thus, based on Eqs. (2) and (3), one may assume the static regime to prevail throughout the temperature interval where EPR line broadening is observed. This implies that the broadening is due to fluctuations in the local order parameter occurring with frequencies lower than the frequency analog of the resonance linewidth. For the resolution of the EPR experiment one can accept the baseline value $\delta H_G(T^*)\sim 0.35$ mT. Hence the characteristic frequencies of the fluctuations resulting in an increase in the inhomogeneous linewidth component should be less than 10^7 Hz. By comparing the above results with data obtained by submillimeter and Raman spectroscopy,[9,10] one can relate the line broadening observed in EPR with the presence of the central peak in the vibrational spectrum of LHG.

[1] H. Volenkle, F. Wittman, and H. Nowotny, Monatsch. Chem. **101**, 46 (1970).
[2] S. Haussuhl, F. Wallrafen, K. Recker, and J. Eckstein, Z. Kristallogr. **153**, 329 (1980).
[3] M. Wada and Y. Ishibashi, J. Phys. Soc. Jpn. **52**, 193 (1983).
[4] M. P. Trubitsyn, M. D. Volnyanskiĭ, and A. Yu. Kudzin, Kristallografiya **36**, 1472 (1991) [Sov. Phys. Crystallogr. **36**, 835 (1991)].
[5] M. P. Trubitsyn, M. D. Volnyanskiĭ, A. Yu. Kudzin, and B. Ashim, Fiz. Tverd. Tela (Leningrad) **34**, 1746 (1992) [Sov. Phys. Solid State **34**, 929 (1992)].
[6] G. F. Reiter, W. Berlinger, K. A. Müller, and P. Heller, Phys. Rev. B **21**, 1 (1980).
[7] S. A. Al'tshuler and B. M. Kozyrev, *Electronic Paramagnetic Resonance of Compounds of Intermediate-Group Elements* [in Russian], Nauka, Moscow, 1972.
[8] Th. von Waldkirch, K. A. Müller, and W. Berlinger, Phys. Rev. B **7**, 1052 (1973).
[9] A. A. Volkov, G. V. Kozlov, Yu. G. Goncharov, M. Wada, A. Sawada, and Y. Ishibashi, J. Phys. Soc. Jpn. **54**, 818 (1985).
[10] Y. Morioka, M. Wada, and A. Sawada, J. Phys. Soc. Jpn. **57**, 3198 (1988).

Translated by G. Skrebtsov